Advanced Physical Chemistry for Process Metallurgy

Edited by

Nobuo Sano
Professor, Department of Metallurgy, The University of Tokyo, Tokyo, Japan

Wei-Kao Lu
Professor, Department of Materials Science and Engineering, McMaster University, Hamilton, Ontario, Canada

Paul V. Riboud
IRSID, Maizières-lès-Metz, France

with

Masafumi Maeda, Secretary of the Committee
Professor, Institute of Industrial Science, The University of Tokyo, Tokyo, Japan

ACADEMIC PRESS
San Diego · London · Boston
New York · Sydney · Tokyo · Toronto

This book is printed on acid-free paper.

Copyright © 1997 by ACADEMIC PRESS

All Rights Reserved.
No part of this publication may be reproduced or transmitted in any form or by any means electronic or mechanical, including photocopy, recording, or any information storage and retrieval system, without permission in writing from the publisher.

Academic Press
525 B Street, Suite 1900, San Diego, California 92101-4495, USA
http://www.apnet.com

Academic Press Limited
24–28 Oval Road, London NW1 7DX, UK
http://www.hbuk.co.uk/ap/

ISBN 0-12-618920-X

Advanced physical chemistry for process metallurgy / edited by Nobuo Sano, Wei-Kao Lu, Paul V. Riboud.
p. cm.
Includes index.
ISBN 0-12-618920-X
1. Metallurgy. 2. Chemistry, Physical and theoretical. I. Sano, Nobuo. II. Lu, W.-K. (Wei-Kao), 1993- III. Riboud, Paul V.
TN673.A325 1997
669–dc20 96-45948
CIP

A catalogue record for this book is available from the British Library

TU Bergakademie Freiberg
Bibliothek
10

97.9447/2
80

Zw 8

Typeset by Paston Press Ltd, Loddon, Norfolk
Printed in Great Britain by Hartnolls Limited, Bodmin, Cornwall

97 98 99 00 01 02 EB 9 8 7 6 5 4 3 2 1

(240.61) 42

Contents

Contributors xiii
Preface xv

I THERMODYNAMICS

Overview 3
Nobuo Sano

1 **Thermodynamics of metallic solutions** 5
Y. Austin Chang and Shuang-Lin Chen
1.1 Introduction 5
1.2 Thermodynamic relationships of solution 6
  1.2.1 Gibbs–Duhem equation and relationship between the partial and integral thermodynamic quantities 6
  1.2.2 Raoult's law, Henry's law, and regular solutions 8
  1.2.3 Excess thermodynamic quantities 11
  1.2.4 Real solutions 12
1.3 Phase equilibria of simple binary systems 14
  1.3.1 Regular solution model 14
  1.3.2 Relationship between the characteristic features of a binary phase diagram and the relative stabilities of the phases 17
1.4 Metastable phase equilibria 35
Acknowledgments 41
References 41

2 **Thermodynamics of slags** 45
Nobuo Sano
2.1 Introduction 45
2.2 Thermodynamics of phosphorus and sulfur in slags 51
  2.2.1 Phosphorus 51
  2.2.2 Sulfur 57
2.3 Thermodynamics of gases in slags 60
  2.3.1 Nitrogen 60
  2.3.2 Water 64
  2.3.3 Carbon 68

2.4 Thermodynamics of transition metals in slags 70
  2.4.1 Manganese 70
  2.4.2 Chromium 71
  2.4.3 Iron 72
  2.4.4 Copper as oxide 75
  2.4.5 Niobium and vanadium 75
  2.4.6 Titanium 78
2.5 Thermodynamics of tramp elements in slags 78
  2.5.1 Elements of groups IV and V 78
  2.5.2 Copper as sulfide 82
References 84

3 Solution models 87
Arthur D. Pelton
3.1 Introduction 87
3.2 Ideal Raoultian solutions 87
3.3 Polynomial models 89
  3.3.1 Regular solution theory 89
  3.3.2 Polynomial expansions 90
  3.3.3 Interaction parameter formalism 90
3.4 Phase diagram calculation/optimization 91
  3.4.1 Ternary and multicomponent phase diagram calculation/estimation with polynomial models 92
3.5 Sublattice models 93
  3.5.1 One sublattice occupied by only one species 93
  3.5.2 Ionic solutions 94
  3.5.3 Interstitial solutions 97
  3.5.4 Ceramic solutions 97
  3.5.5 The compound energy model 98
  3.5.6 Nonstoichiometric compounds 99
  3.5.7 Applications of the sublattice model 100
3.6 Short-range ordering 100
  3.6.1 Quasichemical model 100
  3.6.2 Association models 104
  3.6.3 Coordination cluster model 105
  3.6.4 Two-sublattice model for liquids 106
  3.6.5 Cluster variation method 106
3.7 Slags and glasses 107
  3.7.1 Quasichemical model 107
  3.7.2 Cell model 110
  3.7.3 Sulfide, sulfate, carbonate, etc. 'capacities' in slags and glasses 110

3.8 Applications 113
References 116

II KINETICS

Overview 121
Wei-Kao Lu

4 Fluid dynamics in metallurgical processes 123
Roderick I.L. Guthrie
4.1 Introduction 123
4.2 Theory 124
4.3 The continuity and momentum equations 124
4.4 Newtonian liquids 128
4.5 Turbulence 129
4.6 Differential models of turbulence for bulk convecting flows 131
4.7 Electromagnetically driven flows 133
4.8 Physical and computational models 135
4.9 Recent advances in metallurgical fluid dynamics 140
  4.9.1 Advances resulting from physical modeling 140
  4.9.2 Mathematical models 141
4.10 Conclusions 148
References 148

5 Solidification 151
Merton C. Flemings
5.1 Introduction 151
5.2 Thermodynamics and the liquid–solid interface 151
5.3 The Scheil equation and its modifications 155
5.4 Microsegregation and solidification paths—iron base alloys 159
5.5 Solidification into undercooled melts 162
5.6 Inclusion formation 169
5.7 Macrosegregation 171
5.8 Dendrite arm spacing and grain size 178
5.9 Concluding remarks 180
References 180

6 Interfaces and interfacial reaction of gases with liquid alloys and slags 183
G.R. Belton
6.1 Introduction 183
6.2 Intellectual framework 184

9.2 Principles of removal of dissolved elements and particles in refining reactors 283
9.3 Kinetics and mixing 284
9.4 Batch and continuous reactors 286
9.5 Contact areas 289
9.6 The residence time distribution function 290
9.7 Influence of the residence time distribution on conversion of particles 294
9.8 Heat transfer 297
9.9 Counterflow mass transfer 300
References 306

10 Ironmaking reactions 309
Jean-Marc Steiler
10.1 Outline of the blast furnace process 309
  10.1.1 The three functions of the blast furnace 309
  10.1.2 Systems of importance in ironmaking 310
  10.1.3 The one-dimensional reactor 314
  10.1.4 The two-dimensional blast furnace 321
10.2 The reactions of combustion 323
  10.2.1 The combustion zone 323
  10.2.2 Mechanisms of coal combustion 324
10.3 Physical chemistry of metal and slag formation 326
  10.3.1 Properties of phases 326
  10.3.2 Transfer of elements between metal–slag–gas 329
References 345

11 Iron smelting and steelmaking reactions 347
Richard J. Fruehan
11.1 Introduction 347
11.2 Iron smelting 348
  11.2.1 Process description 348
  11.2.2 Critical process phenomena 350
  11.2.3 Energy and materials balances 350
  11.2.4 Post-combustion 352
  11.2.5 Sulfur and phosphorus 354
  11.2.6 Slag foaming 357
  11.2.7 Reduction 358
11.3 Steelmaking 364
  11.3.1 Decarburization 366
  11.3.2 Slag–metal reactions in steelmaking 369
  11.3.3 The nitrogen reaction 373
References 379

12 Solidification rate in casting processes 381
Klaus Schwerdtfeger
12.1 Introduction 381
12.2 Solidification rate of one-component materials 382
12.3 Solidification rate of alloys 387
12.4 Solidification rate in continuous casting of steel 392
  12.4.1 Heat withdrawal in the mold 394
  12.4.2 Spray cooling 401
  12.4.3 Determination of boundary conditions from measurements of strand surface temperatures 406
12.5 Solidification rate in special continuous casting processes 408
  12.5.1 Solidification rate in thin slab casting with in-line thickness reduction 409
  12.5.2 Productivity of strip casting processes 412
12.6 Concluding remarks 416
Symbols used 417
References 418

Index 421

6.3 The surface constitution of liquid alloys 187
  6.3.1 Ideal adsorption 188
  6.3.2 Nonideal adsorption 191
  6.3.3 Ternary alloys and coadsorption 192
6.4 The surface constitution of liquid slags 195
6.5 The rates of interfacial reactions of gases with metallurgical melts 198
  6.5.1 Oxygen transfer reactions and the decarburization of liquid iron 198
  6.5.2 Nitrogen reactions with liquid iron 206
  6.5.3 The oxidation and reduction of iron oxide slags 211
References 215

7 Kinetics and mechanisms of heterogeneous reactions 219
Wei-Kao Lu
7.1 Fundamentals 219
  7.1.1 Reaction zone 220
  7.1.2 Gradients 221
  7.1.3 Temperature and concentrations in the reaction zone 222
  7.1.4 Moving interface and quasisteady state 223
  7.1.5 The replacement of interfacial quantities 224
  7.1.6 Slag–metal reactions 225
  7.1.7 Multiplicity of interfacial reactions 226
7.2 Gas–metal droplet reactions 227
  7.2.1 Oxidation of liquid iron 227
  7.2.2 Oxidation of Fe–C droplets 228
  7.2.3 Oxidation of Fe–Si droplets 229
7.3 Kinetics of iron ore reduction 230
  7.3.1 Solid-state reduction 231
  7.3.2 Hematite–magnetite interfacial reaction 234
7.4 Slag–metal reactions 237
  7.4.1 Theoretical development 238
  7.4.2 Coupled interfacial reactions 240
7.5 The reduction of iron oxides in liquid state 242
  7.5.1 Gas–liquid reaction 242
  7.5.2 Carbon as the reductant 244
7.6 Industrially important systems 245
References 247

III INDUSTRIAL SYSTEMS

Overview 251
Paul V. Riboud

8 Process modeling 253
B.G. Thomas and J. Keith Brimacombe
8.1 Introduction 253
  8.1.1 What is a process model? 253
8.2 Why model? 254
  8.2.1 Increasing process understanding 255
  8.2.2 Scale-up and design 255
  8.2.3 Design of experiments 255
  8.2.4 Evaluation of experimental results 255
  8.2.5 Property measurement 256
  8.2.6 On-line process control and optimization 257
  8.2.7 Technology transfer 257
8.3 Types of models 257
8.4 Other process development tools 259
  8.4.1 Industry experiments 260
  8.4.2 Pilot plant experiments 260
  8.4.3 Physical model experiments 260
  8.4.4 Laboratory experiments 261
8.5 Development of a process model 261
  8.5.1 Problem definition 262
  8.5.2 Identification of key phenomena 262
  8.5.3 Approach and model complexity 263
  8.5.4 Model formulation 264
  8.5.5 Solution 266
  8.5.6 Model validation 267
  8.5.7 Comparison with experiments 267
8.6 Model implementation 269
  8.6.1 Definition of model implementation 269
  8.6.2 Ways of implementing a model 270
  8.6.3 Fully on-line models 271
  8.6.4 Semi-on-line models 273
  8.6.5 Off-line models 274
  8.6.6 Literature models 276
8.7 Summary 278
References 279

9 Analysis of metallurgical reactors 281
T. Abel Engh
9.1 Introduction 281

Contributors

G. R. Belton *Newcastle Laboratories, BHP Research, Shortland, New South Wales 2307, Australia*

J. Keith Brimacombe *The Centre for Metallurgical Process Engineering, University of British Columbia, 112-2355 East Mall, Vancouver, British Columbia, Canada, V6T 1Z4*

Y. Austin Chang *Department of Materials Science and Engineering, University of Wisconsin, 1509 University Avenue, Madison, Wisconsin 53706-1595, USA*

Shuang-Lin Chen *Department of Materials Science and Engineering, University of Wisconsin, 1509 University Avenue, Madison, Wisconsin 53706-1595, USA*

T. Abel Engh *Norwegian University of Science and Technology, N-7034 Trondheim, Norway*

Merton C. Flemings *Department of Materials Science and Engineering, Massachusetts Institute of Technology, Cambridge, Massachusetts 02139-4307, USA*

Richard J. Fruehan *Department of Materials Science and Engineering, Carnegie Mellon University, Pittsburgh, Pennsylvania 15213-3890, USA*

Roderick I. L. Guthrie *Department of Mining and Metallurgical Engineering, McGill Metals Processing Centre, 3450 University Street, Montreal, Quebec, Canada, H3A 2A7*

Wei-Kao Lu *Department of Materials Science and Engineering, McMaster University, 1280 Mainstreet West, Hamilton, Ontario, Canada, L8S 4L7*

Arthur D. Pelton *Center for Research in Computational Thermochemistry, Ecole Polytechnique de Montreal, C.P. 6079, Succursale "A", Montreal, Quebec, Canada, H3C 3A7*

Paul V. Riboud *Institut de Recherche de la Siderurgie, IRSID, BP.30320, 57283 Maizières-lès-Metz Cedex, France*

Nobuo Sano *Department of Metallurgy, The University of Tokyo, 7-3-1 Hongo, Bunkyo, Tokyo, Japan*

Klaus Schwerdtfeger *Institut für Allgemeine Metallurgie, Technical University Clausthal, Robert-Koch Str. 42, D-38678 Clausthal-Zellerfeld, Germany*

Jean-Marc Steiler *Institut de Recherche de la Siderurgie, IRSID, BP.30320, 57283 Maizières-lès-Metz Cedex, France*

B. G. Thomas *Department of Mechanical and Industrial Engineering, University of Illinois at Urbana-Champaign, 1206 West Green Street, Urbana, IL 61801, USA*

Preface

INTRODUCTION

During the last three decades there have been dramatic changes in the steel industry in terms of the quality of products, processing technology, energy efficiency, labor productivity, and environmental protection. This progress is the result of the adoption of new technologies that are the fruits of efforts in research and development. As in other industries, the direction of research and development in the steel industry is determined by scientific knowledge, economic forecast, and the state of the art of technology. The branch of science which is the foundation of pyrometallurgy, including major operations in the steel industry, i.e., reduction, refining, and solidification, is high-temperature physical chemistry. It consists of the equilibrium as well as nonequilibrium phenomena of physicochemical processes, i.e., the chemical side of process metallurgy.

At the present time, metallurgy has become a part of Materials Science. Consequently, there are fewer metallurgists on faculty in academic institutions. In addition, the once prominent role of the metals industry in national economies is declining in industrialized countries to the point where fewer research engineers are employed in the industry. It is the responsibility of senior research scientists to synthesize the abundant literature we have so that the complex information available can be put into a form that will enable the next generation to take this branch of science as well as the metals industry to new heights.

The scope of this book is limited to selected topics within the field of 'physical chemistry of iron and steelmaking' that are relevant to reduction, refining, and solidification steps in the steel industry. The authors, who are the leaders in the field, had graduate students and research engineers in mind as typical readers of this book while preparing the text.

Practicing engineers, innovators, and managers in technology development hopefully will read and consult this book for inspiration and to check the soundness of their ideas.

OVERVIEW OF THE BOOK

The book consists of three parts: thermodynamics, kinetics, and industrial systems. Each part has an overview written by an editor.

Thermodynamics

Phase equilibria and thermodynamic activities are common to all metallurgical processes from the treatment of ores through to the finished product and are essential from all points of view, whether to describe closely the final stage for a system that reaches equilibrium in relatively short times, or to evaluate the driving forces that govern the course of the reactions. Thermodynamic aspects of the two main types of phases, metal and slag, are treated in Chapter 1 by Chang and Chen, and in Chapter 2 by Sano.

The use of solution models is essential for the description of multicomponent systems encountered in all industrial metallurgical reactors. They are presented by Pelton in Chapter 3.

Kinetics

The reaction kinetics in metallurgical reactors can be subdivided into two broad categories and are presented by Lu in Chapter 7, which is devoted to kinetics and mechanisms of heterogeneous reactions. The categories are: (1) those involving only solids among the condensed phases, such as those occurring in the upper part of the blast furnace and in prereduction units; and (2) those involving one or several liquid phases in which transport is strongly accelerated by natural or forced convection. Since homogeneous reactions are usually considered as very fast in the temperature range of most of these reactors, kinetic limitations result (i) from the time delay due to mixing process and to the transport time to bring reacting species to the interface, as developed by Guthrie, in the fluid mechanics chapter (Chapter 4), and (ii) from interfacial reactions between gases and liquid alloys and slags involving either only transport inside boundary layers, or true interface phenomena retarding or accelerating mass transfer as detailed in Chapter 6 by Belton.

Some reactors involve solid and liquid phases together and thus combine the complexity of the two previous categories. This is particularly the case for the melting zone of the blast furnace, and for the solidification phenomena involved during casting. In the latter case, concerning solidification, fundamental aspects are analyzed in Chapter 5 by Flemings.

It is probably in the description of interfaces, and how their areas and morphologies evolve as a function of time, that the largest efforts remain to be made. The range of magnitude of equilibrium values of interfacial properties is relatively well known for most industrial systems, and is often sufficient for many practical evaluations. However, the most important problems arise when coupling phenomena occur between mass transfer intensity and interface morphology. This is particularly encountered in solidification, and in very fast liquid–liquid reactions.

Industrial systems

Two chapters concern general aspects of process modeling and analysis of metallurgical reactors: one is devoted to process modeling, integrating all local phenomena into the overall process (Chapter 8 by Thomas and Brimacombe); the other considers the reactor as a whole and provides an evaluation of its efficiency in order to define a strategy for optimization (Chapter 9 by Engh).

The last three chapters illustrate the application of all the previously described aspects of physical chemistry to industrial processes and include ironmaking reactions (Chapter 10 by Steiler); iron smelting and steelmaking reactions (Chapter 11 by Fruehan); and solidification rate in casting processes (Chapter 12 by Schwerdtfeger).

In these chapters devoted to examples of industrial processes, each of the systems considered seems completely different from the others; however, several of the physical chemistry tools developed in the first part of the book are common to them. These include the following:

- The evaluation of equilibrium state that limits the driving force of the reactions. The equilibrium state may be described globally or locally.
- Interfacial reactions of surfaces and all types of interfaces—liquid–liquid, liquid–gas, liquid–solid—including interfacial heat and mass transfer and the geometric description of them.
- Local reaction kinetics.
- Fluid mechanics and transport phenomena in each type of phase, i.e., liquid, solid, and gas, to evaluate a macro reaction rate.

All these aspects are interdependent yet have to be integrated for each major part of the reactor and for the whole, taking into account heat and mass balances.

ACKNOWLEDGMENTS

We are particularly grateful for the contribution of Professor Masafumi Maeda, the able Secretary of the Editorial Committee; he played a key role in the scientific and editorial coordination of the whole book. Sincere appreciation should be extended to Ms. Kayoko Saito for her devoted, patient and expert work on gathering and preparing the manuscripts of all authors.

Sincere appreciation should be extended to the guidance provided by the editors of Academic Press, especially Ms. Susan Lord, the former Senior

Editor of the Physical Sciences, Dr. Gioia Ghezzi, the present Senior Editor, and Ms. Joanna Craig, the Associate Editor.

Nobuo Sano
Wei Kao Lu
Paul V. Riboud

Part I

THERMODYNAMICS

Editor of the Physical Sciences, Dr. Gioia Ghezzi, the present Senior Editor, and Ms. Joanna Craig, the Associate Editor.

Nobuo Sano
Wei-Kao Lu
Paul V. Riboud

Overview

Nobuo Sano

Chapters 1 to 3 are devoted to describing the chemical thermodynamics involved in metallurgical processes. Thermodynamic concepts are very important since they show the final states of any kind of physical and chemical changes, including the driving force of the change and its direction.

Chapter 1 is on solution thermodynamics with emphasis on metallic systems. This topic is very common in any metallurgical thermodynamic textbook, but the feature of this chapter is that, as an application, the principle in describing a phase reaction or a phase diagram is described in detail for computer calculation. This feature is continued throughout Chapter 2, in which a variety of solution models are described with many examples of calculation applied to slag and glass systems.

Measurement of the thermodynamic properties of those systems is troublesome and tedious work, so that only for very few multicomponent systems encountered in practice have they been directly determined. In order to cope with this situation, we must somehow estimate them by making assumptions. For example, the activities of the components of a ternary system may be calculated using a model in conjunction with information on the three binary systems concerned. Today computers are common and useful tools for this purpose and without them actual calculation could not be accomplished because they can handle tremendous numbers of operations.

Chapter 3 shows examples of data for slag systems that have been measured with the consumption of much manpower and time.

Some data may be corrected by calculation, models may be modified by comparing the calculated results and actual data, or some parameters needed for calculation are extracted from data. In this way the models can be refined for the estimation of thermodynamic properties of systems that have never been measured. We hope that readers will learn how to estimate them through reading these chapters and make use of this technique in applications to the systems of interest to them.

1

Thermodynamics of metallic solutions

Y. Austin Chang and Shuang-Lin Chen
Department of Materials Science and Engineering, University of Wisconsin, Madison, Wisconsin, USA

1.1. INTRODUCTION

This chapter deals with the basic thermodynamic relationships governing solution thermodynamics and the application of these relationships to materials systems focusing primarily on those of interest to metallurgists and metallurgical engineers. However, the general methodologies used are equally applicable to other materials systems such as semiconductors and ceramics. Since development of the basic laws of thermodynamics and derivations of the basic thermodynamic relationships have been given in numerous text and reference books (Wagner, 1952; Darken and Gurry, 1953; Lewis et al., 1961; Denbigh, 1966; Swalin, 1972; Gokcen, 1975; Gaskell, 1981), they will not be repeated in detail in this chapter. Instead, brief derivations will be made with specific references cited. In general the reader is recommended to consult any of the references cited above for the basic thermodynamic principles and relationships. Specifically, the treatment of Denbigh (1966) is suggested for the development of the laws of thermodynamics, and that of Darken and Gurry (1953) for the derivations of the basic solution thermodynamic relationships.

The major change that has been taking place during the past decades in solution thermodynamics is the availability of personal computers (PCs) and standard commercial software to solve nonlinear mathematical problems. While many of the more complex solution thermodynamic problems were not amenable to slide rules or calculators for solution, they can readily be solved nowadays using PCs with one of the commercial software packages or

ADVANCED PHYSICAL CHEMISTRY FOR PROCESS METALLURGY
ISBN 0-12-618920-X
Copyright © 1997 Academic Press Ltd
All rights of reproduction in any form reserved

more specific software developed primarily for materials scientists and engineers. Some of the examples given in this and subsequent chapters will reflect the technological changes that have made impacts in this field. Undoubtedly, the manner in which solution thermodynamics is taught and used currently and in the future will be different from that in the days of Darken and Gurry (1953).

1.2. THERMODYNAMIC RELATIONSHIPS OF SOLUTION

1.2.1. Gibbs–Duhem Equation and Relationship Between the Partial and Integral Thermodynamic Quantities

The thermodynamic state for a pure substance at constant temperature T and pressure P is defined. In other words, any of the thermodynamic functions for a pure substance, such as the Gibbs energy G, enthalpy H, internal energy E, entropy S, volume V, etc., is a function only of T and P. However, with the addition of other components to form a solution, $(c-1)$ degrees of freedom are introduced, with c being the number of components. In addition to T and P, it is necessary to specify the amounts of these components. The two basic thermodynamic equations which relate the partial and integral thermodynamic properties of the solution are (Darken and Gurry, 1953)

$$Y' = \sum_{i=1}^{c} n_i \bar{Y}_i \tag{1.1}$$

and

$$\sum_{i=1}^{c} n_i \, d\bar{Y}_i = 0 \tag{1.2}$$

Equation 1.2 is the well-known Gibbs–Duhem relationship at constant T and P. The term Y' represents any extensive thermodynamic property of a multicomponent system such as G', H', E', etc.; n_i is the number of moles of component i and $\bar{Y}_i$ is the partial thermodynamic property of component i.

Equations 1.1 and 1.2 can be also written in terms of mole fractions x_i as

$$Y = \sum_{i=1}^{c} x_i \bar{Y}_i \tag{1.3}$$

and

$$\sum_{i=1}^{c} x_i \, d\bar{Y}_i = 0 \tag{1.4}$$

where $Y = Y'/\sum_{i=1}^{c} n_i$. Following the method of Chen et al. (1994) and starting with Equation 1.3, the following equations expressing $\bar{Y}_i$ in terms of Y are obtained:

$$\bar{Y}_1 = Y - \sum_{i=2}^{c} x_i \frac{\partial Y}{\partial x_i} \tag{1.5}$$

and

$$\bar{Y}_i = Y - \sum_{j=2}^{c} x_j \frac{\partial Y}{\partial x_j} + \frac{\partial Y}{\partial x_i} \qquad (i = 2, 3, \ldots, c) \tag{1.6}$$

The above equations are obtained choosing $x_2, x_3, \ldots, x_c$ as the independent composition variables. For a binary system, $c = 2$, the above equations reduce to

$$\bar{Y}_1 = Y - x_2 \frac{dY}{dx_2} \tag{1.7}$$

and

$$\bar{Y}_2 = Y + (1 - x_2) \frac{dY}{dx_2} \tag{1.8}$$

The general relationships given by Equations 1.5 and 1.6 or the specific relationships given by Equations 1.7 and 1.8 are of practical utility since they allow us to obtain the partial quantities from the integral quantities. Conversely, when the partial quantity for one of the components in a binary alloy is known over the entire composition range, we can obtain the partial quantity of the other component from the Gibbs–Duhem relationship and thus the integral quantities. However, before discussing some of the practical methods for making these calculations, it is instructive to discuss the solution behavior of alloys, first for a Raoultian solution, then a Henrian solution, next a regular solution, and lastly a real solution. This discussion should give us a better intuitive appreciation of the solution behavior of alloys and some physical insights into the relationships between the integral and partial quantities.

1.2.2. Raoult's Law, Henry's Law, and Regular Solutions

1.2.2.1. Raoult's law (ideal solution)

Few if any alloys behave truly like an ideal solution, except for the component solvent at infinite dilution. Nevertheless, the concept of an ideal solution is so simple that it provides us with an intuitive feeling about the thermodynamic driving force for the formation of a solution from its component elements. For an ideal solution, there is no difference in the chemical interaction between like and unlike atoms. If we consider only the first nearest-neighbor interaction, the bond energy between the like atoms is the same as that between the unlike atoms. Let us now write the following chemical reaction for the formation of component B in a binary alloy at a specific composition x_2 from its pure state with T and P held constant

$$\mathrm{B}(pure) = \mathrm{B}(soln., x_2) \tag{1.9}$$

In this chapter, we will normally use the subscripts 1 to denote component A and 2 component B. Using the general relationship between the Gibbs energies of reaction and the activity quotient (Darken and Gurry, 1953), we have

$$(\Delta\bar{G}_2)_{x_2} = 0 + RT\ln(a_2)_{x_2} \tag{1.10}$$

for the above reaction. The term R is the universal gas constant and $(a_2)_{x_2}$ is the activity of the component B at x_2. In most cases throughout this chapter, the subscript x_2 for quantities like $(\Delta\bar{G}_2)_{x_2}$, and $(a_2)_{x_2}$ is omitted.

For an ideal solution,

$$a_i = \frac{P_i}{P_i^\circ} = \frac{x_i P_i^\circ}{P_i^\circ} = x_i \qquad (i = 1, 2) \tag{1.11}$$

where P_i is the partial pressure of the component i at a composition of x_i, and P_i° the vapor pressure of pure component i at the same T and P.

Thus, we may write down the partial Gibbs energies of the component elements for an ideal solution as

$$\Delta\bar{G}_i^{\mathrm{id}} = RT\ln x_i \qquad (i = 1, 2) \tag{1.12}$$

Using standard thermodynamic relationships among G, H, E, S, and V, we obtain the following expressions for $\Delta\bar{H}_i^{\mathrm{id}}$, $\Delta\bar{S}_i^{\mathrm{id}}$ and $\Delta\bar{V}_i^{\mathrm{id}}$ for an ideal solution:

$$\Delta\bar{H}_i^{\mathrm{id}} = 0 \tag{1.13}$$

$$\Delta\bar{S}_i^{\mathrm{id}} = -R\ln x_i \tag{1.14}$$

and

$$\Delta\bar{V}_i = 0 \tag{1.15}$$

In view of Equation 1.3, we have the following integral thermodynamic quantities for an ideal solution:

$$\Delta G^{\mathrm{id}} = RT\sum_{i=1}^{c} x_i \ln x_i \tag{1.16}$$

$$\Delta H^{\mathrm{id}} = 0 \tag{1.17}$$

$$\Delta S^{\mathrm{id}} = -R\sum_{i=1}^{c}(x_i \ln x_i) \tag{1.18}$$

and

$$\Delta V^{\mathrm{id}} = 0 \tag{1.19}$$

These results are to be expected from a microscopic point of view. Since interactions between like and unlike atoms are the same, there should not be any enthalpy and volume effect. However, this is not true for the change in Gibbs energy and entropy, for which the driving force is due to the natural tendency for mixing of atoms in order to attain the state of complete randomness.

The compositional dependencies of the integral and partial Gibbs energies of a binary ideal solution normalized by the quantity RT are shown graphically in Fig. 1.1. As shown in this figure, the normalized ideal Gibbs energy of mixing is symmetrical with respect to composition; it attains a minimum value of -0.693 at the equal atomic composition and approaches 0 at the pure component elements. On the other hand, the partial quantities change much more markedly with composition owing to the logarithmic term involved. It approaches 0 as the composition approaches unity and becomes $-\infty$ as the composition approaches 0. The compositional dependencies of the integral and partial entropies for an ideal solution are the same as those of the Gibbs energies normalized by RT except that the sign is positive in contrast to the case for the normalized Gibbs energies.

The fact that the solvent of an alloy at infinite dilution behaves ideally was first observed experimentally by Raoult (1887). This behavior is referred to in the literature as Raoult's law and is understandable from a microscopic point of view. Even if a solution does not behave like an ideal solution over the entire compositional range, as the solute concentration becomes vanishingly small, statistically most of the nearest-neighbor atoms for a solvent atom are also solvent atoms. Accordingly, there is practically no interaction between these atoms and Raoult's law is obeyed.

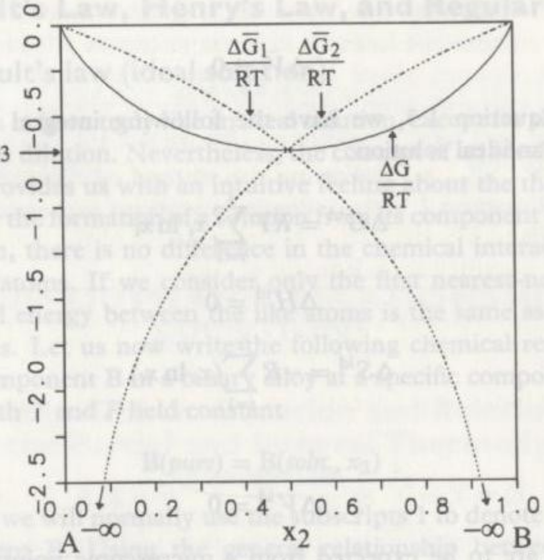

Figure 1.1 Compositional dependencies of the integral and partial Gibbs energies for a binary ideal solution.

1.2.2.2. Henry's law (dilute solution)

In addition to Raoult's law behavior for the solvent component as its composition approaches unity, there is another limiting law for the solute. This is Henry's law, which states that the activity of the solute becomes proportional to its composition at infinite dilution,

$$a_2 = kx_2 \tag{1.20}$$

where k is Henry's law constant. Using the Gibbs–Duhem relationship for a binary solution, Equation 1.4, it can readily be shown that when the solute obeys Henry's law, the solvent must obey Raoult's law. However, the reverse is not necessarily true. As shown later in section 1.2.3, Equation 1.20 is an imprecise definition of Henry's law. More precisely, Henry's law may be restated as saying that the coefficient k reaches a finite value as the concentration of the solute approaches zero.

1.2.2.3. Regular solution

The first attempt used to approximate real solution behavior is the regular solution model proposed by Hildebrand (1929). This model assumes that there is interaction between unlike atoms which makes a contribution to the enthalpy of mixing; but at the same time the interaction is not so strong—the entropy of mixing still follows that of an ideal solution. Accordingly, the Gibbs energy of mixing or formation of such a binary alloy is

$$\Delta G = \varepsilon x_1 x_2 + RT(x_1 \ln x_1 + x_2 \ln x_2) \tag{1.21}$$

where the first term on the right-hand side represents the enthalpy of mixing and the second term the ideal entropy of mixing according to Equation 1.18 for the binary case. The term ε is the regular solution parameter. In view of Equations 1.7 and 1.8, the partial Gibbs energies of the component elements can readily be obtained from Equation 1.21 as

$$\Delta\bar{G}_i = \varepsilon(1 - x_i)^2 + RT \ln x_i \qquad (i = 1,\ 2) \tag{1.22}$$

The parameter ε can be related to the interaction enthalpy of a pair of unlike atoms relative to the average enthalpy of like atom pairs, as given in detail in Swalin (1972).

1.2.3. Excess Thermodynamic Quantities

Using the ideal solution as a frame of reference, an excess thermodynamic quantity, denoted as "xs," is introduced. This is done by expressing a solution thermodynamic property as the sum of two parts,

$$Y = Y^{\mathrm{xs}} + Y^{\mathrm{id}} \tag{1.23}$$

The relative thermodynamic property for the formation of one mole of atoms of an alloy from its component elements is

$$\Delta Y = Y^{\mathrm{xs}} + Y^{\mathrm{id}} - \sum_{i=1}^{c} x_i Y_i^{\circ} \tag{1.24}$$

The corresponding relative partial quantity for component i is

$$\Delta\bar{Y}_i = \bar{Y}_i^{\mathrm{xs}} + \bar{Y}_i^{\mathrm{id}} - Y_i^{\circ} \tag{1.25}$$

The term Y_i° denotes the thermodynamic property of component i in the standard state. Accordingly, the excess partial Gibbs energy of component i is

$$\bar{G}_i^{\mathrm{xs}} = RT \ln(a_i/x_i) = RT \ln \gamma_i \tag{1.26}$$

where γ_i is the activity coefficient of component i. For a regular solution, in view of Equation (1.22), the above equation reduces to

$$\bar{G}_i^{\mathrm{xs}} = \varepsilon(1 - x_i)^2 \tag{1.27}$$

According to Equation 1.27, as $x_i \to 0$, $(\bar{G}_i^{\mathrm{xs}})_{x_i \to 0} \to \varepsilon$ and $(d\bar{G}_i^{\mathrm{xs}}/dx_i)_{x_i \to 0} \to -2\varepsilon$. The second limiting condition at infinite dilution is not in accord with Equation 1.20, an imprecise definition of Henry's law, for which the first derivative of the excess partial Gibbs energy with respect to composition would approach zero as $x_i \to 0$. However, from an experimental point of view, the excess partial Gibbs energy of the solute would appear to be constant as $x_i \to 0$ within the scatter of the data.

1.2.4. Real Solutions

It is convenient to describe the deviations of a real solution from the ideal behavior in terms of the compositional dependencies of the α-function. This function is defined as (Darken and Gurry, 1953; Hultgren et al., 1973)

$$\alpha_i = \frac{\bar{G}_i^{\mathrm{xs}}}{(1 - x_i)^2} = \frac{RT \ln \gamma_i}{(1 - x_i)^2} \qquad (i = 1, 2) \tag{1.28}$$

For an ideal solution, α_i is 0; for a regular solution α_i is a constant which may be positive or negative. For a real solution, α_i varies nonlinearly with composition. However, for the case when α_i varies linearly with composition, a two-parameter model is needed. This type of model is referred to in the literature as a subregular solution model. When α_i varies nonlinearly with composition, more than two parameters are needed. It has been suggested that the name subsubregular solution model (Chuang et al., 1984) be used when three parameters are used. Figures 1.2 and 1.3 show values of the α-function and the corresponding function in terms of the enthalpy of mixing, i.e., $\Delta H/[x_i(1 - x_i)]$, for several liquid alloys. From the relationships between the partial and integral quantities, it is straightforward to show that when the excess partial Gibbs energy is normalized by the quantity $(1 - x_i)^2$, the integral quantity should be normalized by the quantity $x_i(1 - x_i)$.

It is clear from the compositional dependencies of α_i and $\Delta H/[x_i(1 - x_i)]$ for several selected alloys shown in Figs 1.2 and 1.3, the regular solution model is not able to describe the solution behavior for most real solutions quantitatively. On the other hand, except for the liquid Te–Sn alloys (Hsieh et al., 1983), the behavior of the other alloys can be described either by the regular solution model or an extension of this model with additional composition dependent terms.

Many forms of equations have been proposed to represent the excess Gibbs energy and the reader is referred to some of the general references given at the end of this chapter for details. However, all of the polynomial equations given in the literature are mathematically equivalent. In other words, the parameters can readily be converted from one form of the equation to another. The most frequently used expression in the metallurgical literature nowadays is that proposed by Redlich and Kister (1948):

$$G^{\mathrm{xs}} = x_1 x_2 \sum_{j=0}^{n} L_j (x_1 - x_2)^j \tag{1.29}$$

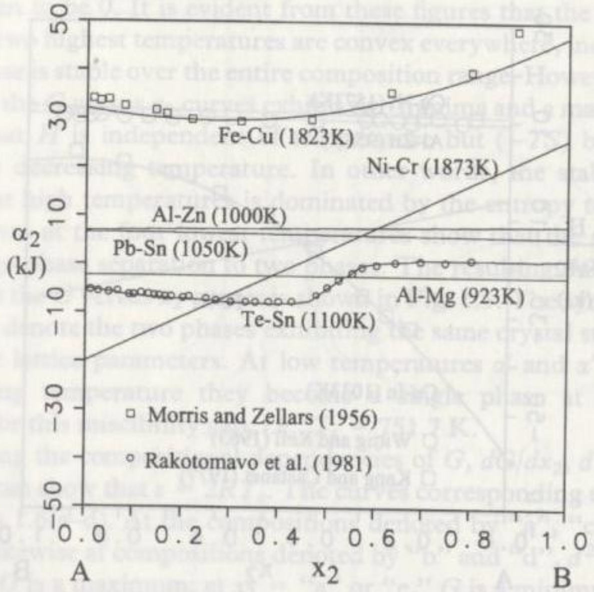

Figure 1.2 Values of the α-function for several liquid alloys. The smoothed values are taken from the literature: Fe–Cu (Chuang et al., 1984), Ni–Cr (Chuang and Chang, 1986), Pb–Sn (Fecht et al., 1989), Al–Zn (Chen and Chang, 1993), Al–Mg (Zuo and Chang, 1993), and Te–Sn (Hsieh et al., 1983).

Equation 1.29 is referred to as the Redlich–Kister equation. When $n = 0$, we have the regular solution model with $L_0 = \varepsilon$; when $n = 1$, we have the subregular solution model; and when $n = 2$, we have the sub-subregular solution model. In principle, we can use more than three parameters at constant T and P. However, inclusion of the fourth parameter may cause a mathematical artifact which would not represent the true behavior of the solution. It can readily be shown mathematically that the α-function may have points of inflection when four parameters are introduced. In developing a model for an alloy phase, every attempt should be made not to use more than three parameters at constant temperature to represent the excess Gibbs energy of a solution.

The L_j parameters represent the thermal part of the Gibbs energy of alloys. In reality, they consist of two parts, i.e., the enthalpy and thermal entropy terms. Accordingly, in practice these parameters are temperature dependent. At high temperatures, i.e., higher than the Debye temperatures, two terms in temperature are often sufficient, one corresponding to enthalpy and the other to entropy.

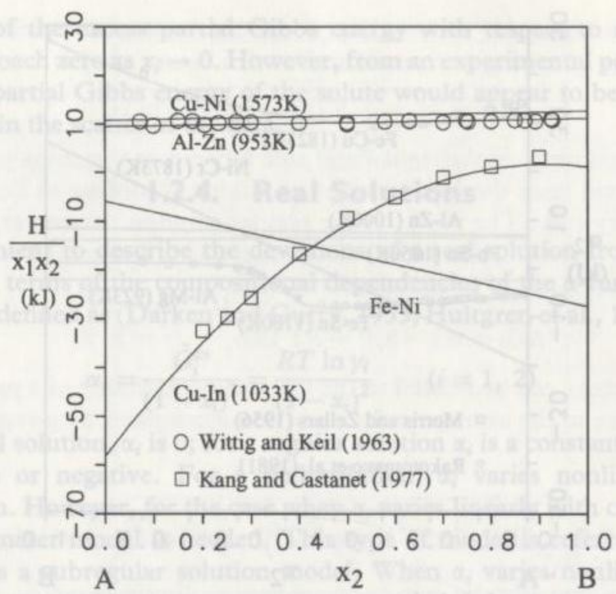

Figure 1.3 Values of the function $\Delta H/(x_1x_2)$ for several liquid alloys. The smoothed values are taken from the literature: Cu–Ni (Chakraborti et al., 1991), Al–Zn (Chen and Chang, 1993), Fe–Ni (Chuang et al., 1986), Cu-In (Kao et al., 1993).

1.3. PHASE EQUILIBRIA OF SIMPLE BINARY SYSTEMS

1.3.1. Regular Solution Model

The regular solution model was introduced in section 1.2.2.3. Even though it does not satisfactorily describe the solution behavior of real alloys, it can be used readily from a pedagogical point of view to show the interrelationship between the characteristic features of phase equilibria and the relative stabilities of phases in an alloy system, i.e., the relative values of the regular solution parameters of the phases.

In this section, the relationship between the critical temperature of a miscibility gap T_c and the regular solution parameter will be presented. It is evident from Equation 1.21 that when the parameter value ε is positive, the G versus x_2 curve will not be convex from $x_2 = 0.0$ to $x_2 = 1.0$ at $T < T_c$. Figures 1.4(a–f) show the $G(H, -TS)$ versus x_2 curves for a regular solution with $\varepsilon = 12.5$ kJ/mol at 850, 751.7, 700, 600, 500, and 400 K, respectively. The Gibbs energy values of the two component elements in their standard states are taken to be 0. It is evident from these figures that the G versus x_2 curves at the two highest temperatures are convex everywhere, indicating that the single phase is stable over the entire composition range. However, at lower temperatures the G versus x_2 curves exhibit two minima and a maximum, due to the fact that H is independent of temperature but $(-TS)$ becomes less negative with decreasing temperature. In other words, the stability of the single phase at high temperatures is dominated by the entropy term. The G versus x_2 curves at the four lowest temperatures show that the single phase would undergo phase separation to two phases. The resulting miscibility gap obtained from the G versus x_2 curves is shown in Fig. 1.5. The symbols α' and α'' are used to denote the two phases exhibiting the same crystal structure but with different lattice parameters. At low temperatures α' and α'' are stable; with increasing temperature they become a single phase at the critical temperature for this miscibility gap, i.e., $T_c = 751.7$ K.

By examining the compositional dependencies of G, dG/dx_2, d^2G/dx_2^2 and d^3G/dx_2^3, we can show that $\varepsilon = 2RT_c$. The curves corresponding to 500 K are shown in Figs 1.6(a–d). At the compositions denoted by "a", "c," and "e", $dG/dx_2 = 0$; likewise at compositions denoted by "b" and "d", $d^2G/dx_2^2 = 0$. At $x_2 =$ "c," G is a maximum; at $x_2 =$ "a" or "e," G is a minimum. In fact, the compositions at "a" and "e" correspond to those of the miscibility at 500 K as shown in Fig. 1.5. An examination of the Gibbs energy curves shows that the five compositions denoted by "a" to "e" approach a single critical composition, $x_{2,c}$, as T approaches T_c. This means dG/dx_2, d^2G/dx_2^2, and d^3G/dx_2^3 are 0 at this temperature and composition. Applying these conditions to Equation 1.21, we obtain $x_{2,c} = 0.5$ and

$$\varepsilon = 2RT_c \tag{1.30}$$

Also shown in Fig. 1.5 as a dashed curve is the locus of compositions where $d^2G/dx_2^2 = 0$. This curve is the spinodal curve and is important in the study of phase transformations of alloys. Let us now refer to this figure to explain the significance of this curve. When a single-phase alloy with a gross composition between the spinodals at a high temperature, i.e., $T > T_c$, is brought to a lower temperature within the miscibility gap, this alloy becomes thermodynamically unstable. It would undergo spontaneous decomposition locally, leading eventually to the equilibrium phases $\alpha'(x_2')$ and $\alpha''(x_2'')$. This can be understood by studying the G versus x_2 curve at a $T < T_c$ given in Fig. 1.7. As shown in this figure, owing to the concave nature of the G versus x_2 curve between the spinodal compositions the Gibbs energy of the single-phase alloy is always higher than that of any two phases that can form from a decomposition of this phase. One such two-phase mixture is shown in this figure with a dash-dotted line. On the other hand, when a single-phase alloy with a composition between the miscibility gap and the nearby spinodal composition is brought to a $T < T_c$, the situation is quite different. Owing to the convex

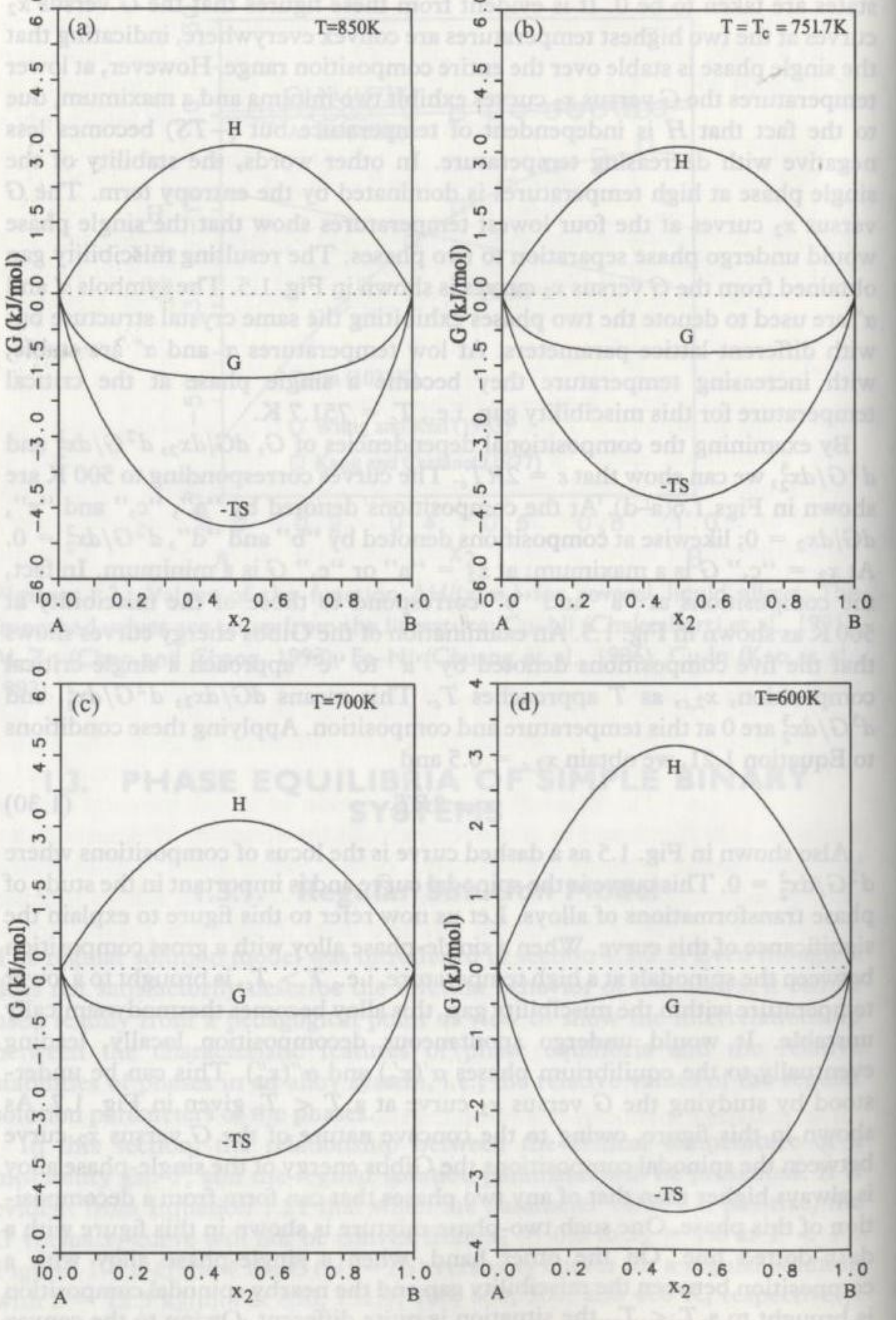

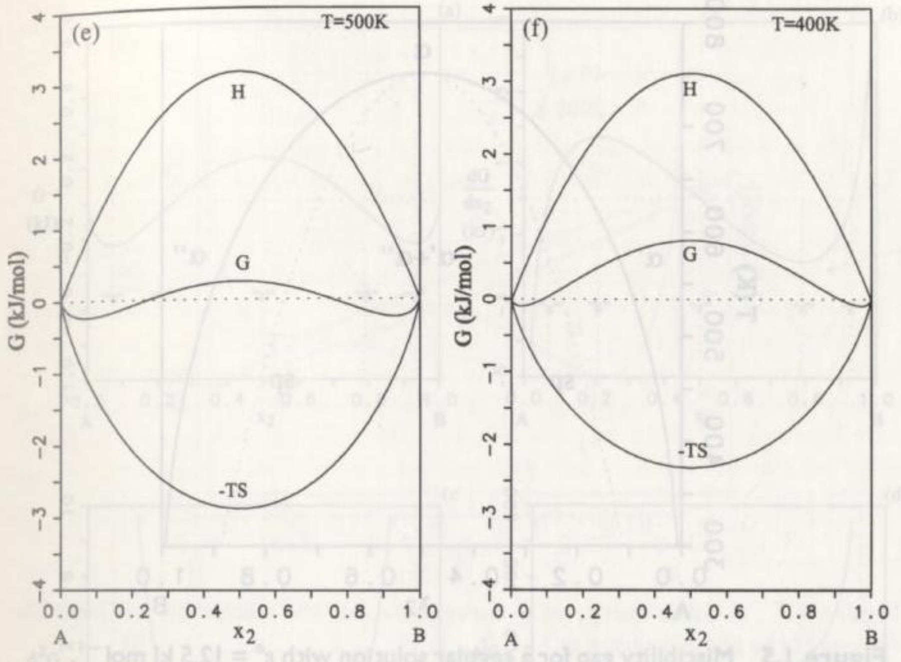

Figure 1.4 Values of G, H and $(-TS)$ for a binary regular solution with $\varepsilon^{\alpha} = 12.5$ kJ mol^{-1} at six temperatures.

nature of the G versus x_2 curve in this composition range, there would be an increase of the Gibbs energy when a single-phase alloy decomposes locally to form a two-phase mixture as also shown in this figure. In other words, there is an activation barrier prior to eventual decomposition of the single-phase alloy to the equilibrium phases $\alpha'(x_2')$ and $\alpha''(x_2'')$. This, of course, is contrary to the behavior of a single-phase alloy whose composition falls between the spinodals.

1.3.2. Relationship Between the Characteristic Features of a Binary Phase Diagram and the Relative Stabilities of the Phases

1.3.2.1 Component elements with the same crystal structure

Figure 1.8(a) shows a binary phase diagram with both components A and B exhibiting the same crystal structure. Figure 1.8(b) shows the Gibbs energy

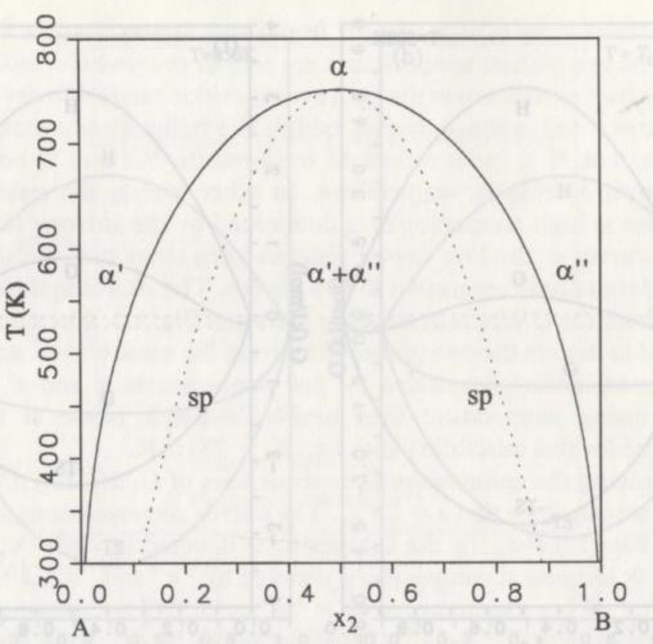

Figure 1.5 Miscibility gap for a regular solution with $\varepsilon^\alpha = 12.5$ kJ mol^{-1}.

curves for the liquid (ℓ) and solid (α) at 900 K. These curves shown are for the case when liquid A and B are taken to be the standard state, i.e., $^\circ G_1^\ell = 0$, $^\circ G_2^\ell = 0$. When the Gibbs energies of both phases are known, the compositions of coexisting ℓ and α can be calculated. These Gibbs energies may be represented by the equations given below:

$$G^\ell = G^{\ell,\mathrm{id}} + G^{\ell,\mathrm{xs}} \qquad (1.31)$$

$$\bar{G}_i^\ell = \bar{G}_i^{\ell,\mathrm{id}} + \bar{G}_i^{\ell,\mathrm{xs}} \qquad (i = 1,\ 2) \qquad (1.32)$$

and

$$G^\alpha = -[(1 - x_2)\Delta G_1^m + x_2\,\Delta G_2^m] + G^{\alpha,\mathrm{id}} + G^{\alpha,\mathrm{xs}} \qquad (1.33)$$

$$\bar{G}_i^\alpha = -\Delta G_i^m + \bar{G}_i^{\alpha,\mathrm{id}} + \bar{G}_i^{\alpha,\mathrm{xs}} \qquad (i = 1,\ 2) \qquad (1.34)$$

The superscript m in ΔG_1^m and ΔG_2^m indicates they are the Gibbs energies of melting for components A and B. As shown in Figs 1.8(a,b), ℓ and α are in equilibrium when the partial Gibbs energies of the component elements are

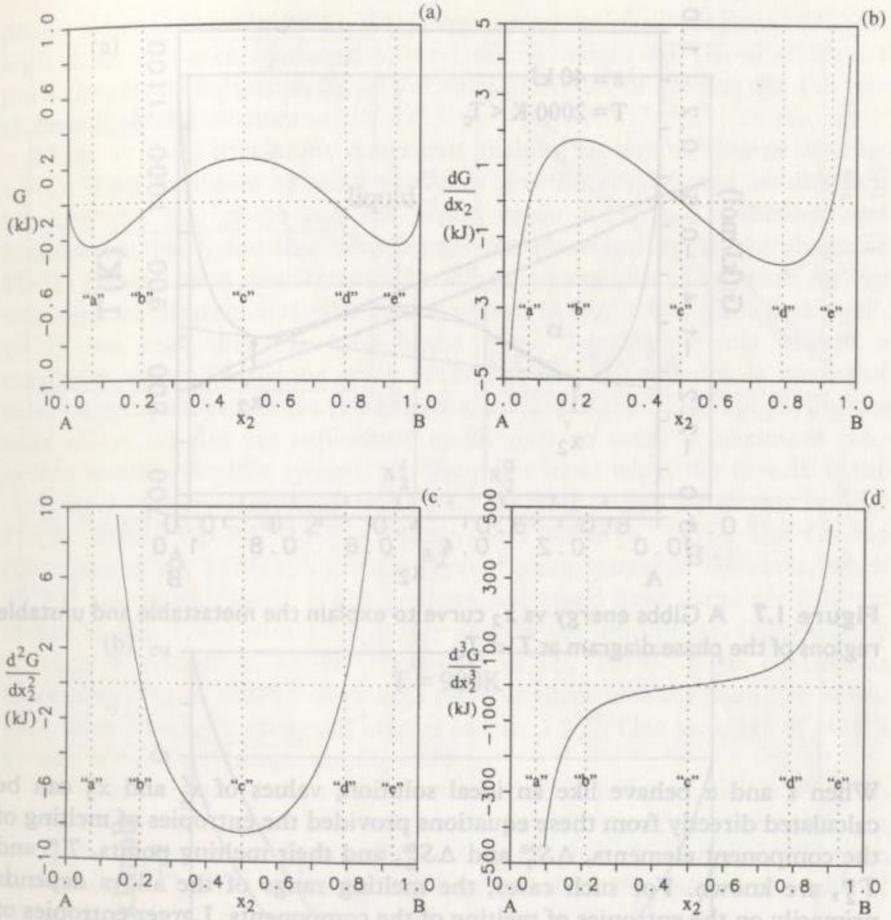

Figure 1.6 Curves of G, dG/dx_2, d^2G/dx_2^2, and d^3G/dx_2^3 vs x_2 for a regular solution with $\varepsilon^\alpha = 12.5$ kJ mol^{-1} at 500 K.

equal, i.e.,

$$\bar{G}^\ell_{i,x_2^\ell} = \bar{G}^\alpha_{i,x_2^\alpha} \qquad (i = 1,\ 2) \qquad (1.35)$$

Substituting Equations 1.32 and 1.34 into Equation 1.35 using the regular solution model to describe the excess Gibbs energy, we obtain the following conditional equations for the coexistence of ℓ and α,

$$RT \ln \frac{x_i^\ell}{x_i^\alpha} = \Delta S_i^m (T - T_i^m) + \varepsilon^\alpha (1 - x_i^\alpha)^2 - \varepsilon^\ell (1 - x_i^\ell)^2 \qquad (i = 1,\ 2) \qquad (1.36)$$

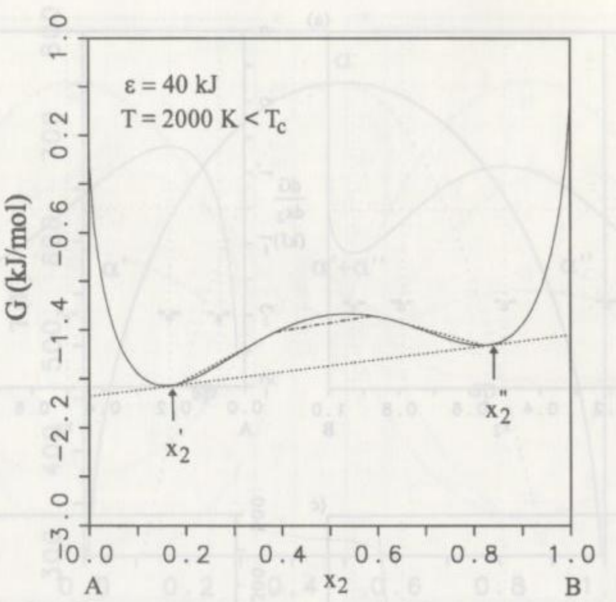

Figure 1.7 A Gibbs energy vs x_2 curve to explain the metastable and unstable regions of the phase diagram at $T < T_c$.

When ℓ and α behave like an ideal solution, values of x_2^ℓ and x_2^α can be calculated directly from these equations provided the entropies of melting of the component elements, ΔS_1^m and ΔS_2^m, and their melting points, T_1^m and T_2^m, are known. For such cases, the melting range of the alloys depends primarily on the entropies of melting of the components. Larger entropies of melting will result in larger melting ranges for the alloys. A simple exercise by the readers will show this indeed is the case!

When the entropies of melting and the melting temperatures of the components remain the same, the characteristic features of the phase diagram are governed by the relative values of the regular solution parameters for the ℓ and α phases. This is evident from Equation 1.36 which shows that the compositions of the coexisting phases are governed by the values of the regular solution parameters. Figures 1.9(a–f) show six simple phase diagrams for different combinations of ε^α and ε^ℓ values. For the phase diagram shown in Fig. 1.9(a), $\varepsilon^\alpha = \varepsilon^\ell$; the freezing range increases with increasing solution parameter values and conversely decreases with decreasing parameter values. Ideal solution behavior is a special case of the phase diagram shown in Fig. 1.9(a). Many binary systems exhibit this type of phase diagrams such as Ag–Au, Ag–Pd, Cd–Mg, Co–Ni (Hultgren et al., 1973) and

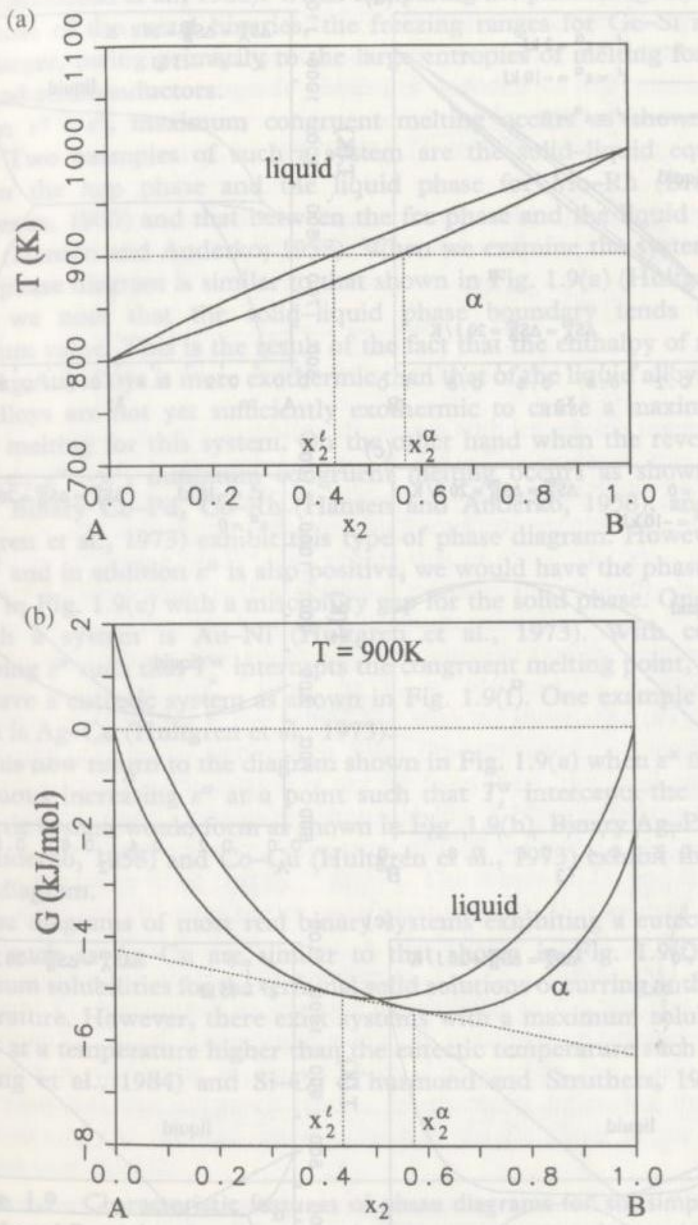

Figure 1.8 (a) Phase diagram for a binary system with continuous solutions for both the liquid and solid phases. (b) Gibbs energy curves for the liquid (ℓ) and the solid (α) phases for the system shown in (a) at 900 K. The standard states are A(ℓ) and B(ℓ); i.e., $°G_1^\ell = 0$, $°G_2^\ell = 0$.

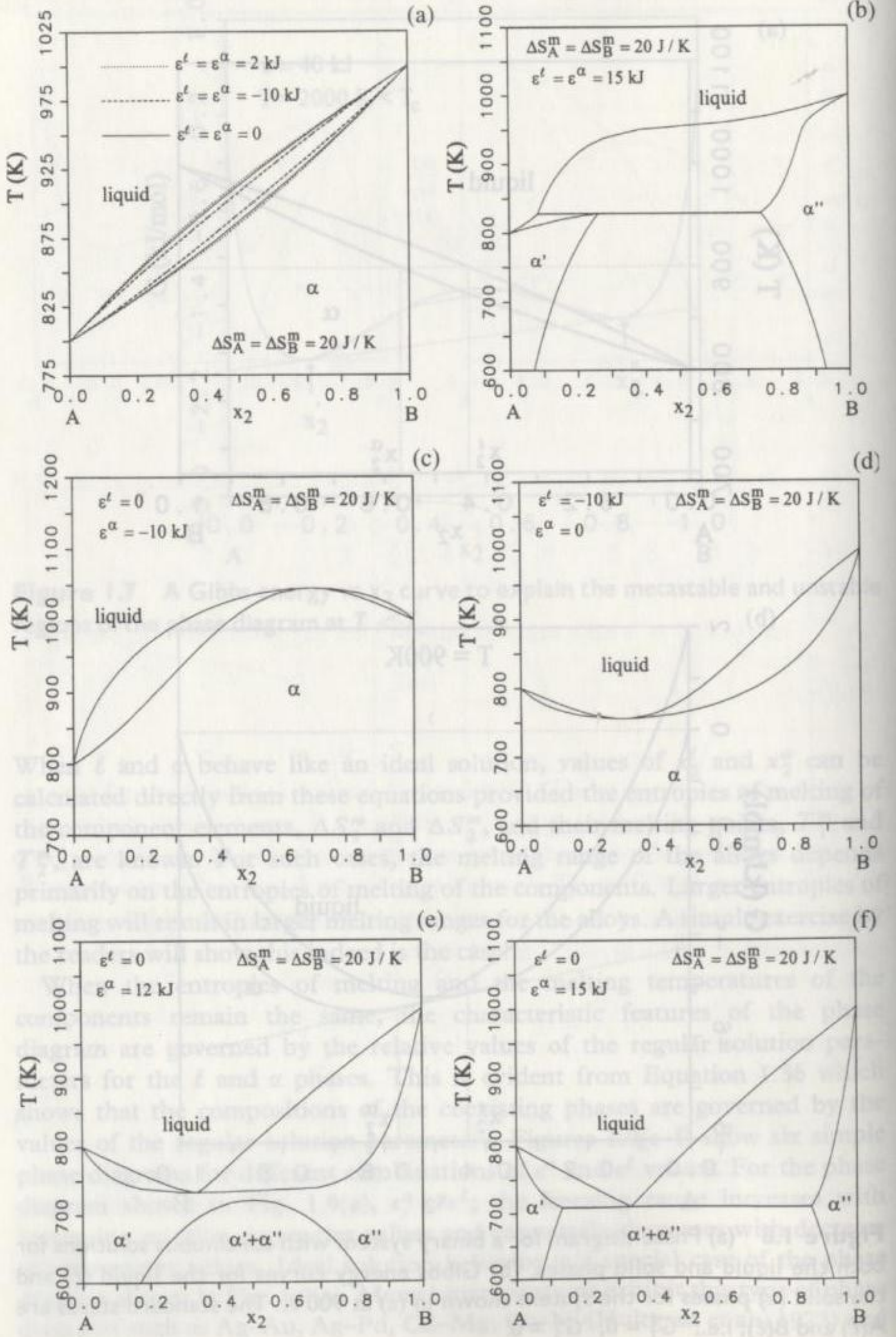

Ge–Si (Massalski et al., 1986). When comparing the phase diagram of Ge–Si with those of the metal binaries, the freezing ranges for Ge–Si alloys are much larger, owing primarily to the large entropies of melting for the two elemental semiconductors.

When $\varepsilon^\alpha < \varepsilon^\ell$, maximum congruent melting occurs as shown in Fig. 1.9(c). Two examples of such a system are the solid–liquid equilibrium between the hcp phase and the liquid phase for Mo–Rh (Brewer and Lamoreaux, 1980) and that between the fcc phase and the liquid phase for Pb–Tl (Hansen and Anderko, 1958). When we examine the system Ag–Au whose phase diagram is similar to that shown in Fig. 1.9(a) (Hultgren et al., 1973), we note that the solid–liquid phase boundary tends toward a maximum value. This is the result of the fact that the enthalpy of mixing of solid (Ag,Au) alloys is more exothermic than that of the liquid alloys. But the solid alloys are not yet sufficiently exothermic to cause a maximum congruent melting for this system. On the other hand when the reverse is the case, i.e., $\varepsilon^\alpha > \varepsilon^\ell$, minimum congruent melting occurs as shown in Fig. 1.9(d). Binary Co–Pd, Co–Rh (Hansen and Anderko, 1958), and Cr–Mo (Hultgren et al., 1973) exhibit this type of phase diagram. However, when $\varepsilon^\alpha > \varepsilon^\ell$ and in addition ε^α is also positive, we would have the phase diagram shown in Fig. 1.9(e) with a miscibility gap for the solid phase. One example of such a system is Au–Ni (Hultgren et al., 1973). With continuous increasing ε^α such that T_c^α intercepts the congruent melting point, we would then have a eutectic system as shown in Fig. 1.9(f). One example of such a system is Ag–Cu (Hultgren et al., 1973).

Let us now return to the diagram shown in Fig. 1.9(a) when $\varepsilon^\alpha \cong \varepsilon^\ell$. With continuous increasing ε^α at a point such that T_c^α intercepts the solidus, a peritectic system would form as shown in Fig. 1.9(b). Binary Ag–Pt (Hansen and Anderko, 1958) and Co–Cu (Hultgren et al., 1973) exhibit this type of phase diagram.

Phase diagrams of most real binary systems exhibiting a eutectic equilibrium such as Ag–Cu are similar to that shown in Fig. 1.9(f) with the maximum solubilities for the terminal solid solutions occurring at the eutectic temperature. However, there exist systems with a maximum solubility that occurs at a temperature higher than the eutectic temperature such as Fe–Cu (Chuang et al., 1984) and Si–Cu (Thurmond and Struthers, 1953). This

Figure 1.9 Characteristic features of phase diagrams for six simple binaries when A and B exhibit the same crystal structure in terms of the relative values of the regular solution parameters for the α and the ℓ phases. (a) $\varepsilon^\alpha = \varepsilon^\ell$. (b) $\varepsilon^\alpha \cong \varepsilon^\ell$ and $\varepsilon^\alpha/2R >$ the solidus temperature. (c) $\varepsilon^\alpha < \varepsilon^\ell$. (d) $\varepsilon^\alpha > \varepsilon^\ell$. (e) $\varepsilon^\alpha > \varepsilon^\ell$ and $\varepsilon^\alpha > 0$. (f) $\varepsilon^\alpha > \varepsilon^\ell$ and $\varepsilon^\alpha/2R >$ the congruent melting temperature.

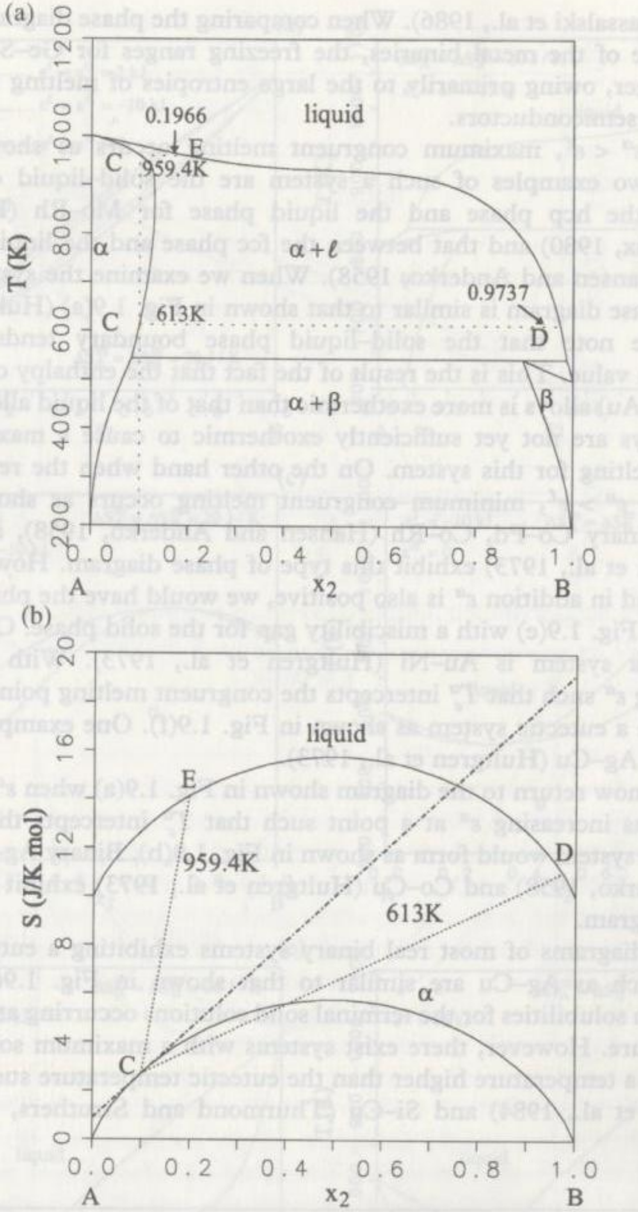

Figure 1.10 (a) A binary phase diagram exhibiting a retrograde solubility with $T_A^{m,\alpha} = 1000$ K, $T_B^{m,\alpha} = 100$ K, $T_A^{m,\beta} = 10$ K, $T_B^{m,\beta} = 500$ K, $\Delta S_A^{m,\alpha} = \Delta S_B^{m,\alpha} = \Delta S_A^{m,\beta} = \Delta S_B^{m,\beta} = 10$ J K^{-1} mol^{-1}, $\varepsilon^\ell = 15$ kJ mol^{-1}, $\varepsilon^\alpha = 8$ kJ mol^{-1}, and $\varepsilon^\beta = 0$. (b) Entropy of mixing curves for the liquid and the α phases of (a) to show that the solubility increases at 613 K but decreases at 959.4 K.

phenomenon is referred to as retrograde solubility. It is due primarily to an increasing value of ε^α relative to that of ε^ℓ. The readers can easily convince themselves by changing the regular solution parameters to obtain a eutectic phase diagram with retrograde solubility for one of the terminal solid solutions. However, it may be instructive to present a thermodynamic treatment first suggested by Meijering (1960) for describing retrograde solubility.

Meijering proposed to evaluate the temperature dependence of the solubility for one of the terminal solid solutions designated as α, i.e., dx_2^α/dT, at any temperature:

$$\frac{dx_2^\alpha}{dT} = \left(\frac{dS^\alpha}{dx_2^\alpha} - \frac{S^\alpha - S^\ell}{x_2^\alpha - x_2^\ell}\right) \Big/ \frac{d^2G^\alpha}{d(x_2^\alpha)^2} \tag{1.37}$$

If dx_2^α/dT is negative, the solubility decreases with increasing temperature, a normal behavior. On the other hand, if dx_2^α/dT is positive, the solubility increases. Retrograde solubility would occur! Since $d^2G^\alpha/d(x_2^\alpha)^2$ is always positive for a stable (even a metastable) equilibrium, the sign of dx_2^α/dT depends on the value of dS^α/dx_2^α versus that of $(S^\alpha - S^\ell)/(x_2^\alpha - x_2^\ell)$. If the difference between these two quantities is positive, the solubility increases as temperature increases, resulting in a retrograde solubility!

Let us next apply this equation to a eutectic system with retrograde solubility shown in Fig. 1.10(a). At $T_1 = 613$ and $T_2 = 959.4$ K, the solubilities of B in α are the same. We wish to show that $(dT/dx_2^\alpha)|_{T_1}$ is positive and $(dT/dx_2^\alpha)|_{T_2}$ is negative. Since the entropy of mixing of solutions for alloys with weak interaction is not far from ideal, the ideal entropies of mixing for the α and ℓ phases are shown in Fig. 1.10(b), referring to solid A and B as the standard state. The entropies of melting of the component elements are taken to be 10 J K^{-1} mol^{-1}. The letters C, D, and E shown in Figs. 1.10(a) and (b) refer to the same compositions. It is evident from Fig. 1.10(b) that dS^α/dx_2^α (shown as a dash-dotted line) is larger than $(S^\alpha - S^\ell)/(x_2^\alpha - x_2^\ell)$ at T_1, but smaller at T_2. This means that dx_2^α/dT is positive at T_1, resulting in an increase of solubility at $T > T_1$. But dx_2^α/dT is negative at T_2. Thus, a maximum solubility would occur between these two temperatures as shown in Fig. 1.10(a). The readers can again convince themselves that this approach works, for example, by taking the solution parameters of the fcc and liquid phases in Cu–Fe given in the literature (Chuang et al., 1984).

1.3.2.2. Component elements with different crystal structures

In the previous section, we discussed the characteristic features of simple binary phase diagrams when both components exhibit the same crystal

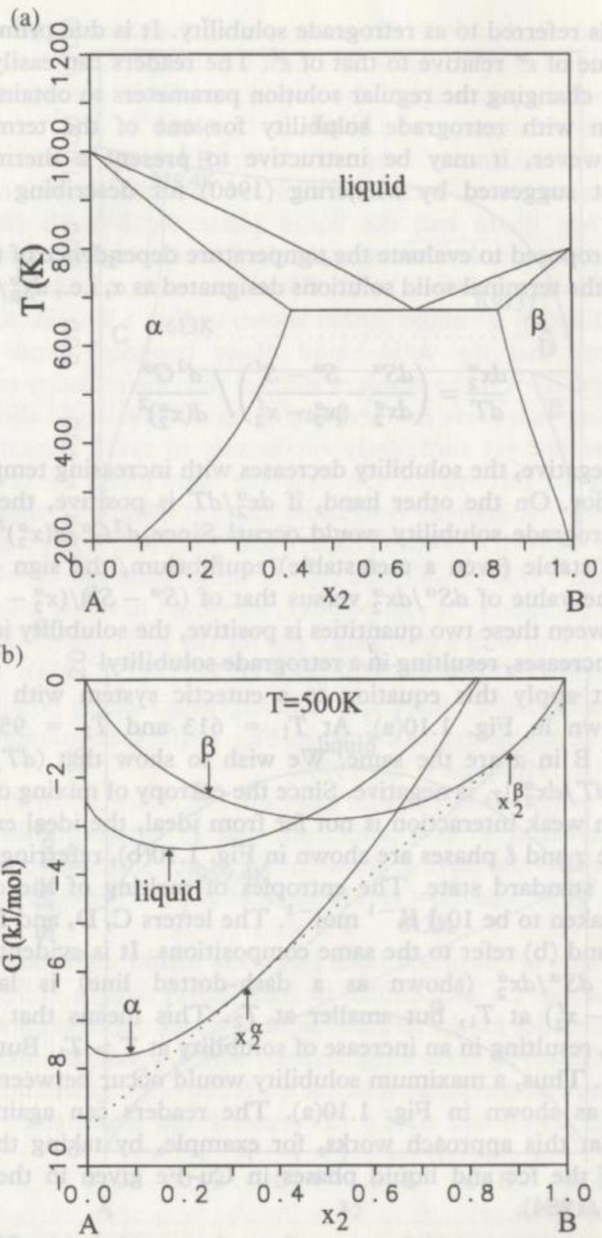

Figure 1.11 (a) A eutectic binary system when the components have different crystal structures as A(α) and B(β). (b) Gibbs energy curves of the ℓ, α and β phases at 500 K of (a) using A(β) and B(β) as the standard states, i.e., ${}^\circ G_1^\beta = 0$ and ${}^\circ G_2^\beta = 0$.

structure. In this section, we will extend our discussion of binaries for systems having component elements with different crystal structures.

Figure 1.11(a) shows a simple eutectic system with A (α) and B (β). Although this phase diagram is similar to that shown in Fig. 1.9(f), the thermodynamic factor which is responsible for the occurrence of a eutectic equilibrium for this case differs from that shown in Fig. 1.9(f). In the present case, the Gibbs energies of transformation for both A and B from α to β also contribute to the occurrence of the eutectic equilibrium. Shown in Fig. 1.11(b) are the Gibbs energy curves for liquid, α and β at 500 K taking A(β) and B(β) to be the standard states. In a similar manner as that by which we obtained Equations 1.31–1.34, we have the following equations for α and β,

$$G^\alpha = [(1 - x_2^\alpha)\Delta G_1^{\beta\to\alpha} + x_2^\alpha\,\Delta G_2^{\beta\to\alpha}] + G^{\alpha,\mathrm{id}} + G^{\alpha,\mathrm{xs}} \tag{1.38}$$

$$\bar{G}_i^\alpha = \Delta G_i^{\beta\to\alpha} + \bar{G}_i^{\alpha,\mathrm{id}} + \bar{G}_i^{\alpha,\mathrm{xs}} \qquad (i = 1,\ 2) \tag{1.39}$$

and

$$G^\beta = G^{\beta,\mathrm{id}} + G^{\beta,\mathrm{xs}} \tag{1.40}$$

$$\bar{G}_i^\beta = \bar{G}_i^{\beta,\mathrm{id}} + \bar{G}_i^{\beta,\mathrm{xs}} \qquad (i = 1,\ 2) \tag{1.41}$$

The conditional equations for the coexistence of the two phases are

$$RT \ln \frac{x_i^\alpha}{x_i^\beta} = -\Delta G_i^{\beta\to\alpha} - \varepsilon^\alpha(1 - x_i^\alpha)^2 + \varepsilon^\beta(1 - x_i^\beta)^2 \qquad (i = 1,\ 2) \tag{1.42}$$

Figures 1.12(a) and (b) show the effect of the regular solution parameter of β, a high-temperature phase, on the characteristic feature of a binary A–B phase diagram. While component B exists as α at low temperatures and transforms to β at 2500 K, with an entropy of transformation of 2.5 J K^{-1} mol^{-1}, component A exists with one crystal structure β over the entire temperature range of interest. The assumption made here is that there is negligible solubility of A in B(α), indicating that the Gibbs energy of transformation for A from β to α is extremely large and that the β-phase is a regular solution. When β behaves ideally, there is a two-phase equilibrium between β and α and the solubility of B in A(β) decreases smoothly with decreasing temperature as shown in Fig. 1.12(a). When $\varepsilon^\beta = 20$ kJ mol^{-1}, there still exists a two-phase equilibrium but the shape of the solubility curve of B in A(β) tends to exhibit a point of inflection. This shape of the solubility curve suggests that immiscibility is imminent at a slightly lower temperature. With further increasing values of ε^β, a miscibility gap of the β phase does occur, resulting in the formation of a monotectoid reaction as shown in Fig. 1.12(b). Two cases are shown with $\varepsilon^\beta = 35$ and 45 kJ mol^{-1}. Also displaced in this diagram for the case of $\varepsilon^\beta = 35$ kJ mol^{-1} are the spinodal curve for the

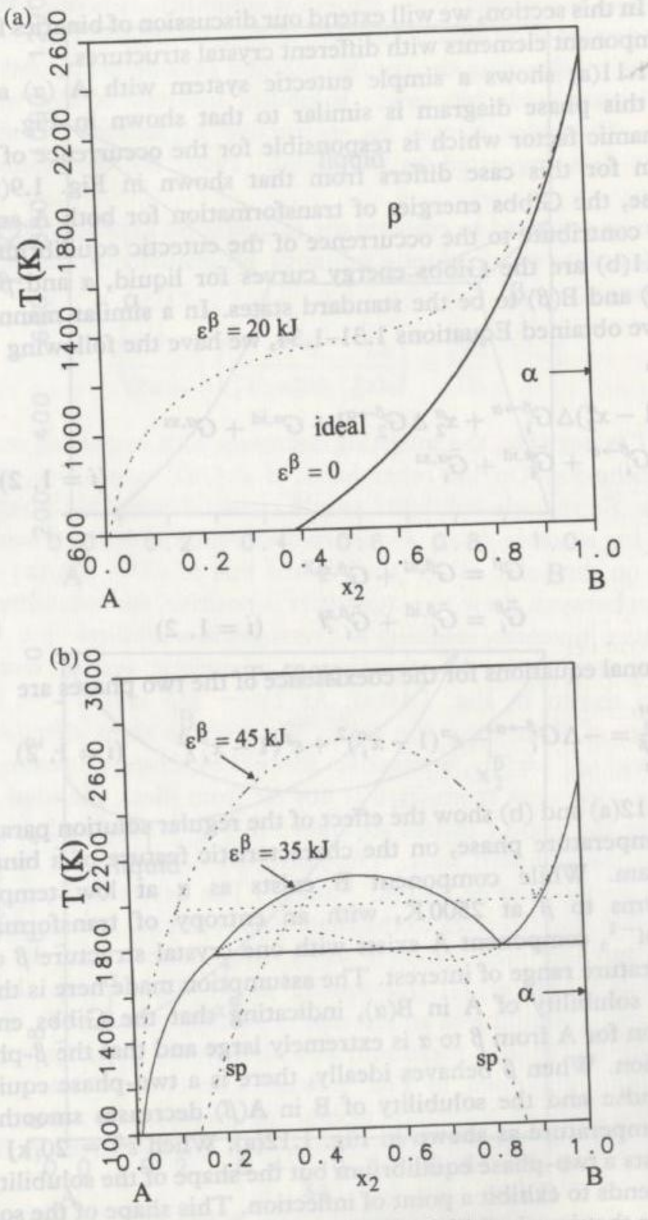

Figure 1.12 Effect of solution behavior of a high-temperature phase β on the characteristic features of the phase equilibria for a hypothetical binary system: component B exists as α at low temperatures and transforms to β at 2500 K with $\Delta H_2^{\alpha\rightarrow\beta} = 6250$ J mol^{-1}. (a) $\varepsilon^\beta = 0$ and $\varepsilon^\beta = 20$ kJ mol^{-1}. (b) $\varepsilon^\beta = 35$ and $\varepsilon^\beta = 45$ kJ mol^{-1}.

β-phase miscibility gap and the metastable extension of the β-phase boundary. The characteristic features of the phase diagram in Fig. 1.12 are similar to those involving a solid and liquid when the enthalpy of mixing of the liquid is highly endothermic. In other words, if we use a regular solution to approximate the liquid behavior, its solution parameter would be large and positive. Examples of binary systems that exhibit the type of phase diagrams shown in Fig. 1.12 are Ti (Hf, Zr)–Nb (Ta, V) (Hansen and Anderko, 1958; Rudy, 1969; Hultgren et al., 1973; Massalski et al., 1986). This is due to the fact that the group IV metals exhibit an hcp structure at low temperatures and transform to a bcc structure at high temperatures, while the group V metals exhibit only the bcc structure.

1.3.2.3. Systems with compound formation

The phase diagrams discussed in the previous two sections are some of the simplest phase relationships for binary systems. The occurrence of these diagrams is due to the fact that the components do not have strong interactions with each other. When strong interactions occur, intermetallic compounds are formed and the resulting phase equilibria are far more complex. However, the basic thermodynamic relationships governing the phase relationships are the same. In this section, we will discuss a case with only one intermediate phase at equal atomic composition. Such a phase diagram is shown in Fig. 1.13(a). The Gibbs energy curves at $T_1 = 1000$ K, which is just below the congruent melting point of the compound, δ, at 50 at% B are shown in Fig. 1.13(b) using A(ℓ) and B(ℓ) as the standard states. It is evident from this figure that

$$\bar{G}^{\ell}_{i,x_2^{\ell,*}} = \bar{G}^{\delta}_{i,x_2^{\delta}=0.5^-} \qquad (i = 1, 2) \tag{1.43}$$

where the symbol 0.5^- indicates that the composition is infinitesimally smaller than 0.5. The integral Gibbs energy of δ at T_1 is

$$G^{\delta} = 0.5\bar{G}_1^{\delta}(x_2^{\delta} = 0.5^-) + 0.5\bar{G}_2^{\delta}(x_2^{\delta} = 0.5^-) = 0.5\bar{G}^{\ell}_{1,x_2^{\ell,*}} + 0.5\bar{G}^{\ell}_{2,x_2^{\ell,*}} \tag{1.44}$$

This means that when the Gibbs energy of the liquid phase is known, the Gibbs energy of δ may be obtained provided the liquidus curve is known. It is noteworthy that the Gibbs energy obtained is referred to A(ℓ) and B(ℓ) since they are taken to be the standard state. In order to refer to A(α) and B(β) as the standard state, we must know the Gibbs energies of melting of A and B. It is obvious from Fig. 1.13(a) that a similar analysis can be carried out for δ and the liquid at the composition $x_2^{\ell,**}$.

In addition, when T_1 is increased to the congruent melting point of δ, the Gibbs energy of the liquid phase at 50 at% B is equal to that of δ. This

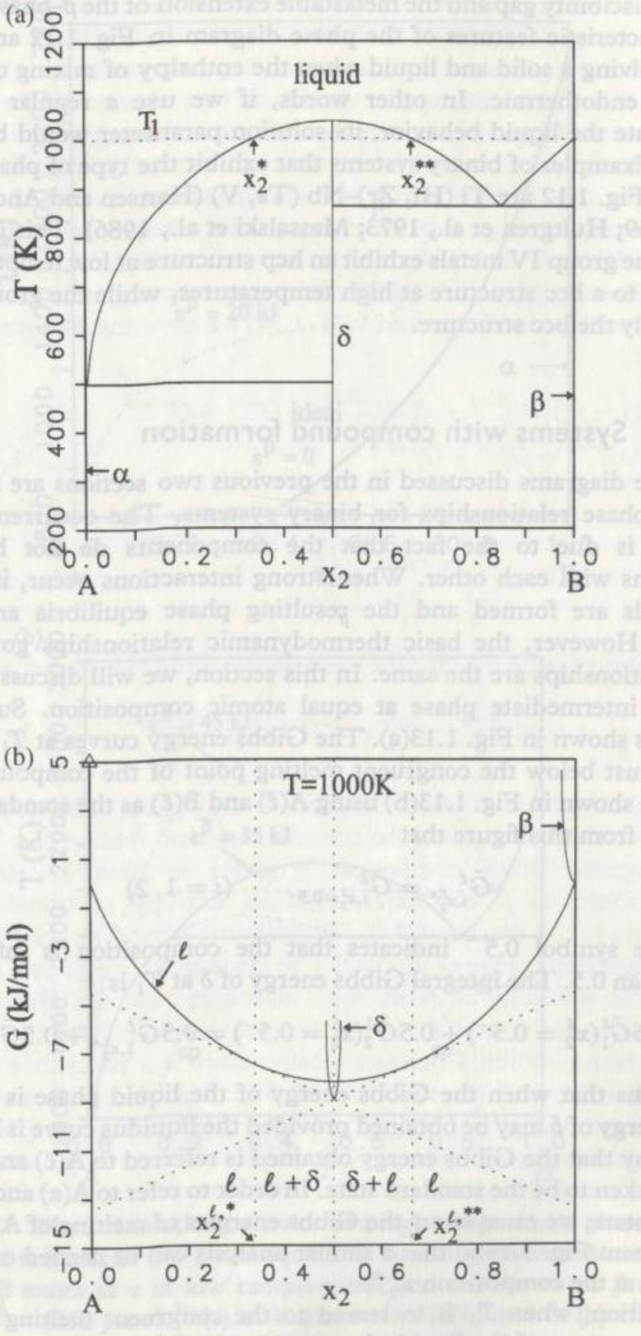

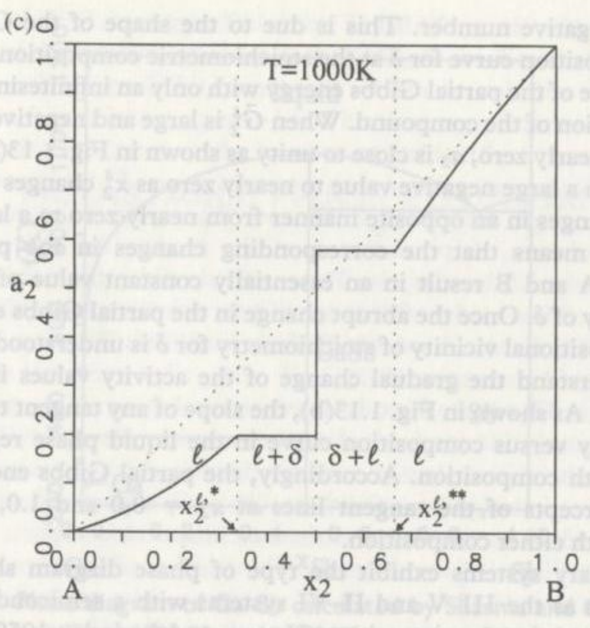

Figure 1.13 (a) A binary phase diagram of A(α) and B(β) with a congruent-melting phase δ at equal atomic composition. $\Delta S_A^m = \Delta S_B^m = 10$ J K⁻¹ mol⁻¹, $\varepsilon^\ell = -10$ kJ mol⁻¹, $\Delta G^\delta = -24000 + 15T$ J mol⁻¹. The standard states are A(ℓ) and B(ℓ). (b) Gibbs energy curves of the liquid and δ phases at $T_1 = 1000$ K of (a). (c) Activity of component B at $T_1 = 1000$ K of (a) using B(ℓ) as the standard state.

means when the Gibbs energy of δ is known, we can also obtain the Gibbs energy of the liquid phase at the congruent melting temperature and composition.

Figure 1.13(c) shows the variation of the activity of B, a_2, as a function of composition at 1000 K. The activity of B, a_2, in the liquid phase increases gradually with increasing composition up to $x_2^{\ell,*}$ and then remains constant within the ($\ell + \delta$) two-phase field until $x_2^\delta = 0.5^-$; it then increases almost abruptly to a much larger value at $x_2^\delta = 0.5^+$. The activity then remains constant within the ($\delta + \ell$) two-phase field at higher concentrations of B until $x_2^{\ell,**}$; it then increases gradually within the single-phase liquid until it reaches unity. The change of the activity values can easily be understood by examining the Gibbs energy values shown in Fig. 1.13(b). Let us first focus on the stoichiometric composition of δ. When $x_2^\delta = 0.5^-$, $\bar{G}_2^\delta$ (which equals $\bar{G}_2^\ell$ at x_2^*) is a large negative number. But when $x_2^\delta = 0.5^+$, $\bar{G}_2^\delta$ (which equals $\bar{G}_2^\ell$ at x_2^{**})

is a small negative number. This is due to the shape of the Gibbs energy versus composition curve for δ at the stoichiometric composition, resulting in a large change of the partial Gibbs energy with only an infinitesimal change in the composition of the compound. When $\bar{G}_2^\delta$ is large and negative, a_2 is small; when $\bar{G}_2^\delta$ is nearly zero, a_2 is close to unity as shown in Fig. 1.13(c). When $\bar{G}_2^\delta$ changes from a large negative value to nearly zero as x_2^δ changes from 0.5^- to 0.5^+, $\bar{G}_1^\delta$ changes in an opposite manner from nearly zero to a large negative value. This means that the corresponding changes in the partial Gibbs energies of A and B result in an essentially constant value of the integral Gibbs energy of δ. Once the abrupt change in the partial Gibbs energy values in the compositional vicinity of stoichiometry for δ is understood, readers can readily understand the gradual change of the activity values in the single-phase liquid. As shown in Fig. 1.13(b), the slope of any tangent to the integral Gibbs energy versus composition curve in the liquid phase region changes smoothly with composition. Accordingly, the partial Gibbs energies, which are the intercepts of the tangent lines at $x_2 = 0.0$ and 1.0, also change smoothly with either composition.

Many binary systems exhibit the type of phase diagram shown in Fig. 1.13(a), such as the III–V and II–VI systems with a semiconducting phase formed at equal atomic composition (Hansen and Anderko, 1958; Hultgren et al., 1973; Massalski et al., 1986). Figure 1.14 shows a phase diagram for Ga–Sb calculated by Sharma et al. (1987), which is in agreement with the experimental phase equilibrium and thermodynamic data. The excess Gibbs energy of the liquid Ga–Sb phase is described by Equation 1.29 with a total of eight parameters and that of the GaSb phase is taken as a line compound with three parameters. These parameters are given in the figure caption. As an exercise, the readers may wish to take the liquid parameters and the known phase boundaries to calculate the Gibbs energy of formation of GaSb and compare the calculated value with the equation given for the Gibbs energy of formation of GaSb.

In the Ga–Sb system, the compound GaSb is taken to be a line compound. In reality many of the intermediate compound phases have wide ranges of homogeneity, particularly for those with predominantly metallic behavior. Even for many compound semiconductors, their ranges of homogeneity at temperatures approaching their melting points also become appreciable. One such example is SnTe, which forms two eutectics with Sn and Te. The thermodynamics of this compound have been modeled in terms of its electronic defects and the phase diagram of the Sn–Te system has also been calculated, as has that for Ga–Sb (Lin et al., 1986; Sharma and Chang, 1986).

Phase equilibria of the systems presented so far have been rather simple in order to illustrate the interrelationships between the relative thermodynamic values of the phases in a system and its phase equilibria. Yet the basic thermodynamic relationships governing the complex systems are the same as those for the simple ones. However, it is worth noting that significant advances have been made in the field of phase diagram calculations in recent decades such that it is possible to calculate the details of a phase diagram for practical applications. As an example, a calculated phase diagram of Ti–Al (Zhang et al., 1997), a rather complex and yet technologically important system, is shown in Fig. 1.15. In the calculation, the following models are used. For the liquid, fcc, hcp, and bcc phases, Equation 1.29 is used; phases with small ranges of homogeneity are taken to be line compounds; and for α_2-Ti_3Al with a DO_{19} structure and γ-TiAl with an $L1_0$ structure, the generalized bond–energy model is used (Chen et al., 1995). This model is an

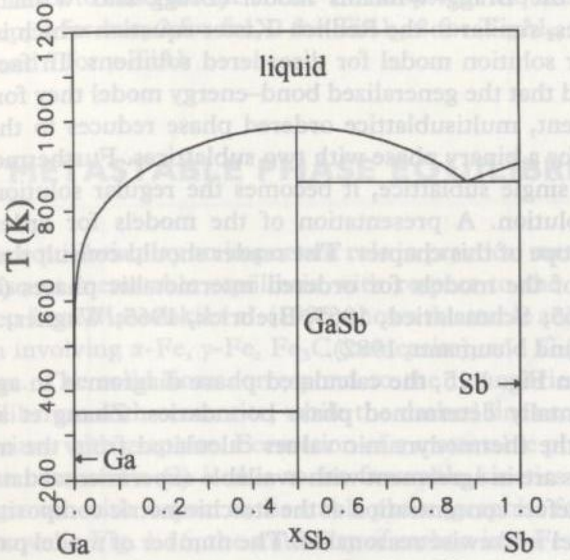

Figure 1.14 Phase diagram of Ga–Sb calculated by Sharma and Chang (1986). $\Delta G_{Ga}^{c\to\ell} = {}^\circ G_{Ga}^{\ell} - {}^\circ G_{Ga}^{c} = 5589.82 - 18.4529T$ J mol^{-1}; $\Delta G_{Sb}^{c\to\ell} = {}^\circ G_{Sb}^{\ell} - {}^\circ G_{Sb}^{c} = 19\,874.0 - 21.9868T$ J mol^{-1}. The Gibbs energy of $Ga_{0.5}Sb_{0.5}$ relative to Ga(c) and Sb(c) is:

$$\Delta G_{f,Ga_{0.5}Sb_{0.5}} = -20\,620.25 - 0.697\,05T + 0.9213T \ln T \text{ J mol}^{-1}$$

The parameters for the excess Gibbs energy of liquid phase in the form of Equation 1.29 are

$$L_0 = -17\,904.2 + 103.214\,57T - 13.631\,22T \ln T \text{ J mol}^{-1}$$
$$L_1 = -2344.6 + 23.637\,12T - 3.129\,81T \ln T \text{ J mol}^{-1}$$
$$L_2 = 1778.4 + 0.361\,66T \text{ J mol}^{-1}$$

extension of the Bragg–Williams model (Bragg and Williams, 1934) for ordered phases, similar to the Redlich–Kister equation which is an extension of the regular solution model for disordered solutions. In fact, Chen et al. (1995) showed that the generalized bond–energy model they formulated for a multicomponent, multisublattice ordered phase reduces to the Bragg–Williams model for a binary phase with two sublattices. Furthermore, when it is reduced to a single sublattice, it becomes the regular solution model for a disordered solution. A presentation of the models for ordered phases is beyond the scope of this chapter. The reader should consult the literature for descriptions of the models for ordered intermetallic phases (Swalin, 1972; Libowitz, 1965; Schmalzried, 1965; Brebrick, 1965; Wagner, 1971; Chang, 1974; Chang and Neumann, 1982).

As shown in Fig. 1.15, the calculated phase diagram is in agreement with the experimentally determined phase boundaries. Zhang et al. (1997) also showed that the thermodynamic values calculated from the models for the various phases are in agreement with available experimental data. For γ-TiAl, the intrinsic defect concentration at the stoichiometric composition calculated from the model is likewise reasonable. The number of model parameters used for each of the phases to describe the entire Ti–Al system is quite reasonable: 4 for L; 4 for hcp, 4 for bcc, 2 for fcc, 2 for $TiAl_2$, 2 for Ti_2Al_5, 2 for $TiAl_3$, 6 for α_2-Ti_3Al, and 7 for γ-TiAl.

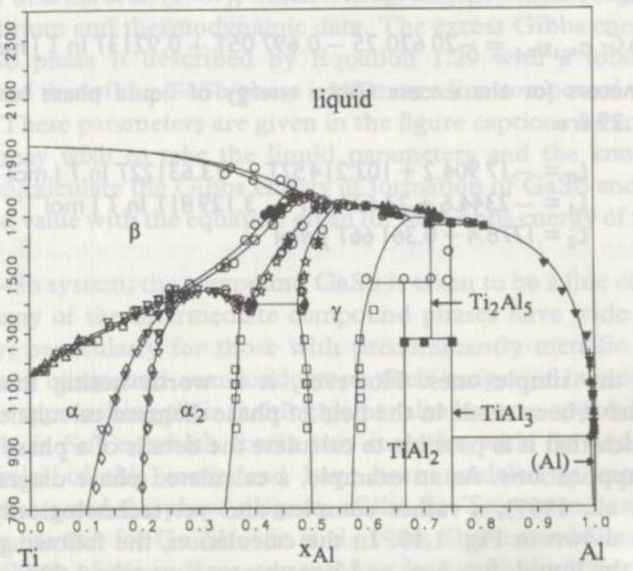

Figure 1.15 Phase diagram of the Ti–Al system: comparison between the calculated diagram by Zhang et al. (1997) and the experimental data with citations given by Zhang et al. (1997).

1.4. METASTABLE PHASE EQUILIBRIA

Since metastable equilibria play an important role in practical metallurgy, it is important to discuss metastable equilibria with respect to the stable ones. Figure 1.16 taken from Massalski et al. (1990) shows the stable and metastable phase equilibria involving α-Fe, γ-Fe, Fe_3C (cementite), and C (graphite) in the Fe–C system. The solid lines correspond to the boundaries of γ-Fe in metastable equilibrium with cementite, while the dashed lines correspond to those in equilibrium with graphite. Formation of a metastable phase (such as cementite in the case of Fe–C) is due to its favorable kinetics in terms of nucleation and growth with respect to the stable phase (graphite for the case in question). As shown in Fig. 1.16, the solubility of carbon in γ-Fe when it is in metastable equilibrium with cementite is greater than that when it is in equilibrium with graphite. This phenomenon can be rationalized readily in terms of the Gibbs energy versus composition curves, as shown schematically in Fig. 1.17, using Fe(γ) and C(gr) as the reference states. In fact, it can be generalized that the solubility of a phase is always increased when it is in metastable equilibrium with a phase.

The availability of novel techniques in the processing and characterization of materials in recent decades has succeeded in making metastable extensions of the stable equilibria which were unthinkable in the past. Two such examples are solubility extension and the formation of a metastable noncrystalline phase. One technique which has been used effectively by metallurgists is rapid quenching of a molten alloy to a low temperature. In the following, we will introduce the concept of the T_0 curve, which may be considered as another feature of the phase diagram. This curve can be used as a thermodynamic constraint for solubility extension by a rapid solidification technique. In the following, we will use two model eutectic systems as examples to explain the utility of the T_0 curve (Boettinger, 1982; Perepezko and Boettinger, 1983; Perepezko et al., 1988).

Figure 1.18(a) shows a calculated model eutectic system with A and B exhibiting the same crystal structure. The liquid phase is taken to be ideal and the solid phase (α) to be regular with $\varepsilon^{\alpha} = 12.5$ kJ mol^{-1}. The entropies of melting for A and B are taken to be 10 J K^{-1} mol^{-1}. The T_0 curve shown as a dashed line is the locus of points where the Gibbs energies of the liquid equal those of the α phase at the same compositions. As is evident from the Gibbs energy curves at 800 K shown in Fig. 1.18(b), the

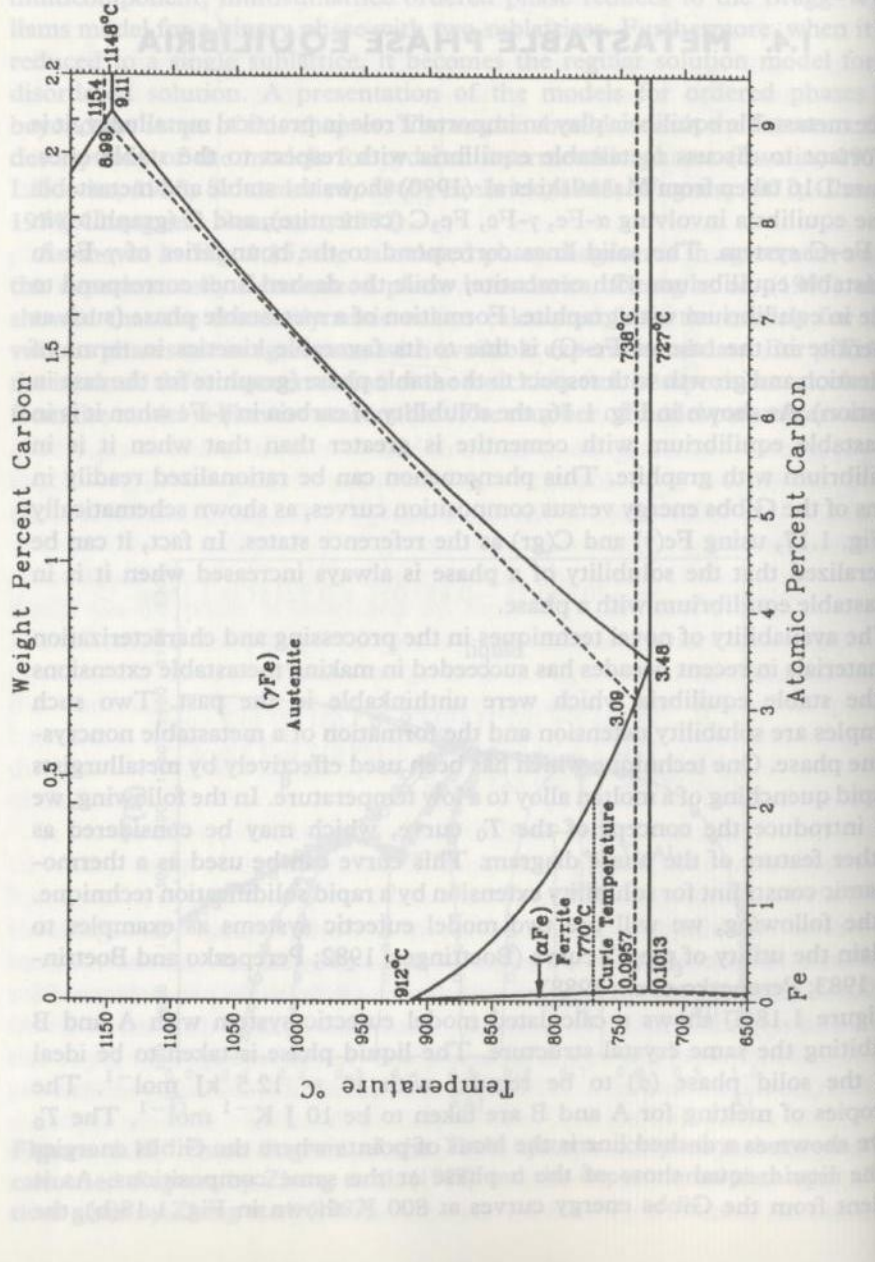

Figure 1.16 Iron–carbon phase diagram involving austenite, ferrite, cementite and graphite (Reproduced from Massalski et al., 1990, with permission).

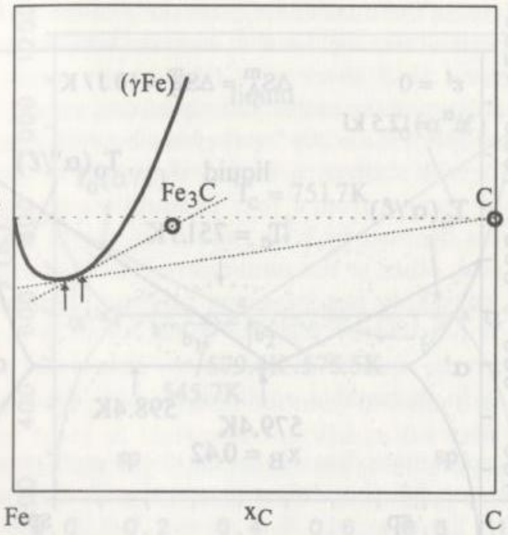

Figure 1.17 A schematic diagram of the Gibbs energy curves for austenite, cementite, and graphite to demonstrate that the solubility of carbon in austenite is greater when it is in metastable equilibrium with cementite than with graphite.

composition of equal Gibbs energies is $x_2 = 0.84$. This composition lies between the equilibrium compositions of the coexisting phases. Let us now refer to Fig. 1.18(a). If we can undercool any of the liquid alloys to the T_0 curve, the undercooled liquid can solidify without partition to form a crystalline solid since the Gibbs energy of the solid phase is the same as that of the liquid phase at the same composition. In reality the liquid must undercool relative to T_0 prior to freezing. This means crystallization would take place at a temperature below the T_0 curve. As shown in Fig. 1.18(a), the mutual solubilities of α' and α'' are rather limited under equilibrium conditions. However, it is possible to obtain a series of metastable α solutions provided the liquid alloys can be undercooled below the T_0 curve. Ag(fcc) and Cu(fcc) have a phase diagram similar to the model one shown in Fig. 1.18. Indeed, using a rapid quenching technique, Duwez et al. (1960) made a continuous solid solution of Ag and Cu in the metastable state. The lattice parameters of the metastable alloys prepared follow Vegard's law. The T_0 curve gives the highest temperatures the liquid alloys need to be undercooled before it is possible to make the solubility extension by a rapid solidification technique.

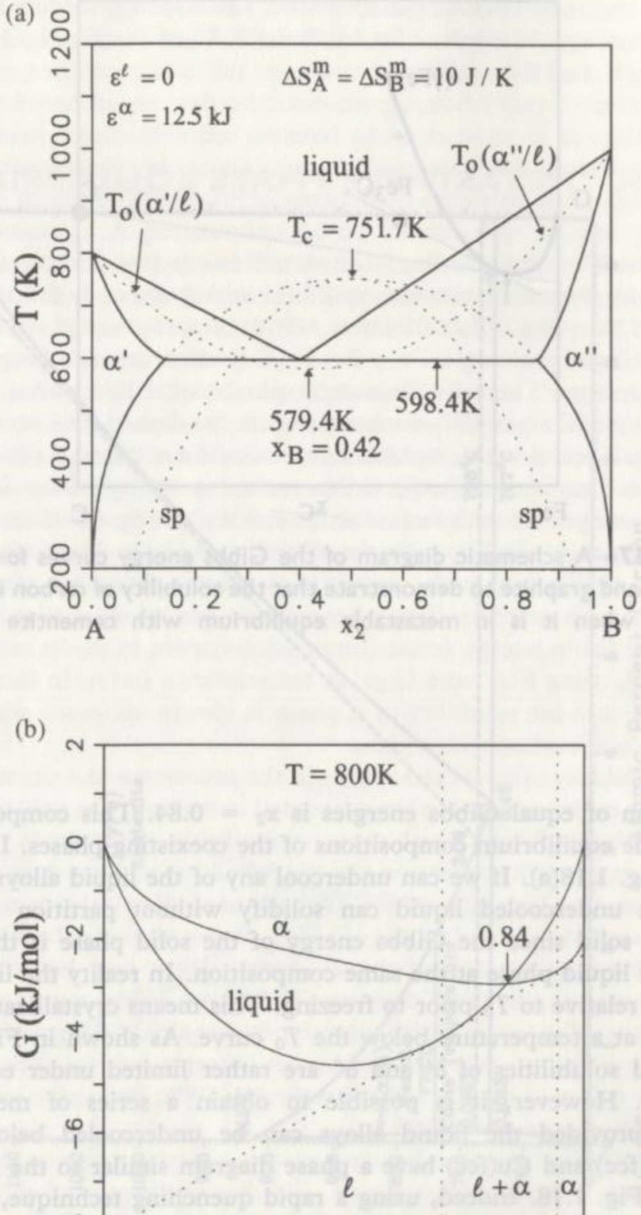

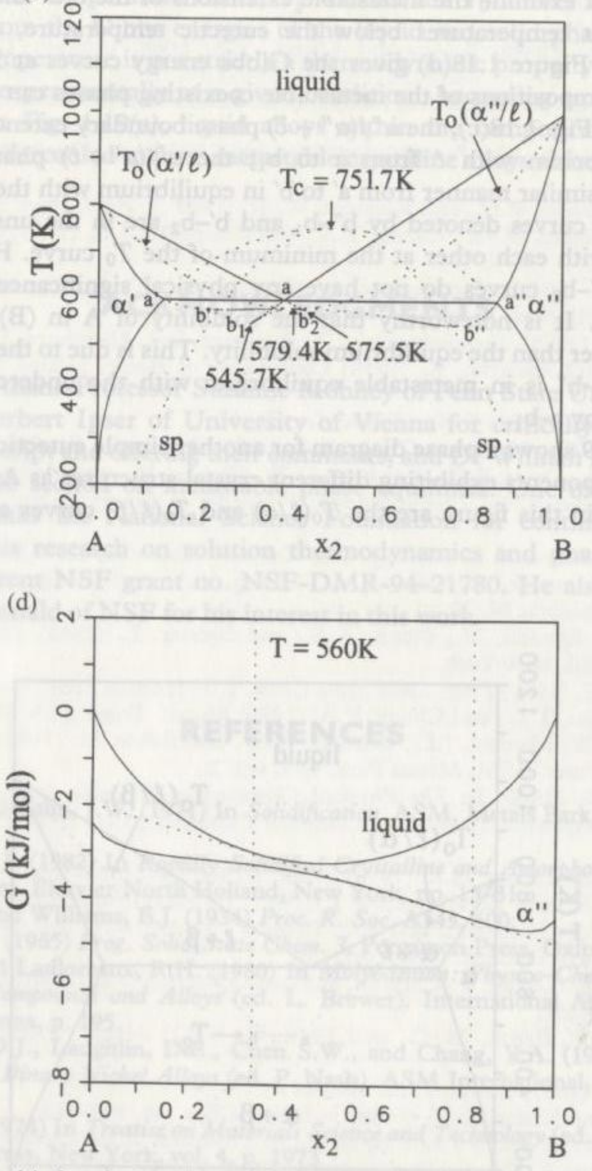

Figure 1.18 (a) A calculated model eutectic phase diagram including the T_0 and spinodal curves. (b) Gibbs energy curves of the liquid and solid phases for the system shown in (a) at 800 K to define T_0. (c) Calculated phase diagram for the system shown in (a) including the T_0 curve and the metastable extension for the solubilities of α′ and α″. (d) Gibbs energy curves of the liquid and solid phases for the system shown in (c) at 560 K.

Let us next examine the metastable extensions of the ℓ/α' and ℓ/α'' phase boundaries at temperatures below the eutectic temperature, as shown in Fig. 1.18(c). Figure 1.18(d) gives the Gibbs energy curves at 560 K; from which the compositions of the metastable coexisting phases can be obtained. As shown in Fig. 1.18(c), the $\alpha''/(\alpha''+\ell)$ phase boundary extends from a″ to b″ in equilibrium with ℓ from a to b_1; the $\alpha'/(\alpha'+\ell)$ phase boundary extends in a similar manner from a′ to b′ in equilibrium with the liquid from a to b_2. The curves denoted by b″–b_1 and b′–b_2 are in the unstable region and merge with each other at the minimum of the T_0 curve. However, the b″–b_1 and b′–b_2 curves do not have any physical significance (Baker and Cahn, 1971). It is noteworthy that the solubility of A in (B) denoted by a″–b″ is greater than the equilibrium solubility. This is due to the fact that the boundary a″–b″ is in metastable equilibrium with the undercooled liquid represented by a–b_1.

Figure 1.19 shows a phase diagram for another simple eutectic system with the two components exhibiting different crystal structures as A(α) and B(β). Also shown in this figure are the $T_0(\ell/\alpha)$ and $T_0(\ell/\beta)$ curves as well as the glass transition temperature curve, T_g. Unlike the T_0 curves which can be calculated from the Gibbs energies of the liquid and solid phases, the glass transition temperature is not strictly a thermodynamic property and must be determined experimentally at a given condition. According to the information given in Fig. 1.19(a), liquid alloys within the composition range a–b cannot be undercooled to form metastable crystaline alloys since T_g is greater than T_0.

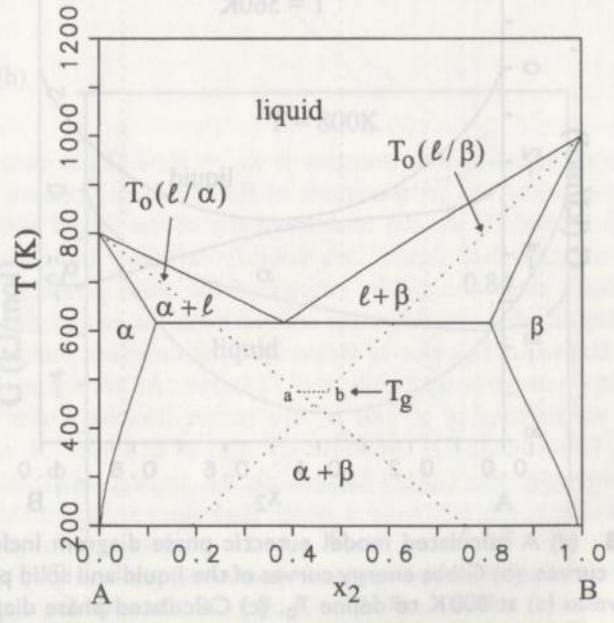

Figure 1.19 A binary eutectic system when the component elements have different crystal structures as A(α) and B(β); also shown are the $T_0(\ell/\alpha)$ and $T_0(\ell/\beta)$ curves and the T_g (glass transition temperature) curve.

ACKNOWLEDGMENTS

The authors thank Professor Suzanne Mohney of Penn State University and Professor Herbert Ipser of University of Vienna for critically reading the entire manuscript and offering their comments, and Dr William Boettinger of NIST for the section on metastable phase equilibria. One of the authors (Y.A.C.) thanks the National Science Foundation for continual financial support of his research on solution thermodynamics and phase equilibria with the current NSF grant no. NSF-DMR-94-21780. He also thanks Dr Bruce MacDonald of NSF for his interest in this work.

REFERENCES

Baker, J.C. and Cahn, J.W. (1971) In *Solidification*. ASM, Metals Park, OH, pp. 23–58.

Boettinger, W.J. (1982) In *Rapidly Solidified Crystalline and Amorphous Alloys* (ed. B.C. Giessen). Elsevier North Holland, New York, pp. 15–31.

Bragg, W.L. and Williams, E.J. (1934) *Proc. R. Soc.* **A145**, 600.

Brebrick, R.F. (1965) *Prog. Solid State Chem. 3*. Pergamon Press, Oxford, ch. 8.

Brewer, L. and Lamoreaux, R.H. (1980) In *Molybdenum: Physico-Chemical Properties of Its Compounds and Alloys* (ed. L. Brewer). International Atomic Energy Agency, Vienna, p. 195.

Chakraborti, D.J., Laughlin, D.E., Chen S.W., and Chang, Y.A. (1991) In *Phase Diagrams of Binary Nickel Alloys* (ed. P. Nash). ASM International, Metals Park, OH, p. 85.

Chang, Y.A. (1974) In *Treatise on Materials Science and Technology* (ed. H. Herman). Academic Press, New York, vol. 4, p. 1973.

Chang, Y.A. and Neumann, J.P. (1982) In *Prog. Solid State Chem* (ed. G.M. Rosenblatt and W.L. Worrell). Pergamon Press, Oxford, vol. 14, pp. 221–301.

Chen, S.-L. and Chang, Y.A. (1993) *CALPHAD* 17, 113.

Chen, S.-L., Oldfield, W., Chang, Y.A., and Thomas, M.K. (1994) *Metall. Mater. Trans. A*. **25A**, 1525.

Chen, S.-L., Kao, C.R., and Chang, Y.A. (1995) *Intermetallics* 3, 233.

Chuang, Y.-Y. and Chang, Y.A. (1986) *Z. Metallk.* 77, 460.

Chuang, Y.-Y., Schmid, R.S., and Chang, Y.A. (1984) *Metall. Trans. A* **15A**, 1921.

Chuang, Y.-Y., Hsieh, K.-C., and Chang, Y.A. (1986) *Metall. Trans. A* **17A**, 1373.

Darken, L.S. and Gurry, R.W. (1953) *Physical Chemistry of Metals*. McGraw-Hill, New York.

Denbigh, K. (1966) *The Principles of Chemical Equilibrium*. Cambridge University Press.

Duwez, P., Willens, R.H., and Klement, W. Jr. (1960) *J. Appl. Phys.* **31**, 1136.

Fecht, H.J., Zhang, M.-X., Chang, Y.A., and Perepezko, J.H. (1989) *Metall. Trans. A* **20A**, 795.

Gaskell, D.R. (1981) *Introduction to Metallurgical Thermodynamics*. 2nd edn. McGraw-Hill, New York.

Gokcen, N.A. (1975) *Thermodynamics*. Techscience, Inc., Hawthorn, CA.

Hansen, M. and Anderko, K. (1958) *Constitution of Binary Alloys*. McGraw-Hill, New York.

Hildebrand, J.H. (1929) *J. Am. Chem. Soc.* **51**, 66.

Hsieh, K.-C., Wei, M.S., and Chang, Y.A. (1983) *Z. Metallk.* **74**, 330.

Hultgren, R.R., Desai, P.D., Hawkins, D.T., Gleiser, M., and Kelley, K.K. (1973) *Selected Values of the Thermodynamic Properties of Binary Alloys*. ASM, Metals Park, OH.

Kang, T. and Castanet, R. (1977) *J. Less-Common Metals* **51**, 125–135.

Kao, C.R., Bolcavage, A., Chen, S.-L., Chang, Y.A., and Romig, Jr. A.D. (1993) *J. Phase Equilibria* **14**, 22.

Lewis, G.N., Randall, M., Pitzer, K.S., and Brewer, L. (1961) *Thermodynamics*. McGraw-Hill, New York.

Libowitz, G.G. (1965) *Prog. Solid State Chem.* 2. Pergamon Press, Oxford, ch. 7.

Lin, J.-C., Ngai, T.L., and Chang, Y.A. (1986) *Metall. Trans.* **17A**, 1241.

Massalski, T.B., Murray, J.L., Bennett, L.H., and Baker, H. (1990) *Binary Alloy Phase Diagrams*. ASM, Metals Park, OH, vol. 2.

Meijering, J.L. (1960) In *The Physical Chemistry of Metallic Solutions and Intermetallic Compounds Symposium*. Chemical Publishing Co., New York, vol. 2, p. 124.

Morris, J.P. and Zellars, G.R. (1956) *Trans. AIME* **206**, 1086–1090.

Perepezko, J.H. and Boettinger, W.J. (1983) In *Alloy Phase Diagrams* (ed. L.H. Bennett, T.B. Massalski, and B.C. Giessen), Mater. Res. Soc. Symp. Proc **19**. Elsevier North Holland, New York.

Perepezko, J.H., Chang, Y.A., Fecht, H.J., and Zhang, M.-X. (1988) *J. Less-Common Metals* **140**, 287.

Rakotomavo, J., Baron, M.-C., and Petot, C. (1981) *Metall. Trans. B* **12B**, 461–467.

Raoult, F.M. (1887) *Compt. Rend.* **104**, 1430.

Redlich, O. and Kister, A. T. (1948) *Ind. Eng. Chem.* **40**, 345–348.

Rudy, E. (1969) *Ternary Phase Equilibria in Transition Metal-Boron-Carbon-Silicon Systems, Part V. Compendium of Phase Diagram Data*. AFML-TR-65-2, Wright-Patterson AFB, OH.

Schmalzried, H. (1965) *Prog. Solid State Chem.* 2. Pergamon Press, Oxford, ch. 8.

Sharma, R.C. and Chang, Y.A. (1986) *Bulletin of Alloy Phase Diagrams* **7**, 72.

Sharma, R.C., Ngai, T.L., and Chang, Y.A. (1987) *J. Electron. Mater.* **16**, 307.

Swalin, R.A. (1972) *Thermodynamics of Solids*, 2nd edn. Wiley, New York.

Thurmond, C.D. and Struthers, J. (1953) *J. Phys. Chem.* **57**, 831.

Wagner, C. (1952) *Thermodynamics of Alloys*. Addison-Wesley, London.

Wagner, C. (1971) *Prog. Solid State Chem.* 6. Pergamon Press, Oxford, ch. 1.

Wittig, F.E. and Keil, G.Z. (1963) *Metallkd.* **54**, 576–590.

Zhang, F. (1996) PhD Preliminary Examination Report, University of Wisconsin-Madison, Madison, WI.

Zuo, Y. and Chang, Y.A. (1993) *CALPHAD* **17**, 177.

Chuang, Y.-Y., [illegible] 1921.
Chuang, [illegible] 1373.
[illegible] New York.
Denbigh, K. (1966) *The Prin*[illegible] Press.
Dewez, P., Willens, R.H., and Klement, W. Jr. (1960) *J. Appl. Phys.* 31, 1136.
Fecht, H.J., Zhang, M.-X., Chang, Y.A., and Perepezko, J.H. (1989) *Metall. Tr A 20A*, 795.
Gaskell, D.R. (1981) *Introduction to Metallurgical Thermodynamics.* 2nd McGraw-Hill, New York.
Gokcen, N.A. (1975) *Thermodynamics*, Techscience, Inc., Hawthorn, CA.
Hansen, M. and Anderko, K. (1958) *Constitution of Binary Alloys.* McGraw- New York.
Hildebrand, J.H. (1929) *J. Am. Chem. Soc.* 51, 66.
Hsieh, K.-C., Wei, M.S., and Chang, Y.A. (1983) *Z. Metallk.* 74, 330.
Hultgren, R.R., Desai, P.D., Hawkins, D.T., Gleiser, M., and Kelley, K.K. (197 *Selected Values of the Thermodynamic Properties of Binary Alloys.* ASM, Me Park, OH.
Kang, T. and Castanet, R. (1977) *J. Less-Common Metals* 51, 125–135.
Kao, C.R., Bolcavage, A., Chen, S.-L., Chang, Y.A., and Romig, Jr. A.D. (19 *J. Phase Equilibria* 14, 22.
Lewis, G.N., Randall, M., Pitzer, K.S., and Brewer, L. (1961) *Thermodynam* McGraw-Hill, New York.
Libowitz, G.G. (1965) *Prog. Solid State Chem.* 2. Pergamon Press, Oxford, ch. 7.
Lin, J.-C., Ngai, T.L., and Chang, Y.A. (1986) *Metall. Trans.* 17A, 1241.
Massalski, T.B., Murray, J.L., Bennett, L.H., and Baker, H. (1990) *Binary A Phase Diagrams.* ASM, Metals Park, OH, vol. 2.
Meijering, J.L. (1960) In *The Physical Chemistry of Metallic Solutions and Inte metallic Compounds Symposium.* Chemical Publishing Co., New York, vol. 2, 124.
Morris, J.P. and Zellars, G.R. (1956) *Trans. AIME* 206, 1086–1090.
Perepezko, J.H. and Boettinger, W.J. (1983) In *Alloy Phase Diagrams* (ed. L Bennett, T.B. Massalski, and B.C. Giessen), Mater. Res. Soc. Symp. Pro Elsevier North Holland, New York.
Perepezko, J.H., Chang, Y.A., Fecht, H.J., and Zhang, M.-X. (1988) *J. Less-Co Metals* 140, 287.
Rakotomavo, J., Baron, M.-C., and Petot, C. (1981) *Metall. Trans. B* 12B, 467.
Raoult, F.M. (1887) *Compt. Rend.* 104, 1430.
Redlich, O. and Kister, A. T. (1948) *Ind. Eng. Chem.* 40, 345–348.
Rudy, E. (1969) *Ternary Phase Equilibria in Transition Metal-Boron-Carbo Systems, Part V. Compendium of Phase Diagram Data.* AFML-TR-65-2, W Patterson AFB, OH.
Schmalzried, H. (1965) *Prog. Solid State Chem.* 2. Pergamon Press, Oxf ch. 8.
Sharma, R.C. and Chang, Y.A. (1986) *Bulletin of Alloy Phase Diagrams* 7, 72.
Sharma, R.C., Ngai, T.L., and Chang, Y.A. (1987) *J. Electron. Mater.* 16, 307.
Swalin, R.A. (1972) *Thermodynamics of Solids,* 2nd edn. Wiley, New York.

2

Thermodynamics of slags

Nobuo Sano
Department of Metallurgy, The University of Tokyo, Japan

2.1. INTRODUCTION

Slags are formed when metals are extracted from ores which contain some gangue minerals such as SiO_2 and Al_2O_3. Therefore, they consist of those gangues and fluxes added to improve their separation from the sought crude metals by lowering their melting temperatures and viscosities. The typical compositions of the industrial slags encountered in various metallurgical processes are given in Table 2.1 (Kawai, 1982). Since SiO_2 is always present in any ore, slags are essentially silicate melts accompanied by various other oxides and in some cases sulfide or halides. Slags are also formed on refining of crude metals. In this case, oxidized impurities of the crude metal are major constituents; examples are MnO, SiO_2, P_2O_5, and FeO in steelmaking slags. Thus, the generation of slags cannot be avoided in metal production as long as original ores are impure.

The most important property a slag should have is good separatability from a metal. For this purpose, the composition of a slag is controlled to have low viscosity and low density. For example, CaO is charged as a flux to an iron blast furnace to give the composition listed in Table 2.1. Another important function is to absorb impurities in the sought metal. Sulfur in blast furnace slags and phosphorus in steel converter slags are examples. Slags also can protect the metal from being contaminated by the environment and reduce excessive heat loss from the metal. For these reasons, slag control has been very important in metallurgical processes.

Molten slags are usually ionic conductors as seen from electric conductivity measurement and so on. Namely, they consist of cations such as Ca^{2+}, Mg^{2+}, and Fe^{2+} and of anions such as O^{2-}, SiO_4^{4-} and PO_4^{3-}. Silicon is coordinated

ADVANCED PHYSICAL CHEMISTRY FOR PROCESS METALLURGY
ISBN 0-12-618920-X
Copyright © 1997 Academic Press Ltd
All rights of reproduction in any form reserved

Table 2.1 Typical composition of industrial slags

	Chemical composition (mass%)					Others
	SiO_2	CaO	FeO	Al_2O_3	MgO	
Blast furnace slag (Cu)	30–40	5–15	35–50	5–10	1–3	Zn,S,Cu
Blast furnace slag (Pb)	25–40	10–25	30–40	5–10	–	Zn,Pb,S
Blast furnace slag (Fe)	30–40	35–45	–	12–18	3–8	MnO
Converter slag (Fe)	10–20	40–50	10–25	–	4–10	MnO,P_2O_5,CaF_2
Electric furnace slag (Fe) (reduction period)	15–20	60–65	< 1.0	< 3.0	5–10	CaF

Source: Kawai, 1982, with permission.

by four O^{2-} to form SiO_4^{4-} having a tetrahedral unit structure. Depending on SiO_2 content, a number of SiO_4^{4-} units are connected as chains or rings, in what is called a network structure, to form a large polymerized ion. Figure 2.1 (Derge and Tenenbaum, 1951) shows the structures of silicate ions with increasing degrees of polymerization. As the size of a silicate ion is increased, the slag viscosity is also increased, as shown in Fig. 2.2 (Ogino and Hara, 1988). The addition of CaF_2 to silicate melts is considered to make them less viscous by breaking a network. However, the exact mechanism is not well understood.

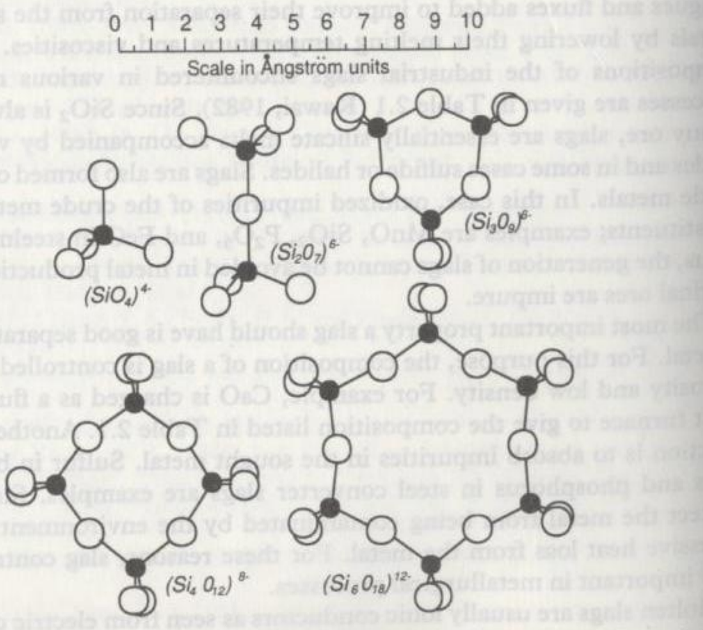

Figure 2.1 Crystalline silicates (Reproduced from Derge and Tenenbaum, 1951, with permission).

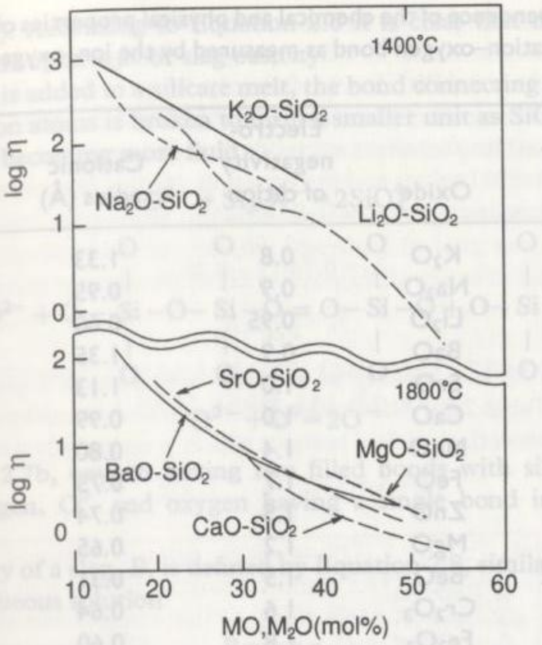

Figure 2.2 Viscosity (η) isotherms for binary silicate melts (Reproduced from Ogino and Hara, 1988, with permission).

Oxides are classified into a donor and an acceptor of oxide ion, O^{2-}, as described by Equations 2.1 and 2.2.

$$CaO = Ca^{2+} + O^{2-} \tag{2.1}$$

$$SiO_2 + 2O^{2-} = SiO_4^{4-} \tag{2.2}$$

A donor is called *basic oxide* and an acceptor is *acidic oxide*. Ward (1962) classified oxides according to their ion–oxygen attraction defined by Equation 2.3:

$$I = \frac{2Z}{d^2} \tag{2.3}$$

where d is the sum of ionic radius of cation and oxygen ion and Z is the valence of the cation. In Table 2.2 (Ban-ya, 1988) K_2O is shown to be most basic and

Table 2.2 Dependence of the chemical and physical properties of binary silicate melts on the cation–oxygen bond as measured by the ion–oxygen attraction

Classification of oxide	Oxide	Electro-negativity of cation	Cationic radius (Å)	Ion–oxygen attraction I
	K_2O	0.8	1.33	0.27
	Na_2O	0.9	0.95	0.36
	Li_2O	0.95	0.60	0.50
BASIC	BaO	0.9	1.35	0.53
	SrO	1.0	1.13	0.63
	CaO	1.0	0.99	0.70
INTERMEDIATE	MnO	1.4	0.80	0.83
	FeO	1.7	0.75	0.87
	ZnO	1.5	0.74	0.87
	MgO	1.2	0.65	0.95
	BeO	1.5	0.31	1.37
	Cr_2O_3	1.6	0.64	1.44
	Fe_2O_3	1.8	0.60	1.50
	Al_2O_3	1.5	0.50	1.66
ACID	TiO_2	1.6	0.68	1.85
	GeO_2	1.8	0.53	2.14
	B_2O_3	2.0	0.20	2.34
	SiO_2	1.8	0.41	2.44
	P_2O_5	2.1	0.34	3.31

Source: Ban-ya (1988), with permission.

P_2O_5 most acidic. In slag melts, acidic oxides exist as complex ions having various coordination numbers for oxygen, such as SiO_4^{4-} (SiO_2), PO_4^{3-} (P_2O_5), AlO_4^{5-} (Al_2O_3), FeO_4^{5-} (Fe_2O_3), TiO_4^{4-} (TiO_2). Neutral oxides between acid and basic oxides behave as amphoteric oxides depending upon other oxides present. For example, in the case of Al_2O_3

$$Al_2O_3 = 2Al^{3+} + 3O^{2-} \tag{2.4}$$

$$Al_2O_3 + 5O^{2-} = 2AlO_4^{5-} \tag{2.5}$$

$$Al^{3+} + 4O^{2-} = AlO_4^{5-} \tag{2.6}$$

Al^{3+} is stable in acidic oxides (Equation 2.4) and AlO_4^{5-} is so in basic ones (Equation 2.5). According to Equation 2.6 it is clear that the predominant species depends upon $a_{O^{2-}}$ or slag basicity.

When CaO is added to a silicate melt, the bond connecting an oxygen atom with two silicon atoms is broken to form a smaller unit as SiO_4^{4-} in Equation (2.7), the slag becoming more fluid.

$$O^{2-} + Si_2O_7^{6-} = 2SiO_4^{4-} \tag{2.7a}$$

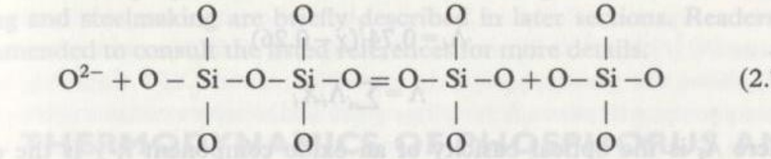

$$\begin{array}{ccccccccc} & & O & & O & & O & & O \\ & & | & & | & & | & & | \\ O^{2-} + & O- & Si & -O- & Si & -O = O- & Si & -O + O- & Si\ -O \\ & & | & & | & & | & & | \\ & & O & & O & & O & & O \end{array} \tag{2.7b}$$

$$O^{2-} + O^0 = 2O^- \tag{2.7c}$$

In Equation 2.7b, oxygen having two filled bonds with silicon is called a bridging oxygen, O^0, and oxygen having a single bond is a nonbridging oxygen, O^-.

The basicity of a slag, B, is defined by Equation 2.8, similar to pH = −log a_{H^+} for an aqueous solution

$$B = \log a_{O^{2-}} \tag{2.8}$$

where $a_{O^{2-}}$ is the activity of oxide ion. However, $a_{O^{2-}}$ cannot be measured in principle like a_{H^+} in an aqueous solution for which the Debye–Hückel theory holds. For this reason a number of measures for slag basicity have been used and a better way of description is still sought. Table 2.3 (Ban-ya, 1988) shows the basicity measures which are conventionally used or have been proposed by various investigators. Recently the solubility of CO_2 in slags and redox equilibria of transition metals have been proposed and will be described in more detail in later sections.

Table 2.3 The concept of quantitative basicity indexes

Vee ratio	mass%CaO/mass%SiO_2
	mass%CaO/(mass%SiO_2 + mass%Al_2O_3) (blast furnace slag)
	mass%CaO/(mass%SiO_2 + mass%P_2O_5) (basic steelmaking slag)
	(mass%CaO + 1.4mass%MgO)/(mass%SiO_2 + 0.84mass%P_2O_5) (ferro-alloy slag)
Excess base	B = mass%CaO–1.86mass%SiO_2–1.19mass%P_2O_5
Excess base	RO–2SiO_2–4P_2O_5–2Al_2O_3–Fe_2O_3 (mole base)
Base–acid ratio	RO/(SiO_2 + 2P_2O_5 + 0.5Al_2O_3 + 0.5Fe_2O_3) (mole base)

Source: Ban-ya (1988), with permission.

Duffy and Ingram (1976) measured the energy shift of the ultraviolet absorption spectrum of Pb^{2+} reflected by the trend for an oxygen ion to release electrons toward Pb^{2+} and defined the value of the shift relative to that of CaO as optical basicity. The measurement is limited to transparent samples which do not contain transition metal oxides. They found good correlation between experimental values and the equation derived from Pauling's electronegativity for various cations (see Table 2.2).

$$\Lambda_i = 0.74/(\chi - 0.26) \tag{2.9}$$

$$\Lambda = \textstyle\sum_i \Lambda_i X_i \tag{2.10}$$

where Λ_i is the optical basicity of an oxide component i; χ is the electronegativity (see Table 2.2); Λ is the optical basicity of a multicomponent slag. Λ is called the theoretical optical basicity which is essentially a calculated one.

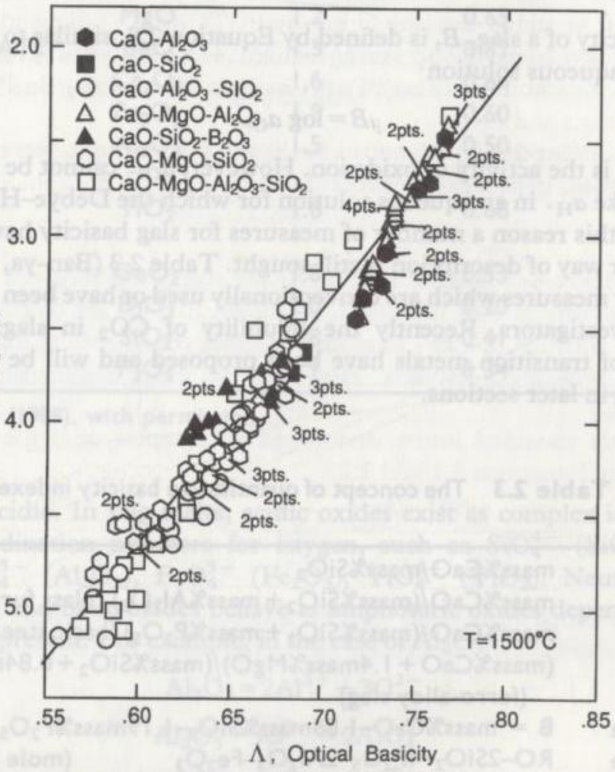

Figure 2.3 Correlation of sulfide capacity data with the calculated optical basicity of slags at 1500°C.

The correlations of this basicity measure and other physicochemical properties have been studied widely. For example, the sulfide capacity (see Equation 2.30) is shown to have good correlation with Λ in Fig. 2.3 (Sosinsky and Sommerville, 1986). However, the correlation is still semiquantitative and, for example, ad hoc adjustments to Pauling's values for χ of BaO and Na_2O have to be made to get a fit.

The chemical properties of some elements in slags encountered in ironmaking and steelmaking are briefly described in later sections. Readers are recommended to consult the listed references for more details.

2.2. THERMODYNAMICS OF PHOSPHORUS AND SULFUR IN SLAGS

2.2.1. Phosphorus

Phosphorus is stable in slags either as PO_4^{3-} or P^{3-}, depending upon the prevailing oxygen partial pressure. Figure 2.4 (Sano, 1991a) shows the critical conditions for stability of $Ca_3(PO_4)_2/Ca_3P_2$ and $Ba_3(PO_4)_2/Ba_3P_2$ as functions of temperature and P_{O_2}.

As the line for $2CO = 2C + O_2$ shows, the P_{O_2} encountered in ironmaking and steelmaking processes favors the presence of phosphate rather than

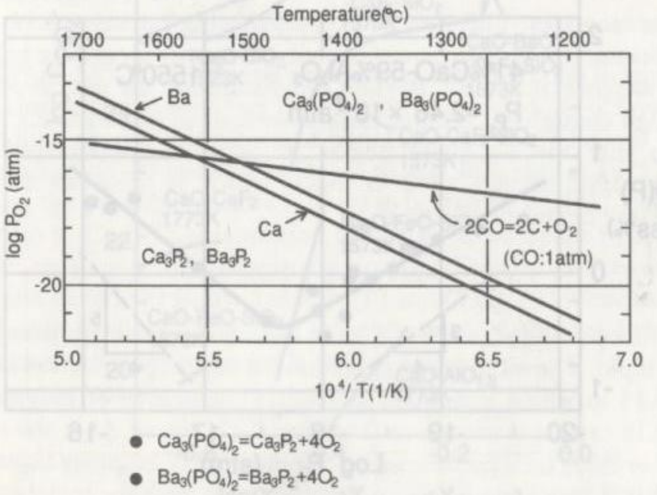

Figure 2.4 The stability of phosphate and phosphide as a function of temperature and partial pressure of oxygen (Reproduced from Sano, 1991a, with permission).

phosphide, so that only dephosphorization by oxidation to $Ca_3(PO_4)_2$ has traditionally been considered. However, this is not the case for dephosphorization of high chromium or manganese steels because the preferred oxidation states of those alloying elements would occur. Accordingly, in these cases, attention has been to dephosphorization by reduction to form Ca_3P_2 in recent years. Technically the treatment of slags containing phosphide is very important because of the generation of hazardous PH_3 when they react with moisture. Equations 2.11 and 2.12 show how phosphorus vapor dissolves into slags as PO_4^{3-} or P^{3-}. Similar to Fig. 2.4, Fig. 2.5 (Momokawa and Sano, 1982) shows the variation of the phosphorus content of a $CaO–Al_2O_3$ melt with oxygen partial pressure on a logarithm scale under a constant phosphorus pressure. The slopes of two straight lines in Fig. 2.5 are expected to be 5/4 and −3/4 for phosphate and phosphide, respectively.

$$\tfrac{1}{2}P_2(g) + \tfrac{5}{4}O_2(g) + \tfrac{3}{2}O^{2-} = (PO_4^{3-}) \tag{2.11}$$

$$\tfrac{1}{2}P_2(g) + \tfrac{3}{2}O^{2-} = (P^{3-}) + \tfrac{3}{4}O_2(g) \tag{2.12}$$

$$C_{PO_4^{3-}} = \frac{(\text{mass\%}PO_4^{3-})}{P_{P_2}^{1/2} \cdot P_{O_2}^{5/4}} = \frac{K_{11} \cdot a_{O^{2-}}^{3/2}}{f_{PO_4^{3-}}} \tag{2.13}$$

In order to express the capacity of a slag to contain phosphorus, the phosphate capacity, $C_{PO_4^{3-}}$ is defined in Equation 2.13 according to Equation 2.11. This

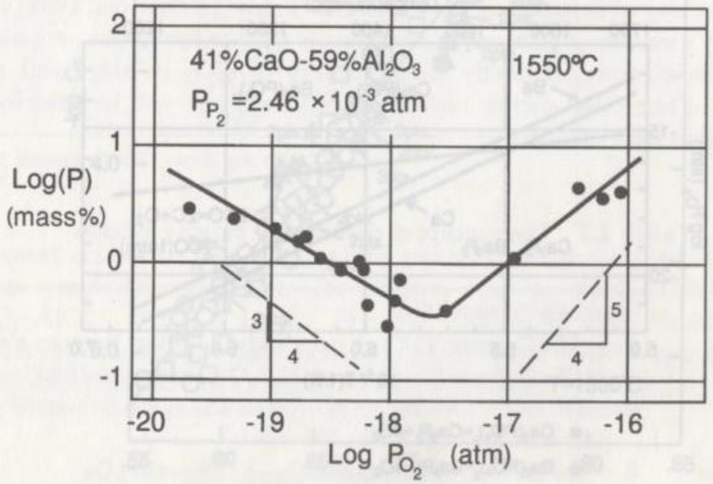

Figure 2.5 Variation in phosphorus content of the $CaO–Al_2O_3$ melt with partial pressure of oxygen (Reproduced from Momakawa and Sano, 1982, with permission).

value may easily be measured by determining the phosphorus distribution ratio between the slag and an appropriate metal under a controlled partial pressure of oxygen, since P_{P_2} in Equation 2.13 can be replaced by the phosphorus content of the metal. According to Equation 2.13, $C_{PO_4^{3-}}$ increases with increasing $a_{O^{2-}}$ or basicity of the slag and increasing K_{11} or decreasing temperature since Equation 2.11 is exothermic. Figure 2.6 (Tsukihashi and Sano, 1994) shows log $C_{PO_4^{3-}}$ as a function of the mole fraction of basic oxide for a variety of basic slags.

The phosphorus distribution ratios obtained in the steelmaking process are plotted in Fig. 2.7 (Kishitaka, 1977) for the quasi-ternary $CaO–SiO_2–FeO$ system. At a constant mass%CaO/SiO₂ ratio, the L_P value has a maximum as

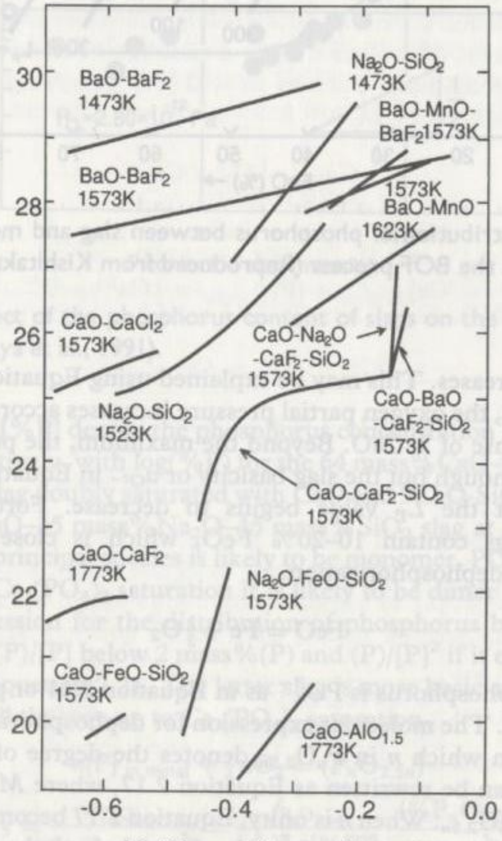

Figure 2.6 Phosphate capacities of various flux systems (Tsukihashi and Sano, 1994).

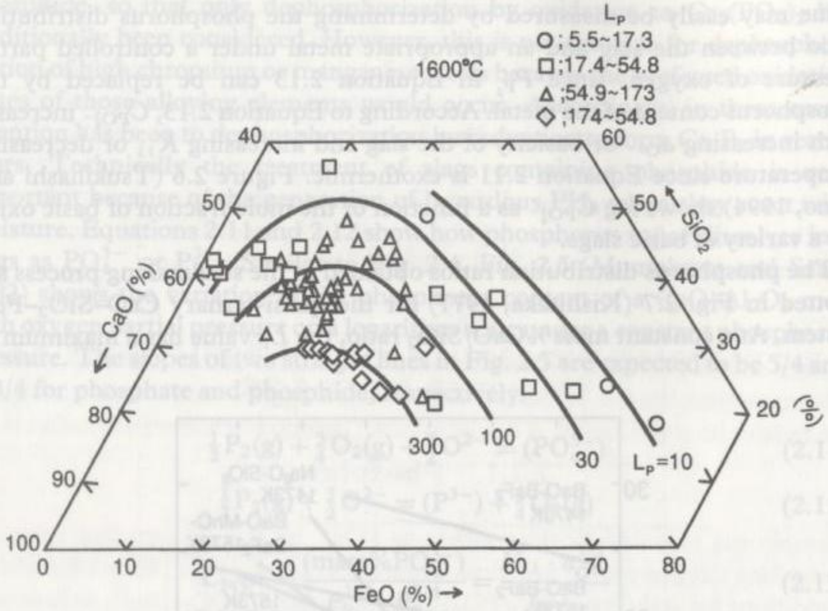

Figure 2.7 Distribution of phosphorus between slag and molten steel at the end of blowing in the BOF process (Reproduced from Kishitaka, 1977, with permission).

FeO content increases. This may be explained using Equation 2.14. Namely, as FeO increases, the oxygen partial pressure increases according to Equation 2.14 at the expense of %CaO. Beyond the maximum, the partial pressure of oxygen is high enough but the slag basicity or $a_{O^{2-}}$ in Equation 2.13 becomes too low so that the L_P value begins to decrease. Fortunately, normal steelmaking slags contain 10–20% FeO, which is close to the optimal composition for dephosphorization.

$$FeO = Fe + \tfrac{1}{2}O_2 \tag{2.14}$$

Whether the phosphorus is PO_4^{3-} as in Equation 2.11 or polymerized is an interesting topic. The molecular expression for dephosphorization is given by Equation 2.15 in which n in $P_nO_{2.5n}$ denotes the degree of polymerization. Equation 2.16 can be rewritten as Equation 2.17, where M is the molecular weight of P or $P_nO_{2.5n}$. When n is unity, Equation 2.17 becomes Equation 2.18 assuming that Henry's law holds for phosphorus in both the metal and slag. It is to be noted that even when the phosphorus content of the slag is high, the molar content of $P_nO_{2.5n}$ can be low enough, because of its large molecular weight. Similarly, for n equal to 2, Equation 2.17 can be rewritten as Equation 2.19. Figure 2.8 (Tagaya et al., 1991) shows the variation of log{(%P)/[%P]},

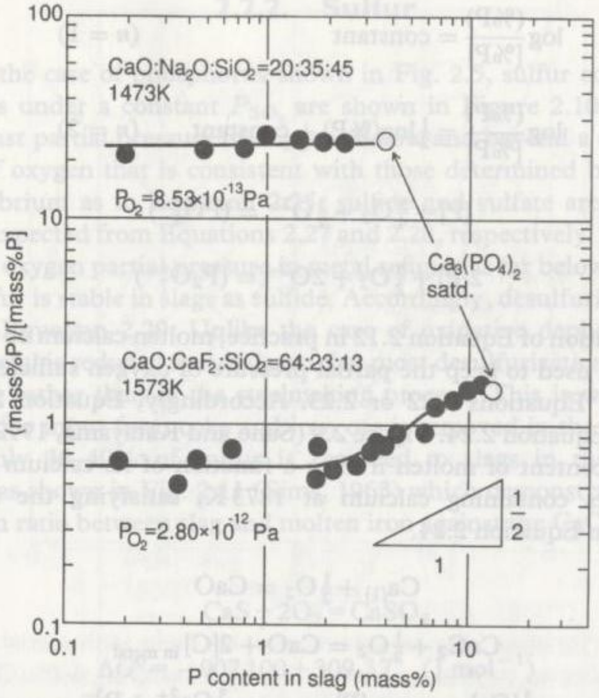

Figure 2.8 Effect of the phosphorus content of slags on the partition ratio of phosphorus (Tagaya et al., 1991).

where (%P) and [%P] denote the phosphorus concentration in mass% of slag and metal respectively, with log(%P) for the 64 mass%CaO–23 mass%CaF$_2$–13 mass%SiO$_2$ slag doubly saturated with CaO and 3CaO·SiO$_2$ at 1573 K and the 20 mass%CaO–35 mass%Na$_2$O–45 mass%SiO$_2$ slag at 1473 K. For the former slag, the principal species is likely to be monomer, PO_4^{3-} up to 2%(P); beyond it up to Ca$_3$(PO$_4$)$_2$ saturation it is likely to be dimer $P_2O_7^{4-}$. In other words, the expression for the distribution of phosphorus between slag and metal should be (P)/[P] below 2 mass%(P) and (P)/[P]^2 if it exceeds 2 mass% as described in Equation 2.21. The latter slag is more basic and the monomer is predominant all the way up to Ca$_3$(PO$_4$)$_2$ saturation.

$$n[P]_{\text{ in metal}} + \tfrac{5}{4}nO_2 = (P_nO_{2.5n}) \tag{2.15}$$

$$K_{15} = \frac{a_{P_nO_{2.5n}}}{(a_P)^n \cdot (P_{O_2})^{\frac{5}{4}n}} = \frac{f_{P_nO_{2.5n}}}{(f_P)^n \cdot [\%P]^n} \cdot \frac{(\%P_nO_{2.5n})}{(P_{O_2})^{\frac{5}{4}n}} \tag{2.16}$$

$$\log\frac{(\%P)}{[\%P]} = \frac{n-1}{n}\log(\%P) + \frac{1}{n}\log\frac{(f_P)^n}{f_{P_nO_{2.5n}}} + \frac{1}{n}\log K_{15} \cdot (P_{O_2})^{\frac{5}{4}n} \cdot \frac{n \cdot M_P}{M_{P_nO_{2.5n}}} \tag{2.17}$$

$$\log\frac{(\%P)}{[\%P]} = \text{constant} \qquad (n = 1) \tag{2.18}$$

$$\log\frac{(\%P)}{[\%P]} = \tfrac{1}{2}\log(\%P) + \text{constant} \qquad (n = 2) \tag{2.19}$$

$$[P] + \tfrac{5}{4}O_2 + \tfrac{3}{2}O^{2-} = (PO_4^{3-}) \tag{2.20}$$

$$2[P] + \tfrac{5}{2}O_2 + 2O^{2-} = (P_2O_7^{4-}) \tag{2.21}$$

In the application of Equation 2.12 in practice, molten calcium or CaC_2–CaF_2 flux has been used to keep the partial pressure of oxygen sufficiently low, as expressed by Equations 2.22 or 2.23. Accordingly, Equation 2.12 can be rewritten as Equation 2.24. Figure 2.9 (Sano and Katayama, 1992) shows the phosphorus content of molten iron as a function of its calcium content for various fluxes containing calcium at 1873 K, satisfying the relationship expected from Equation 2.24.

$$Ca_{(l)} + \tfrac{1}{2}O_2 = CaO \tag{2.22}$$

$$CaC_2 + \tfrac{1}{2}O_2 = CaO + 2[C]_{\text{in metal}} \tag{2.23}$$

$$\tfrac{3}{2}[Ca]_{\text{in metal}} + [P]_{\text{in metal}} = \tfrac{3}{2}Ca^{2+} + P^{3-} \tag{2.24}$$

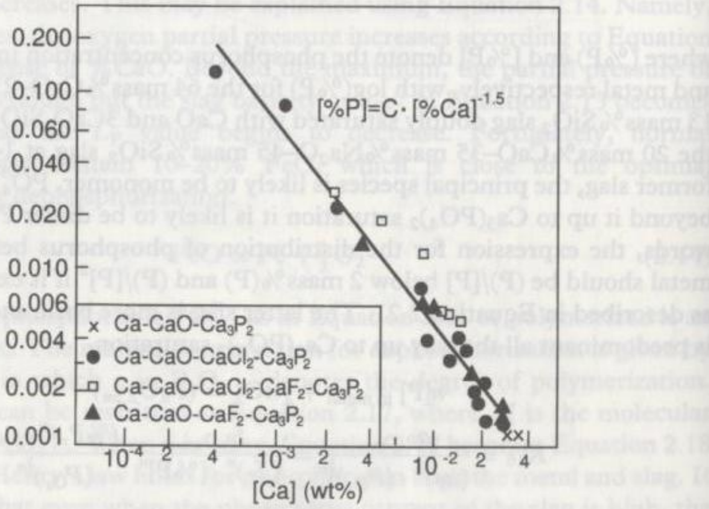

Figure 2.9 Equilibrium diagram of iron melt dephosphorization with calcium (1873 K, P_{Ar}=10 bar (%Ca_3P_2) : 1 ~ 2%) (Sano and Katayama, 1992).

2.2.2. Sulfur

Similar to the case of phosphorus shown in Fig. 2.5, sulfur contents of two oxide melts under a constant P_{SO_2} are shown in Figure 2.10 (McGannon, 1964) against partial pressure of oxygen. Below and beyond a critical partial pressure of oxygen that is consistent with those determined by the $CaSO_4$/CaS equilibrium as in Equation 2.25, sulfide and sulfate are predominant species as expected from Equations 2.27 and 2.28, respectively. As mentioned earlier, the oxygen partial pressure in metal refining is far below those critical values, sulfur is stable in slags as sulfide. Accordingly, desulfurization may be written as Equation 2.29. Unlike the case of oxidative dephosphorization, sulfur in metal is reduced to sulfide, so that most desulfurization occurs in the ironmaking rather than in the steelmaking process. This is why more than 95% of sulfur input from coke and iron ore is removed in the blast furnace, whereas only 30–40% of sulfur is removed to slags in the steelmaking operation, as shown in Fig. 2.11 (Sims, 1963) which demonstrates the sulfur distribution ratio between slag and molten iron against the CaO/SiO_2 ratio of slag.

$$CaS + 2O_2 = CaSO_4 \tag{2.25}$$

$$\Delta G^\circ = -907\,100 + 309.3T \quad (\text{J mol}^{-1}) \tag{2.26}$$

$$\log P_{O_2}(\text{atm}) = -4.44 \text{ at } 1620^\circ\text{C, and } -5.28 \text{ at } 1500^\circ\text{C}$$

$$\tfrac{1}{2}O_2 + SO_2 + O^{2-} = SO_4^{2-} \tag{2.27}$$

$$SO_2 + O^{2-} = S^{2-} + \tfrac{3}{2}O_2 \tag{2.28}$$

$$\tfrac{1}{2}S_2 \text{ or } [S]_{\text{in metal}} + O^{2-} = S^{2-} + \tfrac{1}{2}O_2 \tag{2.29}$$

According to Equation 2.29, the sulfide capacity is defined as Equation 2.30, indicating that this value increases with raising slag basicity ($a_{O^{2-}}$) and temperature because of the endothermic nature of Equation 2.29 and with the presence of components which have greater affinity for sulfur, such as MnO.

$$C_{S^{2-}} = (\%S)\cdot\left(\frac{P_{O_2}}{P_{S_2}}\right)^{1/2} = K_{29}\cdot\frac{a_{O^{2-}}}{f_{S^{2-}}} \tag{2.30}$$

Figure 2.12 (Rachev et al., 1991) shows the $C_{S^{2-}}$ for various slag systems. As far as the present author is aware, the BaO–MnO system has the greatest value, higher than those of the BaO–BaF_2 system for the above-mentioned reason. Another important factor for a slag to be a good desulfurizer is its solubility for sulfide. Since the reciprocal of solubility gives the activity

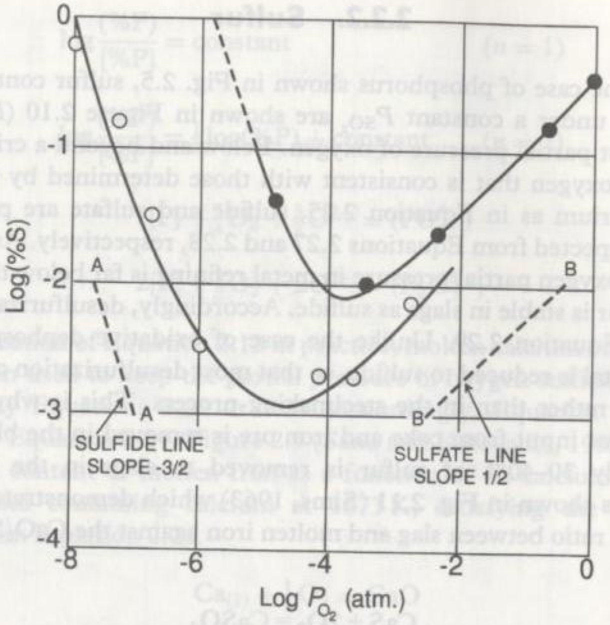

Figure 2.10 Variation in sulfur content of oxide melts with partial pressure of oxygen. (Solid circles: calcium ferrite melts at 1893 K and P_{SO_2} 6–8%. Open circles: calcium-alumino-silicate melts at 1773 K and P_{SO_2} = 2%.) (McGannon, 1964.)

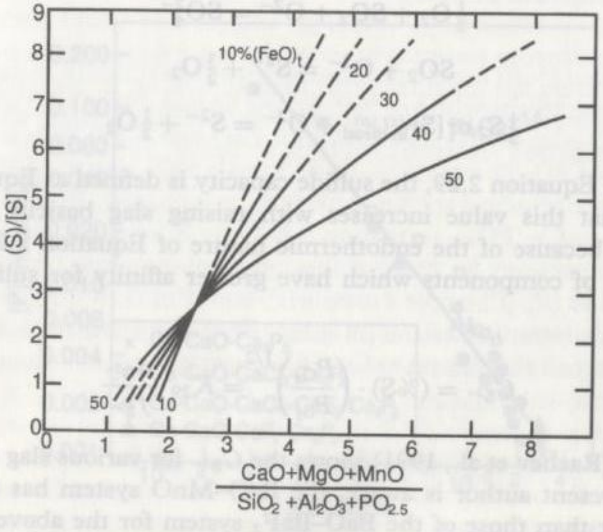

Figure 2.11 Influence of iron oxide and basicity on the desulfurization ratio, 1843–1903 K (Sims, 1963).

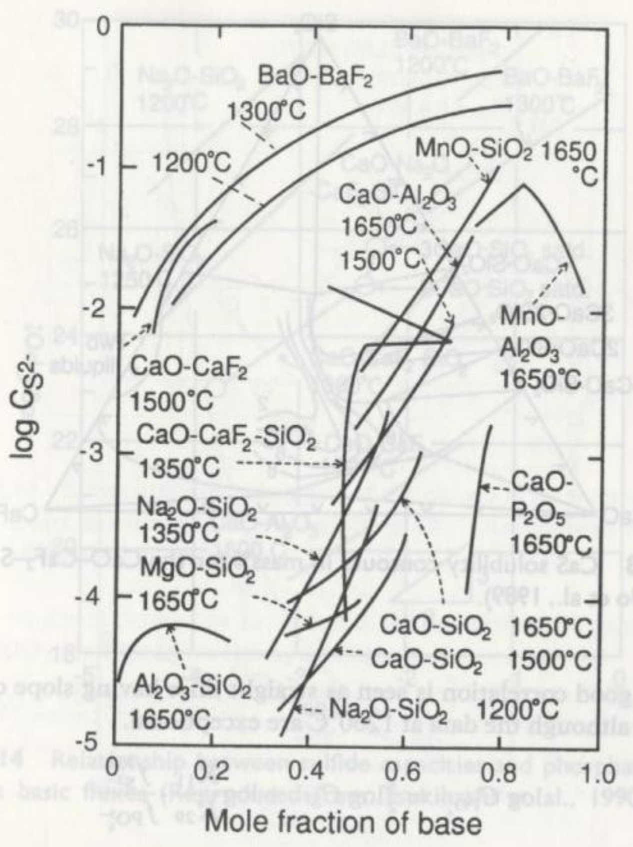

Figure 2.12 Sulfide capacities of various flux systems (Rachev et al., 1991).

coefficient of sulfide, a larger solubility leads to a larger value for $C_{S^{2-}}$ according to Equation 2.30. Besides this effect, the solubility directly affects the amount of slag required for the desired degree of desulfurization. Figure 2.13 (Uo et al., 1989) shows the solubility of CaS for the $CaO–SiO_2–CaF_2$ system used in practice for external desulfurization of a hot metal, which is doubly saturated with CaO and $3CaO \cdot SiO_2$.

Since both the sulfide and phosphate capacities increase with increasing $a_{O^{2-}}$ or basicity of the slag as illustrated by Equations 2.13 and 2.30, elimination of the $a_{O^{2-}}$ term from these equations yields Equation 2.31. If $(f_{S^{2-}})^{3/2}/f_{PO_4^{3-}}$ can be assumed to be independent of the slag system and composition, Equation 2.31 depends only on temperature. Figure 2.14 (Tsukihashi et al., 1990) shows the relationship of two capacities for various

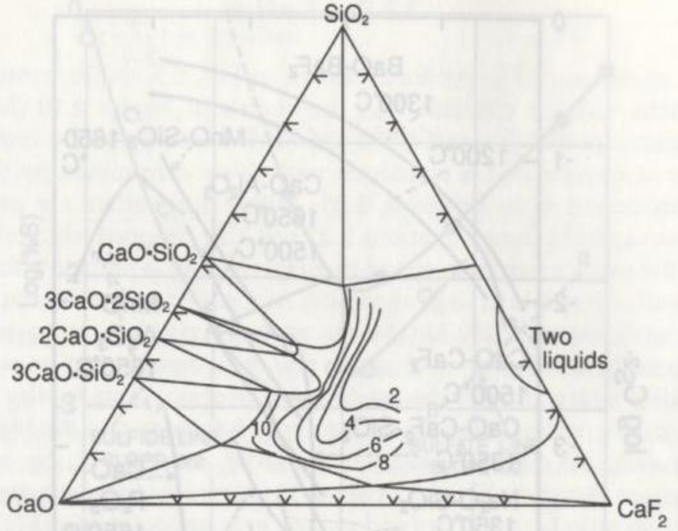

Figure 2.13 CaS solubility contours in mass% for the CaO–CaF₂–SiO₂ system at 1573 K (Uo et al., 1989).

systems. A good correlation is seen as straight lines having slope of approximately 3/2, although the data at 1200°C are exceptional.

$$\log C_{\mathrm{PO}_4^{3-}} = \tfrac{3}{2}\log C_{\mathrm{S}^{2-}} + \log \frac{K_{11}}{K_{29}} \cdot \frac{f_{\mathrm{S}^{2-}}^{3/2}}{f_{\mathrm{PO}_4^{3-}}} \qquad (2.31)$$

2.3. THERMODYNAMICS OF GASES IN SLAGS

2.3.1. Nitrogen

Nitrogen is dissolved as N^{3-} in a slag as expressed by Equation 2.32 so that a more basic slag has a higher solubility as shown in Fig. 2.15 (Martinez and Sano, 1987) for the case of the CaO–CaF_2 system. However, this is not always true. In calcium silicate or aluminate systems, the solubility is observed to decrease with increasing CaO content. This indicates that nitride may dissolve in a slag by being incorporated into a network as expressed by Equation 2.33 or 2.34, where O^- is non-bridging oxygen in a network.

$$\tfrac{1}{2}N_2 + \tfrac{3}{2}O^{2-} = N^{3-} + \tfrac{3}{4}O_2 \qquad (2.32)$$

$$\tfrac{1}{2}N_2 + 3O^{-} = N^{0} + \tfrac{3}{4}O_2 + \tfrac{3}{2}O^{2-} \qquad (2.33)$$

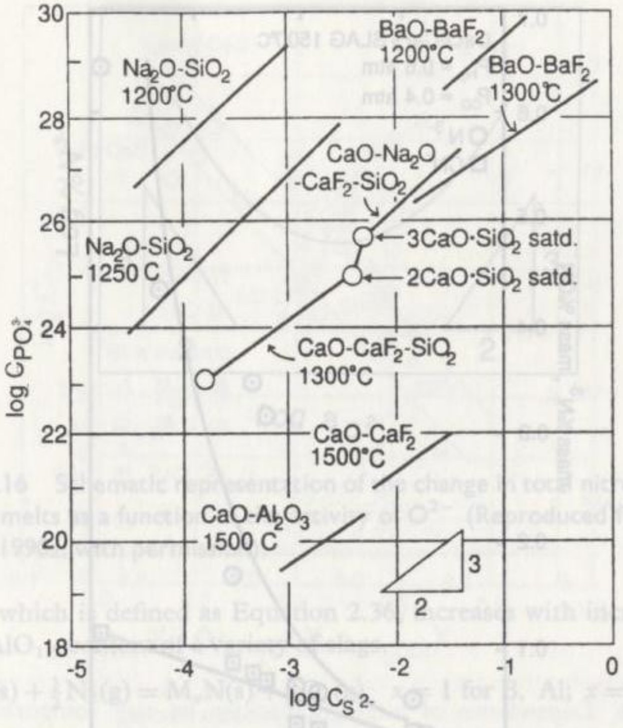

Figure 2.14 Relationship between sulfide capacities and phosphate capacities for various basic fluxes (Reproduced from Tsukihashi et al., 1990, with permission).

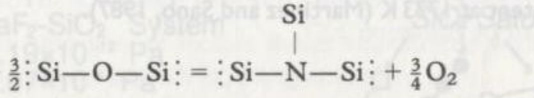

$$\tfrac{1}{2}N_2 + \tfrac{3}{2}\vdots\mathrm{Si{-}O{-}Si}\vdots = \vdots\mathrm{Si{-}}\overset{\overset{\cdots}{\mathrm{Si}}\atop |}{\mathrm{N}}\mathrm{{-}Si}\vdots + \tfrac{3}{4}O_2 \qquad (2.34)$$

Accordingly, nitrogen solubility in slag may be represented schematically as in Fig. 2.16 (Martinez and Sano, 1990a) as a function of slag basicity or $a_{O^{2-}}$, showing its amphoteric nature. For example, Fig. 2.17 (Martinez and Sano, 1990b) shows that the nitrogen solubility of CaO–CaF_2–SiO_2 melts with a constant CaF_2 content decreases with increasing SiO_2 content in accord with a decrease in free N^{3-} content and then starts increasing with an increase in incorporated nitrogen content.

According to this mechanism, slag containing a metal which has a strong affinity for nitrogen is expected to have a larger nitrogen solubility. According to Table 2.4, slag systems containing B_2O_3 or Ti_2O_3 are likely to have greater nitrogen solubility than silicates, incorporating nitrogen in borate or titanate networks. Figure 2.18 (Tomioka and Suito, 1993) shows that the nitride

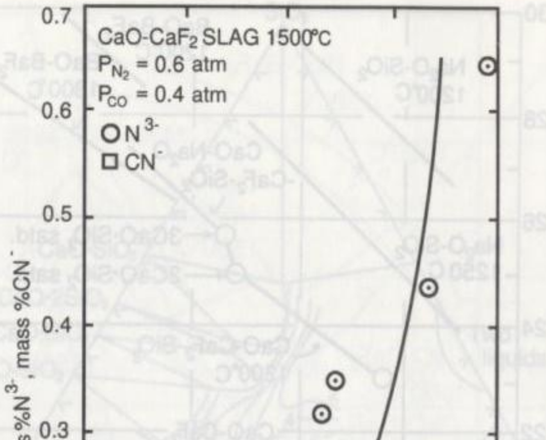

Figure 2.15 Nitride and cyanide contents of CaO–CaF$_2$ slags as a function of CaO content at 1773 K (Martinez and Sano, 1987).

Table 2.4 Enthalpy values for Equation 2.35

M	ΔH (kJ mol^{-1})
B	364
Ti	422
Si	499
Al	518

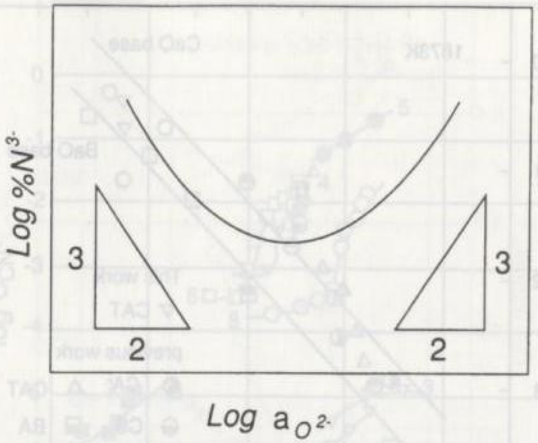

Figure 2.16 Schematic representation of the change in total nitrogen contents of silicate melts as a function of the activity of O^{2-} (Reproduced from Martinez and Sano, 1990a, with permission).

capacity, which is defined as Equation 2.36, increases with increasing SiO_2, TiO_x or $AlO_{1.5}$ content of a variety of slags.

$$M_xO_{1.5}(s) + \tfrac{1}{2}N_2(g) = M_xN(s) + \tfrac{3}{4}O_2(g) \quad x = 1 \text{ for B, Al}; \; x = \tfrac{3}{4} \text{ for Si, Ti} \tag{2.35}$$

$$C_N = \frac{(\%N)\cdot(P_{O_2})^{3/4}}{(P_{N_2})^{1/2}} \tag{2.36}$$

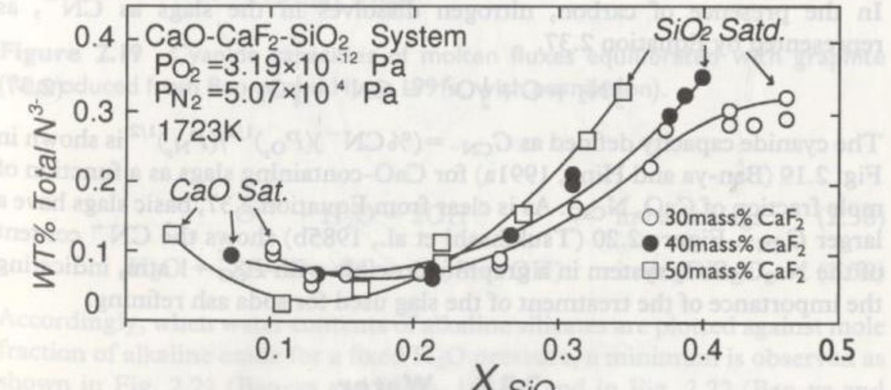

Figure 2.17 Total nitrogen contents of CaO–CaF$_2$–SiO$_2$ melts as a function of SiO$_2$ mole fraction at 1723 K (Reproduced from Martinez and Sano, 1990b, with permission).

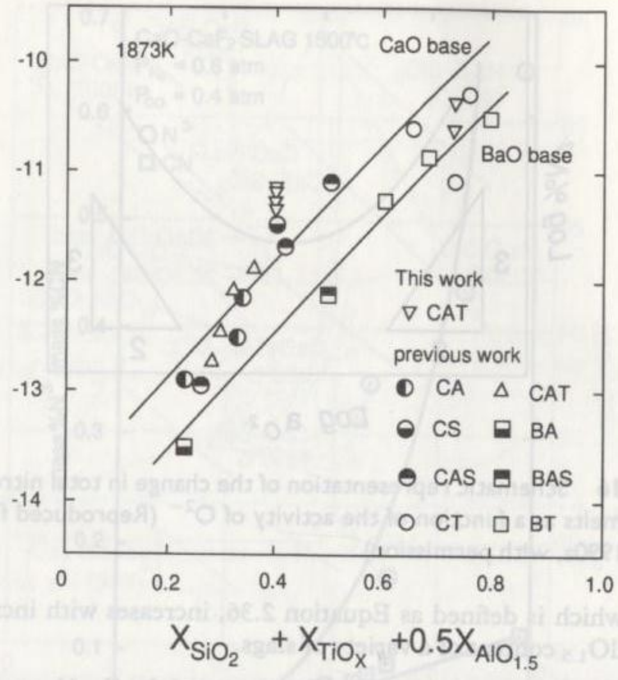

Figure 2.18 Dependence of nitride capacities on slag compositions. A = Al_2O_3; B = BaO; C = CaO; S = SiO_2; T = TiOx (Reproduced from Tomioka and Suito, 1993, with permission).

In the presence of carbon, nitrogen dissolves in the slags as CN^-, as represented by Equation 2.37.

$$\tfrac{1}{2}N_2 + C + \tfrac{1}{2}O^{2-} = CN^- + \tfrac{1}{4}O_2 \qquad (2.37)$$

The cyanide capacity defined as $C_{CN^-} = (\%CN^-)(P_{O_2})^{1/4}/(P_{N_2})^{1/2}$ is shown in Fig. 2.19 (Ban-ya and Hino, 1991a) for CaO-containing slags as a function of mole fraction of CaO, N_{CaO}. As is clear from Equation 2.37, basic slags have a larger C_{CN^-}. Figure 2.20 (Tsukihashi et al., 1985b) shows the CN^- content of the Na_2O–SiO_2 system in a graphite crucible with $P_{CO} = 1$ atm, indicating the importance of the treatment of the slag used for soda ash refining.

2.3.2. Water

Water vapor dissolves into slags in a similar way to nitrogen, as expressed by Equations 2.38 and 2.39.

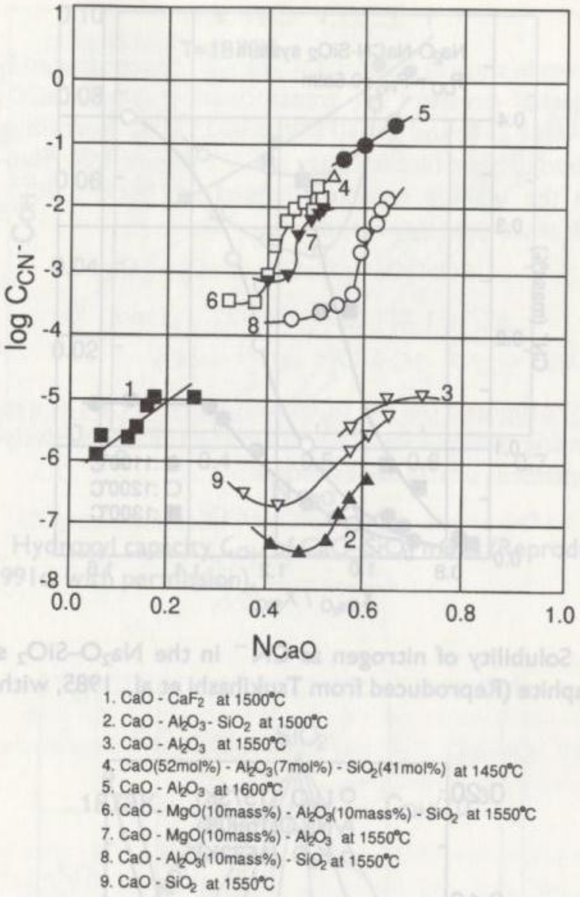

Figure 2.19 Cyanide capacities of molten fluxes equilibrated with graphite (Reproduced from Ban-ya and Hino, 1991a, with permission).

$$O^{2-} + H_2O = 2OH^- \qquad \text{in basic slags} \qquad (2.38)$$

$$H_2O + \vdots Si{-}O{-}Si\vdots = 2(\vdots Si{-}OH) \qquad \text{in acid slags} \qquad (2.39)$$

Accordingly, when water contents of alkaline silicates are plotted against mole fraction of alkaline oxide for a fixed H_2O pressure, a minimum is observed as shown in Fig. 2.21 (Ban-ya and Hino, 1991b) and in Fig. 2.22 (Ban-ya and Hino, 1991c) for the case of the CaO–SiO_2 system. Hydroxyl capacity, defined as $(\text{mass}\%H_2O)/P_{H_2O}^{1/2}$(atm) is shown in Fig. 2.23 (Ban-ya and Hino, 1991d) for the CaO–FeO–SiO_2 system.

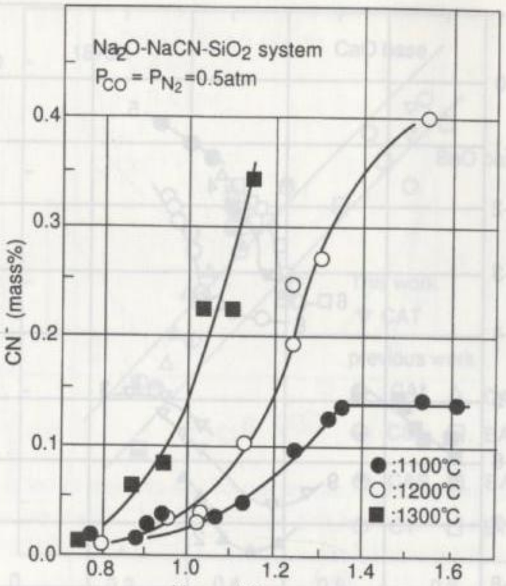

Figure 2.20 Solubility of nitrogen as CN$^-$ in the Na$_2$O–SiO$_2$ system in the presence of graphite (Reproduced from Tsukihashi et al., 1985, with permission).

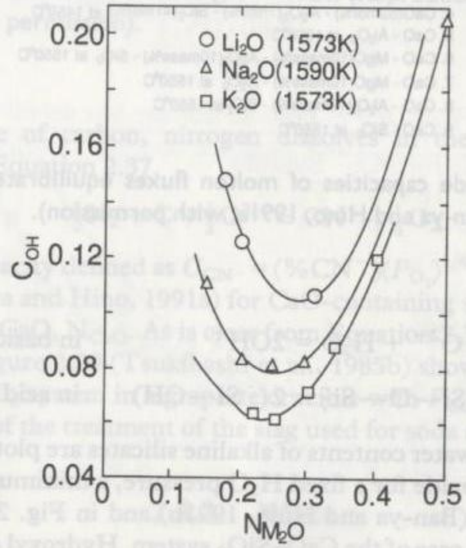

Figure 2.21 Hydroxyl capacity C_{OH} of LiO$_2$–SiO$_2$, Na$_2$O–SiO$_2$ and K$_2$O–SiO$_2$ melts (Reproduced from Ban-ya and Hino, 1991b, with permission).

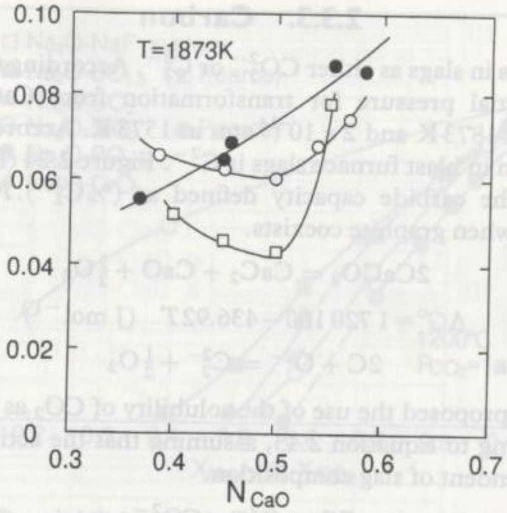

Figure 2.22 Hydroxyl capacity C_{OH} of CaO–SiO$_2$ melts (Reproducd from Ban-ya and Hino, 1991c, with permission).

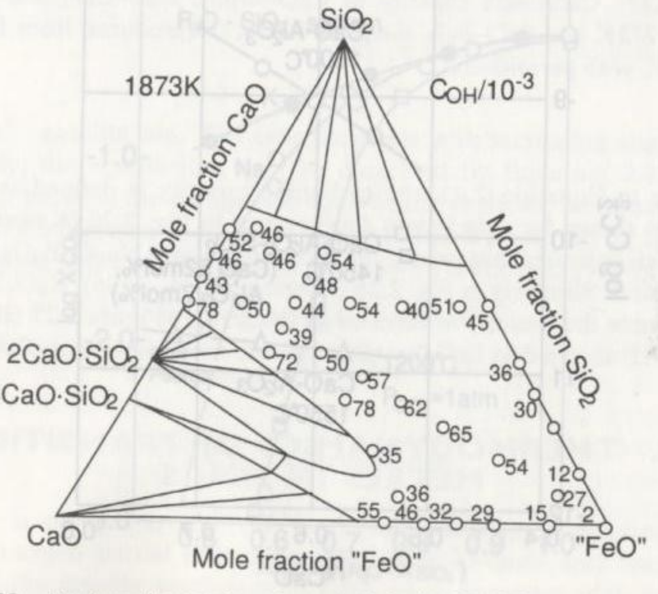

Figure 2.23 Hydroxyl capacity C_{OH} of CaO–'FeO'–SiO$_2$ melts (Reproduced from Ban-ya and Hino, 1991d, with permission).

2.3.3. Carbon

Carbon dissolves in slags as either CO_3^{2-} or C_2^{2-}. According to Equation 2.40, the oxygen partial pressure for transformation from $CaCO_3$ to CaC_2 is 9×10^{-11} atm at 1873 K and 2×10^{-14} atm at 1573 K. Accordingly, the stable species of carbon in blast furnace slags is C^{2-}. Figure 2.24 (Ban-ya and Hino, 1991e) shows the carbide capacity defined as $(\%C_2^{2-}).P_{O_2}^{1/2}$ according to Equation 2.42, when graphite coexists.

$$2CaCO_3 = CaC_2 + CaO + \tfrac{5}{2}O_2 \tag{2.40}$$

$$\Delta G^{\circ} = 1\,720\,100 - 436.92T \quad (\text{J mol}^{-1}) \tag{2.41}$$

$$2C + O^{2-} = C_2^{2-} + \tfrac{1}{2}O_2 \tag{2.42}$$

Wagner (1975) proposed the use of the solubility of CO_2 as a measure of slag basicity according to Equation 2.43, assuming that the activity coefficient of CO_3^{2-} is independent of slag composition.

$$CO_2 + O^{2-} = CO_3^{2-} \tag{2.43}$$

$$C_{CO_3^{2-}} = \frac{(\%CO_3^{2-})}{P_{CO_2}} \tag{2.44}$$

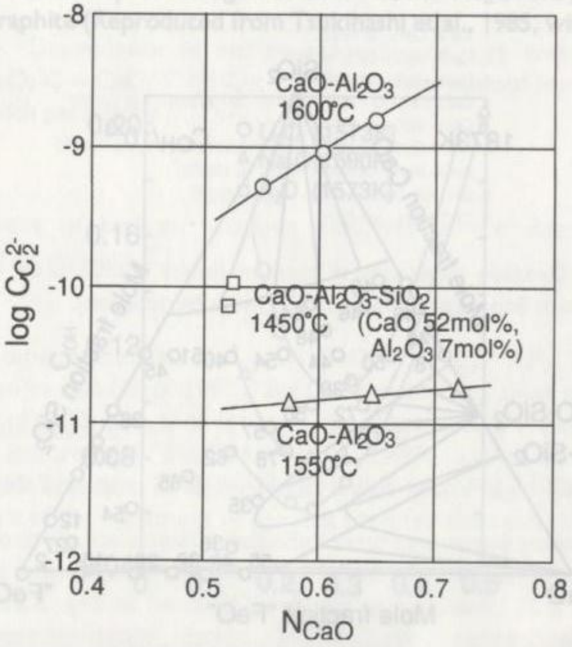

Figure 2.24 Carbide capacities of molten fluxes equilibrated with graphite (Reproduced from Ban-ya and Hino, 1991e, with permission).

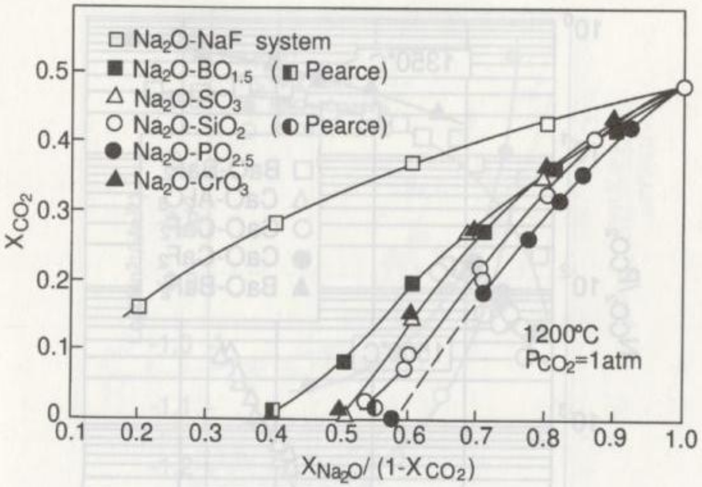

Figure 2.25 CO_2 solubilities in Na_2O-bearing melts at 1473 K (Kawahara et al., 1986).

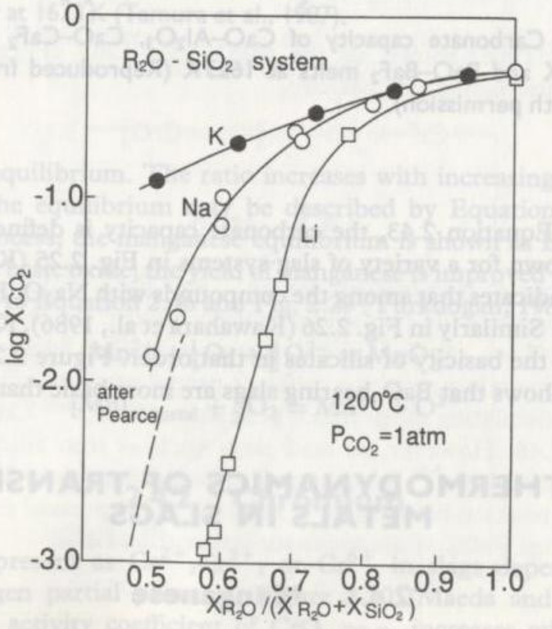

Figure 2.26 CO_2 solubilities in alkaline silicate melts at 1473 K (Kawahara et al., 1986).

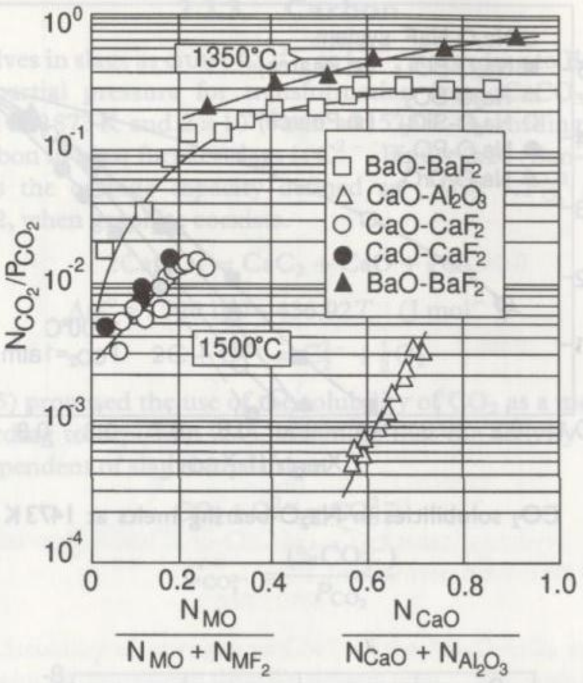

Figure 2.27 Carbonate capacity of CaO–Al_2O_3, CaO–CaF_2 and BaO–BaF_2 melts at 1773 K and BaO–BaF_2 melts at 1623 K (Reproduced from Ban-ya and Hino, 1991f, with permission).

According to Equation 2.43, the carbonate capacity is defined as Equation 2.44 and is shown for a variety of slag systems in Fig. 2.25 (Kawahara et al., 1986) which indicates that among the compounds with Na_2O, B_2O_3 acts as the strongest acid. Similarly in Fig. 2.26 (Kawahara et al., 1986), K_2O, Na_2O, and Li_2O enhance the basicity of silicates in that order. Figure 2.27 (Ban-ya and Hino, 1991f) shows that BaO-bearing slags are more basic than CaO ones.

2.4. THERMODYNAMICS OF TRANSITION METALS IN SLAGS

2.4.1. Manganese

The stable species of manganese in slags is Mn^{2+} in most cases. Even in air, Mn^{3+} is a minor species, as shown in Fig. 2.28 (Tamura et al., 1987) for the Mn^{3+}/Mn^{2+} equilibrium. The ratio increases with increasing slag basicity. Accordingly, the equilibrium may be described by Equation 2.45. In the steelmaking process, the manganese equilibrium is shown as Equation 2.46. Since MnO is a basic oxide, the yield of manganese is improved by using basic slags according to Equation 2.46 and Fig. 2.29 (Turkdogan, 1983b).

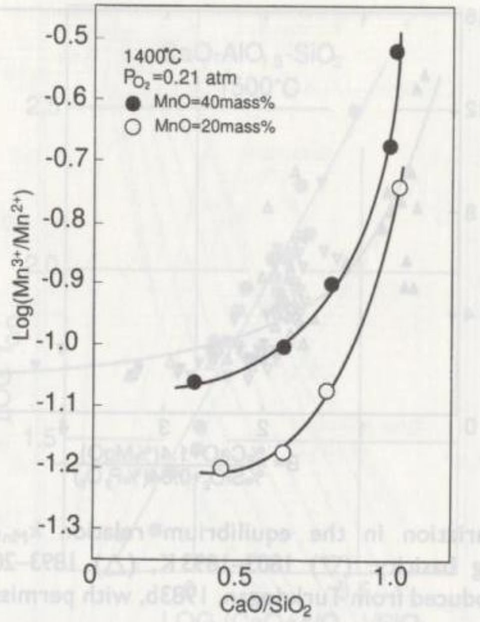

Figure 2.28 Log $(\%Mn^{3+})/(\%Mn^{2+})$ for CaO–MntO–SiO_2 melts as a function of CaO/SiO_2 in air at 1673 K (Tamura et al., 1987).

$$Mn^{2+} + \tfrac{1}{4}O_2 + \tfrac{3}{2}O^{2-} = MnO_2^- \qquad (2.45)$$

$$[Mn]_{\text{in metal}} + \tfrac{1}{2}O_2 = Mn^{2+} + O^{2-} \qquad (2.46)$$

2.4.2. Chromium

Chromium is present as Cr^{2+}, Cr^{3+}, or Cr^{6+} in slags depending on the prevailing oxygen partial pressure. Figure 2.30 (Maeda and Sano, 1982) shows that the activity coefficient of CrO, γ_{CrO}, increases with increasing $(X_{CaO} + X_{AlO_{1.5}})/X_{SiO_2}$, indicating that CrO is a weakly basic oxide in the CaO–$AlO_{1.5}$–SiO_2 system. Cr^{6+} is stable as CrO_4^{2-}, so that as Fig. 2.31

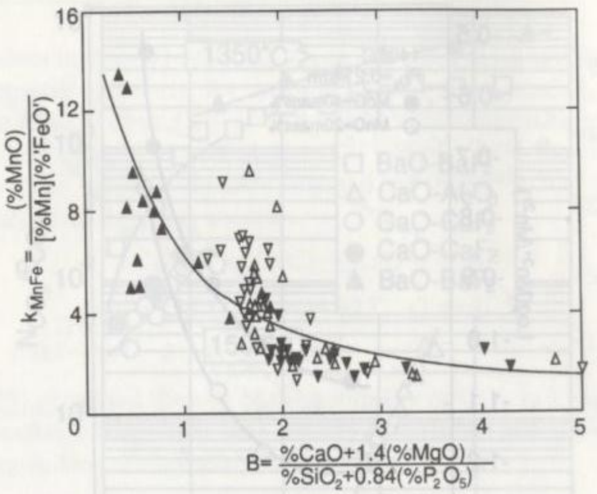

Figure 2.29 Variation in the equilibrium relation k_{MnFe} for manganese reaction with slag basicity: (▽) 1803–1893 K, (△) 1893–2003 K, (▲) 823 K, (▼) 1873 K (Reproduced from Turkdogan, 1983b, with permission).

(Morita et al., 1988) shows for the MgO–SiO_2–CaO system, Cr^{6+}/Cr^{3+} increases with increasing slag basicity.

$$Cr^{3+} + \tfrac{5}{2}O^{2-} + \tfrac{3}{4}O_2 = CrO_4^{2-} \tag{2.47}$$

2.4.3. Iron

The stable forms of iron in slags are Fe^{2+} and Fe^{3+} and in steelmaking or copper smelting slags the two species always coexist. As shown in Fig. 2.32 (Turkdogan, 1983a), the Fe^{3+}/Fe^{2+} increases as CaO content of the CaO–FeO–Fe_2O_3 system increases at a constant partial pressure of oxygen. This is explained by postulating the presence of anions of $FeO_n^{(2n-3)-}$ such as FeO_2^- as in Equation 2.48. However, in acid slags such as iron silicates in copper smelting, the cation Fe^{3+} is suggested to be predominant (Equation 2.49). The exchange reaction between Fe^{3+} and FeO_2^- is expressed as Equation 2.50 and in basic slags FeO_2^- is predominant rather than Fe^{3+}.

$$Fe^{2+} + \tfrac{1}{4}O_2 + \tfrac{3}{2}O^{2-} = FeO_2^- \tag{2.48}$$

$$Fe^{2+} + \tfrac{1}{4}O_2 = Fe^{3+} + \tfrac{1}{2}O^{2-} \tag{2.49}$$

$$Fe^{3+} + 2O^{2-} = FeO_2^- \tag{2.50}$$

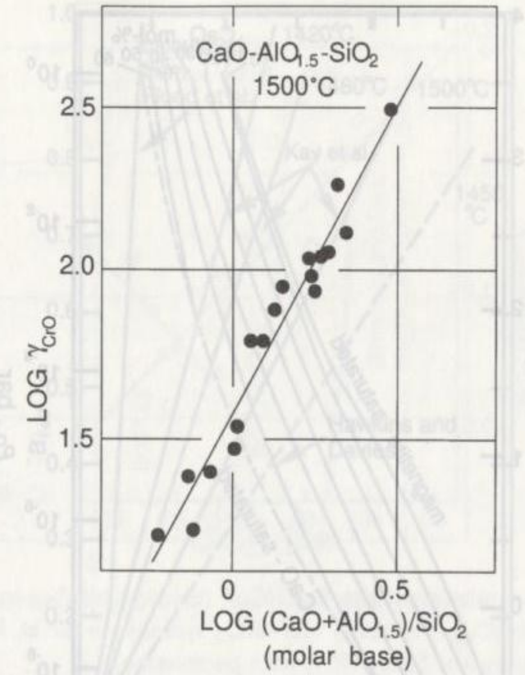

Figure 2.30 Relation between γ_{CrO} and molar $(CaO+AlO_{1.5})/SiO_2$ for the CaO–$AlO_{1.5}$–SiO_2 system (Maeda and Sano, 1982).

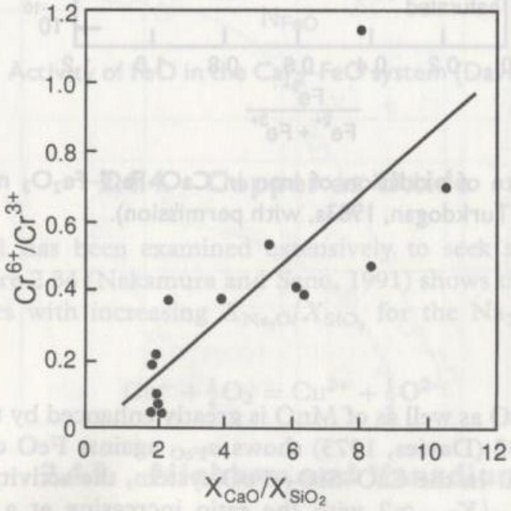

Figure 2.31 Basicity dependence of Cr^{6+}/Cr^{3+} ratio in MgO–SiO_2–CaO–CrO_x melts at 1873 K in air (Morita et al., 1988).

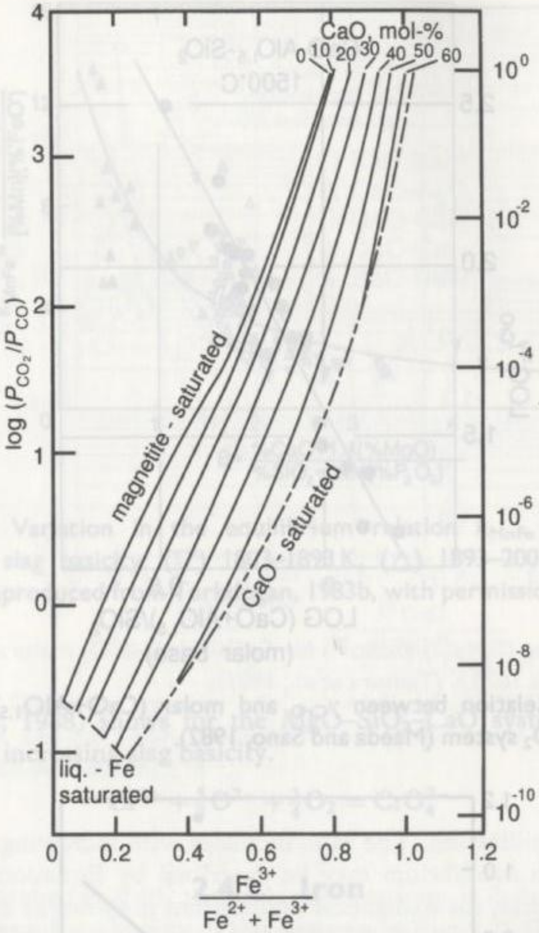

Figure 2.32 State of oxidation of iron in CaO–FeO–Fe_2O_3 melts at 1823 K (Reproduced from Turkdogan, 1983a, with permission).

The activity of FeO as well as of MnO is greatly enhanced by the presence of halide. Figure 2.33 (Davies, 1973) shows a_{FeO} against FeO content for the FeO–CaF_2 system. In the CaO–SiO_2–FeO system, the activity of FeO has a maximum at $X_{CaO}/X_{SiO_2} \cong 2$ with the ratio increasing at a constant FeO content. This may be explained by a fact that the orthosilicate composition is most stable in the CaO–SiO_2 system.

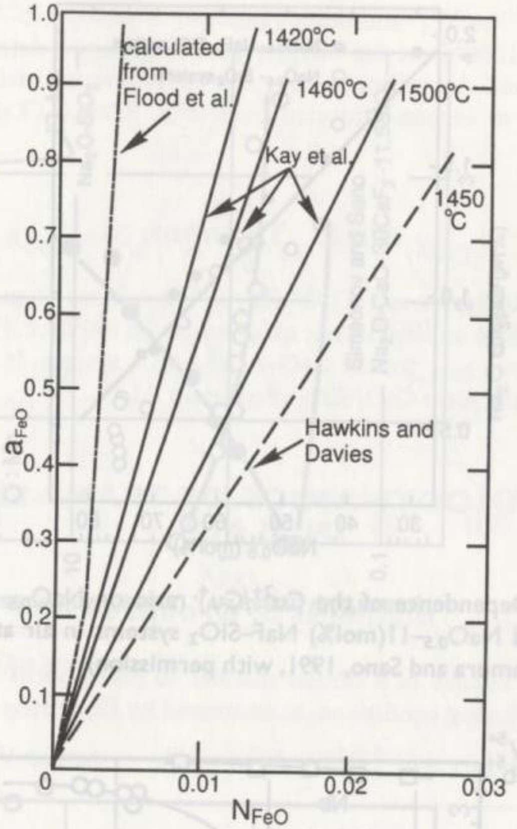

Figure 2.33 Activity of FeO in the CaF_2–FeO system (Davies, 1973).

2.4.4. Copper as Oxide

Equation 2.51 has been examined extensively to seek a measure for slag basicity. Figure 2.34 (Nakamura and Sano, 1991) shows that the ratio Cu^{2+}/Cu^+ decreases with increasing X_{Na_2O}/X_{SiO_2} for the Na_2O–SiO_2 system at 1373 K.

$$Cu^+ + \tfrac{1}{4}O_2 = Cu^{2+} + \tfrac{1}{2}O^{2-} \qquad (2.51)$$

2.4.5. Niobium and Vanadium

These metals exist in basic slags mostly as anions, as shown in Fig. 2.35 (Tsukihashi et al., 1985), which demonstrates that the valence of vanadium

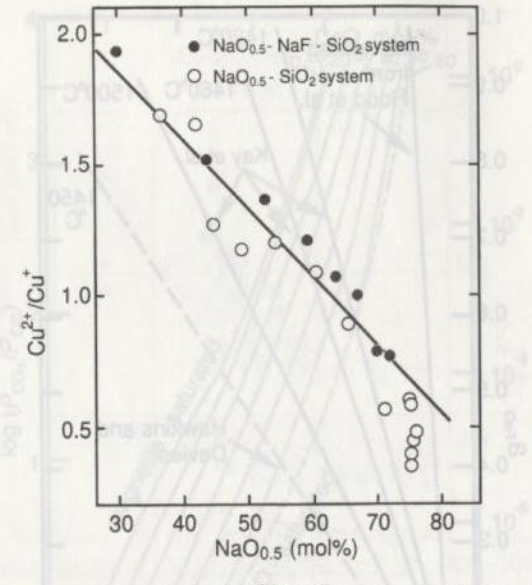

Figure 2.34 Dependence of the Cu^{2+}/Cu^{+} ratio on $NaO_{0.5}$ in mol% for the $NaO_{0.5}$–SiO_2 and $NaO_{0.5}$–11(mol%) NaF–SiO_2 systems in air at 1373 K (Reproduced from Nakamura and Sano, 1991, with permission).

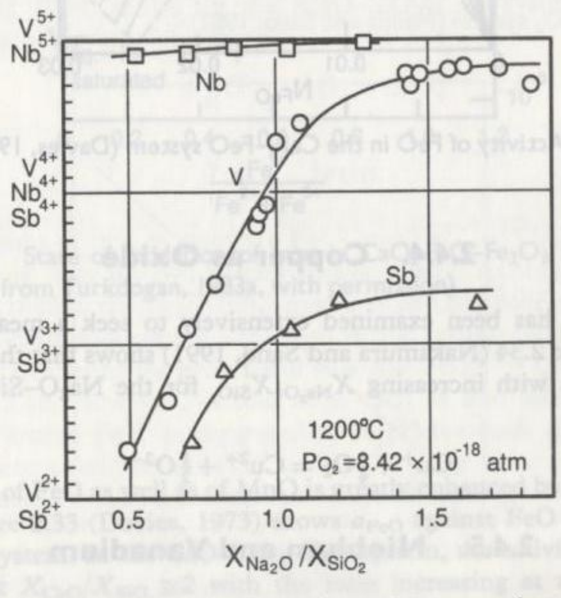

Figure 2.35 Change in valences of vanadium, niobium, and antimony with the composition of the Na_2O–SiO_2 system at 1473 K (Reproduced from Tsakihashi et al., 1985a, with permission).

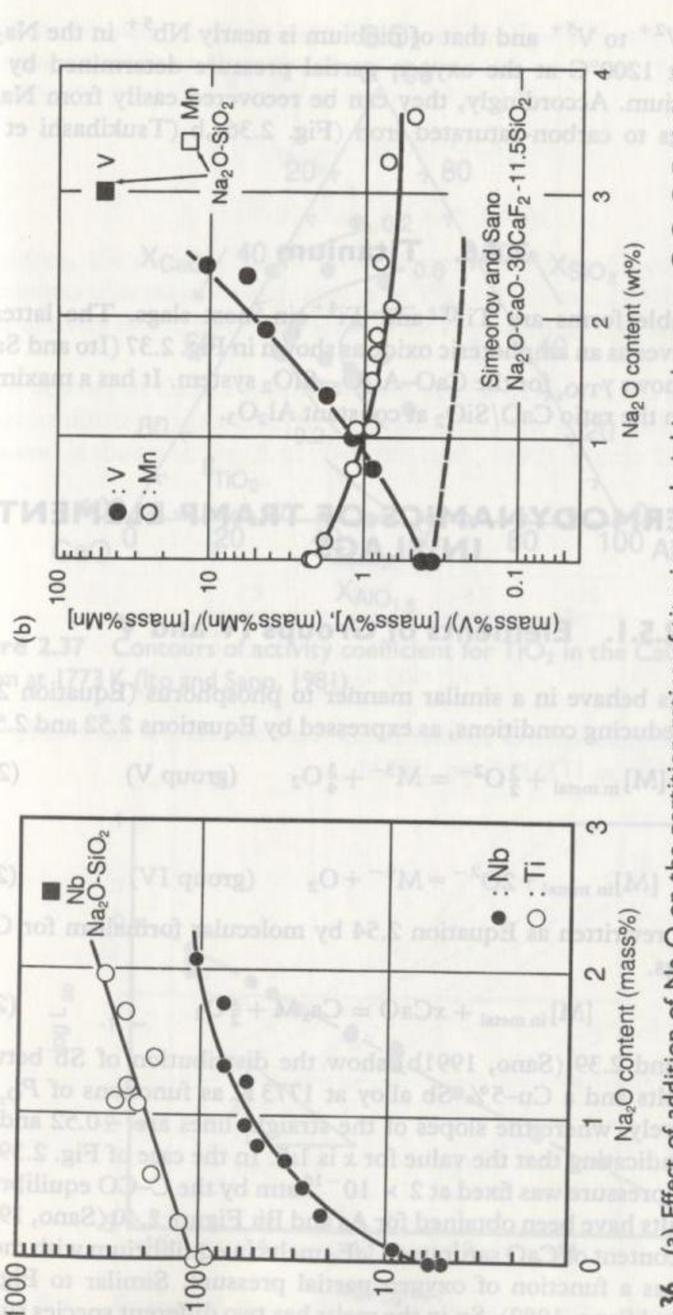

Figure 2.36 (a) Effect of addition of Na_2O on the partition ratios of titanium and niobium between CaO–CaF_2–SiO_2 fluxes saturated with CaO and 3CaO·SiO_2 and carbon-saturated iron at 1573 K with $P_{O_2} = 2.80 \times 10^{-12}$ Pa. (b) Effect of addition of Na_2O on the partition ratios of vanadium and manganese between CaO–CaF_2–SiO_2 fluxes saturated with CaO and 3CaO·SiO_2 and carbon-saturated iron at 1573 K with $P_{O_2} = 2.80 \times 10^{-12}$ Pa (Reproduced from Tsukihashi et al., 1988, with permission).

changes from V^{2+} to V^{5+} and that of niobium is nearly Nb^{5+} in the Na_2O–SiO_2 system at 1200°C at the oxygen partial pressure determined by the C–CO equilibrium. Accordingly, they can be recovered easily from Na_2O-containing slags to carbon-saturated iron (Fig. 2.36a,b (Tsukihashi et al., 1988)).

2.4.6. Titanium

Titanium's stable forms are Ti^{3+} and Ti^{4+} in most slags. The latter in particular behaves as an amphoteric oxide as shown in Fig. 2.37 (Ito and Sano, 1981), which shows γ_{TiO_2} for the $CaO–Al_2O_3–SiO_2$ system. It has a maximum with increase in the ratio CaO/SiO_2 at constant Al_2O_3.

2.5. THERMODYNAMICS OF TRAMP ELEMENTS IN SLAGS

2.5.1. Elements of Groups IV and V

These elements behave in a similar manner to phosphorus (Equation 2.12) under highly reducing conditions, as expressed by Equations 2.52 and 2.53.

$$[M]_{\text{in metal}} + \tfrac{3}{2}O^{2-} = M^{3-} + \tfrac{3}{4}O_2 \qquad \text{(group V)} \qquad (2.52)$$

or

$$[M]_{\text{in metal}} + 2O^{2-} = M^{4-} + O_2 \qquad \text{(group IV)} \qquad (2.53)$$

which may be rewritten as Equation 2.54 by molecular formalism for CaO-containing slags.

$$[M]_{\text{in metal}} + x\text{CaO} = \text{Ca}_x\text{M} + \tfrac{x}{2}O_2 \qquad (2.54)$$

Figures 2.38 and 2.39 (Sano, 1991b) show the distribution of Sb between $CaO–CaF_2$ melts and a Cu–5% Sb alloy at 1773 K as functions of P_{O_2} and a_{CaO}, respectively, where the slopes of the straight lines are −0.52 and 1.2, respectively, indicating that the value for x is 1.5. In the case of Fig. 2.39, the oxygen partial pressure was fixed at 2×10^{-16} atm by the C–CO equilibrium.

Similar results have been obtained for As and Bi. Figure 2.40 (Sano, 1991b) shows the tin content of CaO saturated CaF_2 melts in equilibrium with molten tin at 1773 K as a function of oxygen partial pressure. Similar to Fig. 2.5 (Momokawa and Sano, 1982), Sn in the melts has two different species such as Sn^{4-} and SnO_4^{4-} depending upon P_{O_2} as shown in Figure 2.40. Lead is shown to be stable as Pb^{4-} below approximately $P_{O_2} = 10^{-19}$ atm.

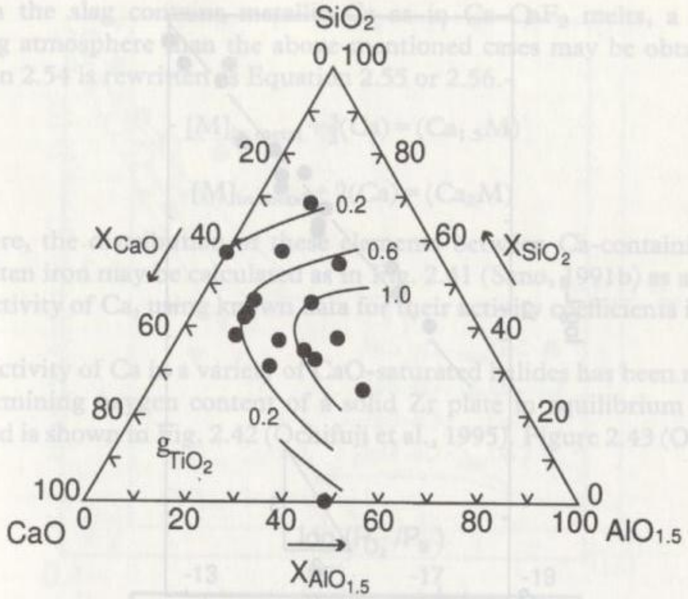

Figure 2.37 Contours of activity coefficient for TiO_2 in the $CaO–AlO_{1.5}–SiO_2$ system at 1773 K (Ito and Sano, 1981).

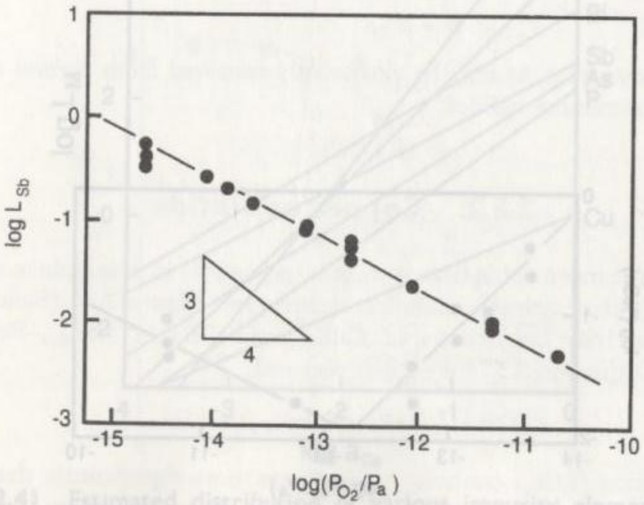

Figure 2.38 Dependence of Sb distribution between Cu and $CaO–CaF_2$ melts on oxygen partial pressure at 1773 K (Sano, 1991b).

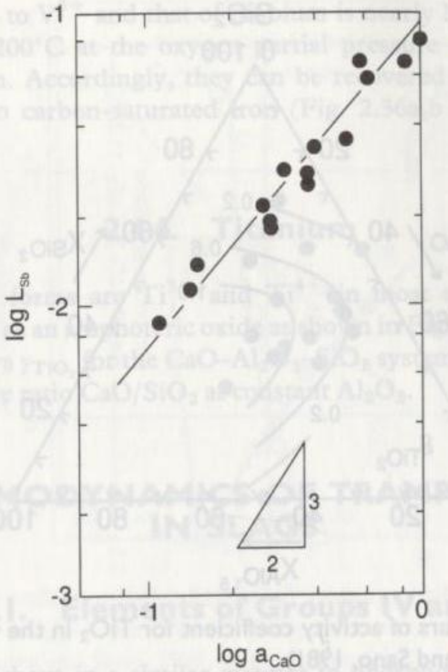

Figure 2.39 Dependence of Sb distribution between Cu and CaO–CaF_2 melts on the CaO activity at 1773 K (Sano, 1991b).

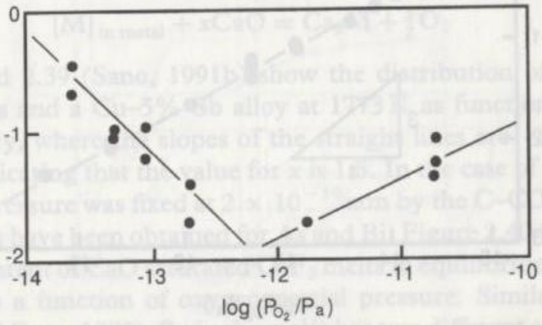

Figure 2.40 Dependence of Sn content of CaO–CaF_2 melts on oxygen partial pressure at 1773 K (Sano, 1991b).

When the slag contains metallic Ca as in Ca–CaF_2 melts, a far more reducing atmosphere than the above-mentioned cases may be obtained and Equation 2.54 is rewritten as Equation 2.55 or 2.56.

$$[M]_{\text{in metal}} + \tfrac{3}{2}(Ca) = (Ca_{1.5}M) \qquad (2.55)$$

or

$$[M]_{\text{in metal}} + 2(Ca) = (Ca_2M) \qquad (2.56)$$

Therefore, the distribution of these elements between Ca-containing melts and molten iron may be calculated as in Fig. 2.41 (Sano, 1991b) as a function of the activity of Ca, using known data for their activity coefficients in molten iron.

The activity of Ca in a variety of CaO-saturated halides has been measured by determining oxygen content of a solid Zr plate in equilibrium with the melts and is shown in Fig. 2.42 (Ochifuji et al., 1995). Figure 2.43 (Ochifuji et

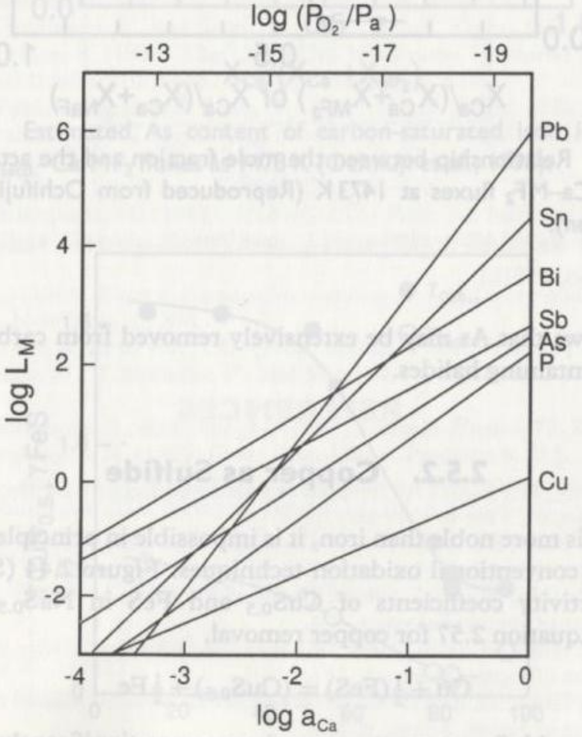

Figure 2.41 Estimated distribution of various impurity elements between molten iron and CaO–CaF_2 melts at 1773 K as a function of the calcium activity or oxygen partial pressure (Sano, 1991b).

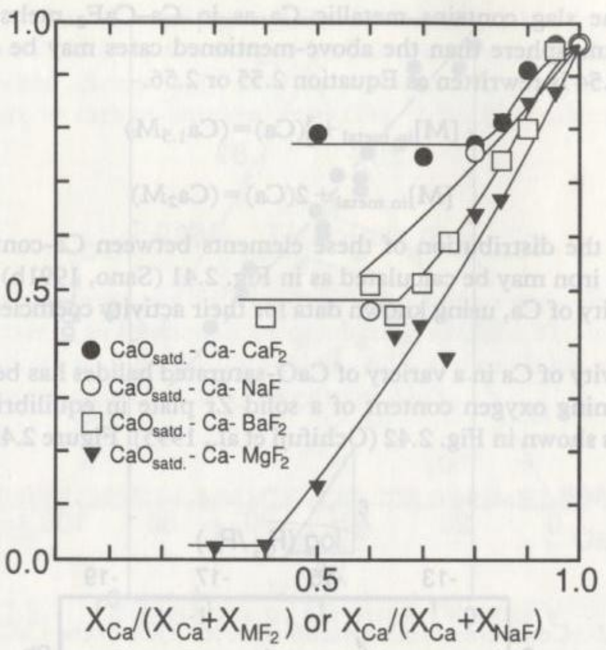

Figure 2.42 Relationship between the mole fraction and the activity of Ca in the $CaO_{satd.}$–Ca–MF_2 fluxes at 1473 K (Reproduced from Ochifuji et al., 1995, with permission).

al., 1995) shows that As may be extensively removed from carbon saturated iron by Ca-containing halides.

2.5.2. Copper as Sulfide

Since copper is more noble than iron, it is impossible in principle to remove it from iron by conventional oxidation techniques. Figure 2.44 (Sano, 1991b) shows the activity coefficients of $CuS_{0.5}$ and FeS in $NaS_{0.5}$–FeS melts, considering Equation 2.57 for copper removal.

$$Cu + \tfrac{1}{2}(FeS) = (CuS_{0.5}) + \tfrac{1}{2}Fe \tag{2.57}$$

With increasing $NaS_{0.5}$ content, $\gamma_{CuS_{0.5}}$ drops more significantly than γ_{FeS} so that the distribution ratio of Cu, L_{Cu}, barely drops, as shown in Fig. 2.45 (Sano, 1991b). However, the value for L_{Cu} is rather low, indicating the difficulty of using this slag for industrial application.

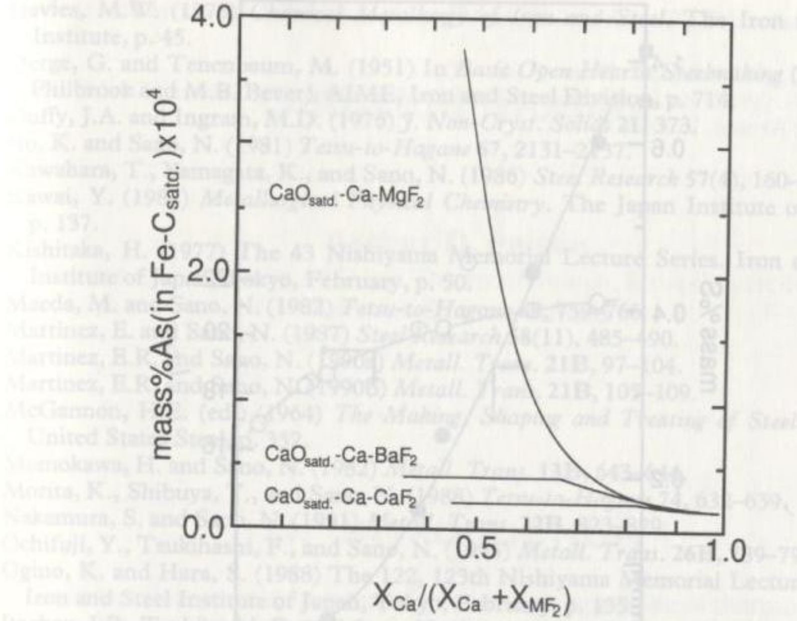

Figure 2.43 Estimated As content of carbon-saturated iron in equilibrium with the $CaO_{satd.}$-Ca-MF_2 fluxes at 1473 K (Ochifuji et al., 1995).

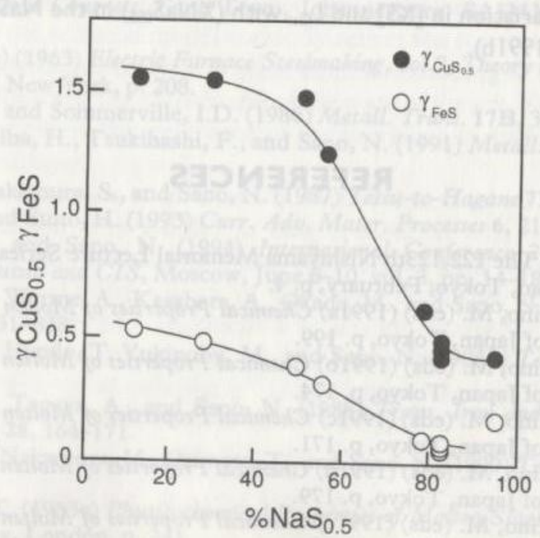

Figure 2.44 Variations in the activity coefficients of $CuS_{0.5}$(l) and FeS(l) with ($\%NaS_{0.5}$) in the $NaS_{0.5}$–FeS system at 1473 K (Sano, 1991b).

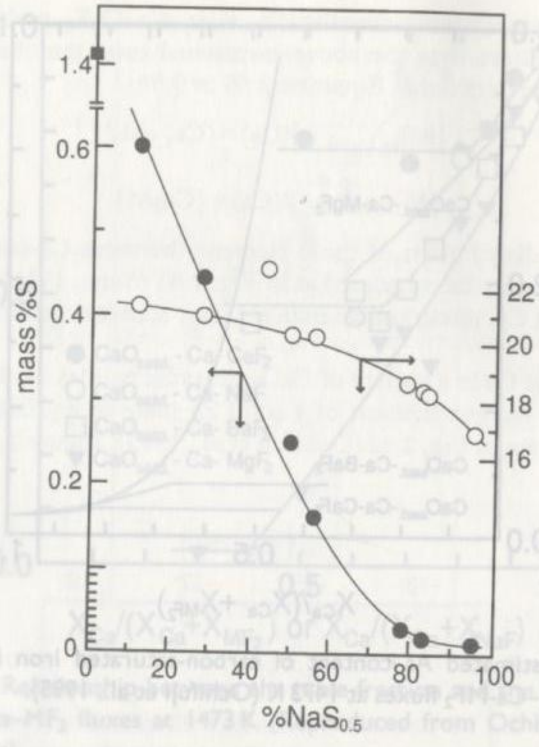

Figure 2.45 Variation in [%S] and L_{Cu} with ($\%NaS_{0.5}$) in the $NaS_{0.5}$–FeS system at 1473 K (Sano, 1991b).

REFERENCES

Ban-ya, S. (1988) The 122,123th Nishiyama Memorial Lecture Series. Iron and Steel Institute of Japan, Tokyo, February, p. 4.

Ban-ya, S. and Hino, M. (eds) (1991a) *Chemical Properties of Molten Slags*, Iron and Steel Institute of Japan, Tokyo, p. 199.

Ban-ya, S. and Hino, M. (eds) (1991b) *Chemical Properties of Molten Slags*, Iron and Steel Institute of Japan, Tokyo, p. 174.

Ban-ya, S. and Hino, M. (eds) (1991c) *Chemical Properties of Molten Slags*, Iron and Steel Institute of Japan, Tokyo, p. 171.

Ban-ya, S. and Hino, M. (eds) (1991d) *Chemical Properties of Molten Slags*, Iron and Steel Institute of Japan, Tokyo, p. 179.

Ban-ya, S. and Hino, M. (eds) (1991e) *Chemical Properties of Molten Slags*, Iron and Steel Institute of Japan, Tokyo, p. 196.

Ban-ya, S. and Hino, M. (eds) (1991f) *Chemical Properties of Molten Slags*, Iron and Steel Institute of Japan, Tokyo, p. 187.

Davies, M.W. (1973) *Chemical Metallurgy of Iron and Steel*. The Iron and Steel Institute, p. 45.

Derge, G. and Tenenbaum, M. (1951) In *Basic Open Hearth Steelmaking* (ed. W.O. Philbrook and M.B. Bever). AIME, Iron and Steel Division, p. 714.

Duffy, J.A. and Ingram, M.D. (1976) *J. Non-Cryst. Solids* **21**, 373.

Ito, K. and Sano, N. (1981) *Tetsu-to-Hagane* **67**, 2131–2137.

Kawahara, T., Yamagata, K., and Sano, N. (1986) *Steel Research* **57**(4), 160–165.

Kawai, Y. (1982) *Metallurgical Physical Chemistry*. The Japan Institute of Metals, p. 137.

Kishitaka, H. (1977) The 43 Nishiyama Memorial Lecture Series. Iron and Steel Institute of Japan, Tokyo, February, p. 50.

Maeda, M. and Sano, N. (1982) *Tetsu-to-Hagane* **68**, 759–766.

Martinez, E. and Sano, N. (1987) *Steel Research* **58**(11), 485–490.

Martinez, E.R. and Sano, N. (1990a) *Metall. Trans.* **21B**, 97–104.

Martinez, E.R. and Sano, N. (1990b) *Metall. Trans.* **21B**, 105–109.

McGannon, H.E. (ed.) (1964) *The Making, Shaping and Treating of Steel 8th edn*. United States Steel, p. 352.

Momokawa, H. and Sano, N. (1982) *Metall. Trans.* **13B**, 643–644.

Morita, K., Shibuya, T., and Sano, N. (1988) *Tetsu-to-Hagane* **74**, 632–639.

Nakamura, S. and Sano, N. (1991) *Metall. Trans.* **22B**, 823–829.

Ochifuji, Y., Tsukihashi, F., and Sano, N. (1995) *Metall. Trans.* **26B**, 789–794.

Ogino, K. and Hara, S. (1988) The 122, 123th Nishiyama Memorial Lecture Series. Iron and Steel Institute of Japan, Tokyo, February, p. 135.

Rachev, I.P., Tsukihashi, F., and Sano, N. (1991) *Metall. Trans.* **22B**, 333–338.

Sano, N. (1991a) *ELLIOTT Symposium Proceedings*. Iron and Steel Society, Warrendale, PA, pp. 173–188.

Sano, N. (1991b) *Bull. Japan Inst. of Metals* **30**, 905–912.

Sano, N. and Katayama, H. (1992). *INFACON6. Proc. 1st International Chromium, Steel and Alloys Congress*, Cape Town, Johannesburg. SAIMM, vol. 2, pp. 25–33.

Sims, C.E. (ed.) (1963) *Electric Furnace Steelmaking, vol.2, Theory and Fundamentals*. Interscience, New York, p. 208.

Sosinsky, D.C. and Sommerville, I.D. (1986) *Metall. Trans.* **17B**, 331.

Tagaya, A., Chiba, H., Tsukihashi, F., and Sano, N. (1991) *Metall. Trans.* **22B**, 499–502.

Tamura, Y., Nakamura, S., and Sano, N. (1987) *Tetsu-to-Hagane* **73**, 2214–2218.

Tomioka, K. and Suito, H. (1993) *Curr. Adv. Mater. Processes* **6**, 215.

Tsukihashi, F. and Sano, N. (1994) *International Conference 21st Century Steel Industry of Russia and CIS*, Moscow, June 6–10, vol. 3, pp. 14–18.

Tsukihashi, F., Werme, A., Kasahara, A., Okada, M., and Sano, N. (1985a) *Tetsu-to-Hagane* **71**, 831–838.

Tsukihashi, F., Hyodo, T. Yukinobu, M., and Sano, N. (1985b) *Tetsu-to-Hagane* **71**, 823–830.

Tsukihashi, F., Tagaya, A., and Sano, N. (1988) *Trans. Iron and Steel Institute of Japan, Tokyo* **28**, 164–171.

Tsukihashi, F., Nakamura, M., Orimoto, T., and Sano, N. (1990) *Tetsu-to-Hagane* **76**, 1664–1671.

Turkdogan, E.T. (1983a) *Physicochemical Properties of Molten Slags and Glasses*. The Metals Society, London, p. 241.

Turkdogan, E.T. (1983b) *Physicochemical Properties of Molten Slags and Glasses*. The Metals Society, London, p. 281.

Uo, M., Sakurai, E., Tsukihashi, F., and Sano, N. (1989) *Steel Research* **60**(11), 496–502.

Wagner, C. (1975) *Metall. Trans. B* **6B**, 405.

Ward, R.G. (1962) *An Introduction to The Physical Chemistry of Iron and Steel Making*. Edward Arnold, London.

3

Solution models

Arthur D. Pelton

Centre de Recherche en Calcul Thermochimique, Ecole Polytechnique,
Montreal, Quebec, Canada

3.1. INTRODUCTION

Solution models permit the interpolation and extrapolation of thermodynamic data and the prediction of the thermodynamic properties of multicomponent solutions. Coupling of evaluated solution databases for metals, mattes, slags, etc. with general Gibbs energy minimization programs permits the calculation of equilibrium conditions in multicomponent, multiphase industrial systems. In order to be useful in interpolations, extrapolations, and predictions, it is essential that the solution model correctly reflect the structure of the solution.

The goal of this chapter is to provide an understanding of the chemistry and of the applicability of the models and of the state of the art. Not all details of all models can be given, but reference to the literature is made for readers who wish to delve deeper.

The thermodynamics of solutions is discussed in Chapter 1; see also Pelton (1991). A notation very similar to that of Chapter 1 is maintained in the present chapter except that lower-case symbols are used for molar properties. Thus, g^{fcc} is the Gibbs energy of one mole of an fcc solution; g_1 is the partial Gibbs energy of component 1 of a solution; $\Delta g_1 = RT \ln a_1$ is the relative partial Gibbs energy; $\Delta g_m = (X_1 \Delta g_1 + X_2 \Delta g_2 + \ldots)$ is the integral molar Gibbs energy of mixing; g^E is the molar excess Gibbs energy; and $g_1^E = RT \ln \gamma_1$ is the partial excess Gibbs energy.

3.2. IDEAL RAOULTIAN SOLUTIONS

Ideal Raoultian solutions were discussed in Chapter 1. In a binary solution the ideal substitutional solution model assumes that atoms or molecules of

ADVANCED PHYSICAL CHEMISTRY FOR PROCESS METALLURGY
ISBN 0-12-618920-X

Copyright © 1997 Academic Press Ltd
All rights of reproduction in any form reserved

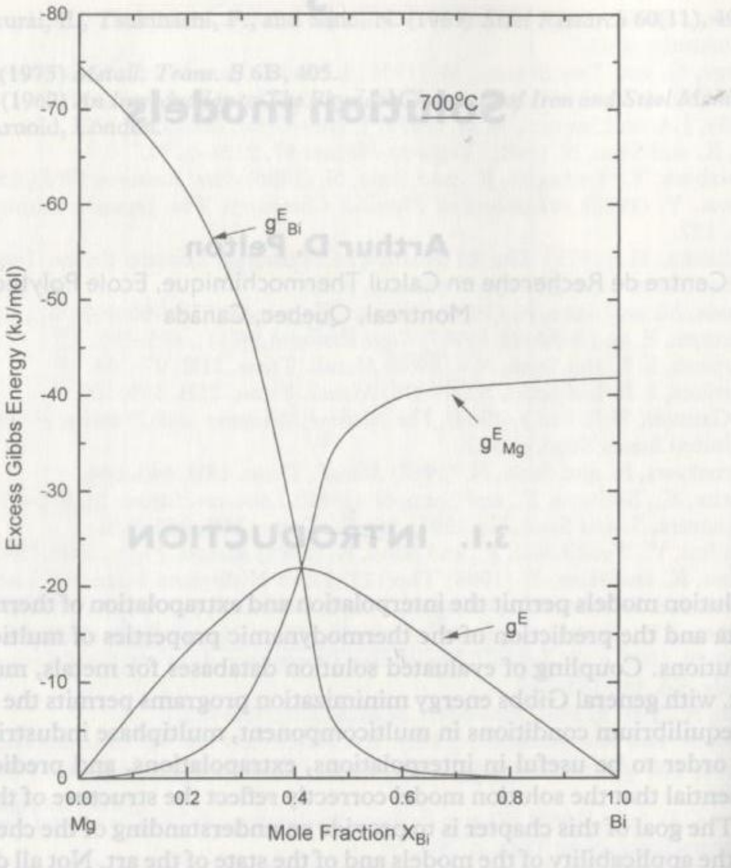

Figure 3.1 Excess Gibbs energies of liquid Mg–Bi solutions at 700°C. (Data from Hultgren et al., 1973.)

components 1 and 2 are very similar so that there will be negligible change in bonding energy or volume upon mixing. Hence, $\Delta h_m^{\text{ideal}} = 0$. Furthermore, and for the same reasons, the atoms or molecules will be randomly distributed over the lattice sites. (In the case of a liquid solution, we can think of the 'lattice sites' as the instantaneous atomic positions.) Boltzmann's equation can then be used (Chapter 1, Equation 1.18) to calculate the ideal, or 'Bragg–Williams', entropy of mixing: $\Delta s_m^{\text{ideal}} = -R\,(X_1 \ln X_1 + X_2 \ln X_2)$.

For liquid Fe–Ni solutions, for example, we might expect the ideal substitutional solution model to apply reasonably well. For these solutions the difference between Δg_m and $\Delta g_m^{\text{ideal}}$ is about 20% (Hultgren et al., 1973), which is, indeed, relatively small. In most solutions encountered in process metallurgy, deviations from ideality are much larger. For example in Fig. 3.1 we see that g^E for liquid Mg–Bi solutions is over three times as large as $\Delta g_m^{\text{ideal}}$.

3.3. POLYNOMIAL MODELS

3.3.1. Regular Solution Theory

A simple *regular solution* in a binary system with components 1 and 2 is defined as one for which:

$$g^E = \alpha X_1 X_2 \qquad g_1^E = \alpha X_2^2 \qquad g_2^E = \alpha X_1^2 \tag{3.1}$$

where α is a parameter independent of composition. Several liquid and solid solutions conform approximately to regular solution behavior, particularly if g^E is small. As an example, liquid Fe–Ni solutions at 1600°C can be approximated to within 0.5 kJ mol^{-1} by the regular equation: $g^E = 11.2\, X_{Fe} X_{Ni}$ kJ mol^{-1}.

To understand why this is so, the very simple model discussed in Chapter 1 suffices. Assume that the atoms or molecules of components 1 and 2 are of similar size and electronic structure such that they form a nearly random substitutional solution. Hence, the configurational entropy of mixing will be nearly ideal. We assume next that the bond energies ε_{11}, ε_{22}, and ε_{12} of nearest neighbor pairs are independent of T and composition, and that the average nearest neighbor coordination number, Z, is also constant. Finally, we assume that the enthalpy of mixing results mainly from the change in the total energy of nearest neighbor bonds. In one mole of solution there are $(N^0 Z/2)$ pair bonds where N^0 is Avogadro's number. Since the distribution is random, the probabilities that a given bond is a 1–1, a 2–2, or a 1–2 bond are X_1^2, X_2^2, and $2X_1X_2$, respectively. The molar enthalpy of mixing is then equal to the sum of the energies of the pair bonds in one mole of solution, less the energy of the 1–1 bonds in X_1 mole of pure component 1 and the energy of the 2–2 bonds in one mole of pure component 2,

$$\begin{aligned}\Delta h_m &= (N^0 Z/2)(X_1^2\varepsilon_{11} + X_2^2\varepsilon_{22} + 2X_1X_2\varepsilon_{12} - X_1\varepsilon_{11} - X_2\varepsilon_{22})\\ &= (N^0 Z)(\varepsilon_{12} - (\varepsilon_{11} + \varepsilon_{22})/2)X_1X_2 = C_1X_1X_2\end{aligned} \tag{3.2}$$

where C_1 is constant. A similar argument, with the 'vibrational entropies of the nearest neighbor pair bonds', σ_{ij}, replacing ε_{ij}, gives the nonconfigurational excess entropy term $s^{E(\text{nonconfig})} = C_2X_1X_2$, where C_2 is constant. Hence, Equation 3.1 results with $\alpha = (C_1 - C_2T)$.

Simple nonpolar molecular solutions and simple ionic solutions often exhibit approximately regular behavior. In such solutions with van der Waals or coulombic forces, the assumption of the additivity of pair bonds is probably realistic. For alloys, the concept of a pair bond is, at best, vague, and metallic solutions tend to exhibit larger deviations from regular behavior. The approximately regular behavior of liquid Fe–Ni solutions has already been mentioned. Liquid Mg–Bi solutions (Fig. 3.1), on the other hand, do not even come close to being regular.

A fundamental problem with regular solution theory arises from the assumption of random mixing. If 1–2 bonds are relatively 'stronger' than 1–1 and 2–2 bonds, then there will be a tendency for the number of 1–2 bonds to be greater than that in a random mixture, since such nonrandomness will decrease the Gibbs energy. Similarly, if 1–2 bonds are relatively weaker, then the number of 1–2 bonds will be less than that in a random distribution. In either case, the configurational entropy is no longer ideal. This problem will be discussed in section 3.6.

3.3.2. Polynomial Expansions

It has been found that the excess properties of simple binary substitutional solutions can often be adequately represented by expanding the enthalpy and excess entropy as polynomials in the component mole fractions:

$$g^E = \alpha X_1 X_2 \qquad \alpha = {}^0L_{12} + {}^1L_{12}(X_1 - X_2) + {}^2L_{12}(X_1 - X_2)^2 + \cdots \tag{3.3}$$

where the ${}^kL_{12}$ are empirical coefficients which, in general, are (usually linear) functions of T. If the series is truncated after the first term, then the solution is regular. The polynomial representation can be considered to be an empirical extension of regular solution theory, and the fundamental assumptions of the polynomial model are the same as those of the regular solution model, namely a substitutional solution with close to random mixing.

As an example, g^E for liquid Fe–Ni solutions at 1600°C can be represented by the sub-regular equation: $g^E = X_{Fe}X_{Ni}\,(-11.22 + 6.16\,(X_{Fe} - X_{Ni}))$ kJ mol^{-1}. This reproduces the experimental data (Hultgren et al., 1973) to ± 0.1 kJ mol^{-1}, which is well within the experimental precison. On the other hand, g^E of liquid Mg–Bi solutions (Fig. 3.1) cannot be adequately represented by polynomial expansions unless an excessive number of terms is employed. This shows that for these solutions the basic assumptions of the model are incorrect.

3.3.3. Interaction Parameter Formalism

The interaction parameter formalism for dilute solutions of several solutes in a solvent was discussed in Chapter 1. The formalism has been modified (Pelton and Bale, 1986; Bale and Pelton, 1990) to be consistent with the Gibbs–Duhem and other necessary thermodynamic relationships. With this modification, the interaction parameter formalism is a polynomial representation which can be simply rearranged into other polynomial forms such as Equations 3.3 or 3.4.

A fundamental weakness of the interaction parameter formalism is the use of ideal configurational entropy terms. For example, a solution of Al and O in molten Fe is treated as a randomly mixed solution, whereas in reality the formation of 'complexes' such as AlO is expected, owing to the strong attractive interaction between Al and O. Neither the temperature dependence nor the composition dependence of such entropic contributions to g^E can be represented simply by the use of a very negative ε_{AlO}. Rather, complex formation should be explicitly taken into account. For further discussions and examples, see Dessureault (1993), Bouchard and Bale (1995a,b), and Heuzey and Pelton (1996).

3.4. PHASE DIAGRAM CALCULATION/OPTIMIZATION

Phase diagrams can be calculated if expressions for the Gibbs energies of the phases as functions of T and composition are available. A primary goal of solution modeling is to provide such Gibbs energy equations in order to permit the calculation of the conditions for phase equilibria in multicomponent systems. Conversely, experimental phase diagrams are a source of thermodynamic data which can be used to test the solution models and to determine the model parameters.

A critical thermodynamic evaluation of a binary system can be carried out by simultaneous *optimization* of all available thermodynamic and phase equilibrium data. Such data may include phase boundary measurements, component activities in solutions, calorimetric data, Gibbs energies of compounds, etc. All data are simultaneously optimized, by a least-squares or similar technique, to obtain one self-consistent set of model parameters, describing the Gibbs energies of all phases, which best reproduces all the data. The resultant parameters can be conveniently stored in computer databases.

For many solutions, a polynomial model is often sufficient. However, if the model equations are subsequently used to extrapolate the data, or as a basis for estimating properties of multicomponent solutions, then it is essential that physically realistic models be used, and a polynomial model may not be adequate.

Techniques of optimization have been discussed by Lukas et al. (1977), Dörner et al. (1980), Bale and Pelton (1983), and Königsberger and Eriksson (1995). A large number of optimizations of binary systems can be found in the *Calphad Journal* (Pergamon Press).

3.4.1. Ternary and Multicomponent Phase Diagram Calculation/Estimation with Polynomial Models

Among 70 metallic elements can be formed 70!/3! 67! = 54 740 ternary and 916 895 quaternary systems. Hence, it is very important to have means of estimating the thermodynamic properties and phase diagrams of ternary and higher-order systems from optimized data for binary subsystems.

To this end, several 'geometrical models', based upon regular solution theory, have been proposed. Three of these are illustrated for a ternary system in Fig. 3.2. In each of these models, g^E in a ternary solution at a composition point p is estimated from the excess Gibbs energies in the three binary subsystems at points a, b, and c by the equation

$$g^E = X_1X_2\alpha_{12(a)} + X_2X_3\alpha_{23(b)} + X_3X_1\alpha_{31(c)} \tag{3.4}$$

where $\alpha_{12(a)}$, $\alpha_{23(b)}$, and $\alpha_{31(c)}$ are the binary 'α-functions', as defined in Equation 3.3, evaluated at points a, b, and c.

If the three binary α-functions are constants, independent of composition, then Equation 3.4 is the expression for g^E of a ternary regular solution. In this case, the three models illustrated in Fig. 3.2 are equivalent. When the α-functions are not independent of composition, then the Kohler model (Kohler, 1960) assumes that the contribution to g^E from pair interactions between i and j atoms or molecules is constant along lines of constant X_j/X_i. The asymmetric Toop model (Toop, 1965) also assumes this for 2–3 interactions, but assumes that the contribution from 1–2 and 3–1 interactions is constant along lines of constant X_1. The Muggianu model (Muggianu et al., 1975) assumes constant i–j interactions along lines of constant $(X_i - X_j)$. Other similar geometrical models have been proposed. If the binary solutions are approximately regular ($\alpha_{ij} \approx$ constant), then all these models give similar estimations of g^E. If the binary solutions exhibit large deviations from regular behavior, then none of these models can be used with confidence, because they are all based upon extensions of regular solution theory.

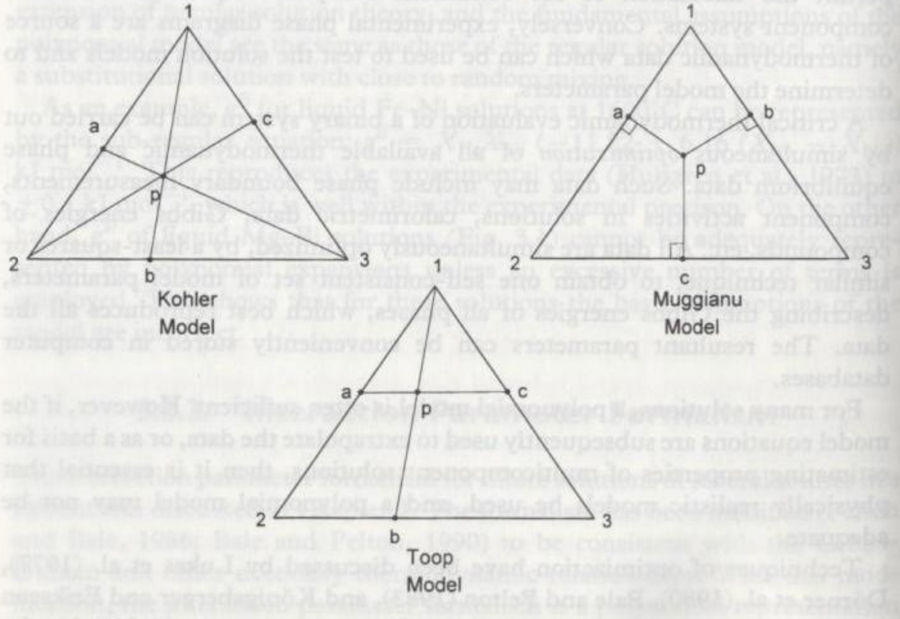

Figure 3.2 Three geometrical models for estimating thermodynamic properties of ternary solutions from binary data.

If some experimental data are available for the ternary system, then 'ternary terms' of the form $aX_1^iX_2^jX_3^k$ can be added to Equation 3.4, where $i > 0$, $j > 0$, and $k > 0$ and a is an adjustable parameter. The extension of the geometrical models to systems of four or more components is straightforward. For discussions, see Ansara (1979), Spencer and Barin (1979), Hillert (1980), and Pelton (1988).

A large number of ternary and multicomponent phase diagram calculations/estimations can be found in the *Calphad Journal*.

3.5. SUBLATTICE MODELS

The sublattice concept has proved to be very useful in thermodynamic modeling. Sublattice models, which were first developed extensively for molten salt solutions, find application in ceramics, interstitial solutions, intermetallic solutions, etc.

3.5.1. One Sublattice Occupied By Only One Species

In the simplest limiting case, one sublattice is occupied by only one species. For example, liquid and solid MgO–CaO solutions can be modeled by assuming an anionic sublattice occupied only by O^{2-} ions, while Mg^{2+} and Ca^{2+} ions mix on a cationic sublattice. In this case the model is formally the same as that of a simple substitutional solution, because the site fractions X_{Mg} and X_{Ca} of Mg^{2+} and Ca^{2+} cations on the cationic sublattice are numerically equal to the overall component mole fractions X_{MgO} and X_{CaO}. Solid and liquid MgO–CaO solutions have been shown (Wu et al., 1993a) to be well represented by simple polynomial equations.

As a second example, the intermetallic ε-FeSb phase exhibits nonstoichiometry toward excess Fe. This phase was modeled (Pei et al., 1995) as a solution of Fe and stoichiometric FeSb by assuming two sublattices: an 'Fe' sublattice occupied only by Fe atoms and an 'Sb sublattice' occupied by both Fe and Sb atoms such that, per gram atom,

$$\Delta g_m = 0.5RT(y_{\mathrm{Fe}} \ln y_{\mathrm{Fe}} + y_{\mathrm{Sb}} \ln y_{\mathrm{Sb}}) + \alpha y_{\mathrm{Fe}} y_{\mathrm{Sb}} \tag{3.5}$$

where $y_{\mathrm{Sb}} = (1 - y_{\mathrm{Fe}}) = 2X_{\mathrm{Sb}}$ is the site fraction of Sb atoms on the 'Sb sites' and α is an empirical polynomial in y_{Sb}.

3.5.2. Ionic Solutions

The structure of ionic liquids has been discussed in Chapter 2. Let us take as example a solution, solid or liquid, of NaF, KF, NaCl, and KCl. Since the number of cations must equal the number of anions, this is a ternary system with two composition variables, the cationic fraction $X_{\mathrm{Na}} = (1 - X_{\mathrm{K}}) = n_{\mathrm{Na}}/(n_{\mathrm{Na}} + n_{\mathrm{K}})$ and the anionic fraction $X_{\mathrm{Cl}} = (1 - X_{\mathrm{F}}) = n_{\mathrm{Cl}}/(n_{\mathrm{F}} + n_{\mathrm{Cl}})$ where n_i is the number of ions i in solution. Compositions in such 'reciprocal' ternary systems are usually plotted on a square as in Fig. 3.3.

If the cations are assumed to mix randomly on a cationic sublattice while the anions mix randomly on an anionic sublattice, then the molar Gibbs energy of the solution can be modeled by the following equation which contains an ideal mixing term for each sublattice:

$$\begin{aligned} g = {} & (X_{\mathrm{Na}}X_{\mathrm{Cl}}g^0_{\mathrm{NaCl}} + X_{\mathrm{K}}X_{\mathrm{F}}g^0_{\mathrm{KF}} + X_{\mathrm{Na}}X_{\mathrm{F}}g^0_{\mathrm{NaF}} + X_{\mathrm{K}}X_{\mathrm{Cl}}g^0_{\mathrm{KCl}}) \\ & + RT(X_{\mathrm{Na}} \ln X_{\mathrm{Na}} + X_{\mathrm{K}} \ln X_{\mathrm{K}}) + RT(X_{\mathrm{F}} \ln X_{\mathrm{F}} + X_{\mathrm{Cl}} \ln X_{\mathrm{Cl}}) + g^E \end{aligned} \tag{3.6}$$

where the factor $(X_{\mathrm{Na}}X_{\mathrm{Cl}})$, for example, is the probability, in a random mixture, of finding a Na ion and a Cl ion as nearest neighbors. Differentiation of Equation 3.6 gives the following expression for the activity of NaF:

$$RT \ln a_{\mathrm{NaF}} = -X_{\mathrm{K}}X_{\mathrm{Cl}}\Delta G^{\mathrm{exchange}} + RT \ln(X_{\mathrm{Na}}X_{\mathrm{F}}) + g^E_{\mathrm{NaF}} \tag{3.7}$$

where $\Delta G^{\mathrm{exchange}}$ is the Gibbs energy change for the following *exchange reaction* among the pure salts:

$$\mathrm{NaCl} + \mathrm{KF} = \mathrm{NaF} + \mathrm{KCl}; \qquad \Delta G^{\mathrm{exchange}} = g^0_{\mathrm{NaF}} + g^0_{\mathrm{KCl}} - g^0_{\mathrm{NaCl}} - g^0_{\mathrm{KF}} \tag{3.8}$$

In this example, $\Delta G^{\mathrm{exchange}} < 0$. The salts NaF and KCl are thus said to form the *stable pair*. The first term on the right of Equation 3.7 is positive. The members of the stable pair thus exhibit positive deviations and in Fig. 3.3 this is reflected by the flat liquidus surfaces for NaF and KCl with widely spaced isotherms. That is, the mixing of pure NaF and KCl is unfavorable because it

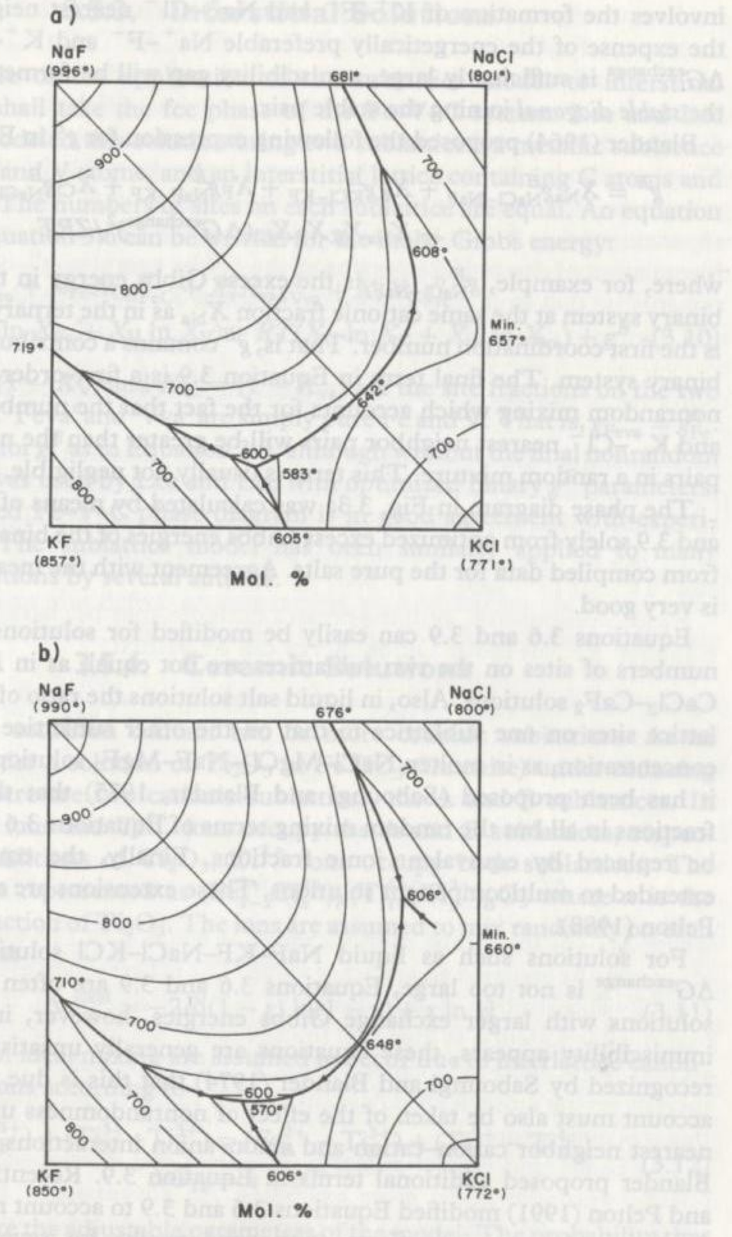

Figure 3.3 Projection of the liquidus surface of the NaF–KF–NaCl–KCl reciprocal ternary system (a) calculated from optimized binary thermodynamic parameters and (b) as reported by Polyakov (1940). (Reproduced from Pelton, 1991, with permission.)

involves the formation of K^+–F^- and Na^+–Cl^- nearest neighbor pairs at the expense of the energetically preferable Na^+–F^- and K^+–Cl^- pairs. If $\Delta G^{\text{exchange}}$ is sufficiently large, a miscibility gap will be formed, centered on the *stable diagonal* joining the stable pair.

Blander (1964) proposed the following expression for g^E in Equation 3.6:

$$g^E = X_{\text{Na}} g^E_{\text{NaCl–NaF}} + X_{\text{K}} g^E_{\text{KCl–KF}} + X_{\text{F}} g^E_{\text{NaF–KF}} + X_{\text{Cl}} g^E_{\text{NaCl–KCl}} - X_{\text{Na}} X_{\text{K}} X_{\text{F}} X_{\text{Cl}} (\Delta G^{\text{exchange}})^2 / ZRT \tag{3.9}$$

where, for example, $g^E_{\text{NaCl–NaF}}$ is the excess Gibbs energy in the NaCl–NaF binary system at the same cationic fraction X_{Na} as in the ternary, and where Z is the first coordination number. That is, g^E contains a contribution from each binary system. The final term in Equation 3.9 is a first-order correction for nonrandom mixing which accounts for the fact that the number of Na^+–F^- and K^+–Cl^- nearest neighbor pairs will be greater than the number of such pairs in a random mixture. This term is usually not negligible.

The phase diagram in Fig. 3.3a was calculated by means of Equations 3.6 and 3.9 solely from optimized excess Gibbs energies of the binary systems and from compiled data for the pure salts. Agreement with the measured diagram is very good.

Equations 3.6 and 3.9 can easily be modified for solutions in which the numbers of sites on the two sublattices are not equal, as in $MgCl_2$–MgF_2–$CaCl_2$–CaF_2 solutions. Also, in liquid salt solutions the ratio of the number of lattice sites on one sublattice to that on the other sublattice can vary with concentration, as in molten NaCl–$MgCl_2$–NaF–MgF_2 solutions. In this case, it has been proposed (Saboungi and Blander, 1975) that the molar ionic fractions in all but the random mixing terms of Equations 3.6 and 3.9 should be replaced by equivalent ionic fractions. Finally, the equations can be extended to multicomponent solutions. These extensions are all discussed by Pelton (1988).

For solutions such as liquid NaF–KF–NaCl–KCl solutions for which $\Delta G^{\text{exchange}}$ is not too large, Equations 3.6 and 3.9 are often sufficient. For solutions with larger exchange Gibbs energies, however, in which liquid immiscibility appears, these equations are generally unsatisfactory. It was recognized by Saboungi and Blander (1974) that this is due to the fact that account must also be taken of the effect of nonrandomness upon the second nearest neighbor cation–cation and anion–anion interactions, and to do this Blander proposed additional terms in Equation 3.9. Recently, Dessureault and Pelton (1991) modified Equations 3.6 and 3.9 to account more rigorously for nonrandom mixing effects, with good results for several molten salt systems with miscibility gaps.

3.5.3. Interstitial Solutions

As an example of the application of the sublattice model to interstitial solutions we shall take the fcc phase of the Fe–V–C system. Lee and Lee (1991) have modeled this solution using two sublattices: a metallic sublattice containing Fe and V atoms, and an interstitial lattice containing C atoms and vacancies, va. The numbers of sites on each sublattice are equal. An equation identical to Equation 3.6 can be written for the molar Gibbs energy:

$$g = X_{\text{Fe}} X_{\text{va}} g^0_{\text{Feva}} + X_{\text{Fe}} X_{\text{C}} g^0_{\text{FeC}} + X_{\text{v}} X_{\text{va}} g^0_{\text{Vva}} + X_{\text{v}} X_{\text{C}} g^0_{\text{vc}} + RT(X_{\text{Fe}} \ln X_{\text{Fe}} + X_{\text{V}} \ln X_{\text{V}}) + RT(X_{\text{C}} \ln X_{\text{C}} + X_{\text{va}} \ln X_{\text{va}}) + g^E \tag{3.10}$$

where $X_{\text{Fe}} = (1 - X_{\text{V}})$ and $X_{\text{C}} = (1 - X_{\text{va}})$ are the site fractions on the two sublattices and 'Feva' and 'Vva' are simply pure Fe and V. That is, $g^0_{\text{Feva}} = g^0_{\text{Fe}}$. An expression for g^E as in Equation 3.9, although without the final nonrandom mixing term, was used by Lee and Lee with optimized binary g^E parameters. Their calculated Fe–V–C phase diagram is in good agreement with experimental data. The sublattice model has been similarly applied to many interstitial solutions by several authors.

3.5.4. Ceramic Solutions

Many ceramic solutions contain two or more cationic sublattices. As an example, consider a solution of Ti_2O_3 in $FeTiO_3$ (ilmenite) under reducing conditions. There are two cationic sublattices, the A and B sublattices. In $FeTiO_3$, Fe^{2+} ions and Ti^{4+} ions occupy the A and B sublattices, respectively. With additions of Ti_2O_3, Ti^{3+} ions occupy both sublattices. The solution can be represented as $(Fe^{2+}_{1-x}Ti^{3+}_x)_A(Ti^{4+}_{1-x}Ti^{3+}_x)_BO_3$ where x is the overall mole fraction of Ti_2O_3. The ions are assumed to mix randomly on each sublattice so that

$$\Delta s^{\text{ideal}} = -2R[(1 - x)\ln(1 - x) + x \ln x] \tag{3.11}$$

Deviations from ideal mixing are assumed to occur due to interlattice cation–cation interactions according to

$$\begin{gathered}(Fe^{2+}_A - Ti^{4+}_B) + (Ti^{3+}_A - Ti^{3+}_B) = (Fe^{2+}_A - Ti^{3+}_B) + (Ti^{3+}_A - Ti^{4+}_B) \\ \Delta G_{12} = a + bT\end{gathered} \tag{3.12}$$

where a and b are the adjustable parameters of the model. The probability that an A–B pair is an $(Fe^{2+}_A - Ti^{3+}_B)$ or a $(Ti^{3+}_A - Ti^{4+}_B)$ pair is equal to $x(1 - x)$. Hence, $g^E = x(1 - x)(a + bT)$.

Similar models can be proposed for other ceramic solutions such as spinels, pseudobrookites, etc. These models can rapidly become very complex mathematically as the number of possible species on the lattices increases. For instance, in Fe_3O_4–Co_3O_4 spinel solutions, Fe^{2+}, Fe^{3+}, Co^{2+}, and Co^{3+} ions are all distributed over both the tetrahedral and octahedral sublattices. Four independent equilibrium constants are required (Pelton et al., 1979) to describe the cation distribution even for the ideal mixing approximation. This complexity has been rendered much more tractable by the 'compound energy model' (Sundman and Ågren, 1981; Hillert et al., 1988). This is not a separate model, but is rather a mathematical formalism permitting the formulation of the model in terms of the Gibbs energies, g^0, of 'pseudocomponents' so that equations similar to Equation 3.6 can be used directly.

3.5.5. The Compound Energy Model

As an example, the model for the $FeTiO_3$–Ti_2O_3 solution in section 3.5.4 will be reformulated. By taking all combinations of an A-sublattice species and B-sublattice species, we define two real components, $(Fe^{2+})_A(Ti^{4+})_BO_3$ and $(Ti^{3+})_A(Ti^{3+})_BO_3$, as well as two 'pseudocomponents,' $(Fe^{2+})_A(Ti^{3+})_BO_3^-$ and $(Ti^{3+})_A(Ti^{4+})_BO_3^+$.

Pseudocomponents, as in the present example, may be charged. Similarly to Equation 3.6, the molar Gibbs energy can be written

$$g = (1-x)^2 g^0_{FeTiO_3} + x^2 g^0_{Ti_2O_3} + x(1-x) g^0_{FeTiO_3^-} + x(1-x) g^0_{Ti_2O_3^+} - T\Delta S^{ideal} \tag{3.13}$$

Note that charge neutrality is maintained in Equation 3.13. The Gibbs energies of the two pseudocomponents are calculated from the equation

$$\Delta G_{12} = a + bT = g^0_{FeTiO_3^-} + g^0_{Ti_2O_3^+} - g^0_{FeTiO_3} - g^0_{Ti_2O_3} \tag{3.14}$$

where ΔG_{12} is the Gibbs energy change of reaction (3.12). One of $g^0_{FeTiO_3^-}$ or $g^0_{Ti_2O_3^+}$ may be assigned an arbitrary value. The other is then given by Equation 3.14. By substitution of Equation 3.14 into Equation 3.13, it may be shown that this formulation is identical to the regular solution formulation given in section 3.5.4. Note that excess terms, g^E, could be added to Equation 3.13, thereby giving more flexibility to the model. In the present example, however, this was not required.

The compound energy model is described and developed by Barry et al. (1992), who give many more examples. An advantage of formulating the sublattice model in terms of the compound energy model is that it is easily extended to multicomponent solutions. It also provides a conceptual framework for treating many different phases with different structures. This facilitates the development of computer software and databases because many different types of solutions can be treated as cases of one general model.

3.5.6. Nonstoichiometric Compounds

Nonstoichiometric compounds are generally treated by a sublattice model. Consider such a compound $A_{1-\delta}B_{1+\delta}$. The sublattices normally occupied by A and B atoms will be called, respectively, the A-sublattice and the B-sublattice. Deviations from stoichiometry (where $\delta = 0$) can occur by the formation of defects such as B atoms on A sites, vacant sites, atoms occupying interstitial sites, etc. Generally, one type of defect will predominate for solutions with excess A and another type will predominate for solutions with excess B. These are called the majority defects.

Consider first a solution in which the majority defects are A atoms on B sites and B atoms on A sites: $(A_{1-x}B_x)_A\,(A_yB_{1-y})_B$. It follows that $\delta = (x-y)$. In the compound energy model formulation we can write, for the molar Gibbs energy,

$$\begin{aligned} g = {} & (1-x)(1-y)g^0_{AB} + (1-x)yg^0_{AA} + x(1-y)g^0_{BB} + xyg^0_{BA} \\ & + RT(x \ln x + (1-x)\ln(1-x) + y\ln y + (1-y)\ln(1-y)) \end{aligned} \tag{3.15}$$

where g^0_{AB} is the molar Gibbs energy of (hypothetical) defect-free stoichiometric AB. Now the defect concentrations at equilibrium are those which minimize g. Therefore, setting $(\partial g/\partial x) = (\partial g/\partial y) = 0$ at constant δ, we obtain

$$\frac{xy}{(1-x)(1-y)} = \exp\left(-(1-x-y)\frac{\Delta g_1 + \Delta g_2}{RT}\right) \tag{3.16}$$

where $\Delta g_1 = (g^0_{AA} - g^0_{AB})$ and $\Delta g_2 = (g^0_{BB} - g^0_{AB})$ are the Gibbs energies of formation of the majority defects and where g^0_{BA} has been set equal to g^0_{AB}. At a given composition $\delta = (x-y)$, and for given values of the parameters Δg_1 and Δg_2, Equation 3.16 can be solved to give x and y, which can then be substituted into Equation 3.15 to give g. The more positive are Δg_1 and Δg_2, the more steeply g rises on either side of its minimum, and the narrower is the range of stoichiometry of the compound.

Consider another model in which the majority defects are vacancies on the B-sublattice and B atoms on interstitial sites. We now have three sublattices with occupancies: $(A)_A\,(B_{1-y}Va_y)_B\,(B_xVa_{1-x})_I$ where 'I' indicates the interstitial sublattice. The A-sublattice is occupied exclusively by A atoms. Va indicates a vacancy. Stoichiometric defect-free AB is represented by (A)(B)(Va) and $(x-y) = 2\delta/(1-\delta)$. Per mole of $A_{1-\delta}\,B_{1+\delta}$, the Gibbs energy is

$$\begin{aligned} g = {} & (1-\delta)[(1-x)(1-y)g^0_{ABVa} + (1-x)yg^0_{AVVa} + x(1-y)g^0_{ABB} + xyg^0_{AVaB} \\ & + RT(x\ln x + (1-x)\ln(1-x) + y\ln y + (1-y)\ln(1-y)] \end{aligned} \tag{3.17}$$

Equation 3.17 is identical to Equation 3.15 apart from the factor $(1-\delta)$, and gives rise to an equilibrium constant as in Equation 3.16. Other choices of majority defects give rise to very similar expressions. The model can easily be modified to account for other stoichiometries A_mB_n, for different numbers of available interstitial sites, etc., and the extension to multicomponent solutions is straightforward.

3.5.7. Applications of the Sublattice Model

The sublattice model has been extensively refined and promoted by SGTE (Scientific Group Thermodynamics Europe). The compound energy model formulation is used in most cases. Frequently, three or more sublattices are postulated. The model is very versatile, being useful, for instance, in describing order–disorder transformations. Although the sublattice concept is very important, it is sometimes used artificially, with the introduction of artificial sublattices populated by artificial species, in order to treat such things as short-range ordering (see section 3.6.4). In such cases in which the model does not correctly reflect the actual structure of the solution, results are often unsatisfactory.

3.6. SHORT-RANGE ORDERING

3.6.1. Quasichemical Model

It was pointed out at the end of section 3.3.1 that there is a basic fallacy in the regular solution model, namely that random mixing occurs even when g^E is not zero. To account for nonrandom mixing, the regular solution model has been extended though the *quasichemical model for short-range ordering* developed by Guggenheim (1935) and Fowler and Guggenheim (1939) and modified by Pelton and Blander (1984, 1986) and Blander and Pelton (1987). The model is outlined below. For a more complete development, see the last two articles cited above as well as Degterov and Pelton (1996).

For a binary system, consider the formation of two nearest neighbor 1–2 pairs from a 1–1 and 2–2 pair:

$$(1\text{–}1) + (2\text{–}2) = 2(1\text{–}2) \tag{3.18}$$

Let the molar Gibbs energy change for this reaction be $(\omega - \eta T)$. Let the nearest neighbor coordination numbers of 1 and 2 atoms or molecules be Z_1 and Z_2. The total number of bonds emanating from an i atom or molecule is Z_iX_i. Hence, mass balance equations can be written as

$$Z_1X_1 = 2n_{11} + n_{12} \qquad Z_2X_2 = 2n_{22} + n_{12} \tag{3.19}$$

where n_{ij} is the number of i–j bonds in one mole of solution. 'Equivalent fractions' may be defined as

$$Y_1 = 1 - Y_2 = \frac{Z_1X_1}{Z_1X_1 + Z_2X_2} \tag{3.20}$$

where the total number of pairs in one mole of solution is $(Z_1X_1 + Z_2X_2)/2$. Letting X_{ij} be the fraction of i–j pairs in solution, Equation 3.19 may be written as

$$2Y_1 = 2X_{11} + X_{12} \qquad 2Y_2 = 2X_{22} + X_{12} \tag{3.21}$$

The molar enthalpy and excess entropy of mixing are assumed to be directly related to the number of 1–2 pairs:

$$\Delta h_m - Ts^{E(\text{nonconfig})} = (Z_1X_1 + Z_2X_2)X_{12}(\omega - \eta T)/4 \tag{3.22}$$

An approximate expression for the configurational entropy of mixing is given by a one-dimensional Ising model:

$$\begin{aligned}\Delta s_m^{\text{config}} = &- R(X_1 \ln X_1 + X_2 \ln X_2) - \frac{R}{2}(Z_1X_1 + Z_2X_2)[X_{11} \ln(X_{11}/Y_1^2) \\ &+ X_{22} \ln(X_{22}/Y_2^2) + X_{12} \ln(X_{12}/2Y_1Y_2)]\end{aligned} \tag{3.23}$$

The equilibrium distribution is calculated by minimizing Δg_m with respect to X_{12} at constant composition. This results in a 'quasichemical' equilibrium constant for reaction (3.18):

$$\frac{X_{12}^2}{X_{11}X_{22}} = 4 \exp\left(-\frac{(\omega - \eta T)}{RT}\right) \tag{3.24}$$

When $(\omega - \eta T) = 0$ the solution of Equations 3.21 and 3.24 gives a random distribution with $X_{11} = Y_1^2$, $X_{22} = Y_2^2$ and $X_{12} = 2Y_1Y_2$, and Equation 3.23 reduces to the ideal Raoultian entropy of mixing. When $(\omega - \eta T)$ becomes very negative, 1–2 pairs predominate. A plot of Δh_m or $s^{E(\text{nonconfig})}$ versus composition then becomes V-shaped and a plot of $\Delta s_m^{\text{config}}$ becomes m-shaped, with minima at $Y_1 = Y_2 = 1/2$, which is the composition of maximum ordering, as illustrated in Fig. 3.4. When $(\omega - \eta T)$ is quite negative, the plot of g^E also has a negative V-shape. Mg–Bi liquid alloys (Fig. 3.1) are an example of a system exhibiting such behavior. To apply the quasichemical model to this solution we would set $Z_{\text{Bi}}/Z_{\text{Mg}} = 2/3$ so that $Y_{\text{Bi}} = 0.5$ when $X_{\text{Bi}} = 0.4$, which is the position of the Gibbs energy minimum.

For Fe–S liquid solutions, the activity coefficients of sulfur as measured by several authors are plotted in Fig. 3.5. It is clear in this case that the model should be applied with $Z_{\text{Fe}} = Z_{\text{S}}$. The curves shown in Fig. 3.5 were calculated from the quasichemical model with $(\omega - \eta T)$ expanded as the

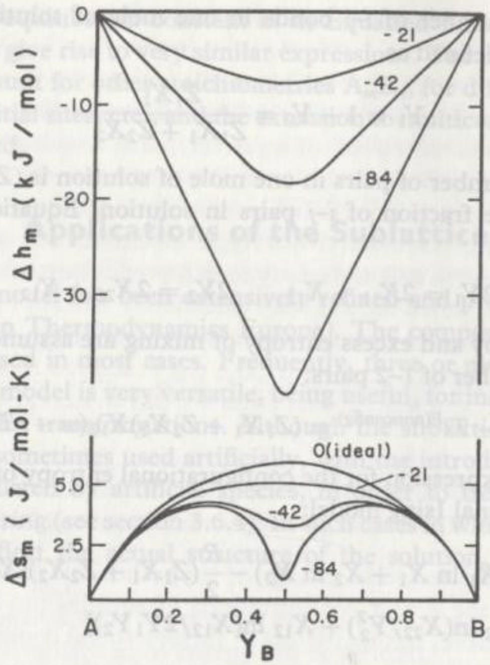

Figure 3.4 Molar enthalpy and entropy of mixing for a system A–B calculated at 1000°C with $Z_1 = Z_2 = 2$ from the quasichemical model for short-range ordering with $(\omega - \eta T)$ = constant = 0, −21, −42, and −84 kJ.

following optimized (Kongoli, 1996) polynomial:

$$(\omega - \eta T) = -(70\,017 + 9T) - 74\,042 Y_S - (798 - 15T) Y_S^3 + 40\,791 Y_S^7 \quad (\text{J mol}^{-1}) \tag{3.25}$$

Far fewer parameters are required than if a polynomial expansion of g^E as in Equation 3.3 were used. Furthermore, and more importantly, the model permits successful predictions of the properties of multicomponent systems as illustrated in Fig. 3.6, where measured sulfur activities in quaternary liquid Fe–Ni–Cu–S solutions are compared with activities calculated (Kongoli, 1996) solely from the optimized model parameters for the Fe–S, Ni–S, and Cu–S binary systems. A pair exchange reaction (3.18) was assumed for each M–S pair (M = Fe, Ni, Cu), and an optimized polynomial expansion of $(\omega_{MS} - \eta_{MS} T)$ as a function of Y_S as in Equation 3.25 was obtained for each binary. Three equilibrium constant equations like Equation 3.24 were written, and it was assumed that $(\omega_{MS} - \eta_{MS} T)$ in the quaternary system was constant at constant Y_S. No adjustable ternary or quaternary parameters

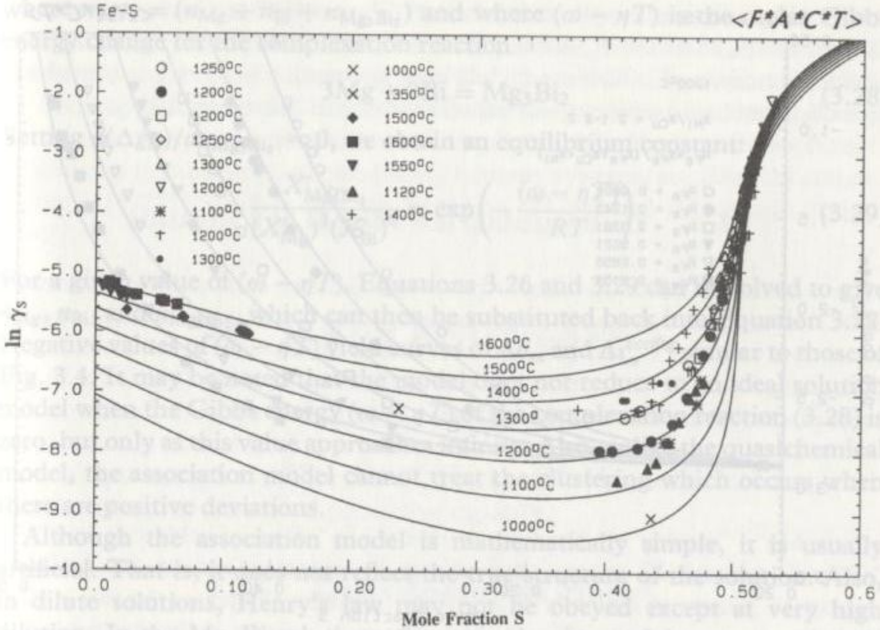

Figure 3.5 Activity coefficient of sulphur in liquid Fe–S solutions calculated from optimized model parameters and comparison with experimental data (Kongoli, 1996).

were required to obtain the agreement shown in Fig. 3.6, although the model permits the inclusion of such terms if required.

The modified quasichemical model has been successful in treating oxide slags and glasses as will be discussed in section 3.7.1.

When $(\omega - \eta T)$ is expanded as a polynomial as in Equation 3.25, the quasichemical model and the polynomial model of section 3.3.2 become identical as $(\omega - \eta T)$ approaches zero. That is, the polynomial model is a limiting case of the quasichemical model when the assumption of ideal configurational entropy is made.

When $(\omega - \eta T)$ is positive, (1–1) and (2–2) pairs predominate. The quasichemical model can thus also treat such clustering which accompanies positive deviations from ideality.

Work is currently in progress in the author's research group to render the model more flexible by permitting the Z_i to vary with composition and by expanding the $(\omega - \eta T)$ as polynomials in the bond fractions X_{ij} rather than the overall component fractions. A merger of the quasichemical and sublattice models is also under development.

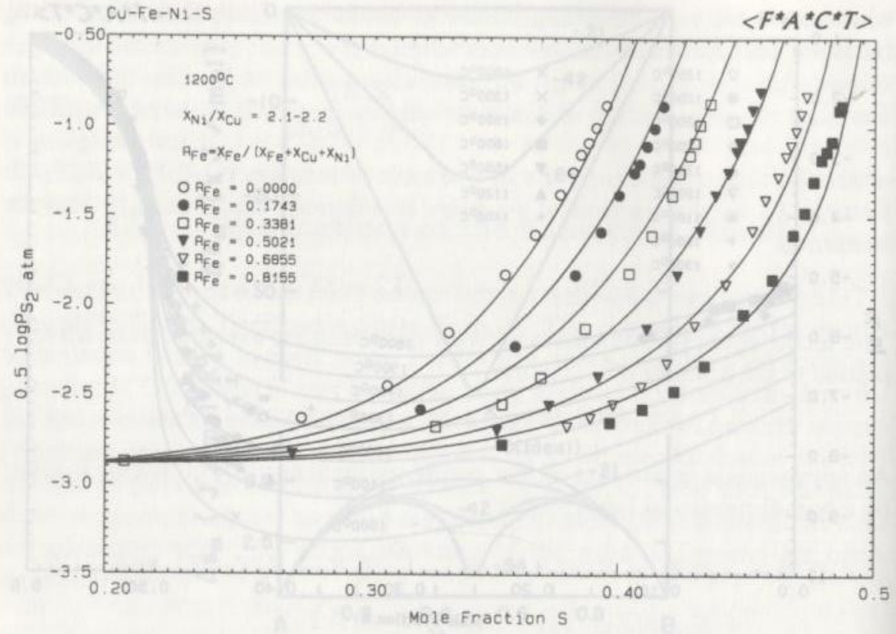

Figure 3.6 Equilibrium partial pressure of S_2 at 1200°C over Fe–Ni–Cu–S mattes predicted by the quasichemical model from binary data (Kongoli, 1996) and comparison with experimental data (C.W. Bale and J. Toguri, private communication, 1996.)

3.6.2. Association Models

V-shaped curves of Δh_m and m-shaped curves of $\Delta s_m^{\text{config}}$ similar to those in Fig. 3.4 for solutions with short-range ordering also result from models which postulate associated species. For example, Mg–Bi liquid alloys (Fig. 3.1) can be modeled by assuming the existence of Mg_3Bi_2 molecular complexes which substitute with unassociated Mg and Bi atoms on one lattice. The mass balance equations are

$$x_{Mg} = n_{Mg} + 3n_{Mg_3Bi_2} \qquad X_{Bi} = n_{Bi} + 2n_{Mg_3Bi_2} \tag{3.26}$$

where $n_{Mg_3Bi_2}$, n_{Mg} and n_{Bi} are the numbers of moles of complexes and of unassociated Mg and Bi atoms per mole of components. Furthermore,

$$\Delta g_m = RT(n_{Mg} \ln X'_{Mg} + n_{Bi} \ln X'_{Bi} + n_{Mg_3Bi_2} \ln X'_{Mg_3Bi_2}) + n_{Mg_3Bi_2}(\omega - \eta T) \tag{3.27}$$

where $X'_{Mg} = (n_{Mg}/n_{TOT})$, $X'_{Bi} = (n_{Bi}/n_{TOT})$ and $X'_{Mg_3Bi_2} = (n_{Mg_3Bi_2}/n_{TOT})$, where $n_{TOT} = (n_{Mg} + n_{Bi} + n_{Mg_3Bi_2})$ and where $(\omega - \eta T)$ is the molar Gibbs energy change for the complexation reaction

$$3Mg + 2Bi = Mg_3Bi_2 \tag{3.28}$$

Setting $d(\Delta g_m)/dn_{Mg_3Bi_2} = 0$, we obtain an equilibrium constant:

$$\frac{X'_{Mg_3Bi_2}}{(X'_{Mg})^3(X'_{Bi})^2} = \exp\left(-\frac{(\omega - \eta T)}{RT}\right) \tag{3.29}$$

For a given value of $(\omega - \eta T)$, Equations 3.26 and 3.29 can be solved to give n_{Mg}, n_{Bi}, and $n_{Mg_3Bi_2}$, which can then be substituted back into Equation 3.27. Negative values of $(\omega - \eta T)$ yield curves of Δh_m and $\Delta s_m^{\text{config}}$ similar to those of Fig. 3.4. It may be noted that the model does not reduce to an ideal solution model when the Gibbs energy $(\omega - \eta T)$ of the complexation reaction (3.28) is zero, but only as this value approaches infinity. Also, unlike the quasichemical model, the association model cannot treat the clustering which occurs when there are positive deviations.

Although the association model is mathematically simple, it is usually artificial. That is, it does not reflect the true structure of the solution. Also, in dilute solutions, Henry's law may not be obeyed except at very high dilution. In the Mg–Bi solutions, for example, the model presumes that Bi atoms, even in dilute solution in Mg, are paired (in the complexes), thereby giving only half the correct partial configurational entropy of Bi. The most serious problem with using an artificial model, however, is that good predictions cannot be made. Molten Fe–Ni–Cu–S solutions have been modeled (Chuang et al., 1985) by assuming NiS, FeS, and Cu_2S associated molecules mixing with unassociated atoms. The properties of the multicomponent solution cannot be predicted from the binary data, and can only be represented through the use of several ternary and quaternary parameters.

3.6.3. Coordination Cluster Model

Association models are, of course, justified when they provide a reasonable approximation of the actual structure of the solution. An example was cited at the end of section 3.3.3. Al and O dissolved in molten Fe can be modeled as forming AlO complexes. This approach for dilute solutions has been extended (Blander et al., 1979) in the 'Coordination Cluster Model' for dilute solutions of a solute in a multicomponent solvent. For a solute C (such as oxygen) in a binary solvent A–B (say Fe–Al) with coordination number Z, each C is assumed to be surrounded by $(Z-i)$ A atoms and i B atoms where $0 \le i \le Z$. One can write $(Z+1)$ equilibria, each with an equilibrium constant:

$$C + (Z-i)A + iB = CA_{Z-i}B_i; \qquad K_i \tag{3.30}$$

where $CA_{Z-i}B_i$ is a 'coordination cluster'. Thus, if C has a higher affinity for B than for A, then the K_i are larger for larger i. Henry's law applies for all species containing C. This model has been shown to give very good results in metallic, ionic, and aqueous solvents (Blander and Saboungi, 1981).

3.6.4. Two-Sublattice Model for Liquids

A *two-sublattice model for liquids* proposed (Hillert et al., 1985; Sundman, 1991) to account for short-range ordering has been quite widely applied recently to molten alloys, sulfides and oxides. It has been used, for instance (Oh et al., 1992) for the optimization of liquid Mg–Bi alloys (Fig. 3.1). In this example the model can be represented as

$$(Mg^{2+})_{2+x-2y}(Bi_x^{3-}Va_{1-x-y}^{2-}Bi_y^0)_2$$

where Mg^{2+} 'cations' are the sole occupants of a 'cationic' sublattice and Bi^{3-} 'anions', neutral Bi atoms, and charged vacancies occupy an 'anionic' sublattice. The ratio $2/(2+x-2y)$ of the numbers of sites on the two lattices varies with composition. The Gibbs energy is written as in the sublattice model (section 3.5.5) with pseudocomponents $Mg_2^{2+}Va_2^{2-}$ (2 moles of pure Mg), $Mg_0^{2+}Bi_2^0$ (2 moles of pure Bi), and $Mg_3^{2+}Bi_2^{3-}$ (a hypothetical completely ordered solution at $X_{Bi} = 0.4$). If ΔG^0 for the formation of $Mg_3^{2+}Bi_2^{3-}$ from $Mg_2^{2+}Va_2^{2-}$ and $Mg_0^{2+}Bi_2^0$ is very negative, then at $X_{Bi} = 0.4$ the solution will be highly ordered, with most anionic sites occupied by Bi^{3-} ions ($x \approx 1$, $y \approx 0$). If ΔG^0 for this reaction is very positive, then there will be very few Bi^{3-} ions at any composition ($x \approx 0$). In this case, the number of Va^{2-} vacancies is equal to the number of Mg^{2+} cations. Hence, $\Delta s_m^{\text{config}}$ for the mixing of the Va^{2-} vacancies and Bi^0 atoms on the anionic sublattice is numerically equal to $\Delta s_m^{\text{config}}$ for an ideal mixture of Mg and Bi.

Polynomial excess terms can be included in the model in the general case of multicomponent solutions. When 'anions' are not present, the model reduces to the polynomial model as in sections 3.3.2 and 3.4.1 (Sundman, 1991). The drawbacks to the model are its mathematical complexity and its artificiality. Also, like the association model, the model cannot treat the clustering which accompanies positive deviations.

3.6.5. Cluster Variation Method

The assumption of random mixing is a zeroth-order approximation. The mixing of pairs, as in the quasichemical model, is a first-order approximation to the configurational entropy. Higher-order approximations take into account the distribution of clusters of three or more particles. A discussion is beyond the scope of the present article. The cluster variation method (CVM) has been applied to *a priori* predictions in alloy systems and to ordering phenomena. Despite its mathematical complexity, it holds promise for future applications in modeling and predicting in many systems; see Kikuchi and de Fontaine (1977), Sanchez and de Fontaine (1978), and Pitsch and Inden (1991).

3.7. SLAGS AND GLASSES

The structure of slags and glasses, particularly silicates, is discussed in Chapter 2. A practical goal is to develop a model which is general, mathematically simple enough to use for calculations in multicomponent solutions, and realistic enough to have good predictive capacity.

3.7.1. Quasichemical Model

Success has been had with the quasichemical model discussed in section 3.6.1. In a binary silicate melt or glass, AO_x–SiO_2 (A = Ca, Mg, Na, ...), the tendency to short-range ordering can be identified with the tendency to form SiO_4^{4-} ions or with the break-up of the silicate network and the resultant formation of second-nearest neighbor A–Si pairs. At the orthosilicate composition, $A_{2/x}SiO_4$, a completely ordered solution can be considered to consist of only A^{2x+} cations and SiO_4^{4-} anions. This is equivalent to saying that there are only A–Si pairs and no A–A of Si–Si pairs. An Si–Si pair can be considered to be joined by a doubly-bonded (network) oxygen, and an A–A pair is a pair of cations separated by an O^{2-} ion. Hence, the quasichemical reaction (3.18) is applied for second-nearest neighbour pairs:

$$(A\text{–}A) + (S\text{–}Si) = 2(A\text{–}Si) \tag{3.31}$$

and this is related to the well-known equilibrium between free, singly-bonded, and doubly-bonded oxygens:

$$O^{2-} + O^0 = 2O^- \tag{3.32}$$

It must be stressed that the modified quasichemical model is not intended as a detailed theory of the melt structure, but rather as a formalism, having the advantages of mathematical simplicity and generality, which appears to have the characteristics required for relatively reliable interpolations and extrapolations of data into unmeasured regions and for extensions to multicomponent solutions.

In systems AO–SiO$_2$ with a divalent cation A, the enthalpy, entropy, and Gibbs energy of mixing pass through a minimum near $X_{SiO_2} = 1/3$. Therefore we set $Z_{Si}/Z_A = 2$. Although there is less evidence in the case of monovalent, trivalent, or tetravalent species, we assume that in these cases the position of maximum ordering also occurs near the orthosilicate composition, so that $Z_{Si}/Z_A = 4$ when A is monovalent and $Z_{Si}/Z_A = 4/3$ when A is trivalent. The values of Z_i used in the model are chosen so that $\Delta s_m^{config} = 0$ at the composition of maximum ordering ($Y_A = Y_{Si} = 1/2$) for a completely ordered solution ($X_{ASi} = 1$) for a system AO–SiO$_2$ where $Z_{Si}/Z_A = 2$. This condition is satisfied when $Z_{Si} = 2.7548$ and $Z_A = 1.3774$ as can be shown from Equation 3.28. In order to maintain the same values of Z_i consistently for all systems containing i, values of $Z_A = 2.0661$, 1.3774, and 0.6887 are used when the cations A are trivalent, divalent, and monovalent, respectively. These nonphysical values of Z_i result from the use of the one-dimensional Ising model in Equation 3.23.

As an example, the calculated optimized (Eriksson et al., 1994) phase diagram of the CaO–SiO$_2$ system is compared to some experimental points in Fig. 3.7. For the molten slag phase, the following quasichemical parameters were obtained by simultaneous optimization of all phase diagram and liquid activity data:

$$(\omega - \eta T) = (-158\,218 + 19.456T) - 37\,932 Y_{Si} - 90\,148 Y_{Si}^5 + (439\,893 - 133.888T) Y_{Si}^7 \quad (\mathrm{J\ mol^{-1}}) \tag{3.33}$$

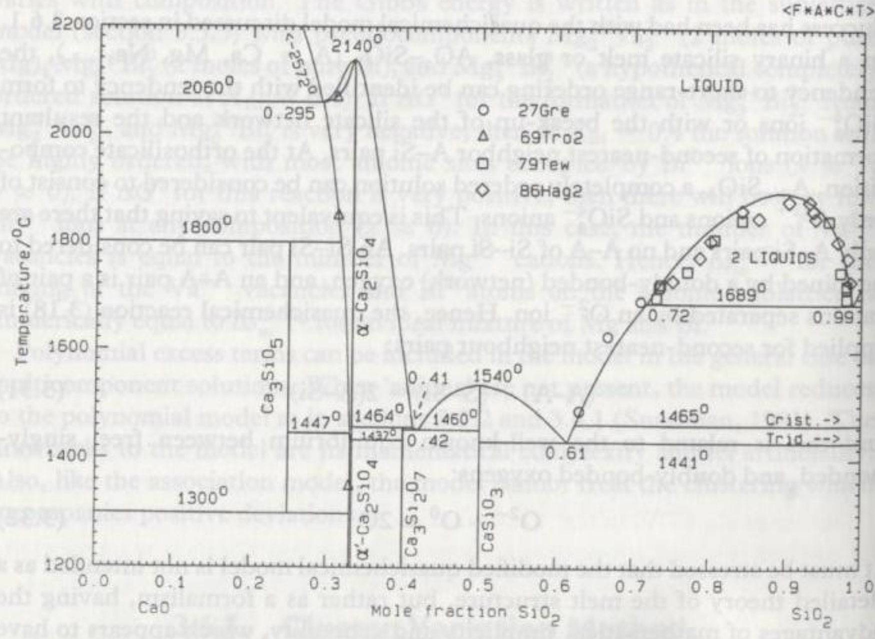

Figure 3.7 CaO–SiO$_2$ phase diagram calculated from optimized parameters and comparison with experimental data. (Reproduced from Eriksson et al. (1994), with kind permission from Elsevier Science Ltd, U.K.)

As described in section 3.6.1, the quasichemical model can be applied to multicomponent solutions. In Fig. 3.8 is shown the phase diagram of the FeO–MgO–SiO$_2$ system in equilibrium with Fe, calculated (Wu et al., 1993b) using the quasichemical model for the liquid phase. No ternary parameters

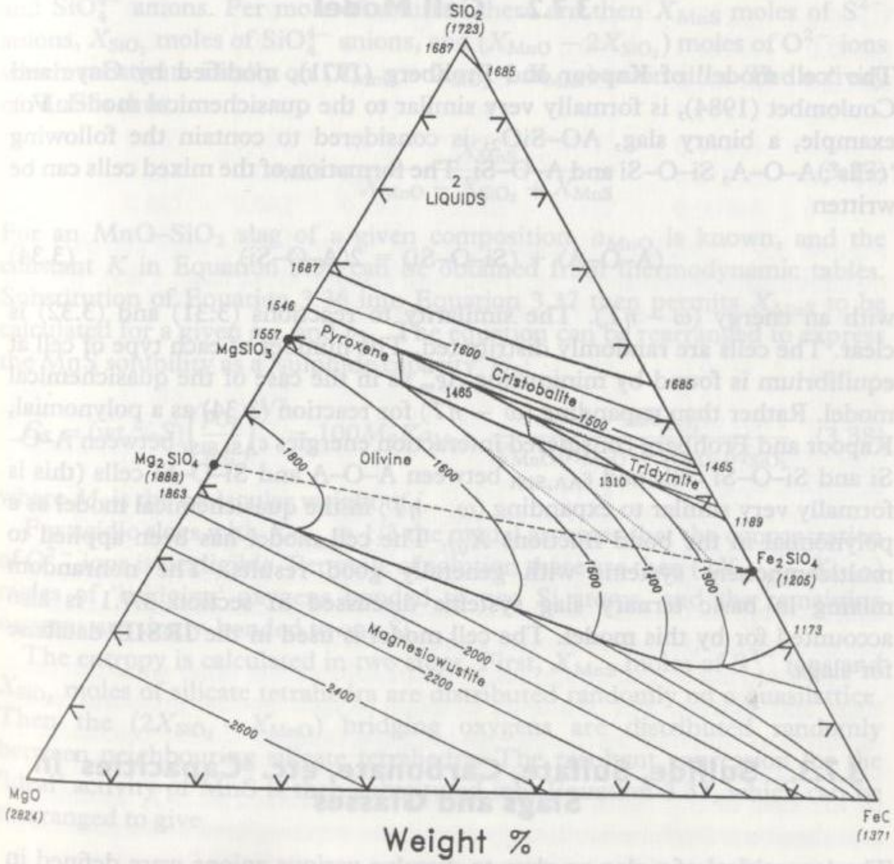

Figure 3.8 Calculated liquidus projection of the FeO–MgO–SiO$_2$ system in equilibrium with Fe. Temperature in °C. (Reproduced from Wu et al., 1993b.) Dotted lines are measured (Bowen and Schairer, 1935). (Originally published in *ISIJ Int* as figure 8.)

were required. The FeO–MgO, $FeSiO_3$–$MgSiO_3$ and Fe_2SiO_4–Mg_2SiO_4 solid solutions were treated as regular, with one parameter each. As discussed by Wu et al. (1993b), the measured liquidus is reproduced very closely at all compositions as are solid–liquid tie-lines for the $FeSiO_3$–$MgSiO_3$ and Fe_2SiO_4–Mg_2SiO_4 joins.

Work is in progress in the author's research group to develop a database for calculating the properties of multicomponent oxide slags and glasses from optimized quasichemical parameters for binary and ternary subsystems. Over 100 systems have already been optimized.

3.7.2. Cell Model

The 'cell model' of Kapoor and Frohberg (1971), modified by Gaye and Coulombet (1984), is formally very similar to the quasichemical model. For example, a binary slag, AO–SiO_2, is considered to contain the following 'cells': A–O–A, Si–O–Si and A–O–Si. The formation of the mixed cells can be written

$$(\text{A–O–A}) + (\text{Si–O–Si}) = 2(\text{A–O–Si}) \tag{3.34}$$

with an energy $(\omega - \eta T)$. The similarity to reactions (3.31) and (3.32) is clear. The cells are randomly distributed. The number of each type of cell at equilibrium is found by minimizing Δg_m as in the case of the quasichemical model. Rather than expanding $(\omega - \eta T)$ for reaction (3.34) as a polynomial, Kapoor and Frohberg considered interaction energies $\varepsilon_{\text{ASi,SiSi}}$ between A–O–Si and Si–O–Si cells and $\varepsilon_{\text{AA,SiSi}}$ between A–O–A and Si–O–Si cells (this is formally very similar to expanding $(\omega - \eta T)$ in the quasichemical model as a polynomial in the bond fractions X_{ij}). The cell model has been applied to multicomponent systems with generally good results. The nonrandom mixing in basic ternary slag systems discussed in section 3.7.1 is also accounted for by this model. The cell model is used in the IRSID database for slags.

3.7.3. Sulfide, Sulfate, Carbonate, etc. 'Capacities' in Slags and Glasses

The 'capacities' of a slag or glass to dissolve various anions were defined in Chapter 2. A very simple model for their calculation was proposed by Reddy and Blander (1987) and modified by Pelton et al. (1993). The model supposes that the activities of the oxide components are known. Let us take as example binary MnO–SiO_2 slags. The exchange of oxygen and sulfur between the slag and other phases can be written

$$\text{MnO(liq)} + \tfrac{1}{2}\text{S}_2\text{(g)} = \text{MnS(liq)} + \tfrac{1}{2}\text{O}_2\text{(g)} \tag{3.35}$$

for which the equilibrium constant is

$$K = \left(\frac{a_{\text{MnS}}}{a_{\text{MnO}}}\right)\left(\frac{p_{\text{O}_2}}{p_{\text{S}_2}}\right)^{1/2} \tag{3.36}$$

where a_{MnS} and a_{MnO} are the activities in the slag. For dilute solutions of MnS the model assumes that S^{2-} ions form an ideal solution, substituting for O^{2-} ions and for SiO_4 groups. Furthermore, for basic slags with $X_{\text{SiO}_2} \leq 1/3$, it is assumed that the only species in solution are Mn^{2+} cations and O^{2-}, S^{2-} and SiO_4^{4-} anions. Per mole of solution there are then X_{MnS} moles of S^{2-} anions, X_{SiO_2} moles of SiO_4^{4-} anions, and $(X_{\text{MnO}} - 2X_{\text{SiO}_2})$ moles of O^{2-} ions which substitute ideally on $(X_{\text{MnO}} - X_{\text{SiO}_2} + X_{\text{MnS}})$ anion sites. The activity of MnS is thus

$$a_{\text{MnS}} = \frac{X_{\text{MnS}}}{X_{\text{MnO}} - X_{\text{SiO}_2} + X_{\text{MnS}}} \tag{3.37}$$

For an MnO–SiO_2 slag of a given composition, a_{MnO} is known, and the constant K in Equation 3.36 can be obtained from thermodynamic tables. Substitution of Equation 3.36 into Equation 3.37 then permits X_{MnS} to be calculated for a given p_{O_2} and p_{S_2}. The equation can be rearranged to express the MnS solubility as a 'sulphide capacity' C_S:

$$C_S = (\text{wt.}\%S)\left(\frac{p_{\text{O}_2}}{p_{\text{S}_2}}\right)^{1/2} = 100M_S K a_{\text{MnO}} \frac{1 - 2X_{\text{SiO}_2}}{X_{\text{MnO}}M_{\text{MnO}} + X_{\text{SiO}_2}M_{\text{SiO}_2}} \tag{3.38}$$

where M_i is the molecular weight of i.

For acidic slags with $X_{\text{SiO}_2} \geq 1/3$ the model assumes that the concentration of O^{2-} ions is negligible. Per mole of solution there are then $(2X_{\text{SiO}_2} - X_{\text{MnO}})$ moles of 'bridging' oxygens bonded to two Si atoms, and the remaining oxygens are singly-bonded to one Si.

The entropy is calculated in two steps. First, X_{MnS} moles of S^{2-} ions and X_{SiO_2} moles of silicate tetrahedra are distributed randomly on a quasilattice. Then the $(2X_{\text{SiO}_2} - X_{\text{MnO}})$ bridging oxygens are distributed randomly between neighbouring silicate tetrahedra. The resultant expression for the 'ideal' activity of MnS is then substituted into Equation 3.37, which can be rearranged to give

$$C_S = 100M_S K a_{\text{MnO}} \frac{X_{\text{SiO}_2}}{X_{\text{MnO}}M_{\text{MnO}} + X_{\text{SiO}_2}M_{\text{SiO}_2}} \left(\frac{1 - X_{\text{SiO}_2}}{2X_{\text{SiO}_2}}\right)^2 \tag{3.39}$$

Sulphide capacities of MnO–SiO_2 slags were calculated from Equations 3.38 and 3.39 with a_{MnO} taken from an earlier optimization of the MnO–SiO_2

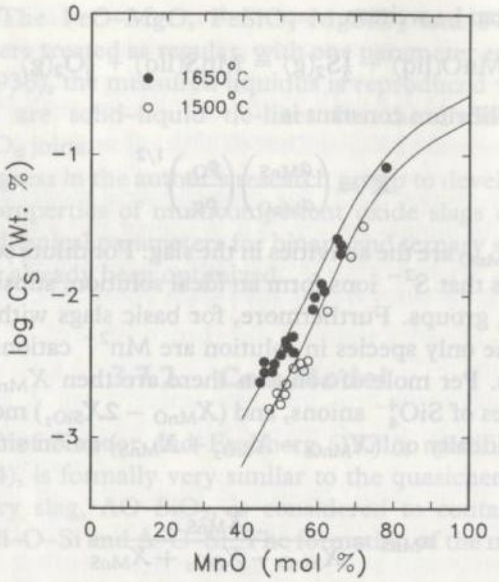

Figure 3.9 Calculated sulphide capacities in MnO–SiO$_2$ slags compared to measured data (Abraham et al., 1960; Sharma and Richardson, 1965). (Reproduced from Pelton et al., 1993, with permission.)

system. The results are shown in Fig. 3.9 to be in very good agreement with measured data. It should be stressed that these are *a priori* calculations involving no adjustable parameters.

Pelton et al. (1993) derived similar equations for C_S of A_nO–SiO$_2$, A_nO–TiO$_2$, A_nO–AlO$_{3/2}$, etc. slags where A_nO is a basic oxide (CaO, FeO, MgO, Na$_2$O, etc.) and SiO$_2$, TiO$_2$, and AlO$_{3/2}$ were taken as acidic. Good agreement with measurements was obtained. The model was also extended to multicomponent solutions with similarly good results.

The same model can be applied to dilute solutions of other anions in oxide slags and glasses. For example, at high oxygen partial pressures sulfur dissolves as sulphate ions, and the sulphate capacity can be calculated by assuming that SO_4^{2-} ions substitute for O^{2-} ions and silicate tetrahedra just as in the case of S^{2-} ions. Sulfate capacities (expressed as SO$_3$ solubilities) calculated *a priori* for a multicomponent glass are compared in Table 3.1 with experimental data. Good results have also been obtained for carbonate and chloride capacities, and reasonable agreement has been found for phosphate capacities. The simple model does not apply, however, for fluoride or hydroxyl capacities, probably because these ions can also bond directly to the silicon atoms in the network.

Table 3.1 Calculated SO$_3$ solubilities[a] in SiO$_2$–CaO–Na$_2$O–(Al$_2$O$_3$–MgO) glasses compared to measurements of Papadopoulos (1973)

	Mole fraction					SO$_3$(mole fraction)	
T (°C)	SiO$_2$	Al$_2$O$_3$	CaO	MgO	Na$_2$O	Exp. (corrected)	Calc.
1370	0.721	0.002	0.136	0.005	0.127	0.00745	0.00715
	0.722	0.001	0.142	0.004	0.123	0.00636	0.00685
	0.741	0.001	0.089	0.003	0.159	0.00664	0.0103
	0.707	0.001	0.200	0.005	0.083	0.00280	0.00417
	0.715	0.001	0.193	0.005	0.083	0.00280	0.00385
	0.710	0.001	0.196	0.005	0.085	0.00238	0.00420
	0.653	0.002	0.195	0.005	0.133	0.01216	0.0162
	0.653	0.002	0.196	0.004	0.132	0.01265	0.0161
	0.657	0.002	0.194	0.005	0.131	0.01050	0.0151
	0.661	0.002	0.195	0.005	0.127	0.00967	0.0137
	0.685	0.002	0.144	0.004	0.154	0.01066	0.0156
	0.778	0.001	0.090	0.004	0.123	0.00360	0.0044
	0.778	0.001	0.144	0.004	0.071	0.00133	0.00185
1373	0.653	0.002	0.196	0.004	0.132	0.0126	0.0157
1397	0.660	0.002	0.198	0.005	0.128	0.0115	0.0108
1403	0.659	0.002	0.194	0.004	0.131	0.0107	0.0108
1427	0.677	0.002	0.187	0.005	0.123	0.0066	0.0060
1433	0.669	0.002	0.192	0.004	0.128	0.0062	0.0069
1451	0.660	0.002	0.201	0.005	0.128	0.0063	0.0063
1453	0.665	0.002	0.194	0.006	0.129	0.0050	0.0058
1483	0.666	0.002	0.199	0.005	0.125	0.0038	0.0040

[a] At $p_{SO_3} = 0.01$ atm.

3.8. APPLICATIONS

In recent years there has been much activity in the development of solution databases through the systematic optimization of data for 2- and 3-component systems using appropriate models. The model parameters are stored in computer databases, and the models are used to predict Gibbs energies of multicomponent solutions. Databases for solutions of alloys, slags and glasses, ceramics, mattes, salts, carbonitrides, etc. have been developed. A summary of

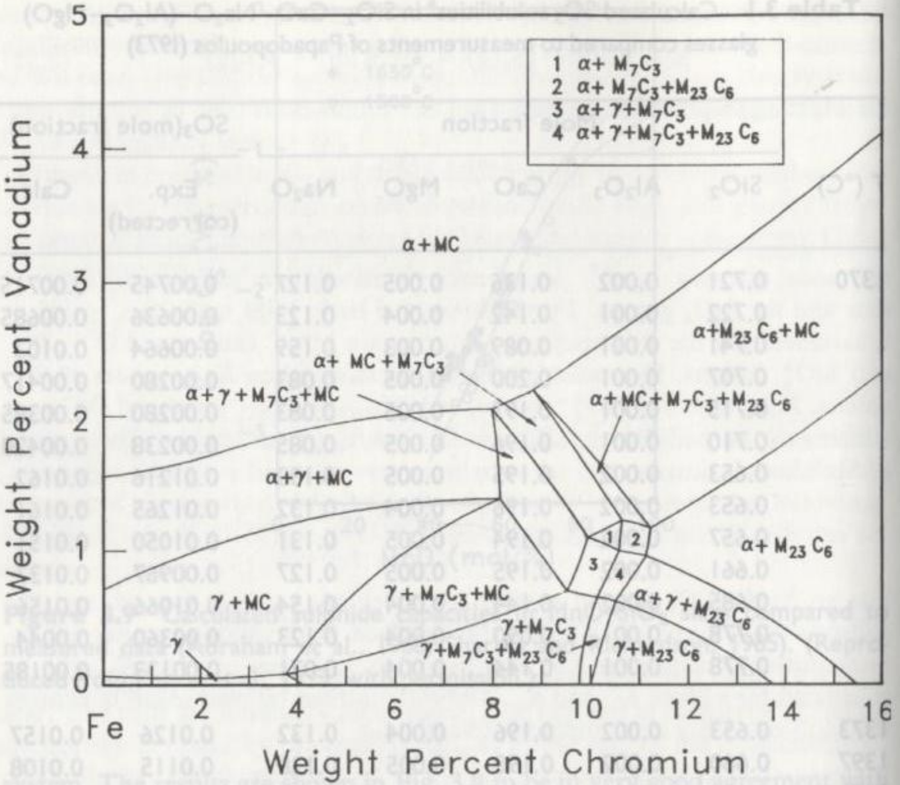

Figure 3.10 Calculated section of the Fe–V–Cr–C phase diagram at 0.3 wt.% C and 850°C (Lee and Lee, 1992). (Reproduced from Pelton (1996), with kind permission from Elsevier Science, The Netherlands.)

thermodynamic databases for metallurgy and materials applications was prepared by Bale and Eriksson (1990). These solution databases are used, along with extensive thermodynamic databases for pure substances and with general Gibbs energy minimization software, in several publicly accessible calculation/database packages for the computation of thermodynamic equilibria in complex systems. Three of the largest such software/database packages are F*A*C*T (Montreal), Thermocalc (Stockholm), and MTDATA (Teddington, UK).

A sample calculation produced with the Thermocalc software (Lee and Lee, 1992) is shown in Fig. 3.10. A calculated section of the Fe–V–Cr–C phase diagram in shown at 0.3 wt.% C at 850°C. Sublattice models were used for all phases, with excess properties expressed as polynomials. For example, the bcc and fcc phases were modeled as interstitial solutions as in section 3.5.3. The

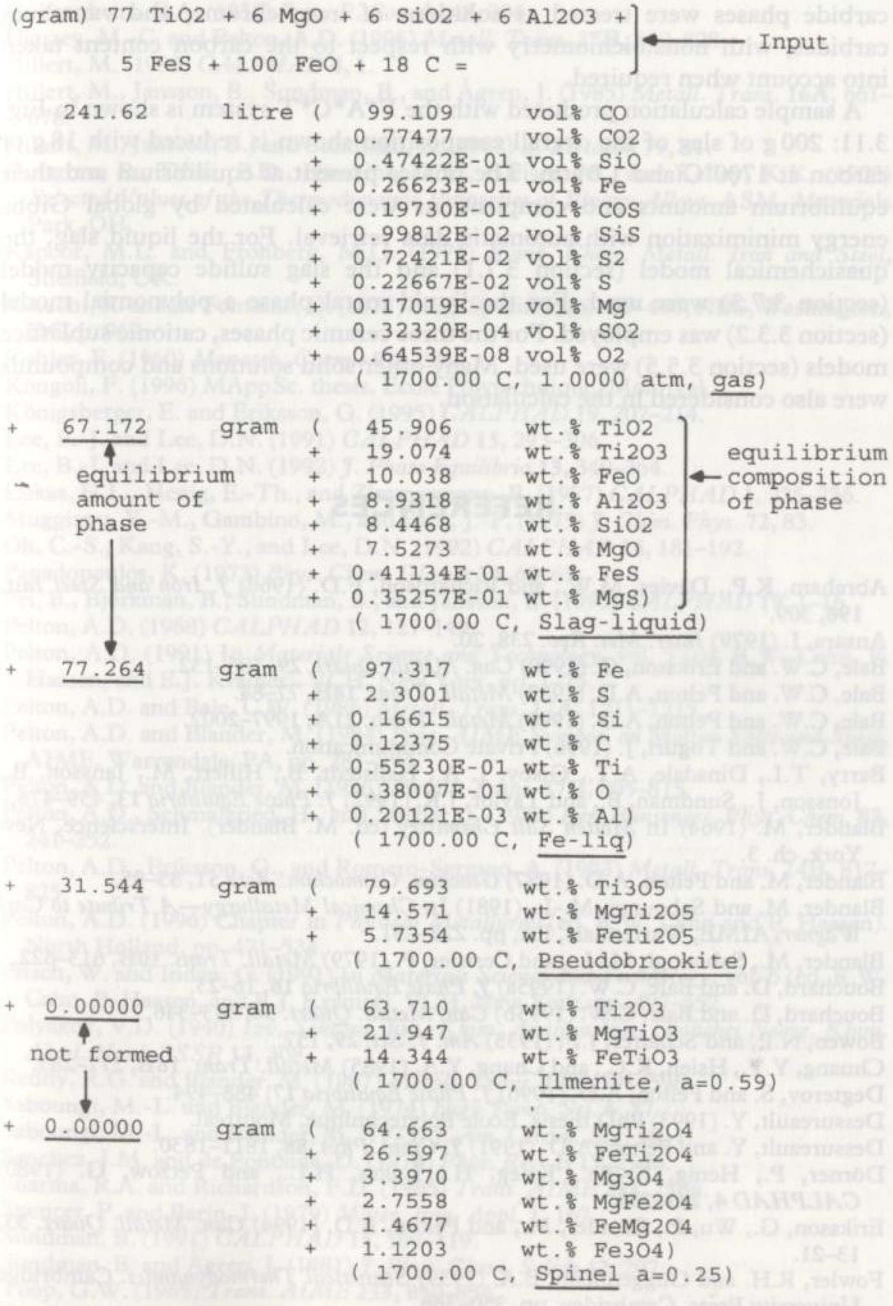
Input
equilibrium amount of phase
equilibrium composition of phase
not formed

```
(gram) 77 TiO2 + 6 MgO + 6 SiO2 + 6 Al2O3 +
   5 FeS + 100 FeO + 18 C =

 241.62    litre (  99.109      vol% CO
                 +  0.77477     vol% CO2
                 +  0.47422E-01 vol% SiO
                 +  0.26623E-01 vol% Fe
                 +  0.19730E-01 vol% COS
                 +  0.99812E-02 vol% SiS
                 +  0.72421E-02 vol% S2
                 +  0.22667E-02 vol% S
                 +  0.17019E-02 vol% Mg
                 +  0.32320E-04 vol% SO2
                 +  0.64539E-08 vol% O2
                    ( 1700.00 C, 1.0000 atm, gas)

+  67.172    gram  (   45.906      wt.% TiO2
                 +    19.074      wt.% Ti2O3
                 +    10.038      wt.% FeO
                 +    8.9318      wt.% Al2O3
                 +    8.4468      wt.% SiO2
                 +    7.5273      wt.% MgO
                 +  0.41134E-01  wt.% FeS
                 +  0.35257E-01  wt.% MgS)
                   ( 1700.00 C, Slag-liquid)

+  77.264    gram  (   97.317      wt.% Fe
                 +    2.3001      wt.% S
                 +  0.16615       wt.% Si
                 +  0.12375       wt.% C
                 +  0.55230E-01  wt.% Ti
                 +  0.38007E-01  wt.% O
                 +  0.20121E-03  wt.% Al)
                   ( 1700.00 C, Fe-liq)

+  31.544    gram  (   79.693      wt.% Ti3O5
                 +    14.571      wt.% MgTi2O5
                 +    5.7354      wt.% FeTi2O5
                   ( 1700.00 C, Pseudobrookite)

+  0.00000   gram  (   63.710      wt.% Ti2O3
                 +    21.947      wt.% MgTiO3
                 +    14.344      wt.% FeTiO3
                   ( 1700.00 C, Ilmenite, a=0.59)

+  0.00000   gram  (   64.663      wt.% MgTi2O4
                 +    26.597      wt.% FeTi2O4
                 +    3.3970      wt.% Mg3O4
                 +    2.7558      wt.% MgFe2O4
                 +    1.4677      wt.% FeMg2O4
                 +    1.1203      wt.% Fe3O4)
                   ( 1700.00 C, Spinel a=0.25)
```

Figure 3.11 Calculated equilibrium conditions when 200 g of a slag is reduced with 18 g of carbon at 1700°C.

carbide phases were treated as solutions of iron, chrome, and vanadium carbides, with nonstoichiometry with respect to the carbon content taken into account when required.

A sample calculation produced with the F*A*C*T system is shown in Fig. 3.11: 200 g of slag of the overall composition shown is reduced with 18 g of carbon at 1700°C and 1.0 atm. The phases present at equilibrium and their equilibrium amounts and compositions were calculated by global Gibbs energy minimization with automatic data retrieval. For the liquid slag, the quasichemical model (section 3.7.1) and the slag sulfide capacity model (section 3.7.3) were used. For the liquid metal phase a polynomial model (section 3.3.2) was employed. For the three ceramic phases, cationic sublattice models (section 3.5.5) were used. Many other solid solutions and compounds were also considered in the calculation.

REFERENCES

Abraham, K.P., Davies, M.W., and Richardson, F.D. (1960) *J. Iron and Steel Inst.* **196**, 309.

Ansara, I. (1979) *Inter. Met. Rev.* **238**, 20.

Bale, C.W. and Eriksson, G. (1990) *Can. Metall. Quart.* **29**, 105–132.

Bale, C.W. and Pelton, A.D. (1983) *Metall. Trans.* **14B**, 77–84.

Bale, C.W. and Pelton, A.D. (1990) *Metall. Trans.* **21A**, 1997–2002.

Bale, C.W. and Toguri, J. (1996) Private Communication.

Barry, T.I., Dinsdale, A.T., Gisby, J. A., Hallstedt, B., Hillert, M., Jansson, B., Jonsson, J., Sundman, B., and Taylor, J.R. (1992) *J. Phase Equilibria* **13**, 459–476.

Blander, M. (1964) In *Molten Salt Chemistry* (ed. M. Blander). Interscience, New York, ch. 3.

Blander, M. and Pelton, A.D. (1987) *Geochim. Cosmochim. Acta* **51**, 85–95.

Blander, M. and Saboungi, M.-L. (1981) In *Chemical Metallurgy—A Tribute to Carl Wagner*, AIME, Warrendale, PA, pp. 223–231.

Blander, M., Saboungi, M.-L., and Cerisier, P. (1979) *Metall. Trans.* **10B**, 613–622.

Bouchard, D. and Bale, C.W. (1995a) *J. Phase Equilibria* **16**, 16–23.

Bouchard, D. and Bale, C.W. (1995b) *Can. Metall. Quart.* **34**, 343–346.

Bowen, N.L. and Schairer, J.F. (1935) *Am. J. Sci.* **29**, 157.

Chuang, Y.Y., Hsieh, K.C., and Chang, Y.A. (1985) *Metall. Trans.* **16B**, 277–285.

Degterov, S. and Pelton, A.D. (1996) *J. Phase Equilibria* **17**, 488–494.

Dessureault, Y. (1993) PhD thesis. Ecole Polytechnique, Montreal.

Dessureault, Y. and Pelton, A.D. (1991) *J. Chim. Phys.* **88**, 1811–1830.

Dörner, P., Henig, E.-Th., Krieg, H., Lukas, H.L., and Petzow, G. (1980) *CALPHAD* **4**, 241–254.

Eriksson, G., Wu, P., Blander, M., and Pelton, A.D. (1994) *Can. Metall. Quart.* **33**, 13–21.

Fowler, R.H. and Guggenheim, E.A. (1939) *Statistical Thermodynamics*. Cambridge University Press, Cambridge, pp. 350–366.

Gaye, H. and Coulombet, D. (1984) Report, Commission European Community, CECA-7210-CF/301.

Guggenheim, E.A. (1935) *Proc. R. Soc.* **A148**, 304.

Heuzey, M.-C. and Pelton, A.D. (1996) *Metall. Trans.* **27B**, 810–828.

Hillert, M. (1980) *CALPHAD* **4**, 1.

Hillert, M., Jansson, B., Sundman, B., and Ågren, J. (1985) *Metall. Trans.* **16A**, 661–678.

Hillert, M., Jansson, B., and Sundman, B. (1988) *Z. Metallk.* **79**, 81.

Hultgren, R., Desai, P.D., Hawkins, D.T., Gleiser, M., and Kelley, K.K. (1973) *Selected Values of the Thermodynamic Properties of Binary Alloys*. ASM, Materials Park, OH.

Kapoor, M.L. and Frohberg, M.G. (1971) *Symp. Chem. Metall. Iron and Steel*, Sheffield, UK.

Kikuchi, R. and de Fontaine, D. (1977) NBS Special Publ. SP-496, NBS, Washington, DC, p. 967.

Kohler, F. (1960) *Monatsh. Chemie* **91**, 738.

Kongoli, F. (1996) MAppSc. thesis. Ecole Polytechnique, Montreal.

Königsberger, E. and Eriksson, G. (1995) *CALPHAD* **19**, 207–214.

Lee, B.-J. and Lee, D.N. (1991) *CALPHAD* **15**, 293–306.

Lee, B.-J. and Lee, D.N. (1992) *J. Phase Equilibria* **13**, 349–364.

Lukas, H.L., Henig, E.-Th., and Zimmermann, B. (1977) *CALPHAD* **1**, 225–236.

Muggianu, Y.-M., Gambino, M., and Bros, J.-P. (1975) *J. Chim. Phys.* **72**, 83.

Oh, C.-S., Kang, S.-Y., and Lee, D.N. (1992) *CALPHAD* **16**, 181–192.

Papadopoulos, K. (1973) *Phys. Chem. Glasses* **14**, 60–65.

Pei, B., Björkman, B., Sundman, B., and Jansson, B. (1995) *CALPHAD* **19**, 1–16.

Pelton, A.D. (1988) *CALPHAD* **12**, 127–142.

Pelton, A.D. (1991) In *Materials Science and Technology*, vol. 5 (ed. R.W. Cahn, P. Haasen, and E.J. Kramer). VCH, New York, pp. 1–75.

Pelton, A.D. and Bale, C.W. (1986) *Metall. Trans.* **17A**, 1211–1215.

Pelton, A.D. and Blander, M. (1984) *Proc. AIME Sympos. on Molten Salts and Slags*. AIME, Warrendale, PA, pp. 281–294.

Pelton, A.D. and Blander, M. (1986) *Metall. Trans.* **17B**, 805–815.

Pelton, A.D., Schmalzried, H., and Sticher, J. (1979) *Ber. Bunsenges. Phys. Chem.* **83**, 241–252.

Pelton, A.D., Eriksson, G., and Romero-Serrano, A. (1993) *Metall. Trans.* **24B**, 817–825.

Pelton, A.D. (1996) Chapter in *Physical Metallurgy* (ed. R.W. Cahn and P. Haasen). North Holland, pp. 471–534.

Pitsch, W. and Inden, G. (1991) In *Materials Science and Technology*, vol. 5 (ed. R.W. Cahn, P. Haasen, and E.J. Kramer). VCH, New York, pp. 497–552.

Polyakov, V.D. (1940) *Izv. Sektora, Fiz.-Khim. Analiza Inst. Obshchei Neorg. Khim. Akad. Nauk SSSR* **13**, 308.

Reddy, R.G. and Blander, M. (1987) *Metall. Trans.* **18B**, 591–596.

Saboungi, M.-L. and Blander, M. (1974) *High Temp. Sci.* **6**, 37.

Saboungi, M.-L. and Blander, M. (1975) *J. Am. Ceram. Soc.* **58**, 1.

Sanchez, J.M. and de Fontaine, D. (1978) *Phys. Rev. B* **17**, 2926.

Sharma, R.A. and Richardson, F.D. (1965) *Trans. AIME* **233**, 1586.

Spencer, P. and Barin, I. (1979) *Mater. Eng. Appl.* **1**, 167.

Sundman, B. (1991) *CALPHAD* **15**, 109–119.

Sundman, B. and Ågren, J. (1981) *J. Phys. Chem. Solids* **42**, 297.

Toop, G.W. (1965) *Trans. AIME* **233**, 850–854.

Wu, P., Eriksson, G., and Pelton, A.D. (1993a) *J. Am. Ceram. Soc.* **76**, 2065–2075.

Wu, P., Eriksson, G., Pelton, A.D., and Blander, M. (1993b) *ISIJ Int.* **33**, 26–35.

Part II

KINETICS

Overview

Wei-Kao Lu

During the 1960s, with the introduction of faster processing facilities, the steel industry realized the necessity of understanding kinetic phenomena in order to have better control in both productivity and quality of products. In this same period of time, transport phenomena were included in the curriculum in metallurgy and metallurgical engineering. It was no surprise to discover that literature in other disciplines has very limited value in solving our problems, which are, in general, multiphase systems at elevated temperatures often involving liquid metal.

The goals of industrial processing are to achieve changes in chemical (e.g., reduction or oxidation) or physical (e.g., melting or solidification) states or both. In general, a gas or a liquid (e.g., slag) is used to process another liquid or solid by carrying heat and chemical reactants. The importance of understanding fluid mechanics in the study of process metallurgy is obvious.

In the chapter on fluid mechanics in metallurgical processes (Chapter 4, Guthrie), the author begins with the formulation of governing equations from the law of conservation of mass, heat, and momentum. To less experienced readers, the insights offered by the author in making acceptable assumptions, with respect to various applications in metallurgical systems, in solving the Navier–Stockes equation are most valuable. The validity of a low-temperature physical model for a high-temperature system is also included.

In the chapter on solidification (Chapter 5, Flemings), the author uses a similar approach but carries it one step further. Solidification of an alloy is a very complex process. The author has succeeded in giving a clear and concise introduction to many engineering aspects of steel solidification processes by starting with a series of simplifying assumptions regarding thermodynamic properties of liquid–solid interfaces and the range of velocity of the solidifying front. The consequence of these assumptions is included in this chapter.

There are two chapters on chemical kinetics but they are sequential in their contents. In the absence of any fundamental law of kinetics or any governing equations, the treatment begins with atoms. In the chapter on interface and interfacial reactions (Chapter 6, Belton), the absolute rate theory is introduced first. It is a theory based on thermodynamic relations and the assumption of partial equilibrium in the system. In the process of formulation of a rate expression, the meanings of a rate constant and of an activation energy are defined. For heterogeneous reactions, the adsorbed state is the beginning of all

ADVANCED PHYSICAL CHEMISTRY FOR PROCESS METALLURGY
ISBN 0-12-618920-X
Copyright © 1997 Academic Press Ltd
All rights of reproduction in any form reserved

reactions. This chapter covers the foundation of chemical kinetics in process metallurgy.

The chapter on kinetics and mechanisms of heterogeneous reactions (Chapter 7, Lu) includes the coupling between interfacial reactions and transport steps in bulk phases. It becomes clear that a theoretician can build a comprehensive mathematical model which is only limited by the size of computer available. On the other hand, the experimental data collected only represents the rate-limiting step prevailing under a given set of conditions. The coupling between simultaneous slag–metal reactions has also been included. The reaction mechanisms, i.e., the rate-limiting step or steps, the knowledge of which would be advantageous in altering or controlling the rate of processing, are covered in the following chapters.

4

Fluid dynamics in metallurgical processes

Roderick I.L. Guthrie
McGill University, Department of Mining & Metallurgical Engineering,
Montreal, Quebec, Canada

4.1. INTRODUCTION

Fluid dynamics, or mechanics, enters into many aspects of metallurgical processing operations involved in the extraction, refining, and casting of ferrous and nonferrous melts. The transport of heat, or mass, or particles, is often associated with such flows. In ironmaking, for example, optimizing gas flows through the burden of a blast furnace is a key factor in assuring high productivity and good gas utilization by the sinter, or pellets, within the burden (Standish, 1975). Similarly, mixing rates of 'raw' liquid steel in a furnace, or in a ladle during alloy additions, play key roles in optimizing a steel's chemistry and in assuring chemical and thermal homogeneity (Guthrie, 1977). Fluid mechanics even enters the field of solidification, in that steel and slag flows within the liquid sump of a casting machine help determine the quality of the final solidified product, in terms of cast microstructure, macrosegregation, the amounts of entrapped inclusions, and even surface characteristics of the solidified products. Similar examples can be quoted for the importance of fluid dynamics for the nonferrous industries, such as the successes achieved in the field of magnetohydrodynamics for the production and casting of aluminum (e.g., Banerjee and Evans, 1990).

Thus, over the last thirty years, significant strides have been made in the improvement and redesign of metallurgical processing operations, based on a growing understanding and appreciation of the relevance of fluid dynamics to such systems and its intrinsic coupling with process kinetics.

ADVANCED PHYSICAL CHEMISTRY FOR PROCESS METALLURGY
ISBN 0-12-618920-X
Copyright © 1997 Academic Press Ltd
All rights of reproduction in any form reserved

4.2. THEORY

The subject of fluid mechanics dates back to at least Egyptian and Grecian times, the theory of static fluids (hydrostatics) being well advanced at that time. Given that a fluid is defined as a substance incapable of withstanding any shear stress without being set in motion, one can easily show that the normal stresses (or pressures) acting on the six surfaces of an imaginary, infinitesimally small cubic element of static fluid must be equal. This basic understanding of fluid statics leads to a fundamental law of hydrostatics, first enunciated by Archimedes of Syracuse, circa 260 BC, to the effect that any object immersed within a static fluid will experience a buoyancy (or anti-gravity directed) force equal to the weight of static fluid displaced by the object (i.e., $F_B = -m_{\text{fluid}}g$). Once a fluid is in motion, however, pressure gradients usually exist, and a dynamic component of pressure, P_d, can be identified. This dynamic component of pressure can be defined as the absolute pressure, P_{Ab}, at a given point, less the static pressure, P_s. When defining a static pressure, P_s, for a fluid *in motion*, this is customarily taken as the mean of three orthogonally directed pressures (or normal stresses, τ_{xx}), so that

$$P_d = P_{ab} - P_s \quad \text{where } P_s = (\tau_{xx} + \tau_{yy} + \tau_{zz})/3 \tag{4.1}$$

In many situations, the dynamic components of pressure driving a given flow are much smaller, numerically, than static components, such as atmospheric pressure and hydrostatic pressure, acting on the flow system. In the art of computational fluid dynamics, to be addressed later, it is therefore more expedient to rewrite the equations of motion governing fluid flow so as to emphasize the influence of the dynamic pressure field on a resulting flow.

4.3. THE CONTINUITY AND MOMENTUM EQUATIONS

The differential equations for fluid motion derive from mathematical statements of conservation of mass and momentum. The continuity equation is a statement of mass conservation, while the momentum equation is an embodiment of Newton's second law of motion. This states that the sum of the forces acting on a body is equal to the product of its mass and its resultant acceleration, or more generally, rate of momentum change, i.e.:

$$\Sigma F_x = Ma_x = \frac{d(MU)}{dt} \tag{4.2}$$

Equation 4.2 is for unidirectional motion, where ΣF_x represents the sum of the x-forces acting on an imaginary cubic element of fluid, M is its mass, and a_x is its resulting acceleration.

In fluid dynamic analyses, it is customary to imagine a cubic element of fluid that is *stationary* (or Eulerian) with respect to time in the eyes of a stationary observer rather than the moving (or Lagrangian) frame of reference implied by Equation 4.2. If we consider Fig. 4.1, therefore, depicting a jet of liquid steel pouring from a ladle into a tundish, we can follow the Lagrangian element of liquid as it moves from position 1 to 2, and apply Equation 4.2 to demonstrate that $a_x = g_x$, or we can change to a stationary (Eulerian) frame of reference by replacing the acceleration term in Equation 4.2, according to

$$\frac{dU}{dt} = \frac{dU}{dx} \cdot \frac{dx}{dt} = U\frac{dU}{dx} \tag{4.3}$$

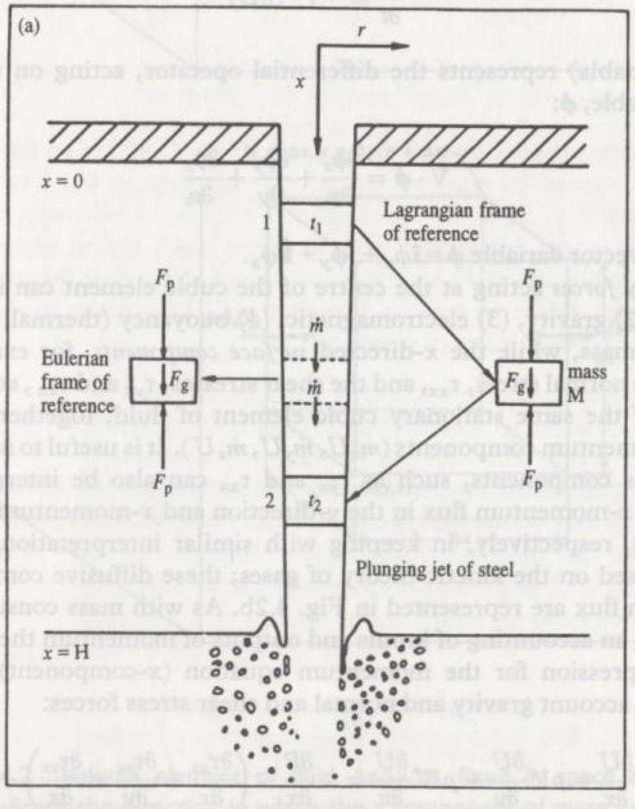

Figure 4.1 Momentum transport processes in fluids illustrated by a plunging jet of liquid steel. Distinction between differential volume elements fixed in space (Eulerian), or moving with the flow (Lagrangian). Reproduced from Guthrie (1992) by permission of Oxford University Press.

giving for the Eulerian frame of reference

$$\Sigma F_x = MU_x \frac{dU}{dx} = \rho A U dx \frac{dU}{dx} \quad \text{or} \quad \dot{m} dU \tag{4.4}$$

These two frames of reference are illustrated in Fig. 4.1.

Figure 4.2a illustrates a more generalized Eulerian situation for three-dimensional flows, in which mass enters and leaves the six surfaces of our imaginary cubic element of fluid. An accounting of inputs and outputs of mass, plus any accumulation of mass in the case of compressible fluids, leads to the continuity equation for the conservation of mass. For a Cartesian-based coordinate system therefore

$$\frac{\partial \rho}{\partial t} = -\nabla \cdot (\rho \mathbf{U}) \tag{4.5}$$

where ∇ (nabla) represents the differential operator, acting on the general vector variable, $\boldsymbol{\phi}$:

$$\nabla \cdot \boldsymbol{\phi} = \frac{\partial \phi_x}{\partial x} + \frac{\partial \phi_y}{\partial y} + \frac{\partial \phi_z}{\partial z}$$

where the vector variable $\boldsymbol{\phi} = \hat{\mathbf{i}}\phi_x + \hat{\mathbf{j}}\phi_y + \hat{\mathbf{k}}\phi_z$.

The *body forces* acting at the centre of the cubic element can include, (1) pressure, (2) gravity, (3) electromagnetic, (4) buoyancy (thermal, mass), and (5) added mass, while the x-directed *surface components*, for example, will include the normal stress, τ_{xx}, and the shear stresses, τ_{yx} and τ_{zx}, acting on the surfaces of the same stationary cubic element of fluid, together with convective momentum components $(\dot{m}_x U, \dot{m}_y U, \dot{m}_z U)$. It is useful to note that the shear stress components, such as τ_{yx} and τ_{zx} can also be interpreted as a transfer of x-momentum flux in the y-direction and x-momentum flux in the z-direction, respectively, in keeping with similar interpretations for shear stresses based on the kinetic theory of gases; these diffusive components of momentum flux are represented in Fig. 4.2b. As with mass conservation, or continuity, an accounting of inputs and outputs of momentum then leads to a general expression for the momentum equation (x-component), explicitly taking into account gravity and normal and shear stress forces:

$$\frac{\partial \rho U}{\partial t} + \rho U \frac{\partial U}{\partial x} + \rho V \frac{\partial U}{\partial y} + \rho W \frac{\partial U}{\partial z} = -\frac{\partial P}{\partial x} - \left(\frac{\partial \tau_{xx}}{\partial x} + \frac{\partial \tau_{yx}}{\partial y} + \frac{\partial \tau_{zx}}{\partial z} \right) + \rho g_x + \Sigma F_x \tag{4.6}$$

where ΣF_x can represent other forces acting on the volume element, such as electromagnetic, added mass, and buoyancy forces.

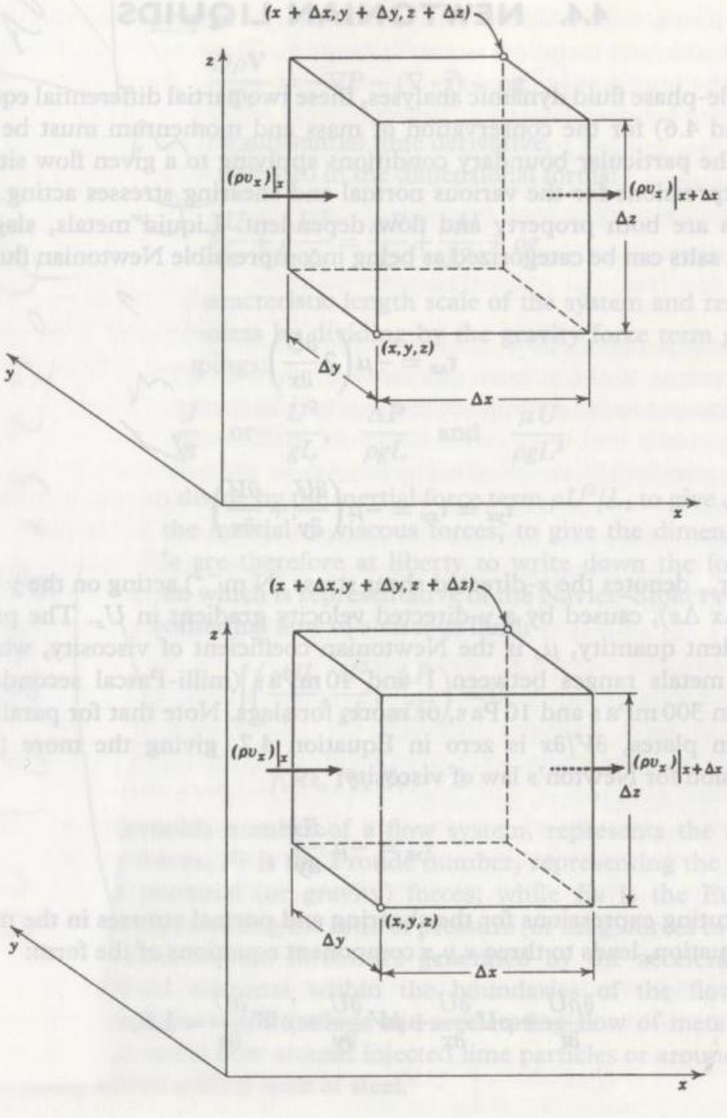

(a)

Figure 4.2 Volume element of fluid $\Delta x \Delta y \Delta z$, fixed in space and time. The arrows indicate the direction in which the x component of mass (upper element) and the diffusive components of x momentum (lower element) are transported through the imaginary surfaces. Reproduced from Guthrie (1992) by permission of Oxford University Press.

4.4. NEWTONIAN LIQUIDS

In single-phase fluid dynamic analyses, these two partial differential equations (4.5 and 4.6) for the conservation of mass and momentum must be solved using the particular boundary conditions applying to a given flow situation, plus expressions for the various normal and shearing stresses acting. These stresses are both property and flow dependent. Liquid metals, slags, and molten salts can be categorized as being incompressible Newtonian fluids, for which

$$\tau_{xx} = -\mu\left(2\frac{\partial U}{\partial x}\right) \tag{4.7}$$

and

$$\tau_{yx} = \tau_{xy} = -\mu\left(\frac{\partial U}{\partial y} + \frac{\partial V}{\partial x}\right) \tag{4.8a}$$

where τ_{yx} denotes the x-directed shear stress (N m^{-2}) acting on the y surface (area $\Delta x\ \Delta z$), caused by a y-directed velocity gradient in U_x. The property dependent quantity, μ, is the Newtonian coefficient of viscosity, which for liquid metals ranges between 1 and 10 mPa s (milli-Pascal seconds), and between 300 mPa s and 10 Pa s, or more, for slags. Note that for parallel flow between plates, $\partial V/\partial x$ is zero in Equation 4.7, giving the more familiar expression for Newton's law of viscosity:

$$\tau_{yx} = -\mu\frac{dU}{dy} \tag{4.8b}$$

Substituting expressions for the shearing and normal stresses in the momentum equation, leads to three x,y,z component equations of the form:

$$\frac{\partial \rho U}{\partial t} + \rho U\frac{\partial U}{\partial x} + \rho V\frac{\partial U}{\partial y} + \rho W\frac{\partial U}{\partial z} = \Sigma F_x \tag{4.9}$$

where

$$\Sigma F_x = -\frac{\partial P}{\partial x} + \mu\left(\frac{\partial^2 U}{\partial x^2} + \frac{\partial^2 U}{\partial y^2} + \frac{\partial^2 U}{\partial z^2}\right) + \rho g_x \tag{4.10}$$

These sets of equations, referred to as the Navier–Stokes equations in honour of two early researchers in the field, can be summarized in vector form as

$$\frac{\partial}{\partial t}(\rho \mathbf{V}) = -[\nabla \cdot \rho \mathbf{V}\,\mathbf{V}] - \nabla P - [\nabla \cdot \bar{\tau}] + \rho \mathbf{g} \tag{4.11}$$

or even more compactly as

$$\frac{D\rho \mathbf{V}}{Dt} = -\nabla P - (\nabla \cdot \bar{\tau}) + \rho \mathbf{g} \tag{4.12}$$

where D/Dt represents the substantial time derivative.

Writing Equations 4.9 and 4.10 in the dimensional forms:

$$\rho\frac{U}{t} + \rho\frac{U^2}{L} = \frac{\Delta P}{L} + \frac{\mu U}{L^2} + \rho g \tag{4.13}$$

where L represents a characteristic length scale of the system and rendering Equation 4.13 dimensionless by dividing by the gravity force term gives us three independent groupings:

$$\frac{U}{gt} \text{ or } \frac{U^2}{gL}, \quad \frac{\Delta P}{\rho g L} \quad \text{and} \quad \frac{\mu U}{\rho g L^2}$$

Alternatively, we can divide by the inertial force term $\rho U^2/L$, to give $\Delta P/\rho U^2$ or take the ratio of the inertial to viscous forces, to give the dimensionless grouping $\rho UL/\mu$. We are therefore at liberty to write down the following dimensionless function which is representative of the Navier–Stokes equation for incompressible isothermal flow of a viscous fluid:

$$f\left(\frac{\rho UL}{\mu}, \frac{U^2}{gL}, \frac{\Delta P}{\rho U^2}\right) = 0 \tag{4.14}$$

or

$$f(Re, Fr, Eu) = 0 \tag{4.15}$$

where Re, the Reynolds number of a flow system, represents the ratio of inertial to gravity forces; Fr is the Froude number, representing the ratio of inertial forces to potential (or gravity) forces; while Eu is the Euler (or Newton) number, representing the ratio of pressure (or drag) forces to inertial forces. The so-called inertial forces are generated by the acceleration or deceleration of fluid elements within the boundaries of the flow field. Metallurgical examples would include the accelerating flow of metal into a teeming nozzle, or metal flow around injected lime particles or around argon bubbles rising within a filled ladle of steel.

4.5. TURBULENCE

In most metallurgical processes, metal and slag flows take place in large processing vessels, such as basic oxygen furnaces, blast furnaces, ladles, and tundishes. As such, attendant Reynolds numbers are extremely high, in the order of 10^3–10^5, indicating that a similar ratio between inertial forces and viscous forces exists. Under such conditions, laminar or layer-like flow is unsustainable and turbulent instabilities set in. These turbulent interactions lead to the interchange of eddies, or 'whorls,' with a resulting exchange of momentum between faster and slower moving regions of liquid. As with the laminar flow implied by Newton's law of molecular viscosity, one may model the equivalent turbulent shear stresses generated by this interchange of momentum according to an equation of the form

$$\tau_{\text{turb},yx} = -\mu_t \frac{d\bar{U}}{dy} \tag{4.16}$$

for turbulent planar flow of liquid across a solid surface. Experimental measurements of the stresses generated by these energy-dissipating eddies, whose sizes are in the submillimeter range and frequencies in the 10^3 to 10^5 Hz range, typically lead to so-called turbulent coefficients of viscosities, μ_t, that are numerically 10^3 to 10^5 times greater than their laminar, or molecular, equivalent.

Equation 4.16, based on Prandtl's theory of turbulence, breaks down in the bulk of a flow system, far away from solid surfaces, where turbulent eddies still exist, together with attendant shearing stresses, even though velocity gradients can approach zero, such as at the center of a pipe through which liquid flows. (Equation 4.16 would predict $\tau_{\text{turb},yx} = 0$ for $dU_x/dy = 0$.)

Various solutions are possible to help represent these effects of turbulence. One is to solve transient forms of the Navier–Stokes (N–S) equations numerically, using micrometer-sized volume elements to faithfully represent the smallest elements of fluid, and thereby model both the macroscopic and microscopic elements of a given flow. This is currently impractical with existing computer technology, so the next recourse is to mimic the role of turbulence in terms of its manifestations at the macroscopic level. The simplest approach is to solve a modified form of the N–S equation, referred to as the Reynold's stress or turbulent Navier–Stokes equation. Thus, by resolving an instantaneous velocity component, U, into a mean component $\bar{U}$, and a fluctuating portion, u', and time averaging according to

$$\bar{U} = \frac{1}{t_2 - t_1}\int_{t_1}^{t_2} U\,dt, \qquad \bar{P} = \frac{1}{t_2 - t_1}\int_{t_1}^{t_2} P\,dt \tag{4.17}$$

where $(t_2 - t_1) \gg$ time period of turbulent fluctuations, one arrives at the time-averaged forms of the continuity and N–S equations for turbulent flow. These can be written compactly, using Cartesian tensor notation, in which i and j take successive values of 1, 2, and 3 to represent vector components in the x_1, x_2, or x_3 (or x, y, z) directions:

$$\frac{\partial \bar{U}_i}{\partial x_i} = 0 \tag{4.18}$$

and

$$\frac{\partial \bar{U}_i}{\partial t} + \bar{U}_j \frac{\partial \bar{U}_i}{\partial x_j} = -\frac{1}{\rho}\frac{\partial \bar{P}}{\partial x_i} + \frac{\partial}{\partial x_i}\left(\nu \frac{\partial \bar{U}_i}{\partial x_j} - \overline{u'_i u'_j}\right) + g_i \tag{4.19}$$

for mass and momentum conservation, respectively, in incompressible, constant density fluids. The only difference between this equation, and the N–S equations for laminar flows are the Reynolds stress terms $\rho u'_i u'_j$. On the basis of the Prandtl approach, these r.m.s. stress products, $u'_i u'_j$, can be replaced by $\nu_t\, \partial U_i/\partial x_j$, where ν_t is the turbulent kinematic viscosity, μ_t/ρ, and $\nu_t \gg \nu$, the 'molecular' kinematic viscosity (μ/ρ).

For many industrial-scale turbulent flow problems, in which inertial forces far outweigh viscous (i.e., Froude dominated flows) one can take ν_t to be constant and produce quite realistic flow fields (e.g., Salcudean and Guthrie, 1978).

However, in order to model convective plus conductive/diffusive flows of heat or mass associated with fluid motions, mass and energy conservation balances on the volume elements depicted in Fig. 4.2 lead to the following form of partial differential equation for energy and/or mass transport:

$$\frac{\partial \rho\phi}{\partial t} + U_i \frac{\partial \rho\bar{\phi}}{\partial x_i} = -\frac{\partial}{\partial x_i}\left(\lambda \frac{\partial \bar{\phi}}{\partial x_i} - \overline{u'_i \phi'}\right) \tag{4.20}$$

where ϕ represents average enthalpy or mass fraction of species i, and λ denotes the molecular conduction or diffusive transport coefficients. By analogy with momentum transport, the fluctuating term $\overline{u'\phi'}$ can be replaced by $\Gamma(\partial\phi/\partial x_i)$ where $\Gamma \gg \lambda$. The symbol Γ represents an eddy diffusivity, D_t, or α_t, a turbulent thermal diffusivity for enthalpy (or heat) transport. It is important to note that Equation 4.20 in comparison to Equation 4.19 lacks a (dominating) pressure gradient term. In consequence, while a precise description of viscosity is not needed in predicting flows within large-scale vessels, and viscosity can even be ignored sometimes when solving the Reynold's equations, the same cannot be held true of associated heat and mass transfer phenomena. For such phenomena, a precise model of turbulence is needed to mimic the all-important $\overline{u'_i\phi'}$ diffusive terms, balancing the convective terms to the left of the equation.

4.6. DIFFERENTIAL MODELS OF TURBULENCE FOR BULK CONVECTING FLOWS

Prandtl and Kolmogorov independently suggested that bulk turbulent viscosity should be determined by way of differential rather than algebraic equations (Kolmogorov, 1941; Antonia et al., 1997), and that the most meaningful way of characterizing velocity fluctuations in high-*Re* turbulent flows (i.e., far from walls or shear flow layers) would be through 'square-rooting' the kinetic energy of turbulence (per unit mass). The turbulence kinetic energy is defined by

$$k = \tfrac{1}{2}\left(\overline{u'^2} + \overline{v'^2} + \overline{w'^2}\right) \tag{4.21}$$

which, for isotropic conditions ($u' = v' = w'$), typical of the eddies containing the major portion of the kinetic energy of turbulence, reduces to

$$k = \tfrac{3}{2}\overline{u'^2} \tag{4.22}$$

We see that the characteristic turbulent velocity component, u_k, becomes

$$u_k \equiv \sqrt{\frac{2}{3}}k^{1/2} \quad \text{or} \quad 0.82\,k^{1/2} \tag{4.23}$$

A transport equation for *k* was therefore obtained by suitable manipulation of the exact, and time-averaged, forms of the Navier–Stokes equation, so as to bring *k* into prominence. This so-called 'one-equation' model represented an important step in the development of more general models of turbulence, in that the direct link between the velocity gradient and the fluctuating velocity component was removed. However, difficulties in specifying a length-scale *l* still remained, as with algebraic models.

Further development in the field led to the development, among others, of a two-equation, *k–ε* model of turbulence. This has been used by many researchers modeling or predicting flows within metallurgical systems. In this model, therefore, the rate of turbulent energy dissipation, $\dot{\varepsilon}$ (which for local isotropy and high *Re* is equal to the molecular viscosity × fluctuating vorticity, $\mu(\partial u_i'/\partial x_j)^2$) is expressed in the form of a further transport equation (4.25), in conjunction with a transport equation for the kinetic energy of turbulence (4.24). Written in index notation, the transport equations for *k* and *ε* take the form:

For turbulence energy transport:

$$\underbrace{\frac{\partial k}{\partial t}}_{\substack{\text{rate of}\\ \text{change}}} + \underbrace{U_i\frac{\partial k}{\partial x_i}}_{\text{convection}} = \underbrace{\frac{\partial}{\partial x_i}\left(\frac{\nu_t}{\sigma_k}\frac{\partial k}{\partial x_i}\right)}_{\text{diffusion}} + \underbrace{\nu_t\left(\frac{\partial U_i}{\partial x_j}+\frac{\partial U_j}{\partial x_i}\right)\frac{\partial U_i}{\partial x_j}}_{\text{generation}} \underbrace{-\dot{\varepsilon}}_{\text{destruction}} \tag{4.24}$$

For turbulence energy dissipation:

$$\underbrace{\frac{\partial \dot{\varepsilon}}{\partial t}}_{\substack{\text{rate of}\\ \text{change}}} + \underbrace{U_i\frac{\partial \dot{\varepsilon}}{\partial x_i}}_{\text{convection}} = \underbrace{\frac{\partial}{\partial x_i}\left(\frac{\nu_\varepsilon}{\sigma_\varepsilon}\frac{\partial \dot{\varepsilon}}{\partial x_i}\right)}_{\text{diffusion}} \underbrace{+C_1\frac{\dot{\varepsilon}}{k}(P)}_{\text{generation}} \underbrace{-C_2\frac{\dot{\varepsilon}^2}{k}}_{\text{destruction}} \tag{4.25}$$

where

$$\nu_t = \frac{\mu_t}{\rho} \quad \text{and} \quad \Gamma = \frac{\nu_t}{\sigma}$$

and

$$\mu_t = (\rho k^{1/2} l) = C_D\frac{\rho k^2}{\dot{\varepsilon}} \tag{4.26}$$

Recommended values for the various empirical constants appearing in Equation 4.25 (Launder and Spalding, 1974) are

C_1	C_2	C_D	σ_k	σ_ε
1.44	1.92	0.09	1.0	1.3

C_D being deduced from Equations 4.24 and 4.26 on the basis of near wall turbulence where convection and diffusion of turbulence can be ignored, C_2 from the decay of turbulence behind a grid, and C_1 from the logarithmic velocity profile that prevails in near-wall turbulence. Since then, a low Reynolds number form of the *k–ε* equation has been developed in which this latter constraint is removed, so as to allow one to model flow fields interacting with interdendritic fluid during metal casting operations, for example. While the *k–ε* equation has been used extensively, certain features of turbulence, such as randomly, slowly shifting flow patterns generated by turbulence phenomena cannot be successfully mimicked. For these situations, the 'large eddy simulation' model of turbulence has met with success in representing flows from nozzles in continuous casting operations, for instance. Further details of turbulence modeling are to be found in the literature. As noted previously, for inertially dominated flows, simple turbulence models, and even a constant (time and space independent) effective viscosity/diffusivity value, can give effective *flow* predictions. Consequently, the level of computational and intellectual effort to be expended by including a particular turbulence model must match the level of information required, and recognize the importance, or otherwise, of turbulence on the particular flow system under investigation.

4.7. ELECTROMAGNETICALLY DRIVEN FLOWS

In recent years, very significant technological advances have been made in the application of electromagnetic force fields aimed at influencing the behavior of liquid metals and alloys during metals and materials processing operations (Asai, 1989). Examples include

1. The electromagnetic stirring of liquid steel in ladles for heating, inclusion removal, and mixing-in of alloy additions

2. Electromagnetic stirring and braking (i.e., flow suppression) in the continuous casting of steel and aluminum for improved microstructures, reduced solute macro-segregation and better metal quality
3. Electromagnetic casting of aluminum in direct chill casting machines for improved ingot surfaces and near surface microstructure
4. The damping of electromagnetically generated waves to allow reduced gaps between the carbon anode and liquid aluminum cathode for reduced electrical energy losses in the molten electrolyte
5. The recent continuous casting of clad steel slabs with a level magnetic field brake (Zeze et al., 1996)

In terms of the phenomena involved, it is commonly understood that if a current is passed through conducting coils that surround a ladle or mold containing an electrical conductor (i.e., the liquid metal) then that primary current will induce a magnetic force field, which in turn will produce motion and heating within the melt.

Maxwell's equations form the basis of any quantitative description of the magnetic fields and forces induced. Thus, Maxwell's equations, using the magnetohydrodynamic (MHD) approximation (Hughes and Young, 1966; Jackson, 1962), can be written

$$\nabla \times \mathbf{E} = -\frac{\partial \mathbf{B}}{\partial t} \qquad (4.27)$$

where **E** is the electric field vector ($\mathrm{V\,m^{-1}}$) and **B** the magnetic flux density vector ($\mathrm{W\,m^{-2}}$ or Tesla). **H**, the magnetic field ($\mathrm{A\,m^{-1}}$), is related to the magnetic flux density according to the relation $\mathbf{B} = \mu(H)\mathbf{H}$, where μ represents the magnetic permeability of the material ($\mathrm{H\,m^{-1}}$). Continuing,

$$\nabla \times \mathbf{H} = \mathbf{J} \qquad (4.28)$$

$$\nabla \cdot \mathbf{J} = 0 \qquad (4.29)$$

$$\nabla \cdot \mathbf{B} = 0 \qquad (4.30)$$

Equations 4.29 and 4.30 represent statements of conservation for **J** and **B** for steady-state flows of electrical and magnetic fluxes. Thus, **J** in Equation 4.28 represents the conduction current density or flux ($\mathrm{A\,m^{-1}}$). The latter is related to a form of Ohm's law that includes the flux of electrical current carried by the moving fluid:

$$\mathbf{J} = \sigma_e[\mathbf{E} + \mathbf{U} \times \mathbf{B}] \qquad (4.31)$$

where σ_e represents the liquid's electrical conductivity ($(\mathrm{ohm\,m})^{-1}$). The second term, however, is often relatively insignificant for typical metal stirring applications and can commonly be ignored.

The Lorentz, or body force, generated on an element of conducting liquid by the electromagnetic force field is given by the cross product of the conduction current density, **J**, and, the magnetic flux density, **B**:

$$\mathbf{F}_{\mathrm{em}} = \mathbf{J} \times \mathbf{B} \qquad (4.32)$$

In magnetohydrodynamic analyses, therefore, the electric and magnetic fields within the system have first to be solved, and the resulting computations for the magnetic force field incorporated into the Reynolds or Navier–Stokes equation, to solve for the resulting flow fields. Fortunately, the two can be treated as uncoupled partial differential equations since the **U** × **B** product is not usually significant.

4.8. PHYSICAL AND COMPUTATIONAL MODELS

Prior to the advent of computers, few, if any, industrial systems involving heat, mass, and fluid flow, were amenable to analytical solutions of the Navier–Stokes, continuity and Maxwell equations just presented. Solutions for viscous creeping flow, in which the inertial terms are ignored, were available, such as Stokes' law for the drag force, F_D, experienced by a sphere of radius R ($F_D = 6\pi\mu R U_\infty$). At the other extreme, flows for which viscosity could be ignored (inviscid flows) led to many analytical solutions of the reduced form of the N-S equation (the Eulerian equation). However, these solutions proved to be unrealistic for diverging flows involving turbulent recirculatory whorls and adverse pressure gradients.

Given this situation, the use of physical models became an important design tool for naval architects in the seventeenth century (Lausanne, 1971). The British Admiralty, for example, required the testing of all 'man of war' sailing ships using faithful replicas (wooden models) of the proposed vessels, at the 1/40th scale. We may find a similar early use of models in metallurgy. For example, Brearly and Brearly, in their book *Ingots and Ingot Moulds*, published 1918, describe the use of molten stearine to study solidification, ingot structure, metal shrinkage, and cavity formation in steel ingot casting operations.

Thus, physical models of systems remain an important part of the armory of a practising engineer in helping to understand, improve, or even design new processes. Useful insight can be gained into the behavior of gas-stirred ladles of liquid steel, for instance, by bubbling gas bubbles through a full-scale (or reduced-scale) water model. Similarly, it is quite commonplace for suppliers of refractories and tundish boards to model the flow of steel in their customer's tundish and to then make design recommendations or propose flow modifications based on measurements of the mean residence times of elements of water within it prior to their exit into the caster(s). By maximizing retention times, conventional wisdom has it that the liquid steel will be cleaner, since more inclusions have the possibility of escaping to the upper surface or slag.

One sees from Equation 4.15 that, provided equality of Froude, Reynolds, and Euler numbers, in geometrically equivalent vessels, is maintained, then the solutions to the Navier–Stokes or the turbulent form of the Navier–Stokes equations will be identical, provided equivalent boundary conditions exist. As such, one can expect a one-to-one ratio between model and prototype of velocities at corresponding positions, and times, during the filling, draining, or steady-state operations within a tundish (provided both systems are essentially isothermal).

Difficulties with the physical modeling approach include the problem of matching, simultaneously, an array of so-called dimensionless π groupings (e.g., *Re*, *Eu*, *Fr*, *We*,...) that may be important, and in finding suitable low-temperature liquids whose physical properties can produce equivalent π groupings in the first place. While modelers are fortunate that the kinematic viscosities of water and liquid steel are practically identical (giving equal Reynold's number), steel's high surface tension ($1.8\,\mathrm{N\,m^{-1}}$), high thermal conductivity, and high electrical conductivity are not matchable with either aqueous or organic liquids. Nonetheless, many useful studies of metallurgical flow systems have been possible using the physical modeling approach, and many important successes can be demonstrated.

Turning to computational fluid mechanics, significant advances have been made in the art since the widespread availability of high-speed digital computers in the early 1960s. The approach involves re-writing the partial differential equations in numerical form, for a two- or three-dimensional array of discrete volume elements, shown in Fig. 4.3a and 4.3b for Cartesian and cylindrical coordinate systems (Guthrie, 1992). However, the development of CFD (computational fluid dynamics) has lagged equivalent advances in computer models for the mechanics of solid structures, or in heat and mass transfer in systems involving solid (nonmoving) bodies. The reason for this has been that while conceptually similar discretization schemes have been developed, it is far more difficult to obtain satisfactory (converged) solutions, since computations require the simultaneous solution of a number of highly nonlinear equations for pressure, velocities, turbulence, and attendant temperature or species concentrations over a discretized domain whose boundaries coincide with the boundaries of the flow field.

CFD schemes can be divided into two classes depending on whether an implicit or explicit numerical scheme is adopted. A further subdivision, into parabolic and elliptic flows, is common depending on whether the downstream flow affects the character of the upstream flow. Typical elliptic flows involve zones of recirculation, and these are common features of many metallurgical systems. Flows which readily come to mind include electromagnetic stirring in continuous casting, fluid flow in filling ladles, and gas-driven recirculatory flows in batch processing operations (e.g., Bessemer or OBM steelmaking vessels).

In terms of numerical schemes for solving discretized forms of the Navier–Stokes, continuity, turbulence, and energy/species partial differential equations, the greatest successes to date have been with the so-called (integral), or control volume, finite difference technique, in which U, V, W, k, ε, C (concentration), and H (enthalpy) flows, into and out of, the many volume elements are taken into account, and balanced on the basis of the prescribed boundary conditions acting on the flow.

Thus, Fig. 4.3c illustrates a typical grid system setup for predicting recirculatory flow of liquid metal within a ladle, the flow being generated by an incoming vertical steel jet, for instance. Note that the volume element for the scalar nodal point volume elements (C, θ, P, k, ε) does not coincide with the two volume elements for vectors V and U, respectively.

Given that all the partial differential equations to be solved can be written in the general form

convection terms = diffusion terms + source term

we can write the general equation

$$\frac{\partial}{\partial t}(\rho\phi) + \mathrm{div}(\rho U\phi) = \mathrm{div}\big(\Gamma_\phi\ \mathrm{grad}\ \phi\big) + \dot{S}_\phi \qquad (4.33)$$

in which ϕ can represent $U, V, W, k, \varepsilon, C, \theta$. The term, Γ_ϕ grad ϕ represents the diffusive flux of ϕ; S_ϕ represents a so-called 'source' term, which essentially involves those residual elements which do not fit into the other three groupings. Discretization of this formula over finite volume elements such as those shown in Fig. 4.3a and b, together with a one-dimensional tridiagonal matrix algorithm for implicit line-by-line solution of nodal ϕ values, plus a Gauss–Siedel routine linking adjacent lines of nodes, can provide an efficient computational scheme for numerical integration (e.g., Patankar, 1980).

Given a typical three-dimensional flow problem, a $40 \times 40 \times 40$ nodal matrix would not be unusual. Combining this with seven variables (U, V, W, P, k, ε, C, and θ (temperature)) implies about a half million calculations, for each successive iteration. The number of iterations before full convergence is achieved may typically range from 1000 to 3000, requiring a total of some 0.5–1.5×10^9 computations.

Alternative schemes based on finite element modeling have also been used in CFD, largely because of their ability to solve heat, mass, and fluid flow taking place in complex geometries. Thus, in the case of finite element modeling (FEM), the calculation domain is typically subdivided into triangular elements. These are certainly more convenient than the regular grids of

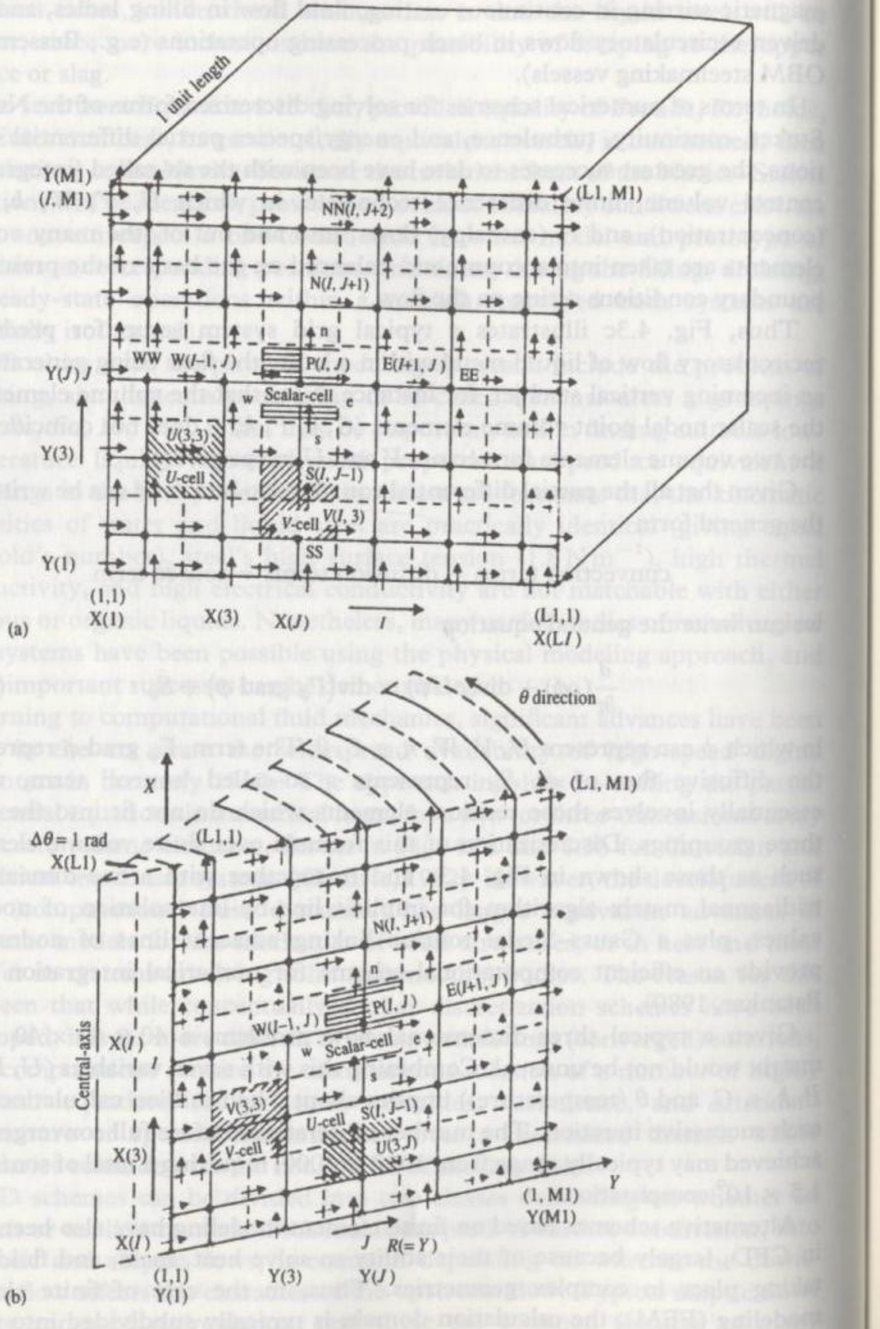

Figure 4.3 (a) and (b).

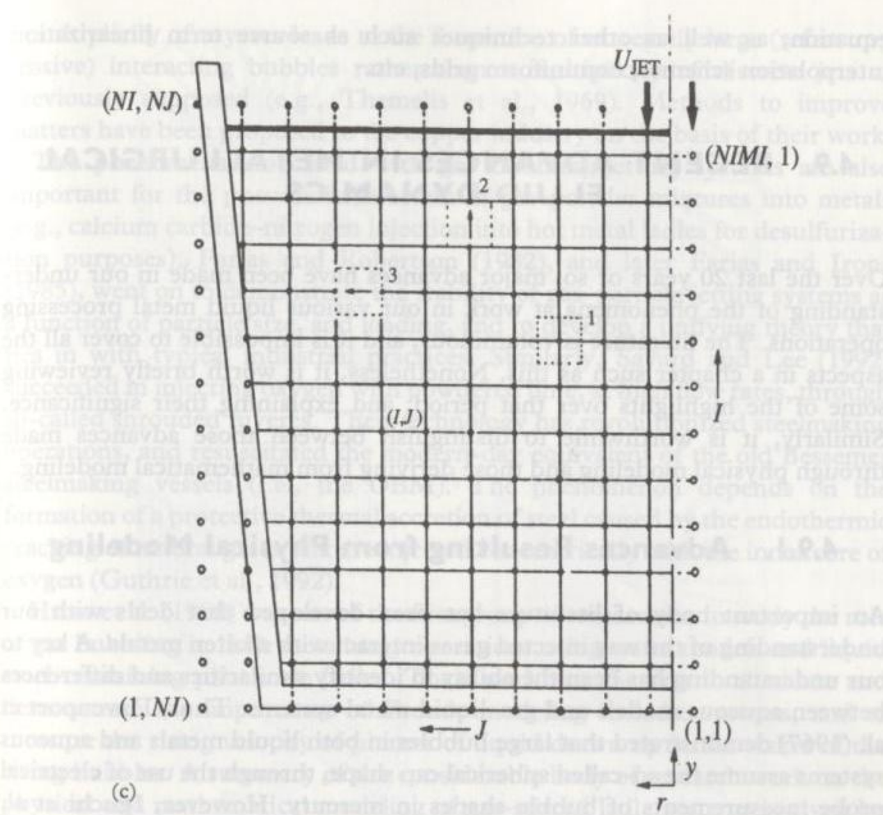

Figure 4.3 Control volume specification in (a) Cartesian mode and (b) cylindrical coordinates for axisymmetric cases. (c) Schematic of idealized axisymmetric flow system for simulating furnace tapping operations into teeming ladles. Reproduced from Guthrie (1992) by permission of Oxford University Press.

the finite difference approach when fitting complex boundary shapes, and are commonly used in calculating the magnetic force fields in MHD computations. The discretization equations are usually derived by the use of a variational principle, or by the Galerkin method, which is a special case of the method of weighted residuals. The majority of CFD commercial codes available for industrial users are still based on the finite difference, control volume method just presented. For complex shapes, the development of a boundary or body-fitted coordinate scheme mitigates many of the objections to the use of integral volume techniques raised by proponents of FEM.

Other topics to which the interested reader is referred include the use of staggered grids (illustrated in Fig. 4.3a) for stabilizing solutions, techniques to solve the dynamic pressure field implicit in the *P* term of the Navier–Stokes equation, as well as other techniques such as source term linearization, interpolation schemes, nonuniform grids, etc.

4.9. RECENT ADVANCES IN METALLURGICAL FLUID DYNAMICS

Over the last 20 years or so, major advances have been made in our understanding of the phenomena at work in our various liquid metal processing operations. The literature is voluminous, and it is impossible to cover all the aspects in a chapter such as this. Nonetheless, it is worth briefly reviewing some of the highlights over that period, and explaining their significance. Similarly, it is worthwhile to distinguish between those advances made through physical modeling and those deriving from mathematical modeling.

4.9.1. Advances Resulting from Physical Modeling

An important body of literature has been developed that deals with our understanding of the way injected gases interact with molten metals. A key to our understanding has been the ability to identify similarities and differences between aqueous models and gas–liquid metal systems. Thus, Davenport et al. (1967) demonstrated that large bubbles in both liquid metals and aqueous systems assume the so-called spherical cap shape, through the use of electrical probe measurements of bubble shapes in mercury. However, Iguchi et al. (1995) propose a bell shape for molten iron systems. Sano and Mori (1977) and Irons and Guthrie (1978) showed that bubbling gases into liquid metals passed through a progression of stages such that, at low flow rates, surface tension versus buoyancy forces governed the size of the resulting bubbles (constant-volume regime) while, at higher flow rates, bubbles formed at orifices became ever larger, their size being determined by the gas flow rate divided by about 11 s^{-1}, the latter being roughly their frequency of formation at an orifice. At still higher flow rates, the phenomenon of jetting takes place. It was demonstrated that nonwetting effects makes bubbles in liquid metal–refractory (bubbling) systems larger than their aqueous counterparts at lower flow rates.

Sano demonstrated that at sufficiently high velocities approaching the velocity of sound, discrete bubble formation at the orifice ceases and a continuous jet of gas is formed. Nilmani and Robertson (1980) showed that the gas/liquid density ratio was an important factor in modeling gas–metal systems at high flow rates. In a similar vein, Hoefele and Brimacombe (1979) and Brimacombe et al. (1985), demonstrated that the side-injection of air into the Pierce–Smith Copper Convertors (horizontal cylindrical vessels) through a multiplicity of tuyeres leads to the formation of extremely large (refractory erosive) interacting bubbles rather than a multiplicity of discrete jets as previously supposed (e.g., Themelis et al., 1969). Methods to improve matters have been proposed to the copper industry on the basis of their work.

The phenomena associated with gas bubbling/jetting systems are also important for the pneumatic injection of gas–powder mixtures into metals (e.g., calcium carbide–nitrogen injection into hot metal ladles for desulfurization purposes). Farias and Robertson (1982), and later Farias and Irons (1985), went on to demonstrate the stability of gas–particle jetting systems as a function of particle size, and loading, and to develop a unifying theory that ties in with typical industrial practices. Similarly, Savard and Lee (1992) succeeded in injecting oxygen with powdered lime, at high flow rates, through so-called shrouded tuyeres. Their technology has revolutionized steelmaking operations, and resuscitated the modern-day equivalent of the old Bessemer steelmaking vessels (i.e., the OBM). The phenomenon depends on the formation of a protective thermal accretion of steel caused by the endothermic cracking of natural gases that are injected concentrically with the inner core of oxygen (Guthrie et al., 1992).

Hsiao et al. (1980) was one of the first group of researchers to study the role of gas bubbling in ladle metallurgy operations using water models and liquid steel-containing pilot scale ladles. Their work was the first to elucidate and demonstrate the importance of Froude modeling in ladle systems, and to measure the rising velocity of plumes of liquid drawn up in the wakes of the rising bubbles. A summary of the considerable body of research work on the physical and mathematical modeling of gas-stirred ladle systems is given by Mazumdar and Guthrie (1995).

Moving on to reactive slag–metal systems, Panda and Robertson (1994) elegantly modeled the reaction of metal droplets in slags by observing the evolution of hydrogen from the interface of a mercury droplet containing dissolved sodium, in contact with water. Ito and Fruehan (1989) made direct x-ray studies of the actual phenomena associated with the injection of a carbon containing droplet of iron within an (oxidizing) steelmaking slag containing lime, silica, and iron oxide. Their work is important in showing the formation of CO–CO_2 gas halos around the reacting droplets that determine the reaction rates possible in slag-based, direct steelmaking operations. Further work along these lines has led to a good understanding of foaming phenomena in metallurgical slags (Lin and Guthrie, 1994; Gou et al., 1996; Fruehan, 1996).

4.9.2. Mathematical Models

Generally, good mathematical models can only be developed provided a clear physical understanding of a phenomenon exists. Thanks to all the work on

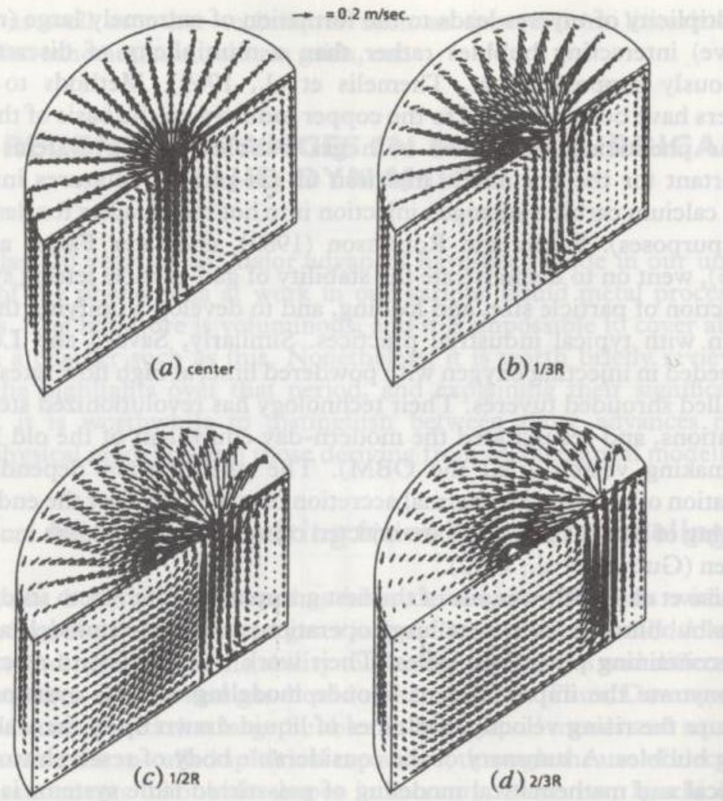

Figure 4.4 Computations illustrating flow patterns developed by submerged gas injection through a single porous plug located at (a) center, (b) one-third, (c) half, and (d) two-thirds radius.

bubble-stirred ladles, for instance, Joo and Guthrie (1992) were able to model three-dimensional flows in ladles and determine where a porous plug gas injector should best be located for the purposes of rapid mixing. Figure 4.4 shows a typical plot of a velocity vector field predicted on the basis of Froude modeling, in which the rotational aspects of the flow help intermix alloy

Figure 4.5 (a) Illustration of predicted 95% per bulk mixing times in a 1/3-scale water model of a 100-tonne ladle for various plug positions and tracer addition points. (Square marks represent measured mixing times.) (b) Illustration of transients in isoconcentrations following (i), center-plume addition of a tracer and (ii) tracer addition just off-center to the gas–liquid plume, during center gas bubbling.

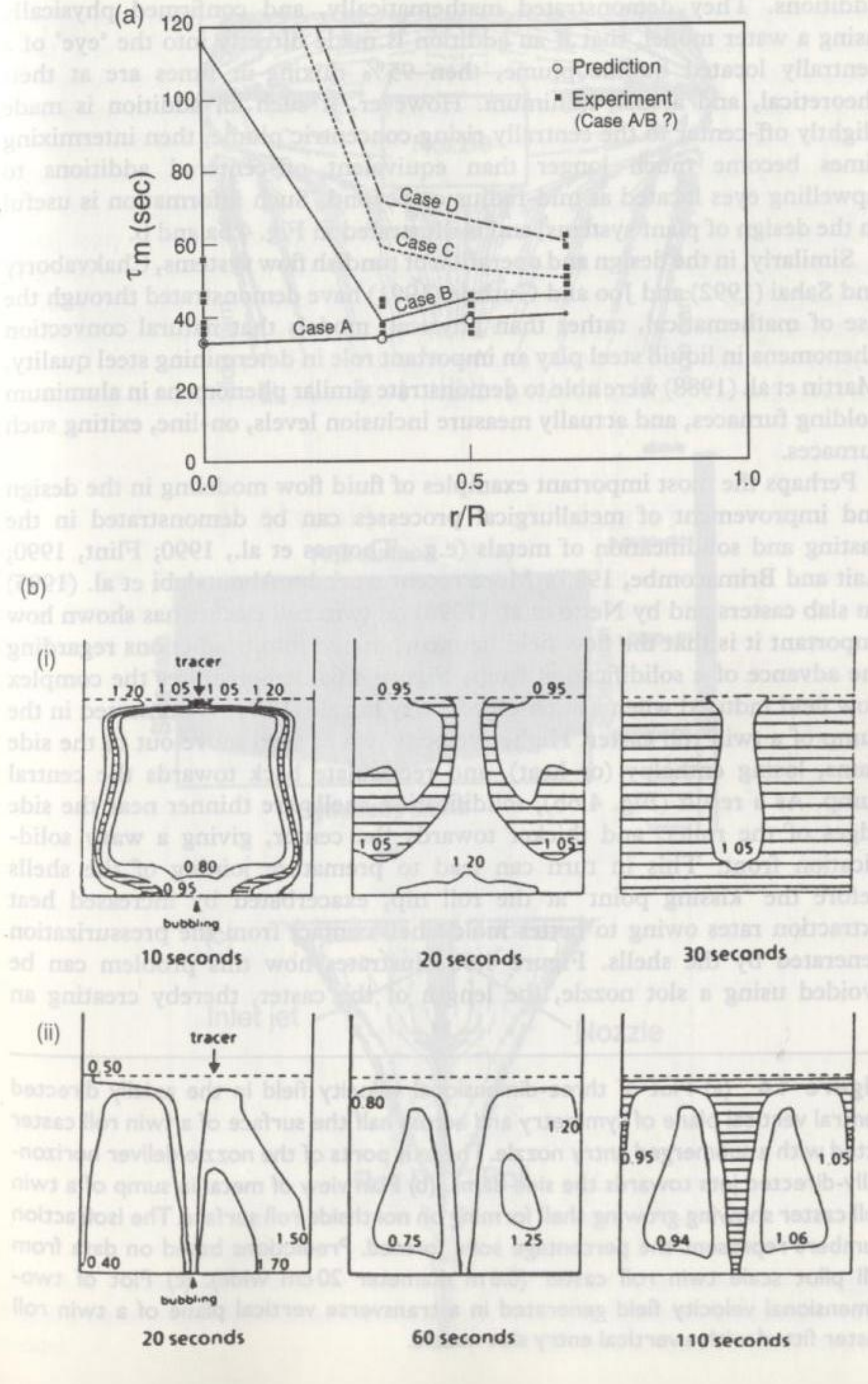

additions. They demonstrated mathematically, and confirmed physically using a water model, that if an addition is made directly into the 'eye' of a centrally located bubble plume, then 95% mixing-in times are at their theoretical, and actual, minimum. However, if such an addition is made slightly off-center to the centrally rising concentric plume, then intermixing times become much longer than equivalent off-centered additions to upwelling eyes located at mid-radius or beyond. Such information is useful in the design of plant systems, and is illustrated in Fig. 4.5a and b.

Similarly, in the design and operation of tundish flow systems, Chakvaborty and Sahai (1992) and Joo and Guthrie (1991) have demonstrated through the use of mathematical, rather than physical, models that natural convection phenomena in liquid steel play an important role in determining steel quality. Martin et al. (1988) were able to demonstrate similar phenomena in aluminum holding furnaces, and actually measure inclusion levels, on-line, exiting such furnaces.

Perhaps the most important examples of fluid flow modeling in the design and improvement of metallurgical processes can be demonstrated in the casting and solidification of metals (e.g., Thomas et al., 1990; Flint, 1990; Lait and Brimacombe, 1983). More recent work by Aboutalebi et al. (1995) on slab casters and by Netto et al. (1996) on twin roll casters has shown how important it is that the flow field be incorporated into predictions regarding the advance of a solidification front. Figure 4.6a demonstrates the complex flow field induced when a submerged entry nozzle (SEN) is immersed in the sump of a twin roll caster. Higher velocity jets of steel move out to the side dams, losing enthalpy (or heat), and recirculate back towards the central sump. As a result (Fig. 4.6b), solidification shells are thinner near the side edges of the roller, and thicker towards the center, giving a wavy solidification front. This in turn can lead to premature joining of the shells before the 'kissing point' at the roll nip, exacerbated by increased heat extraction rates owing to better mold–shell contact from the pressurization generated by the shells. Figure 4.6c illustrates how this problem can be avoided using a slot nozzle, the length of the caster, thereby creating an

Figure 4.6 (a) Plot of three-dimensional velocity field in the axially directed central vertical plane of symmetry and across half the surface of a twin roll caster fitted with a submerged entry nozzle. The exit ports of the nozzle deliver horizontally-directed jets towards the side dams. (b) Plan view of metal in sump of a twin roll caster showing growing shell forming on northside roll surface. The isofraction numbers represent the percentage solid formed. Predictions based on data from IMI pilot scale twin roll caster (0.6 m diameter 20 cm wide). (c) Plot of two-dimensional velocity field generated in a transverse vertical plane of a twin roll caster fitted with a vertical entry slot nozzle.

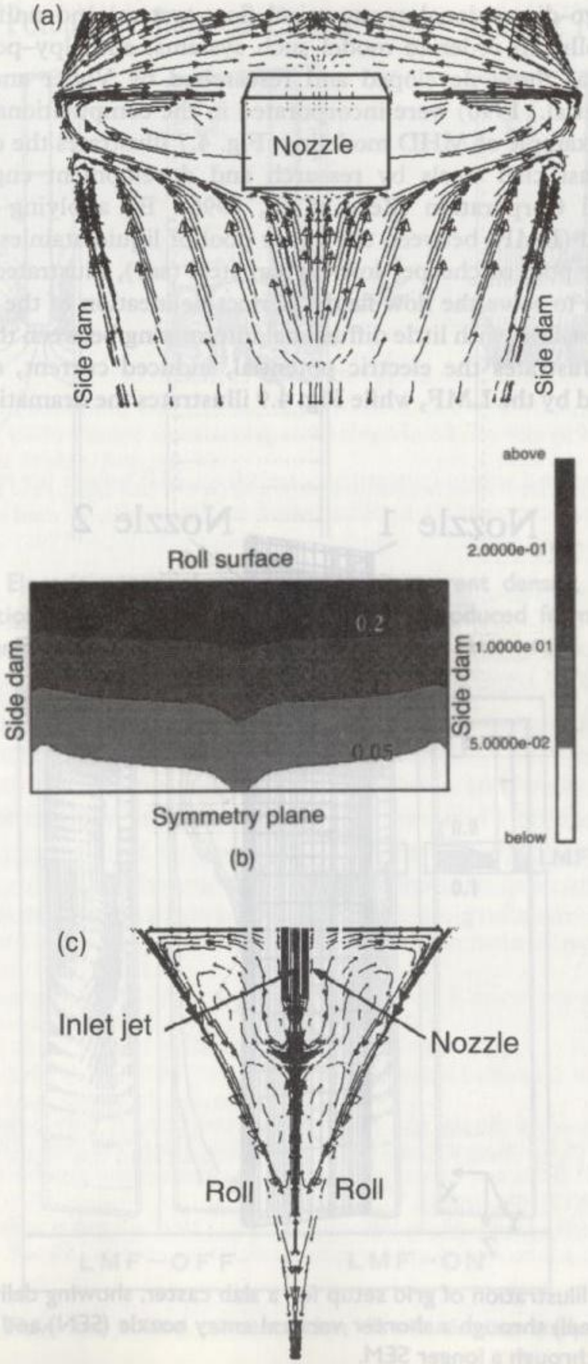

essentially two-dimensional symmetrical flow system, and uniform growth from both rolls. In order to model such systems, enthalpy–porosity techniques such as those developed and researched by Voller and coworkers (e.g., Voller et al., 1990) were incorporated in the computational modeling.

As a final example of MHD modeling, Fig. 4.7 illustrates the development of directly cast clad steels by research and development engineers with Nippon Steel Corporation (Zeze et al., 1996). By applying a level DC magnetic field (LMF) between the upper pool of liquid stainless steel (say), and the lower pool of cheaper low-carbon steel (say), illustrated in the grid system set up to solve the flow fields, perfect delineation of the two pools is technically possible, with little diffusional intermixing between the two pools. Figure 4.8 illustrates the electric potential, induced current, and Lorentz forces induced by the LMF, while Fig. 4.9 illustrates the dramatic differences

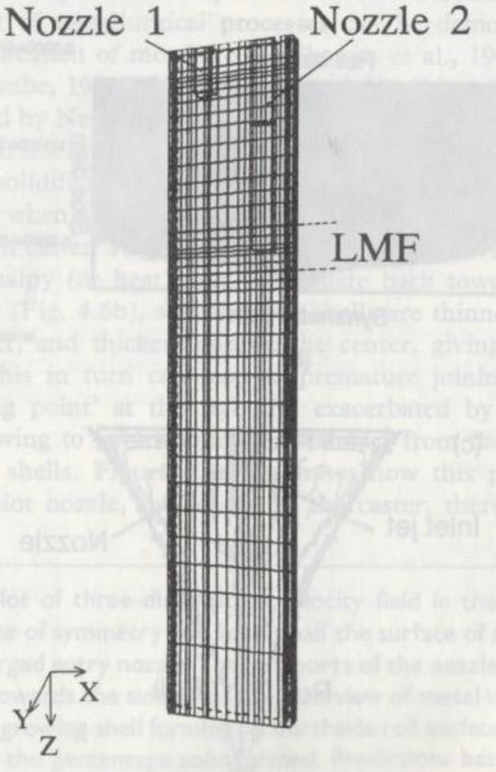

Figure 4.7 Illustration of grid setup for a slab caster, showing delivery of metal A (stainless steel) through a shorter vertical entry nozzle (SEN) and metal B (low carbon steel) through a longer SEM.

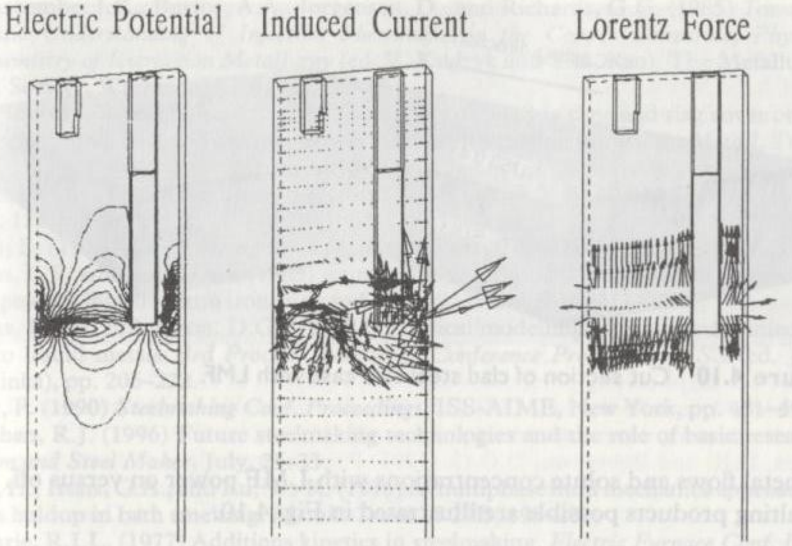

Figure 4.8 Electric potential, induced electric current density, and Lorentz force distributions as analyzed by MHD model. Reproduced from Zeze et al. (1996), with permission.

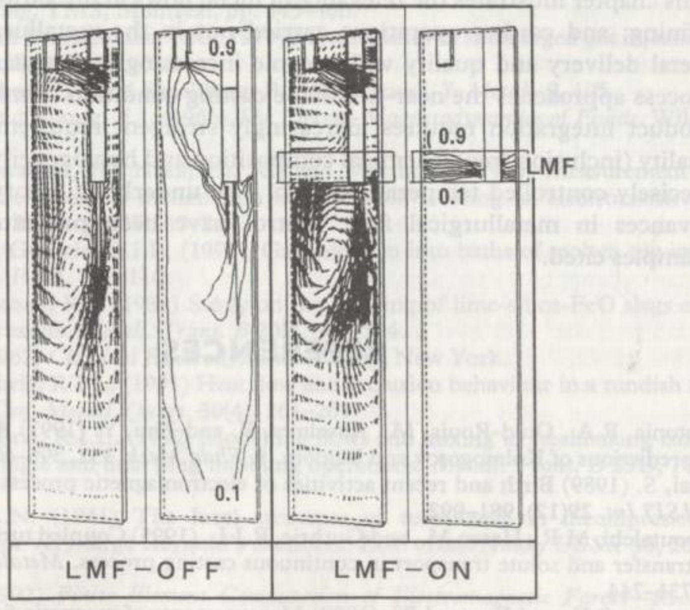

Figure 4.9 Flow and solute concentration distribution as analyzed by MHD model.

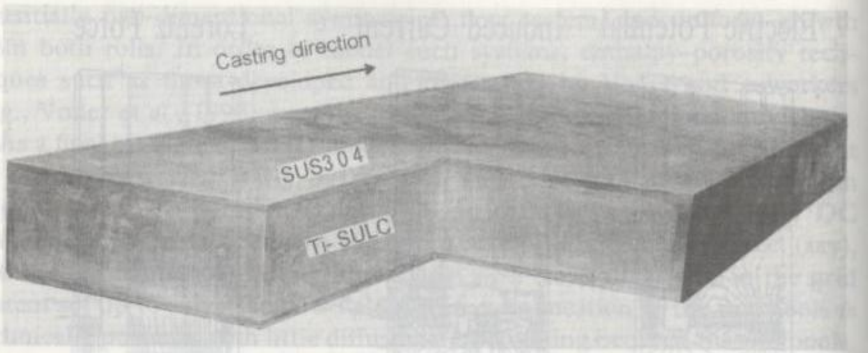

Figure 4.10 Cut section of clad steel slab cast with LMF.

in metal flows and solute concentrations with LMF power on versus off. The resulting products possible are illustrated in Fig. 4.10.

4.10. CONCLUSIONS

This chapter illustrates the relevance of metal flows in the various production, refining, and casting operations carried out in the metallurgical industry. Metal delivery and quality will become increasingly important the closer a process approaches the near-net shape casting condition. Similarly, process–product integration requires increasingly stringent requirements on metal quality (inclusion free), chemical composition and homogeneity, uniform and precisely controlled temperatures, etc. The underlying theory behind these advances in metallurgical flow control have been presented and a few examples cited.

REFERENCES

Antonia, R.A., Ould-Rouis, M., Anselmet, F. and Zhu, Y. (1997) Analogy between predictions of Kolmogorov and Yaglom. *J. Fluid Mech.* **332**, 395–409.

Asai, S. (1989) Birth and recent activities of electromagnetic processing of materials. *ISIJ Int.* **29**(12), 981–992.

Aboutalebi, M.R., Hasan M., and Guthrie, R.I.L. (1995) Coupled turbulent flow, heat transfer and solute transport in continuous casting process. *Metall. Trans. B* **26B**, 731–744.

Banerjee, S.K. and Evans, J.W. (1990) Measurements of magnetic fields and electromagnetically driven melt flow in a physical model of a Hall–Heroult cell. *Metall. Trans. B* **21B**, 59–69.

Brimacombe, J.K., Bustos, A.A., Jorgensen, D., and Richards, G.G. (1985) *Toward a Basic Understanding of Injection Phenomena in the Copper Converter, Physical Chemistry of Extraction Metallurgy* (ed. V. Kudryk and Y.K. Rao). The Metallurgical Society, Warrendale, PA; pp. 327–351.

Chakvaborty, S. and Sahai, Y. (1992) The effect of holding time and slag cover on the flow of liquid steel and heat transfer in continuous casting tundishes. *Metall. Trans. B* **23B**, 152–167.

Davenport, W.G., Richardson, F.D., and Bradshaw, A.V.B. (1967) *Chem. Eng. Sci.* **22**, 1227.

Edita, L. (1971) *The Great Age of Sail.* Viking Press, New York, p. 59.

Farias, L.R. and Irons, G.A. (1985) A unified approach to bubbling jetting phenomena in powder injection into iron and steel. *Metall. Trans. B* **16**, 211–225.

Farias, L. and Robertson, D.G.C. (1982) Physical modelling of gas-powder injection into liquid metals. *3rd Process Technology Conference Proceedings, ISS* (ed. J.W. Hlinka), pp. 206–222.

Flint, P. (1990) *Steelmaking Conf. Proceedings.* ISS-AIME, New York, pp. 481–490.

Fruehan, R.J. (1996) Future steelmaking technologies and the role of basic research. *Iron and Steel Maker*, July, 25–33.

Gou, H., Irons, G.A., and Lu, W.-K. (1996) A multiphase fluid mechanics approach to gas holdup in bath smelting. *Metall. Trans. B* **27B**, 195–201.

Guthrie, R.I.L. (1977) Additions kinetics in steelmaking. *Electric Furnace Conf. Proc.* **35**, 30–41.

Guthrie, R.I.L. (1992) *Engineering in Process Metallurgy.* University Press, Oxford, p. 411 (paperback edition).

Guthrie, R.I.L., Lee, H.C., and Sahai, Y. (1992) On the formation of thermal accretions ('mushrooms') in steelmaking vessels. *Proc. Savard/Lee Int. Symposium on Bath Smelting*, TMS, Montreal, pp. 445–460.

Hoefele, E.O. and Brimacombe, J.K. (1979) Flow regimes in submerged gas injection. *Metall. Trans. B* **10B**, 631–648.

Hsiao, T.C., Lehner, T., and Kejellberg, B. (1980) *Scand. J. Metall.* **9**, 105.

Hughes, W.F. and Young, F.J. (1966) *The Electro-Magnetodynamics of Fluids.* Wiley, New York.

Iguchi, M., Kawabata, H., Nakajima, K., and Morita, Z. (1995) Measurement of bubble characteristic in a molten iron bath at 1600°C using an electroresistivity probe. *Metall. Trans. B* **26B**, 67–74.

Irons, G.A. and Guthrie, R.I.L. (1978). Gas injection into baths of molten pig iron. *Metall. Trans. B* **9B**, 101–110.

Ito, K. and Fruehan, R.J. (1989) Study on the foaming of lime-silica-FeO slags and experimental results. *Metall. Trans. B* **20B**, 509–514.

Jackson, J.D. (1962) *Classical Electrodynamics.* Wiley, New York.

Joo, S. and Guthrie, R.I.L. (1991) Heat flow and inclusion behaviour in a tundish for slab casting. *Can. Metall. Quart.* **30**(4), 261–269.

Joo, S. and Guthrie, R.I.L. (1992) Modelling flows and mixing in steelmaking ladles designed for single and dual plug bubbling operations. *Metall. Trans. B* **23B**, 765–777.

Kolmogorov, A.N. (1941) The local structure of turbulence in incompressible viscous fluid for very large Reynold's numbers. *Dok. Akad Nauk, USSR* **30**, 200–203.

Lavers, J.D. (1992) *Finite Element Computation of Electromagnetic Forces—Recent Developments in Magnetohydrodynamics in Process Metallurgy* (ed. J. Szekely, J.W.

Evans, K. Blazek, and N. El-Kaddah). TMS Symposium Proceedings, San Diego, pp. 27–32.

Lait, J.E. and Brimacombe, J.K. (1993) *Continuous Casting*. ISS-AIME, New York, vol. 2, pp. 171–183.

Launder, B.E. and Spalding, D.B. (1974) The numerical computation of turbulent flows. *Comp. Meth. Mech. Eng*. 3, 269.

Lausanne, E. (1971) *The Age of Sail*. Nepsam Press, p. 179.

Lin, Z. and Guthrie, R.I.L (1994) *Metall. Trans. B* **25B**, 855–864.

Martin, J.-P., Dubé, G., Frayce, D., and Guthrie, R.I.L. (1988) Settling phenomena in casting furnaces—a fundamental and experimental investigation. *Light Metals 1988* (ed. L.G. Boxall). TMS-AIME, New York, pp. 442–456.

Mazumdar, D. and Guthrie, R.I.L. (1995) The physical and mathematical modelling of gas-stirred ladle systems. *ISIJ Int*. 35(1), 1–20.

Netto, P.G.Q., Tavares, R.P., and Guthrie, R.I.L. (1996) Mathematical models for near-net shape casting processes. *ISIJ Int*. **36** (suppl), S175–S178.

Nilmani, M. and Robertson, D.G.C. (1980) Model studies of gas injection at high flowrates using water and mercury. *Trans. IMM* **89**, C42–C58.

Panda, D.K. and Robertson, D.G.C. (1994) Physical modelling of metal drop—slag reactions with gas evolution. *Steelmaking Conference Proceedings, ISS*, pp. 443–456.

Patankar, S.V. (1980) *Numerical Heat Transfer and Fluid Flow*. McGraw-Hill, New York.

Salcudean, M. and Guthrie, R.I.L. (1978) Turbulent flow in filling ladles. *Metall. Trans*. **9B**, 673–680.

Sano, M. and Mori, K. (1977) *Trans JIM (Japan)* 17, 344–352.

Sano, M. and Mori, K. (1992) Fundamentals of gas injection in refining processes. *Proc. Savard/Lee Int. Symp. on Bath Smelting*. TMS, Montreal, pp. 465–479.

Savard, G. and Lee, R. (1992) Submerged oxygen injection for pyrometallurgy. *Proc. Savard/Lee Int. Symp. on Bath Smelting*. TMS, Montreal, pp. 645–660.

Standish, N. (1975) *Blast Furnace Aerodynamics Symposium*, Wollongong. The Australasian Institute of Mining and Metallurgy.

Tavares, R.P. and Guthrie, R.I.L. (1995) *Chiba Proceedings*.

Themelis, N.J., Tarassoff, P., and Szekely, J. (1969) Gas liquid momentum transfer in a copper converter. *Trans. Metall. Soc., AIME* **245**, 2425–2433.

Thomas, B.G., Najsar, F.M., and Mika, L.J. (1990) *Proc. F. Weinberg Int. Symp. on Solidification Processing*, 29th CIM Conf., Hamilton.

Voller, V.R., Swaminathan, C.R., and Thomas, B.G. (1990) Fixed grid techniques for phase change problems: a review. *Int. J. Num. Meth. Eng*. **30**, 875–898.

Zeze, M., Tanaka, H., Takeuchi, E., and Mizoguchi, S. (1996) Continuous casting of clad steel slab with level magnetic field brake. *Proc. 79th Steelmaking Conference*, ISS-AIME, Pittsburgh.

5

Solidification

Merton C. Flemings

Department of Materials Science and Engineering, Massachusetts Institute of Technology, Cambridge, Massachusetts, USA

5.1. INTRODUCTION

The basic engineering principles of solidification that we employ today rest on important fundamental ideas of researchers of fifty and more years ago including, importantly, Gulliver (1992), Scheil (1942, 1947), and Adams (1948). Principles of nucleation were well established soon thereafter through the pathbreaking work of Turnbull (1956) and others. The fresh look at solidification provided by research on semiconductor single crystal growth beginning in the mid-1950s (Pfann, 1966) gave us insights that we incorporate today in our models of dendritic growth.

Understanding of the basic principles of establishment of microsegregation and dendrite arm spacing in castings and ingots came during the 1960s as did the beginnings of our modern understanding of the effects of fluid flow on solidification (Flemings, 1974). In succeeding years, major contributions have been made by many workers to our understanding of relationships between dendrite tip velocity, curvature, and melt undercooling, and to important questions of phase selection during solidification; a notable example is Trivedi and Kurz (1994).

Our current understanding of engineering aspects of solidification, particularly of steel, is summarized in this chapter, beginning with those processes carried out at modest solidification rates, including bloom, billet, and thin slab casting, where the 'Scheil equation' or one of its modifications is applicable.

5.2. THERMODYNAMICS AND THE LIQUID–SOLID INTERFACE

In treating most steel solidification problems we find that rather simple assumptions regarding the liquid–solid interface are sufficient to explain

ADVANCED PHYSICAL CHEMISTRY FOR PROCESS METALLURGY
ISBN 0-12-618920-X

Copyright © 1997 Academic Press Ltd
All rights of reproduction in any form reserved

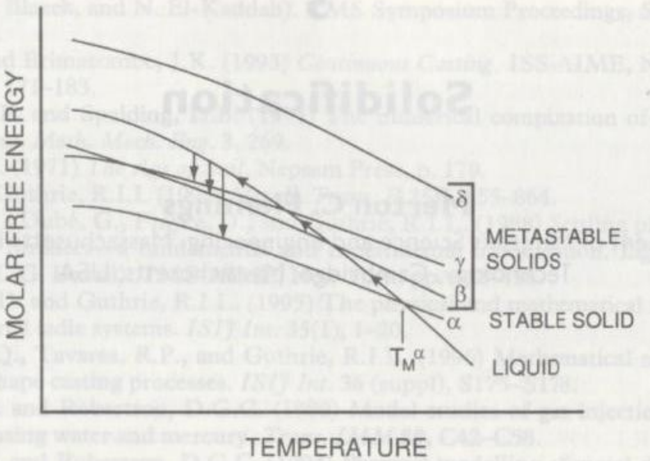

Figure 5.1 Free energies versus temperature for a pure material (Reproduced from Flemings, 1974, with permission).

observed phenomena. The reader should be aware, however, that there is a large and growing body of literature concerning fundamentals of kinetics at the liquid–solid interface, and that this literature is critical to understanding such phenomena as phase selection in metastable (e.g., rapid) solidification. A brief discussion is included here to guide the reader; reviews are to be found in solidification textbooks (Flemings, 1974).

For solidification of a single component at constant pressure, the phase rule tells us that only one phase can exist at equilibrium over a range of temperatures. Two phases coexist at equilibrium only at a single temperature. Figure 5.1 shows the curves of free energy versus temperature of the liquid and a stable solid α; these intersect at the equilibrium melting point T_M^α. Also shown in Fig. 5.1 are the free-energy curves for three metastable phases β, γ, and δ. The β and γ phases are in metastable equilibrium with the liquid at the temperature where their free-energy curves cross that of the liquid. The δ phase has no melting point and can never form from the liquid. This phase can be formed only by some other process such as vapor deposition or electrodeposition.

When a pure liquid is cooled to its equilibrium melting point T_M^α, the α phase may form; alternatively, if nucleation of α is suppressed, the liquid will continue to cool (undercool or supercool). At or below the melting point of β, solidification of this phase could occur. If solidification occurred at the melting point of β, it would be fully thermodynamically reversible, as in the case of a stable phase. The metastable β phase once formed could subsequently transform to the stable phase α, depending on nucleation and growth kinetics of α. If the β phase did not form, cooling would continue until γ might

form. Of course, no crystalline phase at all need form, in which case the liquid (or *glass* if its viscosity reaches a sufficiently high value) remains indefinitely as the metastable phase.

Application of thermodynamics to binary and more complex alloys permits calculation of phase compositions that form under conditions of equilibrium and of different conditions of metastability. A virtually important extension of these concepts incorporates the effect of curvature. Positive radii of curvature on a growing solid may be viewed as lowering the melting point of the solid. This results in a nucleation barrier that must be overcome to initiate solidification, and results also in the coarsening ('ripening') of dendritic structures that occur even during solidification.

In extremis we can imagine two different types of liquid–solid interfaces at the atomic scale—one atomically 'diffuse' and the other atomically 'flat' (Fig. 5.2). We know from the thermodynamics that, for steel, something approaching the diffuse interface of Fig. 5.2 is favored and that, for ordinary solidification rates, atoms reaching the liquid–solid interface have no trouble finding a site at which they can come to rest—i.e., there is no significant barrier of growth due to interface kinetics. On the other hand, at the very rapid solidification rates now achievable, interface attachment kinetics do begin to pose a barrier to growth.

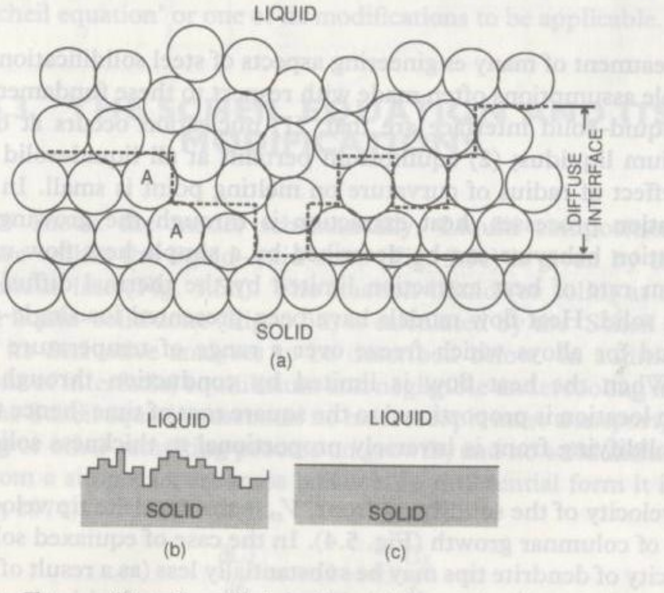

Figure 5.2 Types of liquid–solid interfaces: (a) atomic; (b) a diffuse interface; (c) an atomically flat interface. Reproduced from Flemings (1974), with permission.

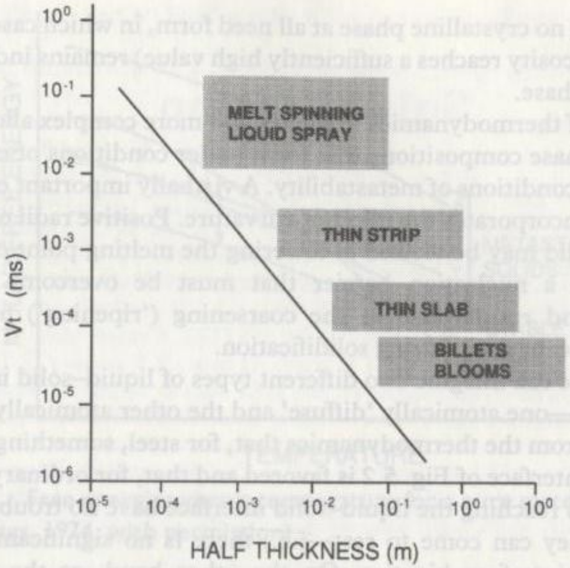

Figure 5.3 Approximate tip velocity for carbon steel versus casting half thickness.

For treatment of many engineering aspects of steel solidification processes, the simple assumptions often made with respect to these fundamental aspects of the liquid–solid interface are that: (1) nucleation occurs at or near the equilibrium liquidus; (2) equilibrium pertains at all liquid–solid interfaces; (3) the effect of radius of curvature on melting point is small. In most such solidification processes, heat extraction is through the growing solid and solidification behavior can be described by a simple heat flow model, with maximum rate of heat extraction limited by the thermal diffusivity of the growing solid. Heat flow models have been presented for single-component alloys and for alloys which freeze over a range of temperature (Flemings, 1974). When the heat flow is limited by conduction through the solid, isotherm location is proportional to the square root of time (hence the velocity of the solidifying front is inversely proportional to thickness solidified; Fig. 5.3).

The velocity of the solidifying front, V_t, is the dendrite tip velocity only in the case of columnar growth (Fig. 5.4). In the case of equiaxed solidification, the velocity of dendrite tips may be substantially less (as a result of new grains forming at the solidification front). For dendrite tip velocities less than about $10^{-2}\,\mathrm{m\,s^{-1}}$, interface kinetics may be assumed to be infinite, and below about $10^{-3}\,\mathrm{m\,s^{-1}}$, the dendrite tip temperature is very near the liquidus temperature (Trivedi and Kurz, 1994). These are the main two conditions necessary for the 'Scheil equation' or one of its modifications to be applicable.

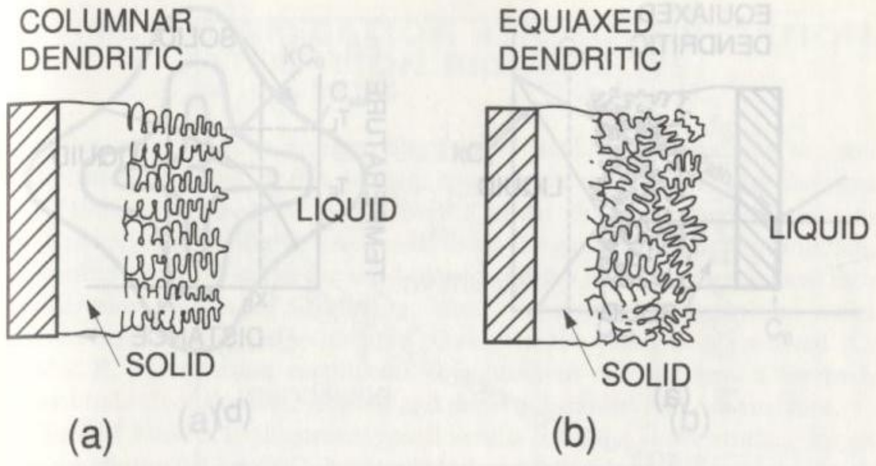

Figure 5.4 Solidification of an alloy against a cold chill wall. (a) Columnar solidification; (b) equiaxed solidification. Reproduced from Flemings (1974), with permission.

5.3. THE SCHEIL EQUATION AND ITS MODIFICATIONS

Figure 5.5 shows the model schematically. Liquid composition at any temperature within the liquid–solid zone (Fig. 5.5c) is given by the equilibrium liquidus line (Fig. 5.5b). The fraction liquid (or solid) at any point within the liquid–solid zone (Fig. 5.5d) is calculated by the 'Scheil equation' or one of its derivative analyses to be described below. In addition to the assumptions of interfacial equilibrium and negligible undercooling implicit in Fig. 5.5, the Scheil equation assumes no macroscopic mass transport, no effect of ripening or other remelting process on growth, and no solid diffusion. It is derived from a simple secure mass balance. In differential form it is written (Flemings, 1974):

$$\frac{\partial C_L}{\partial f_L} = -(1-k)\frac{C_L}{f_L} \tag{5.1}$$

where C_L is liquid composition, f_L is liquid weight fraction, and k is the equilibrium partition ratio. The equilibrium partition ratio, k, equals C_s^*/C_L

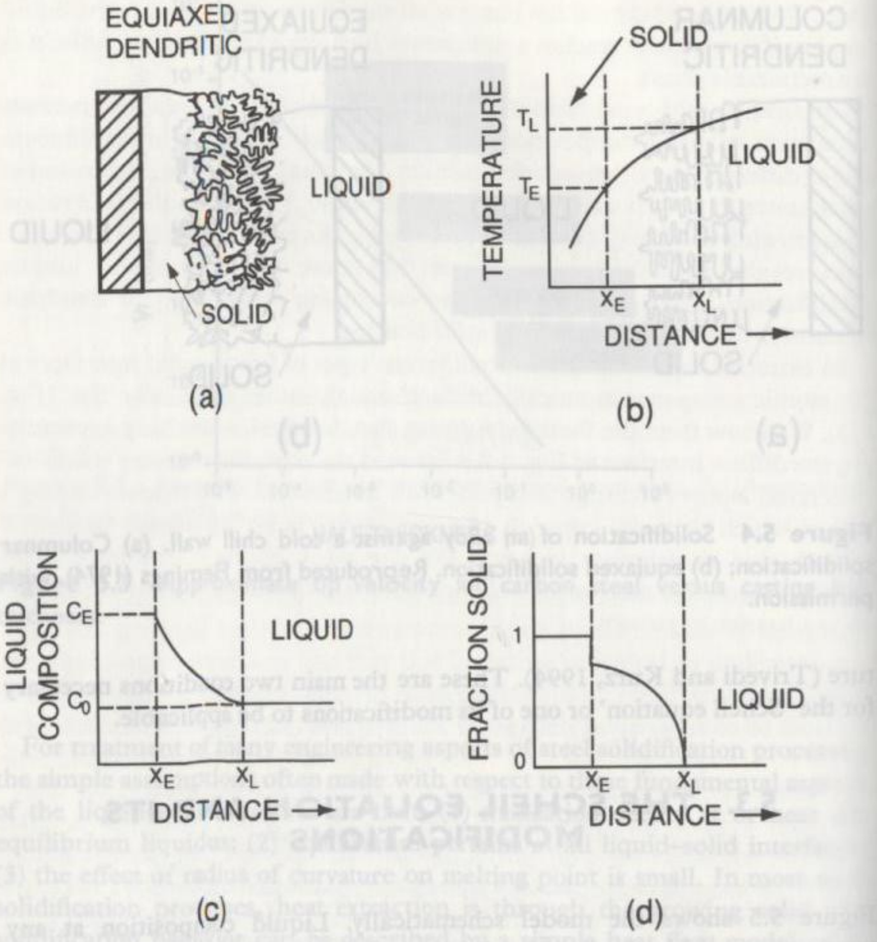

Figure 5.5 Model of solidification, based on Scheil equation. Reproduced from Flemings (1974), with permission.

where C_s^* is solid forming from liquid of composition C_L. Since there is no solid diffusion, the isoconcentrates C_s^* which form on solidification remain after cooling and represent the resulting microsegregation. Rewriting Equation 5.1 in terms of C_s^* and f_s gives the differential equation describing this macrosegregation:

$$\frac{\partial C_s^*}{\partial f_s} = \left(\frac{1-k}{1-f_s}\right) C_s^* \qquad (5.2)$$

Microsegregation calculations for a simple binary alloy using Equation 5.2 are shown schematically in Fig. 5.6.

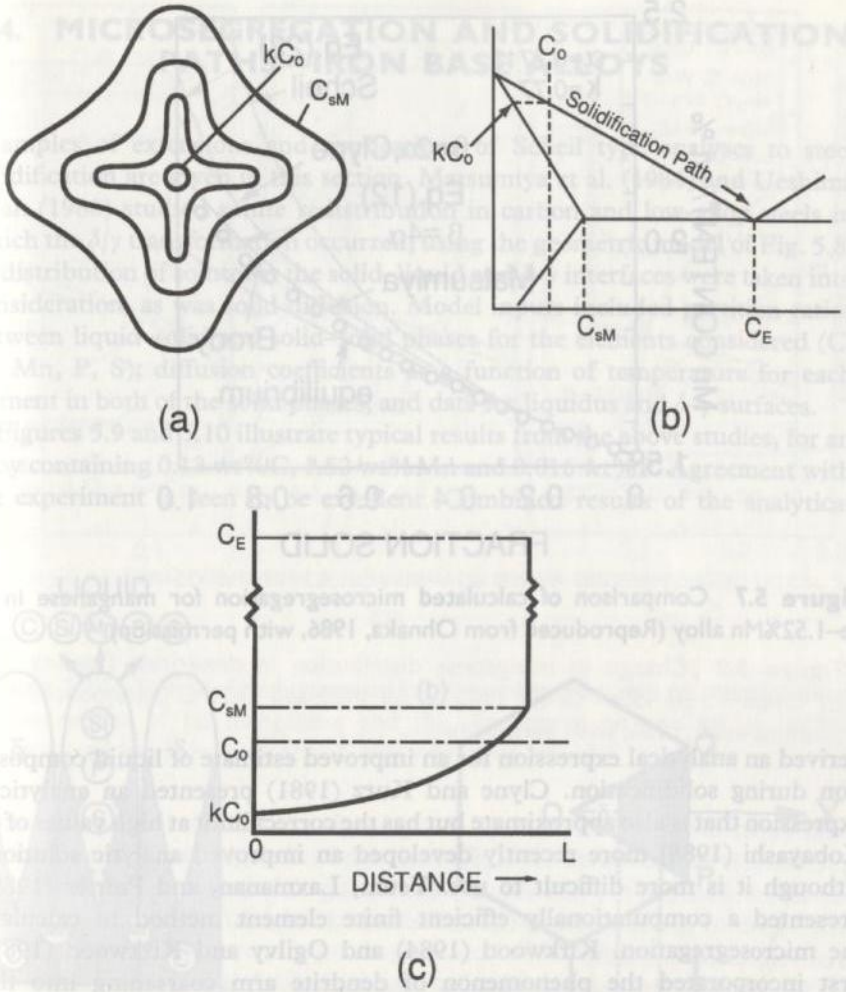

Figure 5.6 Formation of microsegregation, based on Scheil equation. (a) Isoconcentrates as seen in a cross section of a primary columnar dendrite arm after solidification. (b) Phase diagram showing 'solidification path.' (c) Microsegregation, measured along a radial path from the center of the dendrite.

It has long been understood that diffusion during solidification alters segregation in most real systems. This was first analyzed quantitatively by Brody and Flemings (1966) using both a simple analytical model and a computational model for comparison. In subsequent work, Ohnaka (1986)

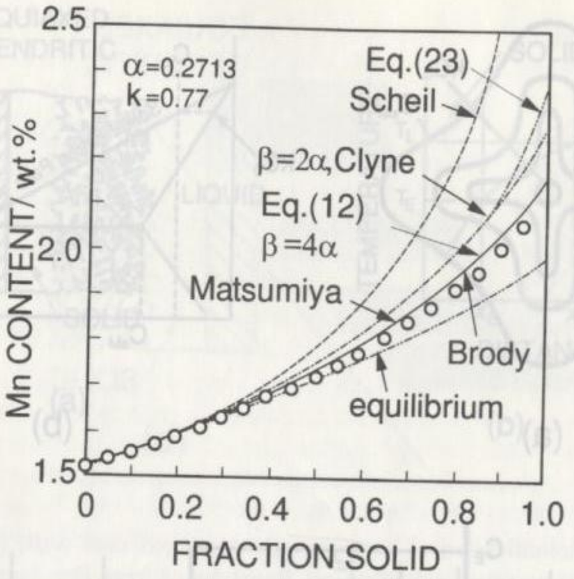

Figure 5.7 Comparison of calculated microsegregation for manganese in a Fe–1.52%Mn alloy (Reproduced from Ohnaka, 1986, with permission).

derived an analytical expression for an improved estimate of liquid composition during solidification. Clyne and Kurz (1981) presented an analytical expression that is also approximate but has the correct limit at high values of α. Kobayashi (1988) more recently developed an improved analytic solution, although it is more difficult to use. Yeum, Laxmanan, and Poirier (1989) presented a computationally efficient finite element method to calculate the microsegregation. Kirkwood (1984) and Ogilvy and Kirkwood (1987) first incorporated the phenomenon of dendrite arm coarsening into the microsegregation model, and Mortensen (1989) later derived an analytical expression for this effect.

In solidification of the type considered in this section, the main factor causing microsegregation (and fraction solid at a given temperature) to deviate from that predicted by the Scheil equation appears to be diffusion in the solid during solidification. Figure 5.7, from Ohnaka (1986), compares calculated results on segregation of manganese in an Fe–1.52 wt%Mn alloy, obtained using several of the different analyses referred to above. The analyses differ only in the analytic or computational method used to account for solid diffusion (including assumed dendrite geometry).

5.4. MICROSEGREGATION AND SOLIDIFICATION PATHS—IRON BASE ALLOYS

Examples of extensions and applications of Scheil type analyses to steel solidification are given in this section. Matsumiya et al. (1984) and Ueshima et al. (1986) studied solute redistribution in carbon and low-alloy steels in which the δ/γ transformation occurred, using the geometric model of Fig. 5.8. Redistribution of solutes at the solid–liquid and δ–γ interfaces were taken into consideration, as was solid diffusion. Model inputs included partition ratios between liquid–solid and solid–solid phases for the elements considered (C, Si, Mn, P, S); diffusion coefficients as a function of temperature for each element in both of the solid phases; and data for liquidus and δ–γ surfaces.

Figures 5.9 and 5.10 illustrate typical results from the above studies, for an alloy containing 0.13 wt%C, 1.52 wt%Mn and 0.016 wt%P. Agreement with the experiment is seen to be excellent. Combined results of the analytical

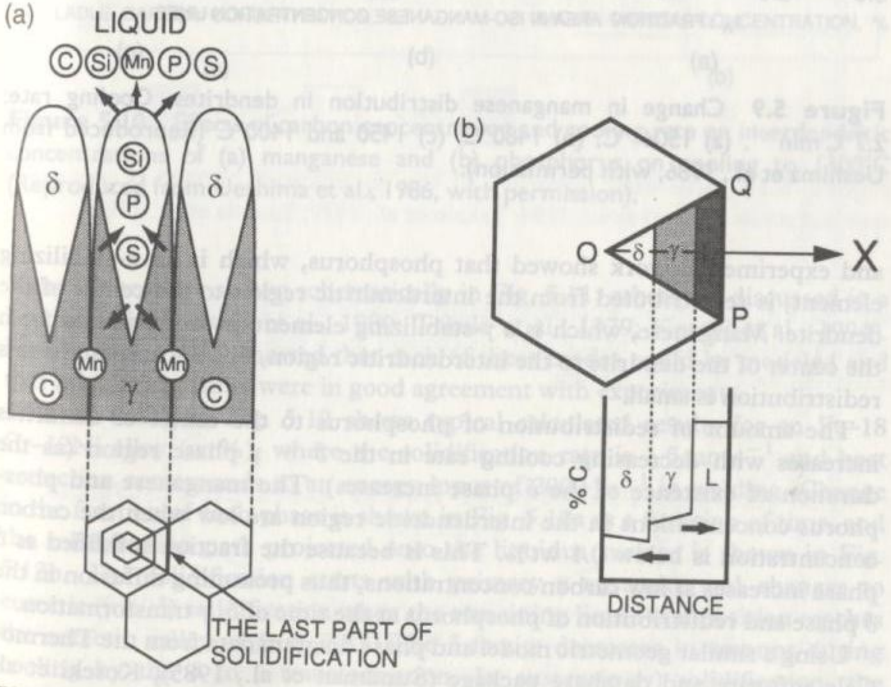

Figure 5.8 (a) Schematic drawing showing the longitudinal and transverse cross sections of dendrites (Reproduced from Ueshima et al., 1986, with permission). (b) Schematic drawing showing the solute distribution in the transverse cross section of dendrite.

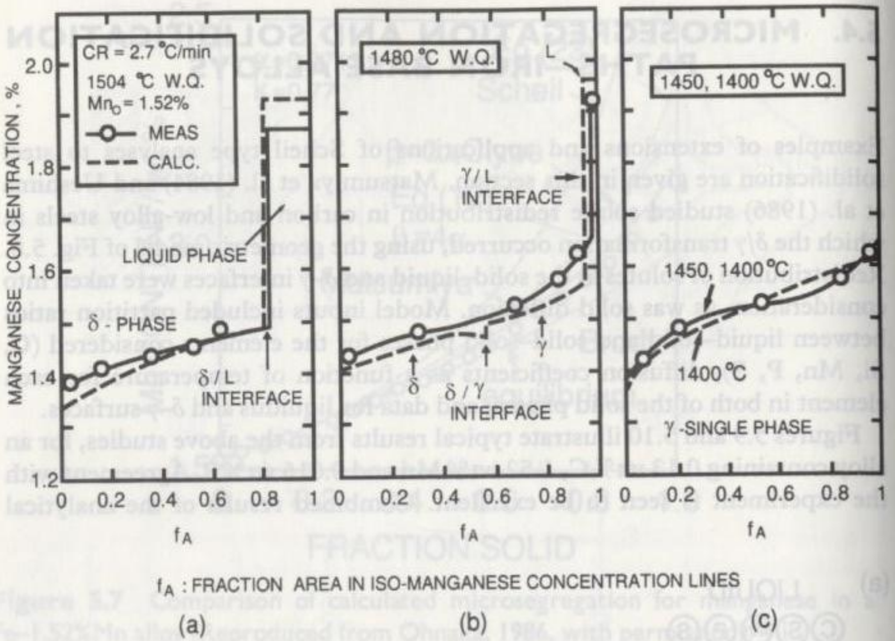

Figure 5.9 Change in manganese distribution in dendrites. Cooling rate: 2.7°C min^{-1}. (a) 1504 °C, (b) 1480°C, (c) 1450 and 1400°C (Reproduced from Ueshima et al., 1986, with permission).

and experimental work showed that phosphorus, which is an α-stabilizing element, is redistributed from the interdendritic region to the center of the dendrite. Manganese, which is a γ-stabilizing element, is redistributed from the center of the dendrite to the interdendritic region, but the amount of this redistribution is small.

The amount of redistribution of phosphorus to the center of dendrites increases with decreasing cooling rate in the δ + γ phase region (as the duration of existence of the δ phase increases). The manganese and phosphorus concentrations in the interdendritic region are low when the carbon concentration is below 0.1 wt%. This is because the fraction solidified as δ phase increases at low carbon concentrations, thus promoting diffusion in the δ phase and redistribution of phosphorus at the time of δ/ γ transformation.

Using a similar geometric model and phase diagram data from the Thermo-Calc software and database package (Sundman et al., 1985), Koseki et al. (1994) performed calculations for Fe–Cr–Ni stainless steels. Complete diffusion was assumed in the δ phase with limited diffusion in the γ phase. Austentic stainless steels exhibit various solidification modes and final microstructures depending on alloy composition and solidification conditions. Some of these are shown schematically in Fig. 5.11; others are discussed in a later section (Suutula et al., 1980; Takalo et al., 1979; Koseki et al., 1994). Koseki et al. (1994) showed that each of these modes could be modeled and that calculated results were in good agreement with experiments.

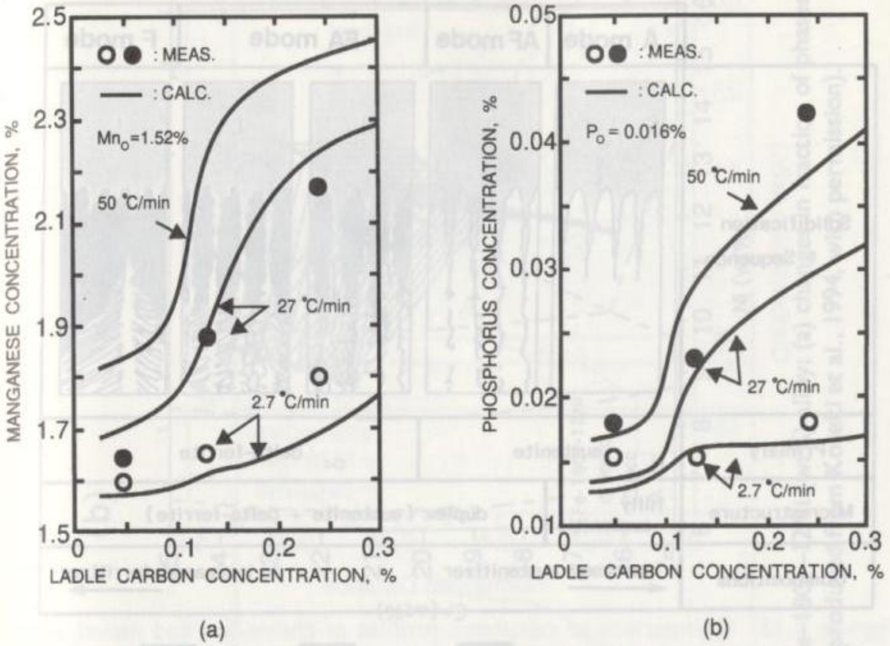

Figure 5.10 Effects of carbon concentration and cooling rate on interdendritic concentrations of (a) manganese and (b) phosphorus on cooling to 1300°C (Reproduced from Ueshima et al., 1986, with permission).

As an example, Fig. 5.12 shows typical calculated results for an Fe–18 Cr–12Ni alloy (wt%), where the solidification rate is 1.5 mm s^{-1} and heat extraction corresponds to an energy input of 2000 J s^{-1} in welding. Change in the fraction of each phase is shown in Fig. 5.10a as a function of time, and the solidification path projected onto the liquidus surface is shown in Fig. 5.12b. The solidification starts with primary γ austenite and changes to eutectic (γ + δ) solidification when the remaining liquid composition reaches the eutectic valley at $f_s \approx 0.83$. The δ ferrite decreases in amount during cooling by the δ to γ transformation. In austentic (γ) solidification, the partitioning of chromium between γ and the liquid is significant, while the partitioning of nickel is relatively insignificant, as seen in Fig. 5.12b. During the eutectic solidification, the liquid composition follows the eutectic valley toward the higher alloy side, forming δ ferrite which is depleted in nickel and

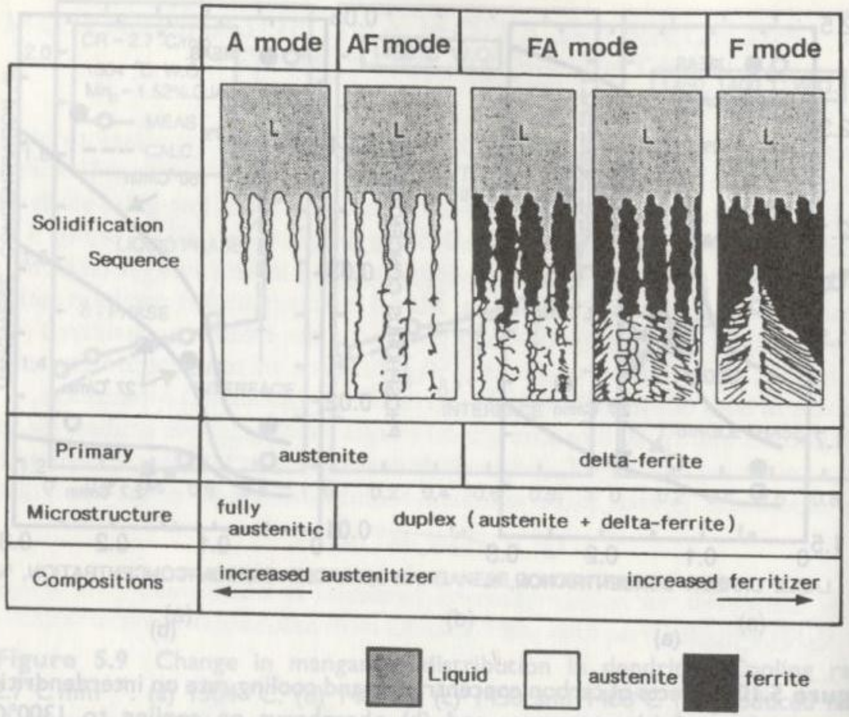

Figure 5.11 Schematic summary of the solidification modes of austenitic stainless steels (Koseki et al., 1994; Takalo et al., 1979; Suutala et al., 1980).

enriched in chromium to a large extent. Figure 5.13 compares experimental and calculated values of Cr and Ni content in a closely similar 'FA' alloy; excellent agreement is shown.

5.5. SOLIDIFICATION INTO UNDERCOOLED MELTS

Except in extremely thin sections (less than tens of micrometers thick) it is not possible to obtain dendrite tip velocities above about 0.1 m s^{-1} when heat extraction must be through the growing solid. In undercooled melts, on the other hand, much higher velocities are possible. Figures 5.14 and 5.15, from work of Barth et al (1991), and analyzed by Trivedi and Kurz (1994), show an example. In this Fe–25 at% Ni alloy, dendrite tip velocities up to 30 m s^{-1} are obtained at undercoolings on the order of 200 K (Fig. 5.14). The dendrite

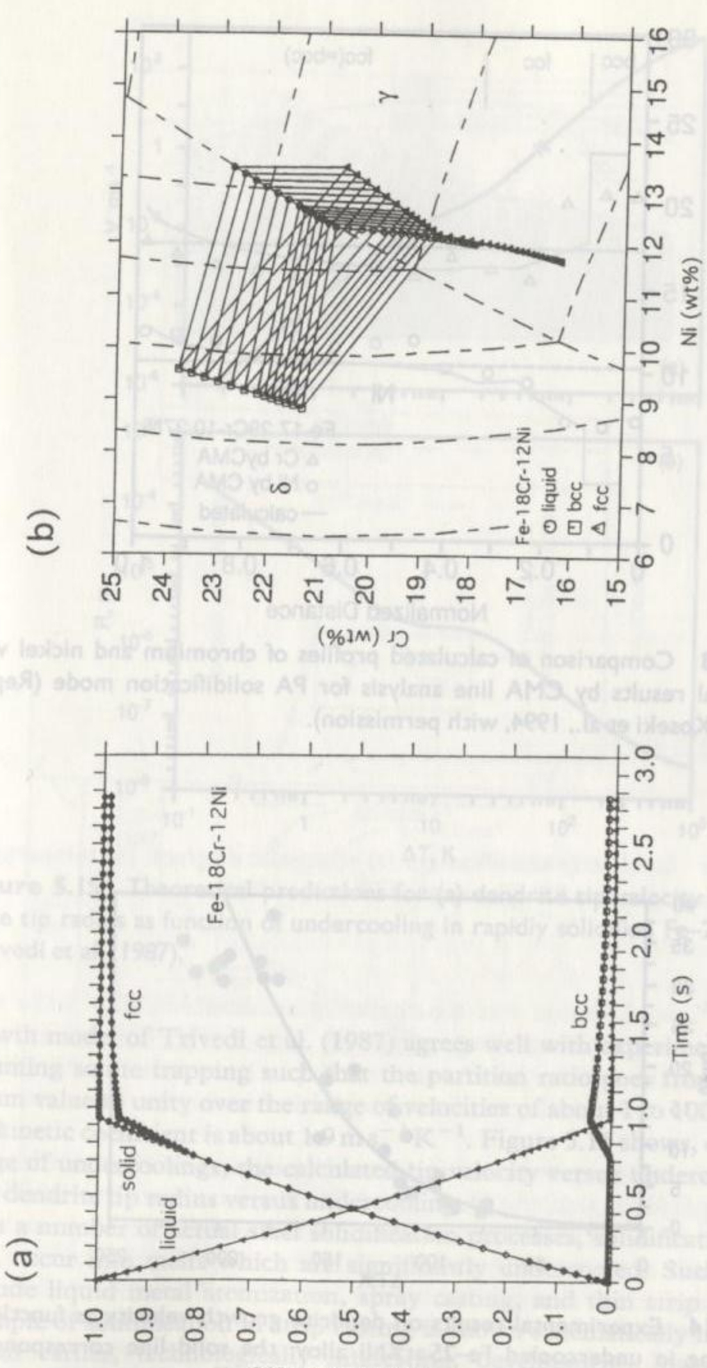

Figure 5.12 Calculated results for the weld solidification of Fe–18Cr–12Ni (wt%) alloy; (a) changes in fraction of phases; and (b) solidification path projected onto the liquidus surface (Reproduced from Koseki et al., 1994, with permission).

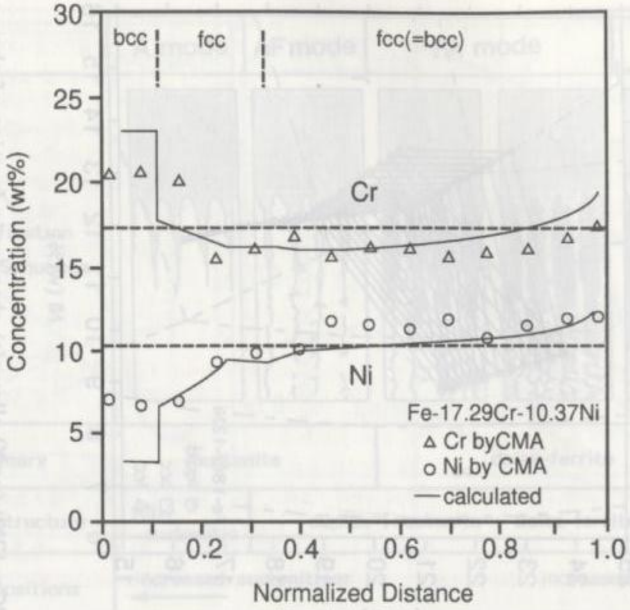

Figure 5.13 Comparison of calculated profiles of chromium and nickel with experimental results by CMA line analysis for PA solidification mode (Reproduced from Koseki et al., 1994, with permission).

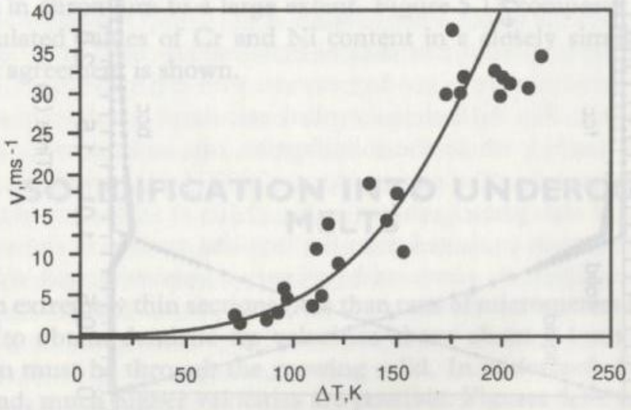

Figure 5.14 Experimental results on dendrite growth velocity as function of undercooling in undercooled Fe–25 at%Ni alloy: the solid line corresponds to predictions of the theoretical model (Trivedi et al., 1987).

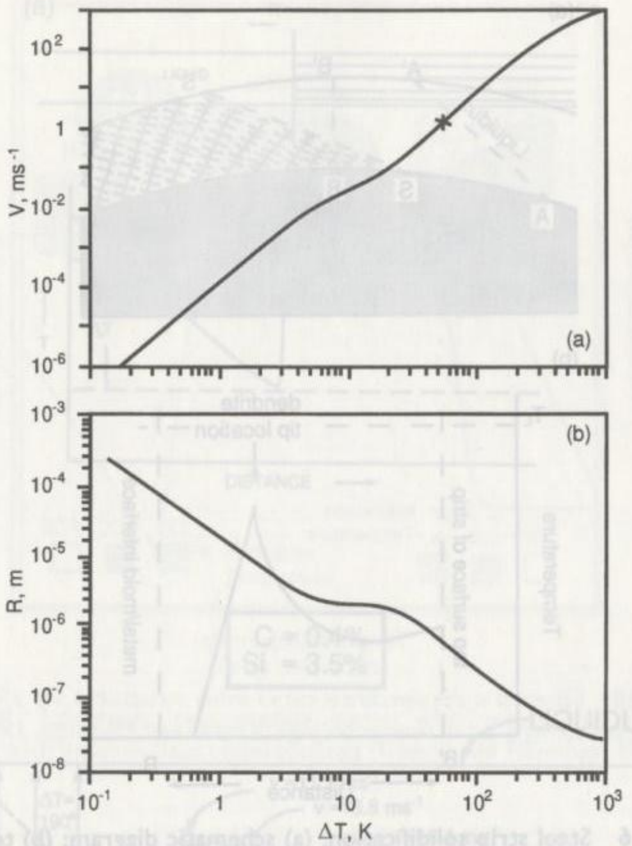

Figure 5.15 Theoretical predictions for (a) dendrite tip velocity and (b) dendrite tip radius as function of undercooling in rapidly solidified Fe–2 at%Ni alloy (Trivedi et al., 1987).

growth model of Trivedi et al. (1987) agrees well with experimental results, assuming solute trapping such that the partition ratio goes from its equilibrium value to unity over the range of velocities of about 1 to 100 m s^{-1}, and the kinetic coefficient is about 1.9 m s^{-1} K^{-1}. Figure 5.15 shows, over a fuller range of undercoolings, the calculated tip velocity versus undercooling, and also dendrite tip radius versus undercooling.

In a number of actual steel solidification processes, solidification may, in fact, occur into melts which are significantly undercooled. Such processes include liquid metal atomization, spray casting, and thin strip casting; an example of solidification in strip casting is shown schematically in Fig. 5.16. In an earlier, technologically interesting, development, Massoubre and Pflieger (1978) 'spun' steel wire of about 200 μm diameter at speeds of

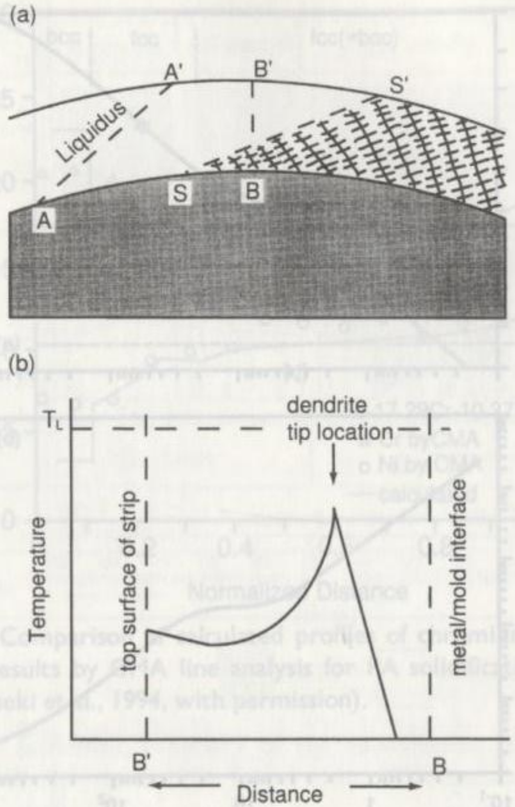

Figure 5.16 Steel strip solidification: (a) schematic diagram; (b) temperature distribution along radius BB' (Flemings and Koseki, 1994).

12–20 m s^{-1}; solidification was schematically as shown in Fig. 5.17a with resulting tip undercoolings diagrammed in Fig. 5.17b. Tip undercooling increases with tip velocity in a manner similar to that of the Fe–Ni alloy of Fig. 5.14; the undercooling is, however, somewhat higher for a given tip velocity.

A recent series of papers based on doctoral thesis work of Koseki (Flemings and Koseki, 1994; Koseki and Flemings, 1995a,b,c) has shown the remarkable range of solidification modes and final microstructures obtainable in stainless steel as a result of variations in amount of undercooling of the metal bath, and of heat extraction rate during solidification. Small droplets of the metal alloys were levitation-melted, with high-speed temperature measurement made during solidification; samples were quenched at various times during and after solidification for structural examination.

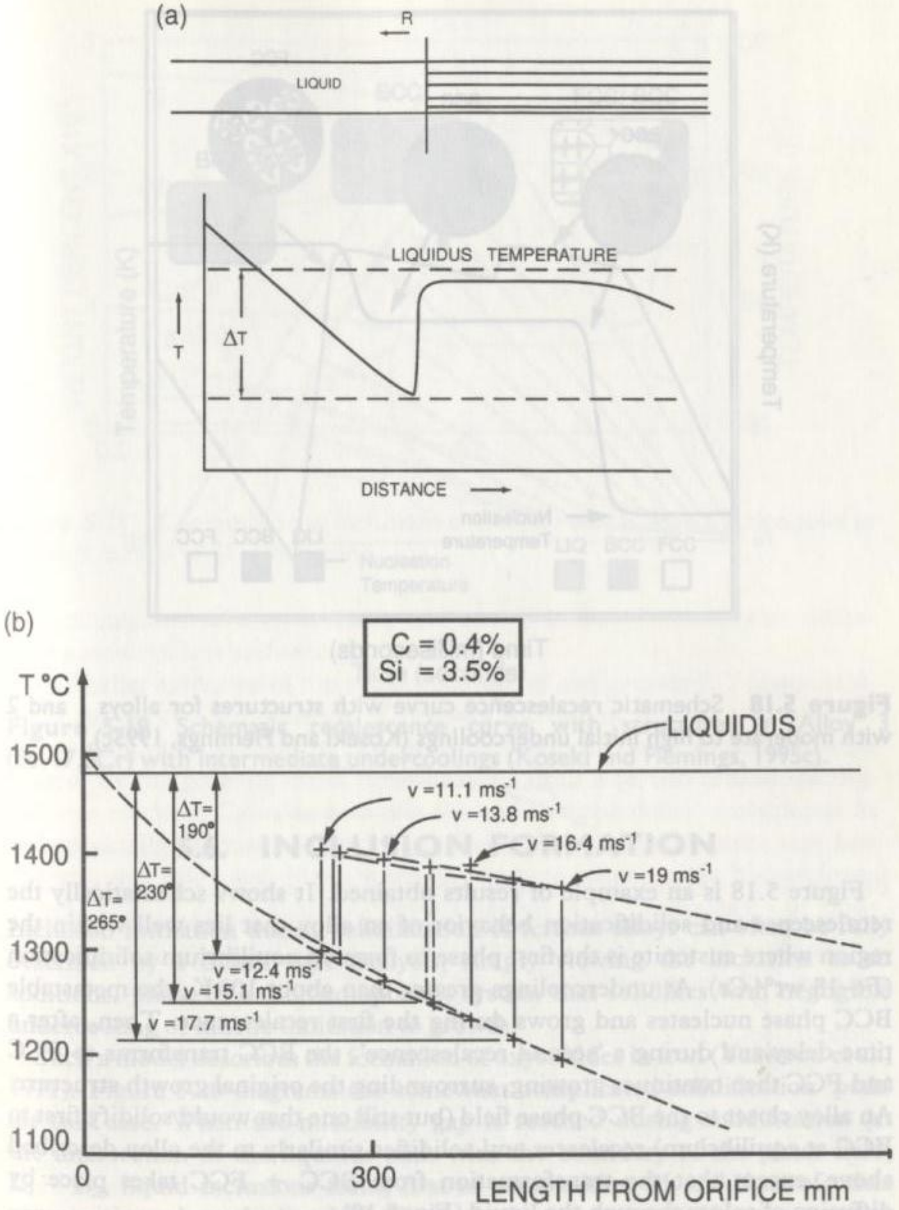

Figure 5.17 (a) Solidification of spun cast wire. At steady state, wire moves to right with velocity R and dendrites grow at constant velocity R into liquid metal undercooled an amount ΔT. (b) Measured temperature distributions along spun wire during steady-state solidification at different velocities (Massoubre and Pflieger, 1978).

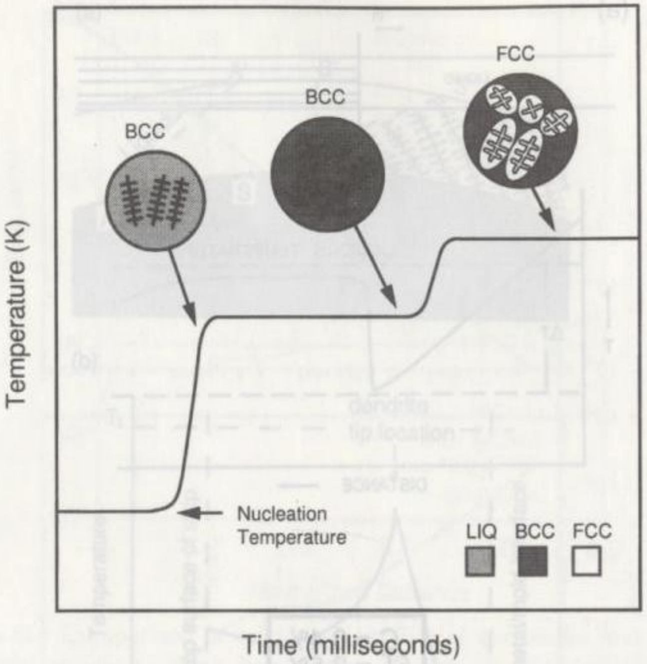

Figure 5.18 Schematic recalescence curve with structures for alloys 1 and 2 with moderate to high initial undercoolings (Koseki and Flemings, 1995c).

Figure 5.18 is an example of results obtained. It shows schematically the recalescense and solidification behavior of an alloy that lies well within the region where austenite is the first phase to form on equilibrium solidification (Fe–18 wt%Cr). At undercoolings greater than about 100 K, the metastable BCC phase nucleates and grows during the first recalescence. Then, after a time delay and during a 'second recalescence', the BCC transforms to FCC and FCC then continues growing, surrounding the original growth structure. An alloy closer to the BCC phase field (but still one that would solidify first to FCC at equilibrium) recalesces and solidifies similarly to the alloy described above, except that the transformation from BCC + FCC takes place by diffusion of solute through the liquid (Fig. 5.19).

It is clear from results of the studies discussed above that newer steel solidification processes which take place in thinner sections and at higher rate may result in quite different structures from those we encounter in traditional processes, and can be understood only with solidification models that go beyond the Scheil model and its derivatives.

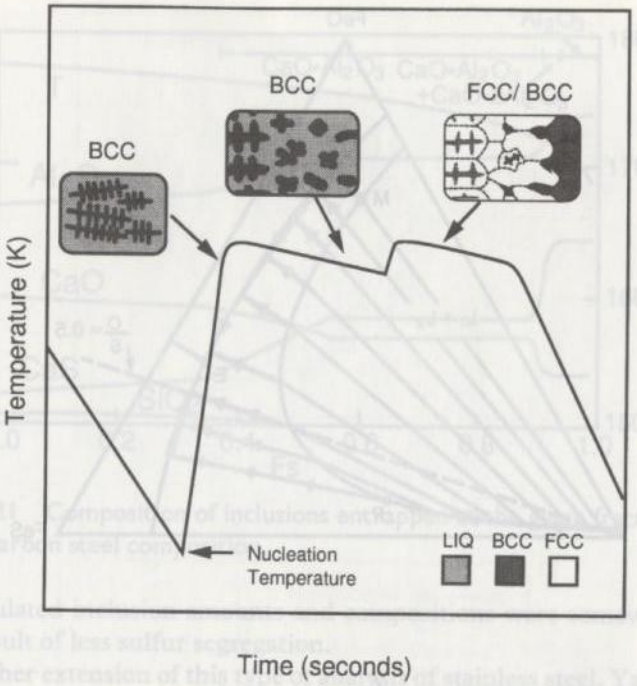

Figure 5.19 Schematic recalescence curve with structures in Alloy 3 (Fe–17.5Cr) with intermediate undercoolings (Koseki and Flemings, 1995c).

5.6. INCLUSION FORMATION

Inclusion formation during solidification of ferrous alloys can often be fully described by a Scheil type analysis, simply viewing the inclusion as an additional phase in a multicomponent system that solidifies with negligible undercooling or kinetic limitation to growth.

Such a model describes the formation of oxysulfides in iron (Yarwood et al., 1971). Figure 5.20 diagrams the somewhat complicated solidification 'path' for this case. When the miscibility gap is reached during solidification (at the intersection of the liquidus path with the boundary of the phase field, $L_1 + L_2$, liquid inclusions form, first of composition M and then of other compositions along the line MP. The inclusions are entrapped in the growing iron and isolated from each other. Each then solidifies along its own solidification path to the final ternary eutectic point E. Because of these multiple 'solidification paths' and the isolation of each individual inclusion, the oxygen/sulfur ratio of the inclusions in the fully solidified material ranges from rich in FeO to rich in FeS. Inclusions in other systems, whether or not

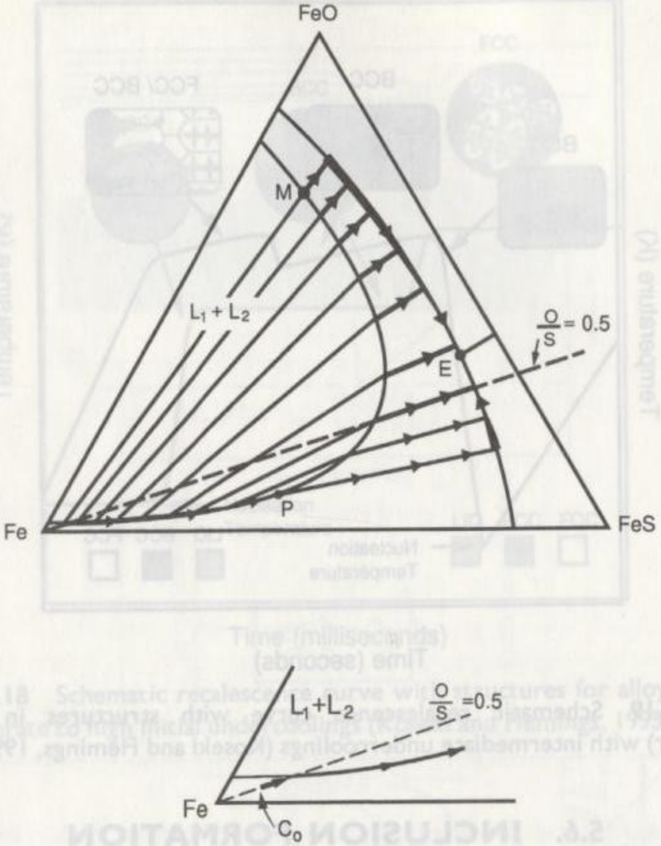

Figure 5.20 Schematic illustration of the liquidus surface of the Fe–FeO–FeS system showing solidification path of an iron-rich alloy of composition C_0. Point P is a minimum on the line of twofold saturation. Insert is enlargement of the Fe-rich corner (Reproduced from Yarwood et al., 1971, with permission).

they obey a Scheil type relation, may be pushed by the growing solid and so end up largely in interdendritic spaces. Silicon inclusions are an example (Myers and Flemings, 1972).

Yamada and coworkers have extended this type of analysis to carbon steels (Ito et al., 1990). Inclusions were assumed to form homogeneously in the interdendritic liquid and to be entrapped by the growing solid. Solgasmix (Eriksson, 1971) was employed to calculate equilibria between the molten steel and complex oxides during solidification. Diffusion in the solid steel was incorporated. Figure 5.21 shows calculated results for a 0.3 wt% carbon steel, solidified with a local solidification time of 200 seconds. At very low cooling rates, calculated inclusion amounts and compositions were somewhat different as a result of less sulfur segregation.

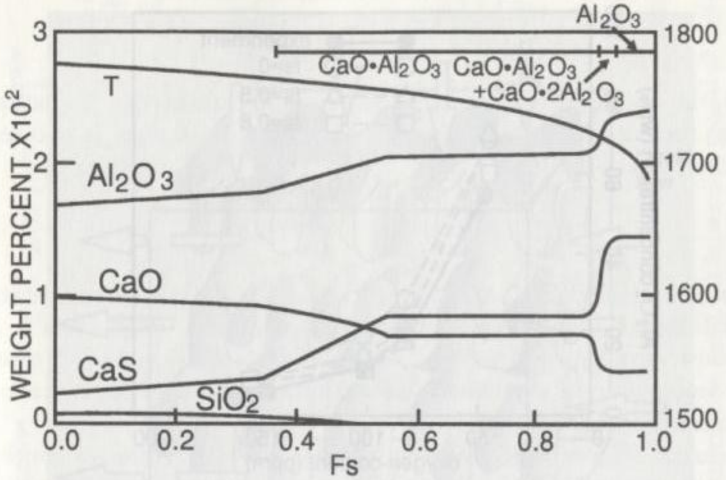

Figure 5.21 Composition of inclusions entrapped at the given fraction solid in a 0.3 wt% carbon steel composition.

In a further extension of this type of analysis of stainless steel, Yamada et al. (1993) considered the presence of primary inclusions, as well as those that form during solidification of the steel, and assumed that inclusions were 'pushed' by the growing metal dendrite arms until a certain critical fraction solid was reached. Calculated results showed that the major constituents in the nonmetallic inclusions were Al_2O_3 when the oxygen content was low (40 ppm) and SiO_2 and MnO when the oxygen content was higher (over 80 ppm) (Fig. 5.22). Calculated results agreed with observations of nonmetallic inclusions in continuously cast stainless steel slabs when the inclusions were assumed to be entrapped at a fraction solid of 0.5 and above.

Other applications of analysis of this type to understanding of steel solidification phenomena may be found in the recent literature. One example is the work of Wintz et al. (1995), who calculated the temperature range over which liquid films may exist in sulfide-containing carbon steel. They showed that in one steel a Mn/S ratio of 15 can result in such films a full 150°C below the liquidus temperature (a condition leading to severe biot tearing).

5.7. MACROSEGREGATION

The cause of macrosegregation in castings and ingots is the physical movement of liquid or solid phases during solidification. Diffusional transport can

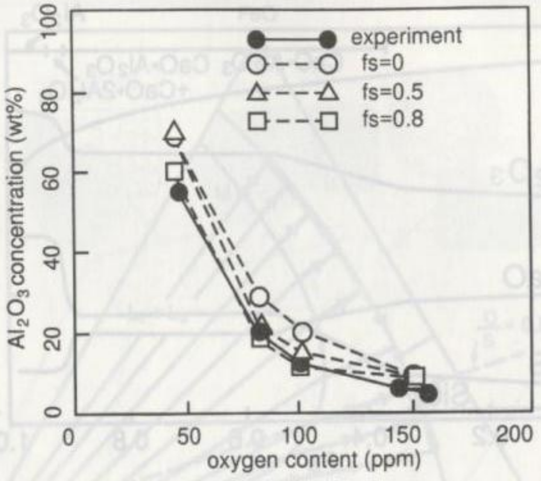

(a) (Al$_2$O$_3$)

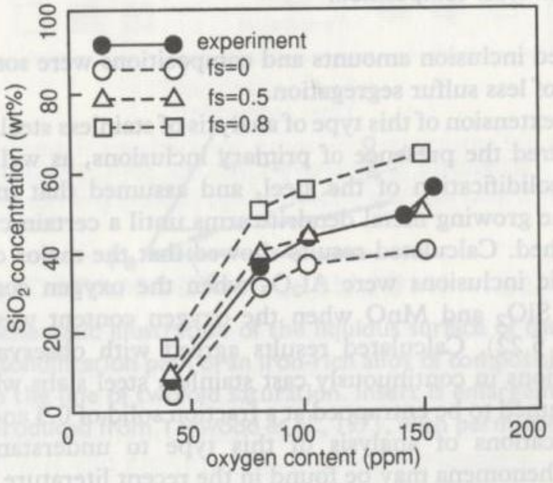

(b) (SiO$_2$)

Figure 5.22 Calculated and experimental Al$_2$O$_3$ (a) and SiO$_2$ (b) concentrations in complex oxide inclusions in a (sus 304) stainless steel. Agreement of theory is best assuming trapping at $f_s = 0.5$ (Reproduced from Yamada et al., 1993, with permission).

be significant only over very small distances. One way in which the physical displacement can occur is by floating or settling of precipitated phases early in solidification (e.g., flotation of inclusions or settling of fine grains early in the solidification process). Most macrosegregation, however, is caused by a different mechanism—the flow of liquid through the interdendritic channels in the liquid–solid zone. Causes of this flow include solidification shrinkage, gravity induced convection, and solid movement (e.g. 'bulging').

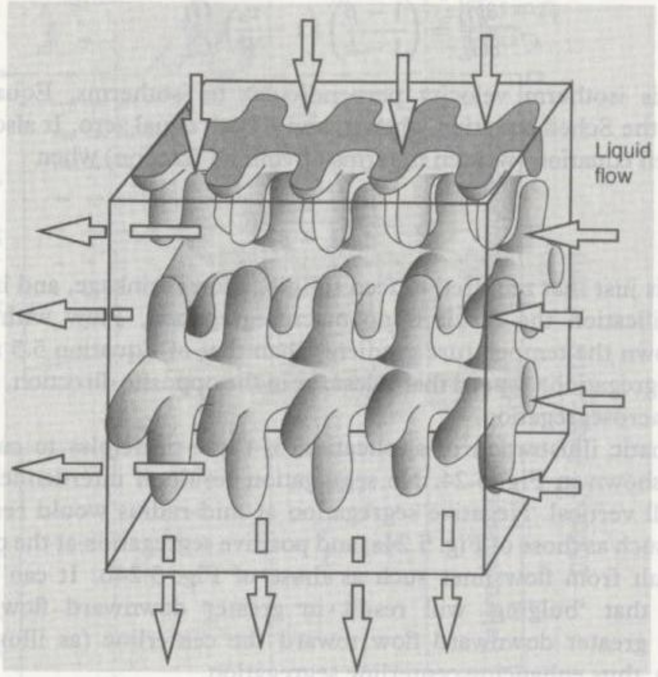

Figure 5.23 Fluid flow through a solidifying 'volume element'.

Figure 5.23 is a schematic diagram of a 'volume element' in the liquid–solid region of a solidifying casting. The element is permeable to liquid flow. Because liquid composition varies spatially within the liquid–solid zone, any interdendritic flow other than that parallel to an isotherm must alter the composition of the volume element. Conservation of solute requires modification of the Scheil equation to a new 'local solute redistribution equation' (Flemings and Nereo, 1967; Mehrabian et al., 1970a):

$$\frac{\partial g_L}{\partial C_L} = \left(\frac{1-\beta}{1-k}\right)\left(1 + \frac{v \cdot \Delta T}{\varepsilon}\right)\frac{G_L}{C_L} \tag{5.3}$$

where β is solidification contraction and ε is rate of temperature change. The physical significance of Equation 5.3 can be seen by considering steady-state solidification with planar isotherms moving with velocity R in the x direction. Equation 5.3 then becomes:

$$\frac{\partial g_L}{\partial C_L} = \left(\frac{1-\beta}{1-k}\right)\left(1-\frac{v_x}{R}\right)\frac{G_L}{C_L} \tag{5.4}$$

where v_x is isotherm velocity perpendicular to isotherms. Equation 5.4 reduces to the Scheil equation when v_x and β both equal zero. It also reduces to the Scheil equation (written in terms of volume fraction) when

$$v_x = -\left(\frac{\beta}{1-\beta}\right)R \tag{5.5}$$

This flow is just that required to feed solidification shrinkage, and in steady-state solidification the result is no macrosegregation. Flow with a speed greater (down the temperature gradient) than that of Equation 5.5 results in negative segregation; a speed that is less, or in the opposite direction, results in positive macrosegregation.

A schematic illustration of application of these principles to continuous casting is shown in Fig. 5.24. No segregation results if interdenderitic flow lines are all vertical. Negative segregation at mid-radius would result from flow lines such as those of Fig. 5.24a, and positive segregation at the centerline would result from flow lines such as those of Fig. 5.24b. It can easily be visualized that 'bulging' will result in greater downward flow and, in particular, greater downward flow toward the centerline (as illustrated in Fig. 5.24c), thus enhancing centerline segregation.

Miyazawa and Schwerdtfeger (1981) were the first to demonstrate the foregoing by quantitative calculation of segregation during bulging in continuous casting. Figure 5.25a illustrates their model, and Fig. 5.25b shows the

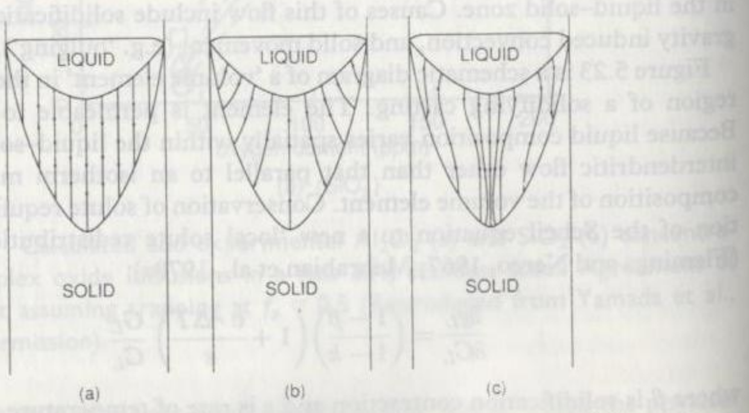

Figure 5.24 Interdendritic fluid flow in a continuous casting. (a) No segregation; (b) negative segregation at mid-radius; (c) positive segregation at centerline (Reproduced from Flemings, 1974, with permission).

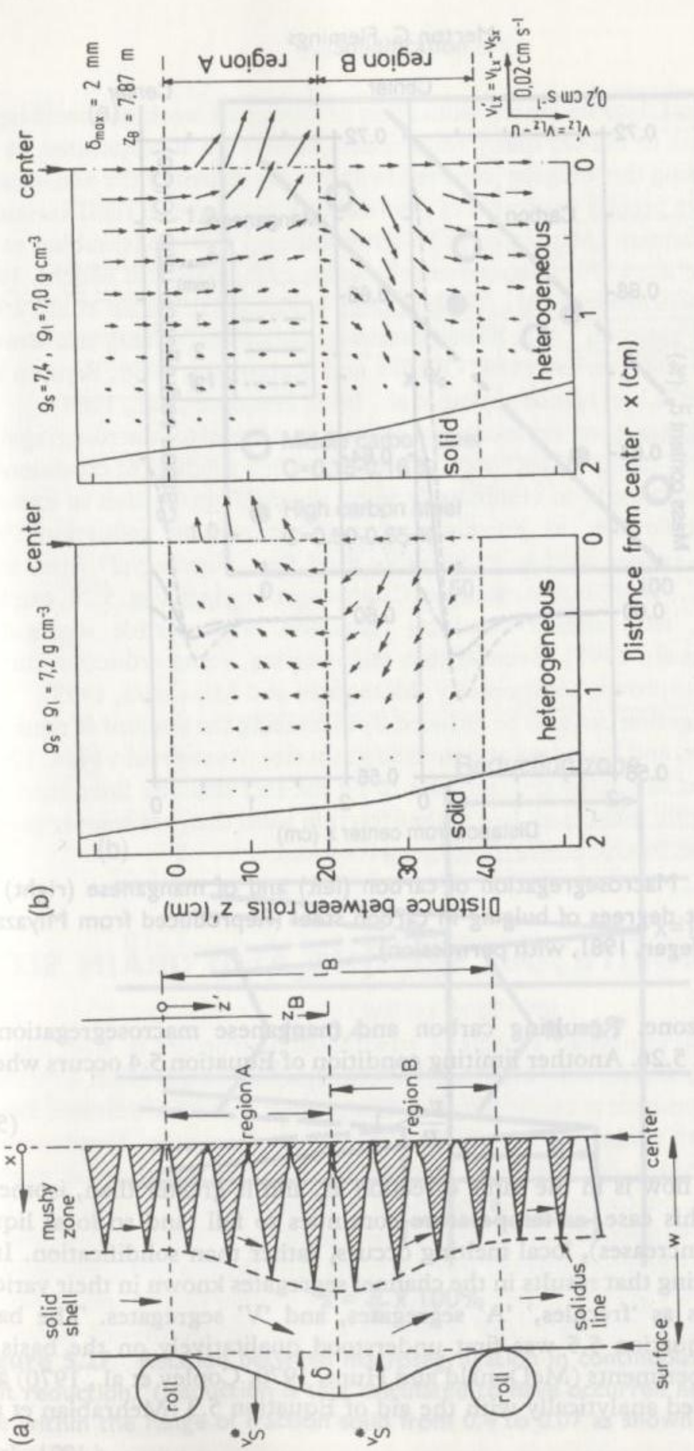

Figure 5.25 Effect of bulging on interdendritic flow in vertically continuous cast carbon steel. (a) Schematic model of half thickness of continuous casting. (b) Left is flow assuming only bulging; right is flow including effects of both bulging and solidification shrinkage (Reproduced from Miyazawa and Schwerdtfeger, 1981, with permission).

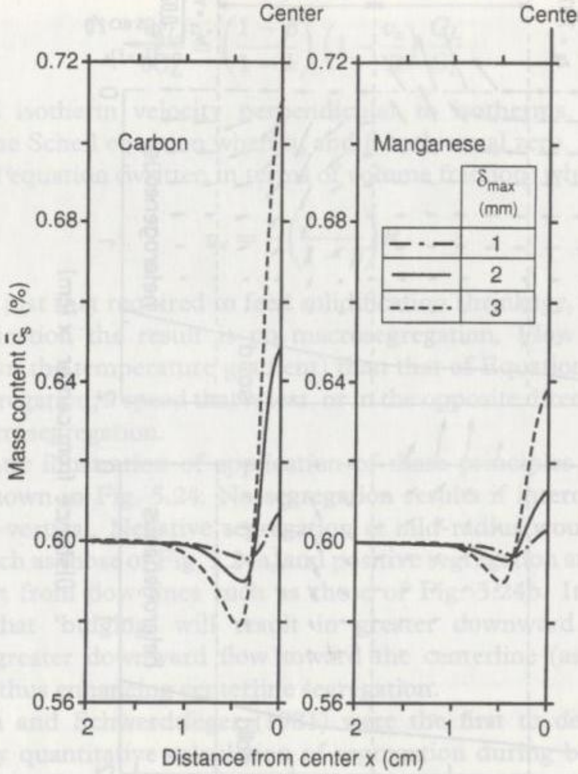

Figure 5.26 Macrosegregation of carbon (left) and of manganese (right) for three different degrees of bulging in carbon steel (Reproduced from Miyazawa and Schwerdtfeger, 1981, with permission).

liquid–solid zone. Resulting carbon and manganese macrosegregation is shown in Fig. 5.26. Another limiting condition of Equation 5.4 occurs when

$$\frac{v_x}{R} > 1 \tag{5.6}$$

that is, when flow is in the same direction as, and is greater than, isotherm velocity. In this case, as temperature continues to fall (and so local liquid composition increases), local melting occurs, rather than solidification. It is this local melting that results in the channel segregates known in their various manifestations as 'freckles,' 'A' segregates, and 'V' segregates. The basic relation of Equation 5.5 was first understood qualitatively on the basis of laboratory experiments (McDonald and Hunt, 1970; Copley et al., 1970) and later interpreted analytically with the aid of Equation 5.3 (Mehrabian et al., 1970b).

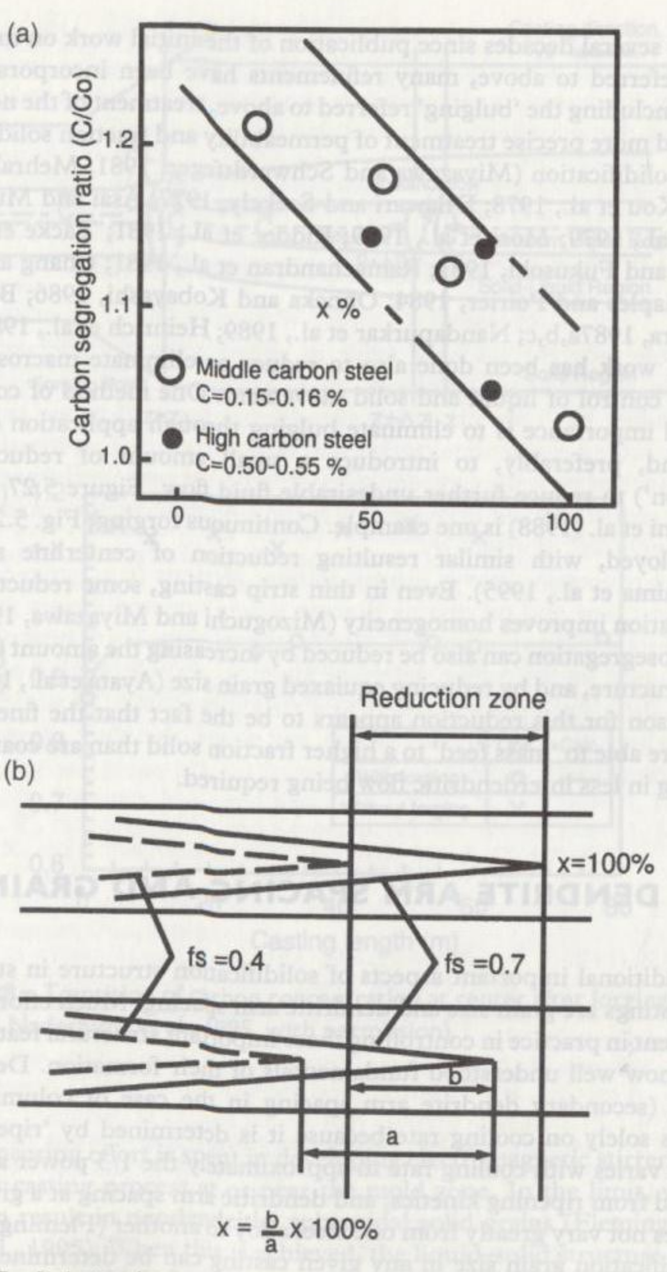

Figure 5.27 Relation between macrosegregation in continuous cast steel and 'soft reduction.' (Reduction is that calculated to have occurred near the centerline within the range of fraction solid from 0.4 to 0.07 as shown in (b).) (Barth et al., 1991.)

In the several decades since publication of the initial work on macrosegregation referred to above, many refinements have been incorporated in the theory, including the 'bulging' referred to above, treatment of the non-steady-state, and more precise treatment of permeability and fraction solid variations during solidification (Miyazawa and Schwerdtfeger, 1981; Mehrabian et al., 1970b; Kou et al., 1978; Dilawari and Szekely, 1977; Asai and Muchi, 1978; Fujii et al., 1979; Mori et al., 1989; Ridder et al., 1981; Tacke et al., 1981; Ohnaka and Fukusoki, 1981; Ramachandran et al., 1981; Chang and Brown, 1983; Maples and Poirier, 1984; Ohnaka and Kobayashi, 1986; Bennon and Incropera, 1987a,b,c; Nandapurkar et al., 1989; Heinrich et al., 1989).

Much work has been done also to reduce or eliminate macrosegregation through control of liquid and solid movement. One method of considerable practical importance is to eliminate bulging through application of external force and, preferably, to introduce a small amount of reduction ('soft reduction') to reduce further undesirable fluid flow. Figure 5.27 from work of Izutani et al. (1988) is one example. Continuous forging, Fig. 5.28, can also be employed, with similar resulting reduction of centerline segregation (Nadeshima et al., 1995). Even in thin strip casting, some reduction during solidification improves homogeneity (Mizoguchi and Miyazawa, 1995).

Macrosegregation can also be reduced by increasing the amount of equiaxed grain structure, and by reducing equiaxed grain size (Ayata et al., 1984, 1995). The reason for this reduction appears to be the fact that the finer equiaxed grains are able to 'mass feed' to a higher fraction solid than are coarser grains, resulting in less interdendritic flow being required.

5.8. DENDRITE ARM SPACING AND GRAIN SIZE

Two additional important aspects of solidification structure in steel continuous castings are grain size and dendritic arm spacing. Much effort continues to be spent in practice in controlling these important structural features, based on the now well understood fundamentals of their formation. Dendrite arm spacing (secondary dendrite arm spacing in the case of columnar grains) depends solely on cooling rate because it is determined by 'ripening.' The spacing varies with cooling rate to approximately the 1/3 power as would be expected from ripening kinetics, and dendritic arm spacing at a given cooling rate does not vary greatly from one steel alloy to another (Flemings, 1974).

Solidification grain size in any given casting can be determined either by extent of nucleation or by the extent of the 'break up' of dendrites which have formed. We now understand that for steel alloys the latter mechanism is by far the most important and this dendrite break up can be enhanced through introduction of convection during the early stages of solidification. Thus, much engineering effort is spent in developing electromagnetic stirrers for the continuous casting process at or near the mold zone. In the limit, vigorous stirring can result in nondendritic, spheroidal solid grains (Flemings, 1991; Blazek et al., 1995). When this is achieved, the liquid–solid structure remains quite fluid to a very high fraction solid.

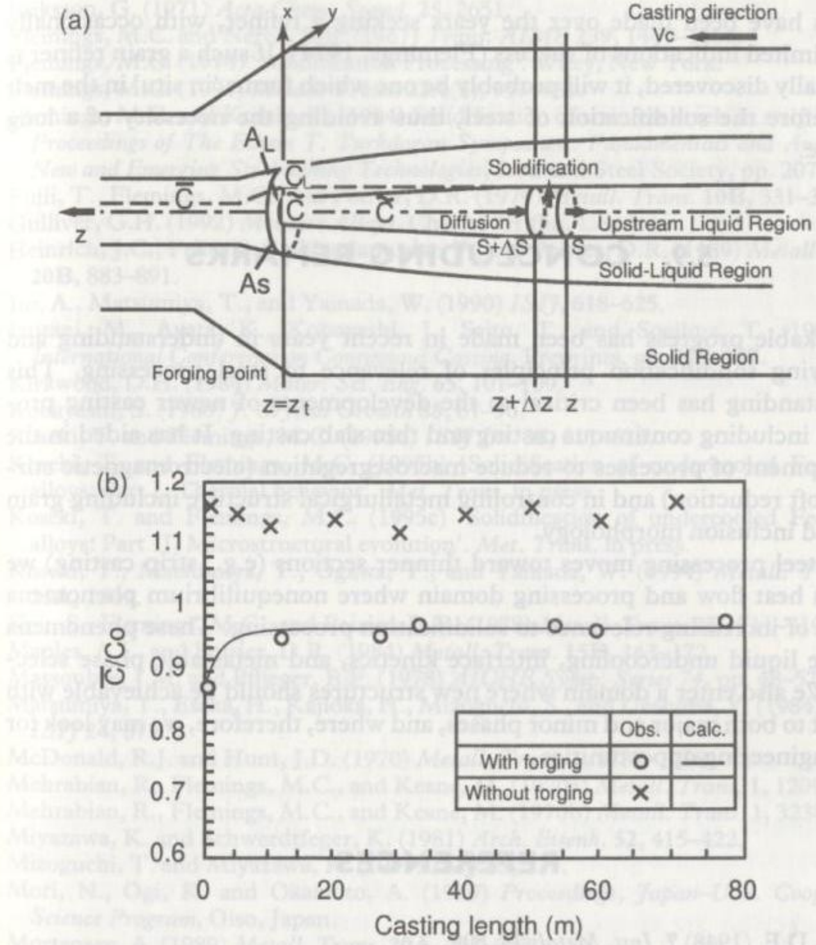

Figure 5.28 Transition of carbon concentration at center after forging (Reproduced from Nadeshima et al., 1995, with permission).

It has long been a dream of ferrous metallurgists to find a heterogeneous nucleating agent ('grain refiner') that would be effective and would have a sufficiently long lifetime in molten steel to be useful in practice. Various studies have been made over the years seeking a refiner, with occasionally some limited indications of success (Flemings, 1974). If such a grain refiner is eventually discovered, it will probably be one which forms 'in situ' in the melt just before the solidification of steel, thus avoiding the necessity of a long lifetime.

5.9. CONCLUDING REMARKS

Remarkable progress has been made in recent years in understanding and employing solidification principles of relevance to steel processing. This understanding has been critical to the developments of newer casting processes, including continuous casting and thin slab casting. It has aided in the development of processes to reduce macrosegregation (electromagnetic stirring, soft reduction) and in controling metallurgical structure including grain size and inclusion morphology.

As steel processing moves toward thinner sections (e.g., strip casting) we enter a heat flow and processing domain where nonequilibrium phenomena will be of increasing relevance to solidification processing. These phenomena include liquid undercooling, interface kinetics, and metastable phase selection. We also enter a domain where new structures should be achievable with respect to both major and minor phases, and where, therefore, we may look for new engineering opportunities.

REFERENCES

Adams, D.E. (1948) *J. Inst. Metals* **75**, 809.
Asai, A. and Muchi, I. (1978) *ISIJ* **18**, 90–98.
Ayata, K., Fujimoto, T., Mori, T., Ohnishi, T., and Wakasugi (1984) *Trans. Iron and Steel Inst. Japan* **24**, 931.
Ayata, K., Matsuda, H., Mori, H., and Taniguchi, K. (1995) *ISIJ* **35**, 680.
Barth, M., Alexander, H., Eckler, K., and Herlach, D.M. (1991) *Mater. Sci. Eng.* **A133**, 790.
Bennon, W.D. and Incropera, F.P. (1987a) *Int. J. Heat Mass Transfer* **30**, 2161–2170.
Bennon, W.D. and Incropera, F.P. (1987b) *Int. J. Heat Mass Transfer* **30**, 2171–2187.
Bennon, W.D. and Incropera, F.P. (1987c) *Metall. Trans.* **18B**, 611–616.
Blazek, K.E., Kelly, J.E., and Pottore, N.S. (1995) *ISIJ* **35**, 813.
Brody, H.D. and Flemings, M.C. (1966) *Trans. AIME* **236**, 615–624.
Chang, C.J. and Brown, R.A. (1983) *J. Crystal Growth* **63**, 343–364.
Clyne, T.W. and Kurz, W. (1981) *Metall. Trans.* **12A**, 965–971.
Copley, S.M., Giamei, A.F., Hornbecker, J.F., and Johnson, S.M. (1970) *Metall. Trans.* **1**, 2193–2204.
Dilawari, A.H. and Szekely, J. (1977) *Metall. Trans.* **8B**, 227–236.

Eriksson, G. (1971) *Acta Chem. Scand.* **25**, 2651.
Flemings, M.C. and Nereo, B.E. (1967) *Trans. AIME* **239**, 1449–1461.
Flemings, M.C. (1974) 'Solidification Processing'. Wiley, New York.
Flemings, M.C. (1991) *Metall. Trans.* **22A**(5), 957–981.
Flemings, M.C. and Koseki, T. (1994) Solidification of stainless steels in strip casting. *Proceedings of The Ethem T. Turkdogan Symposium: Fundamentals and Analysis of New and Emerging Steelmaking Technologies*, Iron and Steel Society, pp. 207–215.
Fujii, T., Flemings, M.C., and Poirier, D.R. (1979) *Metall. Trans.* **10B**, 331–339.
Gulliver, G.H. (1992) *Metallic Alloys*. Charles Griffin, London.
Heinrich, J.C., Felicelli, S., Nandapurdar, P., and Poirier, D.R. (1989) *Metall. Trans.* **20B**, 883–891.
Ito, A., Matsumiya, T., and Yamada, W. (1990) *ISIJ*, 618–625.
Izutani, M., Ayata, K., Kobayashi, J., Saito, T., and Soejima, T. (1988) *4th International Conference on Continuous Casting*, Preprints, pp. 115–127.
Kirkwood, D.H. (1984) *Mater. Sci. Eng.* **65**, 101–109.
Kobayashi, S. (1988) *J. Crystal Growth* **88**, 87–96.
Koseki, T. and Flemings, M.C. (1995a) *ISIJ Int.* **35**, 611–618.
Koseki, T. and Flemings, M.C. (1995b) 'Solidification of undercooled Fe–Cr–Ni alloys: Part I, Thermal behavior'. *Met. Trans.* in press.
Koseki, T. and Flemings, M.C. (1995c) 'Solidification of undercooled Fe–Cr–Ni alloys: Part II, Microstructural evolution'. *Met. Trans.* in press.
Koseki, T., Matsumiya, T., Ogawa, T., and Yamada, W. (1994) *Metall. Trans. A* **25A**, 1309.
Kou, S., Flemings, M.C., and Poirier, D.R. (1978) *Metall. Trans.* **9B**, 711–719.
Maples, A.L. and Poirier, D.R. (1984) *Metall. Trans.* **15B**, 163–172.
Massoubre, J.M. and Pflieger, B.F. (1978) *AICHE Symp. Series 74*, pp. 48–57.
Matsumiya, T., Esaka, H., Kajioka, H., Mizoguchi, S., and Ueshima, Y. (1984) *Trans. ISIJ* **24**, 873.
McDonald, R.J. and Hunt, J.D. (1970) *Metall. Trans.* **1**, 1787–1788.
Mehrabian, R., Flemings, M.C., and Keane, M. (1970a) *Metall. Trans.* **1**, 1209–1220.
Mehrabian, R., Flemings, M.C., and Keane, M. (1970b) *Metall. Trans.* **1**, 3238–3241.
Miyazawa, K. and Schwerdtfeger, K. (1981) *Arch. Eisenh.* **52**, 415–422.
Mizoguchi, T. and Miyazawa, K. (1995) *ISIJ* **35**, 771.
Mori, N., Ogi, K. and Okamoto, A. (1989) *Proceedings, Japan–U.S. Cooperative Science Program*, Oiso, Japan.
Mortensen, A. (1989) *Metall. Trans.* **20A**, 247–253.
Myers, M. and Flemings, M.C. (1972) *Metall. Trans.* **3**, 2225.
Nadeshima, S., Fujii, T., Fujimura, T., Kushida, K., and Nakato, H. (1995) *ISIJ* **35**, 673.
Nandapurkar, P., Felicelli, S., Heinrich, J.D., and Poirier, D.R. (1989) *Metall. Trans.* **20B**, 711–721.
Nereo, G.E., Flemings, M.C., and Polich, R.F. (1965) *Trans. AFS* **73**, 1.
Ogilvy, A.J.W. and Kirkwood, D.H. (1987) *Appl. Sci. Res.* **44**, 43–49.
Ohnaka, I. (1986) *Trans. ISIJ* **26**, 1045–1051.
Ohnaka, I. and Fukusoki, T. (1981) *ISIJ* **21**, 485–494.
Ohnaka, I. and Kobayashi, K. (1986) *ISIJ* **26**, 781–789.
Pfann, W.G. (1966) *Zone Melting*, 2nd edn. Wiley, New York.
Ramachandran, N., Gupta, G.R., and Jaluria, Y. (1981) *Num. Heat Transfer* **4**, 469–484.
Ridder, S.D., Kou, A., and Mehrabian, R. (1981) *Metall. Trans.* **12B**, 435–447.
Scheil, E. (1942) *Z. Metallk.* **34**, 70.

Scheil, E. (1947) *Metallforschung* **2**, 69.
Sundman, B., Andersson, J.O., and Jansson, B. (1985) *CALPHAD* **9**, 153.
Suutala, N., Moisio, T., and Takalo, T. (1980) *Metall. Trans. A* **11A**, 717–725.
Tacke, K.H., Grill, A., Miyazawa, K., and Schwerdtfeger, K. (1981) *Arch. Eisenh.* **52**, 15–20.
Takalo, T., Moisio, T., and Suutala, N. (1979) *Metall. Trans. A* **10A**, 1173–1181.
Trivedi, R. and Kurz, W. (1994) *Int. Mater. Rev.* **39**, 49.
Trivedi, R., Kurz, W., and Lipton, J. (1987) *Acta Metall.* **35**, 965.
Turnbull, D. (1956) 'Solid State Physics.' Academic Press, New York, vol. 3, p. 225.
Ueshima, Y., Kajioka, H., Matsumiya, T., and Mizogushi, S. (1986) *Metall. Trans. B* **17B**, 845.
Wintz, M., Bobadilla, M., Gaye, H., and Lehman, J. (1995) *ISIJ* **35**, 715.
Yamada, W., Fukumoto, S., Matsumiya, T., and Tanaka, S. (1993) *ISIJ* 123–128.
Yarwood, J., Elliott, J.F., and Flemings, M.C. (1971) *Metall. Trans.* **2**, 2573–2582.
Yeum, K.D., Laxmanan, V., and Poirier, D.R. (1989) *Metall. Trans.* **20A**, 2847–2856.

6

Interfaces and interfacial reactions of gases with liquid alloys and slags

G.R. BELTON

BHP Research, Newcastle Laboratories, Shortland, New South Wales, Australia

6.1. INTRODUCTION

A reaction between a gas or gases and a metallurgical melt will generally involve transport processes within one or both of the bulk phases as well as the interfacial chemical step or phase boundary reaction. The unambiguous description of the overall rate of such a reaction requires a knowledge of the rate phenomena involved in the transport steps and the rate law of the interfacial reaction step, unless the molecular processes are sufficiently fast for the interfacial reaction to be at virtual equilibrium with respect to the concentrations of reactants and products at the interface. The rate phenomena which occur in this interfacial chemical step are the subject of the present chapter.

The experimental determination of an empirical rate law together with appropriate rate constants is a useful end in itself, but ultimately we would like to understand enough of the details of the mechanism of the reaction to be able to formulate a rational rate law. Such a rational rate law will usually need to include factors other than simple concentrations of reactants and products to account for the dependence of the rate on the concentrations of other components in the melt. The rational and empirical rate laws must ultimately agree and it is usual to speculate on the mechanism from the empirical law. However, it is seldom that there is sufficient information in a single kinetic study to firmly establish a mechanism. Further information may be needed on

ADVANCED PHYSICAL CHEMISTRY FOR PROCESS METALLURGY
ISBN 0-12-618920-X

Copyright © 1997 Academic Press Ltd
All rights of reproduction in any form reserved

relevant chemisorption equilibria, the rates of possible elementary steps in a proposed reaction sequence, and the steady-state chemical potentials of reaction intermediates (Wagner, 1970).

In reactions with liquid metals it is virtually impossible to ascribe definite electrical charges to absorbing or adsorbing atoms or molecules and rate laws can be formulated usually without inclusion of charge transfer phenomena. In reactions with liquid oxides, an absorbing atomic species must ultimately acquire a reasonably well-defined charge and the condition of electrical neutrality must be included in the overall formulation of the rate law. In principle, the charge transfer process may be rate determining or virtual equilibria in a reaction sequence may need to be formulated in terms of electron donor and acceptor concentrations.

The early work of Kootz (1959) and Naeser and Scholtz (1959) and slightly later work by Schenck et al. (1962), Kozakevitch and Urbain (1963), and Pehlke and Elliott (1963) demonstrated that the presence of the strongly surface-active solutes oxygen and sulfur retarded the rate of reaction of nitrogen with liquid iron. Darken and Turkdogan (1970) reviewed this and other work and showed that under the conditions of near surface saturation by an interfering solute the interfacial rate is often inversely proportional to the activity of the solute, that is, consistent with the reaction occurring on the remaining vacant sites. Thus, reactions at the gas–metal interface involve the interplay of the chemisorption of impurities, reactants, and reaction intermediates with bond breaking and forming kinetics.

6.2. INTELLECTUAL FRAMEWORK

Modern reaction rate theory is based essentially on the concept of the activated complex which, in the rate-determining step, is in virtual equilibrium with reactants, and the presumption that this complex decomposes at a universal rate which is a function only of temperature. For the detailed development of this 'absolute reaction rate theory' from statistical mechanical considerations, the reader is referred to the works of Eyring (1935) and Glasstone et al. (1941).

If we consider a reaction to occur between two species, A and B, which are adsorbed at an interface, we may express the virtual equilibrium between these species and the activated complex, (AB)†, as

$$K^{\dagger} = \frac{a_{\dagger}}{a_A a_B} \tag{6.1}$$

where $K^{\dagger}$ is the equilibrium constant, $a_{\dagger}$ is the activity of the activated complex, and a_A and a_B are the activities of the reactants. This may be further expressed as

$$K^{\dagger} = \frac{\Gamma_{\dagger}\gamma_{\dagger}}{a_A a_B} = e^{-\Delta G_{\dagger}/RT} = e^{-\Delta H_{\dagger}/RT}\, e^{\Delta S_{\dagger}/R} \tag{6.2}$$

where $\Gamma_{\dagger}$ is the surface concentration, $\gamma_{\dagger}$ is the surface activity coefficient, and $\Delta G_{\dagger}$, $\Delta H_{\dagger}$, and $\Delta S_{\dagger}$ are the standard free energy, enthalpy, and entropy, respectively, of formation of the activated complex.

The activities of the reactants may be taken to refer to those in the appropriate bulk phases, e.g., the gas for a gaseous reactant or the liquid metal for a reacting solute, since equilibrium is assumed for all processes before activation. The concentration of activated complexes, $\Gamma_{\dagger}$, is usually expressed in moles per unit area of surface.

The universal rate at which the activated complexes are assumed to decompose to products is $k_B T/h$ per second, where k_B is Boltzmann's constant, h is Planck's constant, and T is the absolute temperature. The reaction rate may then be expressed as $(k_B T/h)\Gamma_{\dagger}$, or about $2.1 \times 10^{10} (T\Gamma_{\dagger})\,\mathrm{mol\,cm^{-2}\,s^{-1}}$. Thus, for a typical reaction rate of $10^{-4}\,\mathrm{mol\,cm^{-2}\,s^{-1}}$ at 1500°C, the steady-state concentration of activated complexes is considered to be of the order of $10^{-18}\,\mathrm{mol\,cm^{-2}}$. This is very small in comparison with typical values for a monolayer coverage of a surface, i.e., about $10^{-9}\,\mathrm{mol\,cm^{-2}}$.

The complete expression for the reaction rate, v, is

$$v = a_A a_B \left(K^{\dagger} \frac{k_B T}{\gamma_{\dagger} h} \right) \tag{6.3}$$

where the bracketed quantity is the rate constant with respect to the product of the activities of the reactants. The temperature dependence of the logarithm of the rate constant will be dominated by the temperature dependence of $\log K^{\dagger}$, i.e., by the enthalpy of formation of the activated complex, plus the temperature dependence of $\log(1/\gamma_{\dagger})$. This net enthalpy will differ only slightly from the empirical Arrhenius activation energy E obtained by assuming that the rate constant is given by the expression

$$k = Ce^{-E/RT} \tag{6.4}$$

where k is now the rate constant and the preexponential factor C is presumed to be a constant.

The surface activity coefficient, $\gamma_{\dagger}$, will generally be a complex function of the coverage of the surface by other adsorbed reactant, intermediate, or impurity species. A first-order simplification may be made by assuming that the activated complex follows a Langmuir adsorption isotherm. This isotherm arises from the assumption that the energy of adsorption of the particular species is independent of the coverage or atomic arrangement of all species on the surface. For single site occupancy and constant temperature we may write

$$\frac{\theta_\dagger}{1-\sum\theta_i}=\frac{\Gamma_\dagger/\Gamma_0}{1-\sum\theta_i}=K_\dagger^s a_\dagger \tag{6.5}$$

where θ_i is a fractional coverage by any adsorbed species, $\theta_\dagger$ is the fractional coverage by the activated complex, Γ_0 is the total number of sites per unit area, and $K_\dagger^s$ is an equilibrium constant (adsorption coefficient).

The forward reaction rate may therefore be written as

$$v=a_A a_B\left(1-\sum\theta_i\right)\left(\frac{k_B T}{h}\,\Gamma_0 K_\dagger K_\dagger^s\right) \tag{6.6}$$

where the quantity in the second set of brackets represents a rate constant, k, at low surface coverage. The two equilibrium constants cannot be operationally separated, and the activation energy obtained from a plot of $\log(k/T)$ versus $1/T$ is identified with the enthalpy of formation of the activated complex on the ideal surface; again, approximately equal to the Arrhenius activation energy. At significant surface coverage, the temperature dependence of the rate will include a factor which is a function of the heats of adsorption of all species other than the activated complex, which, as noted earlier, would be present at very small concentration.

The principle of microscopic reversibility requires the activated complex to be the same for the forward and reverse reactions. Accordingly, for a reaction which is near to equilibrium, the net rate of reaction is given by substitution of the expression $[a_A a_B-(a_A a_B)_{eq}]$ for the term $a_A a_B$ in Equation 6.6, where $(a_A a_B)_{eq}$ is the value which would be in equilibrium with the activities of the reaction products. Although all of the foregoing has been formulated in terms of a bimolecular second-order reaction, the extension of the principles to other orders of reaction is straightforward.

Clearly, a rate expression of the form of Equation 6.6 must be regarded as a first approximation and it is not normally possible to calculate the energetics of formation of proposed activated complexes from first principles. It does, however, provide a useful framework for the analysis of high-temperature rate data and an understanding of the influence of the surface constitution of the melt on rates and rate laws. In the words of the eminent metallurgist John Chipman: 'The usefulness of a scientific law does not depend on its exactness but rather on whether it gets you out of more trouble than it gets you into.'

6.3. THE SURFACE CONSTITUTION OF LIQUID ALLOYS

The several surface spectroscopies are significantly advancing our understanding of surface segregation phenomena in solids, and Grabke and coworkers (1989, 1995) have recently reviewed the results of such studies for mainly ferrous alloys at elevated temperatures. For an introduction to these surface spectroscopies, reference may be made to the text edited by Walls (1989). At present, the only source of quantitative information on adsorption equilibria for high-temperature liquid alloys is the depression of surface tension, although some broad similarities are to be expected in the phenomena which occur in solid and liquid systems.

The Gibbs adsorption isotherm (Gibbs, 1948) for a multicomponent system at constant pressure may be written:

$$d\sigma=-\sum_i\Gamma_i\,d\mu_i \tag{6.7}$$

where σ is the surface tension, Γ_i is a surface concentration (adsorption), and μ_i is the chemical potential of a component. Combination with the Gibbs–Duhem equation gives

$$d\sigma=-\sum_{i=2,3}\left(\Gamma_i-\frac{x_i}{x_1}\right)d\mu_i \tag{6.8}$$

where x_i is a mole fraction and the quantities in brackets, the relative adsorptions $\Gamma_{i,1}$, are invariant with respect to the position of the interface. Component 1 is usually chosen to be the major component or solvent.

For a full didactic discussion of the definitions of relative adsorption, reference is made to the paper by Wagner (1973). In general, approximations or reasonable models need to be used to derive internally consistent surface concentration information from the application of Equation 6.8. Usually, following Butler (1932), the surface phase is considered to be of near single atomic thickness and some area relationship is assumed among the coverages of the several species. A typical relationship is the Lucassen-Reynders (1966) convention:

$$\sum_i\Gamma_i=\Gamma^0 \tag{6.9}$$

where Γ^0 is a saturation coverage which is assumed to be the same for all species, including the solvent.

At low concentration of a solute 2 in a binary system, the limiting form of the adsorption isotherm becomes

$$\left(\frac{\partial\sigma}{\partial \ln a_2}\right)_{P,T} = -RT\Gamma_2 = -RT\theta_2\Gamma_2^0 \qquad (6.10)$$

where a_2 is the activity of the solute 2. The limiting slope in a plot of σ versus $RT \ln a_2$ may be assumed to be the saturation coverage by the solute, Γ_2^0, and Kozakevitch (1968) has shown that for the strongly surface-active group VIb solutes in liquid iron these coverages are often in reasonable accord with a close-packed coverage by the doubly charged negative ion or with the area occupied in a near close-packed plane of the element in an appropriate solid compound for smaller ions.

6.3.1. Ideal Adsorption

If the ideal Langmuir isotherm is assumed, we may write

$$\frac{\theta_2}{1-\theta_2} = K_2^s a_2 \qquad (6.11)$$

Substitution in Equation 6.10 gives, at constant temperature and pressure,

$$\frac{d\sigma}{d \ln a_2} = -RT\Gamma_2^0 \frac{K_2^s a_2}{1+K_2^s a_2} \qquad (6.12)$$

This equation may be integrated between $a_2 = 0$ and $a_2 = a_2$ to give (Belton, 1976a)

$$\sigma^{\mathrm{P}} - \sigma = RT\Gamma_2^0 \ln(1 + K_2^s a_2) \qquad (6.13)$$

where σ^{P} is the surface tension of the pure solvent. This ideal adsorption equation was first deduced empirically in a slightly different form by Szyszkowski (1908) and has been found to describe surface tension data closely for many ionized (Lucassen-Reynders, 1966) and un-ionized (Meissner and Michaels, 1949) surfactants in water. In the form

$$\sigma^{\mathrm{P}} - \sigma = -RT\Gamma_2^0 \ln\left(1 - \frac{\Gamma_2}{\Gamma_2^0}\right) \qquad (6.14)$$

it is known as the Frumkin (1925) equation.

In initial analyses (Belton, 1976a,b), Equation 6.13 was found to give a close description of the available surface tension data for the group VIb elements in some liquid metals and the derived values of the apparent ideal adsorption coefficient for O, S, and Se in liquid iron were shown to be broadly in accord with the effects of the elements in retarding the rate of absorption of nitrogen into liquid iron. The isotherm

$$1788 - \sigma = 195 \ln(1 + 185 a_{\mathrm{S}}) \quad \mathrm{mN\,m^{-1}} \qquad (6.15a)$$

is shown to be in close agreement with the available data (Kozakevitch and Urbain, 1961a; Halden and Kingery, 1955; Van Tszin-Tan et al., 1960; Dyson, 1963; Gaye et al., 1984; Ogino et al., 1984) for the effect of sulfur on the surface tension of liquid iron at 1550–1600°C in Fig. 6.1, where Henry's law is assumed to hold for the dilute solute.

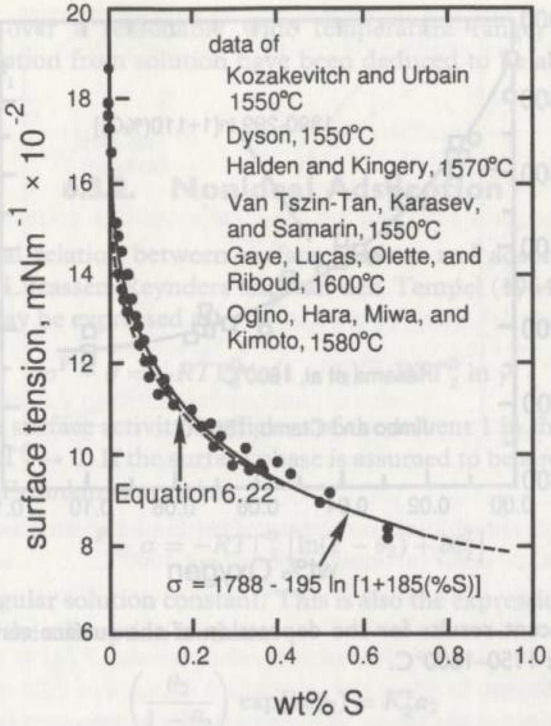

Figure 6.1 The depression of the surface tension of liquid iron by sulfur at 1550–1600°C. Reproduced from Belton (1993), with permission.

For selenium, the consistent isotherm at 1550°C is

$$1788 - \sigma = 176 \ln(1 + 1200 a_{\mathrm{Se}}) \quad \mathrm{mN\,m^{-1}} \qquad (6.15b)$$

where activity is equated with wt%.

The measurement of surface tensions of liquid iron alloys is experimentally difficult and derived values of the limiting slope, $RT\Gamma_2^0$, are uncertain. In addition, the surface tension of 'pure iron' in the extant literature (Keene, 1988) varies over a range of about 700 mN m^{-1}. In applying Equation 6.13 to a set of data, it is probably reasonable to use the value for pure iron from the same study or, at least, from studies using the same technique and closely similar experimental conditions.

Oscillating droplet studies by Kasama et al. (1983) and the more recent

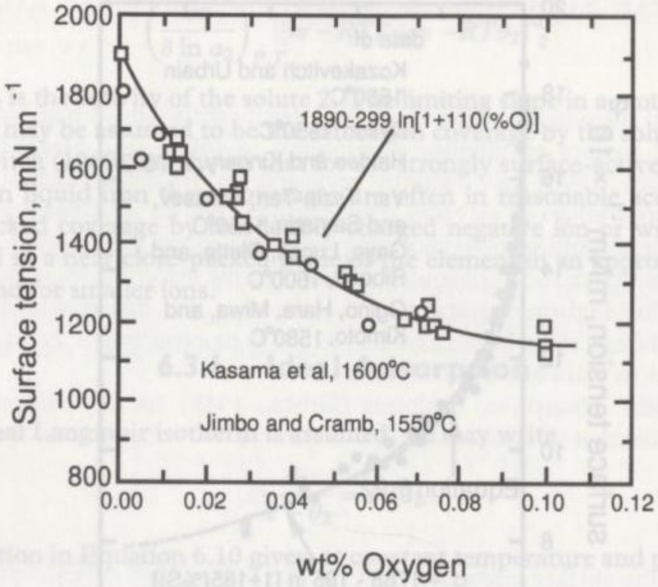

Figure 6.2 Recent results for the depression of the surface tension of liquid iron by oxygen at 1150–1600°C.

sessile droplet studies of Jimbo and Cramb (1992) are, however, in good accord for both the surface tension of pure iron and iron–oxygen alloys. Their results are shown in Fig. 6.2 to be closely described by the isotherm

$$1890 - \sigma = 299 \ln(1 + 110a_O) \ \text{mN m}-1 \tag{6.16}$$

at 1600°C, or the consistent isotherm

$$1905 - \sigma = 291 \ln(1 + 130a_O) \ \text{mN m}-1 \tag{6.17}$$

at 1550°C, within the experimental scatter. There is no independent evidence to support such ideal behavior on liquid iron, but studies on solid metals suggest that this can occur. For example, Auger electron spectroscopy studies by Seah and Lea (1975) have shown that the adsorption of tin on polycrystalline α-iron at 500–850°C is closely described by Langmuir adsorption and that the adsorption coefficients are in good agreement with those deduced from surface tension (zero creep) measurements (Seah and Hondros, 1973) on δ-iron-tin alloys at 1420°C.

Derived values of the apparent ideal adsorption coefficient are uncertain (Belton, 1976a) to at least ±20% and any estimates for the heats of adsorption of the group VIb elements on liquid iron would be too crude to be of value. For sulfur on liquid copper and oxygen on liquid silver, where the isotherms

are available over a reasonably wide temperature range, the respective heats of adsorption from solution have been deduced to be about −170 and −200 kJ mol^{-1}.

6.3.2. Nonideal Adsorption

A more general relation between surface tensions and adsorption has been developed by Lucassen-Reynders and van den Tempel (1964). For a binary system, this may be expressed as

$$\sigma^{\mathrm{P}} - \sigma = -RT\Gamma_2^0 \ln(1 - \theta_2) - RT\Gamma_2^0 \ln \gamma_1^s \tag{6.18}$$

where γ_1^s is the surface activity coefficient of the solvent 1 in the surface phase with $\gamma_1^s \rightarrow 1$ as $\Gamma_2^0 \rightarrow 0$. If the surface phase is assumed to be a regular solution, we obtain the Frumkin expression

$$\sigma^{\mathrm{P}} - \sigma = -RT\Gamma_2^0 \left[\ln(1 - \theta_2) + b\theta_2^2\right] \tag{6.19}$$

where b is a regular solution constant. This is also the expression which would be obtained if the adsorption isotherm

$$\left(\frac{\theta_2}{1 - \theta_2}\right) \exp(2b\theta_2) = K_2^s a_2 \tag{6.20}$$

rather than the ideal Langmuir isotherm were to be substituted in Equation 6.10. Independent information on, or a presumption of the value of the saturation coverage by the solute, Γ_2^0, is needed if these equations are to be applied to surface tension data to examine deviations from ideality.

Auger electron studies of the segregation of oxygen to the surfaces of polycrystalline copper (Guth et al., 1984) and iron (Grabke, 1989) at elevated temperatures have shown a distinct two-stage adsorption behavior. For iron at 800°C, the first step appears to be filling of sites to an O/Fe ratio of 0.25 and the second step to be filling to an O/Fe ratio of 1. The two steps were reasonably well described by Langmuir isotherms. It may be speculated that at the liquid metal surface the group VIb ions, at least, would exhibit strong repulsive interactions and that an initial isotherm could describe adsorption up to a point where strong interactions lower the net adsorption energy. Filling of the remaining sites might then be described by one or more isotherms with progressively lower values of the adsorption coefficient. It can be shown (Belton, 1993) that the expression for the lowering of surface tension of a binary alloy becomes

$$\sigma^{\mathrm{P}} - \sigma = RT\Gamma_2^0 \sum_j \beta_j \ln(1 + K_{(2)j}^s a_2) \tag{6.21}$$

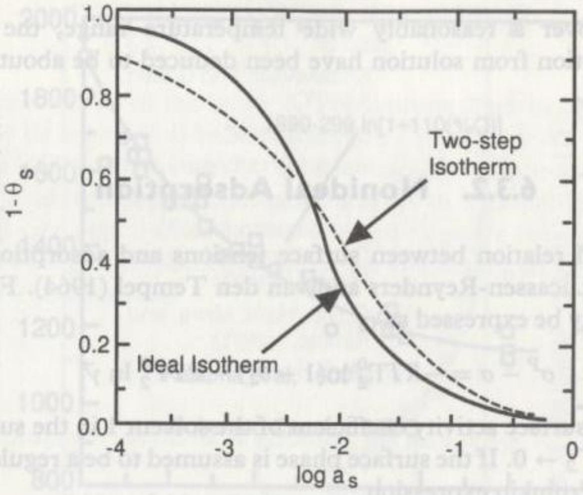

Figure 6.3 Calculated fraction of vacant sites for a two-step isotherm versus an ideal isotherm for sulfur on liquid iron at about 1600°C.

where β_j is the fraction of sites of a given type and $K^s_{(2)j}$ is the associated adsorption coefficient.

Assuming an initial site filling to S/Fe of 0.25, the two-step isotherm

$$1788 - \sigma = 195[0.25\ln(1 + 6000a_S) + 0.75\ln(1 + 60a_S)] \text{ mN m}^{-1} \quad (6.22)$$

has been found to describe the surface tension data for liquid iron–sulfur alloys, as shown by the dashed curve in Fig. 6.1. The calculated fraction of vacant sites, $1 - \theta_S$, for the two-step isotherm and the ideal isotherm are compared in Fig. 6.3. Clearly, very high precision in surface tension data would be required to establish such nonideal behavior and, broadly, if a reaction rate were to be a linear function of the fraction of vacant sites, there would be only a small difference in the functional dependence of the rate on solute concentration.

6.3.3. Ternary Alloys and Coadsorption

At low concentrations of solutes 2 and 3 and constant temperature and pressure, the limiting form of Equation 6.8 may be written as

$$d\sigma = -\Gamma_2\, d\mu_2 - \Gamma_3\, d\mu_3 \quad (6.23)$$

Transformation of this expression to two independent equations has been examined by Whalen et al. (1962) and the present author (Belton, 1972). For constant atom fraction of one solute, the latter work has shown that the dependence of the surface tension on composition becomes

$$-\frac{1}{RT}\left(\frac{\partial\sigma}{\partial\ln x_2}\right)_{x_3} = \Gamma_2\left[x_2\left(\frac{\partial\ln\gamma_2}{\partial x_2}\right)_{x_3} + 1\right] + \Gamma_3 x_2\left(\frac{\partial\ln\gamma_3}{\partial x_2}\right)_{x_3} \quad (6.24)$$

At low concentration and using wt% as the practical composition function, this becomes

$$-\frac{1}{2.303RT}\left(\frac{\partial\sigma}{\partial\log[\%2]}\right) = \Gamma_2(1 + [\%2]e_2^2) + \Gamma_3[\%2]e_3^2 \quad (6.25)$$

where e_i^j represents a practical interaction parameter.

In order to separate out values of Γ_i by applying Equation 6.24 to ternary (or higher-order) systems, there must be sufficient surface tension data and bulk phase thermodynamic data to allow a series of intersecting composition paths of constant mole fraction of a component to be analyzed. This is not usually the case.

Studies of the surface tensions of Fe–O–S alloys have been carried out by Ogino et al. (1983) and their results are in reasonable accord with earlier work by Popel et al. (1975). Unfortunately, the precision in the data is insufficient to apply Equation 6.25 in a detailed analysis, but paths of constant composition for each component clearly show decreasing surface tension with increasing concentration of the second component. Since the terms involving the interaction parameters are small at the low concentrations, this is consistent with coadsorption of the two solutes. The authors concluded from a simplified analysis that the data were consistent with ideal competitive adsorption of the two solutes, i.e., the Langmuir isotherm constants from the binary systems were applicable to the ternary system. This must, however, be regarded as a rough first approximation.

There are cases where pairs of solutes which are separately not very surface active cause a significant depression of the surface tension of liquid iron, and Kozakevitch and Urbain (1961b) suggested that the formation of surface-active molecular groups could be the cause. Auger electron spectroscopy and low-energy electron diffraction studies by Uebing et al. (1989) of single-crystal surfaces of iron alloys at 500–750°C have now demonstrated the formation of the two-dimensional compounds CrC, CrN, and VC under conditions where the activities of the components are too low to form stable precipitates.

Whalen and colleagues (1962) measured surface tensions of liquid Fe–Cr–C alloys at 1350°C and at a constant atom fraction of carbon of 0.125. They observed a minimum in the surface tension at approximately $x_{Cr} = 0.18$. From Equation 6.24, an extremum will exist when

$$0 = \Gamma_{\mathrm{Cr}}\left[1 + x_{\mathrm{Cr}}\left(\frac{\partial \ln \gamma_{\mathrm{Cr}}}{\partial x_{\mathrm{Cr}}}\right)_{x_{\mathrm{C}}}\right] + x_{\mathrm{Cr}}\Gamma_{\mathrm{C}}\left(\frac{\partial \ln \gamma_{\mathrm{C}}}{\partial x_{\mathrm{Cr}}}\right)_{x_{\mathrm{C}}} \tag{6.26}$$

The thermodynamic factors in this equation are well established and it has been shown (Belton, 1972) that the minimum is consistent with $\Gamma_{\mathrm{Cr}} = \Gamma_{\mathrm{C}}$, i.e., adsorption of the stoichiometric compound CrC. This is illustrated in Fig. 6.4.

The existence of strong attractive interactions between solutes at the surface may lead to enhanced adsorption without the formation of apparent stoichiometric compounds. This has been observed in Auger electron spectroscopy studies by Dumoulin and Guttmann (1980) of a series of polycrystalline ternary iron alloys containing Ni, Cr, V, Ti, or Mo with Sb, P, S, C, or N, with 11 of these pairs showing strong cosegregation. A theoretical model of this cosegregation has been developed in terms of the regular solution approximation (Guttmann and McLean, 1979).

Incorporation of this model into expressions such as Equation 6.24 for the depression of the surface tension of liquid alloys would be complex and is not justified because of the lack of experimental data. Qualitatively, however, such cosegregation phenomena appear to occur, as is illustrated by the depression of the surface tension of liquid iron by Si and C, solutes which are not separately significantly surface active (Whalen et al., 1962).

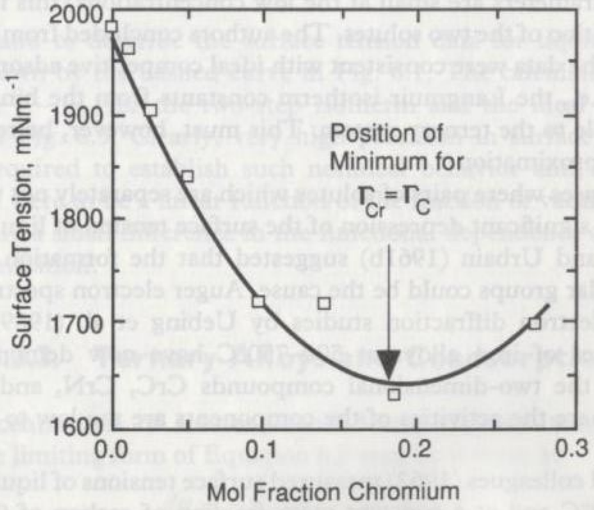

Figure 6.4 Surface tensions of liquid Fe–Cr–C alloys at 1350°C and $x_{\mathrm{Cr}} =$ 0.125. Data of Whalen et al. (1962), after Belton (1972).

6.4. THE SURFACE CONSTITUTION OF LIQUID SLAGS

As in the case of liquid alloys, surface tension measurements are the source of information on the surface constitution of liquid slags. Reference may be made to the review by Mills and Keene (1987) for most of the available surface tension data for slags containing FeO. Broadly, the surface tensions of pure liquid oxides and slags are lower than for the metals and the magnitude of the depression of the surface tension by surface-active components tends to be very much lower than, for example, that by the Group IVb elements in liquid iron.

For binary systems based on liquid FeO, it is found that Al_2O_3 has a negligible effect, SiO_2, TiO_2, CaO, and MnO moderately depress the surface tension, and Na_2O and P_2O_5 are reasonably strongly surface active. A summary of the data for 1420°C, taken from Kozakevitch (1949), is shown in Fig. 6.5. More complete experimental data for iron-saturated FeO–P_2O_5

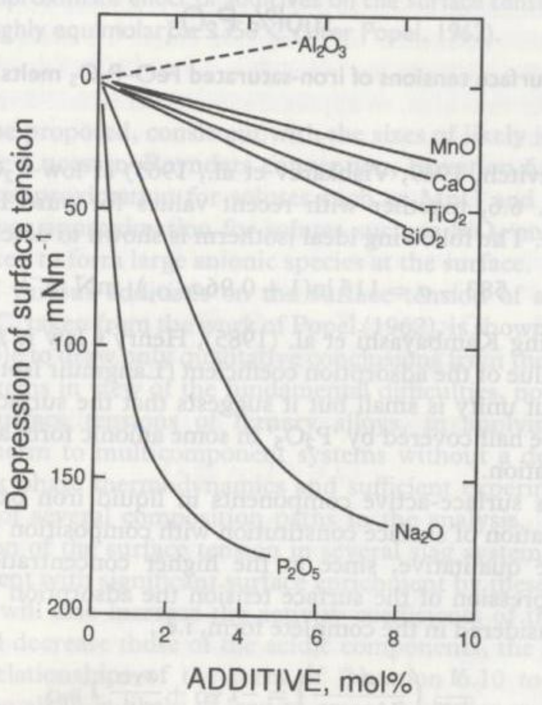

Figure 6.5 Depression of the surface tension of liquid iron oxide at about 1420°C (after Kozakevitch, 1949).

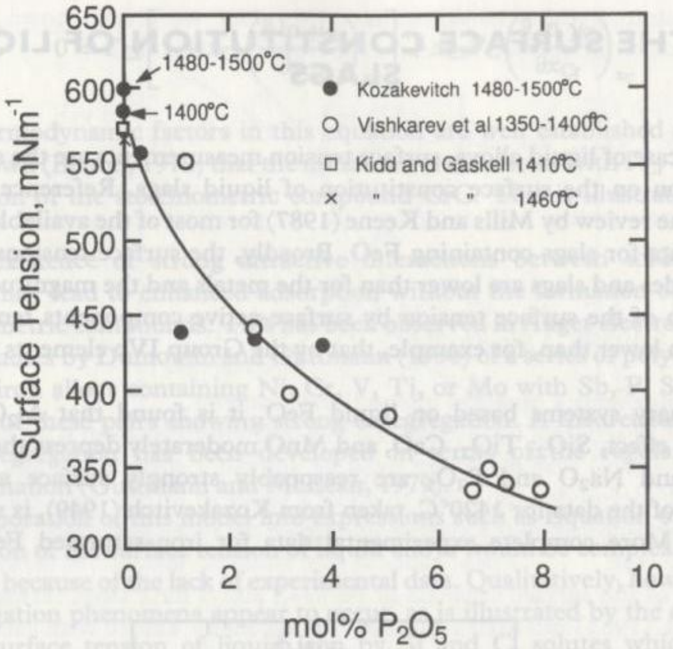

Figure 6.6 Surface tensions of iron-saturated FeO–P_2O_5 melts.

melts (Kozakevitch, 1949; Vishkarev et al., 1965) at low P_2O_5 contents are shown in Fig. 6.6, together with recent values for pure FeO (Kidd and Gaskell, 1986). The following ideal isotherm is shown to describe the data

$$583 - \sigma = 115 \ln(1 + 0.96 a_{P_2O_5}) \text{ mN m}^{-1} \tag{6.27}$$

where, following Kambayashi et al. (1985), Henry's law is assumed for the solute. The value of the adsorption coefficient (Langmuir isotherm constant), $K^s_{P_2O_5}$, of about unity is small but it suggests that the surface of liquid iron oxide would be half covered by 'P_2O_5' in some anionic form at about 1 mol% bulk concentration.

For the less surface-active components in liquid iron oxide, deductions about the variation of surface constitution with composition would generally be even more qualitative, since at the higher concentrations needed for significant depression of the surface tension the adsorption isotherm would need to be considered in the complete form, i.e.,

$$\frac{1}{RT}\left(\frac{d\sigma}{d \ln a_{YO}}\right) = -\Gamma_{YO} + \frac{x_{YO}}{x_{FeO}}\Gamma_{FeO} \tag{6.28}$$

where YO represents the added oxide. A relationship between Γ_{FeO} and Γ_{YO} would need to be proposed, consistent with the sizes of likely ionic species at the surface. The Lucassen–Reynders convention, Equation 6.9, would be a reasonable first approximation for solutes such as MnO and CaO but it is likely to be a poor approximation for solutes such as SiO_2 and P_2O_5 which would be expected to form large anionic species at the surface.

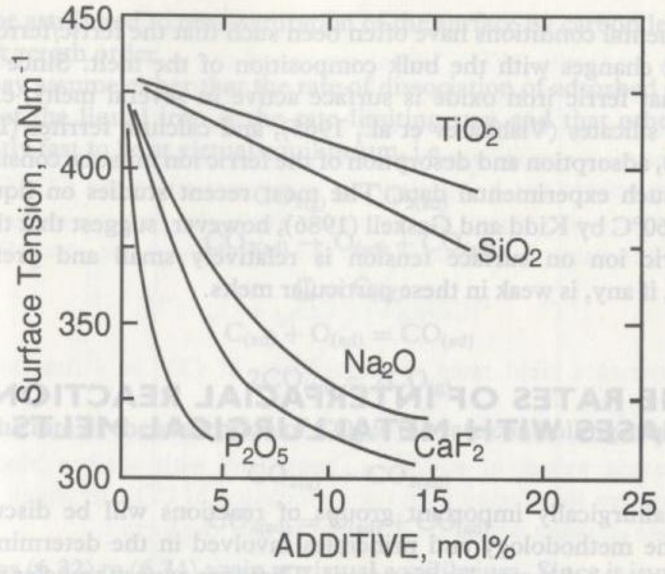

Figure 6.7 Approximate effect of additives on the surface tension of a calcium iron silicate (roughly equimolar) at 1350°C (after Popel, 1962).

The effect of various additives on the surface tension of a calcium iron silicate at 1350°C, taken from the work of Popel (1962), is shown in Fig. 6.7. It is usually possible to draw only qualitative conclusions from these and similar data on slag systems in view of the fundamental difficulties, noted in Section 6.3.3 on the surface tensions of ternary alloys, in applying the Gibbs adsorption isotherm to multicomponent systems without a detailed knowledge of the bulk phase thermodynamics and sufficient experimental data to permit the use of several composition paths in the analysis. The relatively strong depression of the surface tension in several slag systems by the basic alkalis is consistent with significant surface enrichment by these components, but, since they will also increase the activity coefficients of the other basic components and decrease those of the acidic components, the application of even limiting relationships of the form of Equation 6.10 to quantify the adsorption of the alkali is likely to lead to error. A similar argument would hold for the effects of the strongly acidic components, i.e., P_2O_5 and B_2O_3.

Mills and Keene (1987) have noted that for the iron oxide-containing melts the experimental conditions have often been such that the ferric/ferrous ratio of the melt changes with the bulk composition of the melt. Since there is evidence that ferric iron oxide is surface active in several melts, e.g., iron oxide, iron silicates (Vishkarev et al., 1965), and calcium ferrites (Din-Fen et al., 1963), adsorption and desorption of the ferric ion must be considered in analyzing such experimental data. The most recent studies on liquid iron oxide at 1460°C by Kidd and Gaskell (1986), however, suggest that the effect of the ferric ion on surface tension is relatively small and preferential adsorption, if any, is weak in these particular melts.

6.5. THE RATES OF INTERFACIAL REACTIONS OF GASES WITH METALLURGICAL MELTS

Three metallurgically important groups of reactions will be discussed to illustrate the methodology and principles involved in the determination of rate laws and probable rate-limiting steps. These are oxygen transfer reactions and the decarburization of liquid iron, nitrogen reactions with liquid iron, and the oxidation and reduction of iron oxide slags. To avoid complexities in superscripts and subscripts, the symbols v, k_a, and k_0 will generally be used to denote a rate per unit area, an apparent rate constant, and a rate constant at a specifically defined condition, respectively. Where it is necessary to represent the quantities for a reverse reaction, v', k'_a, and k'_0 will be used. The subscript bar _ will be used to denote a dissolved species, and the designation (ad) will be used to denote a species adsorbed on a surface site.

6.5.1. Oxygen Transfer Reactions and the Decarburization of Liquid Iron

The rate of decarburization of liquid iron by the overall reaction

$$CO_2 + \underline{C} = 2CO \qquad (6.29)$$

has been studied at 1200–1600°C under conditions where mass transfer limitations were negligible by Sain and Belton (1976, 1978), Mannion and Fruehan (1989), and Nagasaka and Fruehan (1994a). This body of work has shown that the interfacial rate is first order with respect to the pressure of CO_2 over at least the range 0.1–0.5 atm, independent of the pressure of CO, and, for high-purity iron, independent of carbon concentration from saturation down to at least 1 wt%. It is known that carbon has a negligibly small effect on the surface tension of otherwise pure liquid iron (Kozakevitch and Urbain, 1961b). Accordingly, the independence of the rate from carbon concentration cannot be attributed to near-saturation of the surface by carbon leading to an apparent zeroth order.

We may assume either that the rate of dissociation of adsorbed CO_2 on the surface of the liquid iron is the rate-limiting step and that other steps are sufficiently fast to be at virtual equilibrium, i.e.,

$$CO_{2(g)} = CO_{2(ad)} \qquad (6.30a)$$

$$CO_{2(ad)} \rightarrow O_{(ad)} + CO_{(ad)} \qquad (6.31a)$$

$$\underline{C} = C_{(ad)} \qquad (6.32)$$

$$C_{(ad)} + O_{(ad)} = CO_{(ad)} \qquad (6.33)$$

$$2CO_{(ad)} = 2CO_{(g)} \qquad (6.34)$$

or that the rate of chemisorption of CO_2 is the rate controlling step, i.e.,

$$CO_{2(g)} \rightarrow CO_{2(ad)} \qquad (6.30b)$$

$$CO_{2(ad)} = O_{(ad)} + CO_{(ad)} \qquad (6.31b)$$

with steps (6.32) to (6.34) again at virtual equilibrium. Since it is not possible to distinguish between these two possibilities from the available experimental data, steps (6.30) and (6.31) can be considered in combination and the rate-determining step described as the dissociative chemisorption of CO_2. Thus the activated complex would contain one molecule of CO_2 in the physically or chemically adsorbed state.

At high concentrations of carbon, the virtual equilibrium (6.33) leads to very low values for the steady-state activity of oxygen. This, in turn, indicates that the surface coverage by adsorbed oxygen, calculated from the Langmuir adsorption isotherm (6.11) and values of the adsorption coefficient K_O^s from either (6.16) or (6.17), would be negligibly small. Thus, for high-purity carbon-saturated iron, we may write

$$v = k_0 p_{CO_2} \quad \text{mol cm}^{-2}\,\text{s}^{-1}\,\text{atm} \qquad (6.35)$$

According to Sain and Belton (1976), values for this bare surface rate constant are given by

$$\log k_0 = -\frac{5080}{T} - 0.21 \qquad (6.36)$$

from 1150–1600°C.

Independent measurements of the rate of dissociation of CO_2 on liquid iron have been carried out by Cramb and Belton (1981) through studies of the rate of the isotope exchange reaction

$$^{14}CO_{2(g)} + {}^{12}CO_{(g)} = {}^{14}CO_{(g)} + {}^{12}CO_{2(g)} \qquad (6.37)$$

at 1540–1740°C. For a full description of the principles of isotope exchange methods in heterogeneous reaction studies, the reader is referred to the monograph by Ozaki (1977). Initial studies of the exchange reaction (6.37) on solid metal surfaces were carried out by Grabke (1965, 1967).

Isotope exchange experiments can be carried out over a sufficiently long time that *chemical equilibrium* exists between the gas phase and the specimen; thus measurements can be carried out as a function of the CO_2/CO ratio, i.e., the activity of oxygen in the melt. Since the isotope exchange may reasonably be assumed (Wagner, 1970) to occur through the generalized step

$$ {}^{14}CO_{2(g)} \rightarrow {}^{14}CO_{(g)} + O_{ad} \qquad (6.38) $$

the measurements yield rates of dissociation of CO_2 as a function of the activity of oxygen.

Values of the first-order apparent rate constant, k_a, were found to decrease with increasing values of p_{CO_2}/p_{CO}, consistent with surface blockage by adsorbed oxygen interfering with the dissociation of CO_2. In which case, the apparent rate constant would be expected to take the form

$$ k_a = k_0(1 - \theta_O) \qquad (6.39) $$

where θ_O is the fractional coverage of the surface by oxygen. Assuming the ideal Langmuir isotherm (6.11) holds for the adsorption of oxygen, this becomes

$$ k_a = \frac{k_0}{1 + K_O^s a_O} \qquad (6.40) $$

Taking the reciprocal of this expression and a standard state for oxygen of $p_{CO_2}/p_{CO} = 1$, this becomes

$$ \frac{1}{k_a} = \frac{1}{k_0} + \frac{K_O'^s}{k_0} \frac{p_{CO_2}}{p_{CO}} \qquad (6.41) $$

where $K_O'^s$ is the adsorption coefficient with respect to this particular standard state for oxygen. Data for two temperatures are shown plotted in accordance with Equation 6.41 in Fig. 6.8. Also shown are values for the reciprocal of the rate constant for decarburization from Equation 6.36. There is thus consensus among the experimental studies that the rate-limiting step in the reaction of CO_2 with liquid iron is the dissociative chemisorption of the CO_2 molecule.

Values of the adsorption coefficient for oxygen may be obtained from the values of the slopes and intercepts in Fig. 6.8. Taking data for other temperatures into account, Cramb and Belton (1981) derived the expression

$$ \log K_O'^s = \frac{2910}{T} + 0.47 \qquad (6.42) $$

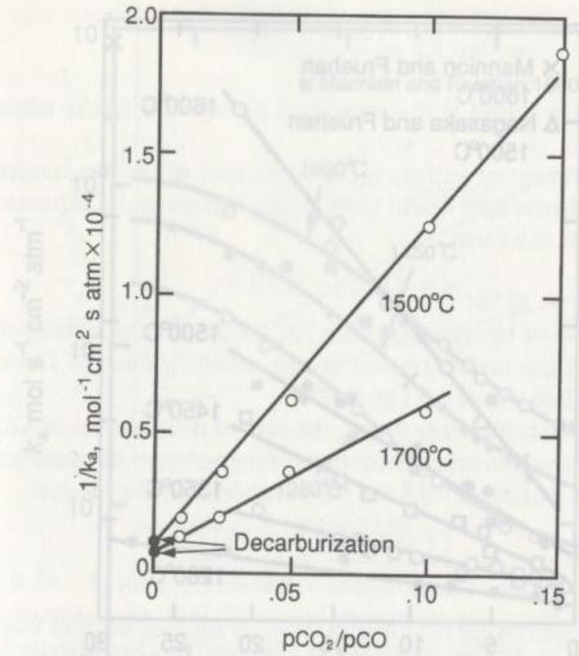

Figure 6.8 Data for the interfacial apparent rate constants for decarburization by CO_2 and the dissociation of CO_2 for very high purity iron at two selected temperatures, plotted in accordance with Equation 6.41. Data of Cramb and Belton (1981) and Sain and Belton (1976).

which, on converting to a standard state for oxygen of the 1 wt% ideal solution, became

$$ \log K_O^s = \frac{11\,370}{T} - 4.09 \qquad (6.43) $$

At 1550°C, the value of K_O^s is about 140. This is in essential agreement with the value of 130 which was deduced from the recent surface tension studies through the Szyszkowski equation (6.17).

6.5.1.1. The effect of sulfur on rates of decarburization

Sulfur has a profound effect in depressing the rate of decarburization of carbon-saturated liquid iron by CO_2 or H_2O. As little as 0.05 wt% S reduces the interfacial rate by more than an order of magnitude. Values of the apparent first-order rate constants for several temperatures, mainly from Sain and Belton (1978), are shown as a function of the reciprocal of the concentration of sulfur in Fig. 6.9, for concentrations above about 0.03 wt%.

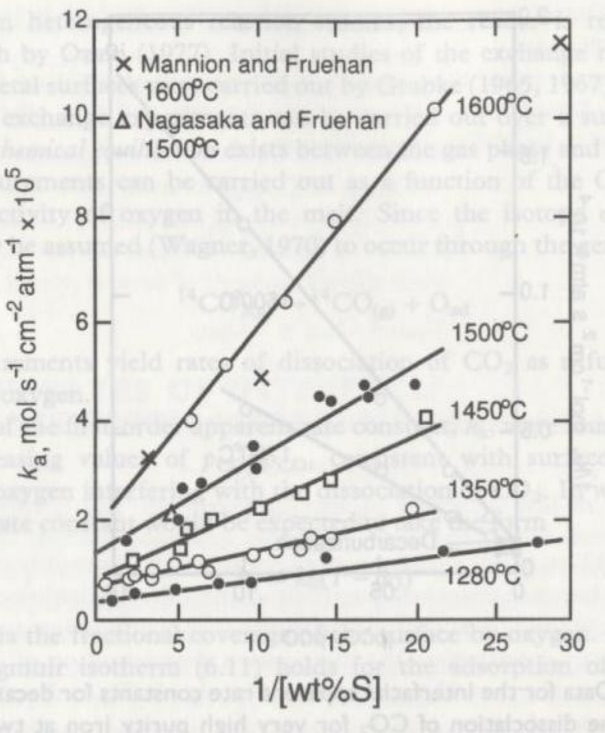

Figure 6.9 Apparent first-order rate constants for the decarburization of carbon-saturated liquid iron by CO_2 versus the reciprocal of the sulfur concentration for wt% S ≥ 0.03; mainly from the data of Sain and Belton (1978).

The data appear to be consistent with a linear dependence, but with a positive intercept, suggesting that a *residual rate* exists on a surface that is saturated with sulfur. A similar, but more marked, residual rate phenomenon has been observed for the retarding effect of sulfur on the free vaporization of liquid iron by Grigoryan et al. (1973), and for the effect of oxygen on the free vaporization of liquid copper and iron by Hayakawa et al. (1982). Clearly, the rate equation will be more complex than that represented by the general rate equation (6.6) with, possibly, an additional rate constant being required to account for a smaller but finite rate of reaction at covered sites or sites which cannot be covered by sulfur.

In the particular case of the decarburization kinetics, the residual rate is about 1.4% of the bare surface rate given by Equation 6.36 independent of temperature. Accordingly, we may propose a semiempirical relationship of the form

$$k_a = k_0[(1-\theta_S) + 0.014\theta_S] \qquad (6.44a)$$

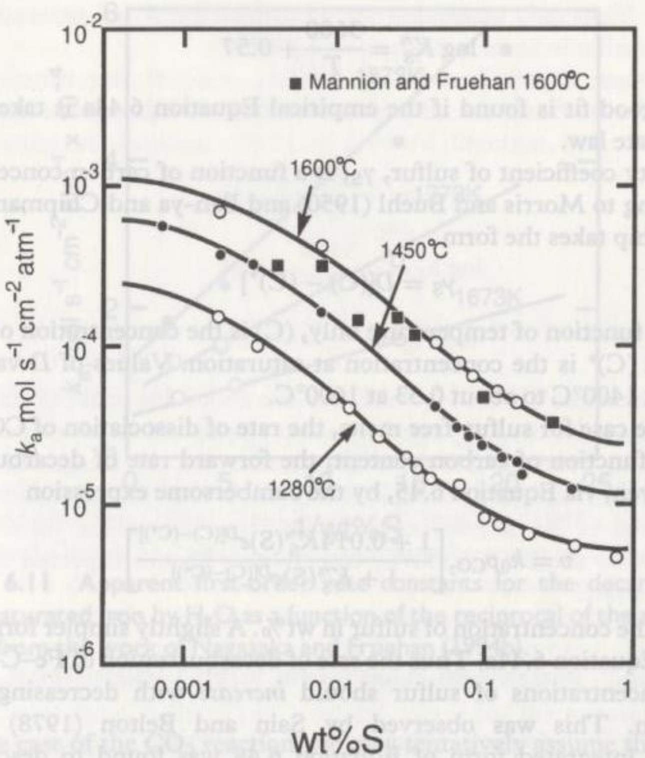

Figure 6.10 Apparent first-order rate constants for the decarburization of carbon-saturated iron by CO_2 as a function of sulfur concentration at three selected temperatures. The curves are calculated from Equations 6.36, 6.45, and 6.46. Reproduced from Belton (1993), with permission.

or

$$k_a = k_0[(1-\theta_S) + 0.014] \qquad (6.44b)$$

On assuming a Langmuir adsorption isotherm for sulfur, Equation 6.44a becomes

$$k_a = \frac{k_0(1 + 0.014K_S'^{s}a_S)}{1 + K_S'^{s}a_S} \qquad (6.45)$$

where k_0 is from Equation 6.36 and $K_S'^{s}$ is the adsorption coefficient for sulfur with respect to a standard state of 1 wt% S in carbon-saturated iron. The close fit with the apparent rate constants over a wide range of sulfur concentration and temperature is illustrated in Fig. 6.10, where the consistent values for $K_S'^{s}$ are given by

$$\log K_S'^s = \frac{3600}{T} + 0.57 \tag{6.46}$$

An equally good fit is found if the empirical Equation 6.44a is taken as the basis of the rate law.

The activity coefficient of sulfur, γ_S, is a function of carbon concentration and, according to Morris and Buehl (1950) and Ban-ya and Chipman (1969), the relationship takes the form

$$\gamma_S = D[(C) - (C)^*] \tag{6.47}$$

where D is a function of temperature only, (C) is the concentration of carbon in wt%, and (C)* is the concentration at saturation. Values of D vary from about 0.39 at 1400°C to about 0.33 at 1600°C.

If, as in the case for sulfur-free melts, the rate of dissociation of CO_2 is not separately a function of carbon content, the forward rate of decarburization should be given, via Equation 6.45, by the cumbersome expression

$$v = k_0 p_{CO_2}\left[\frac{1 + 0.014K_S'^s(S)e^{D[(C)-(C^*)]}}{1 + K_S'^s(S)e^{D[(C)-(C^*)]}}\right] \tag{6.48}$$

where (S) is the concentration of sulfur in wt%. A slightly simpler form would result from Equation 6.44a. Thus the rate of decarburization of Fe–C–S melts at given concentrations of sulfur should *increase* with decreasing carbon concentration. This was observed by Sain and Belton (1978) and an approximate integrated form of Equation 6.48 was found to describe the decarburization of melts containing 0.08 wt% S at 1500°C from carbon saturation down to about 1 wt%.

6.5.1.2. Decarburization by water vapor

The interfacial rate of decarburization of liquid iron by water vapor by the overall reaction

$$H_2O + \underline{C} = H_2 + CO \tag{6.49}$$

was first studied by Shinego et al. (1983). Sasaki and Belton (1986) derived approximate values of the rate constant from this work and concluded that the reaction was about one order of magnitude faster than that for decarburization by CO_2. This led to work by Fruehan et al. (1992) and Nagasaka and Fruehan (1994b) which has established the empirical rate law and the effect of sulfur on the rates from about 1300 to 1600°C.

The rate has been found to be first order with respect to the pressure of water vapor from about 0.002 to 0.3 atm for carbon-saturated melts at fixed sulfur concentrations, thus

$$v = k_a p_{H_2O} \tag{6.50}$$

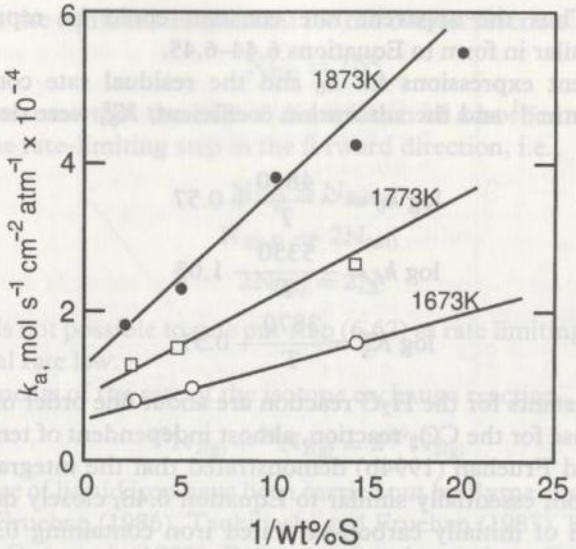

Figure 6.11 Apparent first-order rate constants for the decarburization of carbon-saturated iron by H_2O as a function of the reciprocal of the sulfur concentration, from the work of Nagasaka and Fruehan (1994b).

As in the case of the CO_2 reaction, we may tentatively assume that the rate of dissociation of H_2O on the surface of the liquid iron is the rate-limiting step with other steps, including those represented by Equations 6.32–6.34, at virtual equilibrium, i.e.,

$$H_2O_{(g)} = H_2O_{(ad)} \tag{6.51}$$

$$H_2O_{(ad)} \rightarrow OH_{(ad)} + H_{(ad)} \tag{6.52}$$

$$OH_{(ad)} = O_{(ad)} + H_{(ad)} \tag{6.53}$$

$$2H_{(ad)} = H_{2(g)} \tag{6.54}$$

Independence of the rate from the pressure of hydrogen has not yet been demonstrated, so step (6.53) cannot, in principle, be ruled out as rate limiting at this time.

The effect of sulfur on the rate closely parallels the effect found for the CO_2 reaction. Figure 6.11 shows the values of the apparent first-order rate constants as a function of the reciprocal of the concentration of sulfur for three temperatures from the work of Nagasaka and Fruehan (1994b). Again, a residual rate is observed and the authors deduced that this represented about 1.5% of the rate for sulfur-free melts, but with a small temperature dependence. Thus the apparent rate constant could be represented by expressions similar in form to Equations 6.44–6.45.

The consistent expressions for k_0 and the residual rate constant k_r in mol cm^{-2} s^{-1} atm^{-1} and the adsorption coefficient, K_S'', were deduced to be given by

$$\log k_0 = -\frac{4860}{T} + 0.57 \qquad (6.55)$$

$$\log k_r = -\frac{5350}{T} - 1.03 \qquad (6.56)$$

$$\log K_S'' = \frac{3870}{T} + 0.51 \qquad (6.57)$$

The rate constants for the H_2O reaction are about one order of magnitude higher than those for the CO_2 reaction, almost independent of temperature.

Nagasaka and Fruehan (1994b) demonstrated that the integrated form of the rate equation, essentially similar to Equation 6.48, closely described the decarburization of initially carbon-saturated iron containing 0.1 wt% S at 1600°C down to about 0.2 wt% C, consistent with the expected four-fold *increase* in the rate.

6.5.2. Nitrogen Reactions with Liquid Iron

As noted in the Introduction, it was the work on nitrogen reactions during the period 1959–1963 that first established the effect of surface-active solutes on the interfacial rates of high-temperature reactions with liquid iron. Reference may be made to papers by Battle and Pehlke (1986) and Ban-ya et al. (1988) for an overview of the many studies which were carried out over the following two and a half decades. Studies have included the rates of absorption of nitrogen, the desorption at atmospheric and low pressure, and isotope exchange between nitrogen molecules. For any given composition of the iron, the weight of the evidence is that the interfacial reaction for the absorption is first order with respect to the pressure of nitrogen and that for desorption is second order with respect to the activity of dissolved nitrogen, as required by the principle of microscopic reversibility. Thus the rates of absorption and desorption may be written as

$$v = k_a p_{N_2} \qquad (6.58)$$

and

$$v' = k_a'(a_N)^2 \qquad (6.59)$$

with the relationship between the apparent rate constants being

$$k_a/k_a' = K_N \qquad (6.60)$$

where K_N is the equilibrium constant for the overall reaction

$$N_{2(g)} = 2\underline{N} \qquad (6.61)$$

We may assume that the rate of dissociation of adsorbed nitrogen on the surface is the rate-limiting step in the forward direction, i.e.,

$$N_{2(g)} = N_{2(ad)} \qquad (6.62)$$

$$N_{2(ad)} \rightarrow 2N_{(ad)} \qquad (6.63)$$

$$2N_{(ad)} = 2\underline{N} \qquad (6.64)$$

although it is not possible to rule out step (6.62) as rate limiting on the basis of the empirical rate law.

Measurements of the rate of the isotope exchange reaction

$${}^{28}N_{2(g)} + {}^{30}N_{2(g)} = 2\,{}^{29}N_{2(g)} \qquad (6.65)$$

on the surface of liquid iron have been carried out by Byrne and Belton (1983), Glaws and Fruehan (1986), Tsukihashi and Fruehan (1987), Kobayashi et al. (1993), and Ono et al. (1995). Reference may be made to Byrne and Belton (1983) for a detailed derivation of the kinetic equations and for general experimental details. All the isotope exchange studies have found good agreement with the bulk of the results from the absorption and desorption studies when the compositions of the iron overlap. This is illustrated in Fig. 6.12, adapted from Belton (1993), where values for the apparent first-order rate constant, k_a, at 1600°C are shown as a function of the reciprocal of the sulfur concentration from absorption, desorption, and isotope exchange studies. This is consistent with the mechanism expressed in Equations 6.62–6.64 since the isotope exchange reaction (6.65) must involve the dissociation and reforming of the nitrogen molecule.

6.5.2.1. The effect of sulfur and oxygen

On the basis of their isotope exchange measurements on high-purity zone-refined iron, Byrne and Belton (1983) proposed that the forward rate constant for reaction at the bare surface, in units of mol cm^{-2} s^{-1} atm^{-1}, is given by

$$\log k_0 = -\frac{6340}{T} - 1.38 \qquad (6.66)$$

If ideal Langmuir adsorption is assumed, the strong depression of the value of the apparent rate constant by sulfur at 1600°C, shown in Fig. 6.12, can therefore be described by the expression

$$k_a = \frac{1.7 \times 10^{-5}}{1 + 130a_S} \text{ mol cm}^{-2}\text{ s}^{-1}\text{ atm}^{-1} \qquad (6.67)$$

if it is also assumed that any residual rate is negligibly small.

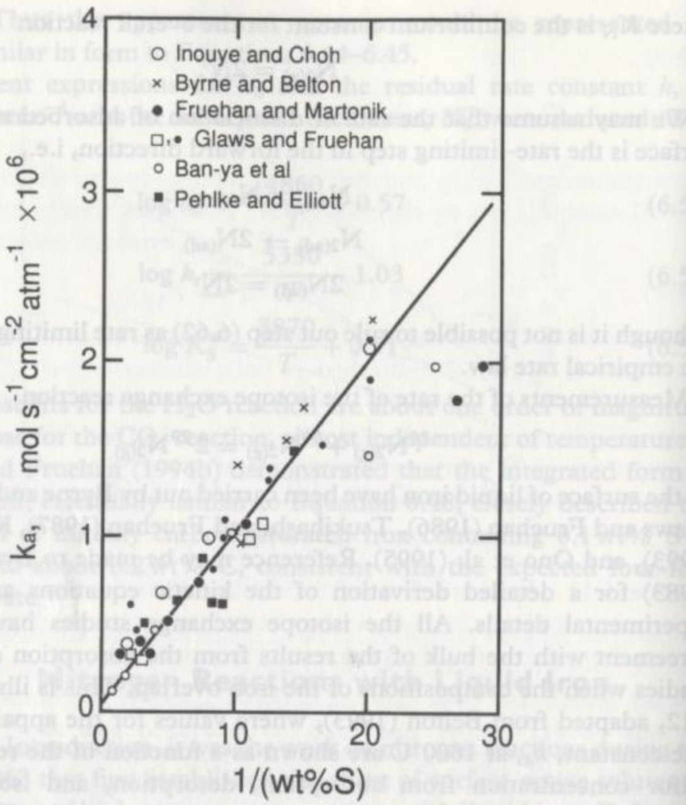

Figure 6.12 Apparent first-order rate constants for the absorption of nitrogen into liquid iron at 1600°C as a function of the reciprocal of the sulfur concentration. Reproduced in a modified form from Belton (1993), with permission.

From a similar treatment of the data for rates of absorption of nitrogen into Fe–O alloys at 1600°C by Fruehan and Martonik (1980) and Inouye and Choh (1968), the following expression was suggested:

$$k_a = \frac{1.7\times10^{-5}}{1+220a_O} \ \text{mol cm}^{-2}\,\text{s}^{-1}\,\text{atm}^{-1} \qquad (6.68)$$

The values of 220 and 130 for the adsorption coefficients of oxygen and sulfur, with the 1 wt% solution as the standard state, are of the same order of magnitude as those derived from the Szyszkowski analyses of the surface tension data—Equations 6.15 and 6.17.

Sulfur and oxygen essentially always coexist in liquid steel, so the combined effect of these solutes is of practical interest. Ban-ya and colleagues (1988), from their analysis of all kinetic data available at that time, proposed that the apparent rate constant for desorption at 1600°C could be closely decribed by the expression

$$k_a = k_0' f_N^2 \left(\frac{1}{1+300a_O+130a_S}\right) \qquad (6.69)$$

where f_N is the Henrian activity coefficient of nitrogen. The consistent value of k_0' was found to be 7.9×10^{-3} mol cm^{-2} s^{-1} which, through Equation 6.60 and the value of the equilibrium constant (Pehlke and Elliott, 1960) gives a value of 1.6×10^{-5} mol cm^{-2} s^{-1} atm^{-1} for k_0, in good accord with the value given by Equation 6.56. Recent studies by Wu et al. (1995) have shown a closer fit with a dependence on $(1 + 220a_O + 130a_S)$ and a slightly smaller value for the bare surface rate constant.

Irrespective of minor differences in values for the adsorption coefficients, the observed dependence is consistent with the fraction of vacant sites being given by

$$1-\sum\theta_i = \frac{1}{1+K_Sa_S+K_Oa_O} \qquad (6.70)$$

It was noted in the earlier discussion of adsorption in ternary alloys that the data of Ogino et al. (1983) were consistent with coadsorption of O and S on liquid iron. Possibly, ideal competitive adsorption of the two solutes is approximated despite the large difference in saturation coverages and ionic sizes of the two species.

6.5.2.2. The effects of other alloying elements

The other strongly adsorbed group IVb elements, Se and Te, lower the rates of the nitrogen reactions by more than an order of magnitude more than do O and S at equivalent mass concentrations, and Wu et al. (1995) have recently shown that this is broadly in accord with the depression of the surface tension by these elements. The adsorption isotherm for Se, Equation 6.15b, is consistent with a value for the adsorption coefficient about one order of magnitude greater than those of O and S.

It is to be expected that any alloying element which has a stronger affinity for nitrogen than does iron would change the energetics of the adsorption of the nitrogen molecule at the surface and, concomitantly, that of the activated complex. The value of $K_\ddagger^s$ in the adsorption isotherm for the activated complex, Equation 6.5, would be expected to increase and, accordingly, the forward rate constant would also be expected to increase. For dilute solutions, it is possible that the kinetics should be treated in terms of parallel paths, i.e.,

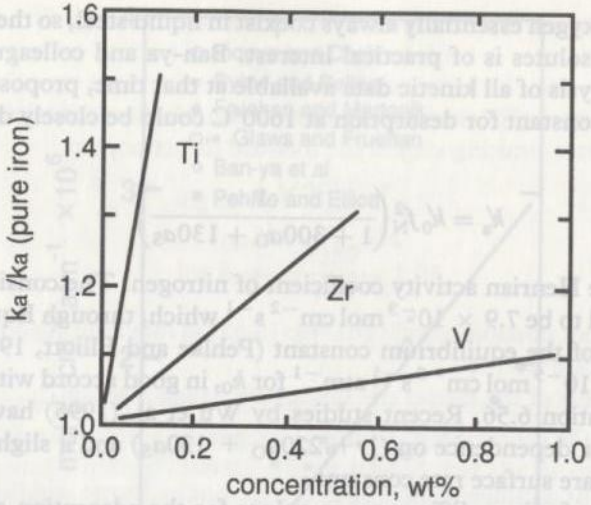

Figure 6.13 Effect of low concentrations of strong nitride-forming elements on the first-order rate constant for absorption of nitrogen in liquid iron at 1600°C (after Ono et al., 1995).

reaction occurring on sites with and without the alloying element in the coordination shell. This has yet to be explored.

Ono et al. (1995) have demonstrated that dilute solutions of the strong nitride-forming elements Ti, Zr, and V in pure liquid iron increase the forward rate constant, as shown schematically in Fig. 6.13. The effect of chromium on the rate of adsorption was found to be weaker, with the rate constant increasing by a factor of about 2 at 28 wt% Cr. For iron–chromium alloys containing sulfur at known activity, Fruehan and Martonik (1981) and Glaws and Fruehan (1986) found a very marked increase in the rate constant with chromium content—up to a factor of about 6 at 18 wt% Cr. It would appear to be a case where the alloying element increases the bare surface rate constant and lowers the adsorption coefficient of the interfering solute.

It has been demonstrated that carbon has no intrinsic effect on the bare surface rate constant (Glaws and Fruehan, 1985; Tsukihashi and Fruehan, 1987). Accordingly, the effect of carbon on the interfacial rates of desorption would be through the effect of carbon on the activity coefficients of sulfur and nitrogen and the rates would still be calculable via Equation 6.69. It is possible that in the more highly alloyed liquid steels, coadsorption and surface compound formation phenomena would influence the rates, but this has yet to be examined.

6.5.3. The Oxidation and Reduction of Iron Oxide Slags

The interfacial rates of reaction of CO and CO_2 with liquid iron oxide and iron oxide-containing slags have been studied by measurements of the rate of reduction to metallic iron by CO under conditions where mass transfer restrictions were avoided (Nagasaka et al., 1986; Nagasaka, 1987; Fine et al., 1985) and by the isotope exchange reaction, Equation 6.27 (Sasaki et al., 1984; El-Rahaiby et al., 1986; Sun et al., 1988). Reviews of these and associated studies have been given elsewhere (Belton, 1984, 1989).

For a given overall composition and a constant activity of oxygen, approximately established by iron saturation in the reduction experiments and explicitly by the CO_2/CO ratio in the isotope exchange experiments, the rates were found to be first order with respect to the pressures of the gaseous species. In the isotope exchange experiments, the apparent rate constant was found to decrease with increasing activity of oxygen, expressed as the value of the CO_2/CO ratio in equilibrium with melt. The apparent rate constant for a particular melt could be expressed as

$$k_a = k_0\left(\frac{p_{CO_2}}{p_{CO}}\right)^{-\alpha} = k_0 a_O^{-\alpha} \qquad (6.71)$$

where k_0 is the value of the rate constant at unit activity of oxygen. The value of the exponent α was found to be close to unity in the cases of liquid iron oxide and the CaO- and SiO_2-saturated binary melts, as is illustrated in Fig. 6.14. For the equimolar calcium iron silicate at 1420°C and a calcium ferrite with Ca/Fe = 0.3 at 1300°C, the respective values of α were established to be about 0.75 and 0.79, respectively. Intermediate values were found for some ternary melts.

Since the ratio of the values of the forward and reverse apparent first-order rate constants must be inversely proportional to the CO_2/CO ratio that would be in equilibrium with the melt, it follows that the reverse rate constant is given by

$$k'_a = k_0 a_O^{1-\alpha} \qquad (6.72)$$

The net rate of reaction of CO with the surface in atmospheres containing CO and CO_2 is therefore given by

$$v' = k_0[p_{CO} a_O^{1-\alpha} - p_{CO_2} a_O^{-\alpha}] \qquad (6.73)$$

or, in the more familiar form, by

$$v' = k_0 a_O^{1-\alpha}[p_{CO} - (p_{CO})_{eq}] \qquad (6.74)$$

where $(p_{CO})_{eq}$ is the partial pressure of CO which would be in equilibrium with the melt and p_{CO_2}. For those melts where $\alpha = 1$, the rate constant for reduction will be independent of the oxygen activity of the melt. Very close

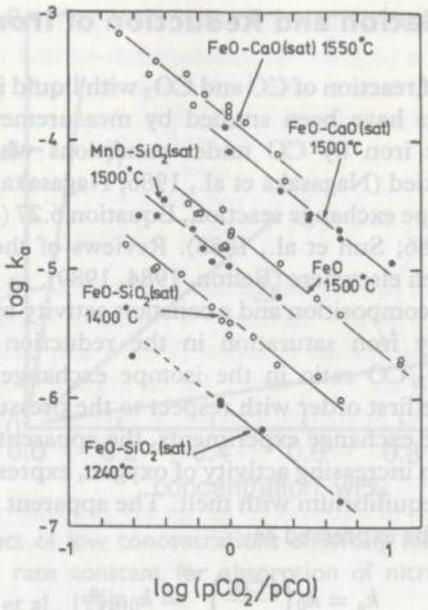

Figure 6.14 Apparent first-order rate constants for the dissociation of CO_2 on liquid iron oxide and some binary oxide melts as a function of the oxygen activity in the melt; data of Sasaki et al. (1984) and El-Rahaiby et al. (1986). Lines are drawn with a slope of −1.

agreement is found between the rates of reduction calculated via Equation 6.74, using values of k_0 from the isotope studies, and those measured directly by Nagasaka et al. (1986) for liquid iron oxide and all the other melts which were common to both sets of studies. Similarly, rates of oxidation of a liquid calcium ferrite in CO_2–CO mixtures at 1360°C, as a function of the activity of oxygen in the melt, were found to be in close accord with rates from isotope exchange studies (Sun et al., 1988).

The strong depression of the rate with increasing activity of oxygen cannot be attributed to the blockage of the surface by oxygen ions or ferric ions since, as pointed out in the discussion of the surface tensions of molten oxides and slags, the available evidence shows that there is probably a negligibly small segregation of oxygen ions to the surface of liquid iron oxide and a fairly weak segregation in the case of the liquid calcium ferrites.

Recognizing that the transfer of oxygen from the CO_2 molecule to the molten oxide must also include the transfer of a fairly well-defined charge, we may propose that the dissociation of the adsorbed unstable ionic species CO_2^{2-} is the rate-determining step. Accordingly, the steps may be represented by

$$CO_{2(g)} = CO_{2(ad)} \tag{6.75}$$

$$CO_{2(ad)} + 2e^- = CO^{2-}_{2(ad)} \tag{6.76a}$$

$$CO^{2-}_{2(ad)} \rightarrow O^{2-}_{(ad)} + CO_{(ad)} \tag{6.77}$$

$$O^{2-}_{(ad)} = \underline{O}^{2-} \tag{6.78}$$

$$CO_{(ad)} = CO_{(g)} \tag{6.79}$$

For iron oxide-containing melts, the ferric–ferrous redox couple would be expected to establish the chemical potential of the electrons in the virtual equilibrium, Equation 6.76. Accordingly, we may write

$$2\underline{Fe}^{2+} + CO_{2(ad)} = CO^{2-}_{2(ad)} + 2\underline{Fe}^{3+} \tag{6.76b}$$

The forward rate for the reaction of CO_2 with the melt would then take the form

$$v = p_{CO_2}\left[k_0^c\left(\frac{Fe^{3+}}{Fe^{2+}}\right)^{-2}\right] \tag{6.80}$$

where k_0^c is a rational rate constant for this model. The quantity in square brackets is the apparent first-order rate constant, k_a. A plot of log k_a versus the logarithm of the Fe^{3+}/Fe^{2+} ratio, rather than the activity of oxygen, should give a staight line of slope −2. This is shown to be closely followed in Fig. 6.15, taken from Belton (1989), for the melts for which data are available.

This rational rate law is not as practically useful as those represented in Equations 6.71–6.74, but it does provide a basis for understanding differences in rate constants between different melts. The basicity of a melt is a measure of the propensity of the melt to transfer charge. Accordingly, the values of the rate constants for different melts might be expected to increase with increasing basicities. A close correlation between values of k_0 at 1520°C and the CaO/SiO$_2$ ratio for calcium iron silicates was found by El-Rahaiby et al. (1986), and by Nagasaka and coworkers (1986, 1987) for the apparent rate constant for reduction, k_a', at 1400°C and iron-saturation for a wide range of binary and ternary melts of CaO, SiO$_2$, Al$_2$O$_3$, TiO$_2$, and MnO with iron oxide. The measure of basicity was taken as the value of the Fe^{3+}/Fe^{2+} ratio at iron saturation. This correlation is shown in Fig. 6.16, where the apparent rate constant is expressed in practical units.

The correlations suggest that the surface constitution is playing only a minor role in influencing the kinetics, in keeping with the relatively small effects of most slag components on the surface tension of liquid iron oxide, as discussed earlier. The exception appears to be the solute P$_2$O$_5$, which shows a depression by a factor of about 2 below the correlation value for an iron oxide-rich calcium iron silicate containing 4 mol% P$_2$O$_5$ (Nagasaka et al., 1989). Sun

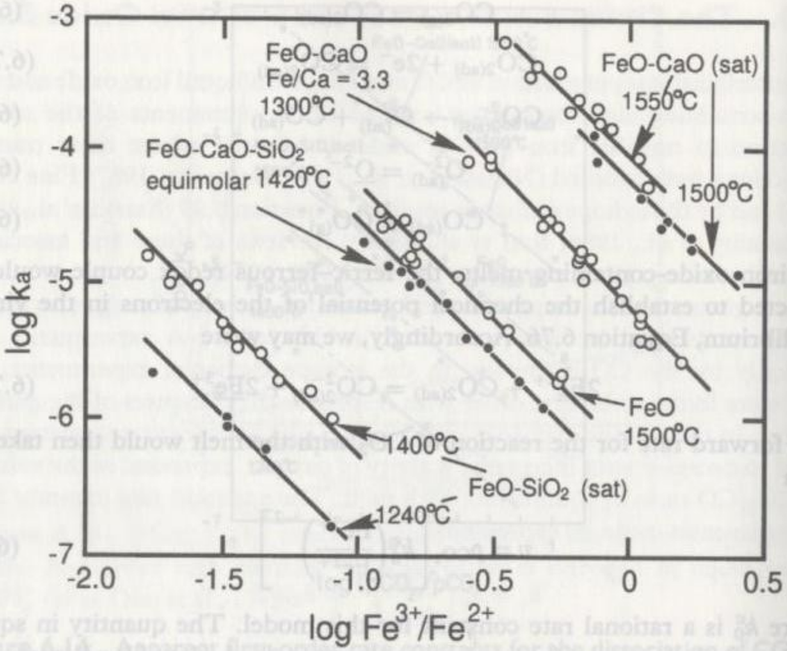

Figure 6.15 Apparent first-order rate constant for the dissociation of CO_2 on iron oxide-containing melts as a function of the Fe^{3+}/Fe^{2+} ratio in the melt, after Belton (1989). Lines are drawn with a slope of −2.

(1988) has shown that the addition of a similar amount of P_2O_5 to liquid iron oxide lowers the apparent rate constant by a factor of about 2.5. It was noted earlier that P_2O_5 could be described as reasonably strongly surface active in liquid iron oxide and that a Szyszkowski analysis, Equation 6.27, gave a value for the adsorption coefficient of about unity. This suggests that the surface would have a significant coverage, possibly about 80%, by phosphate ions at 4 mol% P_2O_5.

P_2O_5 is the least basic of the common component oxides of slag systems, i.e., it has the lowest optical basicity and highest electron density (Nakamura et al., 1986). Possibly, the depression of the rate contant should be attributed to the segregation changing the surface potential or space charge potential rather than in terms of a simple site blockage model. It has been shown that this is quantitatively reasonable (Belton, 1989), but there are no independent measurements available for the typical magnitudes of surface potential changes in high-temperature melts which would help clarify this.

All of the above observations and analysis are based on melts containing more than about 5 or 10 mol% iron oxide. At lower concentrations, the rate

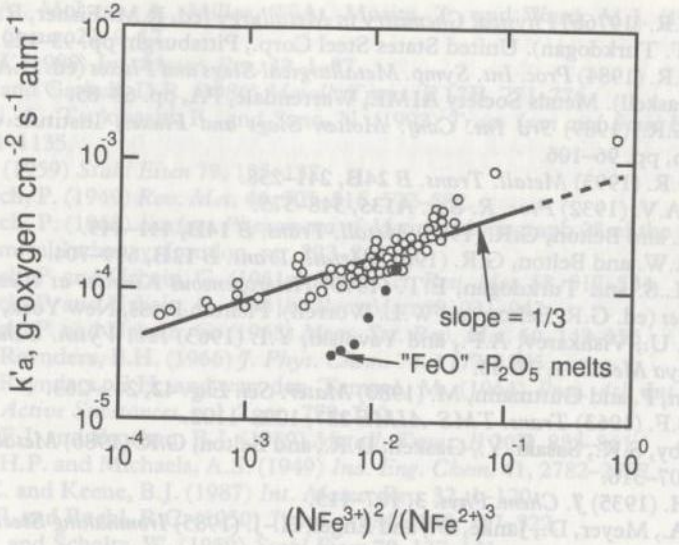

Figure 6.16 Correlation of the apparent rate constants for reduction by CO at iron-saturation of a wide range of binary and ternary melts of iron oxide with CaO, SiO_2, Al_2O_3, TiO_2, MnO, and P_2O_5 with the value of the Fe^{3+}/Fe^{2+} ratio at iron saturation (after Nagasaka et al., 1989).

constants show a more complex behavior (Sun, 1989). The results of these studies have not yet been published in detail.

The very limited amount of work which has been carried out on the reactions of H_2O with SiO_2-saturated iron oxide melts has shown that the dependence of the apparent first-order rate constant on a_O is very similar to that observed in the CO_2 reaction, but with an order of magnitude increase in value of the rate constants (Glaws and Belton, 1990).

REFERENCES

Ban-ya, S. and Chipman, J. (1969) *Trans. TMS-AIME* **245**, 133–143.

Ban-ya, S., Shinohara, T., Tozaki, H., and Fuwa, T. (1974) *Tetsu-to-Hagane* **60**, 1443–1453.

Ban-ya, S., Ishi, F., Iguchi, Y., and Nagasaka, T. (1988) *Metall. Trans. B* **19B**, 233–242.

Battle, T.P. and Pehlke, R.D. (1986) *Ironmaking and Steelmaking* **13**, 179–189.

Belton, G.R. (1972) *Metall. Trans.* **3**, 1465–1469.

Belton, G.R. (1976a) *Metall. Trans. B* **7B**, 35–42.

Belton, G.R. (1976b) *Physical Chemistry in Metallurgy* (ed. R.M. Fisher, R.A. Oriani, and E.T. Turkdogan). United States Steel Corp., Pittsburgh, pp. 93–119.

Belton, G.R. (1984) *Proc. Int. Symp. Metallurgical Slags and Fluxes* (ed. H.A. Fine and D.R. Gaskell). Metals Society AIME, Warrendale, PA, pp. 63–85.

Belton, G.R. (1989) *3rd Int. Conf. Molten Slags and Fluxes*, Institute of Metals, London, pp. 96–106.

Belton, G.R. (1993) *Metall. Trans. B* **24B**, 241–258.

Butler, J.A.V. (1932) *Proc. R. Soc.* **A135**, 348–375.

Byrne, M. and Belton, G.R. (1983) *Metall. Trans. B* **14B**, 441–449.

Cramb, A.W. and Belton, G.R. (1981) *Metall. Trans. B* **12B**, 699–704.

Darken, L.S. and Turkdogan, E.T. (1970) *Heterogeneous Kinetics at Elevated Temperatures* (ed. G.R. Belton and W.L. Worrell). Plenum Press, New York, pp. 25–95.

Din-Fen, U., Vishkarev, A.F., and Yavoiski, Y.I. (1963) *Izv. Vyssh. Ucheb. Zaved., Chernaya Metall.* **1**, 27–33.

Dumoulin, P. and Guttmann, M. (1980) *Mater. Sci. Eng.* **42**, 249–263.

Dyson, B.F. (1963) *Trans. TMS-AIME* **227**, 1098–1102.

El-Rahaiby, S.K., Sasaki, Y., Gaskell, D.R., and Belton, G.R. (1986) *Metall. Trans. B* **17B**, 307–316.

Eyring, H. (1935) *J. Chem. Phys.* **3**, 107–115.

Fine, H.A., Meyer, D., Janke, D., and Engel, H.-J. (1985) *Ironmaking Steelmaking* **12**, 157–162.

Fruehan, R.J. and Martonik, L.J. (1980) *Metall. Trans. B* **11B**, 615–621.

Fruehan, R.J. and Martonik, L.J. (1981) *Metall. Trans. B* **12B**, 379–384.

Fruehan, R.J., Belton, G.R., Mannion, F.J., and Sasaki, Y. (1992) *Metall. Trans. B* **24B**, 45–51.

Frumkin, A. (1925) *Z. Phys. Chem.* **116**, 466–484.

Gaye, H., Lucas, L.D., Olette, M., and Riboud, P.V. (1984) *Can. Metall. Quant.* **23**, 179–191.

Gibbs, J.W. (1948) *Collected Works*, Yale University Press, New Haven, vol. 1, p. 219ff.

Glasstone, S., Laidler, K.J., and Eyring, H. (1941) *The Theory of Rate Processes*. McGraw-Hill, New York.

Glaws, P.C. and Fruehan, R.J. (1985) *Metall. Trans. B* **16B**, 551–559.

Glaws, P.C. and Fruehan, R.J. (1986) *Metall. Trans. B* **17B**, 317–322.

Glaws, P.C. and Belton, G.R. (1990) *Metall. Trans. B* **21B**, 511–519.

Grabke, H.J. (1965) *Proc. 3rd Int. Congr. Catalysis*. North Holland, Amsterdam, pp. 928–938.

Grabke, H.J. (1967) *Ber. Bunsenges. Phys. Chem.* **71**, 1067–1073.

Grabke, H.J. (1989) *ISIJ Int.* **29**, 529–538.

Grabke, H.J., Leroy, V., and Viefhaus, H. (1995) *ISIJ Int.* **35**, 95–113.

Grigoryan, V.A., Aleev, R.A., Kochetov, A.J., and Pryanishikov, M.I. (1973) *Steel in USSR* **3**, 199–200.

Guth, L.A., Luckman, G., and Graham, W.R. (1984) *Surf. Sci.* **136**, 184–194.

Guttmann, M. and McLean, A.D. (1979) *Interfacial Segregation* (ed. W.D. Johnson and J.M. Blakely). ASM, Metals Park, OH.

Halden, F.A. and Kingery, W.D. (1955) *J. Phys. Chem.* **59**, 557–559.

Hayakawa, S., Choh, T., and Inouye, M. (1982) *Trans. Iron and Steel Inst. Japan* **22**, 1989–1994.

Inouye, M. and Choh, T. (1968) *Trans Iron and Steel Inst. Japan* **8**, 134–135.

Jimbo, I. and Cramb, A.W. (1992) *ISIJ Int.* **32**, 26–35.

Kambayashi, S., Awaka, H., and Kato, E. (1985) *Tetsu-to Hagane* **71**, 1911–1918.

Kasama, A., McLean, A., Miller, W.A., Morita, Z., and Ward, M.J. (1983) *Can. Metall. Quart.* **22**, 9–17.

Keene, B.J. (1988) *Int. Mater. Rev.* **33**, 1–37.

Kidd, M. and Gaskell, D.R. (1986) *Metall. Trans. B* **17B**, 771–776.

Kobayashi, A., Tsukihashi, F., and Sano, N. (1993) *Trans Iron and Steel Inst. Japan* **33**, 1131–1135.

Kootz, T. (1959) *Stahl Eisen* **79**, 135–137.

Kozakevitch, P. (1949) *Rev. Met.* **46**, 505–516, 572–582.

Kozakevitch, P. (1968) *Surface Phenomena of Metals*, Monograph 28 of the Society of the Chemical Industry, London, pp. 223–245.

Kozakevitch, P. and Urbain, G. (1961a) *Mem. Sci. Rev. Met.* **58**, 517–534.

Kozakevitch, P. and Urbain, G. (1961b) *Rev. Met.* **58**, 931–947.

Kozakevitch, P. and Urbain, G. (1963) *Mem. Sci. Rev. Met.* **60**, 143–156.

Lucassen-Reynders, E.H. (1966) *J. Phys. Chem.* **70**, 1777–1785.

Lucassen-Reynders, E.H. and van den Tempel, M. (1964) *Proc. 4th Int. Congress Surface Active Substances*, vol. 2, pp. 779–790.

Mannion, F.J. and Fruehan, R.J. (1989) *Metall. Trans. B* **20B**, 853–861.

Meissner, H.P. and Michaels, A.S. (1949) *Ind. Eng. Chem.* **41**, 2782–2787.

Mills, K.C. and Keene, B.J. (1987) *Int. Mater. Rev.* **32**, 1–120.

Morris, J.P. and Buehl, R.C. (1950) *Trans. AIME* **188**, 317–322.

Naeser, G. and Scholtz, W. (1959) *Stahl Eisen* **79**, 137–141.

Nagasaka, T. (1987) *Tetsu-to-Hagane* **73**, S773.

Nagasaka, T. and Fruehan, R.J. (1994a) *ISIJ Int.* **34**, 241–246.

Nagasaka, T. and Fruehan, R.J. (1994b) *Metall. Mater. Trans. B* **25B**, 245–253.

Nagasaka, T., Iguchi, Y., and Ban-ya, S. (1986) *5th Int. Iron Steel Congress*, Iron and Steel Society, Warrendale, PA, vol. 3, pp. 469–477.

Nagasaka, T., Iguchi, Y., and Ban-ya, S. (1989) *Tetsu-to-Hagane* **75**, 74–81.

Ogino, K., Nogi, K., and Yamase, O. (1980) *Tetsu-to-Hagane* **66**, 179–185.

Ogino, K., Nogi, K., and Hosoi, C. (1983) *Tetsu-to-Hagane* **69**, 1989–1994.

Ogino, K., Hara, S., Miwa, T., and Kimoto, S. (1984) *Trans. Iron and Steel Inst. Japan* 24, 522–531.

Ono, H., Morita, K., and Sano, N. (1995) *Metall. Mater. Trans. B* **26B**, 991–995.

Ozaki, P. (1977) *Isotopic Studies of Heterogeneous Catalysis*. Kodansha, Tokyo and Academic Press, New York.

Pehlke, R.D. and Elliott, J.F. (1960) *Trans. TMS-AIME* **218**, 1088–1101.

Pehlke, R.D. and Elliott, J.F. (1963) *Trans. Met. Soc. AIME* **227**, 844–855.

Popel, S.I. (1962) *Metallurgical Slags and Their Use in Building*. Akad. Stroit i Arkhitekt, SSSR, Ural'sk Filial, pp. 97–127.

Popel, S.I., Tsarevskii, B.V., Pavlov, V.V., and Furman. E.K. (1975) *Izv. Akad. Nauk SSSR Met.* **4**, 54–58.

Sain, D.R. and Belton, G.R. (1976) *Metall. Trans. B* **7B**, 235–244.

Sain, D.R. and Belton, G.R. (1978) *Metall. Trans. B* **9B**, 403–407.

Sasaki, Y. and Belton, G.R. (1986) *Trans. Iron and Steel Inst. Japan* **26**, 611–613.

Sasaki, Y., Hara, S., Gaskell, D.R., and Belton, G.R. (1984) *Metall. Trans. B* **15B**, 563–571.

Schenck, H., Frohberg, M.G., and Heinman, H. (1962) *Arch. Eisenh.* **33**, 593–600.

Seah, M.P. and Hondros, E.D. (1973) *Proc. R. Soc.* **A335**, 191–212.

Seah, M.P. and Lea, C. (1975) *Phil. Mag.* **31**, 627–645.

Shinego, Y., Mitsufugi, H., Tokuda, M., and Ohtani, M. (1983) *J. Japan Inst. Met.* **47**, 933–941.

Sun, S. (1989) PhD Dissertation, University of Newcastle.

Sun, S., Sasaki, Y., and Belton, G.R. (1988) *Metall. Trans. B* **19B**, 959–965.

Szyszkowski, B. von (1908) *Z. Phys. Chem.* **64**, 385–414.

Tsukihashi, F. and Fruehan, R.J. (1987) *Trans. Iron and Steel Inst. Japan* **27**, 858–865.

Uebing, C., Viefhaus, H., and Grabke, H.J. (1989) *Ber. Bunsenges. Phys. Chem.* **93**, 1363–1367.

Van Tszin-Tan, Karasev, R.A., and Samarin, A.M. (1960) *Izv. Akad. Nauk SSSR, Met.: Toplivo* **2**, 49–52.

Vishkarev, A.F., Dragomir, J., Din-Fen, U., and Yavoiski, V.J. (1965) *Surface Phenomena in Melts*. Kabardino-Balkarskoe Isdatelstvo, Nalchik, pp. 327–332.

Wagner, C. (1970) *Adv. Catal.* **21**, 25–29.

Wagner, C. (1973) *Nach. Akad. Wiss. Göttingen Math.-Phys.* **3**.

Walls, J.M. (1989) *Methods of Surface Analysis*. Cambridge University Press.

Whalen, T.J., Kaufman, S.M., and Humenic, M. (1962) *Trans. ASM* **55**, 778–785.

Wu, W.P., Lange, K.W., and Janke, D. (1995) *Ironmaking Steelmaking* **22**, 295–309.

7

Kinetics and mechanisms of heterogeneous reactions

Wei-Kao Lu

McMaster University, Hamilton, Ontario, Canada

This chapter bridges the gap between Chapter 4 where the basic science of chemical kinetics is introduced and chapters on ironmaking and steelmaking. Owing to space limitations, only two types of reactions, i.e., iron oxide reduction and oxidation of liquid iron alloys, will be discussed. For extensive reviews, readers are referred to books by Darken and Gurry (1953), Strassburger (1969), Von Bagdandy and Engell (1971), Deo and Boom (1993).

7.1. FUNDAMENTALS

In the steel industry, there are two important chemical processing steps. The winning of metal from its oxide ore under reducing conditions is done in a blast furnace with carbon as the reducing agent as well as fuel. The refining of impure iron to the desired chemical composition under oxidizing conditions is done in a converter with the second condensed phase (slag) as the sink of impurities, e.g., sulfur and phosphorus. The overall chemical reaction of hematite reduction and phosphorus removal as examples may be written as follows:

$$Fe_2O_3(s) + 3C(s) \rightarrow 2Fe(s) + 3CO(g) \tag{7.1}$$

$$2[P]_{metal} + 5[O]_{metal} + 3(CaO)_{slag} \rightarrow (Ca_3(PO_4)_2)_{slag} \tag{7.2}$$

Chemical Equations 7.1 and 7.2 are informative for the overall stoichiometry and useful for some thermodynamic computations.

There is no significant solubility of carbon in hematite and vice versa,

ADVANCED PHYSICAL CHEMISTRY FOR PROCESS METALLURGY
ISBN 0-12-618920-X

Copyright © 1997 Academic Press Ltd
All rights of reproduction in any form reserved

therefore, for Equation 7.1, hematite and carbon must exist as separate grains no matter how finely they have been ground. There is a solid reaction product, iron, in between. Hematite and carbon react initially at the point of contact. As the reaction proceeds in this manner, the solid product iron separates solid reactants and terminates the reaction because the atoms in the carbon grain can no longer reach out to grab the oxygen ions in hematite. Of course, carbon can dissolve in iron and diffuse in iron to reach hematite; however, there is no space to discuss this special case. Industrial practice and laboratory investigations support the mechanism that solid hematite and its suboxides, magnetite and wustite, are reduced by reducing gas in the blast furnaces. Reaction 7.1 may be replaced by two gas–solid reactions:

$$Fe_2O_3(s) + 3CO(g) \rightarrow 2Fe(s) + 3CO_2(g) \qquad (7.1a)$$

and the regeneration of reducing gas at higher temperatures for continuation of the reaction by the following:

$$3C(s) + 3CO_2(g) \rightarrow 6CO(g) \qquad (7.1b)$$

The sum of (7.1a) and (7.1b) equals (7.1).

As the density of the solid product is more than twice that of the solid reactant (hematite), metallic iron formed is quite porous (known as sponge iron) and its pores are connected and easy for gaseous diffusion. When molecules of carbon monoxide reach phase boundaries between iron and iron oxide behind the sponge iron layer, there is always oxide surface uncovered by iron to adsorb CO. The activated complex (see Chapter 4) is in the adsorbed state.

7.1.1. Reaction Zone

In a homogeneous system, all reactants and products are in the same phase and reaction may take place anywhere in the system. Within this phase, there is no restriction for reactants to meet and for the newly formed products to survive. On the contrary, there is no single phase in the heterogeneous system that can accommodate all chemical species involved in the reaction. For example, hematite in (7.1a) and carbon in (7.1b) cannot dissolve gases; therefore, gaseous and solid reactants meet to form the activated complex only at the gas–solid interface or simply on the surface of the solid. In comparison with the homogeneous system, the location where chemical reaction may take place in a gas–solid system is severely restricted. A similar restriction applies for reaction 7.2. Atoms of phosphorus and oxygen in liquid iron can only meet lime at the slag–metal interface to form phosphate, which itself can only survive in the slag phase. It is clear that reaction 7.2 can only initiate and complete in a region accessible to both metal and slag phases, the interfacial region or the reaction zone.

For homogeneous reactions, the three-dimensional reaction zone is everywhere within the phase. For a heterogeneous reaction involving two phases simultaneously, the reaction zone is two-dimensional and the reaction rate has the unit of the number of moles per unit area of interface per unit of time. If one wishes to assign a thickness to the reaction zone at the reacting interface, it should be comparable to the size of the activated complex that forms and decomposes in this region.

In order to carry out this concept a little further, one may consider that the reaction zone in a heterogeneous system involving three phases simultaneously is in the form of a line. This one-dimensional reaction zone may be considered to have a cross-sectional area comparable to the size of the activated complex. The unit of the reaction rate should be in the number of moles per unit length of reaction zone per unit of time. Reaction 7.1a is a three-phase reaction. Its equivalent in the slag–metal system is the reduction of reducible oxides in slag by dissolved carbon in liquid iron, e.g.

$$(SiO_2)_{slag} + 2\,[C]_{metal} \rightarrow [Si]_{metal} + 2\,CO(g) \qquad (7.3)$$

For this reaction to proceed as written above necessitates the presence of a gas bubble at slag–metal interface. The reaction zone is the ring where the bubble pierces the slag–metal interface. In principle, three-phase reactions can take place as illustrated in the aforementioned examples. However, the total number of sites where activated complexes could form in a one-dimensional reaction zone would be negligibly smaller in comparison with the two- and three-dimensional cases in the same system. Reactions 7.1a and 7.3 may proceed by an alternative path of two steps in series with each following a two-phase mechanism.

7.1.2. Gradients

A homogeneous system that is uniform in all concentrations and in temperature before the homogeneous chemical reaction starts will remain spatially uniform even though the concentration and temperature will change with time as the reaction proceeds. That is to say, there will be no gradients of concentrations and temperature created in an initially uniform homogeneous reacting system. In the heterogeneous system the situation is rather different.

The differences in concentrations and temperature between the reaction zone and bulk phases are created and maintained by interfacial reactions. Concentration and temperature gradients induce fluxes of mass and heat to and from the reaction zone. One difference between (7.1a) and (7.1b) is that the solid reactant in (7.1a) could have a range of nonstoichiometry. The removal of each oxygen atom from hematite by the reducing gas will convert two ferric ions to the ferrous form. Interfacial reactions will induce concentration gradients, resulting in diffusive fluxes of ions in hematite. The diffusion process will enlarge the region in which the change in composition is tolerated until the nucleation of magnetite phase takes place. It should be pointed out that the stripping off of oxygen atoms from hematite takes place at the gas–solid interface and the growth of magnetite at solid–solid interface. These two two-phase heterogeneous reactions have different reaction zones, even though they are at the same locality. Reaction (7.1a) may be rewritten as the following three consecutive pairs of two-phase heterogeneous reactions.

At the gas–solid interface:

$$3Fe_2O_3(s) + CO(g) \rightarrow H/M(s) + CO_2(g) \qquad (7.4a)$$

and at the solid–solid interface:

$$H/M(s) \rightarrow M(s). \qquad (7.4b)$$

At the gas–solid interface:

$$Fe_3O_4\,(s) + CO(g) \rightarrow M/W(s) + CO_2(g) \qquad (7.5a)$$

and at the solid–solid interface:

$$M/W(s) \rightarrow W(s). \qquad (7.5b)$$

At the gas–solid interface:

$$FeO(s) + CO(g) \rightarrow W/Fe(s) + CO_2\,(g) \qquad (7.6a)$$

and at the solid–solid interface:

$$W/Fe(s) \rightarrow Fe(s). \qquad (7.6b)$$

where H, M, W, and Fe stand for hematite, magnetite, wustite, and iron phases. H/M stands for a portion of hematite crystal which has a composition of ions close to that of magnetite. Similar meanings apply for M/W and W/Fe.

The morphology of the product phase varies. At higher temperatures the ease of nucleation will result in uniform coverage of the product layer and allow retention of the shape of the parent phase. This situation is called topochemical reduction. When nucleation is difficult at lower temperatures, an uneven growth of the solid product will result in inward growth of magnetite and outward growth of iron whisker.

7.1.3. Temperature and Concentrations in the Reaction Zone

The gas–solid reaction (7.6a) will be used as an example for this part of the discussion. The sum of (7.6a) and (7.6b) gives the usual form of wustite reduction:

$$FeO(s) + CO(g) \rightarrow Fe(s) + CO_2(g) \qquad (7.6)$$

In the reaction zone, there are wustite, iron, and gaseous mixtures of CO and CO_2. For the continuation of the interfacial reaction, reactants must be supplied to and products removed from the reaction zone by transport processes. The instantaneous concentration of carbon monoxide in the reaction zone of (7.6a) is determined by the rate of its consumption at the interface and the rate of supply by diffusion across the sponge iron layer from the main gas stream and the volume of the reaction zone. It is also true, but in the opposite direction, for carbon dioxide. The temperature at the reaction zone is also determined by the rates of supply and consumption of heat in this region. It cannot be overemphasized that the rate equation for the interfacial reaction derived from the Absolute Rate Theory must be expressed in concentrations and the temperature of the reaction zone, not that of bulk phases.

7.1.4. Moving Interface and Quasisteady State

In the category of heterogeneous chemical reactions, the literature on catalysis occupies almost all the space in a typical library. In catalysis, under well-controlled conditions, interfacial reactions may reach a steady state, i.e., constant concentrations and temperature in the reaction zone, to result in a rate of reaction which is non-zero and independent of time. For the case of iron oxide reduction, the solid reactant is being consumed and the interface is receding from the incoming flux of carbon monoxide. The total area of interface decreases and distance of diffusion for gases increases with time. In principle, there will be no steady state even if all conditions outside of the sphere are kept constant.

If there were an approximate steady state in the reaction zone, within a short period of time the following relation would exist for the forward reaction of (7.6a) per unit area of interfacial reaction zone and per unit of time, in number of moles:

Rate of supply of carbon monoxide by diffusion = − rate consumption of carbon monoxide = $R_{CO}(t)$ (7.7a)

Rate of generation of carbon dioxide = − rate of removal of carbon dioxide by diffusion = $R_{CO_2}(t)$ (7.7b)

Rate of generation of metallic iron = − rate of reduction of Wustite = $R_{Fe}(t)$ (7.7c)

In comparison with volumes of neighboring bulk phases, the interfacial reaction zone is negligibly small. Therefore, the cumulative term for mass balance in the reaction zone is ignored, and the stoichiometry of (7.6) gives the following equalities:

$$R_{CO}(t) = R_{CO_2}(t) = R_{Fe}(t) = \text{function of time} \qquad (7.7d)$$

Equation 7.7d shows the coupling between chemical reaction and transport process for each reacting species. It is the most important relation linking interfacial quantities which are needed for interfacial kinetics and those in bulk phases. Equation 7.7d may be called the quasisteady state. For consumable solid reactants in which the interface is receding, the steady state does not exist.

7.1.5. The Replacement of Interfacial Quantities

In this section, a simple rate equation is derived for (7.6) as an example. The simplest rate expression one may assume is first order with respect to each species involved. The rate expression of (7.6), which we write $R(7.6)$, in the reaction zone may be written as follows:

$$R(7.6) = k_f[S]^{(i)}_{wustite}[CO]^{(i)}_{gas} - k_b[S]^{(i)}_{iron}[CO_2]^{(i)}_{gas} \qquad (7.8)$$

where $[\ ]^{(i)}$ are concentrations at the interface or in the reaction zone—for example, $[S]^{(i)}_{wustite}$ is the concentration of reactive sites for adsorption on wustite, which may be altered by dissolved impurities such as CaO and temperature; k_f and k_b are rate constants which are functions of temperature.

The rate expression shown in (7.8) may be reasonable but practically useless because even if we accept the assumed functional form, all concentrations in the reaction zone are unknown values. Experimental techniques for the measurement of concentrations and temperature in the reaction zone are yet to be developed. In order to minimize the number of unknowns to be evaluated from experimental data, (7.8) may be rewritten as follows:

$$R(7.6) = k[CO]^{(i)}_{gas} - k'[CO_2]^{(i)}_{gas} = R_{Fe} \qquad (7.8a)$$

where $k = k_f[S]^{(i)}_{wustite}$ and $k' = k_b[S]^{(i)}_{iron}$; k and k' are products of specific rate and solid reactivity.

For simplicity, the interface is assumed to be flat and the gradients of carbon oxides to be constant across the sponge iron layer of thickness x. Therefore,

$$\text{Flux of CO to the reaction zone} = -D_{CO}\frac{[CO]^{(i)} - [CO]^{(b)}}{x} \qquad (7.9a)$$
$$= R_{CO}$$

$$\text{Flux of } CO_2 \text{ from the reaction zone} = -D_{CO_2}\frac{[CO_2]^{(i)} - [CO_2]^{(b)}}{x} \qquad (7.9b)$$
$$= -R_{CO_2}$$

Following the gaseous reactant, in the reaction path, there are three steps in the series, i.e., the transport of CO to the reaction zone (7.9a); the conversion of CO to CO_2 (7.8a); and the transport of CO_2 from the reaction zone (7.9b). Another simultaneous but parallel step is the removal of heat released in the reaction zone by conduction through solid phases and convection with flowing gases.

Applying the quasisteady state condition (7.7d), two unknowns, $[CO]^{(i)}$ and $[CO_2]^{(i)}$, may be eliminated in the above three equations to result in the following form:

$$R_{Fe} = R_{CO} = R_{CO_2} = \frac{k[CO]^{(b)} - k'[CO_2]^{(b)}}{1 + \dfrac{kx}{D_{CO}} + \dfrac{k'x}{D_{CO_2}}} \qquad (7.10)$$

The relatively simple expression shown in (7.10) is the direct consequence of the linear dependence of gaseous concentrations in (7.8a), (7.9a), and (7.9b). Through the assumed mass transport equations and quasisteady state condition, unknown interfacial concentrations in (7.8a) are replaced by corresponding values of bulk phases as shown in Equation 7.10. The denominator represents the sum of resistances of each of these three steps to the overall reaction. It should be pointed out that this approach is valid only for the isothermal system, otherwise equations for heat generation (consumption) and heat transport must be included in our attempt to replace interfacial properties by corresponding values in the bulk phases.

7.1.6. Slag–Metal Reactions

A steelmaking slag, which contains cations (in number of moles), $n_{Ca^{2+}}$, $n_{Si^{4+}}$, $n_{Mn^{2+}}$, $n_{Fe^{2+}}$, $n_{Al^{3+}}$ and anions $n_{O^{2-}}$, $n_{S^{2-}}$, reacts with liquid iron solution which contains n_{Fe}, n_O, n_S, n_{Si}, n_{Mn}, n_{Al}, n_{Ca}. The basic reaction at the slag–metal interface is the conversion between an atom and an ion, an electrodic reaction. For example,

$$[Si]_{metal} \rightleftarrows (Si^{4+})_{slag} + 4\,[e^-]_{metal} \qquad (7.11a)$$

$$[O]_{metal} + 2\,[e^-]_{metal} \rightleftarrows (O^{2-})_{slag} \qquad (7.11b)$$

where e^- stands for an electron. Electrical neutrality of the slag may be expressed as follows:

$$\sum_i z_i\,\omega_i = 0 \tag{7.12}$$

where $i = 1, 2, 3, \ldots$ for all ions in the slag, z_i = charge for ith ion, ω_i = reaction rate for ith reaction. For the case that there is only one element across the interface, the neutrality condition of (7.12) will be violated.

In order to maintain electrical neutrality in slag, the minimum number of elements to react simultaneously at the slag–metal interface is two. These simultaneous reactions are usually written as the formation and dissolution of neutral compounds, e.g.,

$$[\mathrm{Si}]_{\mathrm{metal}} + 2\,[\mathrm{O}]_{\mathrm{metal}} \rightleftarrows (\mathrm{SiO_2})_{\mathrm{slag}} \tag{7.13a}$$

and displacement reactions

$$[\mathrm{Si}]_{\mathrm{metal}} + 2\,(\mathrm{Fe}^{2+})_{\mathrm{slag}} \rightleftarrows 2\,[\mathrm{Fe}]_{\mathrm{metal}} + (\mathrm{Si}^{4+})_{\mathrm{slag}} \tag{7.13b}$$

One way to avoid the difficulty due to the unknown value of interfacial concentrations is to assume that the equilibrium of the slag–metal reaction under consideration is reached. Then, the interfacial concentration may be calculated from the equilibrium constant for a reaction similar to (7.13) and other necessary assumptions. Therefore, kinetic data may be analyzed as a mass transfer-limited system.

7.1.7. Multiplicity of Interfacial Reactions

The discussion begins with a situation where there is a slag–metal system under an equilibrium condition. The solvent iron dissolves Si, Mn, Al, Ca, O, and S and the slag phase is made up of ions of the same set of chemical elements. This equilibrium state may be disturbed by an increase in one of the elements in liquid iron, e.g., silicon. The reaction path to reach the new equilibrium state would be along the general direction of transferring part of the excess silicon to the slag. The electrical neutrality condition forces other chemical elements to cross the slag–metal interface as well. The events at interface may be illustrated in the following manner.

First, a number of silicon atoms, through their own thermodynamic driving force, become silicon ions at the interface and enter the slag, with electrons left behind in the metal. The consequence of silicon transfer is that the slag becomes positively charged and the metal becomes negatively charged. The electrochemical potential of cations in the slag increases, while that of anions decreases. The thermodynamic driving force for silicon transfer reappears partly in the form of an electric field, centered in the reaction zone, which drives cations to the metal phase and dissolved oxygen and sulfur to become anions. The overall reaction will lead to a new equilibrium state and maintains electrical neutrality in the slag.

A stoichiometric equation representing interfacial reactions may be given as follows:

$$\begin{aligned}
&\alpha_{\mathrm{Si}}[\mathrm{Si}]_{\mathrm{metal}} + \alpha_{\mathrm{O}}[\mathrm{O}]_{\mathrm{metal}} + \alpha_{\mathrm{S}}[\mathrm{S}]_{\mathrm{metal}} + \alpha_{\mathrm{Mn}}\,(\mathrm{Mn}^{2+})_{\mathrm{slag}}\\
&+ \alpha_{\mathrm{Fe}}\,(\mathrm{Fe}^{2+})_{\mathrm{slag}} + \alpha_{\mathrm{Al}}(\mathrm{Al}^{3+})_{\mathrm{slag}} + \alpha_{\mathrm{Ca}}(\mathrm{Ca}^{2+})_{\mathrm{slag}} \rightarrow \alpha_{\mathrm{Si}}(\mathrm{Si}^{4+})_{\mathrm{slag}}\\
&+ \alpha_{\mathrm{O}}(\mathrm{O}^{2-})_{\mathrm{slag}} + \alpha_{\mathrm{S}}(\mathrm{S}^{2-})_{\mathrm{slag}} + \alpha_{\mathrm{Mn}}[\mathrm{Mn}]_{\mathrm{metal}} + \alpha_{\mathrm{Fe}}[\mathrm{Fe}]_{\mathrm{metal}}\\
&+ \alpha_{\mathrm{Al}}[\mathrm{Al}]_{\mathrm{metal}} + \alpha_{\mathrm{Ca}}[\mathrm{Ca}]_{\mathrm{metal}}
\end{aligned} \tag{7.14}$$

where the α are stoichiometric coefficients. The values of this set of coefficients depend on the initial state of the system and should be functions of time to maintain neutrality in the slag. Without drastic assumptions for the simplification of (7.14) to a reaction involving only two chemical elements, the calculation of the equilibrium state at an interface would be extremely difficult based on the current formulism.

7.2. GAS–METAL DROPLET REACTIONS

Significant advances in fundamental studies of oxygen steelmaking reactions were made in the 1960s as the result of two events, the development of the Spray Refining Process by the British Iron and Steel Research Association, and the use of the levitation technique by Professor A.E. Jenkins. In spray steelmaking, droplets of blast furnace hot metal fall through oxidizing gas countercurrently to achieve very fast processing because of large gas–liquid interfacial area. The levitated metal drop, which is stationary in a gas stream of known flow properties, and free from refractory contamination, provides excellent experimental conditions for the study of interfacial reactions. The simplification of the system is that the rate of mass transfer can be calculated and the metal in the droplet is well stirred. In comparison with the steelmaking operation, there are two major differences: (i) the main gas stream is at room temperature, not at the steelmaking temperature, and (ii) the relative velocity between the gas and liquid metal is much lower in a levitation apparatus.

7.2.1. Oxidation of Liquid Iron

Distin and Whiteway (1970) investigated the kinetics of oxidation of the levitated iron droplets by He–O_2 mixtures at about 1750°C for a duration of several hundreds of seconds. It has been found that the ratio of the fraction of oxygen dissolved in the droplet to that terminated in the fume depends on the composition and flow rate of the oxidizing gas. No uptake of oxygen could be detected in droplets levitated for 600 seconds in a gas with p_{O_2} of 5×10^{-5} atm. It should be pointed out that the partial pressure of oxygen in equilibrium with oxygen-saturated iron is only about 10^{-7} atm. at 1750°C.

These observations confirm the mechanism of fume formation (Turkdogan et al., 1963) and the role played by the flux of iron vapor in the oxidation of iron. In Fe–Mn alloys, the vaporization of manganese is usually much more noticeable than that of iron.

7.2.2. Oxidation of Fe–C Droplets

Baker et al. (1964, 1967) studied the rate of decarburization of Fe–C droplets (up to 5.5 wt%C) at 1660°C by CO_2 and O_2. When CO_2 was used as the oxidizing gas, from 1% to 100% of CO_2 in CO_2–CO and CO_2–He mixtures, Baker et al. (1964) found that the rate of decarburization was independent of carbon concentration in the melt (i.e., reaction time) and was slightly affected by the total pressure. Experimental results may be interpreted on the basis of a diffusion model. The rate equation for steady-state diffusion in a binary gas system consisting of A and B molecules is

$$N_A = -D_{AB}\frac{dc_A}{dx} + (N_A + N_B)\frac{p_A}{P} \tag{7.15}$$

where N_A is the rate of diffusion of component A (mol cm^{-2} s^{-1}), D_{AB} is the binary diffusivity for the system A–B (cm^2 s^{-1}), dc_A/dx is the concentration gradient of A (mol cm^{-4}), p_A is the partial pressure of A and P is the total pressure. After integration of (7.15), Ranz and Marshall's correlation was used to evaluate the mass transfer coefficients. Properties of gases in the boundary layer were evaluated at the film temperature, the arithmetic mean of temperatures of the droplet and the incoming gas. Baker et al. (1967) reported that there are two kinetic regions of constant rate of decarburization separated by a period of instability when CO_2 is used as the oxidant at 1.0 and 0.1 atm total pressure. In the first regime where carbon content drops from 5.5% to less than 1%, the constant rate of decarburization reflects the steady state of mass transfer in the gaseous phase. At the onset of the instability, the levitated droplet dilates and ejects materials and, in certain cases, hits the wall of the tube. This is a sign of the internal generation and release of gas bubbles. The end of the period of instability coincides with the appearance of bright spots, probably iron oxide on the surface of the droplet. The results are summarized in Table 7.1.

Belton and coworkers studied the interfacial reaction by blowing the oxidizing gas, above rate-limiting flow rates, onto the surface of iron alloys: see Chapter 4.

Baker et al. (1967) used oxygen at 1%, 10% and 100% in O_2–He mixtures and linear velocities of 12.5 and 62.5 cm s^{-1} flow rates. Graphite spheres were used for comparison with Fe–C droplets of the rate of decarburization under similar conditions. Each molecule of oxygen results in two molecules of CO.

Table 7.1. The rate of decarburization in CO_2 for the two approximately constant-rate regions

	p = 1 atm		p = 0.1 atm	
Constant rate region (s)	0–19	28–40	0–20	40–60
(g-atom cm^{-2}s^{-1}) × 10^6	132	8	114	2
mg cm^{-2}s^{-1}	1.58	0.10	1.39	0.02
Gas-analysis results				
Percent CO	7.9	0.58	6.4	0.15
(mol CO cm^{-2}s^{-1}) × 10^6	270	20	217	5.0
Weight loss (mg cm^{-2}s^{-1})	2.0		1.7	<0.05

Source: Baker et al. (1967)

On the other hand, each molecule of CO_2 only oxidizes one carbon atom to CO. Taking into consideration the differences in properties of these two oxidants, the calculated rate of decarburization by oxygen under the same conditions should be 2.5 times that of CO_2, and this was confirmed experimentally by Baker et al. (1967) in the gaseous diffusion-limited regime. With a 10% oxygen–He mixture, flowing at 62.5 cm s^{-1}, the combustion rate of graphite spheres at 1660°C was (90 ± 5) × 10^{-6} g-atom C cm^{-2} s^{-1}. For an Fe–C droplet under the same conditions, the rate was 76 × 10^{-6} g-atom cm^{-2} s^{-1}.

7.2.3. Oxidation of Fe–Si Droplets

Sano and Matsushita (1971) used the levitation technique for kinetic studies of desiliconization by CO_2–He and O_2–He mixtures. Silicon content in the binary alloy was in the range from 0.15 to 10.60 wt% and the temperature was controlled in the range from 1550 to 1800°C. There are three types of reaction products—SiO gas, iron silicate melt, and solid silica. At 1550°C with a variety of oxidizing gas mixtures, the total amount of silicon removal in these experiments with initial values in the range from 1.2% to 1.6% shows a linear relationship with the square root of reaction time. Data were explained in terms of the diffusion of oxygen ions in the iron silicate melt, which was observed in all runs in this series. When the temperature was raised to 1700°C, keeping other conditions unchanged, considerable fuming was observed close to the droplet surface, being accompanied by greyish brown deposits on the wall of the reaction tube, while the surface was free of any condensed oxide phases. The deposit was found to be solid SiO with a small amount of FeO.

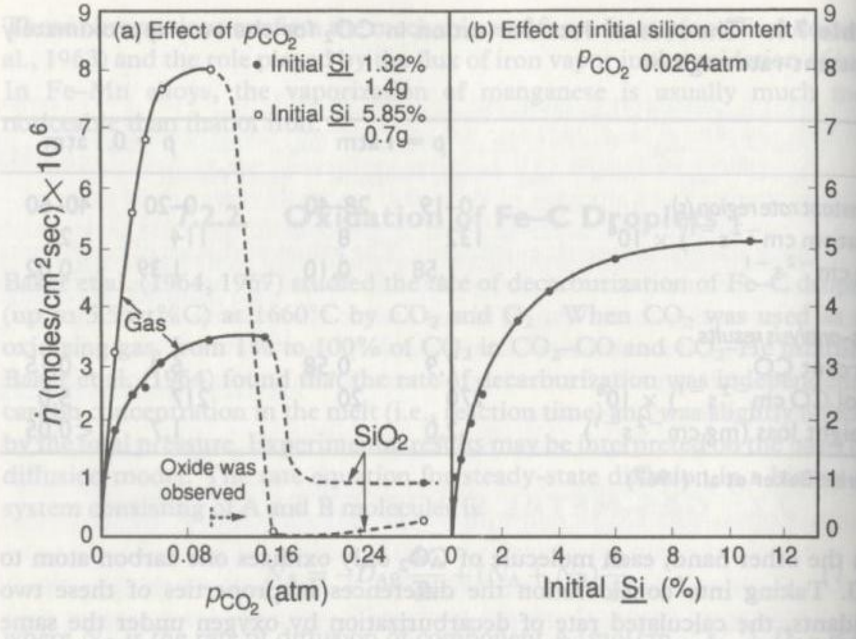

Figure 7.1 Rate of reaction of desiliconization at 1700°C as functions of initial concentration of silicon and partial pressure of CO_2 at a total flow rate of 500 ml min^{-1} (Sano and Matsushita, 1971).

The silicon contents of the droplets changed linearly with time until the surface was covered with liquid iron silicate. The compositional dependence of the reaction rate is clearly shown in Fig. 7.1. The initial reaction rates in the figure are values for the first minute of reaction. This behavior is similar to that of decarburization, where mass transport of oxidizing gas is rate determining. The rate of desiliconization was far greater than at lower temperatures, when rate-limiting step is diffusion in oxide melt. When solid silica formed, the rate of desiliconization became too small to be accurately measured.

Studies of the kinetics of oxidation of falling droplets of iron alloys have been reported by Baker (1967), Baker and Ward (1967), Vig and Lu (1971), and Hamielec et al. (1968). Owing to their complexity, experimental studies with a jet in a crucible will not be reviewed here.

7.3. KINETICS OF IRON ORE REDUCTION

For solid-state reduction of iron ore, there are four porous and impure solid phases with changing pore structures due to sintering at high temperatures. Three reaction zones (H–M, M–W, and W–Fe interfaces) are separated by two intermediate oxides with a wide range of nonstoichiometry. Inside a blast furnace, the temperature of reaction increases as the raw materials descend downward, and there are two reducing gases (CO and H_2). For this five-phase reacting system and for each reducing gas, in order to characterize its kinetic behavior, many kinetic parameters must be evaluated: the forward and backward rate constants for each interfacial reactions and for each solid phase porosity, tortuosity, effective thermal conductivity, solid-state diffusivities for densification, etc. A further complication is that values of temperature-dependent kinetic parameters evaluated from experimental data vary with impurity contents. There is no problem in building comprehensive mathematical models to describe this complicated system. The difficulty is in experimentation to generate data of adequate sophistication so that mechanism can be studied and parameters evaluated. There are two direct consequences: (i) researchers have to simplify the system (e.g., using chemical reagent grade hematite instead of natural ore and conducting experiments under isothermal conditions) for fundamental laboratory studies, and (ii) engineers have to test the reducibility of their iron ore agglomerates in all modern steel plants.

7.3.1. Solid-state Reduction

Joseph (1936) reported that ore properties (porosity, size, and shape) and temperature are important factors in the kinetics of iron ore reduction. In comparative studies of reducibility of different ores he used 14.3-mm cubes cut from lumps and the progress of reduction was monitored by measuring the amount of water vapor and carbon dioxide formed. The time required for 90% reduction was used as the index for reducibility. Tenenbaum and Joseph (1939, 1940) showed that kinetics depends on solid properties (porosity), gas properties (concentration), and temperature when other experimental conditions are kept constant. Their results with the use of hydrogen at lower temperatures are shown in Table 7.2. Their work was invaluable in guiding the development of modern blast furnace ironmaking.

In the interpretation of their data, a pseudohomogeneous rate expression was used even though reduction at the wustite–iron interface was suggested as the slow step.

The next milestone in the kinetic study of iron oxide reduction was the work of McKewan (1958, 1960). The heterogeneous nature of the system was recognized. In the late 1950s, after the commercialization of iron ore pellets, research scientists saw the various advantages of the use of artificial spheres as specimens. Spheres are of simple geometry for mathematical treatment. Specimens with more reproducible properties in terms of impurity contents,

Table 7.2 Effect of doubling pressure on time of reduction by hydrogen

Series	Average porosity, %	Temperature decrease (°C)	Minutes required for 90% reduction			
			1 atm	2 atm	Decrease in time	Percentage decrease
1	37	800	26	16	10	39
2	19	800	51.8	30.5	21.3	41
3	32	600	111.0	82.5	28.5	26
4	29	700	42.5	34.5	8.0	19

Source: Tenenbaum and Joseph (1939)

porosity, and size can be prepared. The availability of continuous electrobalances also contributed to the improvement in kinetic measurements. Data obtained around 1960 were ready for more sophisticated mathematical analysis than that of Tenenbaum and Joseph two decades earlier.

Based on data in the literature, McKewan (1958) proposed that the reaction rate of iron oxide reduction is proportional to the area of reacting interface which is assumed to be topochemical. He has also substantiated his theory with his own results on low-temperature magnetite reduction by hydrogen (McKewan, 1960). An implication of McKewan's theory is that the interfacial concentrations of reacting gases do not change significantly as the interface recedes toward the center.

Using spheres and bars prepared by oxidation of electrolytic iron to produce iron oxide specimens of a porosity of 31%, Kawasaki et al. (1962) carried out reduction experiments and proposed a gaseous diffusion-controlled model. They assumed that the interfacial reaction is essentially under equilibrium conditions and found that the model had difficulties in fitting the data of shorter reaction times.

Both experimental and theoretical results at that time made it obvious that the interfacial concentrations should be influenced by mass transfer resistance and should vary with time. Lu (1963) proposed the mixed control model based on the existence of a quasisteady state with McKewan's model and that of Kawasaki et al. as the limiting cases. He substantiates his own theory with results from artificial specimens and one-dimensional natural ore by using ceramic coatings in later publications (Lu and Bitsianes, 1966, 1968). His theory was improved by Seth and Ross (1965) and by St. Clare (1965). Spitzer et al. (1966) articulated theoretical development up to that time and made it clear that it would be straightforward to extend the modeling to a three-interface system. They assumed linear equations with respect to gaseous concentrations for all steps, quasisteady states and isothermal conditions as all other authors did. The results of Spitzer et al. (1966) are summarized below.

Five kinetic steps are considered, namely, mass transfer of reductant across the boundary layer outside the spherical specimen (7.16a); diffusion of reductant across the porous product layer (7.16b); interfacial reaction (7.16c); diffusion of gaseous product across the solid product layer (7.16d); and mass transfer of gaseous product across the boundary layer (7.16e).

$$\left(\frac{RT}{k_{\mathrm{m(A)}}}\cdot\frac{1}{4\pi\chi_0^2}\right)(-\dot{n}_{\mathrm{O}}) = p_{\mathrm{A}}^{(\mathrm{b})} - p_{\mathrm{A}}^{(\mathrm{o})} \tag{7.16a}$$

$$\left(\frac{RT}{D_{\mathrm{A}}^{(\mathrm{eff})}}\cdot\frac{(\chi_{\mathrm{o}}-\chi_{\mathrm{i}})}{4\pi\chi_{\mathrm{i}}\chi_0}\right)(-\dot{n}_{\mathrm{O}}) = p_{\mathrm{A}}^{(\mathrm{o})} - p_{\mathrm{A}}^{(\mathrm{i})} \tag{7.16b}$$

$$\left(\frac{RT}{k_{\mathrm{r}}}\cdot\frac{1}{4\pi\chi_{\mathrm{i}}^2}\right)(-\dot{n}_{\mathrm{O}}) = p_{\mathrm{A}}^{(\mathrm{i})} - \frac{p_{\mathrm{B}}^{(\mathrm{i})}}{K_{\mathrm{e}}} \tag{7.16c}$$

$$\left(\frac{RT}{K_{\mathrm{e}}D_{\mathrm{B}}^{(\mathrm{eff})}}\cdot\frac{(\chi_{\mathrm{o}}-\chi_{\mathrm{i}})}{4\pi\chi_{\mathrm{i}}\chi_0}\right)(-\dot{n}_{\mathrm{O}}) = \frac{p_{\mathrm{B}}^{(\mathrm{i})}}{K_{\mathrm{e}}} \tag{7.16d}$$

$$\left(\frac{RT}{K_{\mathrm{e}}k_{\mathrm{m(B)}}}\cdot\frac{1}{4\pi\chi_0^2}\right)(-\dot{n}_{\mathrm{O}}) = \frac{p_{\mathrm{B}}^{(\mathrm{o})}}{K_{\mathrm{e}}} - \frac{p_{\mathrm{B}}^{(\mathrm{b})}}{K_{\mathrm{e}}} \tag{7.16e}$$

where the specimen has a radius χ_0 initially, and the unreacted core at time t has radius χ_{i}. $D_{\mathrm{A}}^{(\mathrm{eff})}$, k_{r}, k_{m}, and K_{e} are the effective diffusivity of gas A, forward rate constant of interfacial reaction, mass transfer coefficient, and equilibrium constant, respectively. Gaseous concentrations are expressed in p/RT. $p_{\mathrm{A}}^{(\mathrm{b})}$, $p_{\mathrm{A}}^{(\mathrm{o})}$ and $p_{\mathrm{A}}^{(\mathrm{i})}$ are partial pressures of A at the main gas stream, on the surface of the sphere, and at the interface, respectively. $\dot{n}_{\mathrm{O}}$ stands for the rate of removal of oxygen from the solid oxide to be reduced in gram-atoms per unit time.

Upon algebraic addition of these equations, the interface and surface concentration terms cancel out, yielding an Ohm's law type of relation for the rate of reaction with the driving force expressed in terms of known bulk-phase concentrations:

$$\left[\frac{1}{\alpha 4\pi\chi_0^2} + \frac{\chi_0-\chi_{\mathrm{i}}}{\beta 4\pi\chi_{\mathrm{i}}\chi_0} + \frac{1}{k_{\mathrm{r}}4\pi\chi_{\mathrm{i}}^2}\right]\cdot[-\dot{n}_{\mathrm{O}}] = \frac{1}{RT}\left[p_{\mathrm{A}}^{(\mathrm{b})} - \frac{p_{\mathrm{B}}^{(\mathrm{b})}}{K_{\mathrm{e}}}\right] \tag{7.17}$$

where

$$\alpha = \frac{K_{\mathrm{e}}k_{\mathrm{m(A)}}k_{\mathrm{m(B)}}}{K_{\mathrm{e}}k_{\mathrm{m(B)}} + k_{\mathrm{m(A)}}} \tag{7.17a}$$

$$\beta = \frac{K_e D_A^{(\text{eff})} D_B^{(\text{eff})}}{K_e D_B^{(\text{eff})} + D_A^{(\text{eff})}} \tag{7.17b}$$

Viewing the overall reaction rate as the rate of removal of oxygen, the total resistance to the overall reaction is expressed by the left-hand factor of (7.17), whose terms may be identified respectively as the gas–film, shell-layer, and interface resistances. Equation 7.17 may be integrated for ready comparison with experimental data (Spitzer et al., 1966). Mass transfer coefficients may be calculated based on boundary layer theories and the effective diffusivities may be estimated based on pore structure of shell-layer and gas diffusivity. The evaluation of interfacial rate constants is done by curve-fitting.

It should be noted that, with adjustable parameters in the system, such a complicated model can readily be made to fit a finite set of data. The emphasis of this model is on the interplay between interfacial reactions and mass transfer steps. There are two general assumptions that have not been tested up to that time.

(i) It is an isothermal and isobaric system.
(ii) The interfacial reaction is first order with respect to the concentration of gaseous reactants.

The consequence of invalidity of assumption (i) is that the rate constant obtained by curve-fitting may lead to an erroneous activation energy. If assumption (ii) is not valid, then we have an entirely different mathematical model with which to obtain a different set of kinetic parameters. The examination of assumption (ii) is done below.

7.3.2. Hematite–Magnetite Interfacial Reaction

This investigation was carried out by Nabi and Lu (1974). The initial rates of hematite reduction to magnetite in ternary gas mixtures of H_2, H_2O, and N_2 were measured. Artificial hematite spheres, essentially pore free, were prepared by repeated firing, dipping into slurry of hematite powder, and polishing, with gradually increased firing temperature. The first surprising result was that the reactivity of hematite spheres is very sensitive to the final firing temperatures, as shown in Fig. 7.2. The decrease in reactivity of hematite when the sintering temperature was raised from 1100 to 1200°C was due to grain growth and smoothing of the surface. The increase in reactivity beyond 1200°C sintering temperature was due to further deviation from stoichiometry. For the rest of the kinetic study, all specimens had a final sintering temperature of 1200°C and underwent 5 hours of firing. For this single-interface system, reduction rates were measured continuously using a microbalance up to about 2% (at 650°C) and 6% (at 800°C) of completion of the reaction.

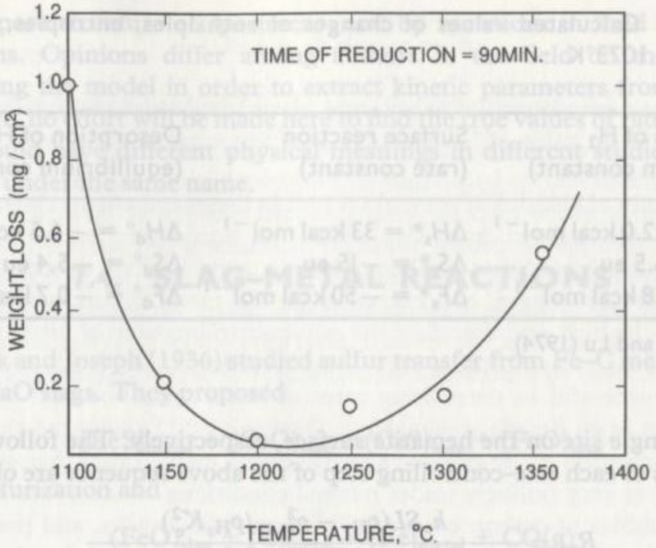

Figure 7.2 Surface reactivity vs. sintering temperature for constant sintering time of 5 hours (Reproduced from Nabi and Lu, 1974, with permission).

Four mechanisms, which differ in the types of adsorbed species and in the way the water molecules are formed, were considered in this study. The first two considered the chemisorption of hydrogen molecules to be nondissociative. The difference between these two mechanisms is that the adsorbed species are hydrogen and water molecules in one, and hydrogen molecules and oxygen atoms in the other. In the other two mechanisms, hydroxyl groups (as the result of dissociative adsorption of hydrogen) and water molecules are the adsorbed species. The difference between these two mechanisms is that in one the adsorbed water molecules are formed as the result of reaction between the adsorbed hydroxyl groups, and in the other as the result of reaction between hydroxyl groups and the hydrogen gas. Only the last mechanism will be discussed here.

$$H_2(g) + O_s\text{–}O_s = HO^*\text{–}HO^* \quad \text{(adsorption)} \tag{7.18a}$$

$$HO^*\text{–}HO^* + H_2(g) = H_2O^*\text{–}H_2O^* \quad \text{(surface reaction)} \tag{7.18b}$$

$$H_2O^* = H_2O(g) + s \quad \text{(desorption)} \tag{7.18c}$$

where * indicates the adsorbed species, and O_s–O_s and s are the dual oxygen

Table 7.3 Calculated values of changes of enthalpies, entropies, and free energies at 1073°K

Adsorption of H_2 (equilibrium constant)	Surface reaction (rate constant)	Desorption of H_2O (equilibrium constant)
$\Delta H_a{}^\circ = -22.0$ kcal mol^{-1}	$\Delta H_s{}^* = 33$ kcal mol^{-1}	$\Delta H_d{}^\circ = -6.5$ kcal mol^{-1}
$\Delta S_a{}^\circ = -16.5$ eu	$\Delta S_s{}^* = -15$ eu	$\Delta S_d{}^\circ = -5.4$ eu
$\Delta F_a{}^\circ = -4.8$ kcal mol^{-1}	$\Delta F_s{}^* = -50$ kcal mol^{-1}	$\Delta F_d{}^\circ = -0.7$ kcal mol^{-1}

Source: Nabi and Lu (1974)

sites and single site on the hematite surface, respectively. The following rate expressions to each rate-controlling step of the above sequence are obtained:

$$R_{ad} = \frac{k_a SL(p_{H_2} - p^2_{H_2O}/p_{H_2}K^2_e)}{2[1 + K_d/(K_s)^{1/2}p_{H_2O}/p^{1/2}_{H_2} + K_d p_{H_2O}]^2} \tag{7.19a}$$

$$R_s = \frac{K_a k_s SL(p^2_{H_2} - p^2_{H_2O}/K^2_e)}{2[1 + (K_a p_{H_2})^{1/2} + K_d p_{H_2O}]^2} \tag{7.19b}$$

$$R_{des} = \frac{k_d(K_s K_a)^{1/2} L(p_{H_2} - p_{H_2O}/K_e)}{[1 + (K_a p_{H_2})^{1/2} + (K_a K_s)^{1/2} p_{H_2}]} \tag{7.19c}$$

where S and L are coordination numbers for close packed plane and site density, respectively. K and k are equilibrium and rate constants. The other nine equations, and detailed mathematical analysis, can be found elsewhere (Nabi and Lu, 1974). Among the 12 equations, only the rate equation for surface reactions (7.19b) satisfies the requirement that all equilibrium constants and rate constants evaluated statistically be positive.

Confirmation of the conclusion that hematite reduction carried out in their study has the surface reaction (7.18b) as the rate-limiting step can be found in the thermodynamic properties of these parameters given in Table 7.3. The values of enthalpy and entropy changes listed agree well with computed values based on statistical thermodynamics according to the proposed mechanism.

There are two important conclusions from this work. (i) The reactivity (i.e., rate constants) of hematite of the same purity may vary widely depending on its thermochemical history. (ii) At least in this case, the interfacial reaction is second order with respect to the gaseous reactants, even for the simpler case of hydrogen. This implies that the popular assumption of first order of reaction for gas–solid iron oxide reduction may not always be valid.

In addition to the uncertainties mentioned above, experimental results reported in the literature are further complicated by the effect of impurities and the pore structure of specimens, and by variations in fluid mechanical conditions. Opinions differ among authors in the field on the need for simplifying the model in order to extract kinetic parameters from the data. Therefore, no effort will be made here to find the true values of rate constants, which could have different physical meanings in different studies although reported under the same name.

7.4. SLAG–METAL REACTIONS

Holbrook and Joseph (1936) studied sulfur transfer from Fe–C melts to SiO_2–Al_2O_3–CaO slags. They proposed

$$[FeS]_{metal} + (CaO)_{slag} \rightleftarrows (CaS)_{slag} + (FeO)_{slag} \tag{7.20}$$

for desulfurization and

$$(FeO)_{slag} + [C]_{metal} \rightarrow [Fe]_{metal} + CO(g) \tag{7.21}$$

for the formation of gas bubbles and metal droplets in slag. They explained the mechanism near the slag–metal interface of formation bubbles which carry over a film of metal to slag. When the bubble breaks, the film of metal becomes droplets in slag. They reported that the metal beads were never found above the metal bath if the metal, as charged, contained no sulfur. This system was investigated more quantitatively by Chang and Goldman (1948), who interpreted their kinetic data based on the following equation. The net transfer of sulfur from metal to slag is given by

$$\frac{dC_s S}{dt} = Ak_m C_m - Ak_s C_s \tag{7.22}$$

where S and A are the mass of slag and slag–metal interfacial area; k_m and k_s are the rate constants; and C_s and C_m are the concentrations. They also recognized that the rate constants are functions of temperature and composition of both phases. Radioactive iron was used as a tracer. They concluded that FeS is one of the constituents going across the interface but not the only one on the basis of mass balance.

Philbrook and Kirkbride (1956) studied reaction (7.21) between carbon-saturated iron and CaO–Al_2O_3–SiO_2 slags containing less than 5% FeO in a graphite crucible. In comparison with Chang and Goldman's work (1948), there was no sulfur in the system but there was substantially more FeO in the slag. They interpreted their data according to the following equation:

$$-\frac{dC_{FeO}}{dt} = k''(C_{FeO})^{\alpha} \tag{7.23}$$

where

$$k'' = \frac{100}{S}(k_1A_1 + k_2A_2)$$

and α is the order of reaction, which was determined to be in the range 1.6–2.3 with the average value of 2. A_1 and A_2 are the areas of slag–metal and slag/graphite interfaces.

In his study of kinetics of the carbon boil in the open hearth, Darken (1951) considered that oxygen from slag enters the liquid steel at the slag–metal interface and assumed that local equilibrium prevails. Experimentally, it was verified that the oxygen concentration in the metal phase was essentially uniform in the bulk and therefore the rate-controlling step of oxygen transfer was considered to be diffusion across the boundary layer. Such computation was very successful in correlating rates of decarburization and manganese oxidation in open hearth steelmaking. Darken (1951) suggested that homogeneous nucleation of the gaseous phase in liquid metal (other than in frothing conditions) is very unlikely under normal conditions for deep-seated carbon boiling. Bubbles of carbon oxides grow at crevices, cracks, and pores in the bottom of the furnace to bypass the nucleation step for normal carbon boil.

7.4.1. Theoretical Development

Systematic analysis of important steps in slag–metal reactions was first reported by Wagner (1956). For the cases in which local equilibrium was assumed, Wagner derived rate expressions based on two-phase film theory. Systems with simultaneous fluxes were treated. The data of Philbrook and Kirkbride (1956) which could be explained in terms of a second-order reaction (7.23), were interpreted by Wagner (1956) in a different way. It may be a gas-stirred (from CO generation) and mass transfer rate-limited system even though it may be a first-order reaction with respect to iron oxide concentration.

Wagner's illustration that slag–metal interfacial reaction is electrochemical in nature is most significant. He demonstrated that anodic reactions (7.11a), and cathodic reaction (7.11b), analogous to corrosion reactions, take place randomly at distinctly different sites on the slag–metal interface.

The rate of anodic dissolution of a metal i, ω_i is equal to the product of the metal–electrolyte interface area A and the current density J_i of this particular process divided by the product of valence z_i and the Faraday constant F:

$$\omega_i = \frac{AJ_i}{z_iF} \tag{7.24}$$

This equation also accounts for cathodic deposition of metal i with a negative value of ω_i for transfer from slag to metal and a negative value for the current

density J_i of the cathodic process. An equation relating current density and electrode potential

$$J_i = k_i'c_i'^{*} \exp[(1-\alpha_i)z_iEF/RT] - k_i''c_i''^{*} \exp[-\alpha_iz_iEF/RT] \tag{7.25}$$

gives the current density as the difference of two terms for anodic dissolution of metal i and its cathodic deposition as individual electrochemical phase-boundary reactions, where E is the potential difference between the electrode under consideration and a reference electrode measured without IR drop in the electrolyte; k_i' and k_i'' are the rate constants for the anodic and the cathodic process, respectively; $c_i'^{*}$ is the interface concentration of the metal to be oxidized anodically; $c_i''^{*}$ is the interfacial concentration of the metal ions to be reduced cathodically; and α_i is a parameter whose values lie between zero and unity.

In general, metal–slag reactions take place without the net flow of electrical current. Thus, we have

$$\Sigma J_i = 0 \tag{7.26}$$

or

$$\Sigma z_i\,\omega_i = 0 \tag{7.27}$$

We have a set of equations (7.25) for the rate of transfer for each constituent between slag and metal in terms of interfacial concentrations and the single electrode potential, E. Equations 7.25 and 7.27 determine the value of E through which all interfacial reactions are coupled.

King and Ramachandran (1956), observed the reversal of silicon and iron transfer when sulfur transfer from carbon-saturated iron to silicate slag was the main driving force (see Fig. 7.3). Interfacial reactions involved five elements, i.e., sulfur, iron, oxygen, silicon, and carbon. Their experimental data and Wagner's theory (1956) were mutually supportive.

Wagner (1956) suggested an experiment on silica reduction to test the electrochemical nature of the slag–metal reaction in a graphite crucible, where a cathodic reaction takes place at the slag–metal interface and an anodic reaction at the slag–graphite interface; and with current carried out by electrons in the metal and graphite and by ions in the slag. With the use of refractory sleeves in some experiments in graphite crucibles, Aurini (1968) confirmed that the electrochemical local cell effect does exist as suggested by Wagner (1956); however, when bare graphite crucibles are used, its contribution to the overall kinetics is insignificant within the experimental error of the method.

Interest in slag–metal reactions was significantly aroused by the work of Wagner (1956) and King and Ramachandran (1956). Several authors tried to extend Wagner's theoretical work but with limited success. De Hemptinne et al. (1961) treated the interface as a membrane in their electrochemical

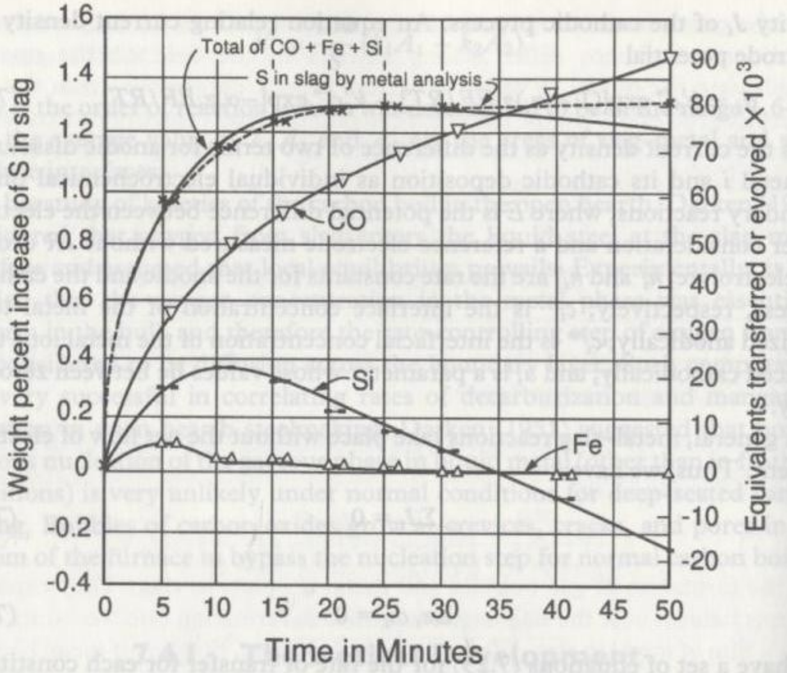

Figure 7.3 Equivalents of S, Fe, and Si transferred from metal to slag and equivalents of CO evolved (Reproduced from King and Ramachandran, 1956, with permission).

theory of smelting. Lu (1971) and Frohberg et al. (1973) studied the coupling of interfacial reactions based on relations of irreversible theomodynamics.

7.4.2. Coupled Interfacial Reactions

The data presented by King and Ramachandran (1956) are extremely interesting, but the generation of bubbles of carbon monoxide creates complications. Bubbles increase the interfacial area by bringing metal droplets to slag and its movement results in stirring.

Ma and Lu (1994) carried out experiments in a carbon-free system of Fe–Mn–Si alloy and CaO–SiO$_2$–Al$_2$O$_3$ slags in capillaries. A further precaution taken to minimize the convective mass transfer was that experiments were conducted at 20°C below the solidus temperature of 1783°C for the alloy. Slag at 1763°C has a viscosity of 8 dynes s cm^{-1}. The reason for choosing this particular system is that the solution thermodynamics and diffusivities of these phases are better known. Four experiments with different slag compositions were conducted. Concentration profiles in both phases, including the interface, in the sectioned reacted specimens were measured by electron microprobe.

A mathematical model of the system was used which consists of two semi-infinite multicomponent diffusional systems with a set of coupled interfacial electrodic reactions as the common boundary conditions at the interface. Diffusion equations for the metallic phase are based on the formalism of Kirkaldy and Young (1987) and coupled diffusion in the ionic phase according to Okongwu et al. (1973). The rate equations for interfacial reactions are according to (7.24)–(7.27), but the equivalent form in terms of electrochemical potential and affinity (Lu, 1971) is as follows:

$$\begin{aligned}\omega_i &= k_i\bar{a}_i - k'_i\bar{a}'_i\bar{a}_e^{z_i}\\ &= k_i\bar{a}_i\left(1 - \frac{k'_i\bar{a}'_i\bar{a}_e^{z_i}}{k_i\bar{a}_i}\right)\\ &= k_i\bar{a}_i\left[1 - \exp\left(-\frac{\bar{A}_i}{RT}\right)\right] \qquad (i = 1, 2, \ldots, n)\end{aligned} \tag{7.28}$$

where $\bar{a}_i$ is the electrochemical activity defined in terms of electrochemical potential,

$$\bar{\mu}_i = \bar{\mu}_i^0 RT\, ln\, \bar{\alpha}_i = \mu_i^0 T\, ln\, \alpha_i + z_i\mathcal{F}\phi$$

and $\bar{A}_i$ is the electrochemical affinity for the *i*th reaction. After resolving the inconsistency in solution thermodynamics of ionic melts (Ma and Lu, 1993), the activity of single ions is uniquely defined so that the linearization of Equation 7.28 (Lu, 1971) is avoided. Equation 7.28 is rearranged and its corresponding form of neutrality condition is given below:

$$\omega_i = k_i\bar{a}_i[1 - L_iU^{z_i}] \quad (i = 1, 2, \ldots, n) \tag{7.29}$$

where
$$U = \bar{a}_e \exp\left[\frac{\mathcal{F}(\Delta\phi - \Delta\phi_{eq})}{RT}\right]$$

and
$$L_i = \frac{k_i\alpha'_i}{k_i\alpha_i} = \frac{\alpha'_i/\alpha_i}{(\alpha'_i/\alpha_i)_{eq}}$$

where a_i and a_i' are chemical activities of the *i*th element in metallic and ionic solutions, respectively; $\Delta\phi(=\phi_s - \phi_m)$ is the electrical overpotential difference between slag and metal, and the subscript eq indicates that these properties are at the state of chemical equilibrium. Therefore, L_i $(i = 1, 2, \ldots, n)$ is a function of thermochemical properties, which are available in the literature. The conversion of single-ion activities to those of neutral compounds is demonstrated elsewhere (Ma and Lu, 1993). The coupling factor, U, characterizes the electrical properties in the interfacial zone through which simultaneous reactions are coupled. That relationship is the constraint of no net electric current, everywhere in the system; therefore (7.27) becomes

$$\sum_{i=1}^{n} z_i k_i \tilde{a}_i [1 - L_i U^{z_i}] = 0 \tag{7.30}$$

Further manipulation of (7.29) and (7.30) before computation is given elsewhere (Ma and Lu, 1994). For computational purposes, the reaction zone, which has layers of slag and metal at the interface, must have a finite size. The thickness of these layers in the reaction zone is assumed in such a way that the total masses on each side of the interface are equal. In view of the resolution of the microprobe, they are assumed to be 1.0 μm for slag and 0.4 μm for metal.

There are initially three elements (Fe, Mn, and Si) in the alloy and four (Al, Ca, Si, and O) in the slags. When reactions proceed, iron and manganese move from the metal to the slag and silicon moves in the opposite direction. In the specimens studied, aluminum, calcium, and oxygen in the alloy may be detected from beams of characteristic x-rays but cannot be analyzed quantitatively for their low concentrations. Thus, measured results are presented in terms of concentration profiles of oxides (MnO, FeO, SiO_2, Al_2O_3, CaO) in the slag and those of manganese and silicon in the alloy, for example, Fig. 7.4. The approximate stoichiometric equation is

$$(SiO_2)_{slag} + [Mn, Fe] \rightarrow (MnO, FeO)_{slag} + [Si]_{metal} \tag{7.31}$$

The ratio between reacted manganese and iron depends on the initial concentrations in the system and changes with time. Details of computation and computational results are available elsewhere (Ma and Lu, 1994). They may be summarized by saying that Wagner's (1956) theory of electrochemical reactions at slag–metal interfaces has been rigorously tested and positively confirmed.

7.5. THE REDUCTION OF IRON OXIDES IN LIQUID STATE

The advancement in this field is mainly due to the efforts of Philbrook, Soma, and Ban-ya and their associates. A comprehensive review of the kinetics of reduction of liquid iron oxides and iron oxide in liquid slag by gases (H_2, CO), solid carbon, and Fe–C melts has been given by Nagasaka and Ban-ya (1992).

7.5.1. Gas–Liquid Reaction

The reaction mechanism of liquid iron oxide reduction by carbon monoxide in a transport bed due to Tsukihashi, Kato, Otsuka, and Soma (1982b) is reviewed. Wustite particles (average size 25 μm) were carried by carbon

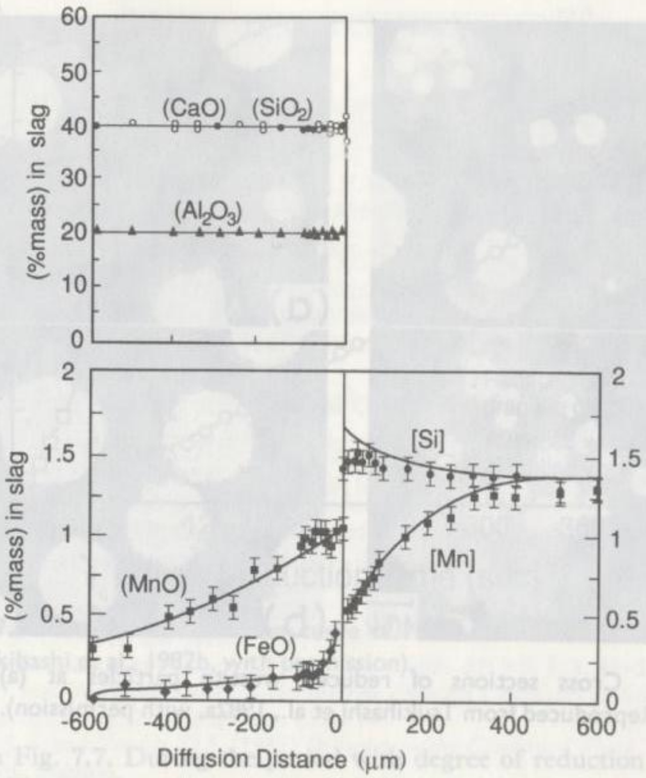

Figure 7.4 Comparison between measured and computed concentration profiles in 10 minutes of reaction (Ma and Lu, 1994).

monoxide through a tubular hot zone 10 cm in length controlled at 1450 or 1600°C. The residence time of particles in the hot zone may be calculated. Micrographs of cross sections of partially reduced specimens are reproduced in Fig. 7.5. Both metal and oxide phases had been in the liquid state and liquid iron did not hinder gas–oxide reaction as sponge iron does. This three-phase reaction actually takes place at two types of interfaces, i.e., gas–oxide for oxygen removal and oxide–iron for metalization. Metal phase is more likely nucleated inside the droplet of wustite, considering the presence of non-spherical metal phase in the interior, rather than sinking in from the surface because the slag–metal interfacial tension is much lower than the surface tension of iron in gas. The significant role played by nucleation of metallic iron in limiting the rate of metalization may explain the following facts observed by Tsukihashi et al. (1982b): (i) the extent of metallization varies from particle to particle; (ii) on the average, smaller particles (16 μm) react

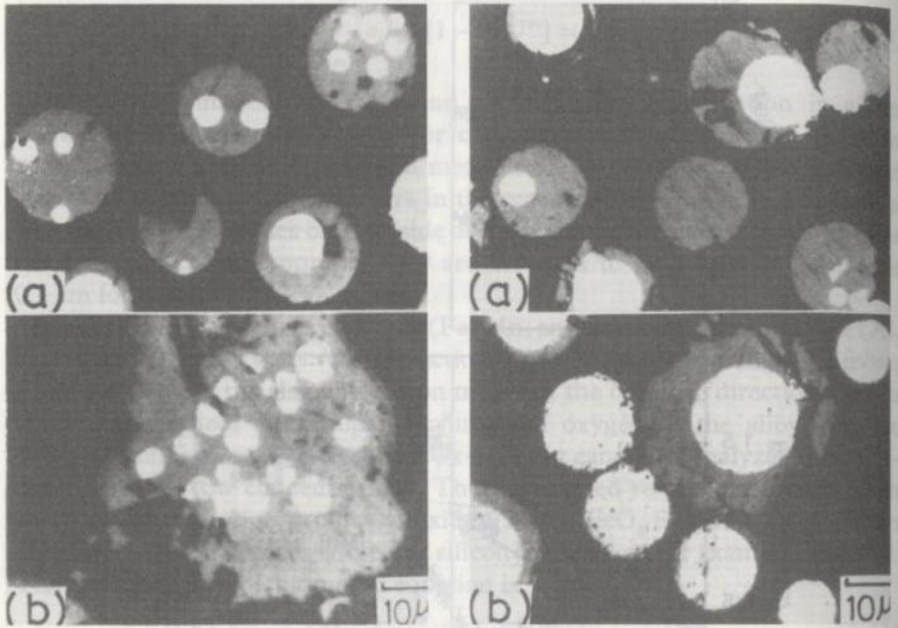

Figure 7.5 Cross sections of reduced wustite particles at (a) 1450°C (b) 1600°C (Reproduced from Tsukihashi et al., 1982a, with permission).

more slowly; and (iii) prereduction (from 0.45 to 0.16 in the ratio of Fe^{3+} to total iron) does not affect the overall rate of metallization.

7.5.2. Carbon as the Reductant

Tsukihashi et al. (1982b) carried out a series of interesting experiments. In each experiment, 10 g of fine iron ore of high purity was introduced to a graphite crucible of 20, 25, or 30 cm diameter which was maintained at 1500 or 1400°C. The kinetics of the system was monitored in two ways: (i) by measuring the total flow rate and composition of exit gas to give the rate of reduction quantitatively; and (ii) by viewing the x-ray transmission image of the graphite crucible and its contents for qualitative investigation of the mechanism.

In a comparative study, with the use of a graphite crucible with alumina sleeves to give constant liquid oxide–reductant interfacial area, two reductants (the bottom of the graphite crucible or about 100 g Fe–C melt at the bottom of the crucible) were used. The results are reproduced in Fig. 7.6. The progress of reduction, in the absence of iron–carbon melt initially, was recorded and is

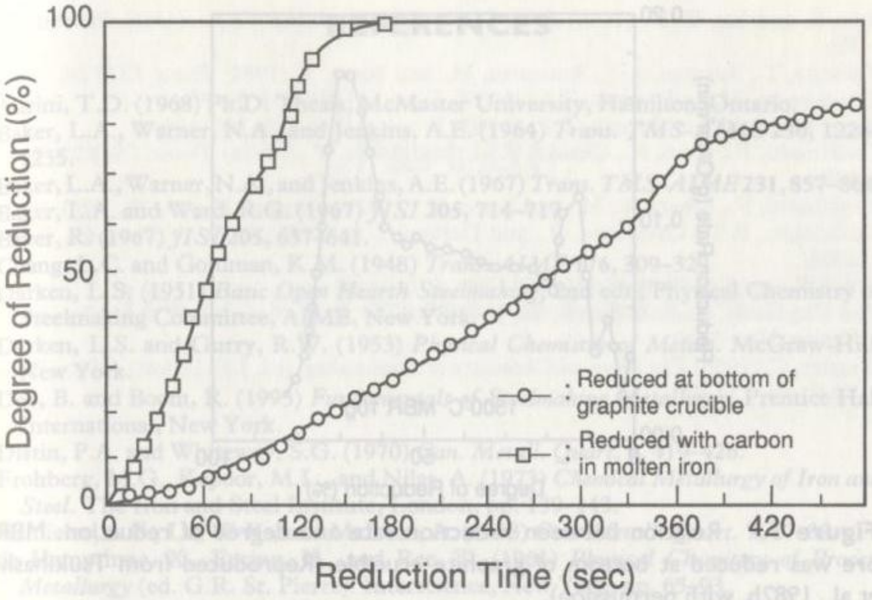

Figure 7.6 Degree of reduction curve of MBR ore at 1500°C (Reproduced from Tsukihashi et al., 1982b, with permission).

shown in Fig. 7.7. During the period with degree of reduction of 30–54% shown in Fig. 7.7, the exit gas has a ratio of $CO_2/(CO_2 + CO)$ of 0.17 which is the equilibrium value with liquid 'FeO' at 1500°C. The increase in the reaction rate after 60% of reducible oxygen was removed may be explained by the participation of the reaction product in the form of Fe–C droplets as reductant. This is consistent with the changes in x-ray transmission image. The extent of foaming shown on x-ray film would make any attempt at modeling challenging. Takaoka et al. (1984) reported that when dissolved carbon in liquid iron is the reductant, under similar conditions, the rate of reduction of liquid iron oxide increases with the increase of carbon content up to 0.3 wt%. Above this value, the rate of reduction was independent of the carbon content.

7.6. INDUSTRIALLY IMPORTANT SYSTEMS

In the 1950s and 1960s, the quality of raw materials for blast furnace ironmaking was dramatically improved. The enhanced process efficiency was partly due to better reducibility (less reductant required), higher strength

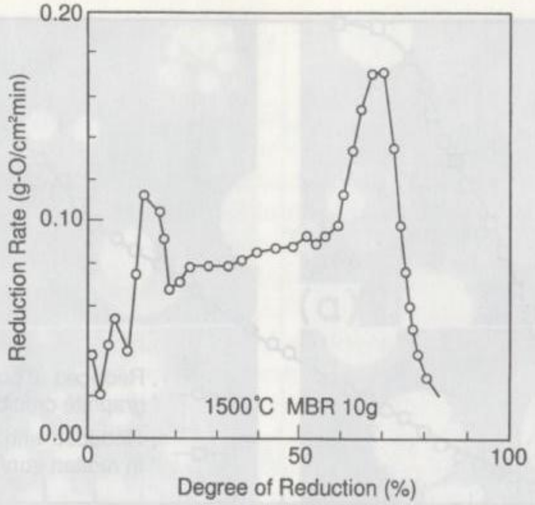

Figure 7.7 Relation between reduction rate and degree of reduction. MBR ore was reduced at bottom of graphite crucible (Reproduced from Tsukihashi et al., 1982b, with permission).

(more permeable furnaces) and higher gaseous pressure. It should be noted that iron ore agglomerates used by industry have a gangue content of 5 wt% or more. The chemical and physical properties of agglomerates of importance to ironmaking processes are usually determined by phases of gangues not by iron oxides. To minimize the use of metallurgical coke, in addition to coal injection to blast furnaces, the use of ore/coal composites is being considered. Study of the kinetics of reduction of these composites, in which heat transfer must be considered, will necessitate the adoption of nonisothermal and nonisobaric models (Sun and Lu, 1996).

The batch processes of steelmaking are relatively better understood. The practical use of kinetic knowledge is still hindered by lack of measurements of interfacial areas in the system. For smelting reduction, the gas–liquid metal–liquid slag system is further complicated by the direct charging of iron ore and coal. Determining the best way to feed carbon to iron melt to reduce iron oxide from slag and at the same time to supply heat and to release gas will be a challenge to practicing engineers as well as researchers.

The study of the kinetics and mechanisms of heterogeneous reactions is also important for reactions in gasification of coal and coke, slagmaking, refractory attack, agglomeration, and vacuum treatment.

REFERENCES

Aurini, T.D. (1968) Ph.D. Thesis, McMaster University, Hamilton, Ontario.

Baker, L.A., Warner, N.A., and Jenkins, A.E. (1964) *Trans. TMS-AIME* **230**, 1228–1235.

Baker, L.A., Warner, N.A., and Jenkins, A.E. (1967) *Trans. TMS-AIME* **231**, 857–864.

Baker, L.A. and Ward, R.G. (1967) *JISI* **205**, 714–717.

Baker, R. (1967) *JISI* **205**, 637–641.

Chang, L.C. and Goldman, K.M. (1948) *Trans. AIME* **176**, 309–329

Darken, L.S. (1951) *Basic Open Hearth Steelmaking*, 2nd edn. Physical Chemistry of Steelmaking Committee, AIME, New York.

Darken, L.S. and Gurry, R.W. (1953) *Physical Chemistry of Metals*. McGraw-Hill, New York.

Deo, B. and Boom, R. (1993) *Fundamentals of Steelmaking Metallurgy*. Prentice Hall International, New York.

Distin, P.A. and Whiteway, S.G. (1970) *Can. Metall. Quart*. **9**, 419–426.

Frohberg, M.G., Kapoor, M.L., and Nilas, A. (1973) *Chemical Metallurgy of Iron and Steel*. The Iron and Steel Institute, London, pp. 139–143.

Hamielec, A.E., Lu, W-K., and McLean, A. (1968) *Can. Metall. Quart*. **7**, 27–33.

de Hemptinne, X., Eyring, H., and Ree, T. (1961) *Physical Chemistry of Process Metallurgy* (ed. G.R. St. Pierre). Interscience, New York, pp. 65–93.

Holbrook, W.F. and Joseph, T.L. (1936) *Trans. AIME* **120**, 99–117.

Joseph, T.L. (1936) *Trans. AIME* **120**, 72–98.

Kawasaki, E., Sanscrainte, J., and Walsh, T.J. (1962) *AIChE. J*. **8**, 48–52.

King, T.B. and Ramachandran, S. (1956) *The Physical Chemistry of Steelmaking* (ed. J.F. Elliott). Wiley, New York, pp. 125–135.

Kirkaldy, J.S. and Young, D.J. (1987) *Diffusion in the Condensed State*. The Institute of Metals, London.

Lu, W-K. (1963) *Trans. Met. Soc. AIME* **227**, 203–206.

Lu, W-K. (1971) *Trans. ISIJ* **11**, 32–39.

Lu, W-K. and Bitsianes, G. (1966) The general rate equation for gas-solid reactions in metallurgical processes. II. *Trans. Met. Soc. AIME* **236**, 531–535.

Lu, W-K. and Bitsianes, G. (1968) Chemical kinetics of gaseous reduction of hematite. *Can. Metall. Quart*. **7**, 3–13.

Ma, D. and Lu, W-K. (1993) *Metall. Trans*. **24B**, 317–323.

Ma, D. and Lu, W-K. (1994) *Metall. Trans*. **25B**, 579–587.

McKewan, W.M. (1958) *Trans. Met. Soc. AIME* **212**, 791–793.

McKewan, W.M. (1960) *Trans. Met. Soc. AIME* **218**, 2–6.

Nabi, G. and Lu, W-K. (1974) *Ind. Eng. Fundamentals* **13**, 311–316.

Nagasaka, T. and Ban-ya, S. (1992) *Tetsu-to-Hagane* **78**, 1753–1767.

Okongwu, D.A., Lu, W-K., Hamielec, A.E., and Kirkaldy, J.S. (1973) *J. Chem. Phys*. **58**, 777–787.

Philbrook, W.O. and Kirkbride, L.D. (1956) *J. Metals* **8**, 351–356.

Sano, N. and Matsushita, Y. (1971) *Trans. ISIJ* **11**, 232–239.

Seth, B.B.L. and Ross, H.U. (1965) *Trans. Met. Soc. AIME* **233**, 180–185.

Spitzer, R.H., Manning, F.S., and Philbrook, W.O. (1966) *Trans. Met. Soc. AIME* **236**, 726–742.

St. Clair, H.W. (1965) *Trans. Met. Soc. AIME* **233**, 1145–1152.

Strassburger, J.H. (Editor-in-Chief) (1969) *Blast Furnace Theory and Practice*. Gordon and Breach, New York.

Sun, S. and Lu, W-K. (1996) *Proc. 55th Ironmaking Conf. ISS. AIME*, Pittsburgh, PA.

Takaoka, T., Suyama, S.-I., Amatatsu, M., and Soma, T. (1984) *Trans. ISIJ* 24, S832.

Tenenbaum, M. and Joseph, T.L. (1939) *Trans. AIME* 135, 59–72.

Tenenbaum, M. and Joseph, T.L. (1940) *Trans. AIME* 140, 106–125.

Tsukihashi, F., Kato, K., Otsuka, K.-I., and Soma, T. (1982a) *Trans. ISIJ* 22, 688–695.

Tsukihashi, F., Amatatsu, M., and Soma, T. (1982b) *Tetsu-to-Hagane* 68, 1880–1888.

Turkdogan, E.T., Grieveson, P., and Darken, L.S. (1963) *J. Phys. Chem.* 67, 1647–1654.

Vig, S.K. and Lu, W-K. (1971) *JISI* 209, 630–634.

Von Bagdandy, L. and Engell, H.-J. (1971) *The Reduction of Iron Ores.* Springer-Verlag, New York.

Wagner, C. (1956) *The Physical Chemistry of Steelmaking* (ed. J.F. Elliott). Wiley, New York, pp. 237–251.

Part III

INDUSTRIAL SYSTEMS

Overview

Paul V. Riboud

The last five chapters concern industrial systems: Chapters 8 and 9, of general scope, describe respectively process modeling and the analysis of metallurgical reactors, while the remaining three concern different types of industrial processes—ironmaking reactions in Chapter 10, iron smelting and steelmaking reactions in Chapter 11, and solidification rate in casting processes in Chapter 12.

GENERAL APPROACH TO SYSTEMS

Two types of approaches are presented: one is through process modeling, integrating all local phenomena into the overall process; the other considers the reactor as a whole and provides an evaluation of its efficiency in order to define a strategy for optimization.

Process modeling

Process modeling, described by Thomas and Brimacombe (Chapter 8), integrates (i) local and overall mass and heat balances, (ii) momentum balance through fluid dynamics or solid particle flow, (iii) shape and surface area of interfaces and (iv) local and overall chemical kinetics.

Using numerical methods, these calculations are becoming accessible for complex reactors with the development of fast computers.

Global reactor approach

This reactor approach is described by Engh in Chapter 9. It considers the whole process, or at least large distinct parts of the overall process, with the objective of increasing efficiency and productivity. The aim is to organize all components of the reactor: (i) their shape, (ii) their reactant feeding and product extraction and (iii) their stirring energy, originating from gravity, mechanical or magnetohydrodynamic forces, or from gas injections.

This approach is often used to compare competing processes, whether batch or continuous, for example, in terms of utilization efficiency of the reactants, or productivity for a given size of reactor. Final results can then be used directly for economic comparisons.

The two types of approaches—integration process model and global reactor—can be used sequentially toward optimization of a process.

APPLICATIONS TO STEELMAKING PROCESSES

Beyond the application of the above process modeling, the three chapters on iron and steelmaking processes make extensive use of the notions developed in the first parts of the book, i.e., thermodynamic and kinetic concepts.

Use of thermodynamics

Examples of the use of phase equilibria and thermodynamic activities are treated (i) in Chapter 10 by Steiler in the case of the reduction of ores in the blast furnace shaft for solid–gas equilibria, and in the case of the blast furnace hearth for metal–slag equilibria, and (ii) in Chapter 11 by Fruehan for metal–slag partition in steelmaking and in smelting.

Use of kinetics

Examples of the kinetics of reactions involving only solids among the condensed phases, such as those occurring in the upper part of the blast furnace, are also presented in Chapter 10. For reactions involving one or several liquid phases, examples are given for the various metal–slag reactions occurring in the blast furnace crucible (Chapter 10) and for the liquid–liquid emulsions encountered in steelmaking and smelting reactors (Chapter 11). Concerning solidification rate, implementation in the various continuous casting processes implies the detailed treatment of heat transfer in the mold and in spray cooling zones, as detailed by Schwerdtfeger in Chapter 12.

8

Process modeling

B.G. Thomas
Department of Mechanical and Industrial Engineering, University of Illinois at Urbana-Champaign, Urbana, Illinois, USA

J. Keith Brimacombe
Centre for Metallurgical Process Engineering, University of British Columbia, Vancouver, British Columbia, Canada

8.1. INTRODUCTION

The silicon chip has changed our approach to process analysis. In an earlier time, some of us actually used a slide rule and drew graphs by hand. There were merits in some of this as we learned to estimate, carry powers of ten, and think about what we were plotting. But, of course, the complexity of real processes eluded us, as only simple balances and analytical solutions were possible.

The burgeoning evolution of the computer and user-friendly software has fundamentally transformed our approach to process analysis and propelled us into the development and application of mathematical process models. The computer has unshackled us from the need to oversimplify. But if we are not careful, it threatens to confuse and overwhelm us with needless complexity.

In this chapter on process modeling, the challenge is addressed of simplifying complex processes while maintaining a strong hold on reality. As shown in Fig. 8.1, we need to balance the mind-set of simplification with the power of complex analysis. And underpinning modeling must be measurements.

8.1.1. What is a Process Model?

A process model is a system of mathematical equations and constants that are usually solved on a computer to make quantitative predictions about some

ADVANCED PHYSICAL CHEMISTRY FOR PROCESS METALLURGY
ISBN 0-12-618920-X
Copyright © 1997 Academic Press Ltd
All rights of reproduction in any form reserved

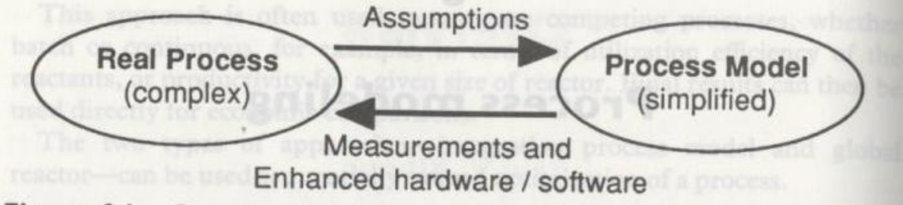

Figure 8.1. Compromise between mathematical simplifications which push the process model away from reality and tools which bring it closer.

aspect(s) of a real process. The specific variables required as input data and generated as output predictions are important features of the model. The equations often stem from a numerical solution to one or more differential equations and their boundary conditions.

The model also includes the constants which represent material properties, empirical relationships, and other knowledge about the process. Considerable effort is usually required to obtain these, normally by experimentation. Thus, general-purpose commercial software packages (e.g., finite element- or finite volume-based codes) are not models in this context. They serve as useful tools, however, by providing frameworks for the development of process models, possibly saving effort in formulating the equations.

Thus, by definition, models require a combination of mathematics and experimental data. To be relevant, they also need to be validated with realistic measurements and finally implemented into practice. These aspects of process models will be treated in subsequent sections, in the context of examples taken from the continuous casting of steel, which is described in Chapter 12.

8.2. WHY MODEL?

There are many different reasons for developing a process model. These include:

- Increasing fundamental understanding of a process
- Assisting in scale-up
- Design of experiments
- Evaluation of experimental results
- Quantifying property measurement
- On-line process control and optimization
- Technology transfer

If a clear reason to develop a model cannot be found, then it should not be developed!

8.2.1. Increasing Process Understanding

Perhaps the most important reason for modeling is to gain fundamental understanding of a process. Without this understanding, improvements can be made only by expensive trial and error, and error is more likely. Models can serve as off-line tools to correct misconceptions, identify what is important, test hypotheses, and perform parametric studies. A validated process model is an ideal tool for isolating the effects of individual phenomena, because each variable of interest can be changed systematically and independently. Off-line study of the influence of different variables on the operation of a process is often the first step in process optimization.

8.2.2. Scale-up and Design

Models are particularly important in the design of new processes and plants. The ability to extrapolate knowledge generated from bench-scale or pilot plant experiments to a commercial-scale operation varies in direct proportion to the accuracy of the process model(s) used. Because there is no existing plant for calibration, it is crucial that models used for this purpose be as mechanistic as possible.

8.2.3. Design of Experiments

Process models can help with experimental design in several ways. One way is to identify the critical location(s) in a process where measurements should be made, in order to get the most use from the experiment. For example, without the aid of a model, thermocouples might be placed needlessly in locations that are not very interesting. Alternatively, there may be too few thermocouples at critical locations where temperatures change rapidly.

Another use of a model is to help identify the process variables which are most critical, or rate-limiting. Experiments can then focus on quantifying the effects of just these variables. Finally, models can help to ensure that an experiment does not forget a crucial phenomenon that governs the real process.

8.2.4. Evaluation of Experimental Results

Off-line process models can help in interpreting the results of experiments. For example, temperature measurements may be converted to heat fluxes with the aid of a model. These heat fluxes enable more meaningful comparison between experimental results, because they are less specific to a particular experimental setup.

Process models are particularly useful when the phenomena are difficult to measure or model physically. Examples relevant to continuous casting include flow in the liquid pool generated by electromagnetic or thermal effects, and thermal stress generation. A good process model can extrapolate the results from a few key experiments to other conditions and help to find the optimal process conditions with less experimental effort.

8.2.5. Property Measurement

Models are very important in the measurement of properties. This is because properties are not measured directly, but are instead derived from measurements using a model. Furthermore, particular property data must only be used with the specific model that was used to extract them from the raw measurements.

For example, thermal conductivity is typically calculated from an experiment which measures two temperatures and the distance between them for a known applied heat flux. Generally, a simple form of Fourier's heat conduction law is used to extract the thermal conductivity. However, if the material is a semitransparent slag, for example, then the measurements will include heat transmitted by both conduction and radiation. The conductivity calculation may or may not account for this radiation. Thus, several different conductivity 'measurements' are possible from the single experiment, depending on the heat transfer model employed in the property calculation. A sophisticated model might even combine the results from several experiments to calculate simultaneously the thermal conductivity and the radiation absorption coefficient.

Future process models using the 'measured' conductivity should separately account for radiation or not, according to the heat transfer model employed in the property calculation. Obviously, it is important that the experimenter reporting the property 'measurements' should clearly indicate the model used in calculating the property data.

This particular example arises when quantifying the thermal properties of molten slag layers. Similar difficulties arise during measurement of other properties whenever there are complicating phenomena which cannot be avoided in the experiment. Other practical examples include inelastic creep relaxation during the measurement of elastic modulus at high temperature, and strain localization during the measurement of critical fracture strain. The lack of complete, fundamental property data in areas such as these is one of the many factors limiting the accuracy of current process models.

Models can contribute to property measurement by providing a framework common to experimenters and modelers alike. The need for general models of fundamental material behavior is growing, as the phenomena of interest grow in complexity and experiments are unable to isolate a single property to be measured. In many cases, sophisticated mechanistic models should be used together with the results of several experiments in order to extract properties that are more fundamental.

8.2.6. On-line Process Control and Optimization

The best way to optimize many processes is to control some aspect of them on-line. This requires a simple model which correctly identifies the key parameters of the process and quantifies how they affect the product. Developing an on-line model and implementing it to control a process is the ultimate reason for modeling and is discussed in further detail in a later section.

8.2.7. Technology Transfer

Finally, models also act as a means of technology transfer which can be embedded in expert systems. An expert system can provide easy access to relatively complex models and a wealth of knowledge without forcing the engineer to read and understand all of the literature.

Models are excellent educational tools. They enable visualization of the phenomena which control a process. The insights gained from careful evaluation of 3D color moving images often cannot be obtained in any other way. Even the act of modeling can produce mental discipline in process analysis and deepen understanding of the phenomena which govern it. With increased process understanding, a process engineer can make better decisions and implement improvements to processes.

8.3. TYPES OF MODELS

All process models can be classified according to their basis as empirical versus mechanistic.

A fully empirical model is created by performing a curve-fitting procedure on the results of a statistical study with no attempt to understand the reasons for the relationships. This type of model is well suited for on-line applications, because the resulting equations are very fast to solve and are robust, avoiding numerical difficulties. However, they usually become very inaccurate if extrapolated beyond the specific range of processing conditions for which they were developed.

A fully mechanistic, or phenomenological, model solves equations based solely on the fundamental laws which govern natural phenomena. These laws include the differential equations governing the conservation and transport of mass, momentum, mechanical force, electromagnetic force, and energy, in addition to thermodynamics, phase equilibria, kinetics, and other relations. Experimental data are incorporated in their most fundamental form, through the material properties. A mechanistic process model can be extended to understand and solve problems with a given process, without knowing the particulars of the problem prior to development of the model.

In practice, all models lie somewhere between these two extremes. No model comes close to being a complete, fully mechanistic process model, despite the claims of some modelers. In reality, it is possible at best to model mechanistically only a tiny fraction of the actual phenomena present in a real process. This is because real industrial processes contain staggering complexities in phenomena at the mechanistic level. The continuous casting process, for example, is governed in part by the following phenomena:

- Fully turbulent, transient fluid motion in a complex geometry (inlet nozzle and strand liquid pool), affected by argon gas bubbles, thermal and solutal buoyancies
- Thermodynamic reactions within and between the powder and steel phases
- Flow and heat transport within the liquid and solid flux layers, which float on the top surface of the steel
- Dynamic motion of the free liquid surfaces and interfaces, including the effects of surface tension, oscillation and gravity-induced waves, and flow in several phases
- Transport of superheat through the turbulent molten steel
- Transport of solute (including intermixing during a grade change)
- Transport of complex-geometry inclusions through the liquid, including the effects of buoyancy, turbulent interactions, and possible entrapment of the inclusions on nozzle walls, gas bubbles, solidifying steel walls, and the top surface
- Thermal, fluid, and mechanical interactions in the meniscus region between the solidifying meniscus, solid slag rim, infiltrating molten flux, liquid steel, powder layers, and inclusion particles
- Heat transport through the solidifying steel shell, the interface between shell and mold (which contains powder layers and growing air gaps), and the copper mold
- Mass transport of powder down the gap between shell and mold
- Distortion and wear of the mold walls and support rolls

- Nucleation of solid crystals, both in the melt and against mold walls
- Solidification of the steel shell, including the growth of grains and microstructures, phase transformations, precipitate formation, and microsegregation
- Shrinkage of the solidifying steel shell due to thermal contraction, phase transformations, and internal stresses
- Stress generation within the solidifying steel shell due to external forces (mold friction, bulging between the support rolls, withdrawal, gravity), thermal strains, creep, and plasticity (which varies with temperature, grade, and cooling rate)
- Crack formation
- Coupled segregation, on both microscopic and macroscopic scales

For an arbitrary problem, any of these phenomena might be critical. Alternatively, the critical phenomena may not yet be identified. Finally, many of the fundamental material properties needed for such a mechanistic model are not yet understood, let alone measured.

Because of this overwhelming complexity, it is unlikely that any model will ever incorporate all of these phenomena mechanistically. Nor should one—the model would be too complex ever to run! All useful models focus on a specific aspect of a process, and mechanistically model only those phenomena most important to that aspect. Other phenomena are either ignored or incorporated empirically. Most models thus contain a significant component of empiricism. The great advantage of mechanistic models is that they can be extrapolated to simulate conditions outside the range of model validation. This makes them useful for design purposes.

Empirically based models are sometimes looked down upon because they are inflexible and serve only a particular purpose. However, empirical models are ideally suited to on-line applications, which are so useful to industry. It is not necessary to achieve full understanding of an existing process before a model can be implemented. The unknowns can be accounted for in the empirical constants. Naturally, the better the understanding, the better the model will be. The challenge is to base the process model on mechanistic understanding without sacrificing speed, simplicity, and robustness.

8.4. OTHER PROCESS DEVELOPMENT TOOLS

As already indicated, mathematical modeling is rarely sufficient, by itself as a mathematical exercise, to analyze the key characteristics of a materials process. Usually, some phenomena, such as the heat flux boundary conditions from a continuously cast strand to the water sprays, are poorly understood and are best treated using measurements. Many thermophysical properties, constitutive behavior, microstructural phenomena, rheological properties, or thermochemistry, have not been quantified and demand determination in building a credible model. Moreover, a process model that has not been tested with measurements can be a most dangerous distraction with the potential to inflict harm to process development.

Consequently, the application of mathematical models to the analysis and design of materials processes must always be set in the context of all of the other tools of process development. These other tools specifically include measurements, which may be conducted in at least four different realms: the real process, pilot plants, physical models, and the laboratory.

8.4.1. Industry Experiments

On an operating process, by definition in the real world of complexity, measurements are obtained only with difficulty, especially in a production environment where pressures to meet schedules are severe and dominant. Commercial materials processes impose difficulties of noise, heat, dust, electrical interference, and time and space constraints. The frustrations of integrating a research program into the production environment are not insignificant, and are sometimes overwhelming; but the rewards, in terms of obtaining real-world data, can be enormous. Much of what we have learned from processes like continuous casting, copper converting, and zinc slag fuming wells up from difficult, time-consuming, and often stressful measurements made on the operating process. Such experiments probe the complexity of fluid interaction, heat flow, and chemical reactions which are not easily replicated under laboratory conditions.

8.4.2. Pilot Plant Experiments

That having been said, the pilot plant, which is a smaller scale of a potential or operating process, can be a powerful tool of process development. The pilot plant affords the opportunity to study, away from the pressures of the production environment, the influence of process parameters on the production rate, quality, safety, and operational care, amongst other things, on the process operation. The size of the pilot plant may vary from laboratory (bench) scale to a larger size, but the goal always is to understand, assess, and develop a process at reduced capital cost which minimizes financial risk.

8.4.3. Physical Model Experiments

The physical model is another tool of process analysis which is aimed at simulating some of the phenomena of a new, or existing, process through the use of more user-friendly systems, such as Plexiglas and water, as compared to molten steel and refractory. Physical models have been employed most frequently to study fluid flow in vessels, such as continuous casting tundishes, where the relevant properties of water and molten metal are similar. In the design of physical models, similarity criteria need to be considered so that the forces at work in the real process are simulated properly. Such forces in fluid flow include inertial, viscous, buoyancy, and surface tension forces, which may be characterized by the Reynolds, Froude, and Weber numbers. It is critical that the dominant forces in a process are evaluated because it is rare that all similarity criteria can be met with the physical model. For example, a hot metallurgical process is accurately simulated with a cold isothermal liquid only when the buoyancy forces are small, as indicated by the size of the modified Froude number. Physical models can be applied to measure mixing conditions or, with the help of sophisticated tools like the laser Doppler velocimeter, turbulence in the fluid. The scaling and use of physical models must be undertaken with considerable forethought and ingenuity, but they can yield important results on complex metals processes at relatively low cost.

8.4.4. Laboratory Experiments

Finally, the process engineer has in his arsenal measurements in the laboratory. Measurements in a carefully controlled laboratory setting may range from determination of thermodynamic activities, to determination of the rate of the Boudouard (C–CO_2) reaction, to the study of sulfide particle disintegration in a flash smelting environment.

It cannot be overemphasized that, in the modeling of complex processes, mathematics can take us only so far. When inevitably we hit the wall of our understanding, measurements must be made. All too frequently, the modeler takes the easy route of making simplifying assumptions to skirt the difficulty and remain at the computer keyboard, rather than move to the laboratory. This is a mistake. Properly formulated, a mathematical model automatically guides us to what we must know, in terms of properties and boundary conditions. What is missing must be measured. Mathematical modeling is often more about measurement than it is about mathematics. A wise process modeler uses all of his tools, including process models, to develop and improve materials processes.

8.5. DEVELOPMENT OF A PROCESS MODEL

The process of developing a process model can be divided into several stages, which are illustrated in Fig. 8.2. In practice, models evolve as understanding improves, so there is cycling between the various steps.

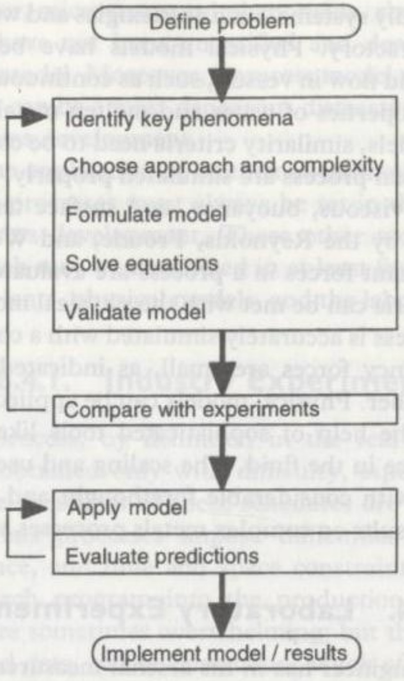

Figure 8.2. Steps in process modeling.

8.5.1. Problem Definition

As in any other endeavor, success in modeling is more likely when there are clear objectives. When developing, applying, evaluating, and implementing a model, a multitude of decisions must be made, such as the choice of phenomena to simplify or ignore. Each decision should be made by considering the exact purpose of the model, or what problem in the real world the model is intended to help solve. Defining the specific reason for the model is the most important step in model development.

8.5.2. Identification of Key Phenomena

An initial goal of the process engineer in developing a process is to identify the rate-limiting steps and to determine how to control, accelerate, or optimize them. The same is true of the process model.

Before developing a process model, it is essential to have a qualitative understanding of the basic phenomena which govern the process. This is because models, at best, can only quantify that understanding and shed insight into the interactions between those chosen phenomena. A model cannot identify phenomena which have been neglected. Important phenomena which are poorly understood, particularly those occurring at the boundaries, are often best treated empirically by calibrating the model with experimental measurements.

To choose the phenomena to model mechanistically, the modeler should bring in as much process understanding as possible from all other available sources. The place to start is with previous literature and experience. This includes the insights from previous laboratory, pilot-plant, and industry experiments, and physical and mathematical models discussed in the previous section. Simple 'back-of-the-envelope' calculations and analytical solutions are invaluable as well. Scaling calculations are a crude preliminary tool to eliminate phenomena that are unimportant.

It is critical to identify correctly the key phenomena or rate-limiting steps which govern the process. Input from all process analysis tools should be gathered together and evaluated carefully before making the choices for this critical stage of model development.

8.5.3. Approach and Model Complexity

Next, the type and complexity of the model must be chosen. Process models range in complexity from simple analytical solutions to fully-coupled, three-dimensional transient numerical simulations. Including another phenomenon often adds another dependent variable (such as concentration, temperature, velocity/pressure, or displacement) or another material property. The purpose of the model should dictate what phenomena are included, and consequently how complex the model should be.

The first guideline is to choose the overall model complexity according to the computing hardware power and time frame available. A common mistake is overcomplexity. Models for eventual on-line use must be kept simple, to run in minutes or less on small computers. Other models can afford to include more mechanistic phenomena, and consequently be more complex. Even then, the developer should consider that a model which requires several weeks of execution time per run on a supercomputer is unlikely to be productive, although it is surprisingly easy for this to happen.

The next guideline is to model phenomena in proportion both to their importance to the problem and to how well they are understood mechanistically. Important phenomena which are well understood are worthy of modeling in detail. For example, detailed simulation of heat conduction in a complex geometry has been the basis of many successful models. Phenomena which are not well understood are best left to simple empirical approximations based on experiments. For example, convective heat transfer between spray water droplets and a hot surface is generally best modeled empirically using correlations from experimental data: heat transfer coefficients.

Another guideline is to keep the relative errors about the same. There is no sense in modeling one aspect of the process (such as the geometric effect of the third dimension) to gain a 1% improvement in accuracy, while at the same time making a 100% error by ignoring another critical aspect of the process altogether (such as transient effects, or upstream process variations).

All process models should aim to simulate phenomena in the real world, which is always three-dimensional. To do this, it is sometimes necessary to discretize all three dimensions, thus producing a '3D model'. Often, however, it is possible to make reasonable approximations which avoid discretizing one or more of the dimensions. This allows huge computational savings because, in general, each dimension discretized increases the complexity of a model by an order of magnitude. Before including that third dimension, it is logical to ensure that no other important phenomena are left out of the model. It is often easier to improve the accuracy of a model by a crude incorporation of some secondary phenomena than by an exact modeling of the primary phenomena in three dimensions.

A process model should be kept as simple as possible, but no simpler! Overly complex models are too difficult and time consuming to run. On the other hand, simplifications which are not reasonable may lead to erroneous conclusions that may be very costly. Thus, it is impossible to create an efficient model of sufficient accuracy without knowing how the model will be used. Granted, this is a difficult task.

8.5.4. Model Formulation

Formulation of the mathematical equations to be solved is often the least difficult of the stages in model development. Naturally, this depends on the complexity of the phenomena to be modeled and on the availability of commercial software packages, which can drastically reduce the time to develop a model. More is said about commercial software in the next section, but these packages should not be used without a sound understanding of the principles and assumptions which underpin them.

An essential aspect of model formulation is the making of assumptions which, if it is done properly, enable us to model the important phenomena more easily and with minimal loss of accuracy. What to assume requires a careful assessment of the process, as described earlier, and good judgment. The wrong assumptions cause us to ignore important phenomena. Too many assumptions oversimplify the model, ultimately leading to greater empiricism and less flexibility. Too few assumptions may overcomplexify a model and create needless expenditure of time and money for no tangible gain. Clearly, the ability to formulate the best assumptions can place the mathematical model on track toward process development, or seriously derail it.

A mathematical model rooted in fundamental laws and mechanisms must conform to the laws of conservation of mass, heat, energy, and momentum. In order to apply conservation, a part of the system must be isolated; and thus a volume element must be defined. This volume element may represent a significant portion of the system, leading to global balance equations. Such could be the case for thermodynamic models or reactor models. Alternatively, the volume element may have small or even infinitesimal dimensions in one, two, or three different coordinate directions, depending on the number of dimensions chosen for the model. The choice involves a balance between model simplicity and potential accuracy, as already discussed.

Having defined the volume element, a balance is performed on the quantity to be conserved (mass, heat, momentum):

$$\begin{array}{c}\text{Input through surfaces}\\ \text{of volume element}\end{array} \quad \begin{array}{c}\text{Output through surfaces}\\ \text{of volume element}\end{array}$$

$$+\begin{array}{c}\text{Generation within}\\ \text{element volume}\end{array} - \begin{array}{c}\text{Consumption within}\\ \text{volume element}\end{array} = \begin{array}{c}\text{Net accumulation}\\ \text{within volume element}\end{array}$$

These balance equations yield the governing equations, which relate the dependent variables to the independent variables of space and time. In the case of a mass balance, the dependent variable is concentration. The heat balance yields temperature, and the momentum/mass balance yields velocity and pressure as dependent variables.

The equations can be built directly into 'finite volume' models by constructing an algebraic equation for each volume element. Alternatively, a partial differential equation form of the balance can be written, based on infinitesimal volume elements, and the discrete system of simultaneous algebraic equations derived using any of a variety of mathematical techniques, such as the Galerkin finite element method (Zienkiewicz and Taylor, 1988).

The final step in the mathematical formulation is the specification of initial and/or boundary conditions subject to which the governing equations are solved. Specification of a particular boundary condition depends on the phenomena occurring at that boundary and is usually relatively straightforward. Determining the coefficients, such as for heat and mass transfer, that appear in the boundary conditions is much more difficult. For most processes, the handbooks do not contain all of the information we need. In the absence of previously published data on a relevant system, measurements are required, as described earlier. An otherwise well-formulated process model with the wrong boundary condition coefficients will yield wrong predictions. The same can be said for the coefficients in the governing equations and initial conditions.

Further details on the equations for modeling specific phenomena are described in other chapters. These include thermodynamic models in Chapter 3, mass balance and reactor models in Chapter 9, fluid flow models in Chapter 7, and heat transfer with solidification in Chapters 6 and 12.

8.5.5. Solution

Next the model equations must be solved, generally by computer. For models which do not have to run on-line, it is often easiest to employ a general-purpose commercial software package to do this, as many powerful programs are now available. These include flowsheet programs, such as METSIM (Bartlett, 1996) for the construction and solution of global balance equations for chemical reactions, based on global balances of mass and heat. These programs include thermodynamic databases and have been used successfully to model both metallurgical and chemical processes, as described in other chapters. Software specifically for thermodynamic calculations includes FACT (Thompson, 1996) and THERMO-CALC (Sundman, 1993).

Fluid flow, including 3D turbulent behavior, can be solved using any of dozens of programs. In complex geometries, finite element software, such as FIDAP (Engleman, 1994), has been used successfully (Najjar et. al., 1995). For simpler geometries, finite difference software, such as FLUENT (1996) may be more computationally efficient. For stress analysis, packages such as ABAQUS (1994) include powerful algorithms for integration of the nonlinear constitutive equations that characterize most materials processes. Most of the fluid flow and stress analysis software can also simulate heat transfer, including complex phenomena such as solidification. These packages offer convenient user interfaces to input choices which define the model equations, material property data, and boundary conditions. Evaluation of results is aided by powerful post-processing abilities built into most packages, such as color movies of contour plots of the solution variables.

It must be emphasized that commercial packages have difficulty solving the complex equations which are most relevant to real processes, even when features to model the desired phenomena are provided. For example, numerical problems are often encountered when simulating multiphase turbulent flow or free-surface movement with current fluid flow programs.

As an alternative to commercial packages, it may be better to develop a special-purpose program to model particular aspects of a specific process. This enables unique features and a faster program which is easier to use. Examples for the process of continuous casting of steel slabs include CON1D (Thomas et. al., 1992) for heat transfer in the mold, and MIX1D (Thomas and Huang, 1994) for intermixing during a grade change. Sometimes, it is convenient to use commercial packages to display the results of a special-purpose program. Software specifically designed for this task includes TEKPLOT (1996) for viewing 3D flow results on a regular grid and GNUPLOT (Williams and Kelley, 1996) for fast, simple 2D graphs on a variety of hardware.

8.5.6. Model Validation

Comparison of the model predictions with known solutions is an important step in model development to verify numerical integrity of the model for all its conceivable uses. The test problem(s) should be chosen such that the model is theoretically capable of an exact match with the known solution. Then, the values of numerical parameters (such as mesh and time step size) required to achieve acceptable accuracy can be clearly identified. To be most useful, the test problem should match the process phenomena and conditions of interest as closely as possible. This stage in model development is particularly important for self-developed codes, to ensure there are no programming errors. Testing of models based on commercial packages also verifies that they are being used correctly. Finally, this stage of model building can also provide early insights into the results, if the test problem is chosen carefully.

Test problems generally must be simple. When validating the model during this stage, however, it is best to use a test problem that invokes as many of the features of the ultimate model as possible. For example, to validate a 3D finite element model using a 1D test problem, it is best to use a single row of 3D elements. Even better is to simulate an axisymmetric test problem with a Cartesian numerical grid. In this way, a 1D solution can validate a 2D numerical scheme. Often, several different test problems are needed to validate all of the features of a process model.

8.5.7. Comparison with Experiments

Comparison of model predictions with experiments is a critical phase of using a model, once its internal numerical consistency has been verified. Important knowledge is always gained, regardless of whether or not there is a match! If the results *do* match experimental observations and measurements, then there is strong circumstantial evidence that both the model and the experiments are correct. This implies that the correct phenomena have been modeled, the assumptions are reasonable, and the constants are valid, to the extent of the match. Of course, it is always possible for a coincidental cancelation of errors, which must be carefully guarded against by comparing with as many experiments as possible.

If the model predictions do not match the experimental measurements, then something is wrong with the model, its input data, or the experiments themselves. In every case, there is an opportunity to learn something.

Sometimes, it is possible to identify a phenomenon which is responsible for the mismatch. If this phenomenon can be accounted for quantitatively in the model by changing only a few parameters, then the model can be 'calibrated' to the experiments by choosing value(s) for the parameter(s) that make the model achieve the match.

Consider, for example, an on-line 1D heat conduction model of continuous casting to trouble-shoot the origin of cracks which form at the solidification front and to optimize cooling water flow rates in the spray zone. The heat transfer coefficients may be obtained as a function of water flow rate using careful laboratory experiments. Suppose that validation of this model using plant data reveals that the model overpredicts the 'metallurgical length' of the strand, which is the distance below the top of the mold where the steel first becomes fully solid. Further comparison with a 3D version of the model on a supercomputer yields similar results, proving that the 1D assumption is not the problem. (This could also have been shown through simple scaling calculations.) The problem with this model is neglect of the tremendous enhancement in heat transfer through the liquid phase which is produced by the turbulent flow inside the solidifying steel strand. Considering the purpose of this model, it is unjustified to include a mechanistic treatment of the liquid phase, even though this could be done. Instead, the 'effective' thermal conductivity of the liquid can be increased until the model predictions match the experiments. The resulting 'calibrated' model can be implemented at the caster to make reliable, quantitative predictions so as to avoid cracks. For its intended purpose, this crude, but calibrated, model is far superior to a fully coupled model of turbulent flow, heat transfer, and solidification, which would be too slow and complex to run at the caster.

Another possibility, if experiments and model predictions do not match, is that one (or more) of the model assumptions is wrong. For example, when attempting to use a coupled thermal-stress model (as an off-line literature model) to simulate the formation of a particular surface shape defect, it was found to be impossible to match any of the facts known about the defect through plant experiments. Checking all of the model assumptions, the only one that seemed highly questionable was the assumption of uniform heat extraction. The model was therefore improved to vary heat extraction by accounting for the lower heat flow across wider interfacial gaps. It was then possible to match the experimental trends (Moitra and Thomas, 1993). Furthermore, the original simulation suggested that the defect might be avoided by finding a means to make the heat extraction more uniform. This example is offered to show that hypothesis testing using the model together with experimental measurements is a good way to gain insight.

Finally, when comparing with experiments, it is important to model the experiment exactly. Even though the experiment might not match the process as intended, it is still of value to model validation, so long as the conditions and results are measured accurately. For example, the steel shell thickness predicted by a solidification model of the continuously-cast strand might not match that measured from a 'breakout shell.' This could be due to conditions unique to the breakout, such as the extra solidification during the time taken for the molten steel to drain from the rupture in the shell. Proper accounting of special effects such as these could enable the model predictions to match the breakout shell (Moitra and Thomas, 1993). Appropriate changes would be made for subsequent use of the model to simulate standard casting conditions. Every experiment has its own potential pitfalls, which should be investigated carefully.

8.6. MODEL IMPLEMENTATION

Hopefully, a better understanding of how models are implemented in practice will lead to more effective model implementation and avoid the all-too-common waste of models that are never implemented. The ultimate goal is not to model, but to develop a process.

8.6.1. Definition of Model Implementation

A model has been 'implemented' only after the modeling exercise has led to some tangible change in the process, that ultimately benefits the industry.

To understand this definition, it must be recognized that the principal aim of industry is to make a profit. In materials processing-based industries, two possible ways to help do this are to improve product quality and to reduce production cost.

One way to improve quality is to eliminate defects. Thus, a reasonable objective for a process model could be to eliminate some defect by specifying achievable changes in the process. Note the two key terms: *eliminate* the defect and *achievable* changes.

Many process modeling efforts aim to predict the occurrence of some kind of defect, such as segregation or impurities in the product. These models may provide valuable insight into the phenomena that underlie the formation of the defect. Before it is truly useful, however, this phenomenological understanding, which is often gained only by the modeler, must be translated into beneficial process changes, such as actually eliminating the defect.

The second point is that process changes need to be achievable. Thus, models should first identify input and output variables that can be changed in the plant. Another pitfall to avoid is running the model for conditions which it is not feasible to achieve in practice. If the model is too complex for anyone else to rerun, then the potential implementation has been lost.

Changes to the plant process can be classified according to the time needed to effect them. 'Design variables' are relatively difficult and time-consuming to change. Standard operating practice, or 'SOP,' variables refer to the set points of process variables that are relatively easy to change. 'Control variables' change rapidly with time, to accommodate variations in input conditions (both accidental and intentional) and customer demands on the product.

In continuous casting, for example, mold geometry and roll spacing are design variables, that require major, expensive plant reconstruction to change. SOP variables include mold water flow rate and tundish level, which are set to desired levels. Slide gate opening position is a control variable that changes continuously to maintain a constant liquid level in the mold. Depending on the availability of on-line models, some variables, such as casting speed, can either be set at SOP levels or controlled to adapt to variations in the process (such as slowing down casting speed temporarily to avoid an impending breakout disaster). Upgrading SOP variables to control variables has obvious advantages for improving the process operation.

For a model to have any impact in industry, it must be implemented. The above definition of model implementation requires that changes take place in the plant. If nothing ever changes as a result of the modeling, then the entire exercise has been wasted. This reasonable definition sets a demanding context for the evaluation of most models reported in the literature. The rest of this section explores how process models are implemented according to this definition, and comments on the implications for process modelers.

8.6.2. Ways of Implementing a Model

There are many paths to model implementation, illustrated in Fig. 8.3. Process models are classified here according to how their results are implemented into practical process changes:

- Fully on-line models
- Semi-on-line models
- Off-line models
- Literature models

On-line models implement beneficial change in the plant directly. Off-line and literature models contribute to process understanding, leading to implementation by others. Semi-on-line models lie somewhere between. The next sections further define and examine how each type of model is implemented, in order of its immediate impact in industry.

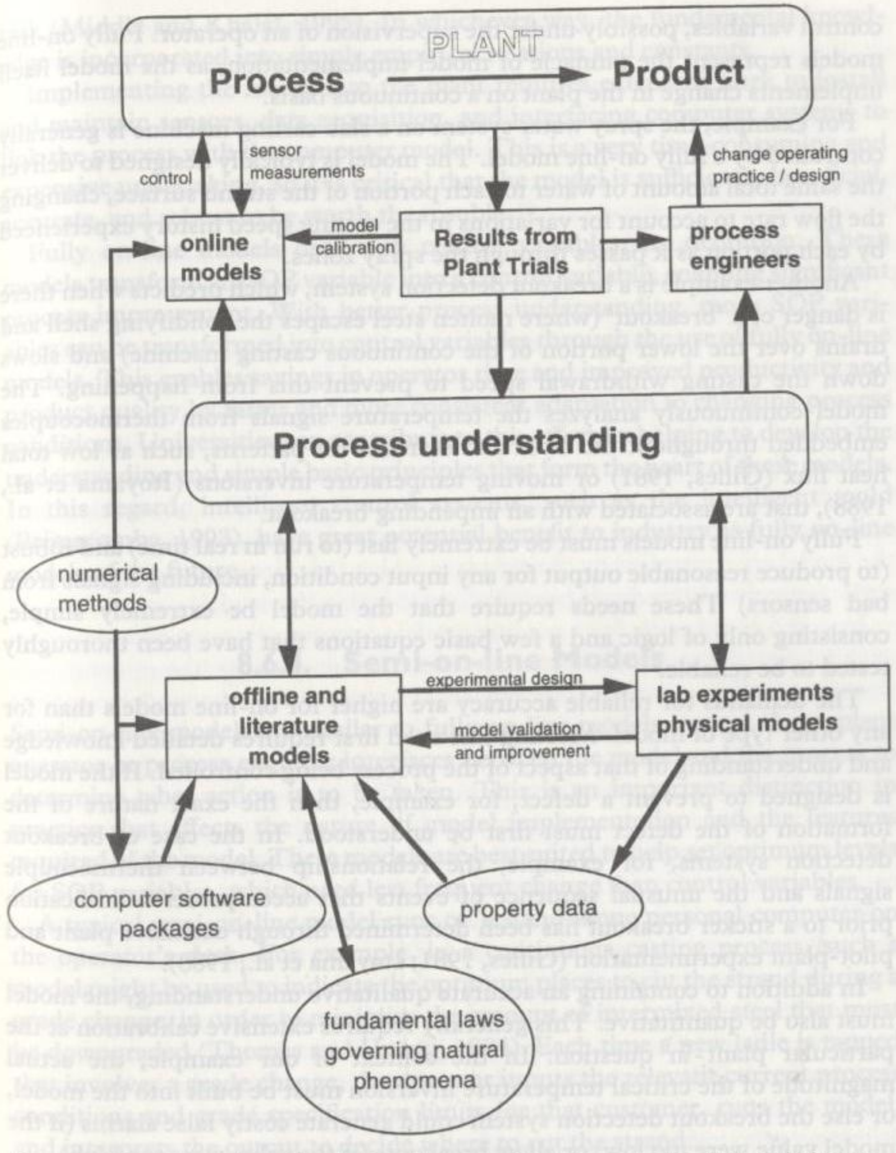
PLANT
Process
Product
control
sensor measurements
change operating practice / design
online models
model calibration
Results from Plant Trials
process engineers
Process understanding
numerical methods
offline and literature models
experimental design
model validation and improvement
lab experiments physical models
computer software packages
property data
fundamental laws governing natural phenomena

Figure 8.3. Flow chart for the implementation of process models in industry.

8.6.3. Fully On-line Models

Fully on-line models are part of the computer system controlling the process at the plant. They obtain their input data directly from the system (which has access to the relevant sensor signals) and make direct changes to specific control variables, possibly under the supervision of an operator. Fully on-line models represent the pinnacle of model implementation, as the model itself implements change in the plant on a continuous basis.

For example, the spray water system on a slab casting machine is generally controlled by a fully on-line model. The model is typically designed to deliver the same total amount of water to each portion of the strand surface, changing the flow rate to account for variations in the casting speed history experienced by each portion as it passes through the spray zones.

Another example is a breakout detection system, which predicts when there is danger of a 'breakout' (where molten steel escapes the solidifying shell and drains over the lower portion of the continuous casting machine) and slows down the casting withdrawal speed to prevent this from happening. The model continuously analyzes the temperature signals from thermocouples embedded throughout the mold and searches for patterns, such as low total heat flux (Gilles, 1981) or moving temperature inversions (Itoyama et al., 1988), that are associated with an impending breakout.

Fully on-line models must be extremely fast (to run in real time) and robust (to produce reasonable output for any input condition, including signals from bad sensors) These needs require that the model be extremely simple, consisting only of logic and a few basic equations that have been thoroughly tested to be reliable.

The demands for reliable accuracy are higher for on-line models than for any other type of model. Meeting this need first requires detailed knowledge and understanding of that aspect of the process being controlled. If the model is designed to prevent a defect, for example, then the exact nature of the formation of the defect must first be understood. In the case of breakout detection systems, for example, the relationship between thermocouple signals and the unusual sequence of events that accompanies solidification prior to a sticker breakout has been determined through extensive plant and pilot-plant experimentation (Gilles, 1981; Itoyama et al., 1988).

In addition to containing an accurate qualitative understanding, the model must also be quantitative. This generally requires extensive calibration at the particular plant in question. In the context of our example, the actual magnitude of the critical temperature inversion must be built into the model, or else the breakout detection system could generate costly false alarms (if the model value were too low) or allow breakouts (if the value were too high).

Generating the knowledge needed, and refining it into a few simple equations, is the most demanding part of fully on-line model development. Fortunately, the model need only produce accurate results for the limited set of process conditions at a particular plant. Therefore, the equations may be based on curve-fits of the results from plant, pilot-plant, physical model, or laboratory-scale measurements, or even sophisticated numerical experiments. Optimization methods such as neural networks provide a useful tool for this task (Middle and Khalaf, 1995). In whichever way, the fundamental knowledge is incorporated into simple empirical relations and constants.

Implementing the model into the plant requires extensive work to install and maintain sensors, data acquisition, and interfacing computer systems to link the process with the computer model. This is a very time-consuming and expensive undertaking, so it is critical that the model is sufficiently beneficial, accurate, and robust to be worth the trouble.

Fully on-line models deal with control variables, by definition. These models transform an SOP variable into a control variable, enabling significant process improvement. With better process understanding, more SOP variables can be transformed into control variables through the use of fully on-line models. This enables savings in operator time and improved productivity and product quality by faster and more consistent adaptation to changing process conditions. Universities can contribute to this effort by helping to develop the understanding and simple basic principles that form the heart of these models. In this regard, intelligent control systems, such as the intelligent mold (Brimacombe, 1993), have great potential benefit to industry as fully on-line models of the future.

8.6.4. Semi-on-line Models

Semi-on-line models are similar to fully on-line models, except that a plant operator or process engineer interfaces between the model and the process to determine what action is to be taken. This is an important distinction in practice that affects the nature of model implementation and the features required of the model. These models are best suited to help set optimum levels for SOP variables, which need less frequent change than control variables.

A typical semi-on-line model runs on a stand-alone personal computer on the operator's desk. For example, in a continuous casting process, such a model might be used to indicate the optimum places to cut the strand during a grade change, in order to minimize the amount of intermixed steel that must be downgraded (Thomas and Huang, 1994). Each time a new ladle is tapped that involves a grade change, the operator inputs the relevant current process conditions and grade specification limits for that customer, runs the model, and interprets the output to decide where to cut the strand.

A semi-on-line model could also act as a tool for trouble-shooting and on-the-spot problem solving. For example, a fully-calibrated, 1D heat-transfer model of a continuous slab caster could be used to determine which rolls to change or realign in order to solve certain types of cracking problems. It does this by calculating the shell thickness as a function of distance down the strand. Misaligned or worn rolls can generate certain types of internal cracks by straining the weak solid at the solidification front. The initiation point of these cracks, measured on a sectioned sample of the slab, corresponds to the location of the solidification front at the time the crack was formed. For this model to be effective, it must be calibrated for the different grades and casting conditions at that plant. In addition, the operator must have access to the metallurgical results and knowledge about the cracks. More advanced semi-on-line models, such as the expert system of billet casting developed by Brimacombe and coworkers (Brimacombe, 1993), make this analysis even easier, and supply useful knowledge to solve other types of problems as well.

Sometimes, a good, well-calibrated model can be implemented in more than one way. For example, the 1D heat conduction model just discussed could also be applied to optimization of cooling water flow rates in the spray zone of the continuous slab casting machine in order to achieve a desired temperature history for the steel surface and thereby avoid surface cracks.

Semi-on-line models have many attributes that are similar to fully on-line models. Both must run very quickly (a decision is often needed within a minute) and make quantitatively accurate predictions, thus requiring extensive model calibration at the plant. In both cases, the potential benefits from the model are controlled by the extent to which the phenomena governing the process are understood and properly quantified in the model.

In comparison with fully on-line models, semi-on-line models are better suited to modeling complex phenomena. This is because the operator can respond to information and circumstances unforeseen by the model to make a better decision. It is also easier for the operator to learn from the semi-on-line model, which serves as a valuable means of technology transfer between the model developer and the plant operator. The semi-on-line model requires substantially less effort to implement into the plant, as fewer computer automation and interfacing systems are needed. It is consequently much easier to change the model, to modify or add new knowledge and capabilities.

An important feature of semi-on-line models is that they must be easy to run and have a very 'user-friendly' interface with the operator. Developing this interface is one of the difficult tasks which separates these models from all others. Semi-on-line models which prove to be worthy might eventually be implemented as fully on-line models. The semi-on-line stage provides the opportunity to learn about the process, and optimize the model by determining all of the essential minimum number of input variables, in addition to refining its accuracy and robustness.

8.6.5. Off-line Models

Off-line models are used by process engineers and designers (in the plant, research, quality control, etc.) to gain personal insights and understanding about a process. The model results are then implemented in the plant by developing new designs or changes to standard operating practices. These models are not as immediately beneficial as on-line models, because off-line models at best can only help to prevent a problem from occurring the *next* time. More importantly, model implementation relies solely on the model user.

To implement beneficial changes, the user of an off-line model must have a thorough understanding of both the process and the model. The model developer should make it clear (through the user manual) what the model assumptions are. To generate the process understanding, Fig. 8.3 illustrates how the off-line model is just one of the tools that can be used. Model results are implemented in combination with the user's personal knowledge obtained from plant, pilot-plant, physical model, and laboratory experiments, and previous literature and other sources.

As shown in Fig. 8.3, the process understanding gained from all of these sources can help a process engineer to implement positive changes in the plant. This can help to avoid the dangerous short cut, also shown in Fig. 8.3, of implementing changes in the plant on the basis of trial results without understanding the process.

Off-line models can help to provide insights in many different ways. They can correct misconceptions about the process, by quantifying phenomena (such as internal temperature and flow patterns) that the process engineer has never seen or measured. The model can also be used for hypothesis testing, by putting numbers on a hand-waving argument. For example, a qualitative mechanism may be suggested to explain some observed event in the plant. A process model could quantify the mechanism, which can then be reevaluated based on how closely the model results match the expected behavior.

Generally, the next stage of implementation is to design plant trials to test the expected improvements. Off-line models can help in this experimental design. They are most useful when the plant trials are very expensive. This is certainly the case when developing a new process. Tracking the effect of a process change on the incidence of a defect in an existing process may also be expensive. This is because it is usually impossible to control plant experiments very well, so that the results are statistical; this situation demands long trials before a conclusion can be made with confidence. Off-line models are also important to understanding the results of plant trials.

Another stage of implementation is finding the 'optimum' way to run the process to save money. Parametric studies or 'numerical experiments' with an off-line model can play an important role in this regard. For example, the model of intermixing during a grade change discussed previously could be used off-line to investigate how to minimize the amount of downgraded steel created. The process engineer could learn by running the model that draining the tundish to a low level before opening the ladle and decreasing the casting speed during the grade change would shorten the downgraded length. Further investigation would be required to determine whether the slowdown in production to save this amount of downgrading is cost-effective. If beneficial, the new practice could be implemented in the plant through changes in the standard operating practice.

Off-line models should be easy to use, leaving time for the user to pursue insights using other tools and to implement the results. Rapid turnaround time between model runs is also important to attain the immediacy needed to understand the behavior of the model. Although commercial packages are the most popular framework for off-line models, they only barely satisfy these requirements. If a process model is too difficult to use, it may be easier to obtain the needed knowledge another way, such as through experiments, or even trial and error in the plant.

To help implement changes, off-line models must be able to simulate process situations outside the scope of prior experience. Thus, the model should be as mechanistic as possible, with its roots grounded solidly in fundamental principles, as illustrated in Fig. 8.3. Properly incorporating the phenomena which govern that aspect of the process being modeled allows the model to make reasonable predictions for new conditions. This enables implementation of new designs and radical changes in operating conditions. It also makes model validation and calibration with experiments easier.

Unfortunately, the same sophistication that enables off-line advances in understanding also tends to complicate and slow down the model. This makes the model difficult to use on-line. Sometimes, a simplified version of an off-line model can be developed for on-line use later.

8.6.6. Literature Models

Literature models are defined here as off-line models which are used only by the person(s) who developed the model. Furthermore, the modeler has no direct contact with the process (working generally in a university or research environment). The only direct way for these models to be implemented (if they are implemented at all!) is by someone else using the reported results.

At their best, literature models can act as off-line models, possibly saving a process engineer time in developing and running a very complex model. Moreover, the literature model can afford the luxury of long computing times (even a week on a supercomputer) and so may include more of the phenomena which govern the process.

As with the off-line model, the knowledge and insights gained by the process engineer are more important than the model itself. It is therefore important that conclusions from the model be communicated clearly. The more practical and specific the insights, the easier for implementation. It is perfectly reasonable to combine the modeling results with experimental results, physical models, and plant data, perhaps found in existing literature. The aim is to present as complete an understanding as possible to the person reading the paper. Ideally, the process engineer can search the literature to learn how to solve his specific problem and implement a course of action in the plant, in a similar manner to a doctor diagnosing and treating a patient.

Because the modeler and user are the same person, significant short-cuts in developing the user interface of the model are permitted. Of course, this usually makes the model too complex and 'user-vicious' to be run by anyone else but the modeler.

A key attribute of the literature model is that there is no opportunity for the process engineer to rerun the model. All of the parametric studies must be done by the original author. For the results to be implemented, it is important that the modeler make reasonable assumptions regarding both the phenomena included in the model and the input conditions adopted in parametric studies. To do this, the modeler must obtain a good understanding of the process.

The implementation value of a model is less when it merely echoes knowledge already known through plant experience or other means. Its value is negative when it contradicts some of that knowledge and fails to explain why. Particularly for well-established processes, there is a great deal of knowledge already in existence. To ensure a positive contribution to industry, this prior knowledge should be taken into account. Well-studied processes generally require more sophisticated models for the contribution of new knowledge than early models of a new process.

To be useful to industry, the results are best presented in the form recommended by Herbertson and Austin (1993) in Fig. 8.4. In this figure, 'you' refers to the process engineer, so ideally the *y* axis should relate to some

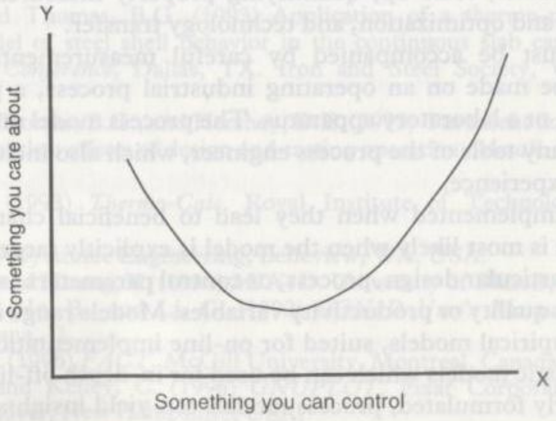

Figure 8.4. Graph containing results that can be implemented.

aspect of quality or productivity. The x axis should contain a design or operating variable which can be changed in the plant.

The modeler should avoid presenting results in terms of intermediate variables, which are difficult to control, or even measure, in practice. For example, it is natural to use a model to find the desired heat flux or heat transfer coefficient needed to optimize some aspect of a given process. This is not as useful as specifying the actual fluid flow rate needed to achieve this heat transfer condition for the specific process under consideration.

The quality of presentation of the results is independent from their accuracy. Potential weaknesses of a model should be identified, in addition to its strong points. It is also useful to point out when the results are known to form upper or lower bounds to the true behavior. To increase the credibility of the entire modeling community, it is the responsibility of each modeler to continually strive for accurate modeling conclusions, by understanding the process of interest and validating the model.

8.7. SUMMARY

The rapid development of computer hardware and software over three decades has made the mathematical model a key component in process development. This chapter has presented some guidelines for the development and implementation of process models.

A successful model must have a purpose, which dictates how choices are made during its development. Reasons for modeling include increasing process understanding, helping with the design of experiments, evaluation of experimental results, scale-up, quantifying property measurement, on-line process control and optimization, and technology transfer.

Modeling must be accompanied by careful measurements as needed, whether they be made on an operating industrial process, a pilot plant, a physical model, or a laboratory apparatus. The process model must be viewed as one of the many tools of the process engineer, which also includes previous literature and experience.

Models are implemented when they lead to beneficial changes to plant operation. This is most likely when the model is explicitly targeted at understanding how particular design, process, or control parameters can be changed to affect specific quality or productivity variables. Models range in complexity from simple empirical models, suited for on-line implementation, to sophisticated mechanistic models which can be used for in-depth off-line analysis.

When properly formulated, process models can yield insights into process behavior that cannot be fathomed by other means, and lead to significant process improvements. However, when key phenomena are ignored, or predictions are analyzed carelessly, great harm can be done. Successful modeling requires understanding of both the industrial process and the computer model. The process engineer has the responsibility to ensure that a process model adequately represents a system and interprets the results appropriately.

REFERENCES

ABAQUS (1994) Hibbitt, Karlsson & Sorensen, Inc., 1080 Main Street, Pawtucket, Rhode Island 02860, USA.

Bartlett, J. (1996) *METSIM*, Proware, 5237 N. Via Velasquez, Tucson, AZ 85750, USA.

Brimacombe, J.K. (1993) Empowerment with knowledge—toward the intelligent mold for the continuous casting of steel billets. *Metall. Trans. B* **24B**, 917–935.

Engleman, M.S. (1994) *FIDAP*, Fluid Dynamics International, Inc., 500 Davis Ave., Suite 400, Evanston, IL 60201, USA.

FLUENT (1996) Fluent, Inc., 10 Cavendish Court, Lebanon, New Hampshire, USA.

Gilles, H.I. (1981) Breakout protection by automatic mold heat removal control. *2nd Process Technology Conference*. Iron and Steel Society, Warrendale, PA, pp. 205–212.

Herbertson, J. and Austin, P. (1993) The application of mathematical models for optimization of continuous casting. *Modeling of Casting, Welding, and Advanced Solidification Processes—VI*, Palm Coast, FL. TMS, Warrendale, PA, pp. 689–700.

Itoyama, S. et. al. (1988) Prediction and prevention system for sticking type breakout in continuous casting. *71st Steelmaking Conference Proceedings*. Iron and Steel Society, Warrendale, PA, pp. 97–102.

Middle, J. and Khalaf, G.H. (1995) Neural network modelling of temperature distribution for control of gas metal arc welding. *Modeling of Casting, Welding, and Advanced Solidification Processes—VII*, London. TMS, Warrendale, PA, pp. 397–405.

Moitra, A. and Thomas, B.G. (1993) Application of a thermo-mechanical finite element model of steel shell behavior in the continuous slab casting mold. *76th Steelmaking Conference*, Dallas, TX. Iron and Steel Society, Warrendale, PA, pp. 657–667.

Najjar, F.M., Thomas, B.G., and Hershey, D.E. (1995) Turbulent flow simulations in bifurcated nozzles: effects of design and casting operation. *Metall. Trans. B* **26B**(4), 749–765.

Sundman, B. (1993) *Thermo-Calc*. Royal Institute of Technology, Stockholm, Sweden.

TEKPLOT (1996) Amtec Engineering, Belleview, WA, USA.

Thomas, B.G. and Huang, X. (1994) *MIX1D*. University of Illinois, Urbana, IL.

Thomas, B.G., Ho, B., and Li, G. (1992) *CON1D User's Manual*. University of Illinois, Urbana, IL.

Thompson, W. (1996) *FACT*. McGill University, Montreal, Canada.

Williams, T. and Kelley, C. (1996) *GNUPLOT*. Pixar Corporation, Dartmouth College, Hanover, New Hampshire, USA.

Zienkiewicz, O.C. and Taylor, R.L. (1988) *The Finite Element Method*, 4th edn. McGraw-Hill, New York.

9

Analysis of metallurgical reactors

T. Abel Engh
Norwegian University of Science and Technology,
Trondheim, Norway

9.1. INTRODUCTION

In a metallurgical reactor usually at least two phases are involved: gas–solid, gas–liquid or liquid–solid (Koros and Pierre, 1991; Rosenqvist, 1983; Tien and Elliott, 1981; Turkdogan, 1980). Heat and/or mass is transferred from one phase to the other (Szekely and Themelis, 1971; Themelis, 1995). Since capital costs depend on the reactor volume, it is important that the contact area between these phases per unit volume is large. Usually productivity is determined by mass and/or heat transfer at this contact area at high temperatures, not by chemical reaction rates.

There are two main idealized types of reactors (see Fig. 9.1)

- Batch reactors, where the variables that describe the state of the reactor change with time (Alcock, 1976; Oeters, 1989)
- Continuous steady-state reactors, where the variables do not change with time (Perry and Green, 1984)

For both reactor types, variables that describe the state of the reactor may change with position in the reactor.

However, in this short chapter it would go too far to deal with systems where the variables such as concentrations and temperatures change with both time and position. To illustrate the behavior of batch and continuous reactors as simply as possible, examples are taken from refining of metals where a small amount of a dissolved impurity is to be removed. In these systems simple approximations for the mass balances may be employed. Also the thermo-

ADVANCED PHYSICAL CHEMISTRY FOR PROCESS METALLURGY
ISBN 0-12-618920-X

Copyright © 1997 Academic Press Ltd
All rights of reproduction in any form reserved

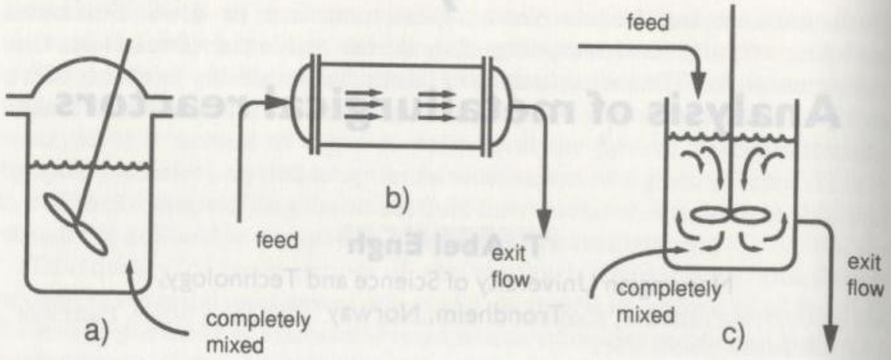

Figure 9.1 Three main types of reactors: (a) completely mixed batch reactor; (b) piston flow reactor; (c) completely mixed continuous reactor.

dynamics may be relatively simple: the impurity obeys Henry's law (Gaskell, 1973).

With low capital costs and high reactant utilization in mind it is important that there are no 'dead volumes' in the reactor. The 'residence time' in continuous reactors should be the same for all parts of a phase fed into the unit. If the residence time is too short, then the reactants are not fully utilized (converted), while too long a residence time only serves to 'fill up the reactor' after conversion is completed. In a continuous shaft furnace (Biswas, 1981), rotary kiln, or fluidized bed (Davidson et al., 1985), solids of the same size and composition (pellets, for instance) should ideally be exposed to the same conditions (gas composition and temperature profiles). Complete conversion would then take place in time t and the residence time should be equal to t. In the design of reactors we seek to attain this ideal. Then, at least as a first approximation, such reactors can be described in terms of the time t elapsed for an element moving along the length, z, of the reactor (or alternatively employing z or a concentration or temperature as independent variable). We call this a linear reactor and, if the residence times are nearly the same, a 'piston flow' reactor (Szekely, 1966). Often we are very far from the ideal of piston flow. This is discussed at some length.

The gas or liquid may move in the same direction as the solids (cocurrent flow) or in the opposite direction (countercurrent flow). To give a high utilization of reactants and efficiency of heat transfer, countercurrent linear reactors (such as the blast furnace) are used. Countercurrent reactors are discussed in some detail in this chapter. It is seen that heat and mass transfer can be described in terms of rate equations that are very similar.

9.2. PRINCIPLES OF REMOVAL OF DISSOLVED ELEMENTS AND PARTICLES IN REFINING REACTORS

As mentioned, refining reactors are treated in order to illustrate in a simple manner important points in the analysis of metallurgical reactors (Coudrier et al., 1985).

In a refining reactor dissolved impurities and unwanted particles (inclusions) are removed. The methods available for removal of dissolved impurities may be listed as follows (Engh, 1992).

- The impurity X reacts with a second phase that may be solid, molten, or gaseous. For instance, sodium is withdrawn from molten aluminum by burning with oxygen in the air at the bath surface.
- X is transferred to another phase—not soluble in the molten metal—where X has a high solubility. An example from steelmaking is the transfer of sulfur from molten iron to slag (Nilsson et al., 1994). For aluminum this mechanism often is undesirable. Thus sodium is 'picked-up' from the cryolite in the Héroult–Hall cell (Grjotheim and Welch, 1988).
- X reacts with another element added to the melt. A well-known example is the reaction of chlorine bubbled through molten aluminum (together with argon) with sodium. The reaction product, whether solid, liquid, or gaseous, has to be removed from the melt. This removal may be produced by the effect of gravity or buoyancy forces, inertial forces, or forces generated by stirring the melt.
- An electric potential is applied to separate X and metal by electrolysis (Claessens and Harris, 1990).
- The molten metal is allowed to solidify partially or a solid is partially melted. X is enriched in either the solid or liquid phase, and this phase is removed (Lux and Flemings, 1979).

All the methods outlined above are applied industrially. The last method is only used for special high-cost materials. The last two methods are not discussed here. The first and third, closely related, methods are widely employed. The essential point is that the impurity is transferred from the molten metal to another phase.

The principles for removal of inclusions are very similar to those applying to dissolved elements. The main difference is that the particles often are not transferred *into* the other phase but only enter or approach the interface between the molten metal and the other phase. For instance, the inclusions may stick to the walls of a ladle, holding furnace, or filter (Raiber et al., 1995) or they may rise to the surface or settle to the bottom of the melt.

An impurity element can never be eliminated completely from the metal.

The sodium content in aluminum may be as low as one part per million. Though low, this level may still play a role in determining the physical and mechanical properties of the final product.

What determines the final levels of an impurity in a melt? Is it the equilibrium between the impurity content in the metal and in the phase that is extracting the undesirable component, or is it mass transfer? Whatever the case, some impurity will remain.

If removal is determined by mass transfer, the rates are governed by the contact area between the two phases and by the driving force. In the most favorable case the driving force is proportional to the concentration x. We realize that as x is reduced in a batch melt, removal becomes slower and slower. Thus a fundamental problem is that the time required may be so long that the cost becomes prohibitive. For continuous reactors we find that this situation becomes even worse.

9.3. KINETICS AND MIXING

Chemical reaction rates increase strongly with temperature (Ward, 1962). The Arrhenius and Eyring (Glasstone et al., 1941) relations tell us that rates increase roughly exponentially with temperature. Thus, in purification operations involving molten metals at high temperatures it is usually assumed that chemical reaction rates are not rate limiting.

Intuitive reasoning suggests that reaction rates are speeded up by increased stirring or 'mixing.' This is only partly true, as seen in the following. Mixing may be performed by the use of mechanical stirrers, oscillating ladles, gas stirring (bubbling), electromagnetic stirring (Szekely, 1979), pouring from one ladle to another (Perrin process), and pumps. Electromagnetic stirring and mixing by pumps seem to be interesting fields for molten metals, though they may not have been properly explored as yet. Stirring by gas is commonly employed (Lehner et al., 1991). A porous plug or lance is often used. However, they often do not give a sufficient metal–gas contact area. Therefore rotors or impellers—usually of graphite—have been developed that both stir the melt and produce small bubbles that give a large contact area (Nagata, 1975).

In the following it will be assumed that mixing or stirring is sufficient to give the same concentration of dissolved elements and inclusions throughout the bath, so that concentration does not depend on spatial coordinates. Then even though the diameter of the impeller is, for instance, only 1/4 of the vessel dimensions, one cannot detect differences between concentrations near the impeller and near the walls. Such a unit is called a backmix tank (see Fig. 9.2).

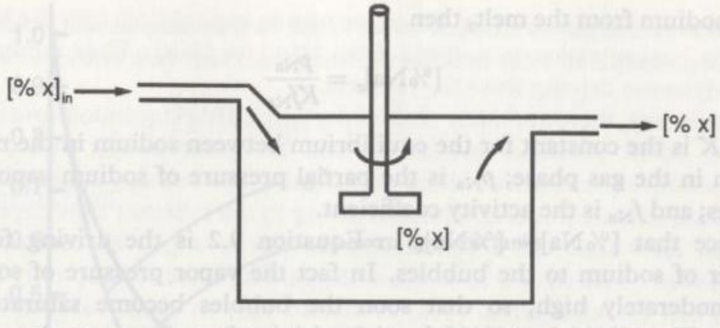

Figure 9.2 Continuous backmix tank (where melt is completely mixed). Surface area of bubbles is A_b.

At the interface between two phases, such as metal and gas, movement is along the interface and not normal to it. Now the main mechanism for transport of a dissolved element or an inclusion is no longer convection or large turbulent eddies. Instead, transport of dissolved elements to a large degree must depend on the slow mechanism of diffusion. The mass transfer coefficient for the melt, k, may be estimated by relations of the type found in penetration theory (Bird et al., 1960):

$$k \sim (D/t)^{1/2} \tag{9.1}$$

where D is the diffusion coefficient and t is the residence time of the melt at the interface.

Often the product of k and the contact area A determines the kinetics of the purification process. This is the case when kA is too small to allow equilibrium to be reached. For transfer between two phases we must in general account for the resistance to transfer on both sides of the interface. In this case a 'total' mass transfer coefficient, k_{tot}, is introduced that takes both resistances into account. At a gas–liquid interface k_{tot} is usually determined by k for the liquid boundary layer (Engh, 1992).

Let us take removal of sodium from molten aluminum as an example to illustrate the kinetics involved. Then the mass of sodium transferred per second, M_{Na}, is given by

$$M_{Na} = \frac{k_{tot}\rho A}{100}([\%Na] - [\%Na]_e) \tag{9.2}$$

where ρ is the density of the aluminum melt. In accordance with the usual practice in refining metallurgy, concentrations are here given in units of mass percent. $[\%Na]_e$ is the hypothetical concentration in the melt in equilibrium with sodium in the other (extracting) phase. For instance, if inert gas is used to purge sodium from the melt, then

$$[\%\mathrm{Na}]_e = \frac{p_{\mathrm{Na}}}{K f_{\mathrm{Na}}} \tag{9.3}$$

where K is the constant for the equilibrium between sodium in the melt and sodium in the gas phase; p_{Na} is the partial pressure of sodium vapor in the bubbles; and f_{Na} is the activity coefficient.

Notice that $[\%\mathrm{Na}] - [\%\mathrm{Na}]_e$ in Equation 9.2 is the driving force for transfer of sodium to the bubbles. In fact the vapor pressure of sodium is only moderately high, so that soon the bubbles become saturated with sodium. Then $[\%\mathrm{Na}]_e \approx [\%\mathrm{Na}]$ and the driving force for removal approaches zero.

If a reactive gas such as chlorine is present in the purge gas, then $[\%\mathrm{Na}]_e$ is determined by the equilibrium

$$\underline{\mathrm{Na}} + \tfrac{1}{2}\mathrm{Cl}_2 = \mathrm{NaCl} \tag{9.4}$$

This reaction is completely displaced to the right so that $[\%\mathrm{Na}]_e$ in Equation 9.2 is effectively zero. This assumption is employed in the following. It is also used for the bath surface where sodium burns with oxygen in the air. This reaction is also displaced far to the right.

9.4. BATCH AND CONTINUOUS REACTORS

Batch and continuous reactors are compared using examples from the refining of aluminum. Batch reactors are common in foundries, while continuous reactors are widely used in the cast-house in the primary aluminum industry. We may set up the following mass balance for sodium in a batch backmix tank:

Reduction of sodium in the melt
= sodium removed by chlorine in bubbles and by oxygen in the air

or

$$-\frac{M}{100}\frac{d[\%\mathrm{Na}]}{dt} = k_b \rho A_b \frac{[\%\mathrm{Na}]}{100} + k_s \rho A_s \frac{[\%\mathrm{Na}]}{100} \tag{9.5}$$

where M is the mass of the melt; k_b and k_s are the total mass transfer coefficients for bubbles and melt surface, respectively; and A_b and A_s are the respective contact areas.

Discarding the common factor 1/100 and integrating, one obtains

$$\frac{[\%\mathrm{Na}]}{[\%\mathrm{Na}]_i} = \exp(-\rho(k_b A_b + k_s A_s)t/M) \tag{9.6}$$

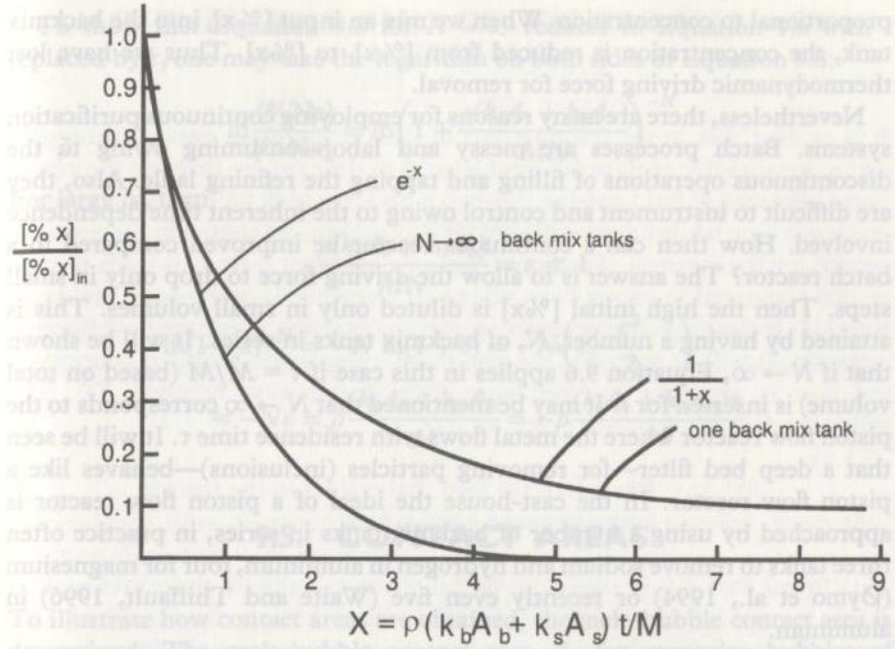

Figure 9.3 Ratio between concentration $[\%x]$ and original concentration $[\%x]_i$ as a function of $X = \rho(k_b A_b + k_s A_s)t/M$. For continuous reactors, τ replaces t.

where $[\%\mathrm{Na}]_i$ is the concentration of sodium in the melt that enters the tank, and $[\%\mathrm{Na}]$ is the concentration that leaves the tank.

The concentration drops exponentially as illustrated in Fig. 9.3. k_b and k_s increase somewhat with the circulation velocity. However, the most effective measure that can be taken to reduce $[\%\mathrm{Na}]$ is to increase the bubble melt contact area, A_b.

Figure 9.2 schematically shows a continuous reactor where the volume and contact areas are the same as for the batch reactor. M is the mass flow of molten aluminum through the reactor. A mass balance, taking sodium as an example, in this case gives that the left-hand side of Equation 9.5 is replaced by $(M/100)([\%\mathrm{Na}]_i - [\%\mathrm{Na}])$. One obtains

$$\frac{[\%\mathrm{Na}]}{[\%\mathrm{Na}]_i} = \left(1 + \frac{\rho(k_b A_b + k_s A_s)}{M}\right)^{-1} \tag{9.7}$$

Equations 9.6 and 9.7 are compared in Fig. 9.3—employing x for concentration in indicating the functional forms. It is seen that removal is much poorer in the continuous reactor, especially at low ratios $[\%x]/[\%x]_i$. It may be fruitful to speculate a little regarding the above result. Removal rates are proportional to concentration. When we mix an input $[\%x]_i$ into the backmix tank, the concentration is reduced from $[\%x]_i$ to $[\%x]$. Thus we have lost thermodynamic driving force for removal.

Nevertheless, there are many reasons for employing continuous purification systems. Batch processes are messy and labor-consuming owing to the discontinuous operations of filling and tapping the refining ladle. Also, they are difficult to instrument and control owing to the inherent time dependence involved. How then can a continuous reactor be improved compared to a batch reactor? The answer is to allow the driving force to drop only in small steps. Then the high initial $[\%x]$ is diluted only in small volumes. This is attained by having a number, N, of backmix tanks in series. It will be shown that if $N \to \infty$, Equation 9.6 applies in this case if $\tau = M/\dot{M}$ (based on total volume) is inserted for t. It may be mentioned that $N \to \infty$ corresponds to the piston flow reactor where the metal flows with residence time τ. It will be seen that a deep bed filter—for removing particles (inclusions)—behaves like a piston flow reactor. In the cast-house the ideal of a piston flow reactor is approached by using a number of backmix tanks in series, in practice often three tanks to remove sodium and hydrogen in aluminum, four for magnesium (Øymo et al., 1994) or recently even five (Waite and Thiffault, 1996) in aluminum.

For N tanks in series it is found by repeatedly using Equation 9.7 where indices 1, 2 refer to the first and second tanks and so on:

$$\frac{[\%x]}{[\%x]_i} = \frac{[\%x]_1}{[\%x]_i}\,\frac{[\%x]_2}{[\%x]_1}\cdots\frac{[\%x]}{[\%x]_{N-1}}$$

Thus if all N tanks have the same contact areas,

$$\frac{[\%x]}{[\%x]_i} = \left(1+\frac{\rho(k_sA_s+k_bA_b)}{\dot{M}N}\right)^{-N} \tag{9.8}$$

Note that the contact areas in each tank are $1/N$th of the total contact area.

For instance if $\rho(k_sA_s + k_bA_b)\dot{M} = 3$ and $N = 3$,

$$\frac{[\%x]}{[\%x]_i} = \left(1+\frac{3}{3}\right)^{-3} = \frac{1}{8}$$

while for the piston flow reactor

$$\frac{[\%x]}{[\%x]_i} = \exp\left(-\frac{\rho(k_sA_s+k_bA_b)\tau}{M}\right) = \exp(-3) = \frac{1}{20}$$

Thus it is seen that if very low impurity levels are required, even three backmix tanks in series can not compete with a piston flow reactor. Here the melt residence time, τ, in the reactor has been introduced, $\tau = M/\dot{M}$.

To show that Equation 9.8 for $N \to \infty$ reduces to Equation 9.6 with t replaced by τ, one may take the logarithm on both sides of Equation 9.8:

$$\ln\frac{[\%\mathrm{Na}]}{[\%\mathrm{Na}]_i} = \ln\left(1+\frac{\rho(k_sA_s+k_bA_b)}{\dot{M}N}\right)^{-N}$$

For large N, then

$$\frac{\rho(k_sA_s+k_bA_b)}{\dot{M}N} = \varepsilon \ll 1$$

$$\ln(1+\varepsilon)^{-N} = -N\ln(1+\varepsilon) = -N\left(\varepsilon-\frac{\varepsilon^2}{2}\cdots\right)$$

$$\approx -N\varepsilon = \rho\frac{(k_sA_s+k_bA_B}{\dot{M}} = -\rho\frac{(k_sA_s+k_bA_b)\tau}{M}$$

9.5. CONTACT AREAS

To illustrate how contact areas are obtained, the melt–bubble contact area is determined. The melt–bubble contact area A_b for monosize bubbles of diameter d is

$$A_b = \dot{n}\pi d^2 \tau_b$$

where $\dot{n}$ is the number of bubbles produced per unit time.

$\dot{n}$ is given by the gas flow rate $\dot{Q}$ in m^3 s^{-1} (SI units are employed)

$$\dot{n} = \dot{Q}\Big/\frac{\pi d^3}{6}$$

τ_b is the residence time of the bubble in the melt, $\tau_b = H/v_b$. These relations give

$$A_b = \frac{6\dot{Q}H}{v_b d} \tag{9.9}$$

where H is the bath height above the gas inlet point and v_b is the rise velocity of the bubble relative to the reactor walls. Equation 9.9 shows that the contact area is inversely proportional to bubble size d, proportional to the gas flow rate $\dot{Q}$ and depth H, and inversely proportional to bubble rise velocity v_b. Equation 9.9 is easily generalized to the practical case where we have (an often wide) distribution of bubble sizes. The most important point is that the contact area is inversely proportional to d. This remark applies also for liquid–droplet, gas–solid and gas–droplet systems if d is taken as the characteristic dimension of the droplets or solids.

9.6. THE RESIDENCE TIME DISTRIBUTION FUNCTION

It is evident that in general elements of fluid or particles passing through a continuous reactor require different lengths of time to pass through the vessel. Some elements of fluid passing through a backmix tank will have a very short residence time while others will stay for a long time. As shown in the previous section for the removal of sodium from an aluminum melt, this leads to poor results compared to piston flow, where all elements have the same residence time τ. It is clear that it is necessary somehow to characterize the flow through a reactor. It will be seen that the minimum information required concerning the flow is given by the residence time distribution function $f(t)$. The following definition may be given for $f(t)$:

$$f(t)\,\Delta t = \text{fraction of the feed that resides in the reactor a time between } t \text{ and } t + \Delta t \tag{9.10}$$

It is found that $f(t)$ is especially useful when calculating the conversion of solids in reactors such as a shaft furnace, rotary kiln, or fluidized bed. One reason for this is that the solids may have kinetics that strongly depend on the residence time t in the reactor.

In principle $f(t)$, at least for fluids, could be obtained from extensive numerical calculations of fluid flow in the reactor. However, hitherto it has been more practical to determine $f(t)$ from tracer measurements (Engh et al., 1971a,b, 1973). A tracer may be defined as an inert addition at the inlet that may be measured at the reactor exit and that flows through the reactor in the same manner as the feed. The mass of the tracer is small compared to the total mass in the reactor.

To illustrate how $f(t)$ may be obtained from the tracer concentration $c(t)$ in (kg tracer)/kg at the exit, let us study a continuous backmix tank. m kmoles of tracer is added to the inlet at time $t = 0$. It is assumed that the tracer is instantly mixed evenly into the whole mass M (Levenspiel, 1972). Then the tracer concentration at $t = 0$ becomes m/M. A mass balance for the tracer gives

$$-M\frac{dc}{dt} = \dot{M}c$$

This equation may be integrated to give

$$c(t) = \frac{m}{M}\exp\left(-\frac{\dot{M}t}{M}\right) \tag{9.11}$$

Now from the definition of $f(t)$ in Equation 9.10 one obtains

$$f(t) = \frac{c(t)\dot{M}}{m} = \frac{\dot{M}}{M}\exp\left(-\frac{\dot{M}t}{M}\right)$$

or

$$f(t) = \frac{\exp(-t/\tau)}{\tau} \tag{9.12}$$

where $\tau = M/\dot{M}$.

Thus for a backmix tank the residence time distribution function is simply a decaying exponential function of time. If the time is given in dimensionless form

$$\theta = \frac{t}{\tau} \tag{9.13}$$

the residence time distribution function becomes even simpler. From the definition, Equation 9.10, we have

$$f(t)\,\Delta t = f(\theta)\,\Delta\theta = f(\theta)\,\Delta t/\tau$$

where from Equation 9.13 $\Delta\theta = \Delta t/\tau$.

So Equation 9.12 becomes

$$f(\theta) = \exp(-\theta) \tag{9.14}$$

In practice we often have several backmix tanks in series. As previously mentioned, examples are found in the refining of aluminum and magnesium. Thus it is important to determine the residence time distribution function $f(t)$ for a number N of backmix tanks in series. A mass balance for tank j then gives

$$\frac{M}{N}\frac{dc_j}{dt} = \dot{M}(c_{j-1} - c_j)$$

Note that the mass in a given tank j is only $1/N$ of the total mass, M. In terms of $\theta^* = tN/\tau$ the equation reduces to

$$\frac{dc_j}{d\theta^*} = c_{j-1} - c_j \tag{9.15}$$

The solution of Equation 9.15 is given by

$$c_j = \exp(-\theta)\int_0^{\theta^*}\exp(\theta)\,c_{j-1}\,d\theta \tag{9.16}$$

This may be checked by insertion of Equation 9.16 into 9.15.

Now for the first tank

$$c_1 = Nm\exp(-\theta^*)/M$$

Then one obtains successively

$$\begin{aligned} c_2 &= Nm \exp(-\theta^*)\, \theta^*/M \\ c_3 &= Nm \exp(-\theta^*)\, \theta^{*2}/2M \\ &\vdots \\ c_N &= \frac{Nm}{M} \exp(-\theta^*)\, \frac{\theta^{*N-1}}{(N-1)!} \end{aligned}$$

From the definition of the residence time distribution function, this gives

$$f(t) = \frac{N}{\tau} \exp(-N(1+\varepsilon))(N(1+\varepsilon))^{N-1} N/N!$$

where $\tau = M/\dot{M}$ and $t = \tau(1 + \varepsilon)$ or, in terms of θ, $\theta = t/\tau = 1 + \varepsilon$ and

$$f(\theta) = f(t)\tau$$

Then

$$f(\theta) = N \exp(-N\theta)(N\theta)^{N-1} N/N! \tag{9.17}$$

For $N > 5$ an accurate approximation for $N!$ is Stirling's formula (Carrier et al., 1966):

$$N! \approx (2\pi N)^{1/2} N^N \exp(-N)$$

Then

$$f(\theta) \approx \left(\frac{N}{2\pi}\right)^{1/2} \exp(-N\varepsilon)\, \frac{(1+\varepsilon)^N}{(1+\varepsilon)}$$

Now we utilize the same expansion of $\ln(1 + \varepsilon)$ as in a previous section:

$$(1+\varepsilon)^N = e^{N \ln(1+\varepsilon)} \approx e^{N(\varepsilon - \varepsilon^2/2 + \varepsilon^3/3 \cdots)}$$

The terms with ε^3 and higher may be neglected for $\varepsilon \ll 1$. Thus the following approximate expression may be employed for $N > 5$

$$f(\theta) \approx \left(\frac{N}{2\pi}\right)^{1/2} \exp(-N\varepsilon^2/2)/(1+\varepsilon) \tag{9.18}$$

Notice that the value of ε that gives a maximum for f is obtained by setting $df/d\varepsilon = 0$. This gives $\varepsilon = -1/N$. For $N > 5$ this maximum is approximately equal to $(N/2\pi)^{1/2}$.

Equations 9.17 or 9.18 are often used to describe the results of tracer studies. In this case the experimentally determined $f(\theta)$ is compared with Fig. 9.4, and the N is chosen which gives the best fit. Then N is in general not an integer number. Sometimes the tanks in series model is expanded to include 'dead volumes,' volumes that exchange liquid slowly with the various backmix tanks, and so on (Himmelblau and Bischoff, 1968; Iyer and Sohn, 1994). This model is then compared with the experimental $f(\theta)$.

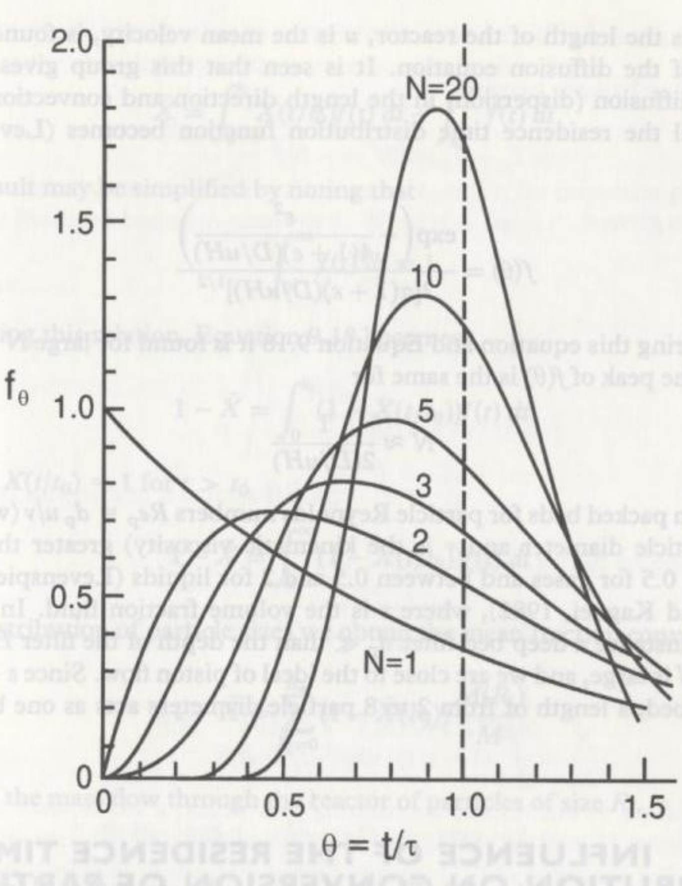

Figure 9.4 Residence time distribution curves for the tanks in series model. From Levenspiel, 1972.

For small deviation from piston flow, a diffusion model (Cussler, 1984) is often employed:

$$\frac{\partial c}{\partial t} + u\,\frac{\partial c}{\partial z} = D\,\frac{\partial^2 c}{\partial z^2}$$

Then mixing in the length direction (z-direction)—for instance in a tabular reactor—is described in terms of a dispersion coefficient D with dimensions of $m^2\,s^{-1}$. The following dimensionless group

$$\frac{D}{uH} = \frac{Dc/H}{uc}$$

where H is the length of the reactor, u is the mean velocity, is found in the solution of the diffusion equation. It is seen that this group gives a ratio between diffusion (dispersion) in the length direction and convection. With this model the residence time distribution function becomes (Levenspiel, 1972)

$$f(\theta) = \frac{\exp\left(-\dfrac{\varepsilon^2}{4(1+\varepsilon)(D/uH)}\right)}{2[\pi(1+\varepsilon)(D/uH)]^{1/2}}$$

By comparing this equation and Equation 9.18 it is found for large N that the shape of the peak of $f(\theta)$ is the same for

$$N \approx \frac{1}{2(D/uH)}$$

For flow in packed beds for particle Reynolds numbers $Re_p = d_p u/\nu$ (where d_p is the particle diameter and ν is the kinematic viscosity) greater than 100, $D\varepsilon/ud_p \approx 0.5$ for gases and between 0.5 and 2 for liquids (Levenspiel, 1972; Wakao and Kaguei, 1982), where ε is the volume fraction fluid. In packed beds, for instance a deep bed filter $d_p \ll$ than the depth of the filter H, D/uH is small, N is large, and we are close to the ideal of piston flow. Since $\varepsilon \sim 0.5$ in a packed bed, a length of from 2 to 8 particle diameters acts as one backmix tank.

9.7. INFLUENCE OF THE RESIDENCE TIME DISTRIBUTION ON CONVERSION OF PARTICLES

The kinetics of conversion of a particle has been treated elsewhere in this book. Here we look only at the effect of mixing on conversion of particles. It is assumed that the temperature and composition of the continuous phase surrounding the particles is the same throughout the reactor. Then knowledge of the residence time distribution allows us to calculate the mean conversion in the reactor. It is assumed that the mass fraction converted of a particle, X, as a function of time is known from kinetic studies conducted in the laboratory at the relevant temperature and composition of the surrounding phase. t_0 is the time when the reaction is complete, so that then $X = 1$. In general t_0 and $X(t/t_0)$ depend on particle size.

For monosized particles the mean conversion in the reactor $\bar{X}$ is given by

$$\bar{X} = \int_0^\infty X(t/t_0) f(t)\, dt$$

or

$$\bar{X} = \int_0^{t_0} X(t/t_0) f(t)\, dt + \int_{t_0}^\infty f(t)\, dt \tag{9.19}$$

This result may be simplified by noting that

$$\int_0^\infty f(t)\, dt = 1 \tag{9.20}$$

Employing this relation, Equation 9.19 becomes

$$1 - \bar{X} = \int_0^{t_0} (1 - X(t/t_0)) f(t)\, dt$$

or since $X(t/t_0) = 1$ for $t > t_0$

$$1 - \bar{X} = \int_0^\infty (1 - X(t/t_0)) f(t)\, dt$$

For a distribution of particle sizes we obtain the mean fraction converted $\bar{X}$:

$$1 - \bar{X} = \sum_{R_j=0}^{R_m} (1 - \bar{X}(R_j)) \frac{\dot{M}(R_j)}{\dot{M}} \tag{9.21}$$

$\dot{M}(R_j)$ is the mass flow through the reactor of particles of size R_j.

Example 1. Drying of particles in a fluidized bed

A powder is to be dried in a continuous fluidized bed. Elutriated particles are collected in a cyclone and returned to the bed. We assume that there is complete mixing in the fluidized bed. The mass of particles is M and the feed rate is $\dot{M}$.

It has been found that heat transfer limits the drying rate. It is assumed that there is no resistance to transfer of moisture inside the particles.

Assume that the particles are spherical and monosize. The heat transfer coefficient h in J m^{-2} °C^{-1} s^{-1} is known. The heat of evaporation (and some sensible heat) is H in J kg^{-1}. The temperatures in particles and gas remain constant at T_p and T_g, respectively. The particle density is ρ [kg/m^{-3}].

(a) Find the mean water content $\bar{X}$ (kg kg^{-1}) in the outgoing stream as a function of the water content in the feed X_0.

(b) What is $\bar{X}/X_0$ if the mean residence time $\tau = M/\dot{M}$ is 3 times greater than the time t_0 it takes to dry a particle completely?

Solution

The enthalpy balance becomes

$$h(T_g - T_p)4\pi R^2 = -H\rho \frac{4\pi R^3}{3}\frac{dX}{dt}$$

Integration gives

$$\frac{X}{X_0} = 1 - \frac{t}{t_0}$$

where

$$t_0 = \frac{\rho R H}{3h(T_g - T_p)}$$

$$\frac{\bar{X}}{X_0} = \int_0^{\infty} \frac{X}{X_0} f(t)\,dt$$

where, since we have a backmix tank,

$$f(t) = \frac{\exp(-t/\tau)}{\tau} \qquad \tau = M/\dot{M}$$

Then

$$\frac{\bar{X}}{X_0} = \int_0^{t_0} (1 - t/t_0)\exp(-t/\tau)\,dt/\tau$$

$$= 1 - \exp(-t_0/\tau) - \frac{\tau}{t_0}\int_0^{t_0/\tau} p\exp(-p)\,dp$$

$$= 1 - \frac{\tau}{t_0}(1 - \exp(-t_0/\tau))$$

$$\frac{\bar{X}}{X_0} = 1 - 3(1 - \exp(-1/3)) = 0.15$$

Thus 15% of the moisture still remains even though the mean residence time is 3 times greater than the time t_0 it takes to dry a particle!

Example 2. Burning of particles in a fluidized bed

Burning of a particle is assumed to be limited by chemical reaction between gas and the shrinking core of the particle. It is found (Levenspiel, 1972) that the kinetics in this case may be described by

$$\frac{r}{R} = 1 - \frac{t}{t_0}$$

where r is the radius of the core, R is the original radius of the spherical particle, t_0 is the time it takes to complete the reaction. If it is assumed that the density of the core does not change, conversion is given by

$$\frac{X}{X_0} = 1 - \left(\frac{r}{R}\right)^3$$

Find the mean conversion $\bar{X}$ as a function of t_0 and τ, for monosize particles in the same fluidized bed as in example 1. What is $\bar{X}$ for $\tau = 3t_0$?

Solution

$$1 - \bar{X} = \int_0^{t_0} (1 - X)\exp(-t/\tau)\,dt/\tau$$

$$= \int_0^{t_0} \left(1 - \frac{t}{t_0}\right)^3 \exp(-t/\tau)\,dt/\tau$$

By partial integration it is found that

$$\bar{X} = 3\frac{\tau}{t_0} - 6\left(\frac{\tau}{t_0}\right)^2 + 6\left(\frac{\tau}{t_0}\right)^3 (1 - \exp(-t_0/\tau))$$

$\tau/t_0 = 3$ gives $\bar{X} = 0.92$, so that 8% remains unconverted.

9.8. HEAT TRANSFER

The heat balance for a piston flow continuous reactor has to be fulfilled for every cross section. The heat supplied by the ascending gas, Q, must be equal to the heat demands of the descending charge, D. The units are J s^{-1}.

$$Q(T_h) = D(T_c) \qquad (9.22)$$

Notice that T_h and T_c, respectively, are the temperatures of the hot gas that supplies heat and cold charge that demands heat. Since heat moves from the higher to the lower temperature, T_h is greater than T_c. In fact transfer of heat is usually described in terms of the temperature difference (Bejan, 1993; Incropera and DeWitt, 1990):

$$dQ = h\,dA\,(T_h - T_c) \qquad (9.23)$$

Here dA is the differential contact area required to transfer a small quantity of heat per second, dQ, from gas to charge; h is the heat transfer coefficient between gas and charge. h has units of J m^{-2} s^{-1} K^{-1} or W m^{-2} K^{-1}.

The heat capacities of the gas and solids are introduced:

$$c_h = |dQ/dT_h|$$
$$c_c = |dD/dT_c|$$

Thus the heat capacities are the product of the mass flow through the cross section and the specific heat. The units are J s^{-1} K^{-1}. Specific heats may be obtained from tables of thermodynamic data, usually as functions of the temperature. The mass flows are determined from the input and output flows for the reactor. When chemical reactions take place, the mass flows are changed accordingly.

Employing the heat balance Equation 9.22, for instance, T_c may be replaced by an expression containing T_h. Then Equation 9.23 can be given in a form that contains only T_h, dT_h, h, c_h, c_c, and dA. If h, c_h, and c_c are taken to be constants, integration can be performed in order to obtain the temperature profiles in gas and solids. It seems to be simpler, however, to carry out the integration in terms of Q instead of T_h. From a Reichardt diagram (Biswas, 1981) as shown in Fig. 9.5 it is seen that

$$T_h = T_a - \frac{Q}{c_h} \tag{9.24a}$$

Furthermore, for the charge one obtains from Equation 9.22

$$T_c = T_e - \frac{D}{c_c} = T_e - \frac{Q}{c_c} \tag{9.24b}$$

Here T_a is the temperature of the gas when it enters the packed bed. If the two expressions are inserted in Equation 9.23, one obtains

$$dQ = h\, dAT_a - T_e + Q(1/c_c - 1/c_h)$$

or

$$dQ/(T_a - T_e + Q(1/c_c - 1/c_h)) = h\, dA$$

The left-hand side of the equation is integrated over Q from $Q = 0$ to Q and the right-hand side over A from $A = 0$ to A. Then taking the antilogarithm of the two sides:

$$1 + Q(1/c_c - 1/c_h)/(T_a - T_e) = \exp(hA(1/c_c - 1/c_h))$$

Inserted in Equation 9.24 this gives

$$\begin{aligned} T_h &= T_a + (T_a - T_e)[1 - \exp(hA(1/c_c - 1/c_h))]c_c/(c_h - c_c) \\ T_c &= T_e + (T_a - T_e)[1 - \exp(hA(1/c_c - 1/c_h))]c_h/(c_h - c_c) \end{aligned} \tag{9.25}$$

If the last equation is subtracted from the one above, one obtains:

$$T_h - T_c = (T_a - T_e)\exp(hA(1/c_c - 1/c_h)) \tag{9.26}$$

For a heat capacity of the charge, c_c, greater than that of the gas, c_h, the expression in the exponent is negative. Then for a large contact area A the temperatures in gas and solids will converge. This is the case in the bottom section of the blast furnace. For c_c smaller than c_h, as in the upper part of the blast furnace, the temperature difference $T_h - T_c$ will increase with A. This is illustrated in Fig. 9.5.

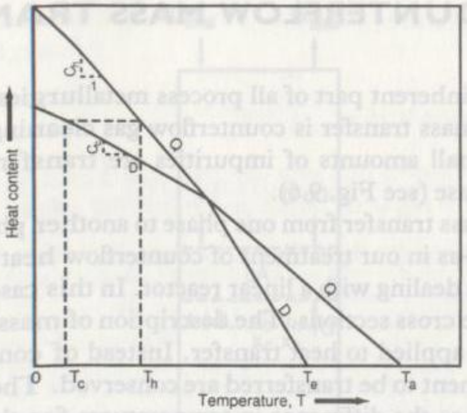

Figure 9.5 A typical schematic Reichardt diagram showing the heat balance of the gas and the solids.

Often it is necessary to determine the heat supplied in terms of the temperatures. This may be accomplished by eliminating the heat capacities in Equation 9.26 using the two Equations 9.24a,b. Then

$$\frac{T_h - T_c}{T_a - T_e} = \exp\left(\frac{hA[(T_h - T_c) - (T_a - T_e)]}{Q}\right)$$

or taking the logarithm:

$$\frac{Q}{hA} = \frac{T_h - T_c - (T_a - T_e)}{\ln((T_h - T_c)/(T_a - T_e))} \tag{9.27}$$

This is a well-known expression for the heat transferred, Q. The right-hand side is called the logarithmic mean temperature difference. The equation is also valid for concurrent flow reactors. In fact, the relations given in this section apply to concurrent flow reactors if c_c is replaced by $-c_c$. In this case, both T_a and T_e are the temperatures going into the heat exchanger.

Equation 9.27 only applies if h, c_h, and c_c can be regarded as constants. If this is not the case, numerical integration must be employed. Then if T_a and T_e are specified, moving up through the shaft in steps of ΔA, holding c_h and c_c constant within each step, temperatures may be calculated in succession. For instance, if the temperatures in grid point i are T_{hi} and T_{ci}, heat capacities between grid points i and $i + 1$ are c_{hi} and c_{ci}, and the heat transfer coefficient is h_i, then by comparison with Equations 9.25 one finds

$$T_{hi+1} = T_{hi} + (T_{hi} - T_{ci})[1 - \exp(h_i\, \Delta A\, (1/c_{ci} - 1/c_{hi}))]\frac{c_{ci}}{(c_{hi} - c_{ci})} \tag{9.28}$$

T_{ci+1} is obtained similarly.

9.9. COUNTERFLOW MASS TRANSFER

Mass transfer is an inherent part of all process metallurgical operations. One simple example of mass transfer is counterflow gas cleaning processes in the special case that small amounts of impurities are transferred from the gas phase to a liquid phase (see Fig. 9.6).

In the study of mass transfer from one phase to another phase moving in the opposite direction—as in our treatment of counterflow heat exchangers—it is assumed that we are dealing with a linear reactor. In this case the flows should be averaged over the cross sections. The description of mass transfer becomes very similar to that applied to heat transfer. Instead of conserving enthalpy, moles of the component to be transferred are conserved. The driving force for heat transfer, given as the difference in temperatures for the two phases, for mass transfer is replaced by the difference in activities of the component in the two phases. In the following, G refers to the amount of impurity component transferred from the phase to be purified (usually gas) while L refers to the amount of impurity accepted by the other phase, for instance a liquid. To simplify the comparison of heat and mass transfer we retain the indices h and c for the gas (hot) phase and liquid (cold) phases, respectively. Then, in summary

$$G(a_h) = L(a_c) \tag{9.29}$$

where a_h, a_c are the activities of the component given in mole fractions in gas and liquid, respectively. For a gas we here define the activity as

$$a_h = \frac{p_h}{p_{total}} \tag{9.30}$$

Equation 9.29 replaces Equation 9.22. The driving force for heat transfer $T_h - T_c$ is replaced by the corresponding driving force for mass transfer $a_h - a_c$. Thus the analog of Equation 9.23 is

$$dG = k_t \rho \, dA \, (a_h - a_c) \tag{9.31}$$

where k_t is a total mass transfer coefficient with units of m s^{-1}, to be discussed in the following. It replaces h. ρ is the density in kmol m^{-3}

For an ideal gas,

$$\rho = \frac{p_{total}}{RT} \tag{9.32}$$

where R is the gas constant, $R = 8314.5 \text{ J K}^{-1} \text{ kmol}^{-1} = 0.083 \text{ bar m}^3 \text{ K}^{-1} \text{ kmol}^{-1}$, and p_{total} is given in bar. All relations derived for heat transfer can be translated to mass transfer if the heat capacities are replaced by 'molar capacities' defined in terms of activities:

$$c_h = |dG/da_h|$$
$$c_c = |dL/da_c|$$

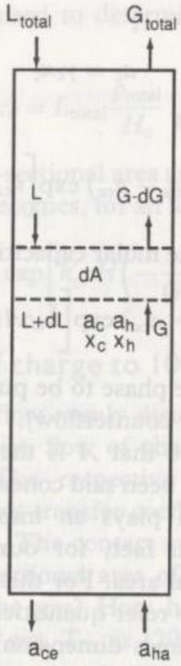

Figure 9.6 In counterflow, column impurity G is transferred to the phase going down. G_{total} gives kmoles per second of phase where amount G is removed. L_{total} gives kmoles per second of phase that extracts amount G.

It is assumed that the content x of the impurity is so small that its contribution to the total molar flow rates is negligible. This means that as an approximation we can write

$$G = G_{total}(x_{ha} - x_h) \tag{9.33}$$

$$L = L_{total}(x_{ce} - x_c) \tag{9.34}$$

where x_{ha} is the mole fraction of the phase to be purified as it enters and x_{ce} is the exit concentration in the other phase. Thus molar capacities are the product of the total molar flow rate times the change of concentration, x, with activity, dx/da.

If we relate activities to concentration in terms of Raoultian activity coefficients,

$$a_h = \gamma_h x_h \tag{9.35}$$

For an ideal gas mixture $\gamma_h = 1$,

$$a_c = \gamma_c x_c \tag{9.36}$$

The analog of Equation 9.26 is

$$a_h - a_c = (a_{ha} - a_{ce}) \exp\left[k_t \rho A \left(\frac{1}{c_c} - \frac{1}{c_h}\right)\right] \tag{9.37}$$

Employing the relations for the molar capacities, Equation 9.37 becomes

$$a_h - a_c = (a_{ha} - a_{ce}) \exp\left[k_t \rho A \left(\frac{\gamma_c}{L_{total}} - \frac{\gamma_h}{G_{total}}\right)\right] \tag{9.38}$$

where a_{ha} is the activity of the phase to be purified as it enters and a_{ce} is exit activity in the other phase (for counterflow).

In Equation 9.38 we notice that A is the contact area between the two phases. However, nothing has been said concerning the cross-sectional area of the column. Now, this area plays an important role in calculating the throughput of a column. In fact, for our linear reactor throughput is proportional to cross-sectional area. For this reason it is practical to look at just 1 m^2 cross section, and to refer quantities such as A, L_{total}, G_{total}, and c_c and c_h to 1 m^2. Then A becomes dimensionless, m^2 of contact area per m^2 cross section. Furthermore, we are interested in the height, H. A is proportional to height. A equals the height, H, times the contact area per unit volume of reactor. This last factor is called specific contact area. In the literature one may find data concerning the specific contact areas and also data for the product of the mass transfer coefficients k_t and the specific contact area, often called volumetric mass transfer coefficient k_t'. Notice that k_t has dimensions of m s^{-1} and specific contact area has dimensions of m^2 m^{-3}. Thus k_t' has the dimension of inverse time since $k_t' = k_t$ times specific contact area.

It is of course important that the specific contact area is large. To attain this, a packed column is often filled with rings or saddles of metal, glass, ceramics, or plastics with small diameters (Raschig rings). It is important that these are wetted by the liquid.

It is often practical to define activities in terms of pressures for both the gas and the liquid phase. Then for the liquid the pressure is obtained from Henrys law:

$$p_c = H_c x_c \tag{9.39}$$

where H_c is the Henry's law constant and x_c is the mole fraction of the impurity in the liquid phase. Equation 9.30 can be employed to relate activity, a_c and concentration x_c:

$$a_c = H_c \frac{x_c}{p_{total}} \tag{9.40}$$

This equation may now be used to determine the capacity c_c as defined above of the liquid phase :

$$c_c = L_{total} \frac{p_{total}}{H_c} \tag{9.41}$$

Now, in terms of the unit cross-sectional area and employing Equations 9.35, 9.39, and 9.41, Equation 9.37 becomes, for an ideal gas mixture,

$$p_h - H_c x_c = (p_{ha} - H_c x_{ce}) \exp\left[k_t' \rho H \left(-\frac{1}{G_{total}} + \frac{H_c}{L_{total} p_{total}}\right)\right] \tag{9.42}$$

Example 3. Preheating of charge to 1000°C by hot process gas

Solids and gas move in piston flow evenly distributed over the cross section in opposite directions. The mass flow of charge is $\dot{M}_c = 10$ kg s^{-1} and for gas $\dot{M}_h = 9$ kg s^{-1}. The respective specific heats are 0.8 and 1.1 kJ kg^{-1} °C^{-1}. The total heat transfer coefficient between solids and gas is $h = 0.125$ kJ m^{-2} s^{-1} °C^{-1}. The contact area between charge and gas is 100 m^2 m^{-3} bed. The cross-sectional area of the charge is 2 m^2. What is the exit temperature T_{he} of the gas? How high must we make the bed? The ingoing temperature of the gas, T_{ha}, is 1200°C while the solids enter at a temperature $T_{c1} = 30$°C.

Solution

A heat balance gives the heat transferred

$$Q = c_c(1000 - 30) = 0.8 \times 10 \times 970 = 7760 \text{ kJ s}^{-1}$$

$$7760 = c_h(1200 - T_{he})$$

or

$$\frac{7760}{1.1 \times 9} = 1200 - T_{he}$$

$T_{he} = 416$°C is the exit temperature of the gas. From Equation 9.27 one obtains for the contact area

$$A = \frac{7760 \ln(200/386)}{0.125(200 - 386)} = 219.45 \text{ m}^2$$

$$A = 100 \times 2 \times H$$

The height of the bed is

$$H = \frac{219.45}{200} = 1.1 \text{ m}$$

Example 4. Absorption of SO_2 process gas by water in a packed tower

Process gas containing SO_2 is to be cleaned in a packed tower with water. Gas and water move in counterflow.

$$x_{SO_2} = \frac{p_{SO_2}}{H_c}$$

Here x_{SO_2} is kg SO_2 per kg H_2O and p_{SO_2} is the partial pressure in bars of SO_2. H_c is Henry's constant $H_c = 10$ bar. G kmol of process gas per second moves up through the tower in piston flow, $G_{total} = 0.003\ \mathrm{kmol\,s^{-1}}$. L_{total} kg of water goes down in piston flow, $L_{total} = 4\ \mathrm{kg\,s^{-1}}$. The cross section of the tower is $A = 4\ \mathrm{m^2}$ and the wetted specific surface area is $a = 100\ \mathrm{m^2/(m^3}$ tower volume). The total mass transfer coefficient $k_t = 4 \times 10^{-5}\ \mathrm{m\,s^{-1}}$. It is assumed that the total pressure $p_{total} = 1$ bar does not change noticeably in the tower. Also the mass fraction SO_2 in the liquid is $\ll 1$. The content of SO_2 of the gas entering the tower is $p^a_{SO_2} = 0.01$ bar. The content in the exit gas is to be reduced to $p^e_{SO_2} = 0.003$ bar. The absolute temperature $T = 295$ K.

1. Determine the exit concentration of SO_2 in the water, $x^e_{SO_2}$.
2. Determine the 'operating line,' i.e., the relation between x_{SO_2} and p_{SO_2} up through the tower.
3. Based on a horizontal slice of the tower, derive a differential balance for SO_2 that relates the thickness ΔH to p_{SO_2} and the change in p_{SO_2}.
4. Eliminate x_{SO_2} from (3) and integrate.
5. Find the height of the tower, H, employing the numbers given above.
6. It is seen that water can be used. However, the amount of gas cleaned is small compared to the flow of water down the column. Would it help if a chemical that reacts with SO_2 was added to the water? Explain why this is the case.

Solution

1. A mass balance over the tower for SO_2 gives

$$\frac{64 G_{total}(p^a_{SO_2} - p^e_{SO_2})}{p_{total}} = L_{total} x^e_{SO_2}$$

where 64 is the molecular mass of SO_2,

$$x^e_{SO_2} = \frac{64 G_{total}(p^a_{SO_2} - p^e_{SO_2})}{p_{total} L_{total}}$$

2. The operating line is given by a mass balance over the lower part of the tower (compare Equations 9.29, 9.33, and 9.34).

$$\frac{64 G_{total}(p^a_{SO_2} - p_{SO_2})}{p_{total}} = L_{total}(x^e_{SO_2} - x_{SO_2})$$

Thus

$$x_{SO_2} = x^e_{SO_2} - \frac{64 G_{total}}{p_{total} L_{total}}(p^a_{SO_2} - p_{SO_2})$$

or

$$x_{SO_2} = \left(x^e_{SO_2} - \frac{64 G_{total} p^a_{SO_2}}{p_{total} L_{total}}\right) + \frac{64 G_{total} p_{SO_2}}{p_{total} L_{total}}$$

3. A mole balance for SO_2 over a slice of the tower of thickness ΔH gives

$$-G_{total} RT \frac{\Delta p_{SO_2}}{p_{total}} = k_t a A\, \Delta H (p_{SO_2} - p^*_{SO_2})$$

where $R = 0.083\ \mathrm{bar\,m^3\,K^{-1}\,kmol^{-1}}$ is the gas constant and T is the absolute temperature. Now $p^*_{SO_2} = x_{SO_2} H_c$. From (2) it is found that

4. $$p^*_{SO_2} = b + B p_{SO_2}$$

where

$$b = \left(x^e_{SO_2} - \frac{64 G_{total} p^a_{SO_2}}{p_{total} L_{total}}\right) H_c = -\frac{64 G_{total} p^e_{SO_2} H_c}{p_{total} L_{total}}$$

and

$$B = \frac{64 G_{total} H_c}{p_{total} L_{total}}$$

Thus the differential expression letting $\Delta H \rightarrow 0$, reduces to

$$-\frac{G_{total} RT\, dp_{SO_2}}{k_t a A p_{total}} = dH(p_{SO_2} - b - B p_{SO_2})$$

or

$$-\frac{G_{total} RT\, dp_{SO_2}}{k_t a A p_{total}(p_{SO_2}(1 - B) - b)} = dH$$

or integrated (compare Equation 9.42)

$$\frac{G_{total} RT}{k_t a A p_{total}(1 - B)} \ln\left(\frac{p^a_{SO_2}(1 - B) - b}{p^e_{SO_2}(1 - B) - b}\right) = H$$

$$B = \frac{64 \times 0.003 \times 10}{4 \times 1} = 0.48$$

$$b = -\frac{64 \times 0.003 \times 0.003 \times 10}{4 \times 1} = -0.001\,44$$

5. $$H = \frac{0.003 \times 0.083 \times 295}{4 \times 10^{-5} \times 100 \times 4 \times 1 \times 0.52} \ln\left(\frac{0.01 \times 0.52 + 0.00144}{0.003 \times 0.52 + 0.00144}\right)$$

$$H = 7.1\ \mathrm{m}$$

6. The main resistance to mass transfer is in the liquid film. If SO_2 reacts at the liquid–gas interface, only the resistance in the gas film remains. Then $k_t = k_{gas}$ is much greater. Also $p^*_{SO_2}$ is lower.

REFERENCES

Alcock, C.B. (1976) *Principles of Pyrometallurgy*. Academic Press, New York.

Bejan, A. (1993) *Heat Transfer*. Wiley, New York.

Bird, R.B., Stewart, W.E., and Lightfoot, E.N. (1960) *Transport Phenomena*. Wiley, New York.

Biswas, A.K. (1981) *Principles of Blast Furnace Ironmaking*. Cootha, Brisbane.

Carrier, G.F., Krook, M., and Pearson, C.E. (1966) *Functions of a Complex Variable*. McGraw-Hill, New York.

Claessens, P.L. and Harris, G.B. (eds) (1990) *Proceedings of the International Symposium on Electrometallurgical Plant Practice*. Pergamon Press, New York.

Coudurier, L., Hopkins, D.W., and Wilkomirsky, I. (1985) *Fundamentals of Metallurgical Processes*. Pergamon Press, Oxford.

Cussler, E.L. (1984) *Diffusion, Mass Transfer in Fluid Systems*. Cambridge University Press.

Davidson, J.F., Clift, R., and Harrison, D. (1985) *Fluidization*. Academic Press, London.

Engh, T.A. (1992) *Principles of Metal Refining*. Oxford Science, Oxford.

Engh, T.A., Hansson, L., Worner, H.K., and Wulff, K. (1971a) Measurement of the residence time distribution function for the WORCRA steel refining launder. *Jernkont. Ann.* **155**, 93–99.

Engh, T.A., Grip, C.-E., Hansson, L., and Worner, H.K. (1971b) A one-dimensional model of the WORCRA steel refining launder. *Jernkont. Ann.* **155**, 553–564.

Engh, T.A., Hansson, L., and Ljunggren, K. (1973) Determination of flow characteristics for a continuous slag-metal reactor. *Nuclear Techniques in the Basic Metal Industries*. International Atomic Energy Agency, Vienna, pp. 251–264.

Gaskell, D.R. (1973) *Introduction to Metallurgical Thermodynamics*. McGraw-Hill, New York.

Glasstone, S., Laidler, K.J., and Eyring, H. (1941) *The Theory of Rate Processes*. McGraw-Hill, New York.

Grjotheim, K. and Welch, B.J. (1988) *Aluminium Smelter Technology*. Aluminium-Verlag, Düsseldorf.

Himmelblau, D.M. and Bischoff, K.B. (1968) *Process Analysis and Simulation*. Wiley, New York.

Incropera, F.P. and DeWitt, D.P. (1990) *Fundamentals of Heat and Mass Transfer*. Wiley, New York.

Iyer, K.M. and Sohn, H.Y. (1994) Physical and mathematical modelling of pyrometallurgical channel reactors. *Metall. Trans. B* **25B**, 207–219.

Koros, P.J. and Pierre, G.R.St. (1991) *Proceedings of the Elliott Symposium on Chemical Process Metallurgy*. Iron and Steel Society, Warrendale, PA.

Lehner, T., Koros, P.J., and Ramachandron, V. (1991) *International Symposium on Injection in Process Metallurgy*. TMS, Warrendale, PA, vol. 2.

Levenspiel, O. (1972) *Chemical Reaction Engineering*. Wiley, New York.

Lux, A.L. and Flemings, M.C. (1979) Refining by fractional solidification. *Metall. Trans. B* **10B**, 71–78, 79–84.

Nagata, S. (1975) *Mixing, Principles and Applications*. Wiley, New York.

Nilsson, R., Seetharaman, S., and Jacob, K.T. (1994) A modified sulphide capacity function. *ISIJ Int.* **34**, 876–882.

Oeters, F. (1989) *Metallurgie der Stahlherstellung*. Springer-Verlag, Berlin.

Øymo, D., Karlsen, D.O., Pinfold, P.M.D., Mellerud, T., and Lie, O. (1994) Particle removal in pure Mg. *Light Metals* (ed. U. Mannweiler). TMS, Warrendale, PA, pp. 1017–1024.

Perry, R.H. and Green, D. (1984) *Perry's Chemical Engineer's Handbook*. McGraw-Hill, New York.

Raiber, K., Hammerschmid, P., and Janke, D. (1995) Experimental studies on Al_2O_3 inclusion removal from steel melts using ceramic filters. *ISIJ Int.* **35**, 380–388.

Rosenqvist, T. (1983) *Principles of Extractive Metallurgy*. McGraw-Hill, New York.

Szekely, J. (1966) *On Some Problems in Continuous Steelmaking* (ed. A.W.D. Hills), Proceedings of a Symposium in Process Metallurgy, Imperial College, London, pp. 115–139.

Szekely, J. (1979) *Fluid Flow Phenomena in Metals*. Academic Press, New York.

Szekely, J. and Themelis, N.J. (1971) *Rate Phenomena in Process Metallurgy*. Wiley-Interscience, New York.

Themelis, N.J. (1995) *Transport and Chemical Rate Phenomena*. Gordon and Breach, Basel.

Tien, J.K. and Elliott, J.F. (1981) *Metallurgical Treatises*. AIME, Warrendale, PA.

Turkdogan, E.T. (1980) *Physical Chemistry of High Temperature Technology*. Academic Press, New York.

Waite, P. and Thiffault, R. (1996) The Alcan Compact Degasser: A Trough-based Aluminium Treatment Process. *Light Metals* (ed. W. Hale). TMS, Warrendale, PA, pp. 1001–1005.

Wakao, N. and Kaguei, S. (1982) *Heat and Mass Transfer in Packed Beds*. Gordon and Breach, New York.

Ward, R.G. (1962) *An Introduction to the Physical Chemistry of Iron & Steelmaking*. Edward Arnold, London.

10

Ironmaking reactions

Jean-Marc Steiler
IRSID, Maizières les Metz, France

10.1. OUTLINE OF THE BLAST FURNACE PROCESS

The blast furnace remains by far the major ironmaking process for the production of high-quality steels in integrated steel plants. During the last decades, blast furnace technology made tremendous progress with respect to effectiveness, productivity, fuel consumption, and hot metal quality. Modern units are now producing, on a routine basis, 11 000 t_{HM} per day, with an iron yield close to 99.5% and an energy efficiency in excess of 90% (Béranger et al., 1996).

The blast furnace is an example of a complex process involving coupled interactions between physical chemistry, heat transfer, and fluid flow phenomena. A gradual improvement of our understanding of the process has been gained over the years from continuous R&D efforts to implement sensors for assessing the actual conditions inside the reactor and to describe and modelize the phenomena.

10.1.1. The Three Functions of the Blast Furnace

The blast furnace is a countercurrent gas–solid reactor, in which the iron oxides are reduced into iron, the iron and gangue are melted, and the liquid metal is separated from slag. The reactor provides three basic metallurgical functions:

- Chemical transfer, with the reduction of iron oxides, the combustion and gasification of carbon, and slag–metal reactions, such as desulfurization.

ADVANCED PHYSICAL CHEMISTRY FOR PROCESS METALLURGY
ISBN 0-12-618920-X
Copyright © 1997 Academic Press Ltd
All rights of reproduction in any form reserved

- Heat transfer, by exchange between gas, solids, or liquids.
- The aerodynamic function of maintaining the permeability of the burden; indeed heat and mass transfer occur in a granular bed and are therefore strongly connected with fluid flow.

The solid charge materials (iron ores and coke) are charged in alternate layers at the top of the furnace. During their descent in the shaft, the iron ores are reduced and subsequently smelted. The impurities, arising from the gangue of coke, coal, and iron ores, can only be separated from iron in the liquid state, which requires them to be heated above their melting temperature; liquid slag and metal are tapped from the furnace at a temperature of ~1500°C.

The reducing gas, a mixture of CO, H_2, and N_2, is produced at the tuyeres at a temperature of 2000 to 2200°C, by partial combustion of coke and auxiliary fuels in the preheated air blast. As it rises through the furnace, the gas, which is always at higher temperature than the solids or liquids, exchanges heat with the latter and provides the necessary enthalpy and reducing power. It leaves the furnace after having lost most of its sensible heat (temperature in the range 80–200°C), but with a significant amount of chemical heat remaining ($\%CO/\%CO_2 \sim 1$), which is used afterwards in the mill. The oxygen potential of the gas increases from bottom to top, but, owing to the countercurrent conditions, the gas always retains reducing potential and heating-up potential with respect to solid; this accounts for the outstanding thermal and chemical efficiency of the blast furnace process.

In the lower part of the furnace, coke is the only solid material. Apart from supplying reducing gas and heat for the process, it provides mechanical support to the burden and acts as a spacer (coke grid) to allow smooth fluid flow conditions for ascending gas and descending liquids through the interstices of coke particles.

10.1.2. Systems of Importance in Ironmaking

10.1.2.1. Fe–O system

Iron forms three stable oxides (Darken and Gurry, 1945): Fe_2O_3 (hematite), Fe_3O_4 (magnetite), and $FeO_{1.056}$ (wustite) (Fig. 10.1). The partial pressures of oxygen in equilibrium with the three couples of oxides are given in Table 10.1.

Hematite is a stoichiometric oxide usually crystallized in a hexagonal lattice. It decomposes at 1457°C into magnetite and oxygen, under atmospheric pressure conditions.

Magnetite exhibits a small stoichiometric range with values of O/Fe ranging from 1.33 to 1.38 at_O/at_{Fe}. Stoichiometric magnetite melts congruently at about 1596°C. The reduction of hematite to magnetite occurs with lattice transformation from hexagonal to cubic, leading to expansion and cracking of the solid structure.

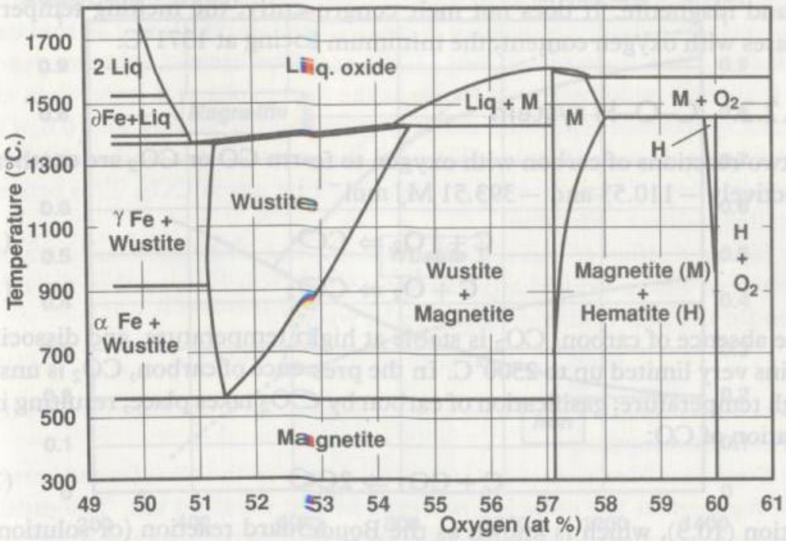

Figure 10.1 The iron–oxygen phase diagram (1 bar total pressure).

Table 10.1 Reduction equilibria of iron oxides

Reaction	Equilibrium partial pressure of O_2		Equilibrium ratio $\%CO/\%CO_2$	
	600°C	950°C	600°C	950°C
Fe_2O_3–Fe_3O_4	5.1×10^{-14}	5.2×10^{-6}	2.0×10^{-6}	1.3×10^{-5}
Fe_3O_4–$FeO_{1.056}$	1.4×10^{-26}	1.4×10^{-14}	0.82	0.25
$FeO_{1.056}$–Fe	1.2×10^{-25}	1.4×10^{-16}	1.25	2.3

Wustite is a nonstoichiometric oxide existing in the temperature range from 570°C to 1424°C. The O/Fe ratio ranges from 1.056 to 1.20 at_O/at_{Fe}; in fact the stoichiometric oxide FeO does not exist. The wustite lattice is deficient in Fe^{2+} ions, and the Fe^{3+}/Fe^{2+} ratio increases with oxygen content. Wustite saturated with iron exhibits a roughly constant O/Fe ratio, which corresponds to the widely used formula $FeO_{1.056}$. Below 570°C, wustite decomposes into iron and magnetite. It does not melt congruently; the melting temperature increases with oxygen content, the minimum being at 1371°C.

10.1.2.2. C–O–H system

The two reactions of carbon with oxygen to form CO or CO_2 are exothermic, respectively −110.53 and −393.51 MJ mol^{-1}.

$$C + \tfrac{1}{2}O_2 \Rightarrow CO \qquad (10.1)$$

$$C + O_2 \Rightarrow CO_2 \qquad (10.2)$$

In the absence of carbon, CO_2 is stable at high temperature, and dissociation remains very limited up to 2300°C. In the presence of carbon, CO_2 is unstable at high temperature; gasification of carbon by CO_2 takes place, resulting in the formation of CO:

$$C + CO_2 \Rightarrow 2CO \qquad (10.3)$$

Reaction (10.3), which is known as the Boudouard reaction (or solution loss reaction) is highly endothermic (172.45 MJ mol^{-1}). The stability of CO_2 in the presence of C is increased as temperature drops or pressure increases (Fig. 10.2). In actual blast furnace operation, this heterogeneous reaction involves coke instead of carbon and occurs with significant kinetics beyond a given threshold temperature in the order of 950°C.

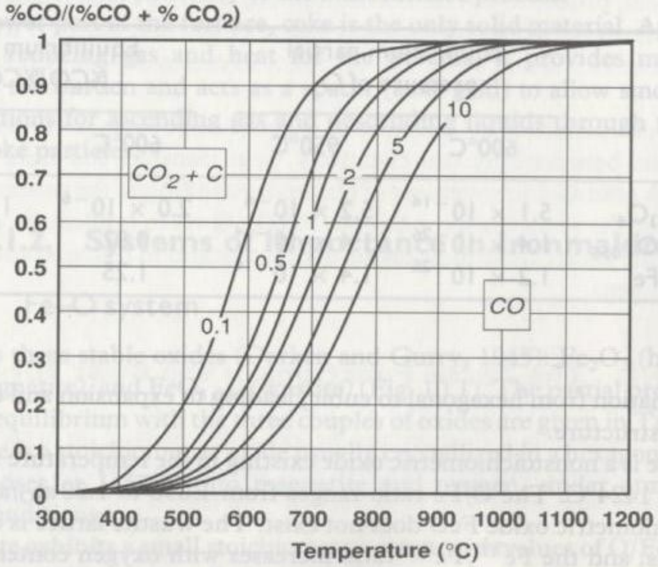

Figure 10.2 The Boudouard reaction equilibrium for different values of total pressure (bar).

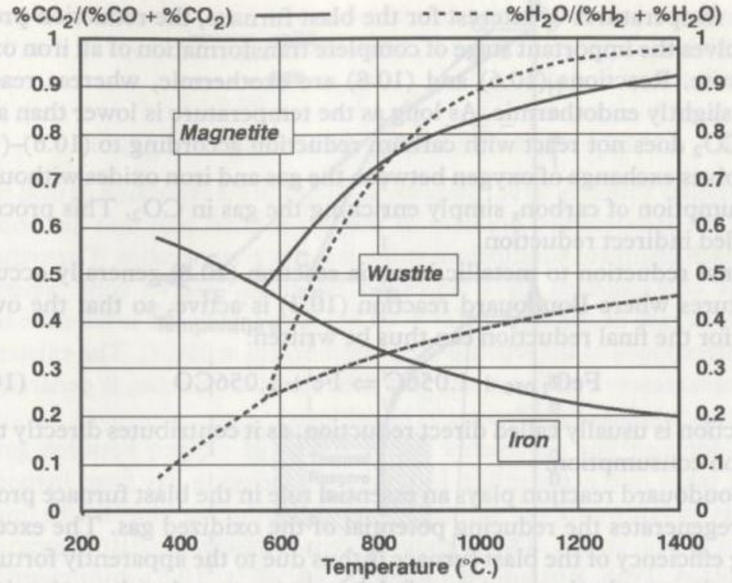

Figure 10.3 The iron oxides reduction diagram (Chaudron equilibria).

Water vapor may also react with carbon, according to reaction (10.4), which resembles the Boudouard reaction.

$$C + H_2O \Rightarrow CO + H_2 \qquad (10.4)$$

$$CO + H_2O \Rightarrow CO_2 + H_2 \qquad (10.5)$$

Equilibration of gaseous C–O–H mixtures is achieved by the watergas shift reaction (10.5); the kinetics of the latter reaction is known to be sluggish below 700°C.

10.1.2.3. Fe–O–C–H system

The stability diagram of iron oxides in the presence of CO–CO_2 mixtures or H_2–H_2O mixtures is shown in Fig. 10.3. The reduction of Fe_2O_3 to iron by CO proceeds through the successive reactions:

$$3Fe_2O_3 + CO \Leftrightarrow 2Fe_3O_4 + CO_2 \qquad (10.6)$$

$$Fe_3O_4 + 0.831CO \Leftrightarrow 3FeO_{1.056} + 0.831CO_2 \qquad (10.7)$$

$$FeO_{1.056} + 1.056CO \Leftrightarrow Fe + 1.056CO_2 \qquad (10.8)$$

Below 570°C, wustite no longer exists, and magnetite is reduced to iron:

$$Fe_3O_4 + 4CO \Leftrightarrow 3Fe + 4CO_2 \qquad (10.9)$$

At the temperatures of interest for the blast furnace, the reduction process thus involves the important stage of complete transformation of all iron oxides into wustite. Reactions (10.6) and (10.8) are exothermic, whereas reaction (10.7) is slightly endothermic. As long as the temperature is lower than about 950°C, CO_2 does not react with carbon; reduction according to (10.6)–(10.8) only involves exchange of oxygen between the gas and iron oxides without any net consumption of carbon, simply enriching the gas in CO_2. This process is often called indirect reduction.

The final reduction to metallic iron via reaction (10.8) generally occurs at temperatures where Boudouard reaction (10.3) is active, so that the overall reaction for the final reduction can thus be written:

$$FeO_{1.056} + 1.056C \Rightarrow Fe + 1.056CO \qquad (10.10)$$

This reaction is usually called direct reduction, as it contributes directly to the net carbon consumption.

The Boudouard reaction plays an essential role in the blast furnace process, since it regenerates the reducing potential of the oxidized gas. The excellent reducing efficiency of the blast furnace is thus due to the apparently fortuitous fact that the two basic reactions of the process, namely, the reduction of wustite to iron by CO and the Boudouard reaction, occur with rapid kinetics in the same range of temperature, thus enabling effective mutual interaction.

10.1.3. The One-Dimensional Reactor

10.1.3.1. Temperature profile and Reichardt diagram

It is known experimentally that the temperature profile of the blast furnace is characterized by the existence of an isothermal zone over a considerable portion of the shaft, where solids and gas are at the same temperature, in the order of 950–1000°C. Very strong heat exchanges from gas to solids occur within the two regions located below or beyond that temperature level, whereas heat exchange vanishes in the isothermal zone, which is therefore called the temperature reserve zone. The heat pattern can be represented in the Reichardt diagram (Reichardt, 1927; Rist and Meysson, 1966) (Fig. 10.4). It shows, with due regard to the second law of thermodynamics, the temperature of gas and the temperature of solids as a function of the heat transferred from the gas. The slope of each line represents the 'average heat capacity' of gas and solid charge respectively; the 'average heat capacity' is a global parameter, including both sensible and latent heat.

The segment SR (see Fig. 10.4) represents the heating of the solid charge from room temperature to the temperature of the reserve zone TR; the heat requirements mostly include heating up of solids and indirect reduction to wustite. The segment RC corresponds to heating up the charge from the temperature of reserve zone to casting temperature TC. The heat requirements involve sensible heat of the charge, heat of fusion, and the heat of endothermic reactions, especially solution loss and direct reduction. The slope of this line is thus markedly higher than the slope of SR line, so that point R becomes a pinch point. The existence of the thermal pinch point is mostly due to the highly endothermic solution loss reaction, leading to drastic cooling of the gas from tuyeres; this effect vanishes below the gasification threshold temperature, i.e., ~950°C.

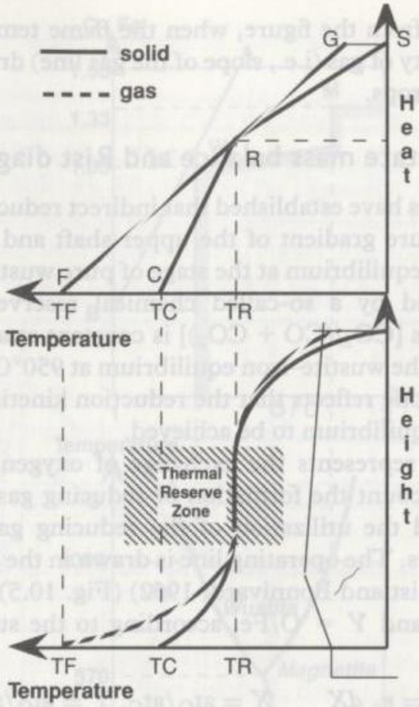

Figure 10.4 Thermal profile of the blast furnace; description of heat exchange by the Reichardt diagram.

The gas line GRF represents the cooling of gas from flame temperature TA down to top gas temperature. The slopes of lines GR and FR are very similar, so that the gas line is generally defined as one segment FG. The distance between the gas and solid lines is a measure of the extent of heat exchange between the phases. The practical significance of the thermal pinch point and the corresponding reserve zone is that the heat transfer kinetics is high enough for establishing conditions of thermal equilibrium between gas and solids in the shaft.

As can be deduced from the figure, when the flame temperature becomes higher, the heat capacity of gas (i.e., slope of the gas line) drops so that the top gas temperature also drops.

10.1.3.2. Steady-state mass balance and Rist diagram

Probes in blast furnaces have established that indirect reduction of iron oxides starts in the temperature gradient of the upper shaft and that gas and iron oxides reach chemical equilibrium at the stage of pure wustite. The reduction profile is characterized by a so-called chemical reserve zone where the oxidation degree of gas [$CO_2/(CO + CO_2)$] is constant at a level close to 0.3, which corresponds to the wustite–iron equilibrium at 950°C. The existence of the chemical reserve zone reflects that the reduction kinetics is generally fast enough for chemical equilibrium to be achieved.

The operating line represents the exchange of oxygen between gas and solids; it takes into account the formation of reducing gas from carbon and oxygen at tuyeres and the utilization of the reducing gas for the indirect reduction of iron oxides. The operating line is drawn in the Rist diagram (Rist and Meysson, 1966; Rist and Bonnivard, 1962) (Fig. 10.5), with coordinates $X = O/C$ in the gas and $Y = O/Fe$, according to the steady state oxygen balance:

$$n_{Fe}\, dY = n_g\, dX \qquad X = at_O/at_C,\ Y = at_O/at_{Fe}$$

with n_{Fe} being the rate of iron production (at_{Fe}) and n_g the rate of gas production (moles).

The slope of the operating line represents the specific gas consumption (moles of reducing gas for the production of 1 at Fe). The total carbon consumption (at_C/at_{Fe}) is equal to this number plus the amount of carbon dissolved in hot metal. As the operating line AB represents the reduction phenomena, it must necessarily remain on the left side of the equilibrium contour derived from the reduction diagram at the reference temperature (generally 950°C.).

In the ideal blast furnace operation, the most favorable conditions with respect to oxygen exchange are achieved when the operating line goes through the point W corresponding to the wustite–iron equilibrium. The oxygen exchange thus provides a 'chemical pinch point,' accounting for the chemical reserve zone. The coordinates of this point are derived from the wustite–iron equilibrium (reaction (10.8)), i.e.,

$X(W) = 1.3$ at 950°C

$Y(W) = 1.056\ at_O/at_{Fe}$ (practically independent from temperature)

In actual operation, it may happen that equilibrium with wustite is not totally achieved at the temperature of the reserve zone, so that the O/Fe ratio of iron oxides is higher than 1.056. The operating line is then located at some distance from point W; conventionally this departure from ideality of reduction is expressed by the parameter ω, the overall oxidation degree of wustite being thus $1.056 + \omega$. Owing to considerable improvement of ferrous burden quality, especially reducibility, it has now become a relatively common practice to operate industrial blast furnaces at about 100% reduction efficiency ($\omega \sim 0$).

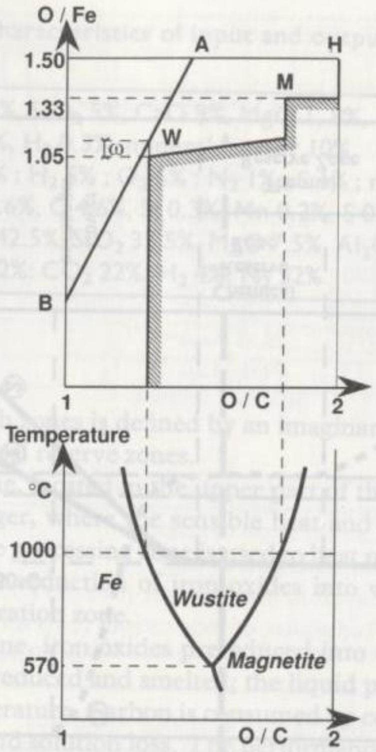

Figure 10.5 The operating line of the blast furnace; description of oxygen exchange by the the Rist diagram.

10.1.3.3. Blast furnace model

The thermal and chemical reserve zones of the blast furnace constitute the fundamental basis of the blast furnace process. This concept led Rist and colleagues (1962, 1966) and Michard (1961; Girard et al., 1971) to develop a blast furnace model involving two superimposed exchangers corresponding respectively to the preparation zone and the processing zone (Fig. 10.6). The

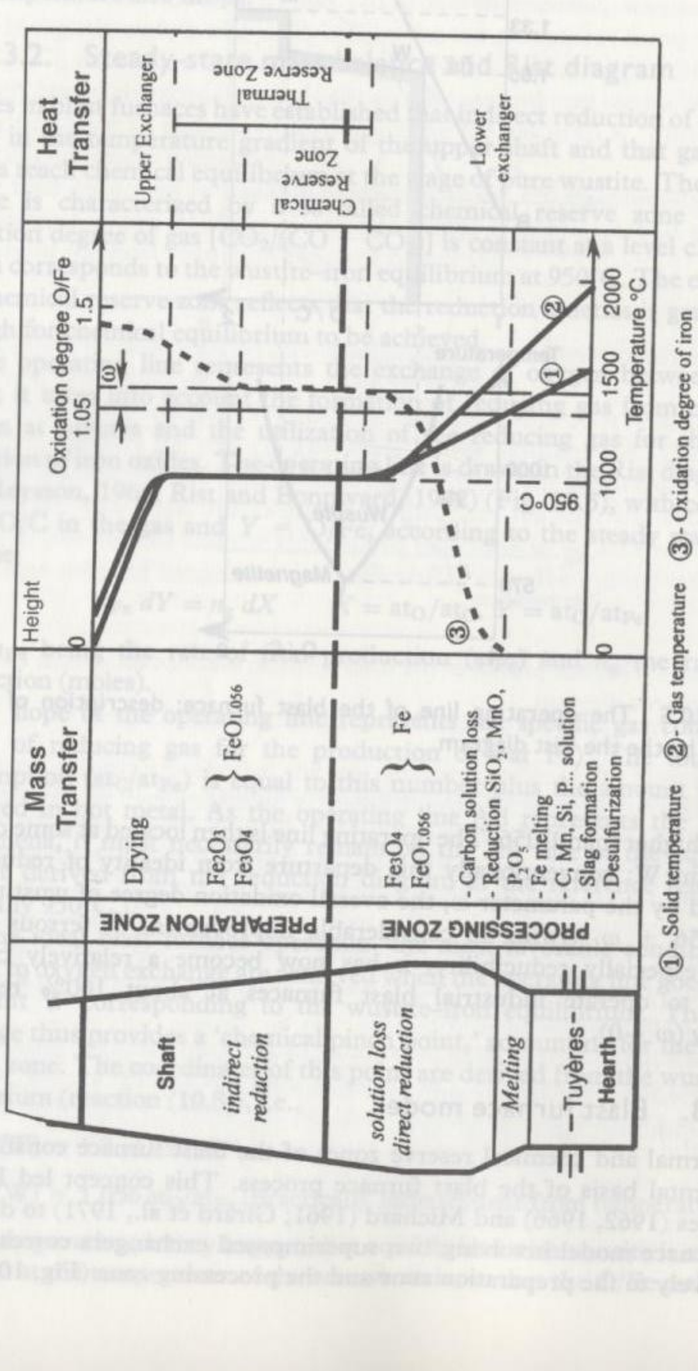

Figure 10.6 Principles of blast furnace process.

Table 10.2 Typical characteristics of input and output feed of blast furnace

Sinter	Fe 58%, SiO_2 5%, CaO 9%, MgO 1, 8%, Al_2O_3 1%
Coke	C 88%, H_2 0.3%, mineral matter 10%
Coal (injection)	C 80% ; H_2 5% ; O_2 6% ; N_2 1% ; S 1% ; mineral matter 5%
Iron	Fe 94.6%, C 4.6%, Si 0.3%, Mn 0.2%, S 0.02%, P 0.08%
Slag	CaO 42.5%, SiO_2 35.5%, MgO 7.5%, Al_2O_3 10.5%, Fe 0.2%, S 1%
Top gas	CO 22%; CO_2 22%; H_2 4%; N_2 52%

boundary between both zones is defined by an imaginary plane cutting across the thermal and chemical reserve zones.

The preparation zone, located in the upper part of the furnace, is merely a heat and mass exchanger, where the sensible heat and reducing potential of the gas delivered by the processing zone is used to heat up the charge to 950°C and to achieve indirect reduction of iron oxides into wustite. No carbon is consumed in the preparation zone.

In the processing zone, iron oxides prereduced into wustite as well as the nonferrous oxides are reduced and smelted; the liquid phases are formed and heated to casting temperature. Carbon is consumed by combustion at tuyeres, dissolution into iron, and solution loss. The performance of the blast furnace, especially the fuel consumption, is mostly determined by the reactions going on in the processing zone.

10.1.3.4. Heat and mass balance

A typical example of heat and mass balance corresponding to modern blast furnace operation is given in Tables 10.2 and 10.3. In integrated ironmaking plants, the major source of iron is sinter and/or pellets, with some additions of lumpy ores. The injection of auxiliary fuels at tuyeres is now a widespread practice, especially of pulverized coal (1 kg of coal is equivalent to ~0.85 kg of coke). Coal injection rate of 180 kg/t_{HM} is now a common industrial practice, and considerable efforts are being expended to further increase this value to 250 kg/t_{HM} in order to reduce the demand for coke.

The smelting reactions and solution loss represent by far the two largest heat requirements of the process. Reduction of iron oxides and heat losses make up a small proportion of the balance. The heat of coke and coal combustion reactions and the enthalpy of hot blast each account for about 50% of the heat supply. The total heat losses are quite low, less than 10% of the requirements.

Table 10.3 Heat and mass balance of blast furnace

(a) Mass balance

Input			Output		
Sinter (58% Fe)	1500	kg t_{HM}^{-1}	Iron	9000	t_{HM} per day
Lumpy ore	150	kg t_{HM}^{-1}	Slag	300	kg t_{HM}^{-1}
Coke (88% C)	300	kg t_{HM}^{-1}	Top gas	1480	N m^3 t_{HM}^{-1}
Coal	180	kg t_{HM}^{-1}	Dust	10	kg t_{HM}^{-1}
Hot blast	970	N m^3 t_{HM}^{-1}			
Oxygen	15	N m^3 t_{HM}^{-1}			

(b) Heat balance

Heat supply (MJ t_{HM}^{-1})	Combustion of coke	1086	26 %
	Combustion of coal	1232	29 %
	Sensible heat of blast (temperature 1180°C)	1738	41 %
	Reduction of iron oxides (overall)	177	4 %
	Total heat supply	**4233**	**100 %**
Heat requirements (MJ t_{HM}^{-1})	Melting and enthalpy of liquids	2005	47 %
	Reduction of non ferrous oxides	83	2 %
	Solution loss reaction	1297	31 %
	Sensible heat of top gas	359	8 %
	Water shift and water cracking reactions	196	5 %
	Heat losses	296	7 %
	Total heat requirements	**4233**	**100%**

10.1.3.5. Aerodynamic aspects and flow conditions

In the blast furnace, hot reducing gas ascends through the coke grid wetted with liquid metal and slag below the melting zone, and travels upward through a column of dry alternate layers of coke and sinter. The gas flow pattern depends upon the resistance it is subjected to during its ascent in the packed bed, whereas the thermal and chemical efficiency of the process depends on the uniformity and time of contact between reacting phases.

At low flow rate the pressure loss in a packed bed is mostly due to viscous flow and is proportional to velocity. At higher velocity, flow becomes turbulent and the pressure drop increases as the square of velocity. The overall pressure drop over the unit height of the column can be expressed by the Ergun relationship:

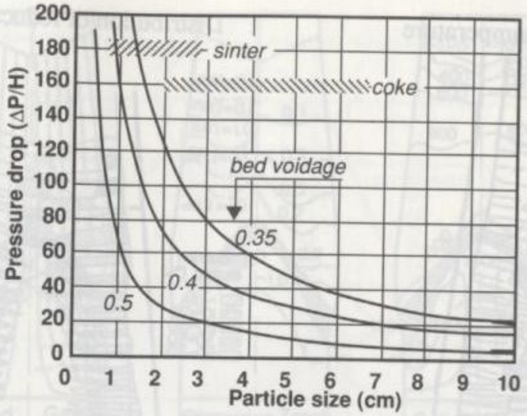

Figure 10.7 Effect of particle size and voidage on the pressure drop in packed bed (Ergun relationship). (Hatched area indicates typical range of sinter and coke particle sizes.)

$$\frac{\Delta P}{H} = A\,\frac{(1-\varepsilon)^2}{\varepsilon^3}\,\frac{\eta}{d^2}\,V + B\,\frac{(1-\varepsilon)}{\varepsilon^3}\,\frac{\rho}{d}\,V^2 \qquad (10.11)$$

with $A \sim 150$, $B \sim 1.75$; ε = voidage of the bed; d = mean diameter of particles (m); η = kinematic viscosity of gas ($m^2\,s^{-1}$); ρ = density of gas; V = velocity of gas ($m\,s^{-1}$).

The respective effects of voidage and particle size on pressure drop are shown in Fig. 10.7. According to its size range, sinter plays a predominant role in pressure drop in packed bed, as compared to coke. For a given particle size, a decrease of voidage by 0.1 results in an increase of pressure drop by 3 to 5 times.

10.1.4. The Two-dimensional Blast Furnace

The two-dimensional model of the blast furnace and the importance of the radial dimension were first emphasized as a result of full-scale experiments carried out in Japan, in which the internal structure of operating blast furnaces was quenched and carefully dissected (ISIJ, 1987) (Fig. 10.8). In the shaft, the ore and coke layers keep their initial stratification and move downward under plug flow conditions. When reaching their softening temperature (~1100°C), the ore layers soften and become impervious to gas,

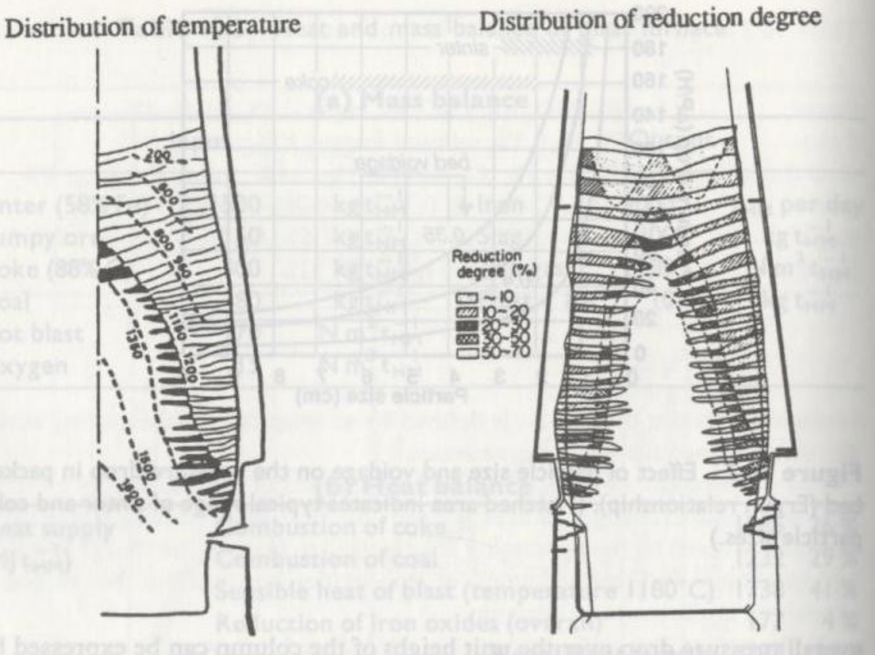
Distribution of temperature

Distribution of reduction degree

Figure 10.8 Structure of inner state of blast furnace, from quenching and dissection (ISIJ, 1987).

forming the so-called 'cohesive zone.' The cohesive zone is located between the softening and the melting isotherms. Liquid phases are formed at ~1350°C. The thermal and chemical path followed by the charge materials and the gas, and consequently the contact conditions between phases and the extent of reaction, are thus strongly dependent upon the radial position.

Considering the flow of ferrous burden, plug flow conditions prevail above the cohesive zone, whereas below the cohesive zone some mixing occurs. From residence time distribution measurements (Nicolle et al., 1986), it has been shown that the plug flow zone occupies ~40% of total volume and the mixing zone ~60%. Obviously these ratios depend on the location of the cohesive zone.

A comprehensive analysis of the blast furnace process thus requires all the coupled phenomena of chemical transfer, heat transfer, and fluid flow to be described in two-dimensional conditions. Sophisticated mathematical models have been developed for this purpose, as for example the BRIGHT model by NSC (Sugiyama et al., 1988); they generally allow the drawing of a complete map of the interior conditions of the furnace, in terms of temperature pattern, gas flow, and progress of reduction (Fig. 10.9).

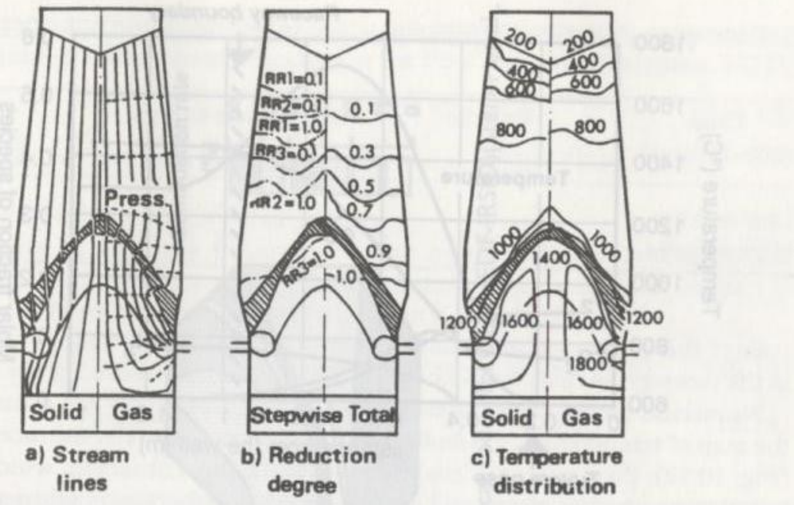
a) Stream lines

b) Reduction degree

c) Temperature distribution

Figure 10.9 Estimation of gas flow, reduction process, and temperature in the blast furnace, using 2D numerical model (BRIGHT model, NSC (Sugiyama et al., 1988)).

10.2. THE REACTIONS OF COMBUSTION

10.2.1. The Combustion Zone

Combustion of coal at tuyeres occurs under very specific conditions with respect to kinetics (ISIJ, 1987) (Fig. 10.10):

- A very short residence time of coal in the oxygen-containing zone, less than 5 ms in the tuyere, less than 20 ms in the raceway.
- A low oxygen/carbon ratio; the stoichiometry for combustion into $CO_2 + H_2O$ is exceeded as soon as coal rate is over $130\,\mathrm{kg/t_{HM}}$.

These detrimental conditions are balanced by some favorable effects:

- High blast temperature, usually in the order of 1200°C, and oxygen enrichment (up to 24% O_2 in blast), both conditions leading to high flame temperature (2100 ± 100°C).
- Very high heating rate (estimated between 1 and $2 \times 10^5\,\mathrm{K\,s^{-1}}$).
- High specific area of finely ground coal particles.

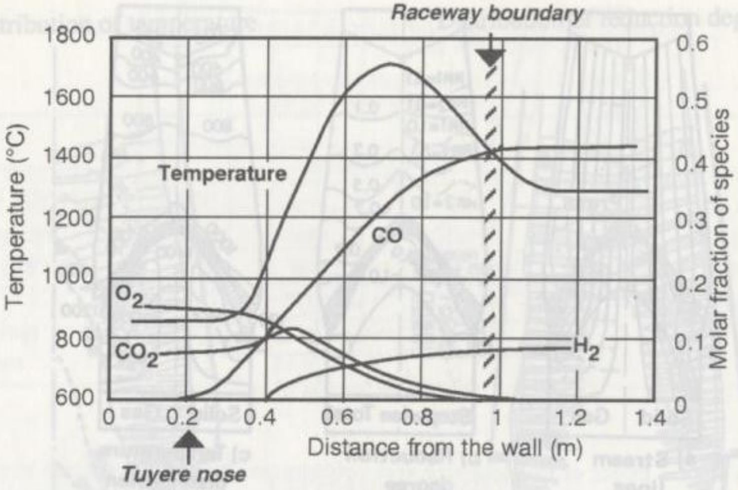

Figure 10.10 Gas composition and temperature distribution in the raceway; measurements on pilot blast furnace (ISIJ, 1987).

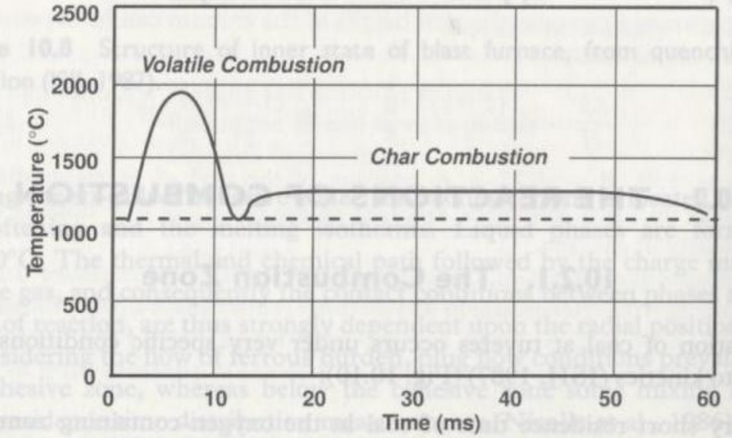

Figure 10.11 Mechanisms of pulverized coal combustion; a two-step reaction (Prado et al., 1988).

10.2.2. Mechanisms of Coal Combustion

Coal combustion is a two-step process (Prado et al., 1988; Kobayashi et al., 1976): a first and fast step of volatile emission and combustion, followed by a much slower step of heterogeneous char combustion (Fig. 10.11). The time

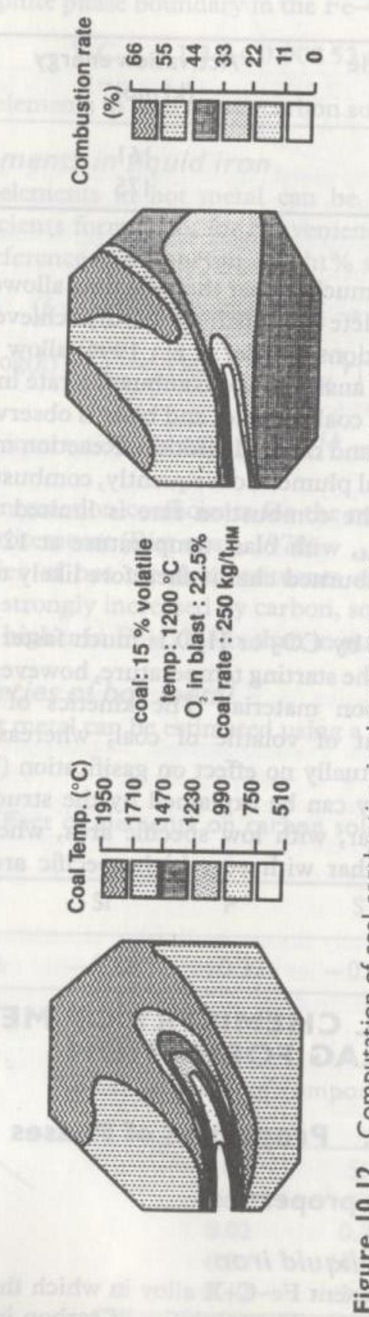

Figure 10.12 Computation of coal combustion in the raceway using numerical code MELODIF (EDF-IRSID)(Steiler et al., 1994): coal temperature and combustion efficiency.

Table 10.4 Kinetics of char gasification with CO_2 or H_2O

Coal (200–250 μm)	Volatile (%)	Activation energy ($kJ\,mol^{-1}$)	Constant ($10^{-3}\,s^{-1}$)
Low volatile	10	161	0.16
High volatile	35	175	0.27

scale of this phenomenon is much higher than the time allowed for coal to stay in the raceway, so that complete combustion is hardly achieved in the raceway.

Numerical model calculations (Steiler et al., 1994) allow the estimation of the map of temperature, gas analysis, and combustion rate in the raceway area (Fig. 10.12). Poor mixing of coal particles and blast is observed, which results in a slow heating up of coal and delayed ignition. Reaction mostly proceeds at the external boundary of coal plume. Consequently, combustion is incomplete in the raceway: typically the combustion rate is limited to ~70% for an injected level of 180 kg/t_{HM}, with blast temperature at 1200°C and oxygen content of 22.5%. Some unburned char is therefore likely to escape from the raceway.

The gasification reaction by CO_2 or H_2O is much faster for char than for coke (Steiler et al., 1994). The starting temperature, however, remains close to 950°C, whatever the carbon material. The kinetics of char gasification increases with the amount of volatile of coal, whereas the preparation conditions of char have virtually no effect on gasification (Table 10.4). This difference in char reactivity can be explained by the structure: low-volatile coals produce compact char, with low specific area, whereas high-volatile coals give 'balloon type' char with very high specific area, enhancing the accessibility of gas.

10.3. PHYSICAL CHEMISTRY OF METAL AND SLAG FORMATION

10.3.1. Properties of Phases

10.3.1.1. Metal phase properties

Solubility of carbon in liquid iron

Hot metal is a multicomponent Fe–C–X alloy in which the degree of carbon saturation is usually 95–100%. The solubility of carbon in pure iron is fixed by the temperature only, according to the following relationship, representing to the liquid–graphite phase boundary in the Fe–C diagram (Chipman, 1972):

$$\%C_{sat} = 1.34 + 0.002\,53\,t\,(°C) \tag{10.12}$$

Other dissolved elements in iron act on carbon solubility (Table 10.5).

Activity of elements in liquid iron

The activity of elements in hot metal can be described according to the interaction coefficients formalism; for convenience, the activity of solute i is expressed with reference to a Henryan weight% standard state:

$$a_i = f_i\,(\%i) \qquad (f_i = \text{activity coefficient};\ f_i \rightarrow 0,\ \text{as}\ (\%i) \rightarrow 0) \tag{10.13}$$

$$\log(f_i) = \sum_j e_i^j\,(\%j) + \sum_j \sum_k r_i^{j,k}\,(\%j)\,(\%k) \tag{10.14}$$

e_i^j = first-order interaction coefficient; $r_i^{j,k}$ = second-order interaction coefficient.

The values of interaction coefficients for the most important elements can be taken from the literature (Rist et al., 1978).

Typical activities of hot metal constituents are reported in Table 10.6. Silicon activity is strongly increased by carbon, so that the activity coefficient of silicon is much higher in Fe–C melts than in pure iron.

Physical properties of hot metal

The density of hot metal can be estimated using a rule of additivity of specific

Table 10.5 Effect of elements on carbon solubility in iron (1500°C)

i	Mn	Si	P	S	Cr	Ti
Δ%C*/Δ%i	0.032	−0.33	−0.32	−0.41	0.08	0.18

Table 10.6 Typical activities of components in hot metal

	Mn	P	S	Si	C	Fe *
%i	0.25	0.08	0.02	0.30	4.85	94.5
f_i	0.3	9.8	6.0	10.5	5.8	0.88
a_i	0.075	0.78	0.12	3.15	28.2	0.83

volume of each component (Lucas, 1964); at 1500°C, the relationship is (density in t m^{-3})

$$\rho = \frac{1}{0.142 + [18.5(\%C) + 13.2(\%P) + 25.5(\%Si) + 3.3(\%Mn)] \times 10^{-4}} \tag{10.15}$$

The viscosity of liquid hot metal varies between 0.4 and 0.6 Pa s for temperature in the range 1450–1550°C; owing to their usually low concentrations in hot metal, components other than carbon can be assumed to have no significant effect on the viscosity of liquid metal. However, if solid particles are precipitated from the liquid (e.g., graphite, titanium carbonitrides, ...) flow behavior may become very poor.

10.3.1.2. Slag properties

Blast furnace slags belong to the CaO–SiO$_2$–Al$_2$O$_3$–MgO system. Minor components MnO, FeO, Na$_2$O, K$_2$O, ... are also present, but their effect on physical and chemical properties is not quantitatively established.

The composition of blast furnace slag is adjusted so as to satisfy the following criteria:

- Liquidus temperature in the range 1350–1400°C
- Good fluidity
- Capacity to retain impurities (S, K), by slag–metal or slag–gas reactions.

The chemical composition of blast furnace slag is typically in the range $0.9 < CaO/\%SiO_2 < 1.2$; $9 < \%Al_2O_3 < 12$; $5 < \%MgO < 10$. Large domains of liquid phases exist in the system CaO–SiO$_2$–Al$_2$O$_3$–MgO at temperature levels of 1350–1400°C (Fig. 10.13). It is generally accepted that the presence of minor components in slag results in a total drop of liquidus temperature by ~50–100°C.

As long as slag is completely liquid, its fluidity is satisfactory, although its viscosity is about 100 times higher than that of liquid hot metal. The viscosity of liquid slag can be well estimated in the system CaO–SiO$_2$–Al$_2$O$_3$–MgO, according to a model derived by Urbain (1987), taking into account temperature and composition (Fig. 10.14). A temperature drop of 50°C results in an increase of viscosity by ~35%.

The activities of components of liquid slags can easily be computed from thermodynamic models, relying on a structural description of the slag (cell assumption) and using actual thermodynamic data (phase diagrams, activities, etc.) to fit some parameters. The most complete model developed by Gaye et al. (1984, 1992) allows the calculation of activities and sulfide capacity in the multicomponent system CaO–SiO$_2$–Al$_2$O$_3$–MgO–MnO–FeO–TiO$_2$ (Fig. 10.15).

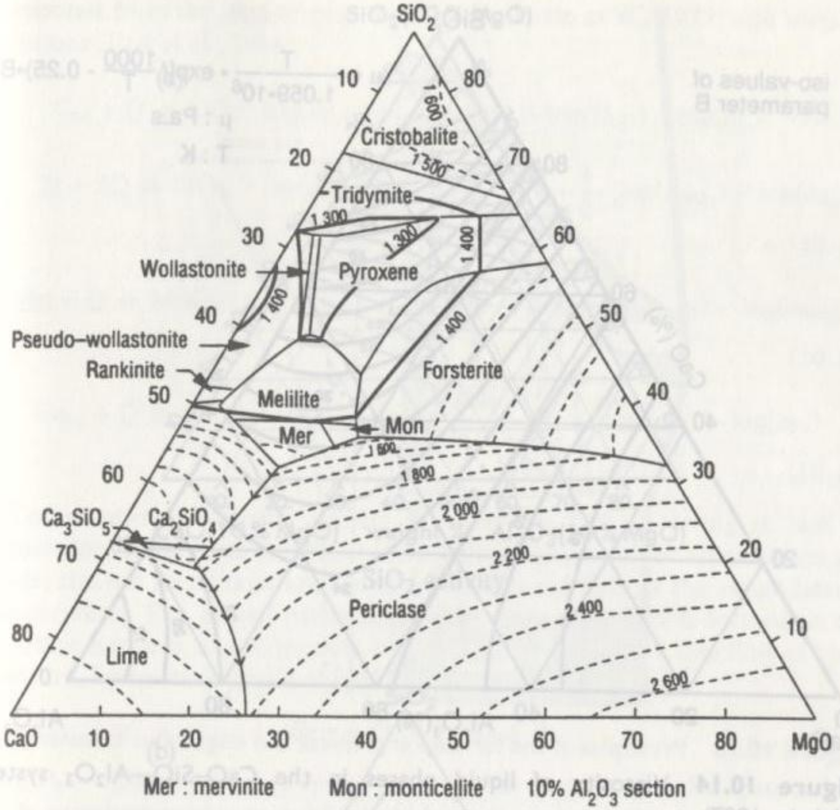

Figure 10.13 Liquidus surface in the system CaO–SiO$_2$–Al$_2$O$_3$–MgO; section at 10% Al$_2$O$_3$.

10.3.2. Transfer of elements between metal–slag–gas

10.3.2.1. Observations on the formation of liquid slag and metal

The formation of liquids occurs in a 'reactor' located between the fusion zone and the hearth of the blast furnace, as a result of heat and material transfer between gas, solids (coke, partly smelted ferrous phases), and liquids (metal and slag) (Fig. 10.16). Complex conditions prevail in that part of the blast furnace, involving cross currents between gas and liquids, inducing strong heterogeneity of the physicochemical conditions across the radius of the furnace. Basically the formation and processing of liquids is governed by three major parameters:

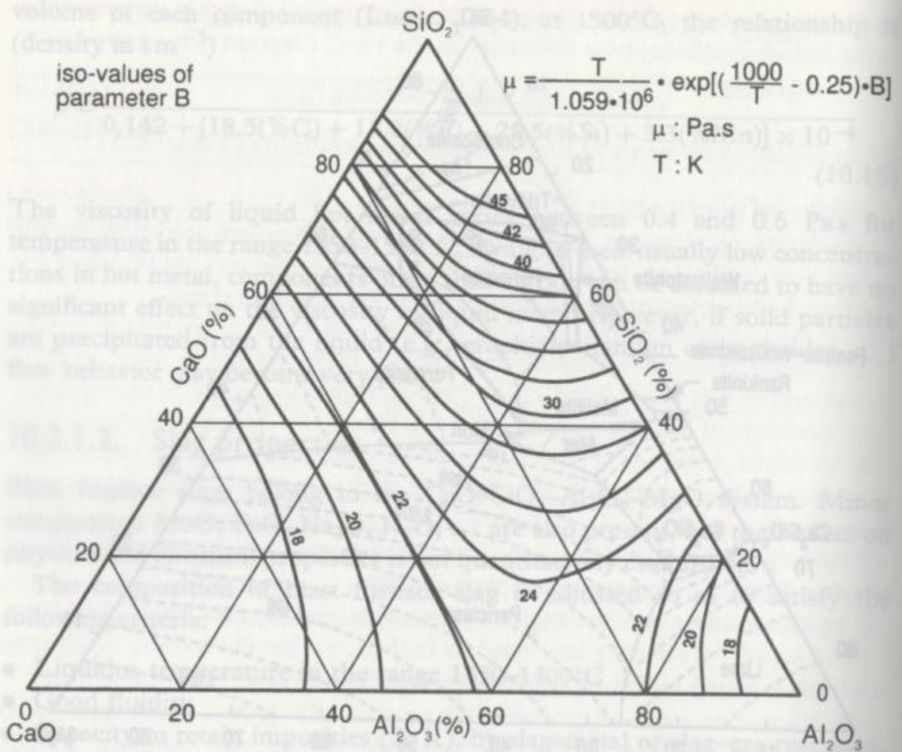

Figure 10.14 Viscosity of liquid phases in the CaO–SiO$_2$–Al$_2$O$_3$ system (Urbain, 1987).

- The temperature at the reaction interface
- The local oxygen potential
- The contact conditions between phases, resulting from the size of the reacting zones and the flow conditions

Formation of liquids (slag and metal) occurs through successive stages of softening and melting within quite a large temperature range (1100–1350°C). The melting temperature of ferrous phases is primarily governed by their residual oxygen content; it is high when the oxygen content is low; consequently, the temperature of liquid formation results not only from the initial chemistry of ferrous burden (basicity, etc.), but predominantly from the progress of the reduction process. The primary slags exhibit a significant amount of FeO (15–20%). At first, the liquid metal contains large amounts of sulfur and phosphorus, both elements lowering the melting temperature of

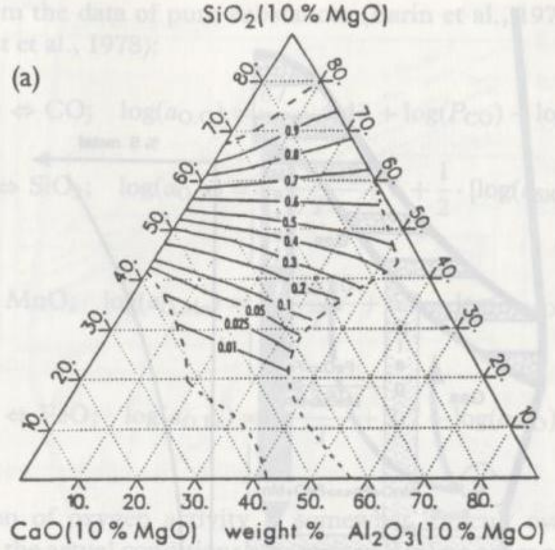

SiO$_2$ activity

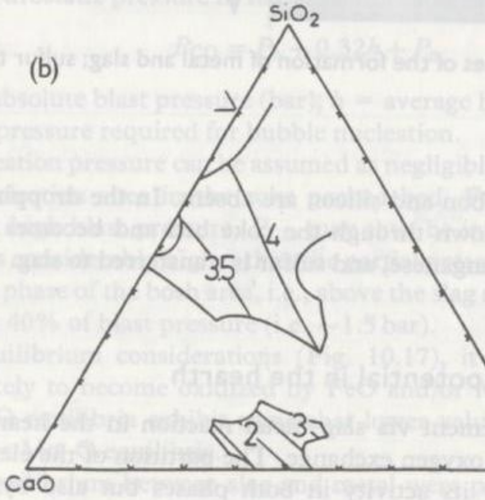

Sulphide capacity (C's)

Figure 10.15 (a) SiO$_2$ activity in the quaternary system CaO–SiO$_2$–Al$_2$O$_3$–MgO at 10% MgO and 1500°C; (b) sulphide capacity (log C'S) in the CaO–SiO$_2$–Al$_2$O$_3$ system at 1500°C (in blast furnace type slags, model computations (Gaye et al., 1984)).

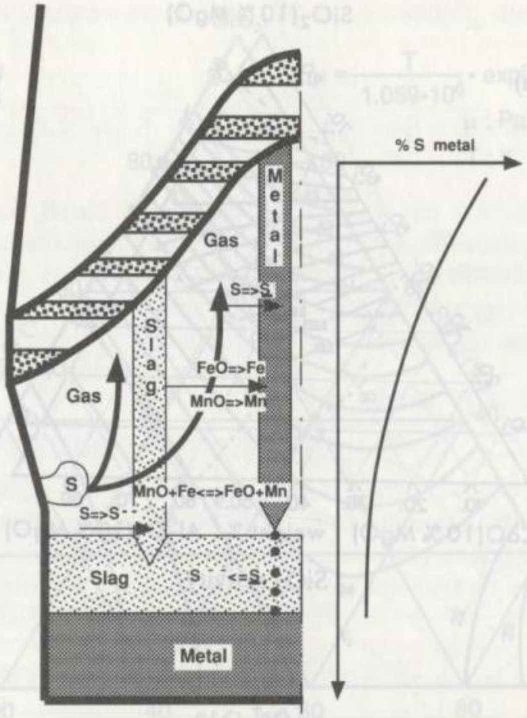

Figure 10.16 Principles of the formation of metal and slag; sulfur transfer.

pure iron, whereas carbon and silicon are absent. In the dropping zone, the metallic phase flows down through the coke bed and becomes enriched in carbon, silicon, and manganese, and sulfur is transferred to slag.

10.3.2.2. Oxygen potential in the hearth

The transfer of an element via slag–metal reaction in the hearth generally involves simultaneous oxygen exchange. The partition of the element is thus governed not only by its activity in both phases but also by the oxygen potential at the reacting interface. This potential can be represented by the partial pressure of oxygen or the oxygen activity at the slag–metal interface. In the hearth conditions, the reacting interface to be considered is that of metal droplets passing through the slag layer in the coke packed bed.

Several metal–slag redox reactions may be used to define the oxygen potential at the interface, some of them listed below. The values can be computed from the data of pure substances (Barin et al., 1977) and metallic solutions (Rist et al., 1978):

$$C_{gr} + \underline{O} \Leftrightarrow CO; \quad \log(a_{O,C}) = \frac{87}{T} - 4.43 + \log(P_{CO}) - \log(a_C) \quad (10.16)$$

$$\underline{Si} + 2\underline{O} \Leftrightarrow SiO_2; \quad \log(a_{O,Si}) = -\frac{15520}{T} + 6 + \frac{1}{2}\cdot[\log(a_{SiO_2}) - \log(a_{Si})] \quad (10.17)$$

$$\underline{Mn} + \underline{O} \Leftrightarrow MnO; \quad \log(a_{O,Mn}) = -\frac{15050}{T} + 6.7 + \log(a_{MnO}) - \log(a_{Mn})] \quad (10.18)$$

$$Fe_{liq} + \underline{O} \Leftrightarrow FeO; \quad \log(a_{O,Fe}) = -\frac{6320}{T} + 2.7 + \log(a_{FeO}) - \log(a_{Fe}) \quad (10.19)$$

Computation of oxygen activity is somewhat difficult owing to lack of knowledge on the actual conditions at interface. Unless other assumptions are made, the hot metal temperature is used as an estimate of the actual hearth temperature. The partial pressure of CO inside the bubbles formed at the interface between metal droplets and slag is estimated as a function of blast pressure, hydrostatic pressure in slag layer, and nucleation:

$$P_{CO} = P_b + 0.32h + P_n$$

with P_b = absolute blast pressure (bar); h = average height of slag layer (m); P_n = extra pressure required for bubble nucleation.

The nucleation pressure can be assumed as negligible, owing to an excess of possible nucleation sites in the coke packed bed. For large blast furnaces operating at high blast pressure, P_{CO} may thus be in the order of 3–4 bars. This value is considerably higher than the partial pressure of CO prevailing in the bulk gas phase of the bosh area, i.e., above the slag surface, where it can be estimated as 40% of blast pressure (i.e. ~1.5 bar).

From equilibrium considerations (Fig. 10.17), it can be observed that silicon is likely to become oxidized by FeO and/or MnO in the hearth. In general, C–O equilibria exhibit somewhat lower values of oxygen potential than Fe–O or Mn–O equilibria.

If total equilibrium between slag and metal were prevailing, the different previous reactions would define one unique value of oxygen activity. In fact, this is scarcely observed, and the various partial equilibria lead to slightly different oxygen potential. Industrial trials involving direct measurement of oxygen activity with an electrochemical cell have shown that the oxygen activity can be reasonably well predicted according to the Si–SiO$_2$ equilibrium (Fig. 10.18).

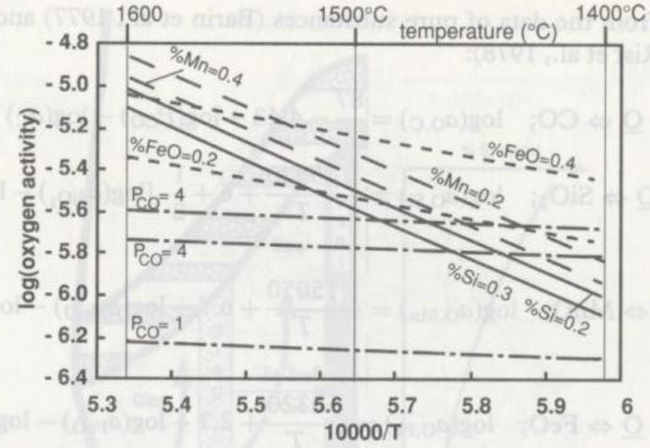

Figure 10.17 Oxygen activity corresponding to different equilibria in the hearth of the blast furnace.

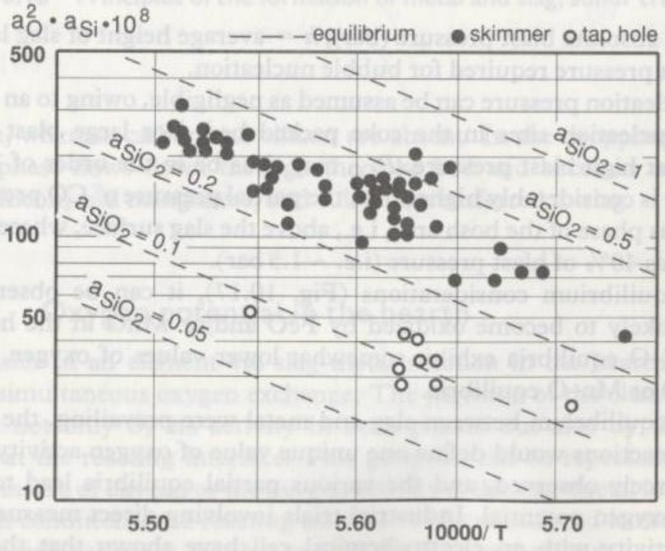

Figure 10.18 Measurement of oxygen activity by electrochemical cell in hot metal: Si–O equilibrium.

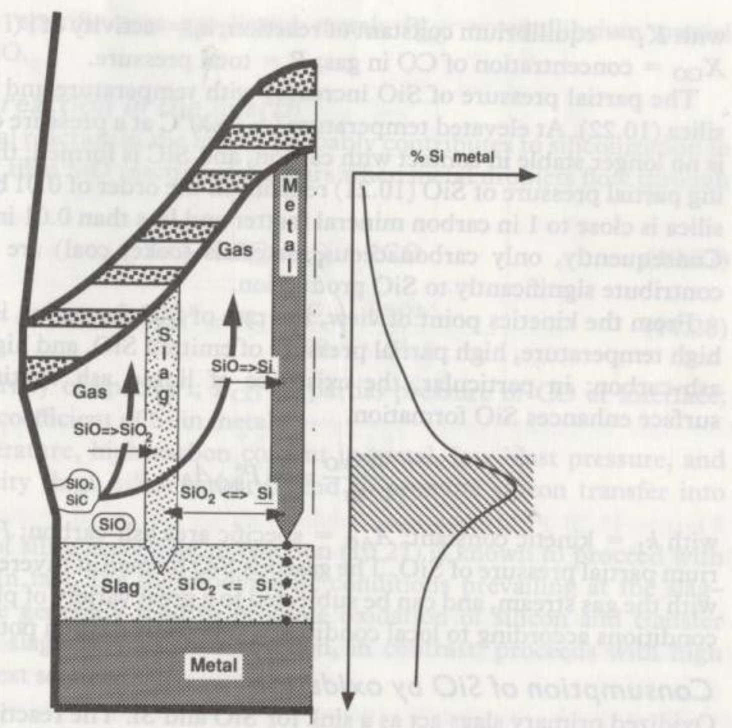

Figure 10.19 Principles of silicon transfer phenomena.

10.3.2.3. Mechanisms of silicon transfer

Reduction of silica in the blast furnace is quite different from the reduction of other oxides (MnO, P_2O_5, etc.), owing to the existence of the gaseous oxide SiO. The mechanisms of silica reduction are thus merely described in terms of formation and consumption of SiO in the reactor located below the cohesive zone (Steiler, 1989; Turkdogan et al., 1980; Tsuchiya et al., 1972; Sugiyama et al., 1990) (Fig. 10.19).

Formation of SiO

The formation of SiO occurs by reduction of silica, according to following reactions:

$$SiO_2 + C \Leftrightarrow SiO + CO \tag{10.20}$$

or

$$SiC + CO \Leftrightarrow SiO + 2\,C \tag{10.21}$$

$$P_{SiO} = K_1 a_{SiO_2} a_C \frac{1}{X_{CO}} \frac{1}{P} \tag{10.22}$$

with K_1 = equilibrium constant of reaction; a_i = activity of i (i = C or SiO_2); X_{CO} = concentration of CO in gas; P = total pressure.

The partial pressure of SiO increases with temperature and the activity of silica (10.22). At elevated temperature (>1620°C at a pressure of 3 bars) SiO_2 is no longer stable in contact with carbon, and SiC is formed; the corresponding partial pressure of SiO (10.21) remains in the order of 0.01 bar. Activity of silica is close to 1 in carbon mineral matter and less than 0.01 in primary slag. Consequently, only carbonaceous materials (coke, coal) are considered to contribute significantly to SiO production.

From the kinetics point of view, the rate of SiO formation is promoted by high temperature, high partial pressure of emitted SiO, and high specific area ash-carbon; in particular, the existence of liquid ash wetting the carbon surface enhances SiO formation.

$$\frac{dn_{SiO}}{dt} = k_1 P^*_{SiO} A_{AC} \tag{10.23}$$

with k_1 = kinetic constant; A_{AC} = specific area ash-carbon; P^*_{SiO} = equilibrium partial pressure of SiO. The gaseous SiO formed at tuyeres flows upward with the gas stream, and can be subjected to a great variety of physicochemical conditions according to local conditions, especially oxygen potential.

Consumption of SiO by oxidation

Oxidized primary slags act as a sink for SiO and Si. The reaction is promoted by high FeO content and high basicity of slag.

Consumption of SiO by reduction

Reduction of SiO by carbon is the effective reaction that contributes to metal siliconization:

$$SiO + \underline{C} \Leftrightarrow \underline{Si} + CO \tag{10.24}$$

$$\%Si^* = K_4 P_{SiO} a_C \frac{1}{P_{CO}} \frac{1}{f_{Si}} \tag{10.25}$$

with a_C = carbon activity in metal; f_{Si} = activity coefficient of Si; $\%Si^*$ = equilibrium silicon content.

The conditions favorable for high equilibrium silicon content in metal are high temperature, high SiO partial pressure, high carbon content in metal droplets, and low partial pressure of CO (i.e., high reducing potential). From the kinetic point of view (Tsuchiya et al., 1972), silicon transfer into metal is enhanced by high emission of SiO, high temperature, and efficient contact conditions: small size droplets, high reaction time (i.e., high cohesive zone, low specific gas flow rate, low throughput).

$$\frac{dn_{Si}}{dt} = k_4 P^*_{SiO} A_{GL} \tag{10.26}$$

with A_{GL} = specific area gas–liquid metal; P^*_{SiO} = equilibrium partial pressure of SiO.

Slag–metal reaction in the hearth

The slag–metal reaction in the hearth probably contributes to siliconization to a lesser extent than SiO reactions; it occurs when metal droplets flow through the slag layer.

$$SiO_2 + 2\underline{C} \Leftrightarrow \underline{Si} + 2CO \tag{10.27}$$

$$\%Si^* = K_5 \left(\frac{a_C}{P_{CO}}\right)^2 \frac{a_{SiO2}}{f_{Si}} \tag{10.28}$$

with a_i = activity of species i; P_{CO} = partial pressure of CO at interface; f_{Si} = activity coefficient of Si in metal.

High temperature, high carbon content in metal, low blast pressure, and low slag basicity (high silica activity) tend to promote silicon transfer into metal.

Reduction of silica according to reaction (10.27) is known to proceed with low kinetics. In fact, the thermodynamic conditions prevailing at the slag–metal interface generally tend to promote oxidation of silicon and transfer from metal to slag; the oxidation reaction, in contrast, proceeds with high kinetics (see next section).

10.3.2.4. Silicon equilibrium in the hearth

Silicon equilibrium (Steiler et al., 1990) between metal and slag is described by Equation (10.29):

$$\log(\%Si^*) = 28700/T - 16.1 + \log(a_{SiO2}) - \log(f_{Si}) + 2\log(a_C) - 2\log(P_{CO}) \tag{10.29}$$

$$A(Si) = -\left[\Delta G^\circ + RT \ln \frac{P^2_{CO}}{a^2_C} \frac{a_{Si}}{a_{SiO2}}\right] \tag{10.30}$$

with ΔG° = Standard Gibbs energy of reaction (10.27).

The affinity of silicon $A(Si)$ is used as a measure of the instantaneous departure from equilibrium: it is zero at equilibrium, whereas a negative value means that the path toward equilibrium corresponds to oxidation of silicon. In addition, the affinity also represents the thermodynamic driving force for the reaction to proceed toward equilibrium.

From the thermodynamic point of view, the bosh conditions tend to promote silicon transfer to metal, whereas hearth conditions promote silicon transfer to slag, by oxidation.

Examination of industrial results shows that slag–metal equilibrium is approximately achieved for silicon, with a partial pressure of CO between 3

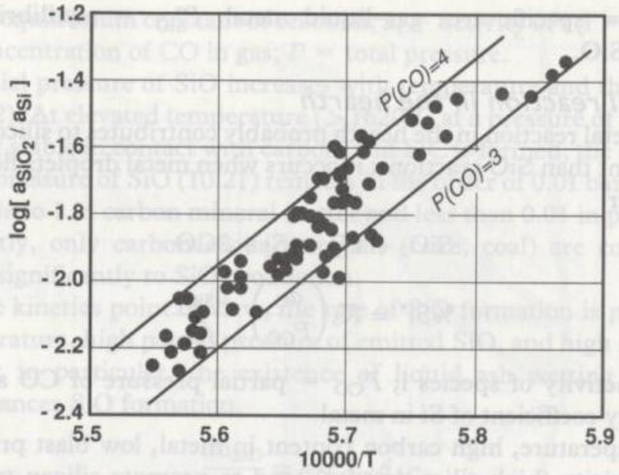

Figure 10.20 Silicon–oxygen equilibrium in hot metal (industrial cast data SOLLAC Fos).

and 4 bars (equivalent to oxygen activity between 1.5×10^{-6} and 2.5×10^{-6}) (Fig. 10.20).

These results suggest that increasing the availability of oxygen at the slag–droplet interface may result in a better approach to equilibrium and a lower silicon content at cast. Industrial application of these principles has shown that it is possible to reduce silicon content by controlling the oxygen potential in the hearth, either by proper action on the position of cohesive zone, or by injection of iron oxides through tuyeres (Brun et al., 1988).

10.3.2.5. Transfer of other elements between metal and slag

The transfer of elements other than silicon involves metal–slag reactions occurring mostly as metal droplets pass through the slag layer (Steiler et al., 1990; Turkdogan et al., 1980). The extent of reaction is defined by the partition ratio:

$$P_X = \%X_{(\mathrm{slag})} / \%\underline{X}_{(\mathrm{in\ metal})} \qquad (10.31)$$

Manganese transfer

Manganese transfer takes place according to the metal–slag reaction:

$$\mathrm{MnO} + \underline{\mathrm{C}} \Leftrightarrow \underline{\mathrm{Mn}} + \mathrm{CO} \qquad (10.32)$$

$$\log(P_{\mathrm{Mn}}) = 13880/T - 8.77 + \log(f_{\mathrm{Mn}}) - \log(\gamma_{\mathrm{MnO}}) + \log(P_{\mathrm{CO}}) - \log(a_{\mathrm{C}}) \qquad (10.33)$$

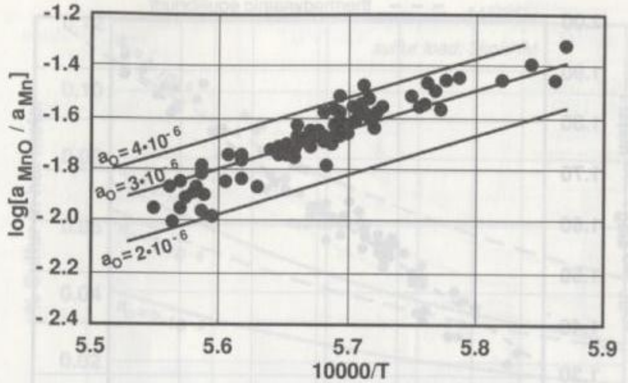

Figure 10.21 Mn–oxygen equilibrium in hot metal (industrial cast data SOLLAC Fos).

with f_{Mn} = activity coefficient of Mn in metal; γ_{MnO} = activity coefficient of MnO in slag.

Manganese recovery in metal is improved by high temperature, high basicity (decrease of activity coefficient of MnO in slag), and low oxygen potential (characterized by the ratio $P_{\mathrm{CO}}/a_{\mathrm{C}}$).

Analysis of industrial results shows that slag–metal equilibrium for manganese would correspond to an oxygen activity in the range 2×10^{-6} to 4×10^{-6}, i.e., somewhat higher than silicon equilibrium (Fig. 10.21).

Sulfur transfer

Sulfur transfer takes place according to the following metal–slag reaction, involving simultaneous oxygen transfer (Fig. 10.16):

$$\underline{\mathrm{S}} + \mathrm{O}^{2-}_{\mathrm{slag}} \Leftrightarrow \underline{\mathrm{O}} + \mathrm{S}^{2-}_{\mathrm{slag}} \qquad (10.34)$$

In the blast furnace, lime is the major desulfurizing agent, so that the previous reaction is often written as

$$\underline{\mathrm{S}} + \mathrm{CaO} \Leftrightarrow \mathrm{O} + \mathrm{CaS} \qquad (10.35)$$

$$K_{\mathrm{S}} = \frac{a_{\mathrm{o}} a_{\mathrm{s}^{2-}}}{a_{\mathrm{s}} a_{\mathrm{o}^{2-}}} = \frac{\%\mathrm{S}_{\mathrm{slag}}}{\%\mathrm{S}_{\mathrm{metal}}} \frac{a_{\mathrm{o}}}{f_{\mathrm{s}}} \frac{f_{\mathrm{s}^{2-}}}{a_{\mathrm{o}^{2-}}} = P_{\mathrm{S}} \frac{a_{\mathrm{o}}}{f_{\mathrm{s}}}, \frac{f_{\mathrm{s}^{2-}}}{a_{\mathrm{o}^{2-}}} \qquad (10.36)$$

with a_i = activity of metallic species in metal or ionic species in slag.

The sulphide capacity of slag C'_{S} (Equation 10.38) is a characteristic property of slag, increasing with temperature and slag basicity; it represents the ability of slag to absorb sulfur under given conditions of oxygen potential and temperature. The sulfur partition ratio is finally expressed as

$$\log(P_{\mathrm{S}}) = \log(C'_{\mathrm{S}}) + \log(f_{\mathrm{S}}) - \log(a_{\mathrm{O}}) \qquad (10.37)$$

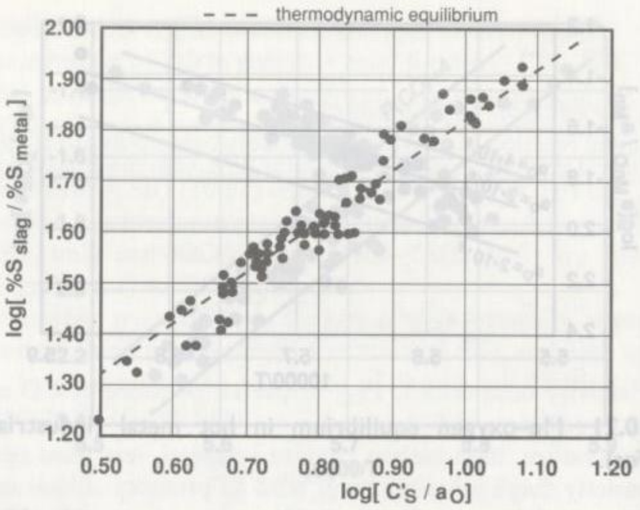

Figure 10.22 Sulfur equilibrium in hot metal (industrial cast data SOLLAC Fos); operational results compared to calculated equilibrium line.

with

$$C'_S = K_S \frac{a_{O^{2-}}}{f_{S^{2-}}} \tag{10.38}$$

The oxygen activity at the slag–metal interface may be defined with the help of Si–SiO_2 or Mn–MnO equilibrium, according to reactions (10.17) or (10.18). The manganese partition ratio is often used as an easy method to get index for oxygen potential, and it is well known that a close decreasing relationship is obtained between sulfur and manganese partition ratios. This result does not mean that the amount of manganese in hot metal exhibits any favorable effect on sulfur transfer; the only governing factor with respect to sulfur transfer is the manganese partition ratio, as an index for oxygen potential.

Analysis of industrial results shows that sulfur transfer is generally close to equilibrium conditions (Fig. 10.22). Sulfur transfer into slag is promoted by high temperature, high slag basicity, and highly reduced slag. Equation 10.39 gives the sulfur content in hot metal, taking into account the mass balance of sulfur in the blast furnace (Fig. 10.23).

$$\%S = \frac{\text{sulfur input (kg t}^{-1})}{10 + 0.01 L C'_S\ (f_S/a_O)} \tag{10.39}$$

with L = slag rate (kg/t_{HM}); %S = sulfur content in metal (%).

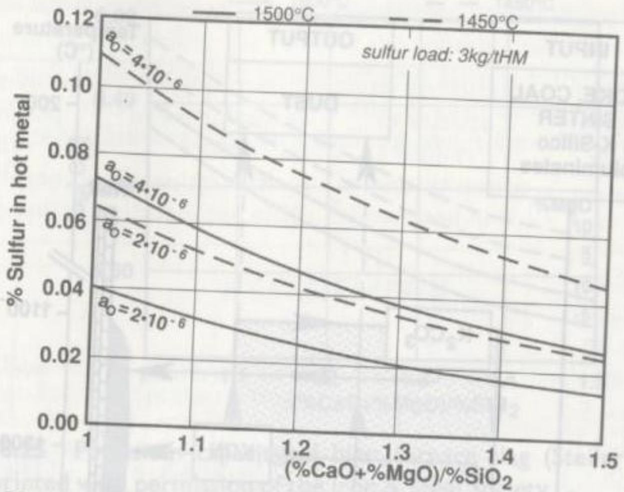

Figure 10.23 Predicted sulfur content in hot metal, as a function of temperature, slag basicity, and oxygen potential (sulfur input 3 kg t_{HM}^{-1}; slag rate 300 kg t_{HM}^{-1}).

10.3.2.6. Alkali transfer

Behavior of alkalis in the blast furnace

The basic features of alkali behavior in the blast furnace are now quite well established, at least qualitatively (Lu, 1973; Steiler et al., 1984). Alkalis enter the furnace as complex silicoaluminates in raw materials (ore, coke, coal, etc.), and leave it mainly dissolved in slag. In the meantime, they are subjected to cycling phenomena, owing to simultaneous countercurrent flow of gas and solids, and gradients of temperature and oxygen potential along the height of the furnace (Fig. 10.24).

Alkalis get concentrated and stored within the areas where their reduction/oxidation reactions are the most active, i.e., in the range 1100–1400°C.

Both sodium and potassium may be subjected to cycling in the blast furnace; despite large similarities in their thermodynamic properties, sodium species are more stable in the solid state than the corresponding potassium species, so that the cycling phenomena are less pronounced for sodium than for potassium.

Alkali equilibria between gas and slag

Alkali dissolution into slag involves simultaneous exchange of oxygen, and can be expressed as

$$K^+ + \tfrac{1}{2}O^{2-} \Leftrightarrow K_g + \tfrac{1}{4}O_2 \tag{10.40}$$

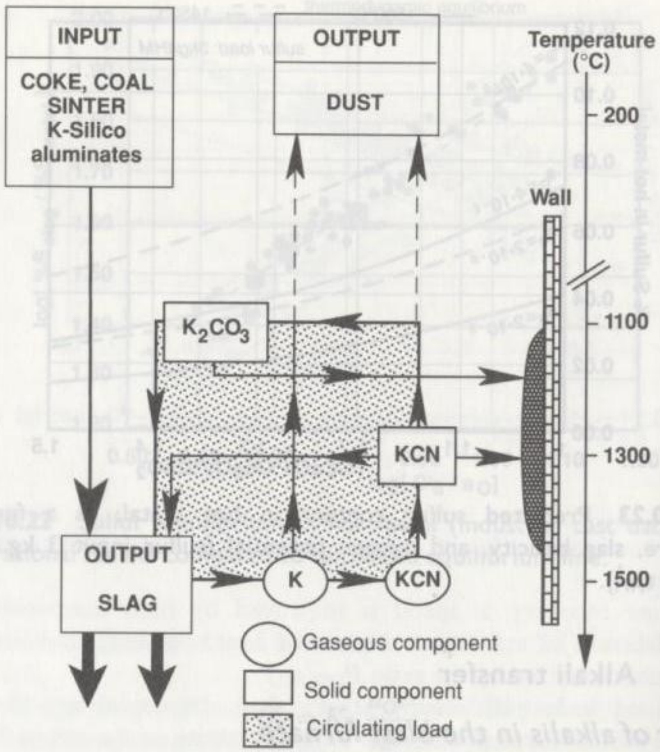

Figure 10.24 Mechanisms of alkali circulation in the blast furnace (Steiler et al., 1984). Reprinted with permission of the Iron & Steel Society.

with

$$K_K = \frac{P_K \sqrt[4]{P_{O_2}}}{a_{K^+} \sqrt{a_{O^{2-}}}} \qquad (10.41)$$

Experimental studies of the thermodynamics of potassium in liquid blast furnace type slags (Steiler et al., 1984) have established that, for limited values of potassium content in slag (<3%), the following relationship holds:

$$a_{K^+} = f_K(\%K_2O) \qquad (10.42)$$

with a_{K^+} = activity of K^+ ion in the slag, referred to a weight % standard state; f_K = activity coefficient of potassium ions; P_K = partial pressure of potassium vapor; P_{O_2} = partial pressure of oxygen.

The previous expressions can be much simplified by introducing the concept of 'potassium capacity' of slag, C_K, which is defined similarly to the sulphide capacity:

$$C_K = \frac{1}{K_K \cdot f_K \cdot \sqrt{a_{O^{2-}}}} \qquad (10.43)$$

The potassium capacity of slag is a characteristic property of slag at a given temperature that provides a measure of the ability of slag to dissolve potassium under given conditions of oxygen potential and partial pressure of potassium. From laboratory investigations, it is known that the potassium capacity of slag is a decreasing function of temperature and slag basicity (Turkdogan et al., 1980; Steiler et al., 1984). In addition, replacement of lime by magnesium oxide at constant basicity ([CaO + MgO]/SiO_2) tends to improve the potassium capacity (Fig. 10.25).

Finally, the content of potassium oxide in slag at equilibrium with gas phase can be derived from the following relationship:

$$(\%K_2O) = C_K \cdot P_K \cdot \sqrt[4]{P_{O_2}} \qquad (10.44)$$

Analysis of operational results generally shows a somewhat scattered relationship between the potassium oxide content in slag and the potassium capacity (Fig. 10.25). In fact the equilibrium potassium content in slag is controlled not only by the slag capacity but also by the oxygen potential and the partial pressure of potassium, which is unknown. Moreover, this pressure probably reflects the extent of the cycling phenomena, and is likely to vary considerably with the gas distribution pattern inside the blast furnace.

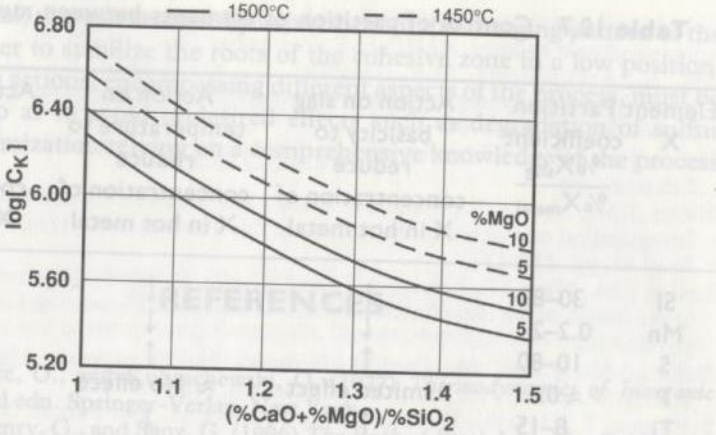

Figure 10.25 Potassium capacity of blast furnace slag (Steiler et al., 1984, 1990). Reprinted with permission of the Iron & Steel Society.

Table 10.7 Control of partition of elements between metal and slag

Element X	Partition coefficient $\frac{\%X_{slag}}{\%X_{metal}}$	Action on slag basicity to reduce concentration of X in hot metal	Action on temperature to reduce concentration of X in hot metal	Action on oxygen potential to reduce concentration of X in hot metal
Si	30–80	↑	↓	↑
Mn	0.2–2	↓	↓	↑
S	10–80	↑	↑	↓
P	≈0.1	Limited effect	≈ No effect	No effect
Ti	8–15	↑	↓	↑
Cr	0.05–0.1	↓	?	↑
Ni, Cu	≈0	No effect	No effect	No effect

10.3.2.7. Summary of chemical transfer in the hearth of the blast furnace

Slag control is a very effective way to govern the behavior of impurities and to adjust the chemistry of hot metal. Typical values for partition ratios of different elements are summarized in Table 10.7, which also indicates the respective effects of slag basicity and temperature on hot metal analysis. The high reducing conditions of the hearth account for the good desulfurizing capacity of blast furnace, which is much higher than for the steel converter. In contrast, for elements such as P, Cu, and Ni, nothing can be done in the blast furnace to modify their partition. The only way to limit their concentration in hot metal is by reducing their input levels in the burden. Some of the objectives in terms of hot metal chemistry may require conflicting actions. For example, lowering the basicity and the temperature to promote alkali dissolution into slag is detrimental to sulfur partition between metal and slag. Replacement of CaO by MgO at constant basicity, leads to a slight increase of potassium capacity of slag, with virtually no effect on sulfur capacity; this can thus help to achieve simultaneous alkali removal and efficient desulfurization. The final choice of slag composition therefore generally represents a compromise, determined by local constraints.

The oxygen potential plays a determinant role in the reactions taking place in the hearth. Its control is somewhat difficult, as it involves the entire blast furnace process, especially the location and shape of the cohesive zone. In this respect, achievement of a safely controlled amount of FeO in the areas where the formation of SiO gas is the most active is a way to depress the siliconization of hot metal; this can be done by adjustment of the charging pattern of the furnace in order to stabilize the roots of the cohesive zone in a low position. However, such actions, encompassing different aspects of the process, must be finely tuned so as to avoid undesired effects such as degradation of sulfur partition. Optimization relying on a comprehensive knowledge of the process is required.

REFERENCES

Barin, I., Knacke, O., and Kubaschewski, O. (1977) *Thermodynamics of Inorganic Substances*, 2nd edn. Springer-Verlag, New York.

Béranger, G., Henry, G., and Sanz, G. (1996) *The Book of Steel*. Lavoisier Publishing Intercept Limited, Paris, ch. 56, pp. 1118–1158.

Brun, G., Nicolle, R., Steiler, J.M., Bouttement, J.L., Eymond, J.L., and Menaut, J.P. (1988) Iron ore injection at tuyeres of blast furnace and control of hot metal silicon. *Revue de Métallurgie*, 21–32.

Chipman, J. (1972) Thermodynamics and phase diagrams of Fe–C system. *Metall. Trans.* 3, 55–64.

Darken, L.S. and Gurry, R.W. (1945) The system iron–oxygen. *J. Am. Chem. Soc.* 67, 1398–1412.

Gaye, H., Riboud, P.V., and Welfringer, J. (1984) Modelling of the thermodynamic properties of complex metallurgical slags. *Proc. 2nd Int. Symposium on Metallurgical Slags and Fluxes*. AIME, pp. 357–375.

Gaye, H., Lehmann, J., Matsumiya, T., and Yamada, W. (1992) A statistical thermodynamic model of slags; application to systems containing S, F, P and Cr oxides. *Proc. 4th Int. Conf. on Molten Slags and Fluxes, Sendai*. ISIJ, pp. 103–108.

Girard, M., Jusseau, N., and Michard, J. (1971) Developments in blast furnace practice; a study using an operating model. *Proc. ICSTIS, Trans. ISIJ* 11, 117–124.

ISIJ (1987) *Blast Furnace Phenomena and Modelling*. Elsevier Applied Science, London, pp. 3–63.

Kobayashi, H., Howard, J.B., and Sarofim, A.F. (1976) Coal devolatilisation at high temperature. *Proc. 16th Int. Symposium on Coal Combustion*, Pittsburgh, pp. 411–425.

Lu, W.K. (1973) Fundamentals of alkali containing compounds. *Proc. MacMaster Symposium*, pp. 2.1–2.17.

Lucas, L.D. (1964) Volume spécifique de métaux et alliages liquides à haute température. *Mem. Sci. Revue Métallurgie* 2, 97–116.

Michard, J.A. (1961) Contribution à l'étude du Haut Fourneau. *Revue de Métallurgie* 58(10), 41.

Nicolle, R., Steiler, J.M., and Libralesso, J.M. (1986) The use of radioactive tracers in the blast furnace. *AIME-ISS Ironmaking Proc.* 45, 565–575.

Prado, G., Charon, O., Soulard, P., Lahaye, J., Offroy, C., Picard, M., and Roth, J.L. (1988) Physical chemistry of coal combustion under blast furnace tuyere conditions. *Revue de Métallurgie* 10, 749–756.

Reichardt, P. (1927) *Archiv Eisenh.* 1, 77.

Rist, A. and Bonnivard, G. (1962) Réduction des oxydes de fer par le gaz. *Revue de Métallurgie* 59, 401.

Rist, A. and Meysson, N. (1966) A dual graphical representation of the blast furnace mass and heat balance. *AIME-ISS, Ironmaking Proc.*, pp. 88–98.

Rist, A., Ancey-Moret, M.F., Gatellier, C., and Riboud, P.V. (1978) Equilibres thermodynamiques dans l'elaboration de la fonte et de l'acier. *Les Techniques de l'ingénieur*, **M**1733, 1–8.

Steiler, J.M. (1989) Silicon transfer in the blast furnace. ECSC Report, EUR 12103, Luxembourg.

Steiler, J.M., Nicolle, R., Metz, B., Wanin, M., Thirion, C., and Flamion, D. (1984) Investigation on potassium behaviour in the blast furnace. *AIME-ISS Ironmaking Proc.* **43**, pp. 427–437.

Steiler, J.M., Gaye, H., Lehmann, J., and Nicolle, R. (1990) Slag–metal gas equilibria in the hearth of the blast furnace. *Proc. 2nd European Ironmaking Congress*, Glasgow, pp. 320–322.

Steiler, J.M., Picard, M., Lao, D., Eymond, J.L., Tieulie, A., Helleisen, M., and Hartig, W. (1994) *Proc. First ICSTI*, Sendai, pp. 517–522.

Sugiyama, T., Hayashi, Y., Sugata, M., Shibaike, H., and Suzuki, N. (1988) *CAMP-ISIJ* **1**, 1.

Sugiyama, T., Matsuzaki, S., and Nakagawa, T. (1990) Analysis of flow and reactions in the lower part of the blast furnace by high precision model. *Proc. 6th Int. Iron and Steel Congress*, Nagoya, pp. 414–421.

Tsuchiya, N., Tokuda, H., and Ohtani, M. (1972) Kinetics of silicon transfer from gas phase to molten iron. *Tetsu-to-Hagane* **58**, 3–15.

Turkdogan, E.T., Kor, G.J.W., and Fruehan, R.J. (1980) Studies of blast furnace reactions. *Ironmaking and Steelmaking* **6**, 268–280.

Urbain, G. (1987) Viscosity estimation of slags. *Steel Research* **58**(3), 111–119.

11

Iron smelting and steelmaking reactions

Richard J. Fruehan

Center for Iron and Steelmaking Research, Department of Materials Science and Engineering, Carnegie Mellon University, Pittsburgh, Pennsylvania, USA

11.1. INTRODUCTION

Owing to the large capital cost and environmental problems associated with the conventional methods of producing iron using a sinter or pellet plant, coke plant, and a blast furnace, there is a worldwide effort to develop a process which eliminates one or more of the existing processes and is less capital intensive. The processes which appear to be most promising are several versions of smelting reduction or bath smelting. In these processes coal is used directly, eliminating the coke plant; in several cases, the ore is also used directly, eliminating agglomeration. Also, owing to the fact the reactions are conducted in an intensely stirred liquid phase, the specific productivity ($t\,m^{-3}\,day^{-1}$) is considerably higher than in the blast furnace.

After iron is produced in a blast furnace, or in a smelting process, it must be further refined to remove unwanted impurities. This is usually accomplished in an oxygen steelmaking (OSM) vessel. In OSM, oxygen oxidizes carbon, silicon, and phosphorus, and sulfur is transferred to a refining slag. The other main method of producing steel is by melting scrap or other forms of iron in an electric arc furnace (EAF).

The oxygen steelmaking and iron smelting processes differ significantly from the iron blast furnace. The OSM and smelting processes utilize liquid metal–slag–gas well stirred reactors. The bulk metal and slag are relatively homogeneous. The chemical reactions are fast, approach equilibrium, and are often controlled by mass transfer. In contrast, a large portion of the blast

ADVANCED PHYSICAL CHEMISTRY FOR PROCESS METALLURGY
Copyright © 1997 Academic Press Ltd
ISBN 0-12-618920-X
All rights of reproduction in any form reserved

furnace, the stack, is a countercurrent gas–solid reactor and in the hearth there is little stirring and complete gas–metal–slag equilibrium is not achieved. Consequently, although iron smelting is basically a reducing process and steelmaking oxidizing, the reactor characteristics and the basic principles governing these two processes are similar and they differ from the blast furnace.

In this chapter the smelting and OSM processes are briefly described. For bath smelting the main reaction is the reduction of the ore which is dissolved in the slag phase, and is discussed in detail. Oxygen steelmaking is the subject of numerous books and thousands of research studies. Consequently, only a brief summary of our current understanding can be presented in this chapter. The most important reaction in OSM is decarburization and many of the other refining reactions depend on this reaction. This reaction is described in some detail but cannot be fully documented; it is adequately described in several sources. The control of nitrogen is becoming more critical and this reaction has not been thoroughly investigated for steelmaking conditions. This reaction also demonstrates many of the fundamental phenomena discussed in previous chapters. Consequently, this reaction will be examined in more detail.

11.2. IRON SMELTING

11.2.1. Process Description

The iron smelting reduction, or bath smelting, processes are not entirely new; versions of these have been attempted for several decades. However, in the last ten years there has been tremendous renewed interest and advances in these technologies. The driving force for these advances are environmental concerns and the need to reduce capital costs associated with current technologies. The iron blast furnace requires coke and the cokemaking process has serious environmental problems; as to a lesser degree do sinter plants and blast furnaces. The capital cost associated with the coke plant, sinter plants, and the blast furnace are enormous compared with the value added to the raw materials. The blast furnace has improved significantly in the past twenty years with regard to productivity and coke rates. However, it will always require some coke and its productivity in theory is limited since it is a countercurrent solid-state reactor. In general, liquid phase reactors provide for faster heat transfer and rates of chemical reactions.

The bath smelter itself may be a vertical or a horizontal reactor. A generic vertical smelter along with the reactions is shown in Fig. 11.1. Preheated and partially prereduced ore and coal are either simply added or injected into the slag or metal bath and oxygen and/or air is blown into the reactor to combust the coal and partially post-combust the reaction gases CO and H_2 to CO_2 and H_2O. When the ore is added to the slag it dissolves into the slag as iron and oxygen ions ('FeO') and then it is reduced by the coal char or carbon dissolved in metal droplets in the slag phase. A key feature of the new generation of smelting processes is post-combustion of the reaction gases above the bath or in the slag. The equilibrium gas without post-combustion would contain primarily CO and H_2. Partially post-combusting these to CO_2 and H_2 provides over 60% of the energy required to the process. However, the post-combustion gas is oxidizing to carbon and, in many cases, iron. Therefore, the heat from post-combustion must be transferred to the bath without extensive oxidation of carbon or iron. The off gas from the process which contains a

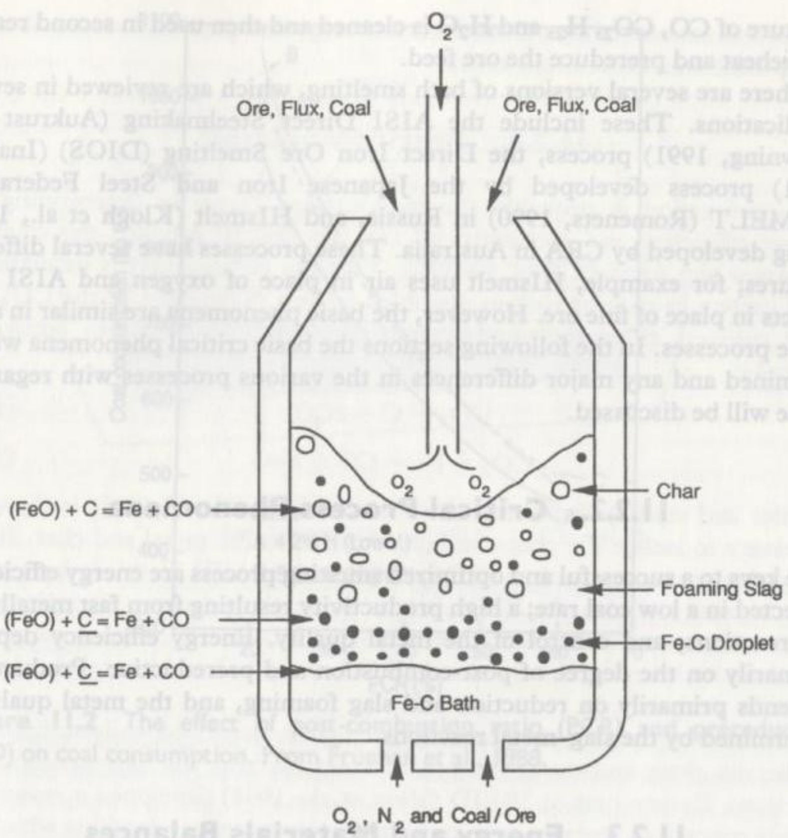

Figure 11.1 Schematic diagram of generic bath smelter indicating chemical reactions.

mixture of CO, CO_2, H_2, and H_2O is cleaned and then used in second reactor to preheat and prereduce the ore feed.

There are several versions of bath smelting, which are reviewed in several publications. These include the AISI Direct Steelmaking (Aukrust and Downing, 1991) process, the Direct Iron Ore Smelting (DIOS) (Inatani, 1991) process developed by the Japanese Iron and Steel Federation, ROMELT (Romenets, 1990) in Russia, and HIsmelt (Klogh et al., 1991) being developed by CRA in Australia. These processes have several different features; for example, HIsmelt uses air in place of oxygen and AISI uses pellets in place of fine ore. However, the basic phenomena are similar in all of these processes. In the following sections the basic critical phenomena will be examined and any major differences in the various processes with regard to these will be discussed.

11.2.2. Critical Process Phenomena

The keys to a successful and optimized smelting process are energy efficiency; reflected in a low coal rate; a high productivity resulting from fast metallurgical reactions; and control of the metal quality. Energy efficiency depends primarily on the degree of post-combustion and prereduction. Productivity depends primarily on reduction and slag foaming, and the metal quality is determined by the slag–metal reactions.

11.2.3. Energy and Materials Balances

The energy and materials balances are complex and depend on several input variables but they are exact for the given set of operating conditions. These balances are discussed in detail in several publications, for example, see Fruehan et al. (1988). The most important input variables are:

- *Coal chemistry:* High-volatile coals usually have lower net heat content and more hydrogen, which makes post-combustion more critical.
- *Prereduction and preheating:* The more highly the ore is prereduced and preheated to higher temperatures, the lower the coal rates.
- *Post-combustion and heat transfer:* With higher post-combustion and heat transfer from post-combustion, the coal rate drops significantly. Although these are set in making the energy and material balances, they depend on the operating parameters and the physics and chemistry of the system. Consequently post-combustion is limited, as discussed in the next section. The effect of post-combustion rates (PCR) on the coal required is shown in Fig. 11.2 for a constant set of operating conditions.

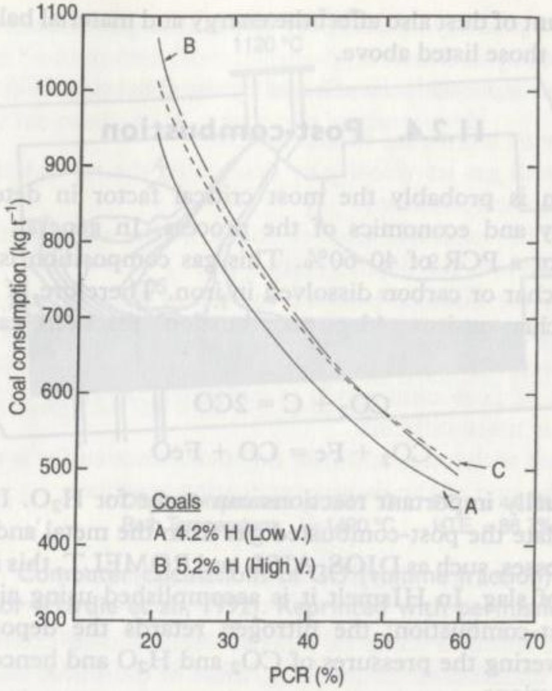

Figure 11.2 The effect of post-combustion ratio (PCR) and prereduction (PRD) on coal consumption. From Fruehan et al., 1988.

$$\mathrm{PCR} = \frac{\%CO_2 + \%H_2O}{\%CO + \%CO_2 + \%H_2 + \%H_2O} \times 100 \qquad (11.1)$$

This figure illustrates that increasing PCR from 25% to 45% decreases fuel consumption by about 200 kg per tonne of metal produced and that PCR is more critical for high-volatile coals. Increasing PCR also reduces the oxygen requirement, which is a major cost consideration.

In general, it is desirable to maximize post-combustion while being consistent with the amount of prereduction required. If the PCR is too high, the off gas will not have the reducing potential required for prereduction. The PCR and prereduction must be optimized simultaneously to give the lowest fuel rate. Since it is easier, both thermodynamically and kinetically, to reduce Fe_2O_3 to FeO than FeO to Fe, all the processes aim to preheat to about 800°C and prereduce the ore to FeO only and attempt to achieve a 40–60% PCR in the smelter. One exception is ROMELT, which does not preheat or prereduce the ore in order to keep the process as simple as possible and capital cost low; however, significantly more coal is required. The ore and slag chemistry, heat losses, and amount of dust also affect the energy and material balances but are less critical than those listed above.

There are several versions of bath smelting, which are reviewed in several publications. These include the AISI Direct Steelmaking (Aukrust and Downing, 1991) process, the Direct Iron Ore Smelting (DIOS) (Inatani, 1991) process developed by the Japanese Iron and Steel Federation, Romelt (Romenets, 1990) in Russia, and HIsmelt (Keogh et al., 1991). The various processes differ in some details but the basic phenomena are similar. In the following sections, the basic critical phenomena will be discussed and any major differences in the various processes with regard to these will be discussed.

11.2.4. Post-combustion

Post-combustion is probably the most critical factor in determining the energy efficiency and economics of the process. In general, the smelting processes aim for a PCR of 40–60%. This gas composition is oxidizing to both carbon as char or carbon dissolved in iron. Therefore, if the CO_2 and H_2O contacts char or iron, 'depostcombustion' reactions can occur, for example:

$$CO_2 + C = 2CO \tag{11.2}$$

$$CO_2 + Fe = CO + FeO \tag{11.3}$$

Similar and equally important reactions can occur for H_2O. It is therefore necessary to isolate the post-combusted gas from the metal and char. In the 'deep slag' processes, such as DIOS, AISI, and ROMELT, this is done with a large quantity of slag. In HIsmelt it is accomplished using air rather than oxygen for post-combustion; the nitrogen retards the depostcombustion reactions by lowering the pressures of CO_2 and H_2O and hence, the driving force for the reactions.

Post-combustion is a very complex phenomenon and depends on fluid flow in the gas phase and the process parameters affecting the depostcombustion reactions. Researchers at IRSID (Huin et al., 1988) developed a reasonably simple concept to describe post-combustion in oxygen steelmaking which can be applied to smelting. The post-combustion (PCR) can be related to the fraction of the off gases, CO and H_2, from the process which are entrained in the oxygen jet (γ) and the fraction of the post-combusted species (CO_2 and H_2O) which react with carbon and iron (α):

$$PCR = (1 - \alpha)(100) \tag{11.4}$$

The model assumes that the species (CO and H_2) entrained into the oxygen jet react upon mixing. The fraction of entrained gases can be computed using various commercially available computer programs describing fluid flow in a single phase.

The fraction of post-combusted gases rereacting (α) is much more difficult to compute. It depends on the surface areas of the char and iron exposed to the gas, mass transfer conditions, and possible chemical kinetics on the surfaces. For example, α increases if there is excess char in the slag, if there is excess bottom stirring, which ejects more metal droplets into the gas phase or the top of the slag phase, or if a gas jet has high velocity, i.e., a 'hard blow', such that the jet penetrates to the metal phase. In most cases, α cannot be computed

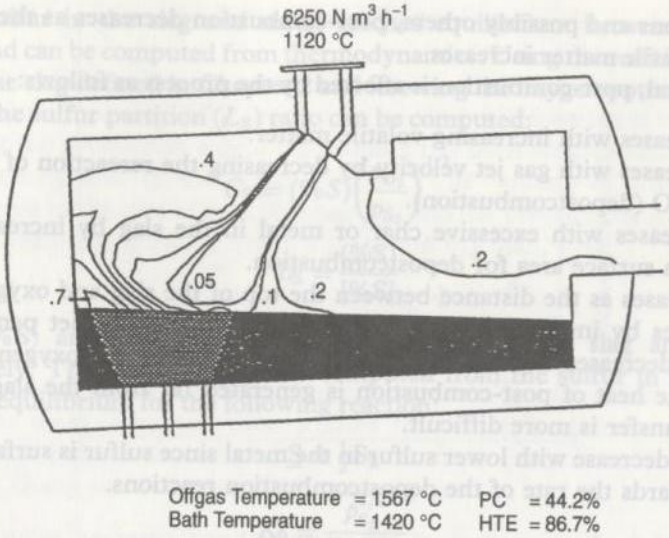

Figure 11.3 Computer calculations of CO (volume fraction) contours in the HIsmelt reactor (Hardie et al., 1992). Reprinted with permission of the Iron & Steel Society.

from basic principles only. It is computed from actual PCR values and computed values of γ. An example of such a calculation for the HIsmelt process is shown in Fig. 11.3 (Hardie et al., 1992) showing the gas composition.

For bath smelting, post-combustion is more extensive and complex than for OSM. In smelting, coal is used which has 10–45% volatile matter (VM). The VM comes off rapidly during heating and the rate of devolatilization is primarily controlled by heat transfer. For top feeding, the coal ranges in size from 2 to 4 cm and most of the volatiles are released in 1 to 3 seconds. The result is that the volatiles are released in one specific area and rapidly. Consequently, it is not possible to entrain as much of the off gas in the oxygen jet as if the gases were evolved uniformly. For processes in which the coal is injected into the metal or slag, the particles are much smaller, in the range of 1 mm or less, and volatilization occurs in a fraction of a second. This results in a small amount of the volatiles dissolving in the metal and more uniform evolution of the VM, which generally results in higher post-combustion.

Another complication with coal is that a large percentage of the post-combusted gas is H_2O. As discussed in Chapter 4, the dissociation of H_2O is an order of magnitude faster than for CO_2. This increases the degree of depostcombustion for gases with higher amounts of H_2O. Consequently, for these reasons and possibly others, post-combustion decreases as the percentage of volatile matter increases.

In general, post-combustion is affected by the process as follows:

- It decreases with increasing volatile matter.
- It decreases with gas jet velocity by decreasing the rereaction of the CO_2 and H_2O (depostcombustion).
- It decreases with excessive char or metal in the slag by increasing the reaction surface area for depostcombustion.
- It increases as the distance between the top of the slag and oxygen lance increases by improving gas entrainment and decreasing jet penetration, which decreases depostcombustion. However, when the oxygen lance is high the heat of post-combustion is generated far from the slag surface heat transfer is more difficult.
- It may decrease with lower sulfur in the metal since sulfur is surface active and retards the rate of the depostcombustion reactions.

11.2.5. Sulfur and Phosphorus

The behavior of sulfur is complex but has been studied extensively and is reasonably well understood. In smelting, most of the sulfur comes from the coal. The sulfur content of bath smelting metal is significantly higher than that from a blast furnace because the sulfur input is greater, since coal is used directly, and the oxygen potential for slag–metal reaction governing the sulfur partition is higher.

When the coal is added to the smelter the sulfur associated with the volatiles—about half—enters the gas phase and reacts to form its equilibrium species, primarily H_2S. As the coal is combusted, some of the mineral sulfur (e.g., FeS) also enters the gas phase because during the combustion of the coal there is a gas surrounding the char, insulating it from the slag but allowing the sulfur to enter the gas phase. The remainder of the sulfur enters the slag and metal. Sulfur also vaporizes from the slag as H_2S at a slow rate. The net result is that a large fraction of sulfur from the coal initially enters the gas phase primarily as H_2S and COS. However, these gaseous species react with iron and CaO in the dust to form FeS and CaS, which are removed in the gas cleaning system:

$$Fe + H_2S = FeS + H_2 \tag{11.5}$$

$$CaO + H_2S = H_2O + CaS \tag{11.6}$$

When the dust is recycled into the smelter the CaS and FeS dissolve in the slag, adding sulfur to the slag and metal. Consequently, the majority of the sulfur enters the slag and metal from the recycled dust.

The sulfur in the slag and metal reaches equilibrium between the two phases and can be computed from thermodynamics. Using the sulfide capacity (C_S) of the slag defined in Chapter 2 and knowing the oxygen potential of the system, the sulfur partition (L_S) ratio can be computed:

$$C_S = (\%S)\left(\frac{p_{O_2}}{p_{S_2}}\right)^{1.2} \tag{11.7}$$

$$L_S = \frac{(\%S)}{[\%S]} \tag{11.8}$$

where (%S) and [%S] are the sulfur contents of the slag and metal, respectively. The sulfur pressure is computed from the sulfur in the metal from the equilibrium for the following reaction:

$$\underline{S} = \tfrac{1}{2}S_2 \tag{11.9}$$

$$K_9 = \frac{p_{S_2}^{1/2}}{[\%S]f_S} \tag{11.10}$$

where f_s is the activity coefficient of sulfur with respect to infinite dilution in liquid iron. The value of f_s increases with increasing carbon content. The oxygen potential is controlled by the Fe–FeO equilibrium. In this chapter the parentheses indicate that the component is dissolved in the slag:

$$\underline{Fe} + \tfrac{1}{2}O_2 = (FeO) \tag{11.11}$$

$$K_{11} = \frac{a_{FeO}}{a_{Fe}p_{O_2}^{1/2}} \tag{11.12}$$

Combining Equations 11.7 through 11.12 the sulfur partition ratio is given by

$$L_S = \frac{C_S f_S a_{FeO} K_9 K_{11}}{a_{FeO}} \tag{11.13}$$

The sulfur distribution ratio increases with C_S and decreases with the activity or concentration of FeO in the slag.

A comparison of the predicted and measured values of L_S is given in Fig. 11.4 (Fruehan et al., 1994) as a function of the FeO content of the slag. In this chapter, all concentrations are in mass-percent unless otherwise stated. The sulfur partition ratio is in the range of 4 to 10, which is considerably lower than for a blast furnace. Furthermore, for a blast furnace, the sulfur input is lower since during cokemaking about half of the sulfur is removed. Consequently, there is considerably more sulfur in the metal for smelting as compared to that produced in the blast furnace. For example, using coal containing 0.7%S the metal from the smelter will contain 0.15–0.3%S compared to less than 0.1% for a blast furnace. The large variation in the

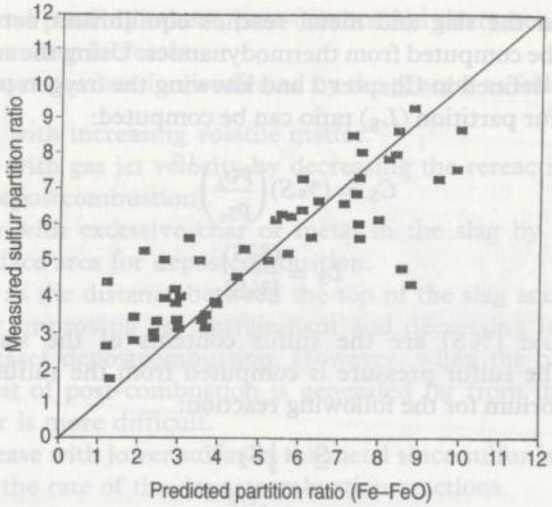

Figure 11.4 A comparison of the computed and observed sulfur partition ratios (L_S) assuming Fe–FeO equilibrium (Fruehan et al., 1994).

sulfur content of smelter metal is primarily due to the variation in the FeO content of the slag, which effect L_S.

The behavior of phosphorus is much simpler and slag–metal equilibrium is obtained. From the definition of the phosphate capacity ($C_{\text{phosphate}}$) the phosphorus distribution ratio (L_P) between the slag and metal can be computed:

$$L_P = \frac{(C_{\text{phosphate}}) f_P p_{O_2}^{5/4} M_P}{K_P M_{PO_4}} \tag{11.14}$$

where f_P is the activity coefficient of phosphorus relative to 1 wt%, K_P is the equilibrium constant for the solution of phosphorus at 1 wt% in iron and M_P and M_{PO_4} are the molecular masses of the P and PO_4, respectively. The oxygen pressure is controlled by the Fe–FeO reaction. The phosphate capacity and, consequently, the phosphorus distribution is very sensitive to temperature; it decreases with increasing temperature.

In smelting, most of the phosphorus enters the process with the ore and is similar to the metal produced in the blast furnace. The phosphate capacities of the slags in both processes are similar. However, the FeO content is higher in bath smelting, resulting in slightly better phosphorus removal; typically smelter metal contains about 20% less phosphorus than blast furnace metal.

11.2.6. Slag Foaming

Owing to the extensive gas evolution the slag in smelting foams, slag foaming plays an important role in the process. In particular, if foaming is excessive it may limit the production rate. Slag foaming has been studied extensively in the laboratory and in the actual process. The volume of foam (V_f) is proportional to the rate of gas evolution (Q) and the proportionality constant has been defined as the foam index (Σ) (Ito and Fruehan, 1989):

$$V_f = \Sigma Q \tag{11.15}$$

The foam index is essentially the time it takes the gas to pass through the foam. The foam index has been studied for over fifty different slags and several foam bubble sizes and its correlation to the properties of the slag is given by (Zhang and Fruehan, 1995)

$$\Sigma = 1.83 \frac{\mu^{1.2}}{\sigma^{0.2} \rho D_b^{0.9}} \tag{11.16}$$

where μ is the viscosity, σ is the surface tension, ρ is the density, and D_b is the diameter of the foam bubbles.

In the actual smelting process, slag foaming is very complex. Specifically,

- It depends on the slag properties and foam bubble size as indicated by (11.16). In general, bubbles formed by the oxidation of char are large and those from reduction by metal drops are small; the small bubbles give a stable foam.
- Char in the slag breaks the foam bubbles and causes the foam to collapse. Typically, if there is 10–20% by weight of char in the slag, the foam is reduced by 50% or more.

Despite these complications, slag foaming can be predicted reasonably well. For typical smelting slags with appropriate amounts of char, the foam volume is proportional to the gas generation rate at the temperature and pressure in the smelter and the foam index is about 0.2 to 0.4 seconds. From the energy and materials balance the total gas flow rate can be computed, and the foam volume using Equation 11.15. A comparison of the actual foam height in the AISI Bath Smelter is compared to that predicted from the foam index and the calculated off gas flow rate in Fig. 11.5 (Fruehan et al., 1994). The foam height is simply computed from the foam volume and the cross-sectional area of the reactor.

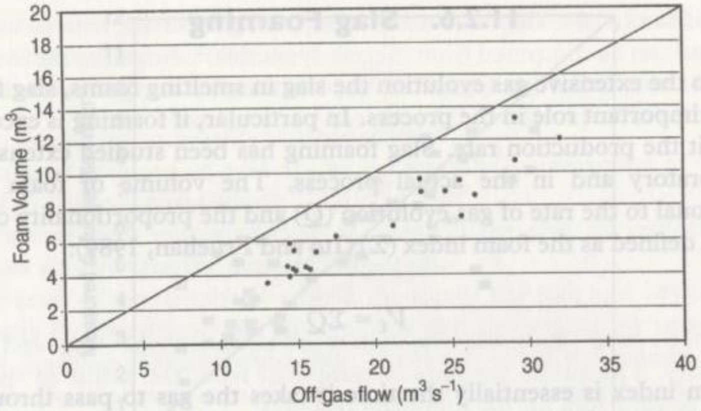

Figure 11.5 Comparison of computed slag foam heights and those measured as a function of off gas for AISI Pilot Plant (Fruehan et al., 1994).

11.2.7. Reduction

The primary reaction in iron smelting is reduction of the iron oxide. Owing to its importance, and since it demonstrates how basic principles can be used to predict and control critical phenomena, this reaction is examined in detail. The partially prereduced ore dissolves in the slag and is reduced by carbon in the coal char or in liquid iron–carbon droplets ejected into the slag from the metal bath. The two reactions contribute about equally to the overall reduction, the exact amounts depending on the quantity of char and metal in the slag. Typically the char and metal droplets are 10–25% of the slag weight. The higher the amount of char and metal the faster reduction, but if there is an excessive amount of metal or char in the slag it will reduce post-combustion and energy efficiency, as discussed previously. The planar surface area between the metal and slag is insignificant compared to the area of the dispersed drops and particles and contributes only about 1% to the overall rate.

The FeO dissolved carbon reaction

The reaction of Fe–C drops with FeO dissolved in bath smelting slags has been studied extensively. Not only has the rate been measured but the actual reaction has been observed using x-ray fluoroscopy by Min and Fruehan (1992b). As the metal droplet is reacting it remains suspended in the slag owing to the gas evolution associated with the reaction. For 3–5 mm drops the reaction takes place in 10 to 60 seconds depending on the droplet size, the FeO content of the slag, and the sulfur content of the metal. The effect of FeO is shown in Fig. 11.6.

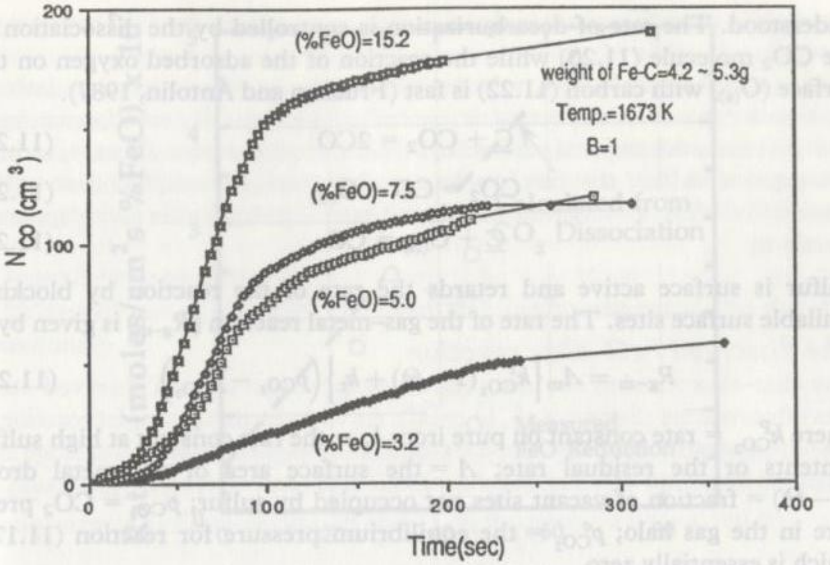

Figure 11.6 Rate of reaction of Fe–C drops with FeO in slag for low-sulfur metal (Min and Fruehan, 1992b).

The overall reaction is given by Equation 11.17 and is proportional to the FeO content of the slag.

$$(\mathrm{FeO}) + \underline{\mathrm{C}} = \mathrm{CO} + \mathrm{Fe} \qquad (11.17)$$

However, during the reaction there is a gas halo surrounding the drop and it is generally accepted that the reaction takes place by two intermediate gas reactions at the slag–gas and metal–gas interfaces, reactions 11.18 and 11.19, respectively:

$$(\mathrm{FeO}) + \mathrm{CO} = \mathrm{CO_2} + \mathrm{Fe} \qquad (11.18)$$

$$\mathrm{CO_2} + \underline{\mathrm{C}} = 2\mathrm{CO} \qquad (11.19)$$

There are several possible rate-controlling mechanisms, including mass transfer in the slag–metal or gas and chemical kinetics for reactions 11.18 or 11.19. Based on the experimental results, mass transfer in the metal, and experimental measurements by Sun et al. (1988), the kinetics of reaction 11.18 can be eliminated as possible rate-controlling steps. Also, since the gas halo is relatively thin, gas phase mass transfer between the slag and metal interface is relatively fast.

Therefore, the two principal rate-controlling steps are mass transfer in the slag phase and kinetics of the CO_2 reaction on the metal droplet surface. The rate of the CO_2 reaction on liquid iron has been studied extensively and is well understood. The rate of decarburization is controlled by the dissociation of the CO_2 molecule (11.20) while the reaction of the adsorbed oxygen on the surface ($O_{(s)}$) with carbon (11.22) is fast (Fruehan and Antolin, 1987).

$$\underline{C} + CO_2 = 2CO \tag{11.20}$$

$$CO_2 = CO + O_{(S)} \tag{11.21}$$

$$\underline{C} + O_{(S)} = CO \tag{11.22}$$

Sulfur is surface active and retards the rate of the reaction by blocking available surface sites. The rate of the gas–metal reaction (R_{g-m}) is given by

$$R_{g-m} = A_m\left\{k^P_{CO_2}(1-\Theta) + k_r\right\}\left(p_{CO_2} - p^e_{CO_2}\right) \tag{11.23}$$

where $k^P_{CO_2}$ = rate constant on pure iron; k_r = the rate constant at high sulfur contents or the residual rate; A = the surface area of the metal drop; $(1-\Theta)$ = fraction of vacant sites not occupied by sulfur; p_{CO_2} = CO_2 pressure in the gas halo; $p^e_{CO_2}$ = the equilibrium pressure for reaction (11.17), which is essentially zero

Since the rate of the gas–slag reaction is relatively fast, it is close to equilibrium and the CO_2 pressure is given by

$$p_{CO_2} = K_{(19)} p^2_{CO} a_{FeO} \tag{11.24}$$

where, $K_{(19)}$ is the equilibrium constant for (11.19); p_{CO} is the equilibrium pressure for (11.4), approximately 1 atm; a_{FeO} is the activity of FeO in the slag.

For the slag composition range of interest the activity of FeO is proportional to its weight percent through a constant (C) and, hence, the rate is given by

$$R_{g-m} = A_m\left(k^P_{CO_2}(1-\Theta) + k_r\right)K_{(19)}C(\%FeO) \tag{11.25}$$

The value of $(k^P_{CO_2}(1-\Theta) + k_r)$ is the rate of the reaction for (11.4) on the Fe–C–S alloy of interest. Note that sulfur decreases the value of $(1-\Theta)$.

As discussed in Chapter 4, the number of vacant sites is related to the activity of sulfur (a_s) and K_s, the adsorption coefficient for sulfur on iron:

$$(1-\Theta) = \frac{1}{1 + K_S a_S} \tag{11.26}$$

Therefore, the rate of the gas–metal reaction is given by

$$R_{g-m} = A_m K_{(19)}\left\{\frac{k^P_{CO_2}}{1 + K_S a_S} + k_r\right\}\%FeO \tag{11.27}$$

At high sulfur contents the rate of the slag–metal reaction is significantly slower than mass transfer and the rate of reduction is given by Equation 11.27.

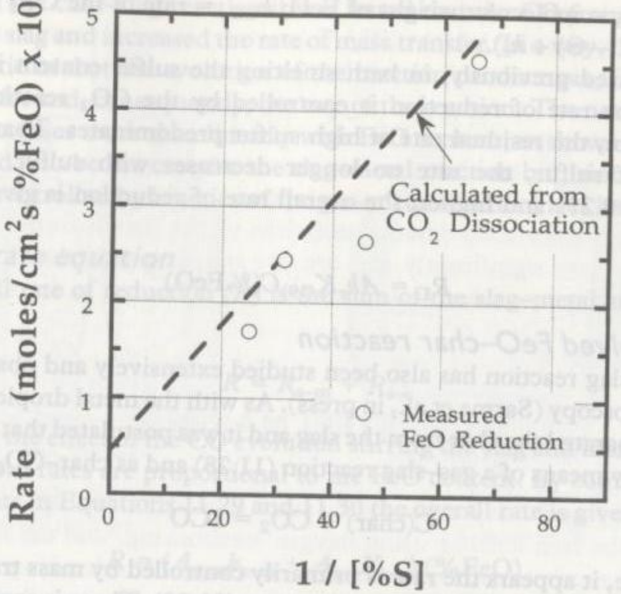

Figure 11.7 Computed rate of reduction of FeO by carbon in iron droplets assuming CO_2 dissociation control compared to the observed rates (Min and Fruehan, 1992b).

Using independent measurements for the rate of the CO_2 reaction on iron, the calculated rate of reduction is in good agreement with the measured rate of reduction as shown in Fig. 11.7.

The rate of mass transfer of 'FeO' in the slag, J, is given by

$$J = \frac{A_S m\rho}{100}(\%FeO - \%FeO^s) \tag{11.28}$$

where A_S = area of the slag around the metal drop (the area of the slag is greater than the area of the metal drop (A_m) because of the gas halo); m = the mass transfer coefficient; ρ = density of the slag; %FeO = the FeO bulk slag content; $\%FeO^s$ = the surface concentration of FeO at the gas–slag interface and is essentially zero. At very low sulfur contents the rate of reduction is controlled by mass transfer.

For the most general case a mixed control model considering both mass transfer and the gas–metal reaction was developed and the rate of reduction is given by:

$$R = \frac{1}{\left(\dfrac{100M_{FeO}}{m_s\rho A_s} + \dfrac{1}{k_{CO_2}A_m C K_{19}}\right)}(\%FeO) \tag{11.29}$$

where M_{FeO} = molecular weight of FeO; $k_{\mathrm{CO_2}}$ = rate of the CO_2 reaction on iron $(k^{\mathrm{P}}_{\mathrm{CO_2}}(1-\Theta)+k_{\mathrm{r}})$.

As discussed previously, in bath smelting the sulfur content is relatively high and the rate of reduction is controlled by the CO_2 reaction on iron. Furthermore, the residual rate at high sulfur predominates. That is, at high coverage of sulfur, the rate no longer decreases with sulfur. For sulfur contents of 0.2% and higher, the overall rate of reduction is given approximately by

$$R_{\mathrm{L}} = Ak_{\mathrm{r}}K_{(19)}C(\%\mathrm{FeO}) \qquad (11.30)$$

The dissolved FeO–char reaction

The char–slag reaction has also been studied extensively and observed using x-ray fluoroscopy (Sarma et al., in press). As with the metal droplet reaction, a gas film separated the char from the slag and it was postulated that the rate also occurred by means of a gas–slag reaction (11.28) and as char–CO_2 reaction

$$\mathrm{C(char)} + \mathrm{CO_2} = 2\mathrm{CO} \qquad (11.31)$$

In this case, it appears the rate is primarily controlled by mass transfer in the slag phase, in which case the rate is given by (11.28). There is some indication that the CO_2–char reaction may also contribute slightly to the overall rate. In the case of the char–slag reaction it was found that the CO from the reaction stirred the slag and increased the rate of mass transfer. In a way, the reaction is self-catalytic in that the evolution of the reaction product gas, CO, increases mass transfer and, consequently, the rate of the reaction. The net result is that the rate increases more than linearly with FeO content, as shown in Fig. 11.8. This would also be the case for the slag–metal reaction but, since that rate is primarily controlled by kinetics of the gas–metal reaction, it is less obvious.

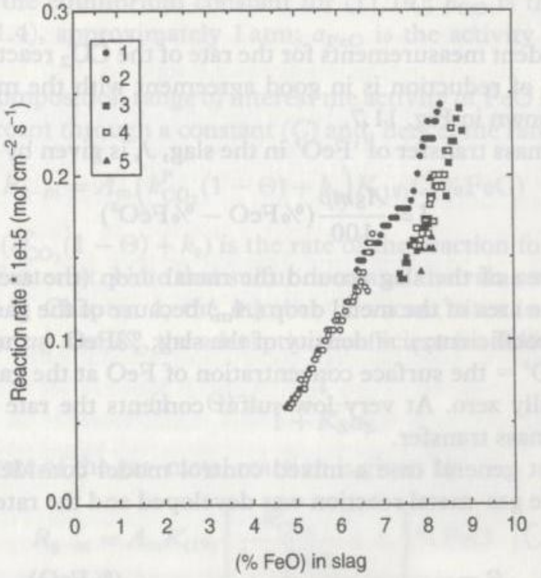

Figure 11.8 Rate of reaction of graphite and coke spheres with bath smelting slags as a function of FeO content (Sarma et al., 1996).

Overall rate equation

The overall rate of reduction (R) is the sum of the slag–metal and slag–char reactions:

$$R = R_{\mathrm{s\text{-}m}} + R_{\mathrm{s\text{-}c}} \qquad (11.32)$$

Neglecting the effect of the CO evolution stirring the slag and increasing mass transfer, both rates are proportional to the FeO content. By combining all of the constants in Equations 11.29 and 11.30 the overall rate is given by

$$R = (A_{\mathrm{s\text{-}m}}k_{\mathrm{s\text{-}m}} + A_{\mathrm{s\text{-}c}}K_{\mathrm{s\text{-}c}})\,(\%\mathrm{FeO}) \qquad (11.33)$$

where $A_{\mathrm{s\text{-}m}}$ and $A_{\mathrm{s\text{-}c}}$ are the areas of the metal droplets and char in the slag, respectively.

From estimates of the areas of the droplets and the particles in the AISI pilot plant smelter, Sarma et al. estimated the overall rate of reaction using Equation 11.30 and the experimentally determined constants. As seen in Fig. 11.9 the observed and computed rates of reduction are in good agreement.

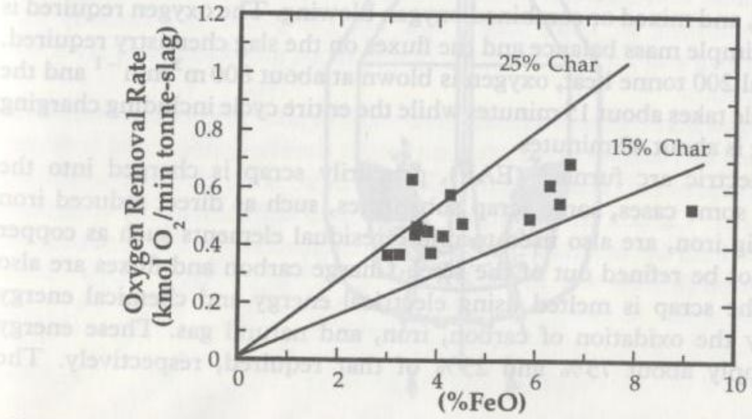

Figure 11.9 Computed rate of reduction from laboratory studies and slag samples compared to those observed in the AISI Pilot Smelter (B. Sarma, AISI, personal communication).

In general the amount of char and metal in the slag phase is approximately proportional to the slag weight (W_s). Therefore, from a practical standpoint the rate can be given approximately by:

$$R = (k'_{s-m} + k'_{s-c})W_s(\%\mathrm{FeO}) \tag{11.34}$$

where k'_{s-m} and k'_{s-c} are the overall rate constants including the relationship between the area of both phases in the slag and the slag weight. This is a crude approximation since the amounts and sizes of the metal droplets and char particles can vary significantly and are not simply proportional to the slag weight. Nevertheless, this simple equation has been used to describe the rate of reduction.

11.3. STEELMAKING

There are two methods for producing steel: refining hot metal from the blast furnace or the iron smelter using oxygen steelmaking, and the melting and refining of scrap in an electric arc furnace. In oxygen steelmaking (OSM), the hot metal and some scrap are charged along with fluxes, primarily lime (CaO), into a vertical converter or furnace. Typically scrap represents about 10–25% of the metallic charge and is melted with the energy released by the oxidation of carbon, silicon, and iron. Oxygen is injected into the metal by means of a top lance or by bottom tuyeres which oxidize the carbon, silicon, and manganese and some iron. These oxides, SiO_2, MnO, and FeO, along with the added CaO, form a slag which removes sulfur and phosphorus from the metal. There are three basic types of OSM furnaces, as shown in Fig. 11.10: top, bottom, and mixed or combined oxygen blowing. The oxygen required is based on a simple mass balance and the fluxes on the slag chemistry required. For a typical 200 tonne heat, oxygen is blown at about 800 $m^3\,min^{-1}$ and the blowing cycle takes about 15 minutes while the entire cycle including charging and tapping is about 40 minutes.

In the electric arc furnace (EAF), primarily scrap is charged into the furnace. In some cases, some scrap substitutes, such as direct reduced iron (DRI) or pig iron, are also used to dilute residual elements such as copper which cannot be refined out of the steel. Charge carbon and fluxes are also charged. The scrap is melted using electrical energy and chemical energy supplied by the oxidation of carbon, iron, and natural gas. These energy sources supply about 75% and 25% of that required, respectively. The

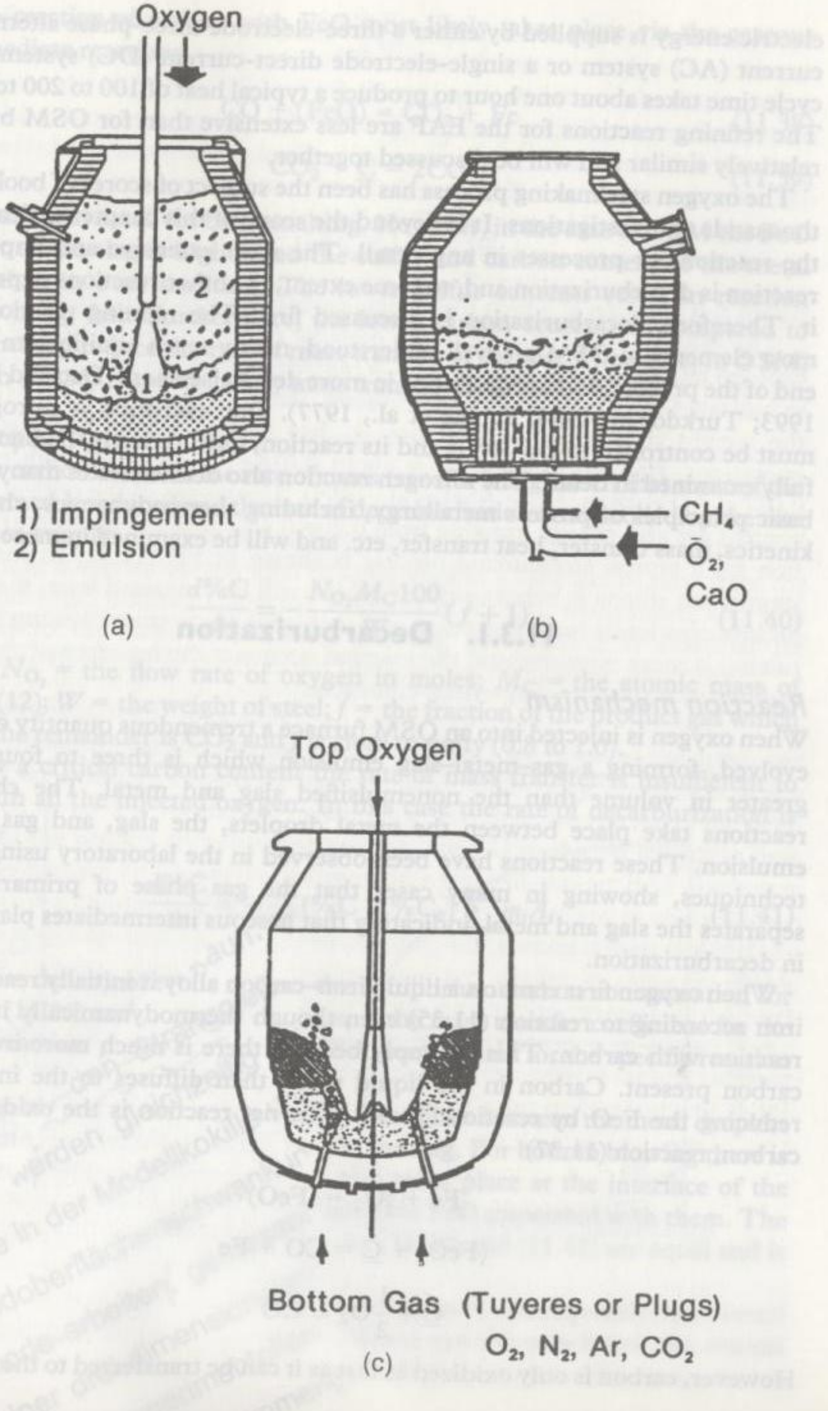

(a) (b) (c)

Figure 11.10 Types of oxygen steelmaking furnaces: (a) BOF or LD, (b) Q-BOP or OBM, (c) combined or mixed blowing.

electric energy is supplied by either a three-electrode three-phase alternating current (AC) system or a single-electrode direct-current (DC) system. The cycle time takes about one hour to produce a typical heat of 100 to 200 tonnes. The refining reactions for the EAF are less extensive than for OSM but are relatively similar and will be discussed together.

The oxygen steelmaking process has been the subject of scores of books and thousands of investigations. It is beyond the scope of this chapter to deal with the reactions or processes in any detail. The most extensive and important reaction is decarburization and, to some extent, the other reactions depend on it. Therefore, decarburization is discussed first. The refining reactions for most elements in OSM are well understood, nearly reach equilibrium at the end of the process, and are described in more detail elsewhere (Deo and Boom, 1993; Turkdogan, 1984; Pehlke et al., 1977). One exception is nitrogen; it must be controlled to low levels and its reaction, until recently, had not been fully examined in detail. The nitrogen reaction also demonstrates many of the basic principles of process metallurgy, including thermodynamics, chemical kinetics, mass transfer, heat transfer, etc. and will be examined in more detail.

11.3.1. Decarburization

Reaction mechanism

When oxygen is injected into an OSM furnace a tremendous quantity of gas is evolved, forming a gas–metal–slag emulsion which is three to four times greater in volume than the nonemulsified slag and metal. The chemical reactions take place between the metal droplets, the slag, and gas in the emulsion. These reactions have been observed in the laboratory using x-ray techniques, showing in many cases that the gas phase of primarily CO separates the slag and metal, indicating that gaseous intermediates play a role in decarburization.

When oxygen first contacts a liquid iron–carbon alloy it initially reacts with iron according to reaction (11.35) even though thermodynamically it favors reaction with carbon. This is simply because there is much more iron than carbon present. Carbon in the liquid metal then diffuses to the interface, reducing the FeO by reaction (11.36). The net reaction is the oxidation of carbon, reaction (11.37).

$$\mathrm{Fe} + \tfrac{1}{2}\mathrm{O_2} = (\mathrm{FeO}) \qquad (11.35)$$

$$(\mathrm{FeO}) + \underline{\mathrm{C}} = \mathrm{CO} + \mathrm{Fe} \qquad (11.36)$$

$$\underline{\mathrm{C}} + \frac{1}{2}\mathrm{O_2} = \mathrm{CO} \qquad (11.37)$$

However, carbon is only oxidized as fast as it can be transferred to the surface.

The reaction of carbon with FeO most likely takes place via the gaseous intermediate reactions:

$$\mathrm{CO} + (\mathrm{FeO}) = \mathrm{CO_2} + \mathrm{Fe} \qquad (11.38)$$

$$\mathrm{CO_2} + \underline{\mathrm{C}} = 2\mathrm{CO} \qquad (11.39)$$

as discussed in detail for bath smelting. However, in the case of OSM the FeO content of the slag is higher and the sulfur and carbon content of the metal lower than in bath smelting. The lower sulfur contents result in reaction (11.39) being fast. Furthermore, the lower carbon contents as compared to iron smelting reduce the rate of mass transfer of carbon. Therefore, in OSM, reaction (11.36) is controlled by mass transfer of carbon.

Rate equations

At high carbon contents the rate of mass transfer is high such that most of the FeO formed is reduced and the rate of decarburization is controlled by the rate of oxygen supply:

$$\frac{d\%\mathrm{C}}{dt} = -\frac{N_{\mathrm{O_2}} M_{\mathrm{C}} 100}{W}(f+1) \qquad (11.40)$$

where, $N_{\mathrm{O_2}}$ = the flow rate of oxygen in moles; M_{C} = the atomic mass of carbon (12); W = the weight of steel; f = the fraction of the product gas which is CO; the remainder is $\mathrm{CO_2}$ and f is close to unity (0.8 to 1.0).

Below a critical carbon content the rate of mass transfer is insufficient to react with all the injected oxygen. In this case the rate of decarburization is given by

$$\frac{d\%\mathrm{C}}{dt} = -\frac{\rho}{W}(\%\mathrm{C} - \%\mathrm{C}_e)\sum m_i A_i \qquad (11.41)$$

where ρ = density of steel; $\%\mathrm{C}_e$ = the equilibrium carbon concentration for reaction (11.36) and is close to zero; m_i = the mass transfer coefficient for the specific reaction site; A_i = the metal–FeO surface area for the specific reaction site.

For top blown processes the reaction takes place between the metal droplets ejected into the emulsion and the FeO in the slag. For bottom blowing there is less of an emulsion and the reaction also takes place at the interface of the metal bath and the rising bubbles which have FeO associated with them. The critical carbon is when the rates given by (11.40) and (11.41) are equal and is typically about 0.3%C.

The actual values of m_i and A_i are not known; consequently, an overall decarburization constant (k_c) can be defined and the rate below the critical carbon content is given by (11.43) and (11.44).

$$k_c = \frac{\rho}{W}\sum_i m_i A_i \tag{11.42}$$

$$\frac{d\%\mathrm{C}}{dt} = -k_c[\%\mathrm{C}] \tag{11.43}$$

or,

$$\ln\left[\frac{\%\mathrm{C}}{\%\mathrm{C}_c}\right] = -k_c(t - t_c) \tag{11.44}$$

where t_c is the time at which the critical carbon content C_c is obtained.

The value of k_c increases with the blowing rate since the amount of ejected droplets and bubbles increases. Also, k_c decreases with the amount of steel, W, as indicated by (11.43). In actual processes, the blowing rate is proportional to the weight of steel and, therefore, k_c has similar values in most OSM operations. For top blowing, k_c is about $0.015\,\mathrm{s}^{-1}$ and for bottom blowing $0.017\,\mathrm{s}^{-1}$ (Fruehan, 1976; Abel et al., 1995). The values of the critical carbon content are also similar, ranging from 0.2 to 0.4%C. The rate of decarburization for a typical steelmaking process is shown in Fig. 11.11. In the initial stage when silicon is being oxidized, which will be discussed later, the rate of decarburization is low. The value of k_c is higher for bottom blowing because mixing is more intensive and the reaction occurs at the interface of the rising bubbles as well as the slag–metal emulsion.

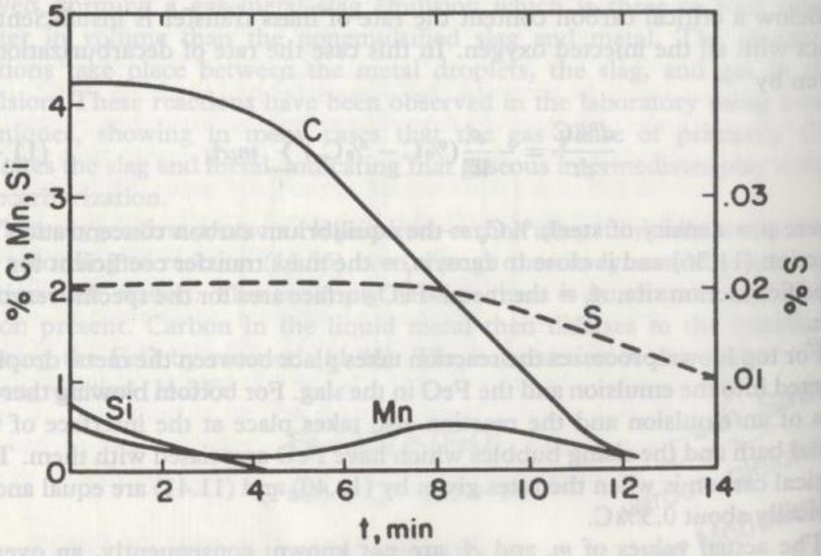

Figure 11.11 Change in the chemical composition of steel during OSM (Pehlke et al., 1977). Reprinted with permission of the Iron & Steel Society.

FeO formation

Below the critical carbon content the rate of mass transfer of carbon is insufficient to reduce all of the FeO formed and, therefore, the FeO content of the slag increases rapidly. In actual processes, initially, some FeO forms because it has a low activity in the slag, resulting in about 5–10% FeO in the slag. The FeO remains constant until the critical carbon content and then increases rapidly. The amount of FeO can be computed from a mass balance for oxygen. Specifically, the oxygen not used for carbon, silicon, or manganese oxidizes iron to FeO. The number of moles of FeO in the slag at any time (N_{FeO}) is given by

$$N_{\mathrm{FeO}} = \int_0^t 2\left[N_{\mathrm{O}_2} - \frac{d\%\mathrm{C}}{dt}\frac{W(1+f)}{M_c 100}\right]dt - (N_{\mathrm{O}_2}^{\mathrm{Si}} + N_{\mathrm{O}_2}^{\mathrm{Mn}}) \tag{11.45}$$

where $N_{\mathrm{O}_2}^{\mathrm{Si}}$ and $N_{\mathrm{O}_2}^{\mathrm{Mn}}$ are the numbers of moles of oxygen consumed in oxidizing Si and Mn. Since the rate of decarburization is slightly higher for bottom and mixed blowing, these processes have lower FeO contents. This results in higher iron yield and higher manganese retention as discussed later.

The slag composition can then be computed as a function of time from the CaO and MgO additions and the amounts of silicon, manganese, and iron oxidized to the bath. Controlling the slag composition is essential for optimizing the refining reactions for phosphorus, manganese, and sulfur.

Decarburization in the EAF

Decarburization is much less extensive than in OSM because the scrap has low carbon contents compared to hot metal: 0.05–1.0% for typical scrap compared to 4.5–5% for the hot metal. However, decarburization in the EAF improves the process by supplying energy; the CO evolution improves heat and mass transfer and removes nitrogen. In a state-of-the-art EAF, carbon is added to the charge so that the 'melt-in' or initial carbon is about 0.5 to 1.0 wt% above the final or aim carbon content. The carbon is then removed by injecting oxygen. The reaction mechanisms are similar to those in OSM; however, since there is not an extensive emulsion and the oxygen is not deeply injected into the bath, the overall decarburization constant is lower, about 0.01 to $0.012\,\mathrm{s}^{-1}$ (Fruehan, 1976). Consequently, the critical carbon content, when mass controls the rate, is higher and for a given carbon content in the metal there is more FeO in the slag.

11.3.2. Slag–Metal Reactions in Steelmaking

In addition to carbon, sulfur, phosphorus, manganese, and silicon are also refined from the metal in steelmaking. These reactions are between the element in the metal and its ion in the slag phase. In many cases these reactions approach equilibrium and can be predicted from thermodynamics.

Extensive reviews of the slag–metal reactions can be found elsewhere (Deo and Boom, 1993; Turkdogan, 1984; Pehlke et al., 1977). Attempts have been made to model the kinetics of these reactions involving simultaneous mass transfer of the relevant reactions (Deo, 1988; Lange, 1986). However, in general, a simple thermodynamic equilibrium analysis gives reasonable predictions of the behavior of these elements.

Silicon

Silicon is oxidized out of hot metal early in the process. The oxidation reaction (11.46), supplies heat and the SiO_2 reacts with the CaO to form the slag.

$$\underline{\mathrm{Si}} + \tfrac{1}{2}\mathrm{O}_2 = (\mathrm{SiO}_2) \tag{11.46}$$

The thermodynamics of the reaction indicate that virtually all of the silicon is oxidized. The rate is controlled by liquid phase mass transfer. The mass transfer can be simplified to mass transfer in the metal and is given by

$$\frac{d\%\mathrm{Si}}{dt} = \frac{A\rho m_{\mathrm{Si}}}{W}[\%\mathrm{Si} - \%\mathrm{Si}_e] \tag{11.47}$$

where m_{Si} = mass transfer coefficient for silicon; $\%\mathrm{Si}_e$ = the silicon content in the metal in equilibrium with the slag and is close to zero.

As with decarburization, an overall parameter for silicon can be defined (k_{Si}) similarly to k_c. Within our ability to estimate k_{Si} it is about equal to k_c since A, W, and ρ are the same and mass transfer coefficients vary only as the diffusivity to the one-half power. Therefore (11.47) simplifies to

$$\ln\left[\frac{\%\mathrm{Si}}{\%\mathrm{Si}^0}\right] = -k_{\mathrm{Si}}t \tag{11.48}$$

where $\%\mathrm{Si}^0$ is the initial silicon and k_{Si} is the overall constant for silicon and is approximately equal to k_c. The rate for silicon oxidation is shown in Fig. 11.11.

Manganese

Manganese is oxidized from the steel by various mechanisms including direct oxidation, enhanced vaporization-deoxidation, and FeO in the slag. In the process, equilibrium for the following reaction is obtained:

$$\underline{\mathrm{Mn}} + (\mathrm{FeO}) = (\mathrm{MnO}) + \mathrm{Fe} \tag{11.49}$$

The activities of MnO and FeO in the slag depend on basicity of the slag defined as the ratio $(\%\mathrm{CaO})/(\%\mathrm{SiO}_2)$. Therefore, the value of k_{Mn} depends on slag chemistry and is not a true equilibrium constant:

$$k_{\mathrm{Mn}} = \frac{(\%\mathrm{MnO})}{[\%\mathrm{Mn}]\,(\%\mathrm{FeO})} \tag{11.50}$$

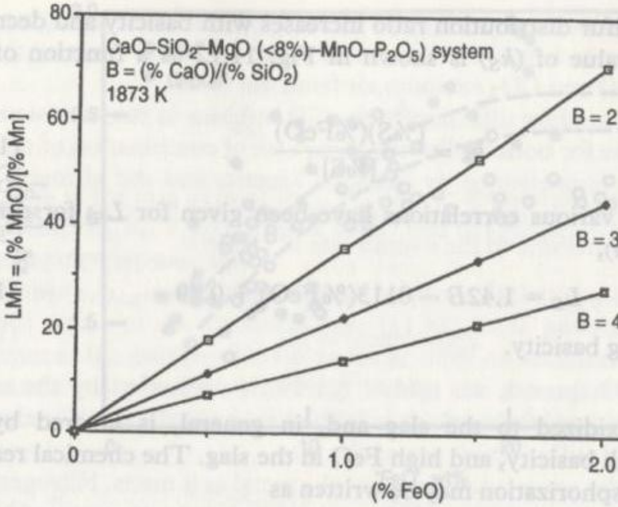

Figure 11.12 Manganese equilibrium between slag and metal or a function of FeO and slag chemistry in OSM (Min and Fruehan, 1992a). Reprinted with permission of the Iron & Steel Society.

The manganese distribution ratio between slag and metal has been reevaluated using the thermodynamic data and is given in Fig. 11.12 (Min and Fruehan, 1992a) as a function of FeO content. As indicated, manganese retention in the metal is favored by high basicities. Also, since in bottom and combined blowing processes, for a given carbon level, the FeO content of the slag is lower, more manganese is retained in the metal.

In top blown processes manganese is oxidized directly by the injected oxygen early in the process, and the manganese content is less than predicted by (11.50). As the process continues, equilibrium is approached and manganese reverts back to the metal. Toward the end of the blowing period when the FeO content of the slag increases, the manganese decreases rapidly. For bottom blowing the manganese follows slag–metal equilibrium and generally is removed late in the process when the FeO content of the slag increases.

Sulfur

About 10–20% of the sulfur reacts directly with the oxygen to form SO_2:

$$\underline{\mathrm{S}} + \mathrm{O}_2 = \mathrm{SO}_2 \tag{11.51}$$

The remainder reaches a slag–metal equilibrium which can be described by

$$\underline{\mathrm{S}} + (\mathrm{CaO}) + \mathrm{Fe} = (\mathrm{FeO}) + (\mathrm{CaS}) \tag{11.52}$$

Therefore, the sulfur distribution ratio increases with basicity and decreases with FeO. The value of (k_S) is shown in Fig. 11.12 as a function of slag basicity.

$$k_S = \frac{(\%S)(\%FeO)}{[\%S]} \tag{11.53}$$

For steelmaking, various correlations have been given for L_S; for example (Turkdogan, 1984),

$$L_S = 1.42B - 0113(\%FeO) + 0.89 \tag{11.54}$$

where B is the slag basicity.

Phosphorus

Phosphorus is oxidized to the slag and, in general, is favored by low temperatures, high basicity, and high FeO in the slag. The chemical reaction describing dephosphorization may be written as

$$\underline{P} + 2.5(FeO) = (PO_{2.5}) + 2.5Fe \tag{11.55}$$

The significance of $PO_{2.5}$ is that, at the low phosphorus levels as in steel, the correct thermodynamic parameter is $(\%P)/[\%P]$ or $(\%P_2O_5)/[\%P]$ not $(\%P)/[\%P]^2$; this is a significant difference at low phosphorus levels. Other complications are that the distribution ratio does not increase with increasing FeO at high FeO contents owing to its dilution effect reducing the CaO content and equilibrium not necessarily being achieved. Typical values of the distribution ratio are shown in Fig. 11.13 (Turkdogan, 1984). For bottom (Q-BOP-OBM) or mixed blowing at a given carbon content, the FeO content is lower but the phosphorus distribution is similar to that in top blowing (BOF).

For EAF steelmaking, the slag basicity is normally low and there is less stirring, making the reaction further from equilibrium. The net result is that the phosphorus distribution ratio is less than 20 compared to 100–300 in OSM. Furthermore, there is less slag in the EAF, making phosphorus removal much less than in OSM.

Oxygen

In steelmaking, a relationship exists between carbon and oxygen:

$$CO = \underline{C} + \underline{O} \tag{11.56}$$

For one atmosphere of CO it follows that:

$$[\%C][\%O] = K_{56} \tag{11.57}$$

where K_{56} is the equilibrium constant for (11.56). For equilibrium and most OSM processes K_{56} is 0.002 and 0.002–0.0025, respectively. For EAF processes there is less stirring and the product is farther from equilibrium and the carbon–oxygen product is about 0.0025–0.0035.

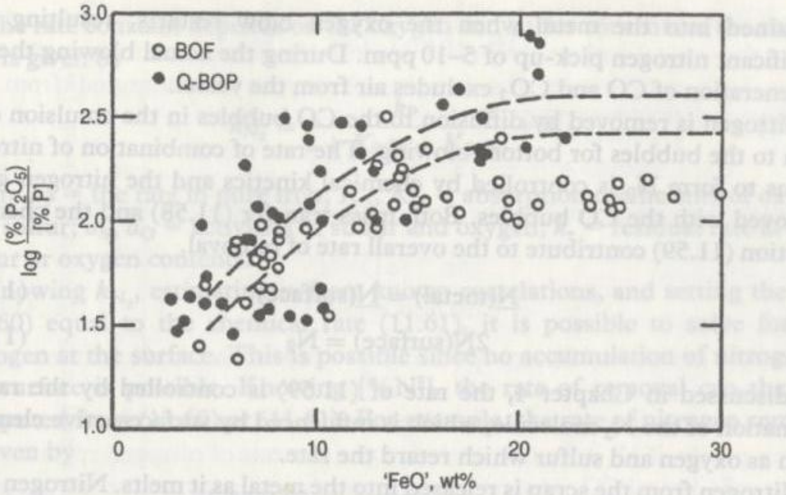

Figure 11.13 Phosphorus equilibrium as a function of slag chemistry in OSM (Turkdogan, 1984).

11.3.3. The Nitrogen Reaction

As demonstrated, the decarburization reaction is reasonably well understood, as well as the slag–metal refining reactions which approach equilibrium. The removal of nitrogen is much more complex and depends on numerous operating variables. With the advent of the production of high-purity interstitial-free (IF) steels, the control of nitrogen has become of great importance. For years there have been 'rules of thumb' for achieving low nitrogen. For example, use of more hot metal and less scrap in the charge and combined blowing, switching the stirring gas from nitrogen to argon, results in lower nitrogen contents. However, there has not been a comprehensive model which indicates how the major variables affect nitrogen and how the process can be optimized to achieve an acceptable nitrogen content at a reasonable cost. Recently, Goldstein and Fruehan (in press) developed such a model, which is summarized below.

11.3.3.1 Reaction mechanisms

The sources of nitrogen in OSM include the hot metal, scrap, impurity nitrogen in the oxygen, and nitrogen in the stirring gas. Nitrogen from the atmosphere is not a major factor unless at first turndown a correction or reblow is required, in which case the furnace fills up with air which is entrained into the metal when the oxygen blow restarts, resulting in a significant nitrogen pick-up of 5–10 ppm. During the actual blowing the rate of generation of CO and CO_2 excludes air from the vessel.

Nitrogen is removed by diffusion to the CO bubbles in the emulsion or in bath to the bubbles for bottom blowing. The rate of combination of nitrogen atoms to form N_2 is controlled by chemical kinetics and the nitrogen gas is removed with the CO bubbles. Both mass transfer (11.58) and the chemical reaction (11.59) contribute to the overall rate of removal.

$$\underline{N}(\text{metal}) = \underline{N}(\text{surface}) \tag{11.58}$$

$$2\underline{N}(\text{surface}) = N_2 \tag{11.59}$$

As discussed in Chapter 4, the rate of (11.59) is controlled by the rate of formation of the N_2 molecule, which is influenced by surface-active elements such as oxygen and sulfur which retard the rate.

Nitrogen from the scrap is released into the metal as it melts. Nitrogen as an impurity in the oxygen or in the stirring gas increases the pressure of N_2 and reduces the rate of (11.59). It is obvious that the amount of CO generated is critical since it provides the reaction surface area and reduces the nitrogen pressure. Therefore, nitrogen removal depends on decarburization. Also, since oxygen and sulfur are surface active, their concentrations on the surface affect the rate of (11.59). Consequently, all these factors much be considered in calculating the net rate of nitrogen removal.

11.3.3.2. Rate equations

There are numerous factors influencing the rate of nitrogen removal. The basic equations are given in this section; a complete description can be found elsewhere (Goldstein and Fruehan, in press). The flux of nitrogen diffusing to the surface of the bubble (J_N) is given by

$$J_N = \frac{m\rho}{100}(\%N - \%N^s) \tag{11.60}$$

where m = mass transfer coefficient; ρ = density of the iron; %N = nitrogen in the bulk metal; $\%N^s$ = nitrogen at the surface of the metal.

The rate of the chemical reaction at the surface (R) is given by

$$R = k_{N_2}\left[p_{N_2} - p_{N_2^e}\right] \tag{11.61}$$

where k_{N_2} = chemical rate constant; p_{N_2} = pressure of nitrogen in the gas; $p_{N_2^e}$ = nitrogen pressure in equilibrium with the nitrogen at surface

$$p_{N_2^e} = [\%N^s]^2\, K_{59} \tag{11.62}$$

and K_{62} = equilibrium constant for reaction (11.59).

The rate constant depends on the oxygen and sulfur contents at the surface and is given by

$$k_{N_2} = \frac{k_P}{1 + K_S a_S + K_O a_O} + k_r \tag{11.63}$$

where k_P = the rate in pure iron; K_S, K_O = absorption coefficients of oxygen and sulfur; a_S, a_O = activities of sulfur and oxygen; k_r = residual rate at high sulfur or oxygen contents.

Knowing k_{N_2}, estimating m from known correlations, and setting the flux (11.60) equal to the chemical rate (11.61), it is possible to solve for the nitrogen at the surface. This is possible since no accumulation of nitrogen at the surface is possible. Knowing [%N^s], the rate of removal can then be computed from (11.60) or (11.61). For example, the rate of nitrogen removal is given by

$$\left[\frac{d[\%N]}{dt}\right]_R = -\frac{Am\rho}{W}[\%N - \%N^s] \tag{11.64}$$

where $[d[\%N]/dt]_R$ = the rate of nitrogen removal; A = the surface areas of the metal droplets; W = the weight of steel, which is a function of time.

There are, however, several complications. For example, all of the rate parameters such as k_P, etc. and the equilibrium constant are functions of temperature. The sulfur content of the metal changes with time and the oxygen content at the surface is considerably different from the bulk concentration. Consequently the temperature and surface contents of oxygen and sulfur must be known as functions of time.

The oxygen activity can be very high at the gas–metal interface and will drastically reduce the rate of nitrogen removal. The oxygen at the surface is computed from the carbon at the surface in equilibrium with CO:

$$C^s + O^s = CO \tag{11.65}$$

where C^s, O^s = the carbon and oxygen at the surface.

It follows that

$$[\%O^s] = \frac{p_{CO}}{[\%C^s]}K_{65} \tag{11.66}$$

where $\%O^s$ = activity or concentration of oxygen at the surface; K_{65} = equilibrium constant for reaction (11.66).

The carbon concentration at the surface is computed by equating the flux of carbon to that consumed by oxygen, as discussed for decarburization reaction:

$$\frac{mA\rho}{100}[\%C - \%C^s] = \dot{N}_{O_2}M_c(100)(f + 1) \tag{11.67}$$

Equation (11.67) is used to compute %C^s above the critical carbon level. Below the critical carbon level there is virtually no carbon at the surface but rather FeO and, hence, the activity of oxygen is computed from the equilibrium for the reaction:

$$\mathrm{Fe} + \mathrm{O} = \mathrm{FeO} \tag{11.68}$$

The carbon concentration at the surface also affects the activity of sulfur (h_S):

$$h_S = f_S[\%\mathrm{S}] \tag{11.69}$$

$$\log f_S = e_S^C[\%\mathrm{C}] \tag{11.70}$$

where f_S = activity coefficient of sulfur; e_S^C = interaction coefficient for carbon on sulfur.

The nitrogen pressure in the slag–metal emulsion is a function of the oxygen purity, if N_2 is used as a stirring gas, the rate of nitrogen removal, and the rate of CO and CO_2 generation. In general nitrogen pressure (p_{N_2}) is given by 11.71 and is a function of time.

$$p_{N_2} = \frac{\dot{N}_{N_2}^{R} + \dot{N}_{N_2}^{O_2} + \dot{N}_{N_2}^{S}}{\dot{N}_{CO(CO_2)} + \dot{N}_{N_2}^{R} + \dot{N}_{N_2}^{O_2} + \dot{N}_{N_2}^{S}} p_T \tag{11.71}$$

where $\dot{N}_{N_2}^{R}$, $\dot{N}_{N_2}^{O_2}$, $\dot{N}_{N_2}^{S}$ = the molar rate of nitrogen removed, in the oxygen, and in the stirring gas; $\dot{N}_{CO(CO_2)}$ = the molar rate of CO and CO_2 generation, which is computed from the rate of decarburization; p_T = total pressure (1 atm).

During the initial stage of the blow no CO is generated since the oxygen is consumed in oxidizing silicon. The rate of oxidation of silicon is controlled initially by the oxygen flow rate but at lower concentrations by mass transfer. During this initial stage of silicon oxidation, no nitrogen is removed. For the latter stage of silicon oxidation, some CO is generated and nitrogen is removed.

Finally, during the OSM process nitrogen is introduced into the metal from the melting scrap. The rate of melting depends on heat and mass transfer and has been modeled by Gaye et al. (1980). The rate of nitrogen pick-up from the scrap is given by

$$\left[\frac{d\%\mathrm{N}}{dt}\right]_S = \frac{[\%N_{sc}]}{W}\left[\frac{dW_{sc}}{dt}\right] \tag{11.72}$$

Also, the weight of the metal (W) used in all the rate equations is computed from the hot metal weight and the rate of scrap melting and the rate of carbon and silicon removed.

$$W = W_{HM} + \int_0^t \frac{dW_{sc}}{dt}\,dt + W_C^R + W_{Si}^R \tag{11.73}$$

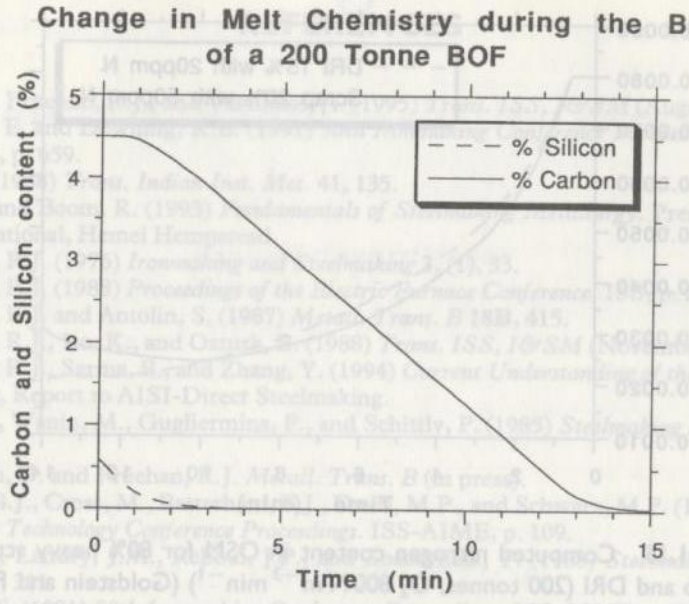

Figure 11.14 Computed carbon and silicon contents of steel in OSM (Goldstein and Fruehan, in press).

In Fig. 11.14 the computed carbon and silicon contents and in Fig. 11.15 the nitrogen contents are shown for two hypothetical cases for a 200 tonne OSM converter blowing oxygen at 800 N m^3 min^{-1}. In one case the charge contains 80% heavy scrap, 16 cm thick and containing 50 ppm nitrogen; in the second case there is no scrap but cooling is achieved by the use of a 15% addition of DRI containing 20 ppm N. The heavy scrap melts late in the process, releasing its nitrogen after most of the CO is generated, causing the nitrogen content to increase to 30 ppm at the end of the blow. With no scrap, the final nitrogen is significantly lower at 20 ppm. The model also indicates if ore which has no nitrogen is used for cooling, about 10 ppm nitrogen can be obtained. In comparing the bulk and surface nitrogen contents it is found that the surface concentration is only slightly less than the bulk, indicating the nitrogen reaction is primarily controlled by chemical kinetics. In particular, toward the end of the blow the oxygen content at the surface is high, retarding the rate. This model is useful for optimizing the process for nitrogen control. For example, the effect of oxygen purity, the time of switching the stirring gas from N_2 to argon, the metal sulfur content, and the amount and size of scrap can be determined. The effect of switching the stirring gas from N_2 to argon is shown in Fig. 11.16.

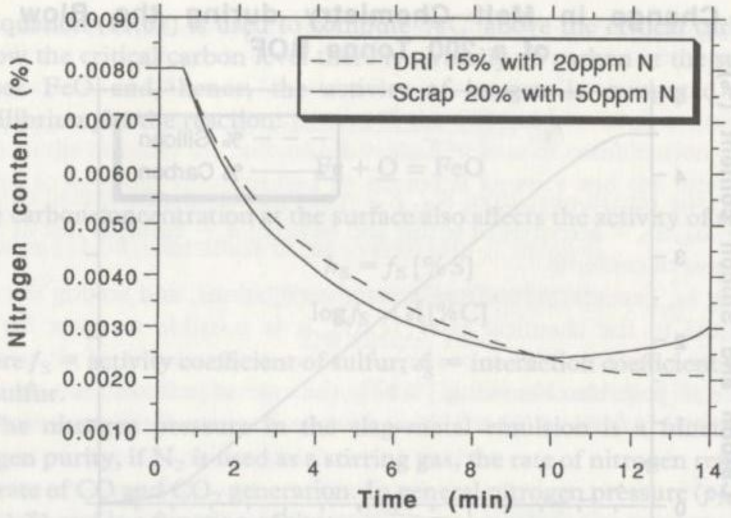

Figure 11.15 Computed nitrogen content in OSM for 80% heavy scrap–20% light scrap and DRI (200 tonnes, O_2 800 N m^{-3} min^{-1}) (Goldstein and Fruehan, in press).

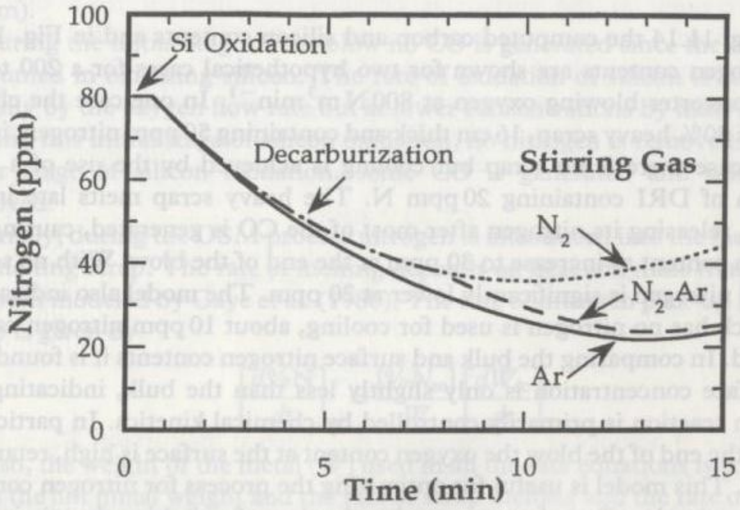

Figure 11.16 The effect of bottom stirring practice on nitrogen removal in the BOF: N_2 entire blow, argon entire blow, and switch at 50% from N_2 to argon.

REFERENCES

Abel, C., Fruehan, R.J., and Vassilicos, A. (1995) *Trans. ISS, I&SM* (August), 49.
Aukrust, E. and Downing, K.B. (1991) *50th Ironmaking Conference Proceedings*. ISS-AIME, p. 659.
Deo, B. (1988) *Trans. Indian Inst. Met.* **41**, 135.
Deo, B. and Boom, R. (1993) *Fundamentals of Steelmaking Metallurgy*. Prentice-Hall International, Hemel Hempstead.
Fruehan, R.J. (1976) *Ironmaking and Steelmaking* **3**, (1), 33.
Fruehan, R.J. (1988) *Proceedings of the Electric Furnace Conference*. ISS, p. 259.
Fruehan, R.J. and Antolin, S. (1987) *Metall. Trans. B* **18B**, 415.
Fruehan, R.J., Ito, K., and Ozturk, B. (1988) *Trans. ISS, I&SM* (November), 83.
Fruehan, R.J., Sarma, B., and Zhang, Y. (1994) *Current Understanding of the Smelting Process*, Report to AISI-Direct Steelmaking.
Gaye, H., Wanin, M., Gugliermina, P., and Schittly, P. (1985) *Steelmaking Proc. ISS* **68**, 11.
Goldstein, D. and Fruehan, R.J. *Metall. Trans. B* (in press).
Hardie, G.J., Cross, M., Batterham, B.J., Davis, M.P., and Schwarz, M.P. (1992) *10th Process Technology Conference Proceedings*. ISS-AIME, p. 109.
Huin, D., Landry, J.M., Reboul, J.P., and Zbaczyniak, Y. (1988) *Steelmaking Proc. ISS* **71**, 311.
Inatani, T. (1991) *50th Ironmaking Conference Proceedings*. ISS-AIME, p. 651.
Ito, K. and Fruehan, R.J. (1989) *Metall. Trans. B* **20B**, 509.
Klogh, J.V., Hardie, G.J., Philip, D.K., and Burke, P.D. (1991) *50th Ironmaking Proceedings*. ISS-AIME, p. 635.
Lange, K. (1986) *Fifth International Iron and Steel Congress*, Washington DC, Book no. 3, p. 231.
Min, D.-J. and Fruehan, R.J. (1992a) *Trans. ISS* 47–52.
Min, D.-J. and Fruehan, R.J. (1992b) *Metall. Trans. B* **23B**, 29.
Pehlke, R.D., Porter, W.F., Urban, R., and Gaines, J.M. (1977) *BOF Steelmaking Series*, ISS-AIME, Warrendale, PA.
Romenets, V.A. (1990) *Steel in Russia* **20**, 366.
Sampaio, R.S., Fruehan, R.J., and Ozturk, B. (1992) *Trans. ISS, I&SM* (August), 49.
Sarma, B., Cramb, A.W., and Fruehan, R.J. (1996) *Metall. Trans. B* **27B**, 717.
Sun, S., Sasaki, Y., and Belton, G.R. (1988) *Metall. Trans. B* **19B**, 959.
Turkdogan, E.T. (1984) *Trans. ISIJ* **24**, 591.
Zhang, Y. and Fruehan, R.J. (1995) *Metall. Trans. B* **25B**, 803.

12

Solidification rate in casting processes

Klaus Schwerdtfeger
Institut für Allgemeine Metallurgie, Technical University Clausthal,
Clausthal-Zellerfeld, Germany

12.1. INTRODUCTION

Most metallic materials are first produced as melts that are subsequently converted to the solid state in a solidification process. Depending on the final application of the material, there are numerous casting and solidification processes, the main groups being continuous casting for long and flat products and the foundry processes for mold castings. The physical and chemical phenomena occurring during solidification exert a strong impact on the properties of the final material, and on its production cost. The basic phenomenon is the transport of heat, which controls the solidification and cooling rate. These rates influence the primary morphological structure (dendrites, grains) and the formation of defects as segregation, internal voids, and cracks, and they determine the technological specifics of the casting process, e.g., the metallurgical length of a continuous casting machine.

This chapter focuses on the solidification and cooling rate of metallic materials. Some fundamentals will be presented in sections 12.2 and 12.3, and the rest of the chapter will be devoted to the continuous casting process. The treatment of solidification and cooling rates is a semitheoretical art. The transport of heat within the solidifying body is described precisely by the differential equation for heat flow. But for making predictions with numerical models many data must be known which can be obtained only by measurements: conditions for heat withdrawal at the surface of the body and material properties. Also, the fluid flow in the remaining melt may influence the solidification rate. However, this chapter is confined to the relatively simple problems in which flow velocities need not be computed explicitly.

ADVANCED PHYSICAL CHEMISTRY FOR PROCESS METALLURGY
ISBN 0-12-618920-X

Copyright © 1997 Academic Press Ltd
All rights of reproduction in any form reserved

The heat flow equation used is that for conduction in only one dimension and for constant density:

$$\rho\left[\frac{\partial H}{\partial t}+\frac{\partial}{\partial x}(v_x H)+\frac{\partial}{\partial z}(v_z H)\right]=\frac{\partial}{\partial x}\left(\lambda\,\frac{\partial T}{\partial x}\right) \tag{12.1}$$

The symbols are explained at the end of the chapter. The second and third terms in the bracket on the LHS of (12.1) account for the movement of the material with respect to the coordinate system. They cancel in the computation of ingot solidification. The third term on the LHS is used in the treatment of conventional continuous casting (section 12.4), both the second and third terms in the treatment of special processes like continuous casting with in-line thickness reduction (section 12.5). Equation 12.1 must be solved numerically, using the computer, for the specific casting process. However, general solutions are available for certain idealized conditions which are quite useful because they show the principal dependencies and may serve, in many cases, for making good first estimates.

12.2. SOLIDIFICATION RATE OF ONE-COMPONENT MATERIALS

Most metallic materials used as practical objects are alloys. However, the solidification rate of many materials with low alloying content, e.g., soft steels, can be predicted satisfactorily with the comparatively simple procedure applicable for one-component materials, and, of course, as a basis for the treatment of alloys, the solidification of pure materials has to be considered first.

One-component materials (pure metals, congruently melting compounds) solidify with a planar solid–liquid interface. Figure 12.1 shows the solidification front in one half of a solidifying ingot of plate geometry (slab) and the temperature profile in the shell at a particular time. The shell thickness, denoted as x_S, and the temperature profile are to be obtained as a function of time by solution of

$$\rho\frac{\partial H}{\partial t}=\frac{\partial}{\partial x}\left(\lambda\,\frac{\partial T}{\partial z}\right) \tag{12.2}$$

If the material properties (c_p, ρ, λ), the heat transfer coefficient h and the reference temperature T_w are taken to be constant, and if the superheat is zero, a rather simple representation of the rate law $x_S(t)$ is possible. With $\partial H = c_p\,\partial T$ and using $\kappa = \lambda/(\rho c_p)$, the Equation 12.2 becomes

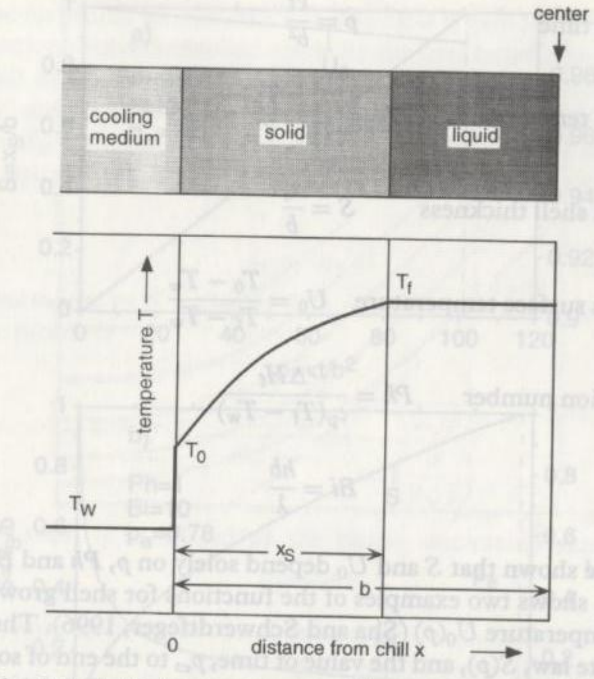

Figure 12.1 Schematic temperature profile in a plate solidifying with planar interface, and extension of solid and liquid regions.

$$\frac{\partial T}{\partial t}=\kappa\frac{\partial^2 T}{\partial x^2} \tag{12.3}$$

The solution is carried out with the initial condition $T = T_f$ (no superheat) and with the boundary conditions at the chill

$$x=0 \qquad \lambda\frac{\partial T}{\partial x}=h(T-T_w) \tag{12.4}$$

and at the solid–liquid interface

$$x=x_s \qquad T=T_f \tag{12.5}$$

$$x=x_s \qquad \lambda\frac{\partial T}{\partial x}=\rho\,\Delta H_f\,\frac{dx_s}{dt} \tag{12.6}$$

The following nondimensional quantities are applied in the numerical computations and in the representation of the results:

Dimensionless x-coordinate $\qquad s=\dfrac{x}{b}$ $\qquad$ (12.7)

Dimensionless time $$p = \frac{\kappa t}{b^2} \tag{12.8}$$

Dimensionless temperature $$U = \frac{T - T_w}{T_f - T_w} \tag{12.9}$$

Dimensionless shell thickness $$S = \frac{x_s}{b} \tag{12.10}$$

Dimensionless surface temperature $$U_0 = \frac{T_0 - T_w}{T_f - T_w} \tag{12.11}$$

Phase conversion number $$Ph = \frac{\Delta H_f}{c_p(T_f - T_w)} \tag{12.12}$$

Biot number $$Bi = \frac{hb}{\lambda} \tag{12.13}$$

It can easily be shown that S and U_0 depend solely on p, Ph and Bi.

Figure 12.2 shows two examples of the functions for shell growth $S(p)$ and for surface temperature $U_0(p)$ (Sha and Schwerdtfeger, 1996). The characteristics of the rate law, $S(p)$, and the value of time, p_e, to the end of solidification, depend strongly on the Biot number (heat transfer coefficient). At low Biot number $S(p)$ becomes close to linear and p_e is large, whereas at high Biot number $S(p)$ approaches the 'square root law' $S \sim \sqrt{p}$. Figure 12.3 gives the correlations between p, S, Bi, and Ph, and Fig. 12.4 those between U_0, S, Bi, and Ph. These two charts can be utilized to draw the $x_S(t)$ and $T_0(t)$ relationships for a broad range of values for λ, ΔH_f, c_p, κ, h, b, T_f, and T_w. For instance, for continuous casting of iron Ph is about 0.22 and Bi is in the range 1 to 10 (spray cooling).

The curves in Fig. 12.3 and the relationship U(s) for the temperature profile approach analytical solutions in certain ranges of SBi and Ph. At low Biot number and high phase conversion number the solution of (12.3) approximates that obtained by setting the LHS equal to zero (so-called steady-state approximation). This means that $\partial^2 T/\partial x^2$ is zero, yielding a linear temperature profile in the shell. The expressions obtained for S and U are

$$S = \sqrt{\frac{1}{Bi^2} + \frac{2p}{Ph}} - \frac{1}{Bi} \tag{12.14a}$$

or

$$\frac{p}{S^2} = Ph\left(\frac{1}{2} + \frac{1}{SBi}\right) \tag{12.14b}$$

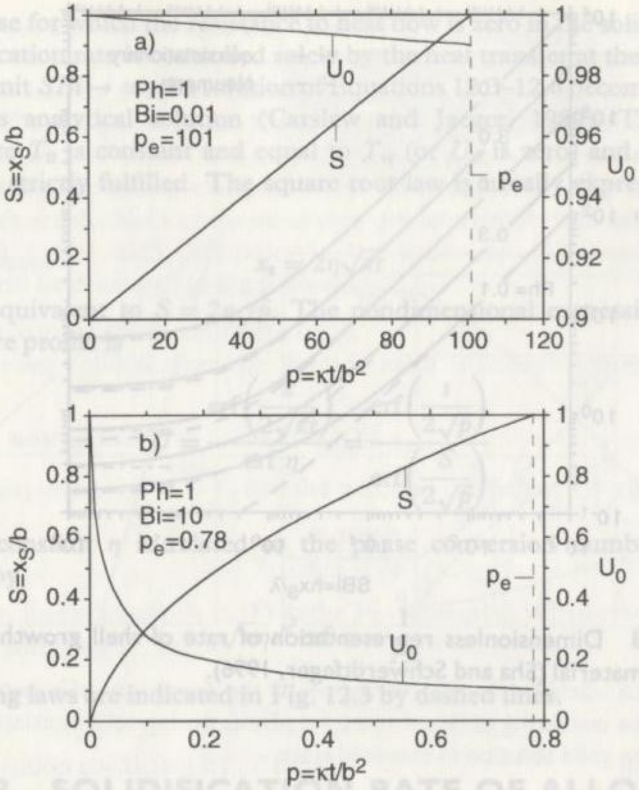

Figure 12.2 Shell growth during solidification of a one-component material as a function of time, showing (a) close to linear behavior at low Biot number, and (b) close to square-root law behavior at high Biot number (Sha and Schwerdtfeger, 1996).

and

$$U = \frac{1 + sBi}{1 + SBi} \tag{12.15}$$

From Equation 12.15, for the surface temperature, $U_0 = 1/(1 + SBi)$. If $SBi \ll 2$,

$$S = \frac{Bi}{Ph} p \tag{12.16}$$

and

$$U = U_0 = 1 \tag{12.17}$$

The expression 12.16 represents the strictly linear rate law $S(p)$ valid in the

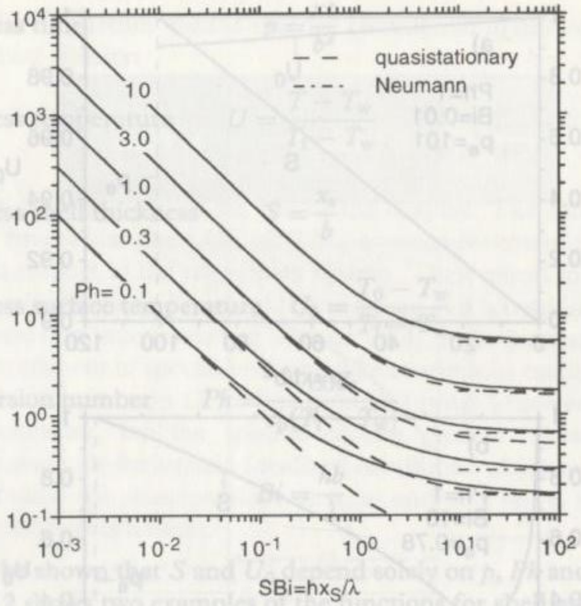

Figure 12.3 Dimensionless representation of rate of shell growth of a one-component material (Sha and Schwerdtfeger, 1996).

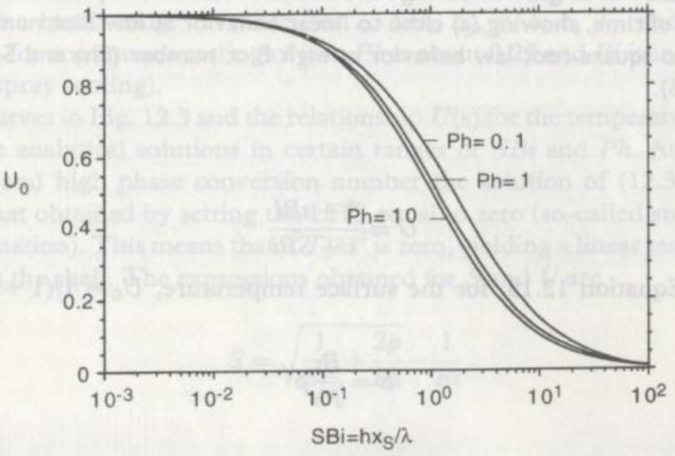

Figure 12.4 Dimensionless representation of surface temperature during solidification of a one-component material (Sha and Schwerdtfeger, 1996).

limiting case for which the resistance to heat flow is zero in the solid shell and the solidification rate is controlled solely by the heat transfer at the chill.

In the limit $SBi \rightarrow \infty$, the solution of Equations 12.3–12.6 becomes equal to Neumann's analytical solution (Carslaw and Jaeger, 1959). The surface temperature T_0 is constant and equal to T_w (or U_0 is zero) and the square root law is strictly fulfilled. The square root law is usually expressed in the form

$$x_s = 2\eta\sqrt{\kappa t} \tag{12.18}$$

which is equivalent to $S = 2\eta\sqrt{p}$. The nondimensional expression for the temperature profile is

$$U = \frac{\mathrm{erf}\left(\frac{x}{2\sqrt{\kappa t}}\right)}{\mathrm{erf}\,\eta} = \frac{\mathrm{erf}\left(\frac{s}{2\sqrt{p}}\right)}{\mathrm{erf}\left(\frac{S}{2\sqrt{p}}\right)} \tag{12.19}$$

The rate constant η is related to the phase conversion number (setting $T_w = T_0$) by

$$\sqrt{\pi}\eta e^{\eta^2}\,\mathrm{erf}\,\eta = \frac{1}{Ph} \tag{12.20}$$

The limiting laws are indicated in Fig. 12.3 by dashed lines.

12.3. SOLIDIFICATION RATE OF ALLOYS

Alloys usually have a freezing range, that is, the solidification starts at the liquidus temperature T_L and ends at the (effective) solidus temperature T_S. In most industrial casting processes the superheat above liquidus is small and, owing to the constitutional undercooling, the planar solid–liquid interface becomes unstable. A heterogeneous zone (mushy zone) consisting of solid and liquid phases is present between the solid shell and the liquid interior (Fig. 12.5). Within the mushy zone the fraction solid f_S increases from the liquidus front where it is zero to the solidus front where it is unity. The content c_L of the solute element in the residual liquid is that of the liquidus line (in a binary system) and increases toward the solidus front corresponding to the decrease of temperature. In a well-developed mushy zone the solid phase grows in the form of dendrites.

The heat flow equation to be used is again Equation 12.2. For the mushy zone, H is composed of the enthalpies H_L and H_S of the liquid and solid phases according to

$$H = f_L H_L + f_S H_S \tag{12.21}$$

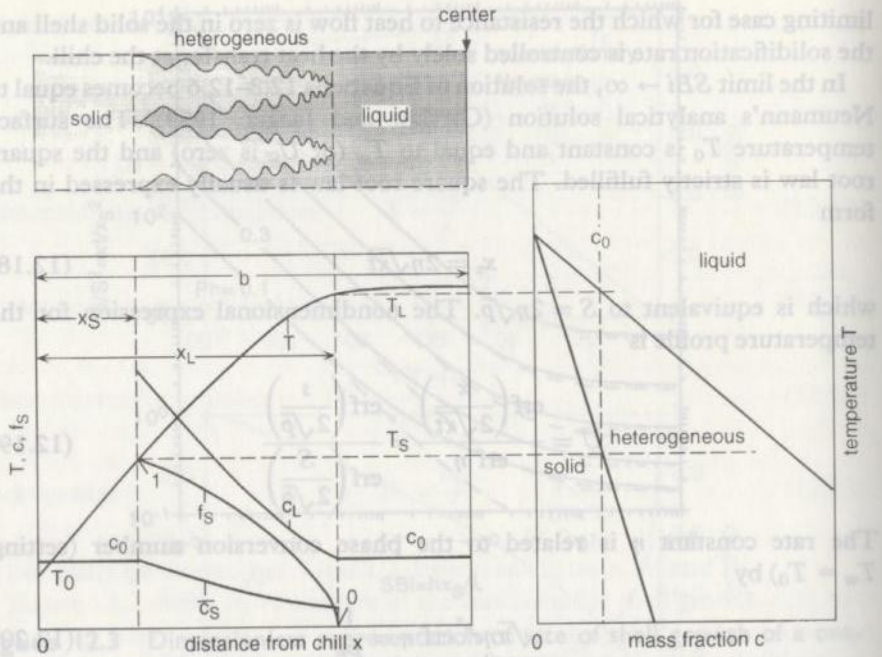

Figure 12.5 Schematic representation of the formation of a heterogeneous (mushy) zone consisting of liquid and solid phases during solidification of a binary alloy forming solid solution in the solid state.

Hence, with $f_L + f_S = 1$ or $\partial f_L = -\partial f_S$, $\partial H/\partial t$ becomes

$$\frac{\partial H}{\partial t} = -(H_L - H_S)\frac{\partial f_S}{\partial t} + f_L\frac{\partial H_L}{\partial t} + f_S\frac{\partial H_S}{\partial t} \tag{12.22}$$

The difference $H_L - H_S$ is the heat of fusion ΔH_f, and $f_L(\partial H_L/\partial t) + f_S(\partial H_S/\partial t)$ can be replaced by $(f_L c_{pL} + f_S c_{pS})\, \partial T/\partial t = c_p\, \partial T/\partial t$. Consequently, the equation for heat conduction in the mushy zone can be written as

$$\rho\left[c_p\frac{\partial T}{\partial t} - \Delta H_f\frac{\partial f_s}{\partial t}\right] = \frac{\partial}{\partial x}\left(\lambda\frac{\partial T}{\partial x}\right) \tag{12.23a}$$

or

$$\rho c_p\left[1 - \frac{\Delta H_f}{c_p}\left(\frac{\partial f_S}{\partial t}\right)\right]\frac{\partial T}{\partial t} = \frac{\partial}{\partial x}\left(\lambda\frac{\partial T}{\partial t}\right) \tag{12.23b}$$

The LHS of Equation 12.23a may be interpreted in such a manner that the first term takes account of the capacitive property of the solid–liquid mixture whereas the second term considers the latent heat of fusion released owing to the liquid–solid phase change. The quantity $\partial f_S/\partial t$, which is the local rate of increase of the fraction solid, is influenced by microsegregation and macrosegregation and its exact computation involves, in general, the additional treatment of these phenomena. However, for equilibrium solidification, that is, in the absence of micro- and macrosegregation, f_S is determined solely by the phase diagram and its computation is quite simple. Binary iron–carbon alloys which are the basis of the mass steel grades exhibit little microsegregation owing to the high diffusivity in the solid iron. Their solidification behavior will be discussed in the following.

Solidification of iron–carbon alloys

In equilibrium solidification the fraction solid is obtained from the mass balance:

$$c_L f_L + c_S f_S = c_0 \tag{12.24}$$

which yields, using $f_L = 1 - f_S$ and the partition coefficient $k = c_S/c_L$,

$$f_S = \frac{c_S - c_0 k}{c_S(1-k)} \tag{12.25}$$

The solidus line of austenite $c_S(T)$ in the Fe–C diagram is described (Chuang and Schwerdtfeger, 1973a) by

$$c_S = \frac{1526.3 - T}{176.9} \tag{12.26}$$

and the partition coefficient by (T in °C)

$$k = 0.3758 + 0.5627 \times 10^{-3}T - 0.3981 \times 10^{-6}T^2 \tag{12.27}$$

Hence, f_S depends only on T and df_S/dT can readily be evaluated.

Figure 12.6 shows the cooling curves at seven distances from the surface in a slab with 0.60% carbon solidifying in a cast iron mold (Chuang and Schwerdtfeger, 1973a). The thickness of the solid shell $x_S = x$ ($f_S = 1$) is obtained, as a function of time, by plotting the position of the thermocouples against the times on the respective cooling curves at which the temperature has dropped to the solidus temperature T_S. Correspondingly, the advancement of fronts with constant fraction solid is determined by relating the positions to the times for the temperature pertaining to the specified fraction solid. Figure 12.7 represents the curves for the progression of the solidus front $x_S = x(f_S = 1)$ and of iso-f_S-fronts for $f_S = 0.1$ and 0.5, as deduced from the cooling curves of Fig. 12.6 in the manner described.

Figure 12.8 gives the theoretical results as obtained by solution of Equation 12.23 using the measured surface temperature $T_0(t)$ (Fig. 12.6) as the boundary condition at $x = 0$. There is close agreement with the measured data. In Fig. 12.8 the square of the coordinate for specified f_S is plotted against time because such a diagram demonstrates that $x(f_S = \text{const})^2$ increases close

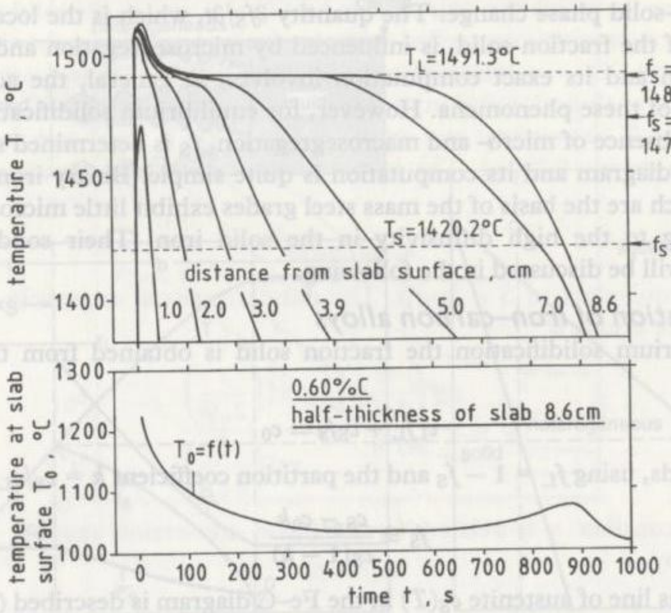

Figure 12.6 Example of mushy zone formation. Experimental cooling curves of an iron–carbon alloy with 0.60% carbon (Chuang and Schwerdtfeger, 1973a).

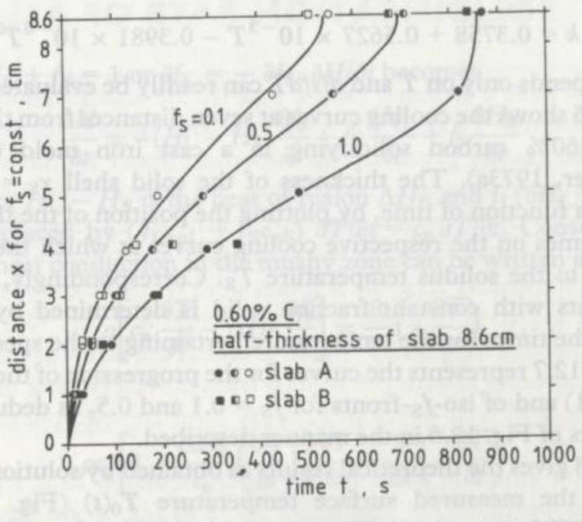

Figure 12.7 Progression of solidus front and iso-f_s-fronts with time, as derived from the experimental cooling curves in Fig. 12.6 (Chuang and Schwerdtfeger, 1973a).

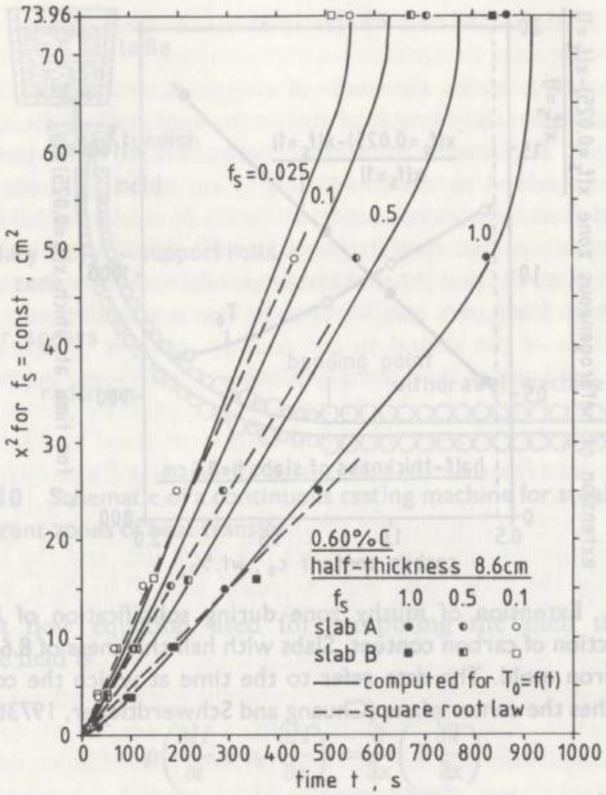

Figure 12.8 Theoretical results for progression of solidus front and iso-f_s-fronts, and comparison with the experimental data. Slab with 0.60% carbon (Chuang and Schwerdtfeger, 1973a).

to linearly with time over most of the total solidification time. That is, under the conditions for ingot casting, the growth of the shell (contour for $f_S = 1$) and the progression of all the contours for f_S = const take place close to the square root dependence over most of the time. But at the end the growth accelerates (Chuang and Schwerdtfeger, 1973a). The border of the mushy zone toward the interior of the slab can be defined as the f_S contour with a certain small f_S value, e.g., $f_S = 0.025$. Hence, in Fig. 12.8 the extension of the mushy zone can be deduced from the curves for $f_S = 0.025$ and $f_S = 1$. This distance increases with time until the contour for $f_S = 0.025$ reaches the center of the slab. It then decreases again, of course. The extension of the mushy zone increases with solute content due to the increase of the freezing range. Figure 12.9 shows the extension of the mushy zone related to the shell

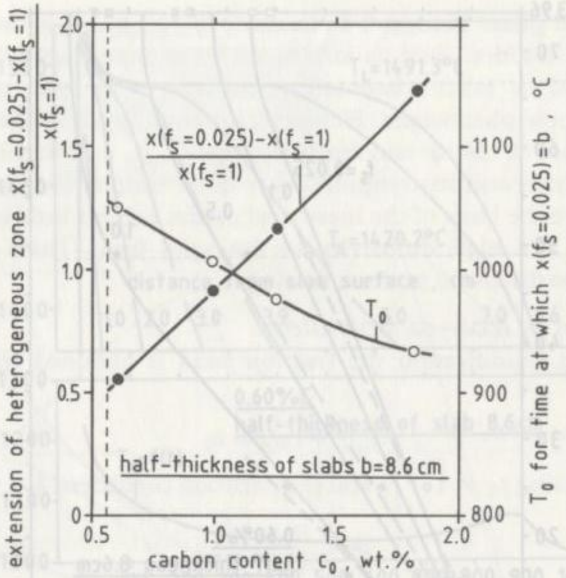

Figure 12.9 Extension of mushy zone during solidification of iron–carbon alloys as a function of carbon content. Slabs with half-thickness of 8.6 cm solidifying in a cast iron mold. The data refer to the time at which the contour with $f_s = 0.025$ reaches the center plane (Chuang and Schwerdtfeger, 1973b).

thickness for iron–carbon alloys, as a function of carbon content (Chuang and Schwerdtfeger, 1973b). At 1.8% carbon the mushy zone is larger by a factor of about 1.7 than the solid shell.

12.4. SOLIDIFICATION RATE IN CONTINUOUS CASTING OF STEEL

Figure 12.10 shows the scheme of a continuous casting machine for steel slabs. The liquid metal is fed from the ladle via a dispenser called a tundish into a water-cooled copper mold. Here, a shell solidifies which attains a thickness of about 1 cm at the end of the mold. The strand is withdrawn continuously from the mold, but its interior is liquid or mushy for many meters downward, depending on the casting rate and the strand thickness. Below the mold, in the so-called secondary cooling zone, the cooling is performed by water sprays and in the lower part of the machine, beyond the spray zone, by radiation. At the end of the caster there is the straightening segment and withdrawal machine.

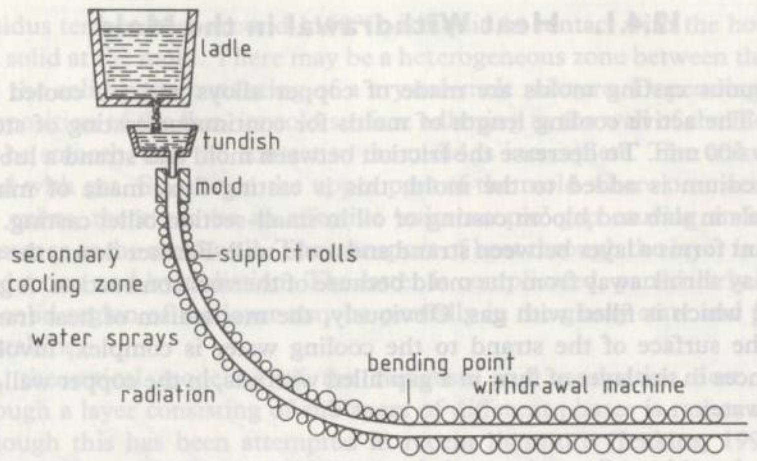

Figure 12.10 Schematic of a continuous casting machine for steel slabs indicating the different zones of heat transfer.

The heat flow equation used for computing the shell thickness and temperature field is

$$\rho\left(\frac{\partial H}{\partial t} + v_{\mathrm{c}}\,\frac{\partial H}{\partial z}\right) = \frac{\partial}{\partial x}\left(\lambda\,\frac{\partial T}{\partial x}\right) \tag{12.28}$$

where $v_c = v_z$ (constant in z-direction) is the rate of strand movement. The origin of the z-coordinate is at the meniscus. Hence, in the steady state which is the normal casting operation Equation 12.28 reduces to

$$\rho v_{\mathrm{c}}\,\frac{\partial H}{\partial z} = \frac{\partial}{\partial x}\left(\lambda\,\frac{\partial T}{\partial x}\right) \tag{12.29}$$

There are two principal methods for determining the boundary conditions at the surface, $x = 0$, of the strand. The main way is to measure cooling water temperatures, mold wall temperatures, strand temperatures, and shell profiles in the actual operation, and then deduce from these data heat flux densities and/or heat transfer coefficients. The other way is to investigate the unit heat transfer operations in the laboratory, viz. heat transfer through layers of casting flux, or heat transfer under spray nozzles. The two methods can be combined. In the following sections the various heat withdrawal phenomena at the strand surface will be discussed.

12.4.1. Heat Withdrawal in the Mold

Continuous casting molds are made of copper alloys and are cooled with water. The active cooling length of molds for continuous casting of steel is usually 600 mm. To decrease the friction between mold and strand a lubrication medium is added to the mold: this is casting flux, made of mineral materials in slab and bloom casting or oil in small-section billet casting. The lubricant forms a layer between strand and mold wall. Farther down, the solid shell may shrink away from the mold because of thermal contraction. A gap is formed which is filled with gas. Obviously, the mechanism of heat transfer from the surface of the strand to the cooling water is complex, involving resistances in the layer of flux, in a gap filled with gas, in the copper wall, and in the water.

12.4.1.1. Heat flow through layers of casting flux

Figure 12.11 shows schematically the flux layer in the upper region of the mold where a macroscopic gas gap does not exist yet, and the temperature profile between the steel shell and the mold wall. The flux, which has a liquidus temperature around 1150°C, is liquid in contact with the hot strand and solid at the mold. There may be a heterogeneous zone between the liquid and the solid parts consisting of a crystal–melt mixture. Depending on the composition of the flux, its cold surface adhering to the wall of the mold may not be smooth, and the contact to the mold is incomplete. The wrinkles are filled with gas. So, also in the upper part of the mold where no macroscopic gap exists, there can be an effective 'microscopic' gap causing an interface resistance at the mold wall. The transport of heat through the layer is both by conduction and by radiation. The latter is complicated, particularly because the solid region of the layer may be partially in the glassy state and partially crystalline.

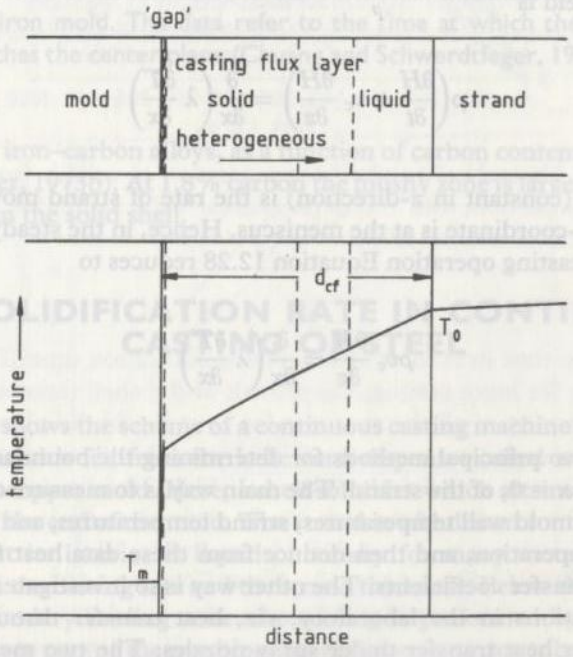

Figure 12.11 Schematic representation of casting flux layer between surface of strand and wall of the mold, and temperature profile. Upper region of mold.

A theoretical modeling of the radiative and conductive heat transfer through a layer consisting of sublayers of different phases is rather difficult, although this has been attempted in recent literature (Jenkins, 1995). For engineering application it suffices to have the experimental data for the overall heat flux, which can be obtained in the laboratory with apparatus designed for this purpose. For instance, the strand can be simulated by a steel plate which is heated by an electric current (Ohmiya et al., 1983; Holzhauser et al., 1990). The plate has a trough in which the casting flux is fused. A copper block, cooled internally with water, serves as the mold. The setup is instrumented with thermocouples for determination of the heat flux (via temperature gradient in the copper) and of the mold and strand side temperatures T_{m} and T_0, respectively. Figure 12.12 shows heat flux densities obtained in such a manner with two different casting powders. The heat flux densities depend on layer thickness d_{cf}. Figure 12.13 gives apparent layer conductivities λ_{app} deduced on the basis of the equation

$$q = \frac{\lambda_{\mathrm{app}}}{d_{\mathrm{cf}}}(T_0 - T_{\mathrm{m}}) \qquad (12.30)$$

which may serve to estimate the heat fluxes at smaller layer thickness. λ_{app} increases with 'strand' temperature T_0 indicating the effect of radiation. There is also a marked influence of composition (compare Figs 12.13a and b) which is caused by the different absorption coefficients of the oxides, and by the effects of the different oxides on making the layer partially crystalline and on producing a nonsmooth interface at the mold side. The total heat transfer resistance between the strand surface and the cooling water in the mold is given as

$$\frac{1}{h} = \frac{1}{h_{\mathrm{w}}} + \frac{d_{\mathrm{m}}}{\lambda_{\mathrm{m}}} + \frac{d_{\mathrm{cf}}}{\lambda_{\mathrm{app}}} \qquad (12.31)$$

where h_{w} is the heat transfer coefficient on the water side of the mold, and d_{m} and λ_{m} are thickness and thermal conductivity, respectively, of the mold plate. Under the normal conditions in continuous casting, the largest part on the

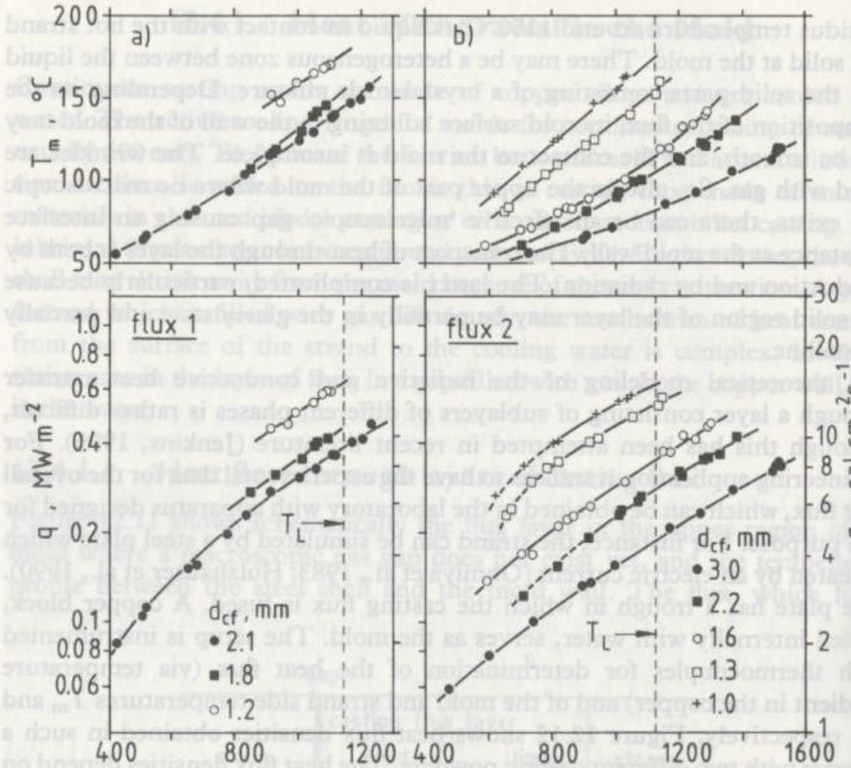

Figure 12.12 Laboratory data on heat transfer through layers of casting fluxes (Ohmiya et al., 1983). (a) Flux 1 (32% SiO_2, 23% Ca, 7.5% Al_2O_3, 4.5% Na_2O, 1.5% Fe_2O_3, 4.5% F, 0.6% MgO, 0.2% TiO_2, 0.3% MnO, 1.0% K_2O, 9% C_{tot} in the powder state, C was removed by preheating in air). (b) Flux 2, same as flux 1, but with 3.5% FeO added.

RHS of Equation 12.31 is the third term; that is, the heat transfer rate is controlled primarily by the properties of the casting flux.

12.4.1.2. Heat flow through a gas gap

When the temperature along the strand surface drops below the solidus temperature of the casting flux, the flux layer becomes completely solid. Owing to the shearing forces caused by the relative motion between strand and mold and to shrinkage of the flux, the coherence of the layer may be destroyed and there will be, at least locally, heat exchange between the strand surface and the mold wall directly over a gas gap. Also, if in the lower part of the mold the conicity of the mold does not balance the shrinkage of the strand shell or if the ferrostatic pressure does not suffice to press the strand shell against the mold, a macroscopic gap will develop. The gas in the gap is formed mainly from air (penetrating into the gap from the lower end of the mold) and consists primarily of nitrogen since most of the oxygen has been removed from the air by reaction with the strand surface. It may contain also some water vapor from the water sprays below the mold and, in the upper part of the mold, hydrogen generated by reduction of water by the steel surface, and possibly some carbon dioxide and monoxide originating from various reactions between the gas, the steel, and the flux.

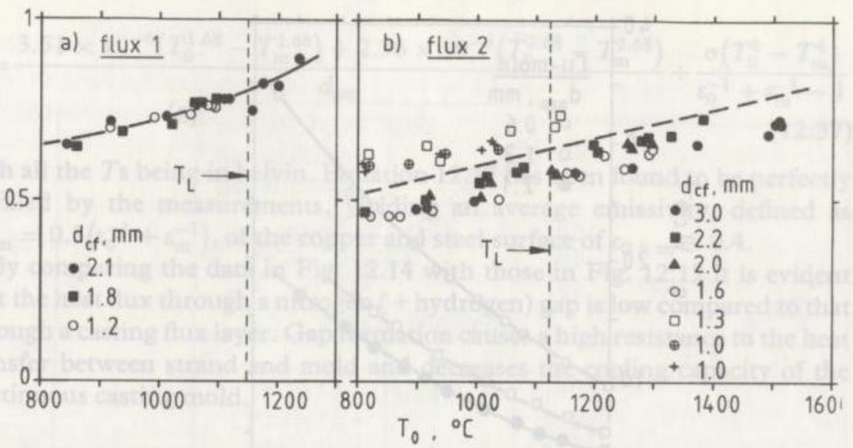

Figure 12.13 Apparent layer thermal conductivities as a function of strand temperature (Ohmiya et al., 1983): (a) flux 1; (b) flux 2.

The heat transfer over a gas gap contained between two parallel metal plates has been investigated with the same setup as described in section 12.4.1.1 (Ohmiya et al., 1983; Holzhauser et al., 1990). In Fig. 12.14a the obtained heat flux densities are plotted against the hot surface temperature T_0 (strand temperature). The cold surface temperature T_m (mold temperature) is given in Fig. 12.14b. Since the optical thickness of a thin gas layer is small, the total heat flux can be written as the sum of conductive and radiative components (Siegel and Howell, 1972):

$$q = q_c + q_r \tag{12.32}$$

which are independent of each other and are given as

$$q_c = \lambda_{gas}\,\frac{\partial T}{\partial x} \tag{12.33}$$

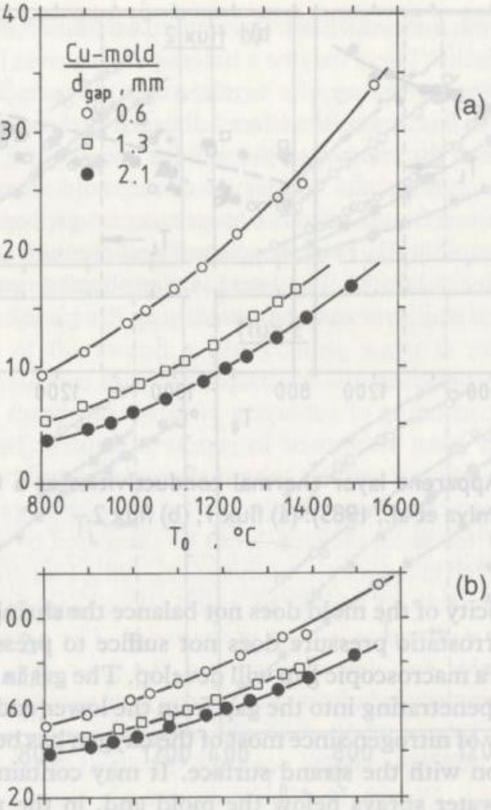

Figure 12.14 Heat transfer through gap filled with nitrogen–hydrogen gas (Holzhauser et al., 1990).

$$q_r = \frac{\sigma(T_0^4 - T_m^4)}{\varepsilon_0^{-1} + \varepsilon_m^{-1} - 1} \tag{12.34}$$

Using the expression

$$\lambda_{95N_2-5H_2} = 5.90 \times 10^{-4} T^{0.68} + 6.32 \times 10^{-8} T^{1.68} \quad \mathrm{W\,m^{-1}\,K^{-1}} \tag{12.35}$$

for the 95% $N_2-5\%$ H_2 layer investigated in the experiments of Fig. 12.14 (Holzhauser et al., 1990), Equation 12.33 can be integrated to yield

$$q_c = \frac{3.51 \times 10^{-4}(T_0^{1.68} - T_m^{1.68}) + 2.36 \times 10^{-8}(T_0^{2.68} - T_m^{2.68})}{d_{gap}} \tag{12.36}$$

Hence, the total heat flux density is given by

$$q = \frac{3.51 \times 10^{-4}(T_0^{1.68} - T_m^{1.68}) + 2.36 \times 10^{-8}(T_0^{2.68} - T_m^{2.68})}{d_{gap}} + \frac{\sigma(T_0^4 - T_m^4)}{\varepsilon_0^{-1} + \varepsilon_m^{-1} - 1} \tag{12.37}$$

with all the *T*s being in kelvin. Equation 12.37 has been found to be perfectly fulfilled by the measurements, yielding an average emissivity, defined as $\varepsilon_{0+m}^{-1} = 0.5(\varepsilon_0^{-1} + \varepsilon_m^{-1})$, of the copper and steel surface of $\varepsilon_{0+m} = 0.4$.

By comparing the data in Fig. 12.14 with those in Fig. 12.12 it is evident that the heat flux through a nitrogen (+ hydrogen) gap is low compared to that through a casting flux layer. Gap formation causes a high resistance to the heat transfer between strand and mold and decreases the cooling capacity of the continuous casting mold.

12.4.1.3. Plant data on mold heat transfer

The laboratory data on the unit heat transfer operations give insight into the different mechanisms operating in the mold and they are useful tools in optimization efforts. But the heat flux existing in reality must be measured on a life continuous casting mold. The main parameter influencing the heat withdrawal in the mold is the casting velocity, but there are several other factors: the taper of the mold, the type of the mold (straight, curved), the guidance system below the mold, the type of the lubricant, of course, the composition of the steel (e.g., carbon content), and the superheat. If the data are to be used in modeling work it is useful to present them in the form of analytical expressions. In this section an equation will be given for the heat flux density as a function of distance *z* from the meniscus and the casting velocity v_c which resulted from an evaluation of literature data (Schwerdtfeger, 1988).

In the mold the maximum of the heat flux density is normally close to the meniscus, that is, the heat flux density decreases downward. There can be small maxima and minima. Also, there may be an increase again at the lower end of the mold. If the gap between mold and strand is of uniform thickness, that is, if the conicity of the mold and the guidance of the strand below the mold are correct, the decrease of the heat flux density along the length of the mold is according to a smooth curve. Examples are shown in Fig. 12.15. To a good approximation, straight lines result in a half-logarithmic plot. Hence, *q* can be described by the exponential law

$$q = q_a\, e^{-\alpha z} \tag{12.38}$$

The exponent α, which results from the slope of the straight lines, is usually about 0.0015 mm^{-1}. Further, the data in Fig. 12.15 demonstrate that the heat flux increases with increasing casting velocity v_c. This effect and the decrease down the mold are caused by the heat flow resistance of the solid steel shell.

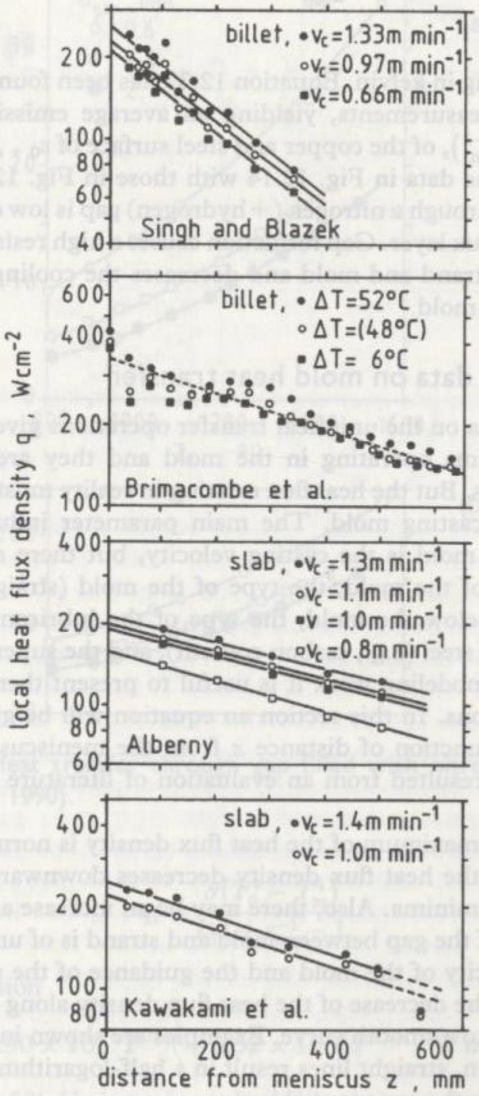

Figure 12.15 Local heat flux density in continuous casting mold according to data in the literature (for original references see Schwerdtfeger, 1988).

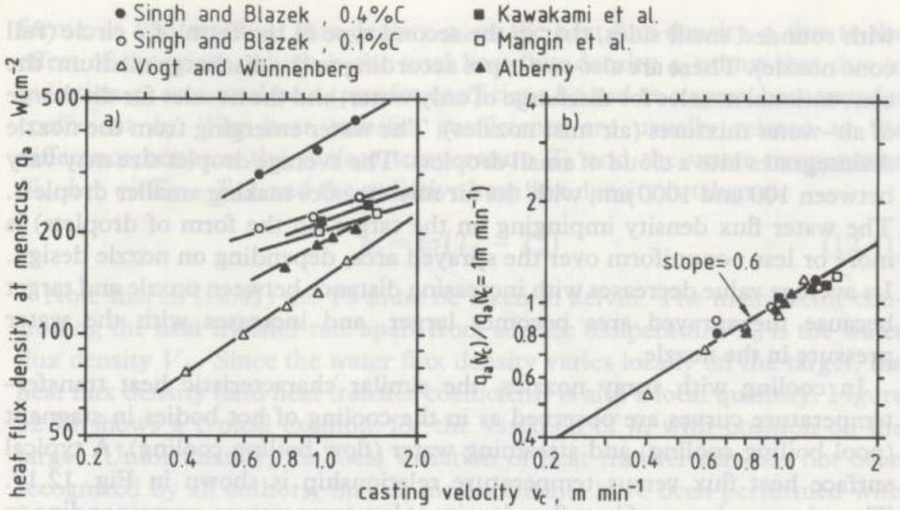

Figure 12.16 Heat flux density at meniscus (extrapolated) as a function of casting rate (for original references see Schwerdtfeger, 1988).

The shell thickness decreases with increasing strand velocity, at given distance z from the meniscus, owing to the shorter solidification time, and it increases, of course, at given casting velocity, v_c, with increasing distance z from the meniscus.

In Fig. 12.16a the heat flux density q_a at the meniscus ($z = 0$), obtained by extrapolation of straight line plots according to Fig. 12.15, is plotted against v_c in log-log scale. From the normalized graph in Fig. 12.16b the relationship

$$q_a = Av_c^{\beta} \tag{12.39}$$

is deduced, with $\beta = 0.6$. Hence, for the mold heat flux density the simple equation

$$q = Av_c^{0.6}\, e^{-0.0015\, z} \tag{12.40}$$

results in which z is in mm. The quantity A is the heat flux density at the meniscus ($z = 0$) if $v_c = 1\text{ m min}^{-1}$. For slab casting A is in the order of $200\text{ W cm}^{-2}\,(\text{m min}^{-1})^{-0.6}$.

12.4.2. Spray Cooling

There are two main types of spray nozzles according to the shape of the wetted area: flat jet nozzles used in slab casting, and cone nozzles used in billet and bloom casting. The wetted area in the first type is in the form of a 'rectangle' with rounded small sides, that in the second type in the form of a circle (full cone nozzle). There are also two types according to the discharge medium: the conventional nozzles for discharge of only water, and the nozzles for discharge of air–water mixtures (air mist nozzles). The water emerging from the nozzle disintegrates into a cloud of small droplets. The average droplet size may vary between 100 and 1000 μm, with the air mist nozzles making smaller droplets. The water flux density impinging on the target (in the form of droplets) is more or less nonuniform over the sprayed area, depending on nozzle design. Its average value decreases with increasing distance between nozzle and target because the sprayed area becomes larger, and increases with the water pressure in the nozzle.

In cooling with spray nozzles, the similar characteristic heat transfer-temperature curves are observed as in the cooling of hot bodies in stagnant (pool boiling cooling) and streaming water (flow boiling cooling). A typical surface heat flux versus temperature relationship is shown in Fig. 12.17. There is a maximum of heat flux density at low temperature, corresponding to the so-called burnout point in pool or flow cooling, and a critical temperature at which the range of stable film boiling commences, corresponding to the Leidenfrost temperature. The cooling characteristics of spray nozzles have been measured by numerous authors. The data are presented in various forms: as the total heat flux density q_t; as the heat flux density q_s due to the effect of the spray, which is the total heat flux density q_t minus that due to radiation q_r; as a total heat transfer coefficient h_t; and as a spray heat transfer coefficient h_s. The heat transfer coefficients are usually related to the difference between the surface temperature T_0 and the water temperature T_w, $h = q/(T_0 - T_w)$, and the radiative heat flux density is taken as

$$q_r = \varepsilon\sigma\left(T_0^4 - T_w^4\right) \qquad (12.41)$$

Note that in (12.41) the Ts must be taken in kelvin. The main factor controlling the heat transfer rate apart from surface temperature T_0 is the water flux density V_w. Since the water flux density varies locally on the target, the heat flux density (and heat transfer coefficient) is also a local quantity. Figure 12.18 shows a typical example for the variation of h_s with position on the target. Unfortunately, the local variation of heat transfer rate has not been recognized by all authors; that is, measurements have been performed with rather large probe areas so that conditions were nonuniform over the area of the probe or it is unclear whether local values or averages over some area are reported.

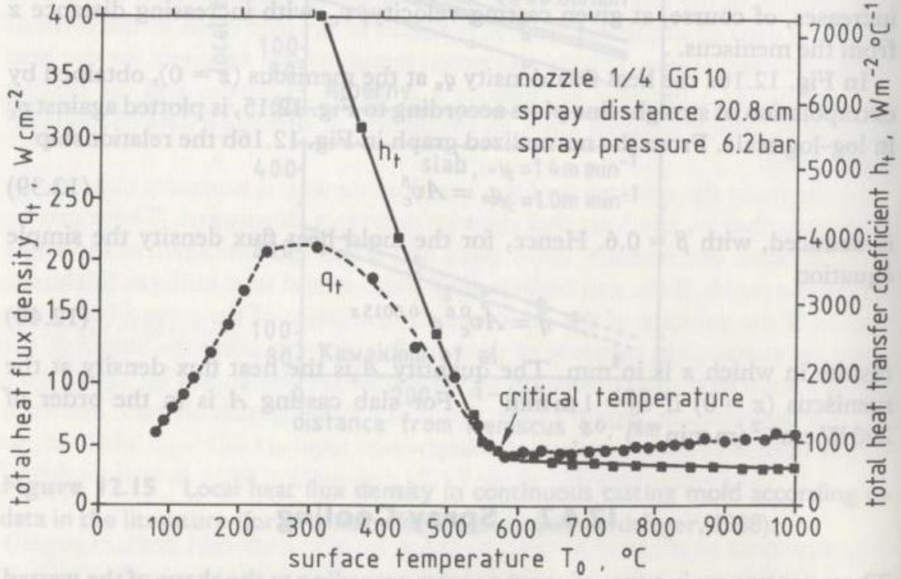

Figure 12.17 Typical heat flux versus temperature relationship in water spray cooling (Mizikar, 1970).

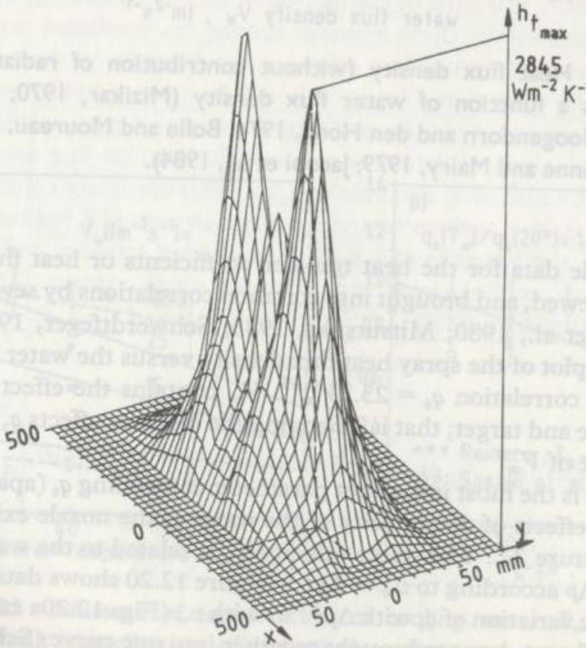

Figure 12.18 Variation of heat transfer coefficient with position on sprayed target (Reiners, 1987).

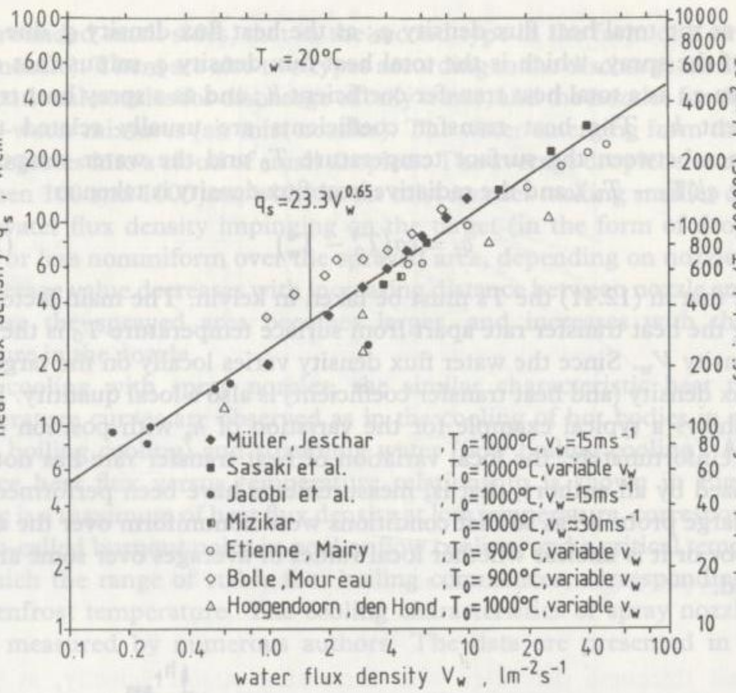

Figure 12.19 Heat flux density (without contribution of radiation) under spray nozzle as a function of water flux density (Mizikar, 1970; Müller and Jeschar, 1973; Hoogendorn and den Hond, 1974; Bolle and Moureau, 1979; Sasaki et al., 1979; Etienne and Mairy, 1979; Jacobi et al., 1984).

The available data for the heat transfer coefficients or heat flux densities have been reviewed, and brought into common correlations by several authors (Brimacombe et al., 1980; Mitsutsuka, 1983; Schwerdtfeger, 1988). Figure 12.19 shows a plot of the spray heat flux density versus the water flux density V_w yielding a correlation $q_s = 23.3V_w^{0.65}$. V_w contains the effect of distance between nozzle and target; that is, changing the distance affects q_s only via the changing value of V_w.

Though V_w is the most important parameter controlling q_s (apart from T_0), there are also effects of the velocity of the water at the nozzle exit and of the water temperature T_w. The water velocity v_w is related to the water pressure in the nozzle Δp according to $v_w \sim \Delta p^{1/2}$. Figure 12.20 shows data of different authors for the variation of q_s with $\Delta p^{1/2}$ or with v_w (Figs 12.20a and b). In Fig. 12.20c the different data are brought together into one curve (Schwerdtfeger, 1988) indicating that the influence of water velocity can be expressed as $q_s \sim v_w^{0.37}$. The available data on the effect of water temperature are presented

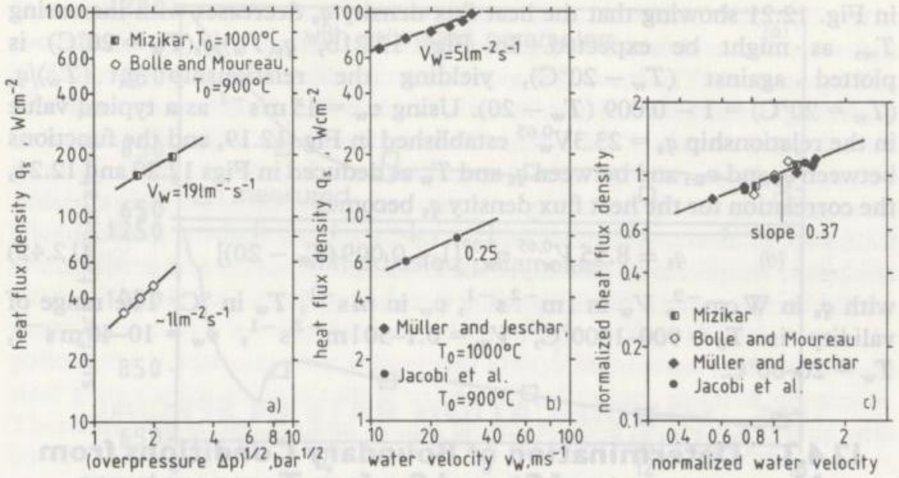

Figure 12.20 Heat flux density under spray nozzle (without contribution of radiation) as a function of pressure at nozzle or of water velocity (Mizikar, 1970; Müller and Jeschar, 1973; Bolle and Moureau, 1979; Jacobi et al., 1984).

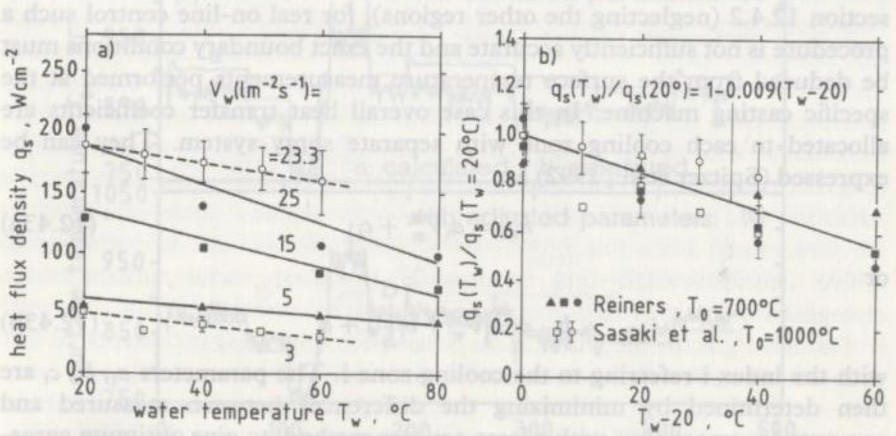

Figure 12.21 Influence of temperature of cooling water T_w, on heat flux density (without contribution of radiation) under spray nozzle. (a) Original literature data (Sasaki et al., 1979; Reiners, 1987); (b) Normalized heat flux versus difference of water temperature with respect to 20°C.

in Fig. 12.21 showing that the heat flux density q_s decreases with increasing T_w, as might be expected. In Fig. 12.21b, $q_s(T_w)/q_s(T_w = 20°C)$ is plotted against $(T_w - 20°C)$, yielding the relationship $q_s\ (T_w)/q_s\ (T_w = 20°C) = 1 - 0.009\ (T_w - 20)$. Using $v_w = 15\,\mathrm{m\,s^{-1}}$ as a typical value in the relationship $q_s = 23.3V_w^{0.65}$ established in Fig. 12.19, and the functions between q_s and v_w, and between q_s and T_w as deduced in Figs 12.20 and 12.21, the correlation for the heat flux density q_s becomes

$$q_s = 8.55\,V_w^{0.65}\,v_w^{0.37}[1 - 0.009\,(T_w - 20)] \qquad (12.42)$$

with q_s in $\mathrm{W\,cm^{-2}}$, V_w in $\mathrm{l\,m^{-2}\,s^{-1}}$, v_w in $\mathrm{m\,s^{-1}}$, T_w in °C. The range of validity is $T_0 = 900$–$1000°C$, $V_w = 0.1$–$50\,\mathrm{l\,m^{-2}\,s^{-1}}$, $v_w = 10$–$40\,\mathrm{m\,s^{-1}}$, $T_w = 20$–$80°C$.

12.4.3. Determination of Boundary Conditions from Measurements of Strand Surface Temperatures

In real continuous casting there can be regions on the strand surface close to the rolls which are not reached by the spray water; also there are the regions of backwater in front of the upper roll of a roll pair where the spray water is collected, and there is a zone of contact between strand and roll at each roll. The heat withdrawal in these regions cannot be predicted so well. For instance, the heat withdrawal in a contact zone depends on the contact area, which is generally unknown. Hence, although first computations of temperatures and shell thickness can be performed using the relationships given in section 12.4.2 (neglecting the other regions), for real on-line control such a procedure is not sufficiently accurate and the exact boundary conditions must be deduced from the surface temperature measurements performed at the specific casting machine. In this case overall heat transfer coefficients are allocated to each cooling zone with separate spray system. They can be expressed (Spitzer et al., 1992) as

$$h_{s,i} = a_i V_w^{b_i} + c_i \qquad (12.43a)$$

or

$$h_{s,i} = a_i V_w^2 + b_i V_w + c_i \qquad (12.43b)$$

with the index i referring to the cooling zone i. The parameters a_i, b_i, c_i are then determined by minimizing the differences between measured and computed temperatures with a least-squares method, to give optimum agreement with surface temperatures measured with pyrometers along the strand.

The optimization procedure can be accelerated by using the inverse heat flow model in which the temperatures are input numbers and the heat transfer coefficients output numbers.

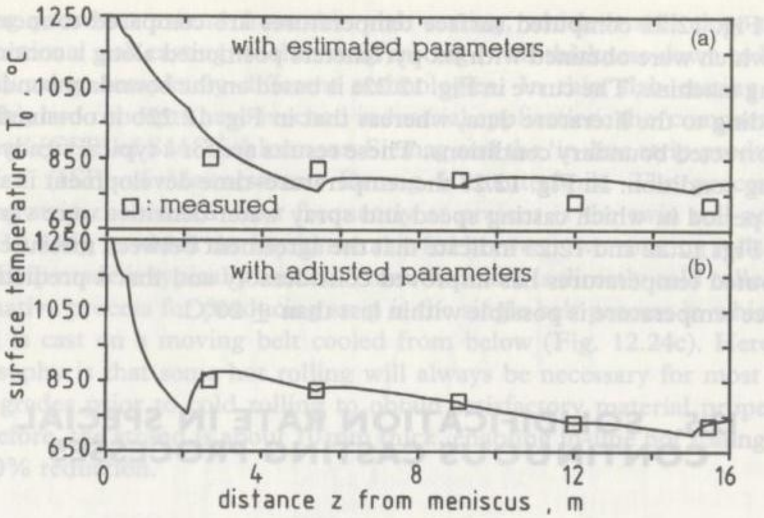

Figure 12.22 Model adjustment to measured surface temperatures along strand in secondary cooling zone (Spitzer et al., 1992).

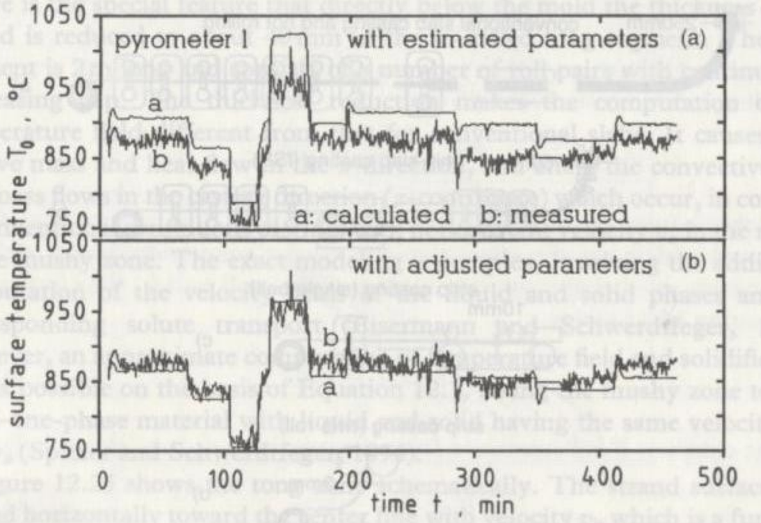

Figure 12.23 Comparision of measured and calculated surface temperatures as a function of time. Position of first thermocouple in Fig. 12.22 (Spitzer et al., 1992).

In Fig. 12.22 computed surface temperatures are compared to measured data which were obtained with six pyrometers positioned along a continuous casting machine. The curve in Fig. 12.22a is based on the boundary conditions according to the literature data, whereas that in Fig. 12.22b is obtained with the corrected boundary conditions. These results are for a typical steady-state casting condition. In Fig. 12.23 the temperature–time development is shown for a period in which casting speed and spray water densities were variable. Both Figs 12.22 and 12.23 indicate that the agreement between measured and computed temperatures has improved considerably and that a prediction of surface temperature is possible within less than ± 20°C.

12.5. SOLIDIFICATION RATE IN SPECIAL CONTINUOUS CASTING PROCESSES

There has been worldwide activity to develop processes for near net shape casting for several years. The advantages of reducing the casting thickness are obvious. The investment cost involved in the hot strip rolling mill is decreased or may even be zero (if hot rolling becomes unnecessary) and the production cost is smaller. The schemes of the new casting processes for flat products and of the conventional casting/hot rolling route are given in Fig. 12.24. The new casting processes extend from thin slab casting, which is still close to the conventional slab casting, to thin strip casting (with thickness down to below 1 mm) using completely different technologies. In thin slab casting (Fig. 12.24b), two concepts have reached industrial application: the 'compact strip process' (CSP) of SMS Schloemann Siemag and the 'in-line strip production process' (ISP) of Mannesmann Demag Hüttentechnik. The process for casting strip considered most frequently at present is the twin roll process (Fig. 12.24d), in which the liquid metal is fed between two rotating rolls. The steel strip made is typically around 3 mm thick and is directly cold rolled. An alternative process for producing strip is the single belt process in which the metal is cast on a moving belt cooled from below (Fig. 12.24c). Here, the philosophy is that some hot rolling will always be necessary for most mass steel grades prior to cold rolling to obtain satisfactory material properties. Therefore, the strand is about 10 mm thick, enabling in-line hot rolling with 50–80% reduction.

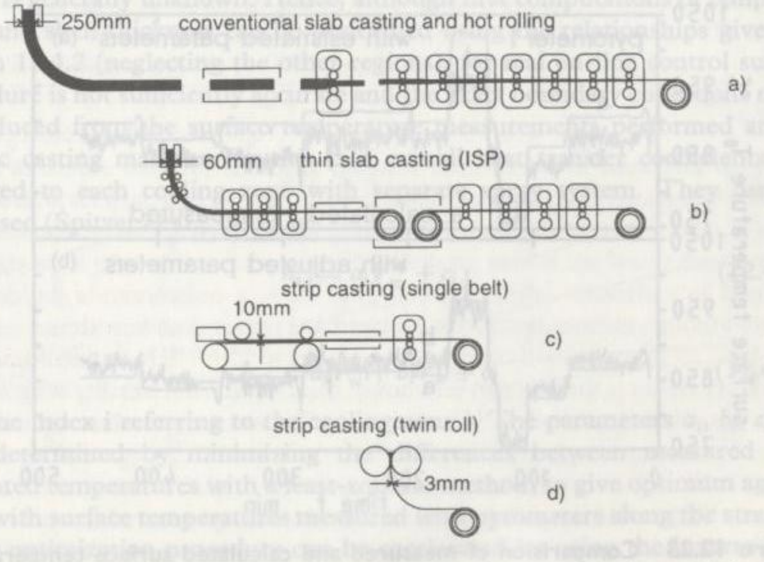
250mm
conventional slab casting and hot rolling
a)
60mm
thin slab casting (ISP)
b)
strip casting (single belt)
10mm
c)
strip casting (twin roll)
3mm
d)

Figure 12.24 Schematic description of several near net shape casting processes.

12.5.1. Solidification Rate in Thin Slab Casting with In-line Thickness Reduction

In the ISP process operated at Arvedi in Italy (Fig. 12.24b), the liquid steel is fed into a mold with parallel walls having interior thickness of 60–70 mm. There is the special feature that directly below the mold the thickness of the strand is reduced to about 40 mm in the so-called tong segment. The tong segment is 2 m long and consists of a number of roll pairs with continuously decreasing gap. The thickness reduction makes the computation of the temperature field different from that for conventional slabs. It causes convective mass and heat flow in the x-direction, and alters the convective heat and mass flows in the casting direction (z-coordinate) which occur, in contrast to conventional continuous casting, with nonconstant velocity v_z in the region of the mushy zone. The exact modeling is complex, involving the additional computation of the velocity fields of the liquid and solid phases and the corresponding solute transport (Eisermann and Schwerdtfeger, 1996). However, an approximate computation of temperature field and solidification rate is possible on the basis of Equation 12.1, taking the mushy zone to be a quasi-one-phase material with liquid and solid having the same velocities v_x and v_z (Spitzer and Schwerdtfeger, 1994).

Figure 12.25 shows the tong zone schematically. The strand surfaces are moved horizontally toward the center line with velocity v_b which is a function of the casting velocity v_c and the angle α:

$$v_b = -v_c \sin \alpha \qquad (12.44)$$

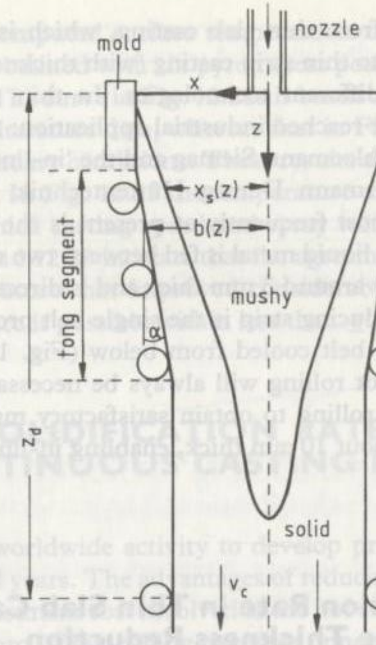

Figure 12.25 Schematic description of casting process with thickness reduction of slab below mold.

The horizontal surface velocity v_b continues into the interior of the strand according to a 'constitutive' equation

$$\frac{\partial v_x}{\partial x} = -B\phi(T, f_L) \tag{12.45}$$

in which the function $\phi(T, f_L)$ is reasonably chosen. For instance, $\phi = f_L$ has been used which has the effect that the mushy zone is deformed with the deformation rate being proportional to the fraction liquid f_L. The integration of Equation 12.45 yields

$$v_x = -B \int_0^x \phi \, dx \tag{12.46}$$

and the constant B is determined from the condition $v_x = v_b$ at $x = b$. Hence,

$$B(z) = -\frac{v_b}{\int_0^b \phi \, dx} \tag{12.47}$$

The z-component of the velocity follows from the continuity equation and is given as

$$v_z = v_c - B \int_z^{z_d} \phi \, dz \tag{12.48}$$

where z_d is some distance from the meniscus, e.g., that of the driver, below the tong segment where $v_z = v_c$.

Figure 12.26 shows some computed results (Spitzer and Schwerdtfeger, 1994). The strand thickness in the mold is 60 mm and the various curves are for different values of total reduction (steps of 2 mm). Thickness reduction has a strong effect on the thermal behavior of the strand. The temperature drop is much faster below the tong segment, and the sump becomes less deep.

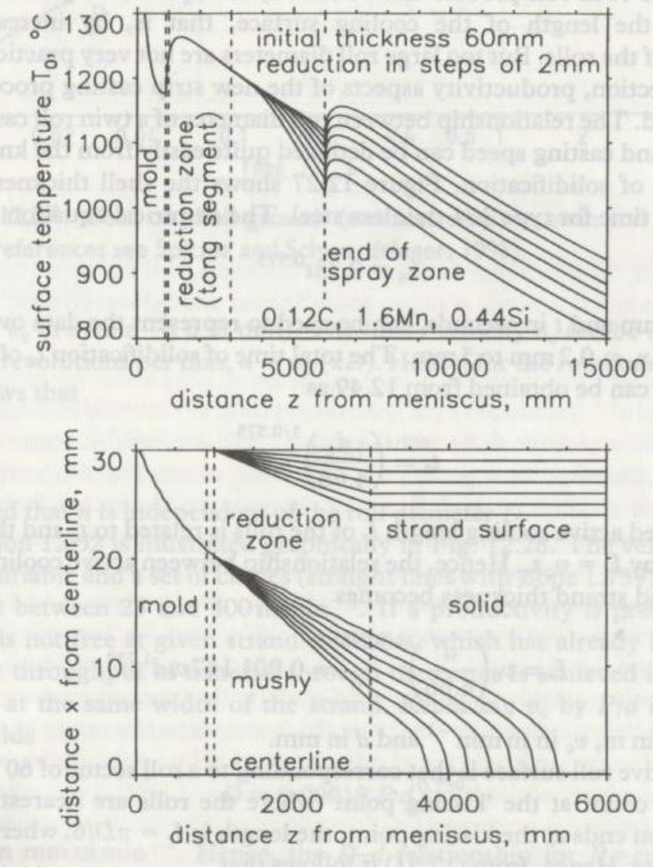

Figure 12.26 Change in surface temperature and shell thickness due to in-line thickness reduction in a slab casting process (Spitzer and Schwerdtfeger, 1994).

12.5.2. Productivity of Strip Casting Processes

The productivity of a casting process is primarily determined by the solidification time of the solidifying body, which is equal to the minimum residence time of the material in the caster. It is very important, when a new casting process is designed, to consider the possible productivity right at the beginning. It is obvious that a new casting process for mass steel grades should have, at least, the same productivity as the conventional process. This means that taking the casting rate of a 250 mm thick slab to be 1 m min^{-1}, the casting speed of a twin roll caster producing 3 mm thick strip of the same width must be 83.3 m min^{-1}. If this condition cannot be fulfilled, for instance, if only 42 m min^{-1} are possible, two casters are needed instead of one, which is not practical and will increase the cost of the process. In principle, the casting speed of the twin roll process can be raised, at required strip thickness, by increasing the length of the cooling surface, that is, by increasing the diameters of the rolls. But too large roll diameters are not very practical either.

In this section, productivity aspects of the new strip casting processes will be discussed. The relationship between roll diameter of a twin roll caster, strip thickness, and casting speed can be deduced quite easily from the known data on the rate of solidification. Figure 12.27 shows the shell thickness x_s as a function of time for type 304 stainless steel. The empirical equation

$$x_s = 2.33t^{0.575} \tag{12.49}$$

with x_s in mm and t in seconds, can be used to represent the data over a wide range from $x_s = 0.2$ mm to 5 mm. The total time of solidification t_e of a strip of thickness d can be obtained from 12.49 as

$$t_e = \left(\frac{d}{4.66}\right)^{1/0.575} \tag{12.50}$$

The required active cooling length L of the rolls is related to t_e and the casting velocity v_c by $L = v_c t_e$. Hence, the relationship between active cooling length, velocity, and strand thickness becomes

$$L = v_c\left(\frac{d}{4.66}\right)^{1/0.575} = 0.001\,147 v_c d^{1.739} \tag{12.51}$$

where L is in m, v_c in m min^{-1} and d in mm.

If the active roll surface is that corresponding to a roll sector of 60° (starting the degree count at the 'kissing point' where the rolls are nearest) and the solidification ends at the kissing point, the length is $L = \pi D/6$, where D is the roll diameter. Hence, from (12.51) it follows that

$$D = 0.00219\, v_c\, d^{1.739} \tag{12.52}$$

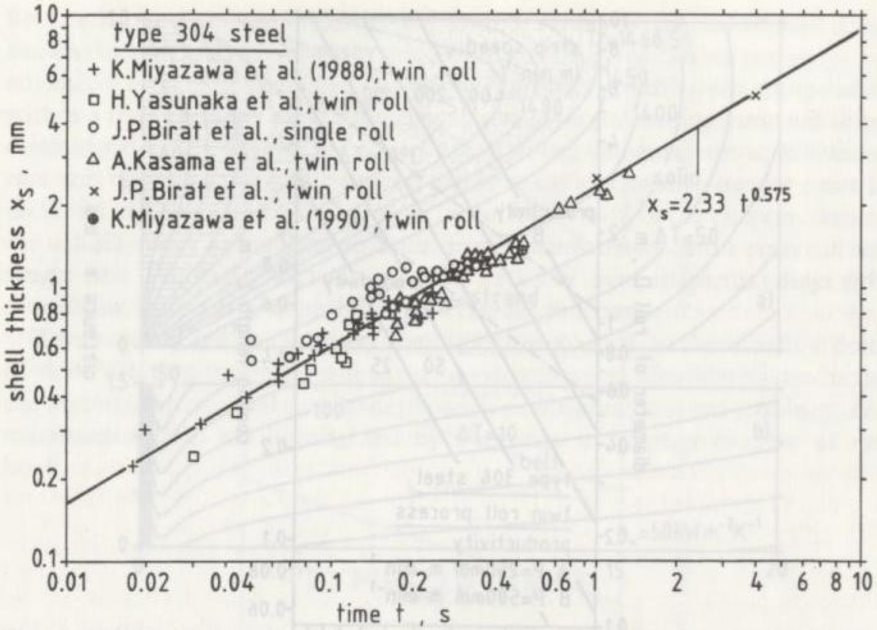

Figure 12.27 Data on shell growth (stainless steel) in twin roll process (for original references see Spitzer and Schwerdtfeger, 1995).

(D in m, v_c in m min^{-1}, d in mm). The linear velocity v_c can be expressed in terms of revolutions per min, $n = v_c/(\pi D)$. Hence, for the rotational frequency n it follows that

$$n = 145d^{-1.739} \tag{12.53}$$

It is noted that n is independent of the roll diameter D.

Equation 12.52 is illustrated graphically in Fig. 12.28. The velocity v_c is a second variable and a set of curves (straight lines with slope 1.739) is given for v_c values between 25 and 400 m min^{-1}. If a productivity is prescribed, the velocity is not free at given strand thickness, which has already been stated. Constant throughput of material through the caster is achieved if $P = dv_c$ is constant at the same width of the strand. Replacing v_c by P/d in Equation 12.51 yields

$$D = 0.00219\, P\, d^{0.739} \tag{12.54}$$

with P in mm m min^{-1}. Hence, the D–d relationship for P = const represents another series of straight lines in the log-log plot of Fig. 12.28 with slope 0.739. Two such lines are drawn for $P = 250$ (productivity A) and

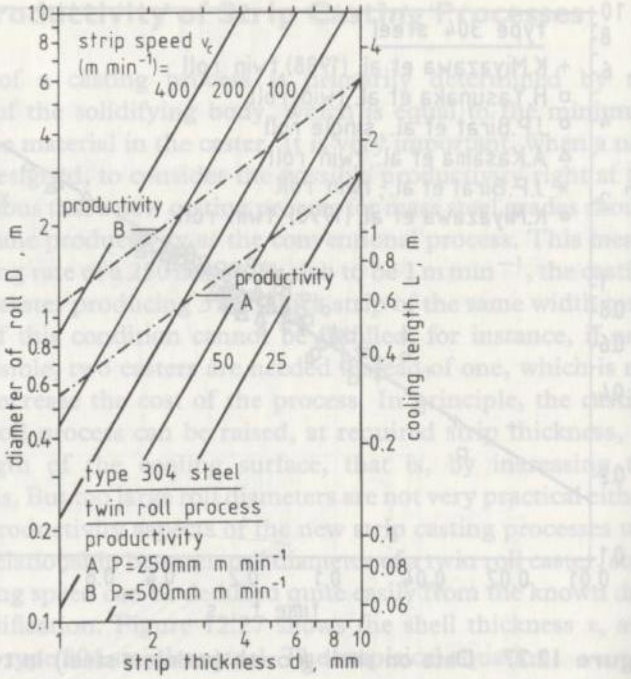

Figure 12.28 Relationship between strip thickness, roll diameter, and casting velocity in twin roll process; stainless steel (Spitzer and Schwerdtfeger, 1995).

500 mm m min^{-1} (productivity B), corresponding to conventional continuous casting of 250 mm thick slabs with 1 m min^{-1} and 2 m min^{-1}, respectively.

The roll diameter and rotational speed for casting of strip with given thickness can readily be read from the diagram or computed from (12.52) and (12.53), respectively. For instance, a strip with 3 mm thickness requires a roll diameter of 1.23 m at productivity A and 2.47 m at productivity B, a thicker strip of 8 mm a roll diameter of 2.55 m at productivity A and of 5.09 m at productivity B. The rotational speed of the rolls is 21.5 rev min^{-1} for the 3 mm strip and 3.9 rev min^{-1} for the 8 mm strip. The productivity A is typical for present-day stainless steel production with conventional continuous casting, and the roll diameter for 3 mm thick strip is in the range of diameters already used in twin roll casting of stainless steel. Mass steel grades are cast in modern steel plants with higher productivity than A. For certain steel grades, high-speed casting is performed with productivity B. Probably the strip must be thicker than 3 mm because some hot rolling is required. The rotational speed decreases with increasing strip thickness, which is favorable, but the required roll diameter will increase to several meters. It may be concluded that high-speed mass steel production seems hardly to be possible with the twin roll process.

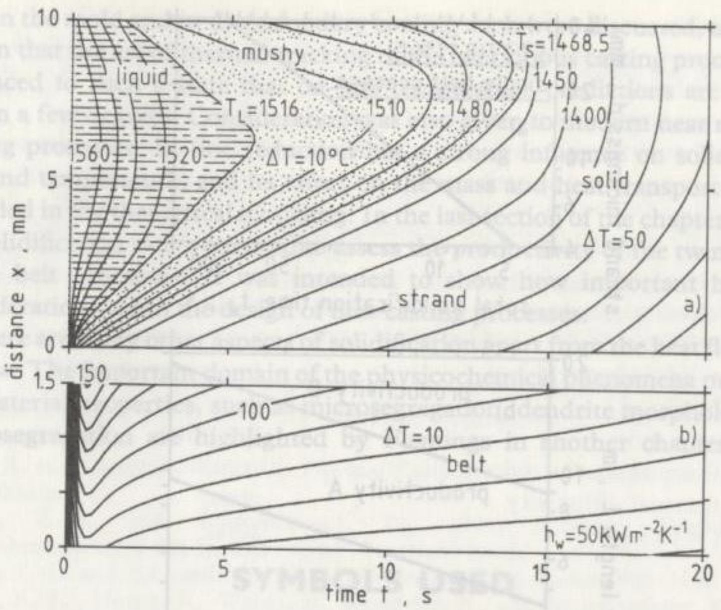

Figure 12.29 Temperature fields in the casting of steel strip of grade ST37 (0.17% C) with the single belt process (Schwerdtfeger et al., 1990). (a) Temperature field in the strand of 10 mm thickness. (b) Temperature field in the belt of 1.5 mm thickness.

In the single belt process (Fig. 12.24c), the cooling surface is horizontal and there are no restrictions, in principle, concerning cooling length. But in this process the total solidification time t_e is larger than in the twin-roll process at the same strip thickness, owing to the slower heat withdrawal at the upper strand surface, and consequently the required cooling length is larger. Figure 12.29 shows the computed temperature field in the strip and in the belt (Schwerdtfeger et al., 1990). The abscissa is time t. The distance z from the feeding nozzle is related to t by $z = v_c t$. The thickness of the strand is 10 mm and the steel grade is ST37 (0.17%C). Owing to the different cooling at the bottom and top surface the temperature field is nonsymmetrical with respect to the center line of the strand. The solidification ends (for these conditions) at $t_e = 14.3$ s. Figure 12.30 represents the results of productivity computations corresponding to those in Fig. 12.28 for the twin roll process. The relationship used between strand thickness and total solidification time (for steel ST37) is shown in Fig. 12.30a. The metallurgical length L (= cooling length on belt to end of solidification) of the machine given by $L = v_c t_e = P t_e / d$ is presented in

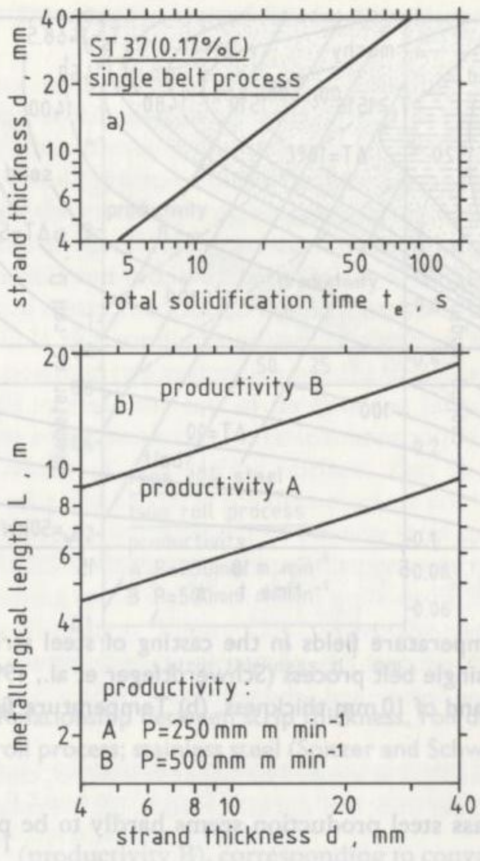

Figure 12.30 Solidification of steel grade ST37 (0.17% C) in the single belt process. (a) Relationship between strand thickness and solidification time. (b) Metallurgical length as a function of strand thickness for two selected productivities (Schwerdtfeger et al., 1990).

Fig. 12.30b as a function of strand thickness *d* for the two productivities A and B.

12.6. CONCLUDING REMARKS

The solidification rate of metallic materials has been treated. Fundamentals were given in the first two sections, and the rest of the chapter focused on the continuous casting of steel. The various factors determining the withdrawal of heat in the mold and in the secondary cooling zone were discussed, and it was shown that the art of thermal tracking of the continuous casting processes has advanced to such a state that on-line temperature predictions are possible within a few degrees. Consideration was also given to modern near net shape casting processes. In-line reduction has a strong influence on solidification rate and temperature, and its effect on the mass and heat transport must be included in the theoretical modeling. In the last section of the chapter, data on the solidification rate were used to assess the productivity of the twin roll and single belt processes. It was intended to show how important heat flow considerations are in the design of new casting processes.

There are many other aspects of solidification apart from the heat flow point of view. The important domain of the physicochemical phenomena producing the material properties, such as microsegregation, dendrite morphology, and macrosegregation are highlighted by Flemings in another chapter of this book.

SYMBOLS USED

D	roll diameter of twin roll caster
L	cooling length, metallurgical length
H	enthalpy
H_L, H_S	enthalpy of liquid and solid phases
ΔH_f	heat of fusion
T	temperature
T_f	melting point of pure metal
T_L, T_S	liquidus and solidus temperatures
Bi	Biot number
Ph	phase conversion number
S	dimensionless shell thickness
U	dimensionless temperature
b	half-thickness of slab
c_0	total mass content of alloying element
c_L, c_S	mass contents of alloying element in liquid and solid phases
c_p	heat capacity
d	strip (strand) thickness
d_{cf}	thickness of casting flux layer
d_{gap}	thickness of gas gap
d_m	thickness of mold wall
f_L, f_S	liquid and solid fractions ($f_L + f_S = 1$)
h	heat transfer coefficient
k	partition coefficient ($= c_S/c_L$)
p	dimensionless time
p_e	dimensionless total solidification time
q	heat flux density (always taken to be positive)
x	coordinate in thickness direction of plate (slab), distance from surface or distance from center plane
z	coordinate in longitudinal direction of strand, distance from meniscus

x_S	thickness of solid shell, coordinate of solidus contour
x_L	coordinate of liquidus contour
s	dimensionless x-coordinate
t	time
t_e	total solidification time of plate (strand, strip)
v_x, v_z	velocity components
v_c	casting velocity, velocity of solidified strand in z-direction
ε	emissivity
λ	thermal conductivity
κ	thermal diffusivity ($= \lambda / (c_p \rho)$)
ρ	density
σ	Stefan–Boltzmann constant ($= 5.669 \times 10^{-12}$ W cm^{-2} K^{-4})
η	rate constant in Neumann's solution

Subscripts on T, U, q, h

o	surface of slab (strand)
m	mold
w	reference temperature, e.g., water temperature
a	meniscus ($z = 0$)
r	radiation
c	conduction
s	spray
t	total

REFERENCES

Bolle, L. and Moureau, J.C. (1979) *Int. Conf. Heat Mass Transfer Metallurgical Processes*, Dubrovnik, pp. 527–534.

Brimacombe, J.K., Agarwal, P.K., Baptista, L.A., Hibbins, S., and Prabhakar, B. (1980) *Steelmaking Proc.* **63**, 235–252.

Carslaw, H.S. and Jaeger, J.C. (1959) *Conduction of Heat in Solids, 2nd edn.* Oxford University Press.

Chuang, Y.-K. and Schwerdtfeger, K. (1973a) *Arch. Eisenh.* **44**, 341–347.

Chuang, Y.-K. and Schwerdtfeger, K. (1973b) *Z. Metallkunde* **64**, 672–677.

Eisermann, H. and Schwerdtfeger, K. (1996) Mathematisches Modell zur Bildung von Makroseigerungen beim Dünnbrammengießen mit In-Line-Dickenreduzierung. Dr.-Ing. Dissertation of H. Eisermann, Technische Universität Clausthal, Germany.

Etienne, A. and Mairy, B. (1979) *C.R.M.* **55**, 3–13.

Holzhauser, J.-F., Spitzer, K.-H., and Schwerdtfeger, K. (1990) The influence of casting aids on the heat transfer in the mold, the surface quality and incidence of breakouts in the continuous casting of steel. ECSC Contract 7210 CA/139. Final Report EUR 12198 DE.

Hoogendorn, C.J. and den Hond, R. (1974) *5th Int. Heat Transfer Conf. IV*, Tokyo. Paper B 3.12, pp. 135–138.

Jacobi, H., Kaestle, G., and Wünnenberg, K. (1984) *Ironmaking and Steelmaking* **11**(3), 132–145.

Jenkins, M.S. (1995) *Steelmaking Conf. Proc 78*, Nashville, TN. Iron and Steel Society, pp. 315–320.

Mitsutsuka, M. (1983) *Tetsu-to-Hagane* **69**(2), 268–274.

Mizikar, E. (1970) *Iron and Steel Engineer* **47**(June), 53–60.

Müller, H. and Jeschar, R. (1973) *Archiv Eisenh.* **44**, 589–594.

Ohmiya, S., Tacke, K.-H., and Schwerdtfeger, K. (1983) *Ironmaking and Steelmaking* **10**, 24–30.

Reiners, U. (1987) Wärmeübertragung durch Spritzwasserkühlung heißer Oberflächen im Bereich der stabilen Filmverdampfung. Dr.-Ing. Dissertation, Technische Universität Clausthal.

Sasaki, K., Sugitani, Y., and Kawasaki, M. (1979) *Tetsu-to-Hagane* **65**(1), 90–96.

Schwerdtfeger, K. (1988) In *Erstarrung metallischer Schmelzen* (ed. P.R. Sahm). DGM Informationsgesellschaft, pp. 205–224.

Schwerdtfeger, K., Spitzer, K.H., Reichelt, W., and Voss-Spilker, P. (1990) *Int. Conf. New Smelting Reduction and Near Net Shape Casting Technologies for Steel, Near Net Shape Casting*, Preprints 2. The Korean Institute Metals & The Institute of Metals UK, pp. 514–524.

Sha, H. and Schwerdtfeger, K. (1996) Computation of the solidification of pure metals in plate geometry using the green's function method. *Int. J. Heat Mass Transfer* (submitted).

Siegel, R. and Howell, J.R. (1972) *Thermal Radiation Heat Transfer*. McGraw-Hill Kogakusha.

Spitzer, K.-H. and Schwerdtfeger, K. (1994) Thermal Tracking für Dünnbrammenguß mit 'in-line rolling', Internal report.

Spitzer, K.-H. and Schwerdtfeger, K. (1995) *Iron and Steelmaker* 1995 (Nov.), 47–35.

Spitzer, K.-H., Harste, K., Weber, B., Monheim, P., and Schwerdtfeger, K. (1992) *ISIJ Int.* **32**(7), 848–856.

Index

Note – Page numbers in *italic* refer to illustrations and tables; **bold** page numbers indicate a main discussion.

- ABAQUS 266
- Absolute Rate Theory 223
- Absorption of SO_2 process gas 304–6
- Acidic oxides 47, 48
- Activity coefficient 204
- Activity quotient 8
- Adsorption coefficient 186, 196, 200, 203, 206, 208, 209
- Adsorption isotherm 187, 209
- Alkali behavior in blast furnace process 341, *342*
- Alkali equilibria between gas and slag 341–3
- Alkali transfer 341–3
- Alloys, solidification rate 387–92, *388*
- α-function 12–13, *13*, *14*
- Amphoteric oxides 48
- Antimony in slags 78, *79*, *80*
- Approximate tip velocity *154*
- Arrhenius activation energy 186
- Arrhenius relation 284
- Arsenic in slags 78
- Association models, short-range ordering 104–5
- Auger electron studies 191
- Austenitic stainless steels 162

- Balance equations 265, 266
- BaO–BaF_2 57, 70, *70*
- BaO–MnO 57
- Basic oxides 47, 48
- Basicity indexes *49*
- Batch backmix tank 286
- Batch processes 288
- Batch reactors 281, 286–9
  - completely mixed *282*
- Bath smelting process 348, *349*
- Binary phase diagrams
  - with different crystal structures 25–9, *26*
  - with same crystal structure 17–25
  - continuous solutions for both liquid and solid phases *21*
  - effect of solution behavior on characteristic features of phase equilibria 27, *28*
  - relative stabilities of the phases **17–34**
  - retrograde solubility *24*
  - with compound formation 29–34
  - with congruent-melting phase at equal atomic composition *31*
- Binary regular solution *17*
- Binary systems, phase equilibria **14–34**
- Bismuth, in slags 78
- Blast furnace hearth
  - silicon equilibrium in 337–8, *338*
  - slag–metal reaction in 336
- Blast furnace model 317–19
- Blast furnace process 309–22
  - aerodynamic aspects 320–1
  - alkali behavior in 341, *342*
  - chemical transfer in hearth 344–5
  - combustion reactions in 323–6
  - combustion zone 323
  - control of partition of elements between metal and slag *344*
  - estimation of gas flow, reduction process and temperature *323*
  - flow conditions 320–1
  - formation of liquid slag and metal 329–32, *332*
  - functions 309–10
  - fundamental basis 317
  - heat balance 319, *320*
  - mass balance 319, *320*
  - one-dimensional model 314–21
  - operating line *317*
  - oxygen potential in hearth 332–3, *334*
  - preparation zone 317–19
  - principles *318*
  - processing zone 317–19
  - silicon transfer in 335–7, *335*
  - structure of inner state, from quenching and dissection *322*
  - temperature profile 314–16
  - two-dimensional model 321–2

Blast furnace slag
  potassium capacity of 343, *343*
  see also Slag(s)
Body forces 126, 134–5
Boudouard reaction 312–13, *312*, 314
Boundary conditions 265
  strand surface temperatures 406–8, *407*
Bragg–Williams model 34
BRIGHT model 322, *323*
Bulk convecting flows, differential models of turbulence for 131–3
Bulk turbulent viscosity 131
Burning of particles in fluidized bed 296–7

CaF_2-FeO *75*
Calcium in slags 81, *81*, *82*
Calcium iron silicate 197, *197*
$CaO-Al_2O_3$ *52*
$CaO-Al_2O_3$ *70*
$CaO-Al_2O_3-SiO_2$ *73*, 237, 240, 330
$CaO-CaF_2$ *62*, *70*
$CaO-CaF_2-SiO_2$ *60*, *63*, *77*
$CaO-FeO-Fe_2O_3$ *74*
$CaO-FeO-SiO_2$ 53, 65, *67*
CaO–MgO 93
$CaO-MgO-Al_2O_3-SiO_2$ 328–9, *329*
$CaO-MnO-SiO_2$ *71*
$CaO-MgO-SiO_2-CrO_x$ *73*
$CaO-SiO_2$ 65, *67*, *108*
$CaO-SiO_2-Al_2O_3-MgO-MnO-FeO-TiO_2$ 328, *331*
Carbide capacities *68*
Carbon in slags 68–70
Carbon solubility in liquid iron 326–7, *327*
Carbon steel, macrosegregation in *176*
Carbonate capacity *70*
  in slags and glasses 110–12
Casting processes, solidification rate in **381–419**
Cation–oxygen bond *48*
Cell model 110
Ceramic solutions 97–8
Characteristic turbulent velocity component 132
Chaudron equilibria *313*
Chemical equilibrium 200
Chromium in slags 71–2
Cluster variation method, short-range ordering 106–7
CO reactions with liquid iron 211–15, *212*, *214*, *215*
CO_2
  dissociation control *361*
  reactions with liquid iron 211–15, *212*, *214*, *215*
  solubilities *69*
Coadsorption in ternary alloys 192–4
Coal combustion 324–6, *324*, *325*
C–O–H system 312–13
Columnar growth 154
Columnar solidification *155*
Combustion reactions in blast furnace process 323–6
Compact strip process (CSP) 409
Compound energy model 98
Computational fluid dynamics (CFD) 136–40
Computational fluid mechanics 136
Computational models 135–40
CON1D 266
Conduction current density 135
Contact areas 289
Continuity equation 124–6
Continuous backmix tank *285*, 290–1
Continuous casting
  carbon steel, interdendritic fluid flow in *175*
  clad steel slabs 134
  interdendritic fluid flow in *174*, *175*
  macrosegregation in steel *177*
  on-line 1D heat conduction model 268
  solidification rate in special processes 408–16
  solidification rate in steel 392–408, *393*
  steel slabs 266
Continuous casting molds
  heat transfer in 399–401, *400*
  heat withdrawal 394–401
Continuous casting process 258
Continuous reactors 286–9, *287*
  completely mixed *282*
Continuous steady-state reactors 281
Control volume specification *139*
Coordination cluster models, short-range ordering 105–6
Copper
  as oxide in slags 75
  as sulfide in slags 82
Counter-current reactors 282
Counterflow gas cleaning processes 300, *301*
Counterflow mass transfer 300–6
Coupled interfacial reactions 240–4, *243*
Cyanide capacities *65*

Debye–Huckel theory 49

Decarburization 366–9
  electric arc furnace 369
  FeO formation in 369
  liquid iron 198–206, *201*, *202*, *203*
    by water vapor 204–6, *205*
  oxygen steelmaking process 367
  rate equations 367–8, *368*
  reaction mechanism 366–9
Dendrites
  arm spacing 178–86
  longitudinal and transverse cross sections *159*
  manganese distribution in 160, *160*
  tip velocity 154
Desulfurization ratio *58*
Differential models of turbulence for bulk convecting flows 131–3
Diffusion coefficients 159
Diffusion during solidification 157
Diffusion model 293
Direct reduced iron (DRI) 364
Dispersion coefficient 293
Dissolved FeO–char reaction 362–3, *362*
Dissolved impurities, removal of 283–4
Drying particles in fluidized bed 295

Electric arc furnace (EAF) 347, 364
  decarburization 369
Electric potential 146–8, *147*
Electrical neutrality 225–6
Electromagnetic casting of aluminum 134
Electromagnetic force field 135
Electromagnetic stirring
  and braking 134
  liquid steel 133
Electromagnetically driven flows 133–5
Elliptic flows 136
Equiaxed solidification *155*
Equilibrium constant 186
Ergun relationship 321
Euler (or Newton) number 129, 136
Eulerian equation 135
Eutectic phase diagram 37, *39*, *40*
Excess thermodynamic quantities 11–12
Expert systems 257
Eyring relation 284

F*A*C*T system 114, *115*, 116, 266
Fe–C droplets, oxidation of 228–9, *229*
Fe–Cr–C 193, *194*
Fe–Cr–Ni 161, *163*
Fe–Cr–Ni stainless steels 160
Fe–FeO reaction 356
Fe–FeO–FeS *170*
Fe–Mn *158*
Fe–Mn–Si 240
Fe–Ni 89, 90, 162–6, *164*, *165*
Fe–Ni–Cu–S 102, *104*, 105
Fe–O 208
Fe–O–C–H 313–14
Fe–O–S 193
Fe–S 101, *103*
Fe–Si droplets, oxidation of 229–30, *230*
Fe–V–C 97
Fe–V–Cr–C phase diagram 114, *114*
FeO
  dissolved carbon reaction 358–62, *359*
  formation in decarburization 369
$FeO-MgO-SiO_2$ 109, *109*
$Fe_3O_4-Co_3O_4$ spinel solutions 98
$FeO-P_2O_5$ 195–6, *196*
$FeTiO_3-Ti_2O_3$ 97, 98
FIDAP 266
Finite element modeling (FEM) 137–9
Flow distribution analysis *147*
Flow predictions 133
FLUENT 266
Fluid dynamics **123–50**
  analyses 125
  recent advances 140–8
  theory 124
Fluid flow through solidifying volume element 173, *173*
Fluid mechanics 124
Fluidized bed
  burning of particles in 296–7
  drying of particles 295–6
Flux layers, heat flow through 394–6, *394*, *396*
Forward reaction rate 186
Free energy versus temperature 152, *152*
Froude modeling 142
Froude number 129, 136, 261
Frumkin equation 188, 191

Ga–Sb 32–3, *33*
Gangue content of iron ore agglomerates 246
Gas bubbling/jetting systems 141
Gas interfacial reaction rates with metallurgical melts 198–215
Gas interfacial reactions with liquid alloys and slags **183–218**
Gas–liquid interface 285

Gas–liquid reaction 242–4, *244*
Gas–metal reaction 227–30, 363
Gas–solid reactions 220, 222
Gases in slags **60–70**
Gasification reaction 326, *326*
Gauss–Siedel routine 137
Gibbs adsorption isotherm 187
Gibbs energy 6–19, *10*, *20*, *21*, *26*, 27, 29, 31–3, *31*, *33*, 36, 37, *37*, *39*, 41
Gibbs–Duhem equation 6–7, 90, 187
Glasses 107–12
  'capacities' 110–12
GNUPLOT 267
Gradients 221–2
Grain size 178–86
Group IV elements in slags 78–82
Group V elements in slags 78–82

Heat balance 297, 298, *299*, 303
Heat capacities 297–8, 300
Heat flow
  equation 387, 393
  through flux layers 394–6, *394*, *396*
  through gas gap 396–9, *398*
Heat flux density at meniscus 401, *401*
Heat transfer 297–9
  in continuous casting molds 399–401, *400*
Heat transfer coefficient 303
Heat withdrawal in continuous casting molds 394–401
Hematite–magnetite interfacial reaction 234–7, *235*, *236*
Henrian activity coefficient of nitrogen 209
Henry's constant 304
Henry's law 10, 106, 189, 196, 282
Heterogeneous reactions **219–40**
  fundamentals 219–27
  moving interface 223–4
  multiplicity of interfacial reactions 226–7
  quasi–steady state 223–4
  rate equation 224–5
  temperature and concentrations in reaction zone 222–3
Homogeneous reactions
  reaction zone 220–1
  three-dimensional reaction zone 221
Hot metal, physical properties 327
Hydroxyl capacity *66*, *67*

Ideal adsorption 188–91
Ideal Langmuir adsorption 207
Ideal Langmuir isotherm 188, 191, 200
Ideal Raoultian solutions 87–8
Inclusions
  formation 169–71, *171*, *172*
  removal of 283
Induced current 146–8, *147*
Industry experiments 260
Inertial forces 129
In-line strip production process (ISP) 409
In-line thickness reduction 409–11, *410*, *411*
Integral thermodynamic quantities 6–7
Integral volume finite difference technique 137
Interaction coefficients 327
  interaction parameter formalism 90–1
Interdendritic concentrations 161
Interdendritic fluid flow in continuous casting *174*, *175*
Interface attachment kinetics 153
Interfacial reactions
  coupled 240–4, *243*
  stoichiometric equation representing 227
Interstitial solutions 97
Ionic solutions 94–6
Ion–oxygen attraction *48*
Iron in slags 72–4
Iron base alloys
  microsegregation 159–62
  solidification 159–62
Iron–carbon alloys, solidification 389–92, *390*, *391*, *392*
Iron–carbon phase diagram 35–6, *36*
Iron melt dephosphorization *56*
Iron ore
  agglomerates, gangue content of 246
  reduction kinetics 230–7, *232*
  solid-state reduction of 230–4, *232*
Iron oxide slags 211–15, *212*, *214*, *215*
Iron oxides *58*, *195*, 197
  reduction diagram *313*
  reduction equilibria *311*
  reduction in liquid state 242–5
Iron–oxygen 190, 310–12
Iron–oxygen phase diagram *311*
Iron smelting process 347–8, **348–64**
  critical process phenomena 350
  energy balance 350–2
  materials balances 350–2
  reduction in 348, 358–64
Iron–sulfur alloys 192

Ironmaking reactions **309–45**
  systems of importance 310–14
  see also Blast furnace process
Isotope exchange
  experiments 200
  measurements 207
  studies 207

k–ε model of turbulence 132, 133
Kohler model *92*, 93
K_2O–SiO_2 *66*

Laboratory experiments 261
Langmuir adsorption 190
Langmuir adsorption isotherm 185
Langmuir isotherm 193
Langmuir isotherm constant 196
Lead in slags 78
Level DC magnetic field (LMF) 146, 148, *148*
Linear reactor 282
LiO_2–SiO_2 *66*
Liquid alloys
  gas interfaces and interfacial reactions with 183–218
  surface constitution of 187–94
Liquid iron
  activity of elements in 327, *327*
  carbon solubility in 326–7, *327*
  nitrogen reactions with 206–10
  oxidation of 227–8
Liquid slags, surface constitution 195–8
Liquid–solid interfaces 151–5
  atomic 153, *153*
  atomically flat interface 153, *153*
  diffuse interface 153, *153*
Literature models 276–8, *277*
Lorentz force 134, 146–8, *147*
Lucassen–Reynders convention 187

Macrosegregation 171–8
  elimination through control of liquid and solid movement 178
  in carbon steel *176*
  in continuous cast steel *177*
Magnetic flux density 135
Magnetohydrodynamic (MHD) modeling 134, 146
Manganese
  distribution in dendrites 160, *160*
  in slags 70–1
  oxidation 370
  transfer 338–9
Manganese–oxygen equilibrium in hot metal *339*
Mass balance 287, 304
Mass transfer 284, 300, 347, 361
Mass transfer coefficient 285, 304
Mathematical models 141–8
Maxwell's equations 134
MBR ore, degree of reduction 244–5, *245*, *246*
Melt–bubble contact area 289
Meniscus, heat flux density at 401, *401*
Metal formation 326–45
Metal phase properties 326–7
Metal–slag–gas, transfer of elements between 329–45
Metallic solutions, thermodynamics **5–44**
Metallurgical reactors **281–307**
  idealized types 281
Metastable phase equilibria **35–41**
METSIM 266
Mg–Bi 88, *88*, 90, 104
$MgCl_2$–MgF_2–$CaCl_2$–CaF_2 96
Microscopic reversibility 186
Microsegregation *158*
  calculations 156, *157*
  iron base alloys 159–62
Miscibility gap 15, *15*
MIX1D 266
Mixing 284–6
MnO–SiO_2 110, 111, *112*
Molar capacities 300–1, 302
Momentum equation 124–6, 128
Momentum transport processes *125*
MTDATA system 114
Muggianu model *92*, 93
Multicomponent phase diagrams, calculation/estimation 92–3

$NaCl$–$MgCl_2$–NaF–MgF_2 solutions 96
$NaCl$–NaF 96
NaF–KF–$NaCl$–KCl solutions *95*, 96
Na_2O-bearing systems *69*
Na_2O–SiO_2 *66*, 75, *76*
Navier–Stokes equation 128–30, 132, 135, 136, 139–40
Near net shape casting processes 408–9, *408*
Neutral oxides 48
Newtonian coefficient of viscosity 128
Newtonian liquids 128–9
Newton's law of molecular viscosity 130

Newton's law of viscosity 128
Newton's second law of motion 124
Niobium in slags 75–8
Nitride capacities *64*
Nitrogen in slags 60–4, *63*, *64*
Nitrogen reactions
  in steelmaking 373–4
  with liquid iron 206–10
    effect of sulfur and oxygen 207–9, *208*
    effects of other alloying elements 209–10, *210*
Nitrogen removal, rate equations for 374
Non–ideal adsorption 191–2
Nonstoichiometric compounds 99–100

One-component materials, solidification rate of 382–7, *383*, *385*, *386*
One-equation model 132
On-line process control 257
Optical basicity 50
Oscillating droplet studies 189
Overall rate of reduction 363, *363*
Oxidation
  of Fe–C droplets 228–9, *229*
  of Fe–Si droplets 229–30, *230*
  of liquid iron 227–8
Oxides 47, 48, 50
Oxygen–carbon relationship in steelmaking 372
Oxygen steelmaking process (OSM) 347–8, 364, *364*
  decarburization in 367
  summary of reactions *373–7*
Oxygen transfer reactions 198–206, *201*, *202*, *203*

PA solidification mode *164*
Parabolic flows 136
Partial thermodynamic quantities 6–7
Particle conversion, effect of mixing 294–7
Particle size, effect on pressure drop in packed bed 321, *321*
Particles
  burning in fluidized bed 296–7
  drying in fluidized bed 295–6
Phase diagrams
  binary. *See* Binary phase diagrams
  calculation/optimization 91–3
  ternary calculation/estimation 92–3
Phase equilibria, binary systems **14–34**
Phase rule 152
Phosphate *51*
Phosphate capacities *53*, *61*
Phosphide *51*
Phosphorus
  behavior in iron smelting 354–6
  distribution ratios 53
  equilibrium as function of slag chemistry *371*
  in slags 51–8, *54*, *55*
  oxidation 372
Physical models 135–41
  experiments 260–1
Pierce–Smith Copper Convertors 140
Pilot plant experiments 260
Piston flow reactor 282, *282*, 297
Polynomial expansions 90
Polynomial models 89–91
Post-combustion 352–3
Post-combustion rates (PCR) 350–1, *351*
Potassium capacity of blast furnace slag 343, *343*
Prandtl's theory of turbulence 130
Preheating of charge by hot process gas 303
Problem definition 262
Process control, on-line 257
Process development tools 259–60
Process modeling **253–79**
  approach and model complexity 263–4
  comparison with experiments 267–9
  definition 253–4
  design of experiments 255
  development process 261–6
  empirical models 257
  evaluation of experimental results 255–6
  flow chart *271*
  formulation 264–6
  fully on-line models 271–3
  identification of key phenomena 262–3
  implementation 269–78
    definition 269–70
    methods 270
  increasing process understanding 255
  literature models 276–8, *277*
  mathematical 264–6
  mechanistic (or phenomenological) models 258
  off-line models 274–6
  property measurement 256–7
  reasons for 254–7
  scale-up and design 255
  semi-on-line models 273–4
  simplification/complexity compromise 253, *254*
  solution of model equations 266–7
  steps involved *262*
  types of models 257–9
  validation 267
Process optimization 257

Quasichemical model
  short-range ordering 100–4, *102*
  slags and glasses 107–10

Raoultian activity coefficients 301
Raoult's law 8–9
Raschig rings 302
Rate equations for nitrogen removal 374
Reaction rate 284
  expression 185
  theory 184–6
Real solutions 12–13
Recalescence curve 168, *169*
Recirculatory flow of liquid metal 137
Redlich–Kister equation 13, 34
Reduction of iron oxides in liquid state 242–5
Reduction process in iron smelting 358–64
Refining reactors 283–4
Regular solutions 89–90
  model 10–11, 14–17
Reichardt diagram *299*, 314–16, *315*
Residence time distribution function 290–4, *293*, 294–7
Retrograde solubility 23–5
Reynolds number 129, 133, 136, 261, 294
Rist diagram 316–17, *317*
ROMELT 351

Scheil equation 155–8, 173, 174
Scheil type analysis 169
Short–range ordering
  cluster variation method 106–7
  coordination cluster models 105–6
  quasichemical model 100–4, *102*
  two-sublattice model for liquids 106
Silicates *46–8*, 49, *63*, *69*
Silicon equilibrium in blast furnace hearth , 337–8, *338*
Silicon oxidation 370
Silicon transfer in blast furnace process 335–7, *335*
Sintering temperature vs. surface reactivity *235*
SiO_2–Al_2O_3–CaO slags 237
SiO_2–CaO–Na_2O–(Al_2O_3–MgO) glasses *113*
SiO
  consumption by oxidation 336
  consumption by reduction 336–7
  formation 335–6
Slab caster, grid setup *146*
Slag foaming 357, *358*
Slag–metal interface 220
Slag–metal reactions 225–6, 237–42
  in blast furnace hearth 337
  in steelmaking process 369–72, *371*, *373*
  theoretical development 238–40, *240*
Slag–metal systems 141
Slags 107–12
  antimony in 78, *79*, *80*
  arsenic in 78
  basicity 49
  bismuth in 78
  calcium in 81, *81*, *82*
  'capacities' 110–12
  carbon in 68–70
  chromium in 71–2
  copper as oxide in 75
  copper as sulfide in 82
  formation 326
  gas interfaces and interfacial reactions with 183–218
  gases in **60–70**
  group V elements in 78–82
  group VI elements in 78–82
  iron in 72–4
  lead in 78
  manganese in 70–1
  niobium in 75–8
  nitrogen in 60–4, *63*, *64*
  phosphorus in 51–8, *54*, *55*
  properties 328
  sulfur in 57–60
  thermodynamics **45–86**
  tin in 78, *80*
  titanium in 78, *79*
  tramp elements in **78–82**
  transition metals in **70–8**
  typical composition *46*
  vanadium in 75–8
  water vapor in 64–5
Solid–liquid interface 382, 383
Solid–solid interface 222
Solid-state reduction of iron ore 230–4, *232*

Solidification **151–82**
  against cold chill wall *155*
  diffusion during 157
  into undercooled melts 162–8
  iron base alloys 159–62
  shrinkage 174
  spun cast wire 165–6, *167*
  steel 154, 165, 168
  steel strip 165, *166*
Solidification model, Scheil equation *156*
Solidification path *157*
Solidification rate
  alloys 387–92, *388*
  casting processes **381–419**
  continuous casting of steel 392–408, *393*
  one-component materials 382–7, *383*, *385*, *386*
  special continuous casting processes 408–16
  thin slab casting 409–11, *410*, *411*
Solidifying front 154
Solute concentration distribution analysis *147*
Solute distribution *159*
Solution databases 113–16
Solution models **87–117**
  applications 113–16
Solution thermodynamics, thermodynamic relationships governing 5–44
Spray cooling 401–6, *402–5*
Spun cast wire, solidification of 165–6, *167*
Stable diagonal 96
Stable pair 94
Standard Gibbs energy of reaction 337
Steady-state mass balance 316–17, *317*
Steady-state solidification 173, 174
Steel solidification processes 154, 165, 168
Steel strip solidification 165, *166*
Steelmaking process **364–77**
  slag–metal reactions in 369–72, *371*, *373*
  see also Electric arc furnace; Oxygen steelmaking process (OSM)
Stoichiometric coefficients 227
Stoichiometric equation representing interfacial reactions 227
Stokes' law 135
Strand surface temperature measurement 406–8, *407*
Strip casting processes 412–16, *413–16*
Sublattice models 93–100
  applications 100
Submerged entry nozzle (SEN) 144, *144*
Submerged gas injection through single porous plug *142*
Sulfate capacities in slags and glasses 110–12
Sulfide capacities 50, 51, *59*, *61*
  in slags and glasses 110–12
Sulfur
  behavior in iron smelting 354–6, *356*
  content in hot metal *341*
  content of oxide melts *58*
  equilibrium in hot metal *340*
  in slags 57–60
  oxidation 371–2
  transfer 339–40
Surface activity coefficient 185
Surface components 126
Surface concentration 185
Surface constitution
  liquid alloys 187–94
  liquid slags 195–8
Surface reactivity vs. sintering temperature *235*
Surface tension 188, *189*, *190*, 193, *194*, *195*, 197, *197*, 198
Szyszkowski equation 201

Technology transfer 257
TEKPLOT 267
Ternary alloys, coadsorption 192–4
Ternary phase diagrams, calculation/estimation 92–3
THERMO–CALC 160, 266
Thermodynamics
  metallic solutions **5–44**
  slags **45–86**
Thin slab casting, solidification rate in 409–11, *410*, *411*
Three-dimensional flows 126, *127*, 137, 142
Three-dimensional velocity field 144, *144*
Ti–Al phase diagram 34–5, *34*
Tin in slags 78, *80*
Titanium in slags 78, *79*
Toop model *92*, 93
Tramp elements in slags **78–82**
Transition metals in slags **70–8**
Transport equations 132
Turbulence 129–31
  differential models for bulk convecting flows 131–3
  energy dissipation 132
  energy transport 132

  kinetic energy 132
  large eddy simulation model 133
Twin roll caster 144, *144*
Two-sublattice model for liquids, short-range ordering 106

Undercooled melts, solidification into 162–8

Vanadium in slags 75–8
Viscous creeping flow 135
Voidage effect on pressure drop in packed bed 321, *321*
Volatile matter (VM) 353
Volume element 173, *173*, 265

Water vapor, in slags 64–5
Weber number 261
Wustite 311–14
  particle reduction 242–4, *244*